NONLINEAR POSE CONTROL AND ESTIMATION FOR SPACE PROXIMITY OPERATIONS: AN APPROACH BASED ON DUAL QUATERNIONS

A Dissertation
Presented to
The Academic Faculty

by

Nuno Filipe

In Partial Fulfillment
of the Requirements for the Degree
Doctor of Philosophy in the
Daniel Guggenheim School of Aerospace Engineering

Georgia Institute of Technology
December 2014

NONLINEAR POSE CONTROL AND ESTIMATION FOR SPACE PROXIMITY OPERATIONS: AN APPROACH BASED ON DUAL QUATERNIONS

Approved by:

Professor Panagiotis Tsiotras, Advisor
Committee Chair
Daniel Guggenheim School of
Aerospace Engineering
Georgia Institute of Technology

Professor Ryan P. Russell
Department of Aerospace Engineering
and Engineering Mechanics
The University of Texas at Austin

Professor Robert D. Braun
Daniel Guggenheim School of
Aerospace Engineering
Georgia Institute of Technology

Dr. Morgan Baldwin
Space Vehicles Directorate
U.S. Air Force Research Laboratory

Professor Marcus Holzinger
Daniel Guggenheim School of
Aerospace Engineering
Georgia Institute of Technology

Date Approved: 17 November 2014

To my grandfather.

ACKNOWLEDGEMENTS

I would like to express my sincere gratitude to my advisor, Prof. Panagiotis Tsiotras. First of all, for accepting me in his group when I first arrived at Georgia Tech and for his continuous guidance and support since then. His responsiveness and brilliance are unparalleled and have been and will continue to be an inspiration to me. He has taught me to set high goals in research and in life and to not be afraid of the unknown.

I would also like to express my gratitude to the members of my advisory committee, Prof. Robert D. Braun, Prof. Marcus Holzinger, Prof. Ryan P. Russell, and Dr. Morgan Baldwin, for their insightful comments that helped improve the quality of this dissertation. I am also very grateful to Prof. Mark Costello, for his absolutely outstanding advanced dynamics class.

I am in debt to the International Fulbright Science and Technology Award and to the Air Force Research Laboratory for their financial support, without which this dissertation would have not been possible.

I would like to thank all the members of the Dynamics and Control Systems Laboratory their friendship and help. In particular, I will never forget the joys and sorrows that I shared with Dr. Michail Kontitsis and Guangcong Zhang while working on the platform. I am also grateful to Alfredo Valverde for his help with some of the simulations presented in this dissertation. Finally, I would like to thank Oktay Arslan, one of the best persons I have ever met, for his friendship throughout the years.

Last but definitely not the least, I would like thank my beautiful and brilliant girlfriend and best friend Niki for her unconditional love, support, and patience. Without her, I would have lost my sanity and happiness a long time ago. All the

accomplishments of this dissertation are meaningless compared to winning her heart.

Claro está, esta secção não estaria completa sem um agradecimento enorme aos meus amigos Paulo, Fred e Tatiana que através do Skype me ajudaram a sentir mais perto de casa. O seu apoio e amizade foi fundamental, especialmente durante os meus primeiros meses nos Estados Unidos.

Finalmente, quero agradecer o apoio e amor incondicionais da minha mãe e do meu pai. Devo-lhes tudo. Esteja onde estiver, sempre os amarei. Por último, quero agradecer à minha avó e muito especialmente ao meu avô, a quem dedico esta tese.

TABLE OF CONTENTS

LIST OF TABLES

LIST OF FIGURES

LIST OF SYMBOLS AND ACRONYMS

OPERATORS

$\circ$	Dual quaternion circle product.
$\star$	Multiplication of a 8-by-8 matrix with a dual quaternion.
$*$	Multiplication of a 4-by-4 matrix with a quaternion.

SUBSCRIPTS

$_0$	Scalar part of quaternion.
$_c$	Control signal.
$_{c_i}$	Gimbal and wheel of VSCMG i.
$_d$	Dual part of dual quaternion or effect due to disturbance, depending on the context.
$_{\nabla g}$	Effect due to gravity-gradient.
$_f$	Bus of the upper stage of the 5-DOF platform (does not include the gimbals and wheels of the VSCMGs).
$_g$	Effect due to gravity or to the ground/epoxy floor of the ASTROS facility, depending on the context.
$_{g_i}$	Gimbal of VSCMG i, without the wheel.
$_{J_2}$	Effect due to Earth's oblateness.
$_l$	Lower stage of the 5-DOF platform.
$_m$	Measurement.
$_r$	Real part of dual quaternion.
$_s$	Upper stage of the 5-DOF platform, including the gimbals and wheels of the VSCMGs.
$_{T_i}$	Effect due to thruster i.
$_{w_i}$	Wheel of VSCMG i.

SUPERSCRIPTS

$^-$	Value before measurement.
$^+$	Value after measurement.

ACCENTS

$\hat{}$	Mean/estimated value.

SYMBOLS

$\bar{0}$	$\bar{0} = [0, 0, 0]^{\intercal}$.
$\mathbf{0}$	$\mathbf{0} = \mathsf{0} + \epsilon\mathsf{0}$.
$0_{m\times n}$	m-by-n matrix of zeros.
$\mathsf{0}$	$\mathsf{0} = (0, \bar{0})$.
$\mathbf{1}$	$\mathbf{1} = \mathsf{1} + \epsilon\mathsf{0}$.
$1_{m\times n}$	m-by-n matrix of ones.
$\mathsf{1}$	$\mathsf{1} = (1, \bar{0})$.
$\bar{a}^{\mathrm{X}}_{\mathrm{Y/Z}}$	Linear acceleration vector of point Y (if Y is a point) or of the origin of the Y-frame (if Y is a frame) with respect to the Z-frame expressed in the X-frame.
$a^{\mathrm{X}}_{\mathrm{Y/Z}}$	$a^{\mathrm{X}}_{\mathrm{Y/Z}} = (0, \bar{a}^{\mathrm{X}}_{\mathrm{Y/Z}})$.
A_g	$A_g = [\bar{I}^{\mathrm{S}}_{\mathrm{G}_1}, \bar{I}^{\mathrm{S}}_{\mathrm{G}_2}, \bar{I}^{\mathrm{S}}_{\mathrm{G}_3}, \bar{I}^{\mathrm{S}}_{\mathrm{G}_4}]$.
$\boldsymbol{a}^{\mathrm{X}}_{g}$	$\boldsymbol{a}^{\mathrm{X}}_{g} = a^{\mathrm{X}}_{g} + \epsilon\mathsf{0}$.
$\boldsymbol{a}^{\mathrm{X}}_{J_2}$	$\boldsymbol{a}^{\mathrm{X}}_{J_2} = a^{\mathrm{X}}_{J_2} + \epsilon\mathsf{0}$.
$\bar{\alpha}^{\mathrm{X}}_{\mathrm{Y/Z}}$	Angular acceleration vector of the Y-frame with respect to the Z-frame expressed in the X-frame.
$\alpha^{\mathrm{X}}_{\mathrm{Y/Z}}$	$\alpha^{\mathrm{X}}_{\mathrm{Y/Z}} = (0, \bar{\alpha}^{\mathrm{X}}_{\mathrm{Y/Z}})$.
$A_s(\gamma)$	$A_s(\gamma) = [\bar{J}^{\mathrm{S}}_{\mathrm{G}_1}(\gamma_1), \bar{J}^{\mathrm{S}}_{\mathrm{G}_2}(\gamma_2), \bar{J}^{\mathrm{S}}_{\mathrm{G}_3}(\gamma_3), \bar{J}^{\mathrm{S}}_{\mathrm{G}_4}(\gamma_4)]$.
$A_t(\gamma)$	$A_t(\gamma) = [\bar{K}^{\mathrm{S}}_{\mathrm{G}_1}(\gamma_1),\ \bar{K}^{\mathrm{S}}_{\mathrm{G}_2}(\gamma_2),\ \bar{K}^{\mathrm{S}}_{\mathrm{G}_3}(\gamma_3),\ \bar{K}^{\mathrm{S}}_{\mathrm{G}_4}(\gamma_4)]$.
$\boldsymbol{b_\omega}$	Dual bias: $\boldsymbol{b_\omega} = b_\omega + \epsilon b_v$.
b_n	$b_n = (0, \overline{b}_n)$.
$\overline{b}_n$	Bias of the non-dimensional specific force measurement.
b_ω	$b_\omega = (0, \overline{b}_\omega)$.
$\overline{b}_\omega$	Bias of the angular velocity measurement.
b_v	$b_v = (0, \overline{b}_v)$.

$\overline{b}_v$	Bias of the linear velocity measurement.
c	Scaling constant defined in the user manual of the IMU: $c = 9.8$ m/s^2.
$\textcircled{\bullet}_*$	Center of mass of $*$.
CR	Center of rotation of the 5-DOF platform.
$\Delta \boldsymbol{f}_d^{\mathrm{B}}$	Estimation error of $\boldsymbol{f}_d^{\mathrm{B}}$.
ΔM^{B}	Estimation error of M^{B}.
$\delta q_{\mathrm{B/I}}$	Unit error quaternion: $\delta q_{\mathrm{B/I}} = \hat{q}^*_{\mathrm{B/I}} q_{\mathrm{B/I}}$.
$\delta \boldsymbol{q}_{\mathrm{B/I}}$	Unit dual error quaternion: $\delta \boldsymbol{q}_{\mathrm{B/I}} = \hat{\boldsymbol{q}}^*_{\mathrm{B/I}} \boldsymbol{q}_{\mathrm{B/I}}$.
$\Delta^\star$	Optimal Kalman state update.
ΔV	Change in velocity associated with an orbital maneuver.
ϵ	Dual unit.
η_n	$\eta_n = (0, \overline{\eta}_n)$.
$\overline{\eta}_n$	Noise of the non-dimensional specific force measurement assumed to be a Gaussian white-noise process.
η_ω	$\eta_\omega = (0, \overline{\eta}_\omega)$.
$\overline{\eta}_\omega$	Noise of the angular velocity measurement assumed to be a Gaussian white-noise process.
$\boldsymbol{\eta_\omega}$	Dual noise: $\boldsymbol{\eta_\omega} = \eta_\omega + \epsilon \eta_v$.
η_v	$\eta_v = (0, \overline{\eta}_v)$.
$\overline{\eta}_v$	Noise of the linear velocity measurement assumed to be a Gaussian white-noise process.
$\bar{f}^{\mathrm{X}}$	Force vector expressed in the X-frame.
$\bar{f}_{c,*/\#}$	Contact force vector acting on $*$ due to $\#$.
$\boldsymbol{f}^{\mathrm{X}}_{\nabla g}$	$\boldsymbol{f}^{\mathrm{X}}_{\nabla g} = 0 + \epsilon \tau^{\mathrm{X}}_{\nabla g}$.
f^{X}	$f^{\mathrm{X}} = (0, \bar{f}^{\mathrm{X}})$.
γ	$\gamma = [\gamma_1, \gamma_2, \gamma_3, \gamma_4]^\intercal$.
γ_i	Gimbal angle of VSCMG i.
$\mathbb{H}$	Set of quaternions.

${}^{P}\bar{H}_{*/\mathrm{Z}}$	Angular momentum vector of $*$ with respect to the Z-frame about point P.
$\mathbb{H}_d$	Set of dual quaternions.
$\mathbb{H}_d^r$	Set of dual scalar quaternions with zero dual part.
$\mathbb{H}_d^s$	Set of dual scalar quaternions.
$\mathbb{H}_d^u$	Set of unit dual quaternions.
${}^{P}\boldsymbol{H}^{\mathrm{X}}_{*/\mathrm{Z}}$	Dual momentum of $*$ with respect to the Z-frame about point P expressed in the X-frame.
$\mathbb{H}_d^v$	Set of dual vector quaternions.
$\mathbb{H}^s$	Set of scalar quaternions.
$\mathbb{H}^u$	Set of unit quaternions.
$\mathbb{H}^v$	Set of vector quaternions.
I^{B}	$I^{\mathrm{B}} = \begin{bmatrix} 1 & 0_{1\times 3} \\ 0_{3\times 1} & \bar{I}^{\mathrm{B}} \end{bmatrix}$.
$\bar{I}_{\mathrm{Y}}$	First axis of the Y-frame.
I_{cg}	$I_{cg} = \mathrm{diag}([{}^{\bullet_{c_1}}I^{\mathrm{G}1}_{c_1,11}, {}^{\bullet_{c_2}}I^{\mathrm{G}2}_{c_2,11}, {}^{\bullet_{c_3}}I^{\mathrm{G}3}_{c_3,11}, {}^{\bullet_{c_4}}I^{\mathrm{G}4}_{c_4,11}])$.
I_{cs}	$I_{cs} = \mathrm{diag}([{}^{\bullet_{c_1}}I^{\mathrm{G}1}_{c_1,22}, {}^{\bullet_{c_2}}I^{\mathrm{G}2}_{c_2,22}, {}^{\bullet_{c_3}}I^{\mathrm{G}3}_{c_3,22}, {}^{\bullet_{c_4}}I^{\mathrm{G}4}_{c_4,22}])$.
I_{ct}	$I_{ct} = \mathrm{diag}([{}^{\bullet_{c_1}}I^{\mathrm{G}1}_{c_1,33}, {}^{\bullet_{c_2}}I^{\mathrm{G}2}_{c_2,33}, {}^{\bullet_{c_3}}I^{\mathrm{G}3}_{c_3,33}, {}^{\bullet_{c_4}}I^{\mathrm{G}4}_{c_4,33}])$.
${}^{P}\bar{I}^{\mathrm{X}}_{*}$	Mass moment of inertia of $*$ about point P expressed in the X-frame.
$I_{n\times n}$	n-by-n identity matrix.
I_{ws}	$I_{ws} = \mathrm{diag}([{}^{\bullet_{c_1}}I^{\mathrm{G}1}_{w_1,22}, {}^{\bullet_{c_2}}I^{\mathrm{G}2}_{w_2,22}, {}^{\bullet_{c_3}}I^{\mathrm{G}3}_{w_3,22}, {}^{\bullet_{c_4}}I^{\mathrm{G}4}_{w_4,22}])$.
J_2	$J_2 = 0.0010826267$.
$\bar{J}_{\mathrm{Y}}$	Second axis of the Y-frame.
$\bar{K}_{\mathrm{Y}}$	Third axis of the Y-frame.
M^{X}	Dual inertia matrix about the center of mass expressed in the X-frame.
m	Mass.
$\boldsymbol{M}^{\mathrm{X}}$	Dual inertia operator about the center of mass expressed in the X-frame.
μ	Earth's gravitational parameter: $\mu = 398600.4418$ km^3/s^2.

$n^{\mathrm{B}}_{\mathrm{A/I}}$	$n^{\mathrm{B}}_{\mathrm{A/I}} = (0, \overline{n}^{\mathrm{B}}_{\mathrm{A/I}})$.
$\overline{n}^{\mathrm{B}}_{\mathrm{A/I}}$	Non-dimensional specific force at the location of the accelerometer with respect to the inertial frame expressed in the body frame.
ν_m	Innovation/residual of EKF with m dimensions.
Ω	$\Omega = [\Omega_1, \Omega_2, \Omega_3, \Omega_4]^{\intercal}$.
$\bar{\omega}^{\mathrm{X}}_{\mathrm{Y/Z}}$	Angular velocity vector of the Y-frame with respect to the Z-frame expressed in the X-frame.
Ω_i	Angular speed of the wheel of VSCMG i.
$\omega^{\mathrm{X}}_{\mathrm{Y/Z}}$	$\omega^{\mathrm{X}}_{\mathrm{Y/Z}} = (0, \bar{\omega}^{\mathrm{X}}_{\mathrm{Y/Z}})$.
$\boldsymbol{\omega}^{\mathrm{X}}_{\mathrm{Y/Z}}$	Dual velocity of the Y-frame with respect to the Z-frame expressed in the X-frame.
$\phi_{\mathrm{Y/Z}}$	Roll angle of the Euler angles in aerospace sequence that represent the orientation of the Y-frame with respect to the Z-frame.
$\psi_{\mathrm{Y/Z}}$	Yaw angle of the Euler angles in aerospace sequence that represent the orientation of the Y-frame with respect to the Z-frame.
$p^{\mathrm{X}}_{\mathrm{Y/Z}}$	First coordinate of $\bar{\omega}^{\mathrm{X}}_{\mathrm{Y/Z}}$.
$\boldsymbol{q}_{\mathrm{Y/Z}}$	Unit dual quaternion that represents the pose of the Y-frame with respect to the Z-frame.
$q_{\mathrm{Y/Z}}$	Unit quaternion that represents the orientation of the Y-frame with respect to the Z-frame.
$q^{\mathrm{X}}_{\mathrm{Y/Z}}$	Second coordinate of $\bar{\omega}^{\mathrm{X}}_{\mathrm{Y/Z}}$.
$\bar{r}^{\mathrm{X}}_{\mathrm{Y/Z}}$	Translation vector from point Z (if Z is a point) or from the origin of the Z-frame (if Z is a frame) to point Y (if Y is a point) or to the origin of the Y-frame (if Y is a frame) expressed in the X-frame.
R_e	Earth's mean equatorial radius: $R_e = 6378.137$ km.
$\mathbb{R}^{m \times n}$	Set of m-by-n matrices.
$\mathbb{R}^n$	Set of n-dimensional column vectors.
$R^{\mathrm{X} \leftarrow \mathrm{Y}}$	Rotation matrix in 3-dimensional space that transforms the coordinates of a vector for the Y-frame to the X-frame.
$r^{\mathrm{X}}_{\mathrm{Y/Z}}$	$r^{\mathrm{X}}_{\mathrm{Y/Z}} = (0, \bar{r}^{\mathrm{X}}_{\mathrm{Y/Z}})$ or third coordinate of $\bar{\omega}^{\mathrm{X}}_{\mathrm{Y/Z}}$, depending on the context.
$\boldsymbol{r}^{\mathrm{X}}_{\mathrm{Y/Z}}$	$\boldsymbol{r}^{\mathrm{X}}_{\mathrm{Y/Z}} = r^{\mathrm{X}}_{\mathrm{Y/Z}} + \epsilon 0$.

SO(3)	Special orthogonal group of all rotations about the origin of three-dimensional Euclidean space.
T	$T = [T_1, T_2, ..., T_{12}]^\intercal$.
${}^P\bar{\tau}^{\mathrm{X}}$	Moment vector about point P expressed in the X-frame.
${}^P\bar{\tau}_{c,*/\#}$	Contact moment vector acting on $*$ due to $\#$ about point P.
${}^P\tau^{\mathrm{X}}$	${}^P\tau^{\mathrm{X}} = (0, {}^P\bar{\tau}^{\mathrm{X}})$.
$\theta_{\mathrm{Y/Z}}$	Pitch angle of the Euler angles in aerospace sequence that represent the orientation of the Y-frame with respect to the Z-frame.
T_i	One of the coordinates of $\bar{f}^{\mathrm{S}}_{T_i}$ (see Section 6.4.2).
$T_{i,\max}$	Maximum thrust of thruster i measured experimentally.
$T_{i,\max,\mathrm{LP}}$	Upper bound on T_i defined by the user and enforced as an inequality constraint on the LP problem.
$T_{i,off}$	Lower threshold of the hysteresis loop of the Schmitt trigger on T_i.
$T_{i,on}$	Upper threshold of the hysteresis loop of the Schmitt trigger on T_i.
$u^{\mathrm{X}}_{\mathrm{Y/Z}}$	First component of $\bar{v}^{\mathrm{X}}_{\mathrm{Y/Z}}$.
$\bar{v}^{\mathrm{X}}_{\mathrm{Y/Z}}$	Linear velocity vector of point Y (if Y is a point) or of the origin of the Y-frame (if Y is a frame) with respect to the Z-frame expressed in the X-frame.
$\mathrm{v}(M^{\mathrm{B}})$	Vectorized version of M^{B}: $\mathrm{v}(M^{\mathrm{B}}) = [I_{11}\ I_{12}\ I_{13}\ I_{22}\ I_{23}\ I_{33}\ m]^\intercal$.
v_m	Measurement noise of EKF with m dimensions.
$v^{\mathrm{X}}_{\mathrm{Y/Z}}$	$v^{\mathrm{X}}_{\mathrm{Y/Z}} = (0, \bar{v}^{\mathrm{X}}_{\mathrm{Y/Z}})$ or second component of $\bar{v}^{\mathrm{X}}_{\mathrm{Y/Z}}$, depending on the context.
w_p	Process noise of EKF with p dimensions.
$w^{\mathrm{X}}_{\mathrm{Y/Z}}$	Third component of $\bar{v}^{\mathrm{X}}_{\mathrm{Y/Z}}$.
x_n	State of EKF with n dimensions.
$x^{\mathrm{X}}_{\mathrm{Y/Z}}$	First coordinate of $\bar{r}^{\mathrm{X}}_{\mathrm{Y/Z}}$.
$y^{\mathrm{X}}_{\mathrm{Y/Z}}$	Second coordinate of $\bar{r}^{\mathrm{X}}_{\mathrm{Y/Z}}$.
$z^{\mathrm{X}}_{\mathrm{Y/Z}}$	Third coordinate of $\bar{r}^{\mathrm{X}}_{\mathrm{Y/Z}}$.

ACRONYMS

ARRM	Asteroid Redirect Robotic Mission.

ASTROS	Autonomous Spacecraft Testing of Robotic Operations in Space.
AWGN	Additive White Gaussian Noise.
CMG	Control Moment Gyro.
CW	Clohessy-Wiltshire.
DART	Demonstration of Autonomous Rendezvous Technology.
DQ-MEKF	Dual Quaternion Multiplicative Extended Kalman Filter.
ECI	Earth-Centered-Inertial.
EKF	Extended Kalman Filter.
FREND	Front-end Robotics Enabling Near-term Demonstration.
GEO	Geosynchronous Earth Orbit.
GLPK	GNU Linear Programming Kit.
GNC	Guidance, Navigation, and Control.
GSSAP	Geosynchronous Space Situational Awareness Program.
KYP	Kalman-Yakubovich-Popov.
LIIVe	Low-design Impact Inspection Vehicle.
LP	Linear Programming.
LQ	Linear Quadratic.
LQG	Linear Quadratic Gaussian.
LTI	Linear Time-Invariant.
LTV	Linear Time-Varying.
MEV	Mission Extension Vehicle.
MPC	Model Predictive Control.
NASA	National Aeronautics and Space Administration.
NRL	Naval Research Laboratory.
PWM	Pulse-Width-Modulator.
Q-MEKF	Quaternion Multiplicative Extended Kalman Filter.
QP	Quadratic Programming.

QV-AEKF	Quaternion-Vector Additive Extended Kalman Filter.
RAAN	Right Ascension of the Ascending Node.
RW	Reaction Wheel.
SIS	Space Infrastructure Servicing.
SQV-AEKF	Split Quaternion-Vector Additive Extended Kalman Filter.
SUMO	Spacecraft for the Universal Modification of Orbits.
TH	Tschauner-Hempel.
USAF	United States Air Force.
VSCMG	Variable-Speed Control Moment Gyro.
ZOH	Zero-Order-Hold.

SUMMARY

The term proximity operations has been widely used in recent years to describe a wide range of space missions that require a spacecraft to remain close to another space object. Such missions include, for example, the inspection, health monitoring, surveillance, servicing, and refueling of a space asset by another spacecraft. One of the biggest challenges in autonomous space proximity operations, either cooperative or uncooperative, is the need to autonomously and accurately track time-varying relative position and attitude references, i.e., pose references, with respect to a moving target, in order to avoid on-orbit collisions and achieve the overall mission goals. In addition, if the target spacecraft is uncooperative, the Guidance, Navigation, and Control (GNC) system of the chaser spacecraft must not rely on any help from the target spacecraft. In this case, vision-based sensors, such as cameras, are typically used to measure the relative pose between the spacecraft. Although vision-based sensors have several attractive properties, they introduce new challenges, such as no direct linear and angular velocity measurements, slow update rates, and high measurement noise.

This dissertation investigates the problem of autonomously controlling and estimating the pose of a chaser spacecraft with respect to a moving target spacecraft, possibly uncooperative. Since this problem is inherently hard, the standard approach in the literature is to split the attitude-tracking problem from the position-tracking problem. Whereas the attitude-tracking problem is relatively simple, since the rotational motion is independent from the translational motion, the position-tracking problem is more complicated, as the translational motion depends on the rotational

motion. Hence, whereas strong theoretical results exist for the attitude problem, the position problem typically requires additional assumptions. An alternative, more general approach to the pose control and estimation problems is to consider the fully coupled 6-DOF motion. However, fewer results exist that directly address this higher dimensional problem.

The main contribution of this dissertation is to show that dual quaternions can be used to extend the theoretical results that exist for the attitude motion into analogous results for the combined position and attitude motion. Moreover, this dissertation shows that this can be accomplished by (almost) just replacing quaternions by dual quaternions in the original derivations. This is because dual quaternions are built on and are an extension of classical quaternions. Dual quaternions provide a compact representation of the pose of a frame with respect to another frame.

Using this approach, three new results are presented in this dissertation. First, a pose-tracking controller that does not require relative linear and angular velocity measurements is derived with vision-based sensors in mind. Compared to existing literature, the proposed velocity-free pose-tracking controller guarantees that the pose of the chaser spacecraft will converge to the desired pose independently of the initial state, even if the reference motion is not sufficiently exciting. In addition, the convergence region does not depend on the gains of the controller.

Second, a Dual Quaternion Multiplicative Extended Kalman Filter (DQ-MEKF) is developed from the highly successful Quaternion MEKF (Q-MEKF) as an alternative way to achieve pose-tracking without velocity measurements. Existing dual quaternion EKFs are additive, not multiplicative, and have two additional states. The DQ-MEKF is experimentally validated and compared with two conventional EKFs on the 5-DOF platform of the Autonomous Spacecraft Testing of Robotic Operations in Space (ASTROS) facility at the School of Aerospace Engineering at Georgia Tech.

Finally, the velocity-free pose-tracking controller is compared qualitatively and quantitatively to a pose-tracking controller that uses the velocity estimates produced by the DQ-MEKF through a realistic proximity operations simulation.

Third, a pose-tracking controller that does not require the mass and inertia matrix of the chaser satellite is suggested. This inertia-free controller takes into account the gravitational acceleration, the gravity-gradient torque, the perturbing acceleration due to Earth's oblateness, and constant – but otherwise unknown – disturbance forces and torques. Sufficient conditions on the reference pose are also given that guarantee the identification of the mass and inertia matrix of the satellite. Compared to the existing literature, this controller has only as many states as unknown elements and it does not require a priori known upper bounds on any states or parameters.

Finally, the inertia-free pose-tracking controller and the DQ-MEKF are tested on a high-fidelity simulation of the 5-DOF platform of the ASTROS facility and also experimentally validated on the actual platform. The equations of motion of the 5-DOF platform, on which the high-fidelity simulation is based, are derived for three distinct cases: a 3-DOF case, a 5-DOF case, and a (2+1)-DOF case. Four real-time experiments were run on the platform. In the first, a sinusoidal reference attitude with respect to the inertial frame is tracked using VSCMGs. In the second, a constant reference attitude is maintained with respect to a target object using VSCMGs and measurements from a camera. In the third, the same sinusoidal reference attitude with respect to the inertial frame tracked in the first experiment is now tracked using cold-gas thrusters. Finally, in the fourth and last experiment, a time-varying 5-DOF reference pose with respect to the inertial frame is tracked using cold-gas thrusters.

CHAPTER I

INTRODUCTION

Although the term *proximity operations* has been widely used in recent years to describe a wide range of missions in space, it is hard to find a proper definition for it. The *Dictionary of Militarily Terms and Acronyms* by the *U.S. Department of Defense* [90] defines proximity operations as:

In space operations, on-orbit activities of a resident space object that deliberately and necessarily maintains a close distance from another space object for a specific purpose. Two objects in space that pass each other by natural orbital mechanics (e.g., routine orbital conjunctions or close approaches) or Department of Defense space systems which are designated to utilize cluster or formation flight to maintain required proximity to provide required system functionality do not fall within this definition.

Under this definition, proximity operations in space include, for example, the inspection, health monitoring, surveillance, servicing, and refueling of a spacecraft by another spacecraft in orbit [93, 51, 52, 73]. Depending on the author, the former may be called the *chief*, *leader*, or *target* spacecraft, whereas the latter may be called the *deputy*, *follower*, or *chaser* spacecraft. In this dissertation, they are called the target and chaser spacecraft, respectively.

Proximity operations in space can be classified as *autonomous* or *non-autonomous* and *cooperative* or *non-cooperative*. Even today, most proximity operations in space are non-autonomous and cooperative. In other words, they require a human in the loop and some kind of cooperation between the two spacecraft.

1.1 Proximity Operation Missions

A well known example of non-autonomous cooperative proximity operations in space is the docking of the Space Shuttle with the *International Space Station* (ISS). In this operation, all docking maneuvers up to the last one were controlled from the ground, whereas the last arc, up to contact, was manually controlled by the pilot using a black and white pattern on the ISS [26].

A more sophisticated approach to dock with the ISS is used by the European *Automated Transfer Vehicle* (ATV). Whereas the ATV docks autonomously (no humans in the loop) with the ISS, it requires cooperation between the two vehicles. First, it requires both vehicles to share their *Global Positioning System* (GPS) measurements in order to implement *Relative GPS* (RGPS). Second, the ATV relies on an optical sensor and on a known optical pattern on the ISS to estimate relative range, *Line-Of-Sight* (LOS) direction, and attitude [26, 89]. Other vehicles that have used autonomous cooperative systems include the Russian Soyuz and Progress spacecraft, which use the Kurs relative navigation system. The Kurs system is based on an S-band radio transponder (transmitter-responder) that measures relative range, range-rate, pitch, and yaw [89]. The Orbital Express mission by the *Defense Advanced Research Projects Agency* (DARPA) also performed autonomous cooperative docking by using retro-reflective visual markers on a target satellite to estimate the full 6-*Degree-Of-Freedom* (DOF) relative state [46]. A similar approach has been used by the *Centre National d'Études Spatiales* (CNES) in their Prisma mission, where *Light-Emitting-Diode* (LED) patterns on a target satellite were used to perform autonomous rendezvous from 10 km to 50 m [23]. The *Synchronized Position Hold Engage Reorient Experimental Satellites* (SPHERES) from the *Massachusetts Institute of Technology* (MIT) are yet another example of an autonomous cooperative system. The three SPHERES micro-satellites have been operating inside the crew volume of the ISS since 2006. In 2012, they were upgraded with a vision-based

navigation system. The target micro-satellite has a set of textured stickers applied to it to increase its visual texture. However, this visual pattern is not preprogrammed into the chaser's memory [89, 88]. Finally, the *Engineering Test Satellite #7* (ETS-VII) launched in 1997 by the *National Space Development Agency of Japan* (NASDA) successfully performed autonomous cooperative rendezvous and docking between two satellites using RGPS (beyond 500 m from the target), a laser radar (between 2 m and 520 m), and a CCD camera (within 2 m) [72, 49].

The more challenging problem of uncooperative autonomous proximity operations has been tackled by at least three missions. The first one, the *eXperimental Satellite System-11* (XSS-11) by the *Air Force Research Laboratory* (AFRL), demonstrated rendezvous and proximity operations with its expended rocket body [2]. The second one, the *Demonstration of Autonomous Rendezvous Technology* (DART) mission by the *National Aeronautics and Space Administration* (NASA), did not complete its mission. During proximity operations, the spacecraft began using more propellant than expected. When the craft detected that its propellant supply was depleting faster than expected, it began a series of maneuvers to departure from the target satellite and de-orbit. Although not known at the time, it made contact with target satellite and boosted its orbit by 1.2 nautical miles. The target satellite was not damaged [70]. The third one, the *Geosynchronous Space Situational Awareness Program* (GSSAP) by the *U.S. Air Force* (USAF) consists of two satellites launched in July 2014 designed to monitor and collect images of other satellites near the geosynchronous belt. According to the USAF, they have the capability to perform rendezvous and proximity operations.

Currently ongoing projects include SUMO/FREND (*Spacecraft for the Universal Modification of Orbits/Front-end Robotics Enabling Near-term Demonstration*), sponsored by DARPA and managed by the *Naval Research Laboratory* (NRL). The goal

of SUMO/FREND is to demonstrate the feasibility of autonomously servicing uncooperative satellites in *Geosynchronous Earth Orbit* (GEO) using robotic arms [71]. Another ongoing project is DARPA's Phoenix project, which envisions a servicing spacecraft that could remove components from a defunct satellite and transport them to another satellite [53]. Finally, NRL's *Low-design Impact Inspection Vehicle* (LIIVe) consists of a small and inexpensive spacecraft capable of autonomously inspecting a host vehicle. Operationally, LIIVe would be docked to its host and would be released in case of a deployment failure or another issue in orbit [45].

Although all the projects mentioned above are government-sponsored, proximity operations are also starting to get some traction in the private sector. A joint venture between ATK Space Systems and U.S. Space called ViviSat is currently offering a life extension service to satellites in GEO through their *Mission Extension Vehicle* (MEV). This vehicle is designed to rendezvous and dock with a customer's satellite. Once docked, it uses its own thrusters to provide orbit and attitude control to the client satellite. At the AIAA Space 2014 Conference and Exposition, ViviSat announced having procured its first paying customers. MDA has a competing design for the refueling of satellites in orbit called *Space Infrastructure Servicing* (SIS) vehicle. However, no clients are known at this time. Finally, Skycorp's CEO Dennis Wingo has recently announced that his company is currently working with NASA to send a servicing spacecraft to the ISS for testing.

1.2 Pose Control and Estimation in Space Proximity Operations

As demonstrated by past, ongoing, and future missions, the interest among the aerospace community for proximity operations is substantial, and so are its applications.

One of the biggest challenges in autonomous space proximity operations, either

cooperative or uncooperative, is the need to autonomously and accurately track time-varying relative position and attitude references with respect to a moving target, in order to avoid on-orbit collisions and achieve mission goals. In addition, if the target spacecraft is uncooperative, the *Guidance, Navigation, and Control* (GNC) system of the chaser spacecraft must not rely on any help from the target spacecraft, such as a priori known visual reference markers or other fiducials. In an extreme case, even the general shape of the target spacecraft might be unknown. In this case, vision-based sensors, such as cameras, are typically used to measure the relative position and attitude between the spacecraft. Although vision-based sensors have several attractive properties, e.g., small size, passive, low power requirements, and no moving parts, they also introduce new challenges, like no direct linear and angular velocity measurements, slow update rates, and high measurement noise.

This dissertation investigates the problem of autonomously controlling and estimating simultaneously the attitude and position of a chaser spacecraft with respect to a moving target spacecraft. From now on, the term *pose* will be used to designate both position and attitude.

1.3 Literature Review

Since the problem of controlling and estimating the attitude and position of a chaser spacecraft with respect to a moving target spacecraft is inherently hard, the standard approach in literature is to split the attitude problem from the position problem. This section reviews some interesting solutions to each problem and a few solutions that attempt to solve both problems simultaneously. This review does not intend to be comprehensive as the literature on these topics is vast.

1.3.1 Relative Attitude Control and Estimation

Let frame B and frame D be two moving frames defined with respect to the chaser and target spacecraft, respectively. Then, the angular acceleration of frame B with

respect to frame D is given by

$$\bar{\alpha}_{\mathrm{B/D}} = \bar{\alpha}_{\mathrm{B/I}} - \bar{\alpha}_{\mathrm{D/I}} - \bar{\omega}_{\mathrm{D/I}} \times \bar{\omega}_{\mathrm{B/I}}, \tag{1}$$

where $\bar{\omega}_{\mathrm{Y/Z}}$ is the angular velocity of frame Y with respect to frame Z, $\bar{\alpha}_{\mathrm{Y/Z}}$ is the angular acceleration of frame Y with respect to frame Z, and frame I is an inertial frame. According to this equation, the relative angular motion between the two spacecraft does not depend on the linear motion. Hence, the relative angular motion can be treated as uncoupled from the linear motion, which simplifies the problem substantially. Note that $\bar{\alpha}_{\mathrm{B/I}}$ might depend on the linear motion if one or more external torques acting on the chaser spacecraft dependent on the linear motion. One such external torque is the gravity-gradient torque. However, since this external torque is usually small, it is reasonable to assume that the relative angular motion is independent from the linear motion.

The literature on *nonlinear control* of the relative angular motion is substantial. Nonlinear control is the area of control engineering that deals directly with nonlinear systems, like Eq. (1). For example, in Ref. [100], three attitude-tracking controllers are given: one that does not require knowledge of the inertia matrix of the chaser satellite under some conditions on the desired attitude; one that does require knowledge of the inertia matrix of the chaser satellite but yields better transient response; and an adaptive controller with gains that dependent on bounds on the eigenvalues of the inertia matrix. In Ref. [1], another adaptive attitude-tracking controller is given that requires no knowledge about the inertia matrix of the chaser satellite and, under some conditions on the desired attitude, can even estimate it. Reference [79] proposes an adaptive attitude-tracking controller that eliminates the degradation of the closed-loop dynamics caused by the estimation of the inertia matrix and stops the estimation process if the true inertia matrix is found. However, the controller has 27 states, which may limit its applicability to small satellites with limited on-board computational resources. In Ref. [3], an attitude-tracking controller is given that, unlike the previous

controllers, only requires measurements of the relative attitude between the B-frame and the D-frame, in other words, it does not require measurements of $\bar{\omega}_{\mathrm{B/D}}$. However, the controller in Ref. [3] requires full knowledge of the inertia matrix of the chaser. An attitude-tracking controller that also does not require measurements of $\bar{\omega}_{\mathrm{B/D}}$ and only requires bounds on the eigenvalues of the inertia matrix is given in Ref. [20]. As far as the author knows, the controller in Ref. [20] is the only attitude-tracking controller that requires neither measurements of $\bar{\omega}_{\mathrm{B/D}}$ nor full knowledge of the inertia matrix.

In Ref. [67], an attitude-tracking controller is given that requires neither measurements of $\bar{\omega}_{\mathrm{B/D}}$ nor any information about the inertia matrix. However, this controller cannot guarantee that the relative attitude error between the B-frame and the D-frame will converge to zero.

1.3.2 Relative Position Control and Estimation

The linear acceleration of the B-frame with respect to the D-frame is given by

$$\bar{a}_{\mathrm{B/D}} = \bar{a}_{\mathrm{B/I}} - \bar{a}_{\mathrm{D/I}} - \bar{\alpha}_{\mathrm{D/I}} \times \bar{r}_{\mathrm{B/D}} - \bar{\omega}_{\mathrm{D/I}} \times (\bar{\omega}_{\mathrm{D/I}} \times \bar{r}_{\mathrm{B/D}}) - 2\bar{\omega}_{\mathrm{D/I}} \times \bar{v}_{\mathrm{B/D}}, \tag{2}$$

where $\bar{a}_{\mathrm{Y/Z}}$ is the linear acceleration of the origin of frame Y with respect to frame Z, $\bar{r}_{\mathrm{Y/Z}}$ is the position vector from the origin of frame Z to the origin of frame Y, and $\bar{v}_{\mathrm{Y/Z}}$ is the velocity of the origin of frame Y with respect to frame Z. This equation shows that the relative linear motion between the two spacecraft depends on the angular motion. Hence, unlike the relative angular motion, the relative linear motion cannot be treated as an uncoupled problem. The only way to treat it as an uncoupled problem is to assume that the angular motion is known.

This coupling between the linear and angular motions is studied in Ref. [66] in the context of a spacecraft orbiting a small celestial body. The trajectory of the rigid body is compared to that of a point mass having the same mass as the rigid body and the same initial states. The numerical results show that the trajectory of

the rigid body is substantially different from the trajectory of the point mass. It is concluded that the coupling between the linear an angular motions is indeed an important perturbation that needs to be accounted for during small body proximity operations.

By far, the most common assumption to decouple the relative linear motion from the angular motion is to assume that the target spacecraft is fixed to the *Hill frame* of a circular Earth orbit [26, 98]. If, in addition, Eq. (2) is linearized, then the resulting equations are the celebrated *Clohessy-Wiltshire* (CW) equations. The CW equations give the position of the chaser spacecraft with respect to the origin of the Hill frame. They are especially attractive because they form a *Linear Time-Invariant* (LTI) system. Hence, several well-known linear control techniques can be applied. Several assumptions limit however the usefulness of the CW equations:

1) The CW equations do not take into account that the target spacecraft might be rotating/tumbling with respect to the Hill frame and that the desired motion might be defined with respect to the rotating target spacecraft.

2) By assuming that the target spacecraft is in a circular orbit, the CW equations assume that the target's orbit has constant radius, constant orbital angular velocity, and zero orbital angular acceleration.

3) These equations do not take into account that the orbital plane of the target satellite might be rotating due to orbital perturbations such as Earth's oblateness.

4) Whereas Eq. (2) explicitly takes into account that the target satellite might activate its thrusters and momentum exchange devices through $\bar{\alpha}_{\mathrm{D/I}}$ and $\bar{a}_{\mathrm{D/I}}$, the CW equations do not.

5) Since the CW equations are a linearized version of Eq. (2), they are only valid close enough to the target spacecraft.

6) Finally, the CW equations do not take into account the fact that the two spacecraft may be affected differently by the same orbital perturbations. For example, if the target is larger than the chaser, atmospheric drag may affect the former more than the latter.

In Ref. [98], the CW equations are used to implement a relative position controller based on *Linear-Quadratic* (LQ) *Model Predictive Control* (MPC) with dynamically reconfigurable linear constraints. The MPC controller prescribes impulsive velocity changes and can handle 3D LOS cone constraints, exhaust-plume magnitude and direction constraints, in-track target overshoot constraints, thrust-vector alignment constraints, and contact speed constraints. An *Extended Kalman Filter* (EKF) is employed to estimate the relative linear and angular velocity. In Ref. [11], the same control framework is used to handle thrust magnitude constraints and a target tumbling with respect to the Hill frame with constant angular velocity perpendicular to the orbital plane. In Refs. [98] and [11], nonlinear constraints are linearized so that efficient and computationally affordable *Quadratic Programming* (QP) algorithms can be used. However, this MPC controller suffers from the same limitations of the CW equations. In particular, it cannot handle elliptical orbits. Moreover, the docking phase is treated as a stabilization problem, where the position and velocity of the docking port are the time-invariant reference. Hence, all the constraints must be taken into account in the design of the MPC controller. If, instead, the docking phase had been treated as a tracking problem, all the constraints could have been (at least softly) satisfied by properly designing a time-varying reference, thus, greatly simplifying the design of the controller.

An advancement with respect to the CW equations is to consider that the target spacecraft is in an elliptical orbit and nadir pointing. In this case, the linearization of Eq. (2) leads to the *Tschauner-Hempel* (TH) equations. A good description of

these equations and of their analytical solutions is given in Ref. [81]. The Tschauner-Hempel equations are no longer LTI, like the CW equations, but rather *Linear Time-Varying* (LTV). The TH equations are applied in Ref. [99] together with a *Linear Quadratic Gaussian* (LQG) controller to spacecraft rendezvous. Another feature of this controller is that the Riccati equations are integrated forward in time and not backwards. Moreover, the LQG controller does not require relative velocity measurements. However, if one looks again at the assumptions associated with the CW equations, this new formulation only removes assumption 2). Assumptions 1), 3), 4), 5), and 6) still hold. Moreover, this controller, like the controller in Ref. [98], is a stabilizing controller and, therefore, cannot handle time-varying references.

Similarly to Ref. [99], Ref. [51] considers that the target spacecraft is in an elliptical orbit and nadir pointing. However, instead of using the linearized TH equations, it uses the nonlinear version of these equations to develop five different nonlinear tracking controllers. The mass of the chaser spacecraft and all orbital disturbances are assumed to be known. Hence, Ref. [51] deals with assumptions 2) and 5), but not with assumptions 1), 3), 4), and 6).

1.3.3 Relative Pose Control and Estimation

A more general approach is to consider the fully nonlinear, coupled, angular and linear, relative equations of motion given by Eqs. (1) and (2). Obviously, this formulation does not require the angular motion to be known a priori as in Section 1.3.2. In fact, this formulation removes all the assumptions of the CW equations listed in Section 1.3.2.

Some interesting results based on these more general equations are given in this section. Additional references and details are given at the beginning of each chapter, when appropriate.

In Ref. [73], using the *vectrix formalism*, a nonlinear adaptive tracking controller is

designed that guarantees almost global asymptotic stability of the linear and angular tracking errors. As is usually done in the literature, the terminology *almost* global asymptotic stability is used in this dissertation to designate stability over an open and dense set. It has been shown that this is the best one can achieve with a continuous controller for the rotational motion, because the special group of rotation matrices SO(3) is a compact manifold [7]. This controller does not require the mass and inertia matrix of the chaser spacecraft to be known. However, it has 392 states, which substantially limits its applicability.

In Ref. [104], another nonlinear adaptive tracking controller is designed based on the vectrix formalism. In this case, the mass and inertia matrix of the chaser spacecraft need to be known, but no measurements of the linear and angular velocity between the spacecraft are required. However, this controller suffers from two problems. First, the attitude of the chaser cannot be more than 180 deg away from the desired attitude. Second, the region of convergence is dependent on the gains chosen by the user. In other words, an infinitely large region of convergence requires infinitely large gains.

In Ref. [52], the authors of Ref. [51] extend their relative position controllers to relative position and attitude controllers. They present three nonlinear controllers for 6-DOF space proximity operations: a passivity-based PD+ controller, a sliding surface controller, and an integrator backstepping controller. All controllers require velocity measurements and knowledge of the mass and inertia matrix of the chaser spacecraft. Moreover, like in Ref. [52], the authors use a relative translation model that assumes that the target satellite is in an elliptical elliptical orbit and nadir pointing. Hence, their controllers cannot handle tumbling targets. A similar translation model is used in Ref. [82], which presents a relative pose tracking controller that requires no linear and angular velocity measurements and no mass and inertia matrix information. However, this controller cannot guarantee that the relative pose error

will converge to zero, since this controller is based on Ref. [67].

In Ref. [61], it is shown that a locally asymptotically stable closed-loop system can be obtained by combining an almost globally asymptotically stable attitude-only tracking controller with a locally exponentially convergent angular velocity observer. Although the theory presented in Ref. [61] can in principle be extended to combined attitude and position control, only attitude control is demonstrated. Reference [10] only addresses the pose stabilization problem and is neither model-independent nor velocity-free.

Finally, in Ref. [93], an adaptive terminal sliding-mode pose tracking controller is proposed based on *dual quaternions* that does not require full knowledge of the mass and inertia matrix of the chaser spacecraft. This controller takes into account the gravitational acceleration, the gravity-gradient torque, constant – but otherwise unknown – disturbance forces and torques, but not the perturbing acceleration due to Earth's oblateness. Moreover, this controller requires a priori knowledge of upper bounds on the mass, on the maximum eigenvalue of the inertia matrix, on the constant but otherwise unknown disturbance forces and torques, on the desired relative linear and angular velocity between the spacecraft and their first derivative, on the linear and angular velocity of the chaser spacecraft with respect to the inertial frame, and on the position of the chaser spacecraft with respect to the inertial frame. In addition, the convergence region is not specified.

1.3.4 Summary

The different results applicable to space proximity operations described in Section 1.3 are summarized in Table 1.

[1]This controller cannot guarantee convergence of the attitude error to zero.
[2]This controller cannot guarantee convergence of the pose error to zero.
[3]The region of convergence is dependent on the gains chosen by the user.
[4]Although pose control might be possible, only attitude control is demonstrated.

Table 1: Summary of the literature review. Legend: Ref. - Reference; L/N - Linear or Nonlinear; PC - Position Control; AC - Attitude Control; MI - Model-Independent; VF - Velocity-Free; S/T - Stabilization or Tracking; TT - Tumbling Target.

Ref.	L/NL	PC	AC	MI	VF	S/T	TT
[100]	NL	no	yes	bounds required	no	T	yes
[1]	NL	no	yes	yes	no	T	yes
[79]	NL	no	yes	yes	no	T	yes
[3]	NL	no	yes	no	yes	T	yes
[20]	NL	no	yes	bounds required	yes	T	yes
[67]	NL	no	yes	yes[1]	yes	T	yes
[98]	L	yes	no	no	no (EKF used)	S	no
[11]	L	yes	no	no	no	S	partially
[99]	L	yes	no	no	yes	S	no
[51]	NL	yes	no	no	yes	T	no
[82]	NL	yes	yes	yes[2]	yes	T	yes
[73]	NL	yes	yes	yes (392 states)	no	T	yes
[104]	NL	yes	yes	no	yes[3]	T	yes
[52]	NL	yes	yes	no	no	T	no
[61]	NL	yes	yes	no	yes[4]	T	yes
[10]	NL	yes	yes	no	no	S	no
[93]	NL	yes	yes	bounds required	no	T	yes

1.4 Dual Quaternions

As stated in Section 1.2, this dissertation investigates the problem of controlling and estimating simultaneously the attitude and position of a chaser spacecraft with respect to a moving target spacecraft. As shown in Section 1.3, this problem can be tackled in two ways: as two separate 3-DOF problems or as one 6-DOF problem. The biggest disadvantage of tackling this problem as two separate 3-DOF problems is that the linear motion is not independent from the angular motion. Hence, the only way to treat the linear motion by itself is to assume that the angular motion is known. Since the target spacecraft might be uncooperative, the angular motion may not be

known. Hence, this dissertation focuses on the combined 6-DOF problem.

One of the conclusions that can be taken from Table 1 is that the 6-DOF problem is harder than each individual 3-DOF problem. For example, all the pose controllers listed in Table 1 require at least partial knowledge of the mass and inertia matrix of the chaser spacecraft. The only exception is Ref. [73], which has 392 states. However, the attitude-only controller presented in Ref. [1] does not require knowledge about the inertia matrix of the chaser spacecraft and has only 6 states. Moreover, all the pose controllers listed in Table 1 require relative linear and angular velocity measurements. The only exception is Ref. [104], whose region of convergence depends on the gains chosen by the user. However, the attitude-only controller presented in Ref. [3] does not require relative angular velocity measurements and its region of convergence does not depend on the selected gains. Hence, instead of tackling the 6-DOF problem head on, this dissertation proposes taking advantage of these existing attitude-only results. By using *dual quaternions*, this dissertation shows how these and other attitude-only results can be extended into combined position and attitude results.

Dual quaternions were first introduced by Clifford in 1873 [17]. They provide a compact representation of the attitude and position of a frame with respect to another frame. They are built on and are an extension of classical quaternions. Dual quaternions are closely related to *Chasles Theorem*, which states that the general displacement of a rigid body can be represented by a rotation about an axis (called the *screw axis*) and a translation along that axis, creating a screw-like motion [105, 69]. Compared to other representations of this screw-like motion, such as dual orthogonal 3-by-3 matrices, dual special unitary 2-by-2 matrices, and dual Pauli spin matrices, dual quaternions have been found to be the most efficient representation to perform basic pose transformations in terms of storage requirements and number of operations [37]. Under the same metrics, dual quaternions have also been

found to be more efficient than 4-by-4 homogeneous matrix transformations and Rodriguez parameters/translation vector pairs for solving the direct kinematic problem in robotics [5]. Moreover, dual quaternions allow attitude and position controllers to be written as a single control law. It has also been shown that they automatically take into account the natural coupling between the linear and angular motions [44, 43]. Dual quaternions have been successfully applied to inertial navigation [105], rigid body control [75, 24, 44, 43, 95, 55, 96, 93, 56], inverse kinematic analysis [38, 74], and computer vision [22, 40] and animation [39]. The connections between dual quaternions and Lie algebra are analyzed in Refs. [18, 94].

The most useful property of dual quaternions is that the combined translational and rotational kinematic and dynamic equations of motion written in terms of dual quaternions have the same form as the rotational-only kinematic and dynamic equations of motion written in terms of quaternions. This is shown in Chapter 2. Inspired by this property, this dissertation derives combined position and attitude results from existing attitude-only results by almost simply replacing quaternions by dual quaternions in the original derivations.

The proposed approach based on dual quaternions to develop combined position and attitude controllers has some advantages over techniques based on differential algebra, where rotations are represented directly by rotation matrices [54, 61, 10]. In the latter, asymptotically stability of the combined rotational and translational motion is proven by either defining two different error functions for the position and attitude [10] or, in two steps, by first proving the asymptotic stability of the rotational motion before the asymptotic stability of the translational motion can be proven [54] (recall that the translational motion depends on the rotational motion). With dual quaternions, a single error function, the *error dual quaternion* (defined analogously to the error quaternion) is used to represent the combined position and attitude error. As a result, the asymptotic stability of the combined rotational and

translational motion is proven in a single step by using a Lyapunov function with the same form as the Lyapunov function used to prove the asymptotic stability of the rotational-only controller. Moreover, whereas quaternions produce two closed-loop equilibrium points (since quaternions cover SO(3) twice [12], both representing the identity rotation matrix), rotation matrices produce a minimum of four closed-loop equilibrium points [61, 54], only one of which is the identity rotation matrix. On the other hand, dual quaternions inherit the so-called *unwinding phenomenon* from classical quaternions [7]. This problem is well documented and possible solutions exist in literature [43, 7, 63, 93].

1.5 Outline of the Dissertation

A condensed description of the contributions of this dissertation, per chapter, is given next.

- Chapter 2 - Quaternion and Dual Quaternion Algebra

  This chapter provides a comprehensive introduction to quaternion and dual quaternion algebra. It is important to note that dual quaternion algebra is constructed on top of quaternion algebra. It is impossible to completely grasp the former without a good understanding of the latter. All operations on and properties of dual quaternions used in this dissertation are presented or deduced in this chapter. Although a significant part of the material given in this chapter is not original, some is. In particular, Lemmas 33, 38, and 55 are new and essential to prove Theorems 2 and 3. However, the most important contribution of this chapter is the derivation of an alternative representation of the rigid body dynamics in terms of dual quaternions. This representation is based on the *dual inertia matrix*, an 8-by-8 symmetric positive definite matrix constructed from the mass and inertia matrix of the rigid body.

- Chapter 3 - Pose-Tracking Without Relative Linear and Angular Velocity Feedback

  Since vision-based sensors typically cannot measure the relative linear and angular velocities between two spacecraft, it is useful to develop pose-tracking controllers that do not require such measurements. Hence, using dual quaternions, an attitude-only tracking controller that does not require relative angular velocity measurements [3] is extended in this chapter into a pose-tracking controller that does not require relative linear and angular velocity measurements [29, 28, 36]. Compared to existing literature, the velocity-free pose-tracking controller presented in this chapter is almost globally asymptotically stable. In particular, this controller guarantees that the pose of the chaser spacecraft will converge to the desired pose independently of the initial state and even if the reference motion is not sufficiently exciting. In addition, the convergence region does not depend on the gains chosen by the user. This controller is verified through simulation in the last section of this chapter.

- Chapter 4 - Dual Quaternion Multiplicative Extended Kalman Filter (DQ-MEFK) for Spacecraft Pose Estimation

  An alternative way to perform pose-tracking when the relative linear and angular velocities are not known is to estimate them from relative pose measurements via a filter. A comprehensive survey of nonlinear estimation methods [21] concluded that the classical *Extended Kalman Filter* (EKF) is still the most useful and practical solution to estimate the attitude and angular velocity of a spacecraft. Hence, based on the highly successful *Quaternion Multiplicative Extended Kalman Filter* (Q-MEKF) for spacecraft attitude and angular velocity estimation, this chapter proposes a *Dual Quaternion Multiplicative Extended Kalman*

Filter (DQ-MEKF) for spacecraft pose and linear and angular velocity estimation [32, 33]. By using the concept of error dual quaternion, defined analogously to the concept of error quaternion in the Q-MEKF, this chapter proposes, as far as the author knows, the first multiplicative EKF for pose estimation. Compared to existing results, only six elements of the dual quaternion are used in the state of the DQ-MEKF, instead of eight, resulting in obvious computational savings. The state estimate of the DQ-MEKF can be used directly by the pose-tracking controllers proposed in Chapters 3 and 5, without any additional conversions. Three formulations of the DQ-MEKF are presented. The first takes continuous-time linear and angular velocity measurements with noise and bias and discrete-time pose measurements with noise. The second takes only discrete-time pose measurements with noise and, hence, is the one suitable for uncooperative satellite proximity operation scenarios where the chaser satellite has only access to measurements of the relative pose, but requires the relative linear and angular velocities for control. The third formulation takes continuous-time angular velocity and linear acceleration measurements with noise and bias and discrete-time pose measurements with noise. The DQ-MEKF is experimentally validated and compared with two alternative EKF formulations on a 5-DOF air-bearing platform. Finally, the velocity-free pose-tracking controller presented in Chapter 3 is compared qualitatively and quantitatively to a pose-tracking controller that uses the velocity estimates produced by the DQ-MEKF, through a realistic proximity operations simulation.

- Chapter 5 - Pose-Tracking Without Mass and Inertia Matrix Information

  Whereas pose-stabilization controllers do not require the mass and inertia matrix to be precisely known, pose-tracking controllers typically do. However, the mass and inertia matrix of most satellites are not precisely known, especially once they are in orbit. Hence, a pose-tracking controller for space proximity

operations that does not require the mass and inertia matrix of the satellite is derived in this chapter [27, 35, 30, 31]. This controller is a direct extension of the attitude-tracking controller presented in Ref. [1]. This controller takes into account the gravitational acceleration, the gravity-gradient torque, the perturbing acceleration due to Earth's oblateness, and constant – but otherwise unknown – disturbance forces and torques. Sufficient conditions on the reference pose to identify the mass and inertia matrix of the satellite are also given. Compared to existing results, this controller has only as many states as unknown parameters and is almost globally asymptotically stable. In particular, this controller does not require a priori known upper bounds on the states and parameters of the problem. Two numerical examples are included to demonstrate the approach. In the first, the controller is used to approach, circumnavigate, and dock with a target satellite in a Molniya orbit. In the second, the controller is used to identify the mass and inertia matrix of a satellite in GEO. The controller is further tested in Chapter 6.

- Chapter 6 - High-Fidelity Simulation and Experimental Results

  In Chapter 6, the inertia-free pose-tracking controller described in Chapter 5 and the DQ-MEKF described in Chapter 4 are tested on a high-fidelity simulation of the 5-DOF platform of the *Autonomous Spacecraft Testing of Robotic Operations in Space* (ASTROS) facility at the School of Aerospace Engineering of the Georgia Institute of Technology and also experimentally validated on the actual platform [110]. Most of this chapter is dedicated to the derivation of the equations of motion of the 5-DOF platform, on which the high-fidelity simulation is based. Three cases are considered: a 3-DOF case, a 5-DOF case, and a (2+1)-DOF case. The allocation of the control moment to the *Variable-Speed Control Moment Gyros* (VSCMGs) on the platform and the allocation of the control moment and force to the thrusters is addressed. The conversion from

continuous thrust to on-off commands is also explained.

- Chapter 7 - Conclusion

  Finally, in Chapter 7, the main conclusions of this dissertation are stated and recommendations for future work are given.

CHAPTER II

QUATERNION AND DUAL QUATERNION ALGEBRA

This chapter provides an introduction to quaternion and dual quaternion algebra. Since dual quaternions are constructed on top of quaternions, it is important to address the latter first.

2.1 Quaternion Algebra

Quaternions were first introduced by Hamilton in 1843 [44]. They are an extension of complex numbers to $\mathbb{R}^4$. A quaternion is defined as $q = q_0 + q_1 i + q_2 j + q_3 k$, where q_0, q_1, q_2, $q_3 \in \mathbb{R}$ and i, j, and k satisfy $i^2 = j^2 = k^2 = -1$, $i = jk = -kj$, $j = ki = -ik$, and $k = ij = -ji$ [44]. A quaternion can also be represented as the ordered pair $q = (q_0, \bar{q})$, where $\overline{q} = [q_1 \ q_2 \ q_3]^\intercal \in \mathbb{R}^3$ is the *vector part* of the quaternion and $q_4 \in \mathbb{R}$ is the *scalar part* of the quaternion. *Vector quaternions* and *scalar quaternions* are quaternions with zero scalar part and vector part, respectively. The set of quaternions, vector quaternions, and scalar quaternions will be denoted by $\mathbb{H} = \{q : \ q = q_0 + q_1 i + q_2 j + q_3 k, \ q_0, q_1, q_2, q_3 \in \mathbb{R}\}$, $\mathbb{H}^v = \{q \in \mathbb{H} : \ q_0 = 0\}$, and $\mathbb{H}^s = \{q \in \mathbb{H} : \ q_1 = q_2 = q_3 = 0\}$, respectively.

The basic operations on quaternions are defined as follows:

$$\text{Addition: } a + b = (a_0 + b_0, \bar{a} + \bar{b}) \in \mathbb{H}, \tag{3}$$

$$\text{Multiplication by a scalar: } \lambda a = a\lambda = (\lambda a_0, \lambda \bar{a}) \in \mathbb{H}, \tag{4}$$

$$\text{Multiplication: } ab{=}(a_0 b_0 - \bar{a} \cdot \bar{b}, a_0 \bar{b} + b_0 \bar{a} + \bar{a} \times \bar{b}) \in \mathbb{H}, \tag{5}$$

$$\text{Conjugation: } a^* = (a_0, -\bar{a}) \in \mathbb{H}, \tag{6}$$

$$\text{Dot product: } a \cdot b = \tfrac{1}{2}(a^* b + b^* a) = \tfrac{1}{2}(ab^* + ba^*) = (a_0 b_0 + \bar{a} \cdot \bar{b}, \bar{0}) \in \mathbb{H}^s, \tag{7}$$

$$\text{Cross product: } a \times b = \tfrac{1}{2}(ab - b^* a^*) = (0, b_0\bar{a} + a_0\bar{b} + \bar{a} \times \bar{b}) \in \mathbb{H}^v, \tag{8}$$

$$\text{Norm: } \|a\|^2 = aa^* = a^* a = a \cdot a = (a_0^2 + \bar{a} \cdot \bar{a}, \bar{0}) \in \mathbb{H}^s, \tag{9}$$

$$\text{Scalar part: } \mathrm{sc}(a) = (a_0, \bar{0}) \in \mathbb{H}^s, \tag{10}$$

$$\text{Vector part: } \mathrm{vec}(a) = (0, \bar{a}) \in \mathbb{H}^v, \tag{11}$$

where $a, b \in \mathbb{H}$, $\lambda \in \mathbb{R}$, and $\bar{0} = [0\ 0\ 0]^\intercal$. The quaternion addition is commutative and associative, whereas the quaternion multiplication is associative and distributive [40], but not commutative. In fact, some authors [57] define Eq. (5) as ba, and not as ab as originally defined by Hamilton [42]. This work follows the original definition by Hamilton. Finally, the quaternions $(1, \bar{0})$ and $(0, \bar{0})$ will be denoted by `1` and `0`, respectively.

The bijective mapping between the set of quaternions and $\mathbb{R}^4$ will be denoted by $[\,\cdot\,] : \mathbb{H} \to \mathbb{R}^4$, where $[q] = [q_0\ q_1\ q_2\ q_3]^\intercal$. Under this mapping, the square of the quaternion norm and the dot product on $\mathbb{H}$ correspond to the square of the Euclidean norm and to the dot (inner) product on $\mathbb{R}^4$, respectively. Moreover, using this mapping, the cross product of $a \in \mathbb{H}^v$ with $b \in \mathbb{H}^v$ can be computed as $[a \times b] = [a]^\times [b]$, where $[\,\cdot\,]^\times : \mathbb{H}^v \to \mathbb{R}^{4\times 4}$ is defined as

$$[a]^\times = \begin{bmatrix} 0 & 0_{1\times 3} \\ 0_{3\times 1} & [\overline{a}]^\times \end{bmatrix}, \text{ where } [\overline{a}]^\times = \begin{bmatrix} 0 & -a_3 & a_2 \\ a_3 & 0 & -a_1 \\ -a_2 & a_1 & 0 \end{bmatrix}. \tag{12}$$

Likewise, the left quaternion multiplication of $a \in \mathbb{H}$ with $b \in \mathbb{H}$ can be computed as $[ab] = [a]^{\mathrm{L}} [b]$, where $[\,\cdot\,]^{\mathrm{L}} : \mathbb{H} \to \mathbb{R}^{4\times 4}$ is defined as

$$[a]^{\mathrm{L}} = \begin{bmatrix} [a]^{\mathrm{L}}_{4\times 1} & [a]^{\mathrm{L}}_{4\times 3} \end{bmatrix}, \ [a]^{\mathrm{L}}_{4\times 1} \triangleq \begin{bmatrix} a_0 \\ \overline{a} \end{bmatrix}, \text{ and } [a]^{\mathrm{L}}_{4\times 3} \triangleq \begin{bmatrix} -\overline{a}^\intercal \\ a_0 I_{3\times 3} + [\overline{a}]^\times \end{bmatrix}. \tag{13}$$

The multiplication of a matrix $M \in \mathbb{R}^{4\times 4}$ with a quaternion $q \in \mathbb{H}$ will be defined

as $M * q = (M_{11}q_0 + M_{12}\overline{q}, M_{21}q_0 + M_{22}\overline{q}) \in \mathbb{H}$, where

$$M = \begin{bmatrix} M_{11} & M_{12} \\ M_{21} & M_{22} \end{bmatrix},$$

$M_{11} \in \mathbb{R}$, $M_{12} \in \mathbb{R}^{1\times 3}$, $M_{21} \in \mathbb{R}^{3\times 1}$, and $M_{22} \in \mathbb{R}^{3\times 3}$. This definition is analogous to the multiplication of a 4-by-4 matrix with a 4-dimensional vector.

The $\mathcal{L}_\infty$-norm of a function $u : [0, \infty) \to \mathbb{H}$ is defined as $\|u\|_\infty = \sup_{t\geq 0} \|u(t)\|$. Moreover, the function $u \in \mathcal{L}_\infty$, if and only if $\|u\|_\infty < \infty$.

The following properties follow from the previous definitions.

Lemma 1. *If $a, b \in \mathbb{H}$, then $a \cdot b = b \cdot a$.*

Proof. If $a, b \in \mathbb{H}$, then $a \cdot b = (a_0b_0 + \bar{a} \cdot \bar{b}, \bar{0}) = (b_0a_0 + \bar{b} \cdot \bar{a}, \bar{0}) = b \cdot a$. □

Lemma 2. *If $a, b, c \in \mathbb{H}$, then $(a + b) \cdot c = a \cdot c + b \cdot c$ and $a \cdot (b + c) = a \cdot b + a \cdot c$.*

Proof. If $a, b, c \in \mathbb{H}$, then $(a+b)\cdot c = (a_0+b_0, \bar{a}+\bar{b})\cdot(c_0, \bar{c}) = (a_0c_0+b_0c_0+\bar{a}\cdot\bar{c}+\bar{b}\cdot\bar{c}, \bar{0}) = a\cdot c+b\cdot c$ and $a\cdot(b+c) = (a_0, \bar{a})\cdot(b_0+c_0, \bar{b}+\bar{c}) = (a_0b_0+a_0c_0+\bar{a}\cdot\bar{b}+\bar{a}\cdot\bar{c}, \bar{0}) = a\cdot b+a\cdot c$.

□

Lemma 3. *If $a, b, c \in \mathbb{H}$, then $(a+b)\times c = a\times c+b\times c$ and $a\times(b+c) = a\times b+a\times c$.*

Proof. If $a, b, c \in \mathbb{H}$, then $(a + b) \times c = (0, c_0(\bar{a} + \bar{b}) + (a_0 + b_0)\bar{c} + (\bar{a} + \bar{b}) \times \bar{c}) = (0, c_0\bar{a} + c_0\bar{b} + a_0\bar{c} + b_0\bar{c} + \bar{a} \times \bar{c} + \bar{b} \times \bar{c}) = a \times c + b \times c$ and $a \times (b + c) = (0, (b_0 + c_0)\bar{a} + a_0(\bar{b} + \bar{c}) + \bar{a} \times (\bar{b} + \bar{c})) = (0, b_0\bar{a} + c_0\bar{a} + a_0\bar{b} + a_0\bar{c} + \bar{a} \times \bar{b} + \bar{a} \times \bar{c}) = a \times b + a \times c$. □

Lemma 4. *If $a, b \in \mathbb{H}$ and $\lambda \in \mathbb{R}$, then $(\lambda a) \cdot b = a \cdot (\lambda b) = \lambda(a \cdot b)$.*

Proof. If $a, b \in \mathbb{H}$ and $\lambda \in \mathbb{R}$, then $(\lambda a) \cdot b = ((\lambda a_0)b_0 + (\lambda\bar{a}) \cdot \bar{b}, \bar{0}) = (a_0(\lambda b_0) + \bar{a} \cdot (\lambda\bar{b}), \bar{0}) = a \cdot (\lambda b) = (\lambda(a_0b_0) + \lambda(\bar{a} \cdot \bar{b}), \bar{0}) = \lambda(a \cdot b)$. □

Lemma 5. *If $a, b \in \mathbb{H}$ and $\lambda \in \mathbb{R}$, then $(\lambda a) \times b = a \times (\lambda b) = \lambda(a \times b)$.*

Proof. If $a, b \in \mathbb{H}$ and $\lambda \in \mathbb{R}$, then $(\lambda a) \times b = (0, b_0(\lambda\bar{a}) + (\lambda a_0)\bar{b} + (\lambda\bar{a}) \times \bar{b}) = (0, (\lambda b_0)\bar{a} + a_0(\lambda\bar{b}) + \bar{a} \times (\lambda\bar{b})) = a \times (\lambda b) = (0, \lambda(b_0\bar{a}) + \lambda(a_0\bar{b}) + \lambda(\bar{a} \times \bar{b})) = \lambda(a \times b)$. □

Lemma 6. *If $a, b \in \mathbb{H}$, then $(ab)^* = b^*a^*$.*

Proof. If $a, b \in \mathbb{H}$, then $(ab)^* = (a_0b_0 - \bar{a} \cdot \bar{b}, -a_0\bar{b} - b_0\bar{a} - \bar{a} \times \bar{b}) = (b_0a_0 - \bar{b} \cdot \bar{a}, -b_0\bar{a} - a_0\bar{b} + \bar{b} \times \bar{a}) = b^*a^*$. □

Lemma 7. *If $a, b, c \in \mathbb{H}$, then $a \cdot (bc) = b \cdot (ac^*) = c \cdot (b^*a)$.*

Proof. If $a, b, c \in \mathbb{H}$, then $a \cdot (bc) = \frac{1}{2}(a(c^*b^*) + (bc)a^*) = \frac{1}{2}((ac^*)b^* + b(ca^*)) = (ac^*) \cdot b = b \cdot (ac^*)$ and $a \cdot (bc) = \frac{1}{2}(a^*(bc) + (c^*b^*)a) = \frac{1}{2}((a^*b)c + c^*(b^*a)) = (b^*a) \cdot c = c \cdot (b^*a)$. □

Lemma 8. *If $a \in \mathbb{H}$, then $(a^*)^* = a$.*

Proof. If $a \in \mathbb{H}$, then $(a^*)^* = (a_0, -\bar{a})^* = (a_0, \bar{a}) = a$. □

Lemma 9. *If $a, b \in \mathbb{H}$, then $a^* \cdot b^* = a \cdot b$.*

Proof. If $a, b \in \mathbb{H}$, then $a^* \cdot b^* = (a_0b_0 + (-\bar{a}) \cdot (-\bar{b}), \bar{0}) = (a_0b_0 + \bar{a} \cdot \bar{b}, \bar{0}) = a \cdot b$. □

Lemma 10. *If $a, b \in \mathbb{H}$, then $\|ab\| = \|a\|\|b\|$.*

Proof. If $a, b \in \mathbb{H}$, then $\|ab\| = \sqrt{abb^*a^*} = \sqrt{\|a\|^2\|b\|^2} = \|a\|\|b\|$. □

Lemma 11. *If $a, b \in \mathbb{H}$ and $M \in \mathbb{R}^{4\times4}$, then $(M * a) \cdot b = a \cdot (M^\intercal * b)$.*

Proof. If $a, b \in \mathbb{H}$ and $M \in \mathbb{R}^{4\times4}$, then $(M*a)\cdot b = (M_{11}a_0 + M_{12}\overline{a}, M_{21}a_0 + M_{22}\overline{a}) \cdot b = ((M_{11}a_0) \cdot b_0 + (M_{12}\overline{a}) \cdot b_0 + (M_{21}a_0) \cdot \bar{b} + (M_{22}\overline{a}) \cdot \bar{b}, \bar{0}) = (a_0 \cdot (M_{11}^\intercal b_0) + \overline{a} \cdot (M_{12}^\intercal b_0) + a_0 \cdot (M_{21}^\intercal \bar{b}) + \overline{a} \cdot (M_{22}^\intercal \bar{b}), \bar{0}) = a \cdot (M_{11}^\intercal b_0 + M_{21}^\intercal \bar{b}, M_{12}^\intercal b_0 + M_{22}^\intercal \bar{b}) = a \cdot (M^\intercal * b)$. □

Lemma 12. *If $a \in \mathbb{H}$, then $\|a^*\| = \|a\|$.*

Proof. If $a \in \mathbb{H}$, then $\|a^*\| = \sqrt{a^*(a^*)^*} = \sqrt{a^*a} = \|a\|$. □

Lemma 13. *If $a, b \in \mathbb{H}$, then $|a \cdot b| \leq \|a\|\|b\|$.*

Proof. If $a, b \in \mathbb{H}$ and using Cauchy-Schwarz inequality, $|a \cdot b| = (|a_0 b_0 + a_1 b_1 + a_2 b_2 + b_3 b_3|, \bar{0}) \leq \|a\|\|b\|$. □

Lemma 14. *If $a, b \in \mathbb{H}$, then $\frac{\mathrm{d}}{\mathrm{d}t}(ab) = \dot{a}b + a\dot{b}$.*

Proof. If $a, b \in \mathbb{H}$, then $\frac{\mathrm{d}}{\mathrm{d}t}(ab) = (\dot{a}_0 b_0 + a_0 \dot{b}_0 - \dot{\bar{a}} \cdot \bar{b} - \bar{a} \cdot \dot{\bar{b}}, \dot{a}_0 \bar{b} + a_0 \dot{\bar{b}} + \dot{b}_0 \bar{a} + b_0 \dot{\bar{a}} + \dot{\bar{a}} \times \bar{b} + \bar{a} \times \dot{\bar{b}}) = (\dot{a}_0 b_0 - \dot{\bar{a}} \cdot \bar{b}, \dot{a}_0 \bar{b} + b_0 \dot{\bar{a}} + \dot{\bar{a}} \times \bar{b}) + (a_0 \dot{b}_0 - \bar{a} \cdot \dot{\bar{b}}, a_0 \dot{\bar{b}} + \dot{b}_0 \bar{a} + \bar{a} \times \dot{\bar{b}}) = \dot{a}b + a\dot{b}$.

□

Lemma 15. *If $a, b \in \mathbb{H}$, then $\frac{\mathrm{d}}{\mathrm{d}t}(a \cdot b) = \dot{a} \cdot b + a \cdot \dot{b}$.*

Proof. If $a, b \in \mathbb{H}$, then $\frac{\mathrm{d}}{\mathrm{d}t}(a \cdot b) = \frac{\mathrm{d}}{\mathrm{d}t}(\frac{1}{2}(a^* b + b^* a)) = \frac{1}{2}(\dot{a}^* b + a^* \dot{b} + \dot{b}^* a + b^* \dot{a}) = \frac{1}{2}(\dot{a}^* b + b^* \dot{a}) + \frac{1}{2}(a^* \dot{b} + \dot{b}^* a) = \dot{a} \cdot b + a \cdot \dot{b}$. □

Lemma 16. *If $a, b \in \mathbb{H}$, then $\frac{\mathrm{d}}{\mathrm{d}t}(a \times b) = \dot{a} \times b + a \times \dot{b}$.*

Proof. If $a, b \in \mathbb{H}$, then $\frac{\mathrm{d}}{\mathrm{d}t}(a \times b) = \frac{\mathrm{d}}{\mathrm{d}t}(\frac{1}{2}(ab - b^* a^*)) = \frac{1}{2}(\dot{a}b + a\dot{b} - \dot{b}^* a^* - b^* \dot{a}^*) = \frac{1}{2}(\dot{a}b - b^* \dot{a}^*) + \frac{1}{2}(a\dot{b} - \dot{b}^* a^*) = \dot{a} \times b + a \times \dot{b}$. □

Lemma 17. *If $M \in \mathbb{R}^{4\times 4}$ and $q \in \mathbb{H}$, then $\frac{\mathrm{d}}{\mathrm{d}t}(M * q) = \frac{\mathrm{d}M}{\mathrm{d}t} * q + M * \frac{\mathrm{d}q}{\mathrm{d}t}$.*

Proof. If $M \in \mathbb{R}^{4\times 4}$ and $q \in \mathbb{H}$, then $\frac{\mathrm{d}}{\mathrm{d}t}(M * q) = \frac{\mathrm{d}}{\mathrm{d}t}(M_{11} q_0 + M_{12} \overline{q}, M_{21} q_0 + M_{22} \overline{q}) = (\dot{M}_{11} q_0 + M_{11} \dot{q}_0 + \dot{M}_{12} \overline{q} + M_{12} \dot{\overline{q}}, \dot{M}_{21} q_0 + M_{21} \dot{q}_0 + \dot{M}_{22} \overline{q} + M_{22} \dot{\overline{q}}) = (\dot{M}_{11} q_0 + \dot{M}_{12} \overline{q}, \dot{M}_{21} q_0 + \dot{M}_{22} \overline{q}) + (M_{11} \dot{q}_0 + M_{12} \dot{\overline{q}}, M_{21} \dot{q}_0 + M_{22} \dot{\overline{q}}) = \frac{\mathrm{d}M}{\mathrm{d}t} * q + M * \frac{\mathrm{d}q}{\mathrm{d}t}$. □

Lemma 18. *If $A, B \in \mathbb{R}^{4\times 4}$ and $q \in \mathbb{H}$, then $A * (B * q) = (AB) * q$.*

Proof. If $A, B \in \mathbb{R}^{4\times 4}$ and $q \in \mathbb{H}$, then $A * (B * q) = A(B_{11} q_0 + B_{12} \overline{q}, B_{21} q_0 + B_{22} \overline{q}) = (A_{11} B_{11} q_0 + A_{11} B_{12} \overline{q} + A_{12} B_{21} q_0 + A_{12} B_{22} \overline{q}, A_{21} B_{11} q_0 + A_{21} B_{12} \overline{q} + A_{22} B_{21} q_0 + A_{22} B_{22} \overline{q}) = ((A_{11} B_{11} + A_{12} B_{21}) q_0 + (A_{11} B_{12} + A_{12} B_{22}) \overline{q}, (A_{21} B_{11} + A_{22} B_{21}) q_0 + (A_{21} B_{12} + A_{22} B_{22}) \overline{q}) = (AB) * q$. □

Lemma 19. *If $A, B \in \mathbb{R}^{4\times 4}$ and $q \in \mathbb{H}$, then $(A + B) * q = A * q + B * q$.*

Proof. If $A, B \in \mathbb{R}^{4\times4}$ and $q \in \mathbb{H}$, then $(A+B)*q = ((A_{11}+B_{11})q_0+(A_{12}+B_{12})\overline{q}, (A_{21}+B_{21})q_0)+(A_{22}+B_{22})\overline{q}) = (A_{11}q_0+A_{12}\overline{q}, A_{21}q_0)+A_{22}\overline{q})+(B_{11}q_0+B_{12}\overline{q}, B_{21}q_0)+B_{22}\overline{q}) = A*q+B*q$. □

Lemma 20. *If $M \in \mathbb{R}^{4\times4}$ and $a, b \in \mathbb{H}$, then $M*(a+b) = M*a+M*b$.*

Proof. If $M \in \mathbb{R}^{4\times4}$ and $a, b \in \mathbb{H}$, then $M*(a+b) = (M_{11}(a_0+b_0)+M_{12}(\overline{a}+\overline{b}), M_{21}(a_0+b_0)+M_{22}(\overline{a}+\overline{b})) = (M_{11}a_0+M_{12}\overline{a}, M_{21}a_0+M_{22}\overline{a})+(M_{11}b_0+M_{12}\overline{b}, M_{21}b_0+M_{22}\overline{b}) = M*a+M*b$. □

Lemma 21. *Let $M \in \mathbb{R}^{4\times4}$ be a symmetric (i.e., $M = M^\intercal$) positive-definite matrix (i.e., $x^\intercal Mx > 0$, $x \neq 0$) of the form*

$$M = \begin{bmatrix} M_{11} & M_{12} \\ M_{12}^\intercal & M_{22} \end{bmatrix}, \quad M_{11} \in \mathbb{R}, \quad M_{12} \in \mathbb{R}^{1\times3}, \quad M_{22} \in \mathbb{R}^{3\times3}. \tag{14}$$

Then, the function $V_1 : \mathbb{H} \to \mathbb{R}$ defined as $V_1(a) = a \cdot (M*a)$ satisfies $V_1(a) > 0$ for $a \in \mathbb{H}\backslash\{0\}$ and $V_1(a) \to \infty$ as $\|a\| \to \infty$.

Moreover, if $N \in \mathbb{R}^{4\times4}$ is of the form

$$N = \begin{bmatrix} N_{11} & N_{12} \\ N_{21} & N_{22} \end{bmatrix}, \tag{15}$$

where $N_{22} \in \mathbb{R}^{3\times3}$ is a symmetric positive-definite matrix, then the function $V_2 : \mathbb{H}^v \to \mathbb{R}$ defined as $V_2(a) = a \cdot (N*a)$ satisfies $V_2(a) > 0$ for $a \in \mathbb{H}^v\backslash\{0\}$ and $V_2(a) \to \infty$ as $\|a\| \to \infty$.

Proof. By definition, $V_1(a) = a \cdot (M*a) = (a_0, \bar{a}) \cdot (M_{11}a_0+M_{12}\bar{a}, M_{12}^\intercal a_0+M_{22}\bar{a}) = (a_0M_{11}a_0+a_0M_{12}\bar{a}+\bar{a}\cdot(M_{12}^\intercal a_0)+\bar{a}\cdot(M_{22}\bar{a}), \bar{0}) = ([a_0\ \bar{a}^\intercal]M[a_0\ \bar{a}^\intercal]^\intercal, \bar{0})$, which is strictly positive for all $a \in \mathbb{H}\backslash\{0\}$ and radially unbounded since M is a symmetric positive-definite matrix. Likewise, $V_2(a) = a \cdot (N*a) = (0, \bar{a}) \cdot (N_{12}\bar{a}, N_{22}\bar{a}) = (\bar{a} \cdot (N_{22}\bar{a}), \bar{0})$, which is strictly positive for all $a \in \mathbb{H}^v\backslash\{0\}$ and radially unbounded since N_{22} is a symmetric positive-definite matrix. □

Finally, note that the dot product and cross product of two vector quaternions are composed by the dot product and cross product of their vector parts, respectively, i.e., $a \cdot b = (\bar{a} \cdot \bar{b}, \bar{0}) \in \mathbb{H}^s$ and $a \times b = (0, \bar{a} \times \bar{b}) \in \mathbb{H}^v$, where $a, b \in \mathbb{H}^v$. Hence, many of the properties of the dot product and cross product of vectors in $\mathbb{R}^3$ can be extended to the dot product and cross product of vector quaternions. In particular, the following properties hold for vector quaternions:

$$a \cdot (b \times c) = b \cdot (c \times a) = c \cdot (a \times b), \quad a, b, c \in \mathbb{H}^v, \tag{16}$$

$$a \times a = 0, \quad a \in \mathbb{H}^v, \tag{17}$$

$$a \times b = -b \times a, \quad a, b \in \mathbb{H}^v. \tag{18}$$

2.1.1 Attitude Representation with Unit Quaternions

The relative orientation of a body frame with respect to an inertial frame can be represented by the *unit quaternion*

$$q_{\mathrm{B/I}} = \left(\cos(\frac{\phi}{2}), \sin(\frac{\phi}{2}) \bar{n} \right),$$

where the body frame is said to be rotated with respect to the inertial frame about the unit vector $\bar{n}$ (i.e., $\bar{n} \cdot \bar{n}$=1) by an angle ϕ. Note that it does not make a difference whether $\bar{n}$ is written in the inertial frame or in the body frame as the coordinates of $\bar{n}$ are invariant under the rotation [64]. The quaternion $q_{\mathrm{B/I}}$ is a unit quaternion because it belongs to the set $\mathbb{H}^u = \{q \in \mathbb{H} : \ q \cdot q = 1\}$. From this constraint and assuming that $-180 < \phi < 180$ deg, the scalar part of a unit quaternion can be computed from

$$q_0 = \sqrt{1 - \|\overline{q}\|^2}, \tag{19}$$

where $\| \cdot \|$ denotes the usual Euclidean norm in $\mathbb{R}^3$.

The body coordinates of a vector, $\bar{v}^{\mathrm{B}}$, can be calculated from the inertial coordinates of that same vector, $\bar{v}^{\mathrm{I}}$, and vice-versa, through

$$v^{\mathrm{B}} = q^*_{\mathrm{B/I}} v^{\mathrm{I}} q_{\mathrm{B/I}} \qquad \text{and} \qquad v^{\mathrm{I}} = q_{\mathrm{B/I}} v^{\mathrm{B}} q^*_{\mathrm{B/I}}, \tag{20}$$

where $v^{\mathrm{B}} = (0, \bar{v}^{\mathrm{B}})$ and $v^{\mathrm{I}} = (0, \bar{v}^{\mathrm{I}})$. This is equivalent to $\overline{v}^{\mathrm{B}} = R^{\mathrm{B}\leftarrow\mathrm{I}}\overline{v}^{\mathrm{I}}$ and $\overline{v}^{\mathrm{I}} = R^{\mathrm{I}\leftarrow\mathrm{B}}\overline{v}^{\mathrm{B}}$, where $R^{\mathrm{X}\leftarrow\mathrm{Y}}$ is the rotation matrix that transforms the coordinates of a vector from the Y-frame to the X-frame.

Another important result about unit quaternions and attitude representation is given by the following lemma [100].

Lemma 22. *Let the relative orientation of frame Y with respect to frame Z be given by the unit quaternion $q_{\mathrm{Y/Z}}$. Then, $q_{\mathrm{Y/Z}}$ and $-q_{\mathrm{Y/Z}}$ represent the same relative orientation between the two frames.*

Proof. Given the coordinates of a vector in the Z-frame, the coordinates of that same vector in the Y-frame are given by

$$v^{\mathrm{Y}} = q^{*}_{\mathrm{Y/Z}} v^{\mathrm{Z}} q_{\mathrm{Y/Z}} \text{ or } v^{\mathrm{Y}} = (-q^{*}_{\mathrm{Y/Z}}) v^{\mathrm{Z}} (-q_{\mathrm{Y/Z}}). \qquad \square$$

In particular, when $q_{\mathrm{Y/Z}} = \mathtt{1}$ and $q_{\mathrm{Y/Z}} = -\mathtt{1}$, the two frames have the same orientation.

2.1.2 Quaternion Representation of the Relative Rotational Kinematic Equations

The rotational kinematic equations of the body frame and of a frame with some desired orientation, both with respect to the inertial frame and represented by the unit quaternions $q_{\mathrm{B/I}}$ and $q_{\mathrm{D/I}}$, respectively, are given by [105]

$$\dot{q}_{\mathrm{B/I}} = \tfrac{1}{2} q_{\mathrm{B/I}} \omega^{\mathrm{B}}_{\mathrm{B/I}} = \tfrac{1}{2} \omega^{\mathrm{I}}_{\mathrm{B/I}} q_{\mathrm{B/I}} \quad \text{and} \quad \dot{q}_{\mathrm{D/I}} = \tfrac{1}{2} q_{\mathrm{D/I}} \omega^{\mathrm{D}}_{\mathrm{D/I}} = \tfrac{1}{2} \omega^{\mathrm{I}}_{\mathrm{D/I}} q_{\mathrm{D/I}}, \tag{21}$$

where $\omega^{\mathrm{X}}_{\mathrm{Y/Z}} = (0, \bar{\omega}^{\mathrm{X}}_{\mathrm{Y/Z}})$, and $\bar{\omega}^{\mathrm{X}}_{\mathrm{Y/Z}} = [p^{\mathrm{X}}_{\mathrm{Y/Z}}, q^{\mathrm{X}}_{\mathrm{Y/Z}}, r^{\mathrm{X}}_{\mathrm{Y/Z}}]^{\intercal}$ is the angular velocity of the Y-frame with respect to the Z-frame expressed in the X-frame. The error quaternion [101, 103]

$$q_{\mathrm{B/D}} = q^{*}_{\mathrm{D/I}} q_{\mathrm{B/I}} \tag{22}$$

is the unit quaternion that rotates the desired frame onto the body frame. By differentiating Eq. (22) and using Eq. (21), the kinematic equations of the error quaternion

turn out to be

$$\dot{q}_{\mathrm{B/D}} = \tfrac{1}{2} q_{\mathrm{B/D}} \omega^{\mathrm{B}}_{\mathrm{B/D}} = \tfrac{1}{2} \omega^{\mathrm{D}}_{\mathrm{B/D}} q_{\mathrm{B/D}}, \tag{23}$$

where $\omega^{\mathrm{B}}_{\mathrm{B/D}} = \omega^{\mathrm{B}}_{\mathrm{B/I}} - \omega^{\mathrm{B}}_{\mathrm{D/I}}$ (and $\omega^{\mathrm{D}}_{\mathrm{B/D}} = \omega^{\mathrm{D}}_{\mathrm{B/I}} - \omega^{\mathrm{D}}_{\mathrm{D/I}}$). Note that $q_{\mathrm{B/D}}$ is a better representation of the error between $q_{\mathrm{B/I}}$ and $q_{\mathrm{D/I}}$ than $q_{\mathrm{B/I}} - q_{\mathrm{D/I}}$. Like $q_{\mathrm{B/I}}$ and $q_{\mathrm{D/I}}$, $q_{\mathrm{B/D}}$ belongs to $\mathbb{H}^u$, whereas $q_{\mathrm{B/I}} - q_{\mathrm{D/I}}$ does not. Hence, $q_{\mathrm{B/I}} - q_{\mathrm{D/I}}$ does not represent a relative orientation between two frames.

2.1.3 Quaternion Representation of the Relative Rotational Dynamic Equations

In quaternion algebra, the rotational(-only) dynamic equations of a rigid body about its center of mass with respect to a rotating frame are given by [93]

$$\dot{\omega}^{\mathrm{B}}_{\mathrm{B/D}} = (I^{\mathrm{B}})^{-1} * \Big(\tau^{\mathrm{B}} - (\omega^{\mathrm{B}}_{\mathrm{B/D}} + \omega^{\mathrm{B}}_{\mathrm{D/I}}) \times \big(I^{\mathrm{B}} * (\omega^{\mathrm{B}}_{\mathrm{B/D}} + \omega^{\mathrm{B}}_{\mathrm{D/I}}) \big) \Big) - q^{*}_{\mathrm{B/D}} \dot{\omega}^{\mathrm{D}}_{\mathrm{D/I}} q_{\mathrm{B/D}} - \omega^{\mathrm{B}}_{\mathrm{D/I}} \times \omega^{\mathrm{B}}_{\mathrm{B/D}}, \tag{24}$$

where

$$I^{\mathrm{B}} = \begin{bmatrix} 1 & 0_{1\times 3} \\ 0_{3\times 1} & \bar{I}^{\mathrm{B}} \end{bmatrix}, \quad \bar{I}^{\mathrm{B}} = \begin{bmatrix} I_{11} & I_{12} & I_{13} \\ I_{12} & I_{22} & I_{23} \\ I_{13} & I_{23} & I_{33} \end{bmatrix}, \tag{25}$$

$\bar{I}^{\mathrm{B}} \in \mathbb{R}^{3\times 3}$ is the mass moment of inertia of the body about its center of mass expressed in the body frame, $\tau^{\mathrm{B}} = (0, \bar{\tau}^{\mathrm{B}})$, and $\bar{\tau}^{\mathrm{B}} = [\tau^{\mathrm{B}}_1, \tau^{\mathrm{B}}_2, \tau^{\mathrm{B}}_3]^{\intercal}$ is the total external moment vector applied to the body about its center of mass expressed in the body frame.

2.2 Dual Quaternion Algebra

Dual quaternions were introduced by Clifford in 1873 [17]. A dual quaternion is defined as $\boldsymbol{q} = q_r + \epsilon q_d$, where ϵ is the *dual unit* defined by $\epsilon^2 = 0$ and $\epsilon \neq 0$. The quaternions $q_r, q_d \in \mathbb{H}$ are called the *real part* and the *dual part* of the dual quaternion, respectively.

Dual vector quaternions and *dual scalar quaternions* are dual quaternions formed from vector quaternions (i.e., $q_r, q_d \in \mathbb{H}^v$) and scalar quaternions (i.e., $q_r, q_d \in$

$\mathbb{H}^s$), respectively. The set of dual quaternions, dual scalar quaternions, dual vector quaternions, and dual scalar quaternions with zero dual part will be denoted by $\mathbb{H}_d = \{\boldsymbol{q} : \ \boldsymbol{q} = q_r + \epsilon q_d, \ q_r, q_d \in \mathbb{H}\}$, $\mathbb{H}_d^s = \{\boldsymbol{q} : \ \boldsymbol{q} = q_r + \epsilon q_d, \ q_r, q_d \in \mathbb{H}^s\}$, $\mathbb{H}_d^v = \{\boldsymbol{q} : \ \boldsymbol{q} = q_r + \epsilon q_d, \ q_r, q_d \in \mathbb{H}^v\}$, and $\mathbb{H}_d^r = \{\boldsymbol{q} : \ \boldsymbol{q} = q_r + \epsilon \mathsf{0}, \ q_r \in \mathbb{H}^s\}$, respectively.

The basic operations on dual quaternions are defined as follows [43, 93]:

$$\text{Addition: } \boldsymbol{a} + \boldsymbol{b} = (a_r + b_r) + \epsilon(a_d + b_d) \in \mathbb{H}_d, \tag{26}$$

$$\text{Multiplication by a scalar: } \lambda\boldsymbol{a} = \boldsymbol{a}\lambda = (\lambda a_r) + \epsilon(\lambda a_d) \in \mathbb{H}_d, \tag{27}$$

$$\text{Multiplication: } \boldsymbol{ab} = (a_r b_r) + \epsilon(a_r b_d + a_d b_r) \in \mathbb{H}_d, \tag{28}$$

$$\text{Conjugation: } \boldsymbol{a}^* = a_r^* + \epsilon a_d^* \in \mathbb{H}_d, \tag{29}$$

$$\text{Swap: } \boldsymbol{a}^{\mathsf{s}} = a_d + \epsilon a_r \in \mathbb{H}_d, \tag{30}$$

$$\text{Dot product: } \boldsymbol{a}\cdot\boldsymbol{b} = \tfrac{1}{2}(\boldsymbol{a}^*\boldsymbol{b} + \boldsymbol{b}^*\boldsymbol{a}) = \tfrac{1}{2}(\boldsymbol{a}\boldsymbol{b}^* + \boldsymbol{b}\boldsymbol{a}^*) = a_r \cdot b_r + \epsilon(a_d \cdot b_r + a_r \cdot b_d) \in \mathbb{H}_d^s, \tag{31}$$

$$\text{Cross product: } \boldsymbol{a} \times \boldsymbol{b} = \tfrac{1}{2}(\boldsymbol{a}\boldsymbol{b} - \boldsymbol{b}^*\boldsymbol{a}^*) = a_r \times b_r + \epsilon(a_d \times b_r + a_r \times b_d) \in \mathbb{H}_d^v, \tag{32}$$

$$\text{Dual norm: } \|\boldsymbol{a}\|_d^2 = \boldsymbol{a}\boldsymbol{a}^* = \boldsymbol{a}^*\boldsymbol{a} = \boldsymbol{a}\cdot\boldsymbol{a} = (a_r \cdot a_r) + \epsilon(2a_r \cdot a_d) \in \mathbb{H}_d^s, \tag{33}$$

$$\text{Scalar part: } \mathrm{sc}(\boldsymbol{a}) = \mathrm{sc}(a_r) + \epsilon\,\mathrm{sc}(a_d) \in \mathbb{H}_d^s, \tag{34}$$

$$\text{Vector part: } \mathrm{vec}(\boldsymbol{a}) = \mathrm{vec}(a_r) + \epsilon\,\mathrm{vec}(a_d) \in \mathbb{H}_d^v, \tag{35}$$

where $\boldsymbol{a}, \boldsymbol{b} \in \mathbb{H}_d$ and $\lambda \in \mathbb{R}$. The dual quaternion addition is commutative and associative, whereas the dual quaternion multiplication is associative and distributive. However, the dual quaternion multiplication is not commutative. Finally, the dual quaternions $\mathsf{1} + \epsilon\mathsf{0}$ and $\mathsf{0} + \epsilon\mathsf{0}$ will be denoted by $\mathbf{1}$ and $\mathbf{0}$, respectively.

Since the dot product and dual norm yield in general a dual scalar quaternion (and not a dual scalar quaternion with zero dual part), the *norm* of a dual quaternion will be defined as [9, 93]

$$\|\boldsymbol{a}\|^2 = \boldsymbol{a} \circ \boldsymbol{a} \in \mathbb{H}_d^r, \tag{36}$$

where $\circ$ denotes the dual quaternion *circle product* given by

$$\boldsymbol{a} \circ \boldsymbol{b} = a_r \cdot b_r + a_d \cdot b_d \in \mathbb{H}_d^r, \tag{37}$$

where $\boldsymbol{a}, \boldsymbol{b} \in \mathbb{H}_d$. Other authors have used alternative norms, for example, based on the logarithm of the dual quaternion [94, 96, 97, 44, 95]. In this work, the dual quaternion norm is defined as in Eq. (36) because the real part of Eq. (36) matches the quaternion norm used in Ref. [1]. Since dual quaternions are used in this work to extend the attitude-only results presented in Ref. [1], selecting this dual quaternion norm facilitates this extension.

The bijective mapping between the set of dual quaternions and $\mathbb{R}^8$ will be denoted by $[\,\cdot\,] : \mathbb{H}_d \to \mathbb{R}^8$, where $[\boldsymbol{q}] = [[q_r]^\intercal [q_d]^\intercal]^\intercal$. Using this mapping, the square of the dual quaternion norm and the circle product on $\mathbb{H}_d$ correspond to the square of the Euclidean norm and to the dot (inner) product on $\mathbb{R}^8$, respectively. Moreover, using this mapping, the left dual quaternion multiplication of $\boldsymbol{a} \in \mathbb{H}_d$ with $\boldsymbol{b} \in \mathbb{H}_d$ can be computed as $[\boldsymbol{ab}] = [\boldsymbol{a}]^{\mathrm{L}}[\boldsymbol{b}]$, where $[\,\cdot\,]^{\mathrm{L}} : \mathbb{H}_d \to \mathbb{R}^{8\times 8}$ is defined as

$$[\boldsymbol{a}]^{\mathrm{L}} = \begin{bmatrix} [a_r]^{\mathrm{L}} & 0_{4\times 4} \\ [a_d]^{\mathrm{L}} & [a_r]^{\mathrm{L}} \end{bmatrix}. \tag{38}$$

Finally, it is convenient to define $\overline{\cdot} : \mathbb{H}_d \to \mathbb{R}^6$ as $\overline{\boldsymbol{a}} = [\overline{a}_r^\intercal \ \overline{a}_d^\intercal]^\intercal$, $[\overline{\cdot}]^\times : \mathbb{H}_d \to \mathbb{R}^{6\times 6}$ as

$$[\overline{\boldsymbol{a}}]^\times = \begin{bmatrix} [\overline{a}_r]^\times & 0_{3\times 3} \\ [\overline{a}_d]^\times & [\overline{a}_r]^\times \end{bmatrix}, \tag{39}$$

and $[\,\cdot\,]^{\mathrm{L}}_{8\times 6} : \mathbb{H}_d \to \mathbb{R}^{8\times 6}$ as

$$[\boldsymbol{a}]^{\mathrm{L}}_{8\times 6} = \begin{bmatrix} [a_r]^{\mathrm{L}}_{4\times 3} & 0_{4\times 3} \\ [a_d]^{\mathrm{L}}_{4\times 3} & [a_r]^{\mathrm{L}}_{4\times 3} \end{bmatrix}. \tag{40}$$

The multiplication of a matrix $M \in \mathbb{R}^{8\times 8}$ with a dual quaternion $\boldsymbol{q} \in \mathbb{H}_d$ will be defined as $M \star \boldsymbol{q} = (M_{11} * q_r + M_{12} * q_d) + \epsilon(M_{21} * q_r + M_{22} * q_d)$, where

$$M = \begin{bmatrix} M_{11} & M_{12} \\ M_{21} & M_{22} \end{bmatrix}, \quad M_{11}, M_{12}, M_{21}, M_{22} \in \mathbb{R}^{4\times 4}.$$

This definition is analogous to the multiplication of a 8-by-8 matrix with a 8-dimensional vector.

The $\mathcal{L}_\infty$-norm of a function $\boldsymbol{u} : [0, \infty) \to \mathbb{H}_d$ is defined as $\|\boldsymbol{u}\|_\infty = \sup_{t \geq 0} \|\boldsymbol{u}(t)\|$. Moreover, the function $\boldsymbol{u} \in \mathcal{L}_\infty$, if and only if $\|\boldsymbol{u}\|_\infty < \infty$.

The following properties follow from the previous definitions.

Lemma 23. *If* $\boldsymbol{a}, \boldsymbol{b} \in \mathbb{H}_d$, *then* $\boldsymbol{a} \cdot \boldsymbol{b} = \boldsymbol{b} \cdot \boldsymbol{a}$.

Proof. If $\boldsymbol{a}, \boldsymbol{b} \in \mathbb{H}_d$, then $\boldsymbol{a} \cdot \boldsymbol{b} = a_r \cdot b_r + \epsilon(a_d \cdot b_r + a_r \cdot b_d) = b_r \cdot a_r + \epsilon(b_r \cdot a_d + b_d \cdot a_r) = \boldsymbol{b} \cdot \boldsymbol{a}$. □

Lemma 24. *If* $\boldsymbol{a}, \boldsymbol{b} \in \mathbb{H}_d$, *then* $\boldsymbol{a} \circ \boldsymbol{b} = \boldsymbol{b} \circ \boldsymbol{a}$.

Proof. If $\boldsymbol{a}, \boldsymbol{b} \in \mathbb{H}_d$, then $\boldsymbol{a} \circ \boldsymbol{b} = a_r \cdot b_r + a_d \cdot b_d = b_r \cdot a_r + b_d \cdot a_d = \boldsymbol{b} \circ \boldsymbol{a}$. □

Lemma 25. *If* $\boldsymbol{a}, \boldsymbol{b}, \boldsymbol{c} \in \mathbb{H}_d$, *then* $(\boldsymbol{a} + \boldsymbol{b}) \cdot \boldsymbol{c} = \boldsymbol{a} \cdot \boldsymbol{c} + \boldsymbol{b} \cdot \boldsymbol{c}$ *and* $\boldsymbol{a} \cdot (\boldsymbol{b} + \boldsymbol{c}) = \boldsymbol{a} \cdot \boldsymbol{b} + \boldsymbol{a} \cdot \boldsymbol{c}$.

Proof. If $\boldsymbol{a}, \boldsymbol{b}, \boldsymbol{c} \in \mathbb{H}_d$, then $(\boldsymbol{a}+\boldsymbol{b}) \cdot \boldsymbol{c} = ((a_r + b_r) + \epsilon(a_d + b_d)) \cdot (c_r + \epsilon c_d) = (a_r + b_r) \cdot c_r + \epsilon((a_r + b_r) \cdot c_d + (a_d + b_d) \cdot c_r) = (a_r \cdot c_r + b_r \cdot c_r) + \epsilon(a_r \cdot c_d + b_r \cdot c_d + a_d \cdot c_r + b_d \cdot c_r) = \boldsymbol{a} \cdot \boldsymbol{c} + \boldsymbol{b} \cdot \boldsymbol{c}$ and $\boldsymbol{a} \cdot (\boldsymbol{b} + \boldsymbol{c}) = (a_r + \epsilon a_d) \cdot ((b_r + c_r) + \epsilon(b_d + c_d)) = a_r \cdot (b_r + c_r) + \epsilon(a_d \cdot (b_r + c_r) + a_r \cdot (b_d + c_d)) = (a_r \cdot b_r + a_r \cdot c_r) + \epsilon(a_d \cdot b_r + a_d \cdot c_r + a_r \cdot b_d + a_r \cdot c_d) = \boldsymbol{a} \cdot \boldsymbol{b} + \boldsymbol{a} \cdot \boldsymbol{c}$. □

Lemma 26. *If* $\boldsymbol{a}, \boldsymbol{b}, \boldsymbol{c} \in \mathbb{H}_d$, *then* $(\boldsymbol{a} + \boldsymbol{b}) \circ \boldsymbol{c} = \boldsymbol{a} \circ \boldsymbol{c} + \boldsymbol{b} \circ \boldsymbol{c}$ *and* $\boldsymbol{a} \circ (\boldsymbol{b} + \boldsymbol{c}) = \boldsymbol{a} \circ \boldsymbol{b} + \boldsymbol{a} \circ \boldsymbol{c}$.

Proof. If $\boldsymbol{a}, \boldsymbol{b}, \boldsymbol{c} \in \mathbb{H}_d$, then $(\boldsymbol{a} + \boldsymbol{b}) \circ \boldsymbol{c} = ((a_r + b_r) + \epsilon(a_d + b_d)) \circ (c_r + \epsilon c_d) = a_r \cdot c_r + b_r \cdot c_r + a_d \cdot c_d + b_d \cdot c_d = \boldsymbol{a} \circ \boldsymbol{c} + \boldsymbol{b} \circ \boldsymbol{c}$ and $\boldsymbol{a} \circ (\boldsymbol{b} + \boldsymbol{c}) = (a_r + \epsilon a_d) \circ ((b_r + c_r) + \epsilon(b_d + c_d)) = a_r \cdot b_r + a_r \cdot c_r + a_d \cdot b_d + a_d \cdot c_d = \boldsymbol{a} \circ \boldsymbol{b} + \boldsymbol{a} \circ \boldsymbol{c}$. □

Lemma 27. *If* $\boldsymbol{a}, \boldsymbol{b}, \boldsymbol{c} \in \mathbb{H}_d$, *then* $(\boldsymbol{a} + \boldsymbol{b}) \times \boldsymbol{c} = \boldsymbol{a} \times \boldsymbol{c} + \boldsymbol{b} \times \boldsymbol{c}$ *and* $\boldsymbol{a} \times (\boldsymbol{b} + \boldsymbol{c}) = \boldsymbol{a} \times \boldsymbol{b} + \boldsymbol{a} \times \boldsymbol{c}$.

Proof. If $\boldsymbol{a}, \boldsymbol{b}, \boldsymbol{c} \in \mathbb{H}_d$, then $(\boldsymbol{a}+\boldsymbol{b}) \times \boldsymbol{c} = ((a_r + b_r) + \epsilon(a_d + b_d)) \times (c_r + \epsilon c_d) = (a_r + b_r) \times c_r + \epsilon((a_r + b_r) \times c_d + (a_d + b_d) \times c_r) = (a_r \times c_r + b_r \times c_r) + \epsilon(a_r \times c_d + b_r \times c_d + a_d \times c_r + b_d \times c_r) =$

$\boldsymbol{a}\times\boldsymbol{c}+\boldsymbol{b}\times\boldsymbol{c}$ and $\boldsymbol{a}\times(\boldsymbol{b}+\boldsymbol{c}) = (a_r+\epsilon a_d)\times((b_r+c_r)+\epsilon(b_d+c_d)) = a_r\times(b_r+c_r)+\epsilon(a_d\times(b_r+c_r)+a_r\times(b_d+c_d)) = (a_r\times b_r+a_r\times c_r)+\epsilon(a_d\times b_r+a_d\times c_r+a_r\times b_d+a_r\times c_d) = \boldsymbol{a}\times\boldsymbol{b}+\boldsymbol{a}\times\boldsymbol{c}$.

□

Lemma 28. *If $\boldsymbol{a},\boldsymbol{b}\in\mathbb{H}_d$ and $\lambda\in\mathbb{R}$, then $(\lambda\boldsymbol{a})\cdot\boldsymbol{b} = \boldsymbol{a}\cdot(\lambda\boldsymbol{b}) = \lambda(\boldsymbol{a}\cdot\boldsymbol{b})$.*

Proof. If $\boldsymbol{a},\boldsymbol{b}\in\mathbb{H}_d$ and $\lambda\in\mathbb{R}$, then $(\lambda\boldsymbol{a})\cdot\boldsymbol{b} = ((\lambda a_r)+\epsilon(\lambda a_d))\cdot(b_r+\epsilon b_d) = (\lambda a_r)\cdot b_r+\epsilon((\lambda a_r)\cdot b_d+(\lambda a_d)\cdot b_r) = a_r\cdot(\lambda b_r)+\epsilon(a_r\cdot(\lambda b_d)+a_d\cdot(\lambda b_r)) = \boldsymbol{a}\cdot(\lambda\boldsymbol{b}) = (\lambda(a_r\cdot b_r))+\epsilon(\lambda(a_r\cdot b_d)+\lambda(a_d\cdot b_r)) = \lambda(\boldsymbol{a}\cdot\boldsymbol{b})$. □

Lemma 29. *If $\boldsymbol{a},\boldsymbol{b}\in\mathbb{H}_d$ and $\lambda\in\mathbb{R}$, then $(\lambda\boldsymbol{a})\times\boldsymbol{b} = \boldsymbol{a}\times(\lambda\boldsymbol{b}) = \lambda(\boldsymbol{a}\times\boldsymbol{b})$.*

Proof. If $\boldsymbol{a},\boldsymbol{b}\in\mathbb{H}_d$ and $\lambda\in\mathbb{R}$, then $(\lambda\boldsymbol{a})\times\boldsymbol{b} = ((\lambda a_r)+\epsilon(\lambda a_d))\times(b_r+\epsilon b_d) = (\lambda a_r)\times b_r+\epsilon((\lambda a_r)\times b_d+(\lambda a_d)\times b_r) = a_r\times(\lambda b_r)+\epsilon(a_r\times(\lambda b_d)+a_d\times(\lambda b_r)) = \boldsymbol{a}\times(\lambda\boldsymbol{b}) = (\lambda(a_r\times b_r))+\epsilon(\lambda(a_r\times b_d)+\lambda(a_d\times b_r)) = \lambda(\boldsymbol{a}\times\boldsymbol{b})$. □

Lemma 30. *If $\boldsymbol{a},\boldsymbol{b}\in\mathbb{H}_d$ and $\lambda\in\mathbb{R}$, then $(\lambda\boldsymbol{a})\circ\boldsymbol{b} = \boldsymbol{a}\circ(\lambda\boldsymbol{b}) = \lambda(\boldsymbol{a}\circ\boldsymbol{b})$.*

Proof. If $\boldsymbol{a},\boldsymbol{b}\in\mathbb{H}_d$ and $\lambda\in\mathbb{R}$, then $(\lambda\boldsymbol{a})\circ\boldsymbol{b} = ((\lambda a_r)+\epsilon(\lambda a_d))\circ(b_r+\epsilon b_d) = (\lambda a_r)\cdot b_r+(\lambda a_d)\cdot b_d = a_r\cdot(\lambda b_r)+a_d\cdot(\lambda b_d) = (a_r+\epsilon a_d)\circ((\lambda b_r)+\epsilon(\lambda b_d)) = \boldsymbol{a}\circ(\lambda\boldsymbol{b}) = \lambda(a_r\cdot b_r)+\lambda(a_d\cdot b_d) = \lambda(\boldsymbol{a}\circ\boldsymbol{b})$. □

Lemma 31. *If $\boldsymbol{a},\boldsymbol{b}\in\mathbb{H}_d$, then $(\boldsymbol{a}\boldsymbol{b})^* = \boldsymbol{b}^*\boldsymbol{a}^*$.*

Proof. If $\boldsymbol{a},\boldsymbol{b}\in\mathbb{H}_d$, then $(\boldsymbol{a}\boldsymbol{b})^* = (a_rb_r)^*+\epsilon(a_rb_d+a_db_r)^* = (b_r^*a_r^*)+\epsilon(b_d^*a_r^*+b_r^*a_d^*) = (b_r^*+\epsilon b_d^*)(a_r^*+\epsilon a_d^*) = \boldsymbol{b}^*\boldsymbol{a}^*$. □

Lemma 32. *If $\boldsymbol{a},\boldsymbol{b},\boldsymbol{c}\in\mathbb{H}_d$, then $\boldsymbol{a}\cdot(\boldsymbol{b}\boldsymbol{c}) = \boldsymbol{b}\cdot(\boldsymbol{a}\boldsymbol{c}^*) = \boldsymbol{c}\cdot(\boldsymbol{b}^*\boldsymbol{a})$.*

Proof. If $\boldsymbol{a},\boldsymbol{b},\boldsymbol{c}\in\mathbb{H}_d$, then $\boldsymbol{a}\cdot(\boldsymbol{b}\boldsymbol{c}) = (a_r+\epsilon a_d)\cdot((b_rc_r)+\epsilon(b_rc_d+b_dc_r)) = (a_r\cdot(b_rc_r))+\epsilon(a_r\cdot(b_rc_d)+a_r\cdot(b_dc_r)+a_d\cdot(b_rc_r)) = (c_r\cdot(b_r^*a_r))+\epsilon(c_d\cdot(b_r^*a_r)+c_r\cdot(b_d^*a_r)+c_r\cdot(b_r^*a_d)) = (c_r+\epsilon c_d)\cdot((b_r^*a_r)+\epsilon(b_d^*a_r+b_r^*a_d)) = \boldsymbol{c}\cdot(\boldsymbol{b}^*\boldsymbol{a})$ and $\boldsymbol{a}\cdot(\boldsymbol{b}\boldsymbol{c}) = (a_r\cdot(b_rc_r))+\epsilon(a_r\cdot(b_rc_d)+a_r\cdot(b_dc_r)+a_d\cdot(b_rc_r)) = (b_r\cdot(a_rc_r^*))+\epsilon(b_r\cdot(a_rc_d^*)+b_d\cdot(a_rc_r^*)+b_r\cdot(a_dc_r^*)) = (b_r+\epsilon b_d)\cdot((a_rc_r^*)+\epsilon(a_rc_d^*+a_dc_r^*)) = \boldsymbol{b}\cdot(\boldsymbol{a}\boldsymbol{c}^*)$. □

Lemma 33. *If* $\boldsymbol{a}, \boldsymbol{b}, \boldsymbol{c} \in \mathbb{H}_d$, *then* $\boldsymbol{a} \circ (\boldsymbol{bc}) = \boldsymbol{b}^{\mathsf{s}} \circ (\boldsymbol{a}^{\mathsf{s}}\boldsymbol{c}^*) = \boldsymbol{c}^{\mathsf{s}} \circ (\boldsymbol{b}^*\boldsymbol{a}^{\mathsf{s}})$.

Proof. If $\boldsymbol{a}, \boldsymbol{b}, \boldsymbol{c} \in \mathbb{H}_d$, then $\boldsymbol{a} \circ (\boldsymbol{bc}) = (a_r + \epsilon a_d) \circ ((b_r c_r) + \epsilon(b_r c_d + b_d c_r)) = a_r \cdot (b_r c_r) + a_d \cdot (b_r c_d) + a_d \cdot (b_d c_r) = c_r \cdot (b_r^* a_r) + c_d \cdot (b_r^* a_d) + c_r \cdot (b_d^* a_d) = (c_d + \epsilon c_r) \circ ((b_r^* a_d) + \epsilon(b_r^* a_r + b_d^* a_d)) = (c_d + \epsilon c_r) \circ ((b_r^* + \epsilon b_d^*)(a_d + \epsilon a_r)) = \boldsymbol{c}^{\mathsf{s}} \circ (\boldsymbol{b}^*\boldsymbol{a}^{\mathsf{s}})$ and $\boldsymbol{a} \circ (\boldsymbol{bc}) = a_r \cdot (b_r c_r) + a_d \cdot (b_r c_d) + a_d \cdot (b_d c_r) = b_r \cdot (a_r c_r^*) + b_r \cdot (a_d c_d^*) + b_d \cdot (a_d c_r^*) = (b_d + \epsilon b_r) \circ ((a_d c_r^*) + \epsilon(a_r c_r^* + a_d c_d^*)) = (b_d + \epsilon b_r) \circ ((a_d + \epsilon a_r)(c_r^* + \epsilon c_d^*)) = \boldsymbol{b}^{\mathsf{s}} \circ (\boldsymbol{a}^{\mathsf{s}}\boldsymbol{c}^*)$. □

Lemma 34. *If* $\boldsymbol{a} \in \mathbb{H}_d$, *then* $(\boldsymbol{a}^*)^* = \boldsymbol{a}$.

Proof. If $\boldsymbol{a} \in \mathbb{H}_d$, then $(\boldsymbol{a}^*)^* = (a_r^* + \epsilon a_d^*)^* = a_r + \epsilon a_d = \boldsymbol{a}$. □

Lemma 35. *If* $\boldsymbol{a}, \boldsymbol{b} \in \mathbb{H}_d$, *then* $\boldsymbol{a}^* \cdot \boldsymbol{b}^* = \boldsymbol{a} \cdot \boldsymbol{b}$.

Proof. If $\boldsymbol{a}, \boldsymbol{b} \in \mathbb{H}_d$, then $\boldsymbol{a}^* \cdot \boldsymbol{b}^* = (a_r^* + \epsilon a_d^*) \cdot (b_r^* + \epsilon b_d^*) = (a_r^* \cdot b_r^*) + \epsilon(a_r^* b_d^* + a_d^* b_r^*) = (a_r \cdot b_r) + \epsilon(a_r b_d + a_d b_r) = \boldsymbol{a} \cdot \boldsymbol{b}$. □

Lemma 36. *If* $\boldsymbol{a}, \boldsymbol{b} \in \mathbb{H}_d$, *then* $\boldsymbol{a}^* \circ \boldsymbol{b}^* = \boldsymbol{a} \circ \boldsymbol{b}$.

Proof. If $\boldsymbol{a}, \boldsymbol{b} \in \mathbb{H}_d$, then $\boldsymbol{a}^* \circ \boldsymbol{b}^* = (a_r^* + \epsilon a_d^*) \circ (b_r^* + \epsilon b_d^*) = a_r^* \cdot b_r^* + a_d^* \cdot b_d^* = a_r \cdot b_r + a_d \cdot b_d = \boldsymbol{a} \circ \boldsymbol{b}$. □

Lemma 37. *If* $\boldsymbol{a}, \boldsymbol{b} \in \mathbb{H}_d$, *then* $\boldsymbol{a}^{\mathsf{s}} \circ \boldsymbol{b}^{\mathsf{s}} = \boldsymbol{a} \circ \boldsymbol{b}$.

Proof. If $\boldsymbol{a}, \boldsymbol{b} \in \mathbb{H}_d$, then $\boldsymbol{a}^{\mathsf{s}} \circ \boldsymbol{b}^{\mathsf{s}} = (a_d + \epsilon a_r) \circ (b_d + \epsilon b_r) = a_d \cdot b_d + a_r \cdot b_r = \boldsymbol{a} \circ \boldsymbol{b}$. □

Lemma 38. *If* $\boldsymbol{a}, \boldsymbol{b} \in \mathbb{H}_d$, *then* $\|\boldsymbol{ab}\| \leq \sqrt{3/2}\, \|\boldsymbol{a}\| \|\boldsymbol{b}\|$.

Proof. By definition, $\|\boldsymbol{ab}\|^2 = \|(a_r b_r) + \epsilon(a_r b_d + a_d b_r)\|^2 = \|a_r b_r\|^2 + \|a_r b_d + a_d b_r\|^2 \leq \|a_r b_r\|^2 + (\|a_r b_d\| + \|a_d b_r\|)^2 = \|a_r b_r\|^2 + \|a_r b_d\|^2 + \|a_d b_r\|^2 + 2\|a_r b_d\| \|a_d b_r\| = \|a_r\|^2 \|b_r\|^2 + \|a_r\|^2 \|b_d\|^2 + \|a_d\|^2 \|b_r\|^2 + 2\|a_r\| \|b_d\| \|a_d\| \|b_r\| = \|a_r\|^2 (\|b_r\|^2 + \|b_d\|^2) + \|a_d\|^2 \|b_r\|^2 + 2\|a_r\| \|b_d\| \|a_d\| \|b_r\|$. Using $\|a_r\| \|a_d\| \leq \frac{1}{2}(\|a_r\|^2 + \|a_d\|^2) = \frac{1}{2}\|\boldsymbol{a}\|^2$ and $\|b_r\| \|b_d\| \leq \frac{1}{2}(\|b_r\|^2 + \|b_d\|^2) = \frac{1}{2}\|\boldsymbol{b}\|^2$, yields $\|a_r\| \|b_d\| \|a_d\| \|b_r\| \leq \frac{1}{4}\|\boldsymbol{a}\|^2 \|\boldsymbol{b}\|^2$. It follows that $\|\boldsymbol{ab}\|^2 \leq \|a_r\|^2 \|\boldsymbol{b}\|^2 + \|a_d\|^2 \|\boldsymbol{b}\|^2 + \frac{1}{2}\|\boldsymbol{a}\|^2 \|\boldsymbol{b}\|^2 = (\|a_r\|^2 + \|a_d\|^2) \|\boldsymbol{b}\|^2 + \frac{1}{2}\|\boldsymbol{a}\|^2 \|\boldsymbol{b}\|^2 = \|\boldsymbol{a}\|^2 \|\boldsymbol{b}\|^2 + \frac{1}{2}\|\boldsymbol{a}\|^2 \|\boldsymbol{b}\|^2 = \frac{3}{2}\|\boldsymbol{a}\|^2 \|\boldsymbol{b}\|^2$. The result follows by taking the square root of both sides of the last inequality. □

Lemma 39. *If $\boldsymbol{a}, \boldsymbol{b} \in \mathbb{H}_d$ and $M \in \mathbb{R}^{8\times 8}$, then $(M \star \boldsymbol{a}) \circ \boldsymbol{b} = \boldsymbol{a} \circ (M^{\intercal} \star \boldsymbol{b})$.*

Proof. If $\boldsymbol{a}, \boldsymbol{b} \in \mathbb{H}_d$ and $M \in \mathbb{R}^{8\times 8}$, then $(M \star \boldsymbol{a}) \circ \boldsymbol{b} = ((M_{11} * a_r + M_{12} * a_d) + \epsilon(M_{21} * a_r + M_{22} * a_d)) \circ (b_r + \epsilon b_d) = (M_{11} * a_r) \cdot b_r + (M_{12} * a_d) \cdot b_r + (M_{21} * a_r) \cdot b_d + (M_{22} * a_d) \cdot b_d = a_r \cdot (M_{11}^{\intercal} * b_r) + a_d \cdot (M_{12}^{\intercal} * b_r) + a_r \cdot (M_{21}^{\intercal} * b_d) + a_d \cdot (M_{22}^{\intercal} * b_d) = (a_r + \epsilon a_d) \circ ((M_{11}^{\intercal} * b_r + M_{21}^{\intercal} * b_d) + \epsilon(M_{12}^{\intercal} * b_r + M_{22}^{\intercal} * b_d)) = \boldsymbol{a} \circ (M^{\intercal} \star \boldsymbol{b})$. □

Lemma 40. *If $\boldsymbol{a} \in \mathbb{H}_d$, then $\|\boldsymbol{a}^*\| = \|\boldsymbol{a}\|$.*

Proof. If $\boldsymbol{a} \in \mathbb{H}_d$, then $\|\boldsymbol{a}^*\| = a_r^* \cdot a_r^* + a_d^* \cdot a_d^* = a_r \cdot a_r + a_d \cdot a_d = \|\boldsymbol{a}\|$. □

Lemma 41. *If $\boldsymbol{a} \in \mathbb{H}_d$, then $\|\boldsymbol{a}^{\mathsf{s}}\| = \|\boldsymbol{a}\|$.*

Proof. If $\boldsymbol{a} \in \mathbb{H}_d$, then $\|\boldsymbol{a}^{\mathsf{s}}\| = a_d \cdot a_d + a_r \cdot a_r = \|a\|$. □

Lemma 42. *If $\boldsymbol{a}, \boldsymbol{b} \in \mathbb{H}_d$, then $(\boldsymbol{a} + \boldsymbol{b})^{\mathsf{s}} = \boldsymbol{a}^{\mathsf{s}} + \boldsymbol{b}^{\mathsf{s}}$.*

Proof. If $\boldsymbol{a}, \boldsymbol{b} \in \mathbb{H}_d$, then $(\boldsymbol{a} + \boldsymbol{b})^{\mathsf{s}} = ((a_r + b_r) + \epsilon(a_d + b_d))^{\mathsf{s}} = (a_d + b_d) + \epsilon(a_r + b_r) = (a_d + \epsilon a_r) + (b_d + \epsilon b_r) = \boldsymbol{a}^{\mathsf{s}} + \boldsymbol{b}^{\mathsf{s}}$. □

Lemma 43. *If $\boldsymbol{a}, \boldsymbol{b} \in \mathbb{H}_d$, then $|\boldsymbol{a} \circ \boldsymbol{b}| \leq \|\boldsymbol{a}\|\|\boldsymbol{b}\|$.*

Proof. If $\boldsymbol{a}, \boldsymbol{b} \in \mathbb{H}_d$, then $|\boldsymbol{a} \circ \boldsymbol{b}| = |a_r \cdot b_r + a_d \cdot b_d| \leq |a_r \cdot b_r| + |a_d \cdot b_d| \leq \|a_r\|\|b_r\| + \|a_d\|\|b_d\| \leq \|a_r\|\|b_r\| + \|a_d\|\|b_d\| + \|a_r\|\|b_d\| + \|a_d\|\|b_r\| = \|\boldsymbol{a}\|\|\boldsymbol{b}\|$. □

Lemma 44. *If $\boldsymbol{a}, \boldsymbol{b} \in \mathbb{H}_d$, then $\frac{\mathrm{d}}{\mathrm{d}t}(\boldsymbol{a}\boldsymbol{b}) = \dot{\boldsymbol{a}}\boldsymbol{b} + \boldsymbol{a}\dot{\boldsymbol{b}}$.*

Proof. If $\boldsymbol{a}, \boldsymbol{b} \in \mathbb{H}_d$, then $\frac{\mathrm{d}}{\mathrm{d}t}(\boldsymbol{a}\boldsymbol{b}) = \frac{\mathrm{d}}{\mathrm{d}t}((a_r b_r) + \epsilon(a_r b_d + a_d b_r)) = (\dot{a}_r b_r + a_r \dot{b}_r) + \epsilon(\dot{a}_r b_d + a_r \dot{b}_d + \dot{a}_d b_r + a_d \dot{b}_r) = ((\dot{a}_r b_r) + \epsilon(\dot{a}_r b_d + \dot{a}_d b_r)) + ((a_r \dot{b}_r) + \epsilon(a_r \dot{b}_d + a_d \dot{b}_r)) = \dot{\boldsymbol{a}}\boldsymbol{b} + \boldsymbol{a}\dot{\boldsymbol{b}}$.

□

Lemma 45. *If $\boldsymbol{a}, \boldsymbol{b} \in \mathbb{H}_d$, then $\frac{\mathrm{d}}{\mathrm{d}t}(\boldsymbol{a} \cdot \boldsymbol{b}) = \dot{\boldsymbol{a}} \cdot \boldsymbol{b} + \boldsymbol{a} \cdot \dot{\boldsymbol{b}}$.*

Proof. If $\boldsymbol{a}, \boldsymbol{b} \in \mathbb{H}_d$, then $\frac{\mathrm{d}}{\mathrm{d}t}(\boldsymbol{a} \cdot \boldsymbol{b}) = \frac{\mathrm{d}}{\mathrm{d}t}((a_r \cdot b_r) + \epsilon(a_r \cdot b_d + a_d \cdot b_r)) = (\dot{a}_r \cdot b_r + a_r \cdot \dot{b}_r) + \epsilon(\dot{a}_r \cdot b_d + a_r \cdot \dot{b}_d + \dot{a}_d \cdot b_r + a_d \cdot \dot{b}_r) = ((\dot{a}_r \cdot b_r) + \epsilon(\dot{a}_r \cdot b_d + \dot{a}_d \cdot b_r)) + ((a_r \cdot \dot{b}_r) + \epsilon(a_r \cdot \dot{b}_d + a_d \cdot \dot{b}_r)) = \dot{\boldsymbol{a}} \cdot \boldsymbol{b} + \boldsymbol{a} \cdot \dot{\boldsymbol{b}}$. □

Lemma 46. *If* $\boldsymbol{a}, \boldsymbol{b} \in \mathbb{H}_d$, *then* $\frac{\mathrm{d}}{\mathrm{d}t}(\boldsymbol{a} \times \boldsymbol{b}) = \dot{\boldsymbol{a}} \times \boldsymbol{b} + \boldsymbol{a} \times \dot{\boldsymbol{b}}$.

Proof. If $\boldsymbol{a}, \boldsymbol{b} \in \mathbb{H}_d$, then $\frac{\mathrm{d}}{\mathrm{d}t}(\boldsymbol{a} \times \boldsymbol{b}) = \frac{\mathrm{d}}{\mathrm{d}t}((a_r \times b_r) + \epsilon(a_r \times b_d + a_d \times b_r)) = (\dot{a}_r \times b_r + a_r \times \dot{b}_r) + \epsilon(\dot{a}_r \times b_d + a_r \times \dot{b}_d + \dot{a}_d \times b_r + a_d \times \dot{b}_r) = ((\dot{a}_r \times b_r) + \epsilon(\dot{a}_r \times b_d + \dot{a}_d \times b_r)) + ((a_r \times \dot{b}_r) + \epsilon(a_r \times \dot{b}_d + a_d \times \dot{b}_r)) = \dot{\boldsymbol{a}} \times \boldsymbol{b} + \boldsymbol{a} \times \dot{\boldsymbol{b}}$. □

Lemma 47. *If* $\boldsymbol{a}, \boldsymbol{b} \in \mathbb{H}_d$, *then* $\frac{\mathrm{d}}{\mathrm{d}t}(\boldsymbol{a} \circ \boldsymbol{b}) = \dot{\boldsymbol{a}} \circ \boldsymbol{b} + \boldsymbol{a} \circ \dot{\boldsymbol{b}}$.

Proof. If $\boldsymbol{a}, \boldsymbol{b} \in \mathbb{H}_d$, then $\frac{\mathrm{d}}{\mathrm{d}t}(\boldsymbol{a} \circ \boldsymbol{b}) = \frac{\mathrm{d}}{\mathrm{d}t}(a_r \cdot b_r + a_d \cdot b_d) = \dot{a}_r \cdot b_r + a_r \cdot \dot{b}_r + \dot{a}_d \cdot b_d + a_d \cdot \dot{b}_d = \dot{\boldsymbol{a}} \circ \boldsymbol{b} + \boldsymbol{a} \circ \dot{\boldsymbol{b}}$. □

Lemma 48. *If* $M \in \mathbb{R}^{8\times 8}$ *and* $\boldsymbol{a} \in \mathbb{H}_d$, *then* $\frac{\mathrm{d}}{\mathrm{d}t}(M \star \boldsymbol{a}) = \frac{\mathrm{d}M}{\mathrm{d}t} \star \boldsymbol{a} + M \star \frac{\mathrm{d}\boldsymbol{a}}{\mathrm{d}t}$.

Proof. If $M \in \mathbb{R}^{8\times 8}$ and $\boldsymbol{a} \in \mathbb{H}_d$, then $\frac{\mathrm{d}}{\mathrm{d}t}(M \star \boldsymbol{a}) = \frac{\mathrm{d}}{\mathrm{d}t}((M_{11} * a_r + M_{12} * a_d) + \epsilon(M_{21} * a_r + M_{22} * a_d)) = (\dot{M}_{11} * a_r + M_{11} * \dot{a}_r + \dot{M}_{12} * a_d + M_{12} * \dot{a}_d) + \epsilon(\dot{M}_{21} * a_r + M_{21} * \dot{a}_r + \dot{M}_{22} * a_d + M_{22} * \dot{a}_d) = (\dot{M}_{11} * a_r + \dot{M}_{12} * a_d) + \epsilon(\dot{M}_{21} * a_r + \dot{M}_{22} * a_d) + (M_{11} * \dot{a}_r + M_{12} * \dot{a}_d) + \epsilon(M_{21} * \dot{a}_r + M_{22} * \dot{a}_d) = \dot{M} \star \boldsymbol{a} + M \star \dot{\boldsymbol{a}}$. □

Lemma 49. *If* $M, N \in \mathbb{R}^{8\times 8}$ *and* $\boldsymbol{a} \in \mathbb{H}_d$, *then* $M \star (N \star \boldsymbol{a}) = (MN) \star \boldsymbol{a}$.

Proof. If $M, N \in \mathbb{R}^{8\times 8}$ and $\boldsymbol{a} \in \mathbb{H}_d$, then $M \star (N \star \boldsymbol{a}) = M \star ((N_{11} * a_r + N_{12} * a_d) + \epsilon(N_{21} * a_r + N_{22} * a_d)) = [M_{11} * (N_{11} * a_r) + M_{11} * (N_{12} * a_d) + M_{12} * (N_{21} * a_r) + M_{12} * (N_{22} * a_d)] + \epsilon[M_{21} * (N_{11} * a_r) + M_{21} * (N_{12} * a_d) + M_{22} * (N_{21} * a_r) + M_{22} * (N_{22} * a_d)] = [(M_{11}N_{11}) * a_r + (M_{11}N_{12}) * a_d + (M_{12}N_{21}) * a_r + (M_{12}N_{22}) * a_d)] + \epsilon[(M_{21}N_{11}) * a_r + (M_{21}N_{12}) * a_d + (M_{22}N_{21}) * a_r + (M_{22}N_{22}) * a_d] = [(M_{11}N_{11} + M_{12}N_{21}) * a_r + (M_{11}N_{12} + M_{12}N_{22}) * a_d] + \epsilon[(M_{21}N_{11} + M_{22}N_{21}) * a_r + (M_{21}N_{12} + M_{22}N_{22}) * a_d] = (MN) \star \boldsymbol{a}$. □

Lemma 50. *If* $M, N \in \mathbb{R}^{8\times 8}$ *and* $\boldsymbol{a} \in \mathbb{H}_d$, *then* $(M + N) \star \boldsymbol{a} = M \star \boldsymbol{a} + N \star \boldsymbol{a}$.

Proof. If $M, N \in \mathbb{R}^{8\times 8}$ and $\boldsymbol{a} \in \mathbb{H}_d$, then $(M + N) \star \boldsymbol{a} = [(M_{11} + N_{11}) * a_r + (M_{12} + N_{12}) * a_d] + \epsilon[(M_{21} + N_{21}) * a_r + (M_{22} + N_{22}) * a_d] = [M_{11} * a_r + N_{11} * a_r + M_{12} * a_d + N_{12} * a_d] + \epsilon[M_{21} * a_r + N_{21} * a_r + M_{22} * a_d + N_{22} * a_d] = M \star \boldsymbol{a} + N \star \boldsymbol{a}$. □

Lemma 51. *If $M \in \mathbb{R}^{8\times 8}$ and $\boldsymbol{a}, \boldsymbol{b} \in \mathbb{H}_d$, then $M \star (\boldsymbol{a} + \boldsymbol{b}) = M \star \boldsymbol{a} + M \star \boldsymbol{b}$.*

Proof. If $M \in \mathbb{R}^{8\times 8}$ and $\boldsymbol{a}, \boldsymbol{b} \in \mathbb{H}_d$, then $M \star (\boldsymbol{a} + \boldsymbol{b}) = M \star [(a_r + b_r) + \epsilon(a_d + b_d)] = [M_{11} * a_r + M_{11} * b_r + M_{12} * a_d + M_{12} * b_d] + \epsilon[M_{21} * a_r + M_{21} * b_r + M_{22} * a_d + M_{22} * b_d] = M \star \boldsymbol{a} + M \star \boldsymbol{b}$. □

Lemma 52. *Let $M \in \mathbb{R}^{8\times 8}$ be a symmetric (i.e., $M = M^\intercal$) positive-definite matrix (i.e., $x^\intercal M x > 0$, $x \neq 0$) of the form*

$$M = \begin{bmatrix} M_{11} & M_{12} \\ M_{12}^\intercal & M_{22} \end{bmatrix}, \quad M_{11}, M_{12}, M_{22} \in \mathbb{R}^{4\times 4}. \tag{41}$$

Then, the function $V_1 : \mathbb{H}_d \to \mathbb{R}$ defined as $V_1(\boldsymbol{a}) = \boldsymbol{a} \otimes (M \star \boldsymbol{a})$ satisfies $V_1(\boldsymbol{a}) > 0$ for $\boldsymbol{a} \in \mathbb{H}_d \backslash \{\mathtt{0}\}$ and $V_1(\boldsymbol{a}) \to \infty$ as $\|\boldsymbol{a}\| \to \infty$.

Moreover, if $N \in \mathbb{R}^{8\times 8}$ is of the form

$$N = \begin{bmatrix} N_{11} & N_{12} & N_{13} & N_{14} \\ N_{21} & N_{22} & N_{23} & N_{24} \\ N_{31} & N_{32} & N_{33} & N_{34} \\ N_{41} & N_{24}^\intercal & N_{43} & N_{44} \end{bmatrix} \tag{42}$$

where $N_{11}, N_{13}, N_{31}, N_{33} \in \mathbb{R}$, $N_{12}, N_{14}, N_{32}, N_{34} \in \mathbb{R}^{1\times 3}$, $N_{22}, N_{24}, N_{44} \in \mathbb{R}^{3\times 3}$, and $N_{21}, N_{23}, N_{41}, N_{43} \in \mathbb{R}^{3\times 1}$, and the submatrix

$$\bar{N} = \begin{bmatrix} N_{22} & N_{24} \\ N_{24}^\intercal & N_{44} \end{bmatrix} \in \mathbb{R}^{6\times 6} \tag{43}$$

is a symmetric positive-definite matrix, then the function $V_2 : \mathbb{H}_d^v \to \mathbb{R}$ defined as $V_2(\boldsymbol{a}) = \boldsymbol{a} \otimes (N \star \boldsymbol{a})$ satisfies $V_2(\boldsymbol{a}) > 0$ for $\boldsymbol{a} \in \mathbb{H}_d^v \backslash \{\mathtt{0}\}$ and $V_2(\boldsymbol{a}) \to \infty$ as $\|\boldsymbol{a}\| \to \infty$.

Proof. By definition, $V_1(\boldsymbol{a}) = \boldsymbol{a} \otimes (M \star \boldsymbol{a}) = (a_r + \epsilon a_d) \otimes ((M_{11} * a_r + M_{12} * a_d) + \epsilon(M_{12}^\intercal * a_r + M_{22} * a_d)) = a_r \cdot (M_{11} * a_r) + a_r \cdot (M_{12} * a_d) + a_d \cdot (M_{12}^\intercal * a_r) + a_d \cdot (M_{22} * a_d) = ([a_{r,0}\ \bar{a}_r^\intercal\ a_{d,0}\ \bar{a}_d^\intercal] M [a_{r,0}\ \bar{a}_r^\intercal\ a_{d,0}\ \bar{a}_d^\intercal]^\intercal, \bar{0})$, which is strictly positive for all $\boldsymbol{a} \in \mathbb{H}_d \backslash \{\mathtt{0}\}$ and radially unbounded since M is a symmetric positive-definite matrix. Likewise,

$V_2(\boldsymbol{a}) = \boldsymbol{a} \otimes (N * \boldsymbol{a}) = ([0\ \overline{a}_r^{\mathsf{T}}\ 0\ \overline{a}_d^{\mathsf{T}}]N[0\ \overline{a}_r^{\mathsf{T}}\ 0\ \overline{a}_d^{\mathsf{T}}]^{\mathsf{T}}, \bar{0}) = ([\overline{a}_r^{\mathsf{T}}\ \overline{a}_d^{\mathsf{T}}]\bar{N}[\overline{a}_r^{\mathsf{T}}\ \overline{a}_d^{\mathsf{T}}]^{\mathsf{T}}, \bar{0})$, which is strictly positive for all $\boldsymbol{a} \in \mathbb{H}_d^v \backslash \{0\}$ and radially unbounded since $\bar{N}$ is a symmetric positive-definite matrix. □

Lemma 53. *The unit dual quaternion* $\boldsymbol{q}_{\mathrm{Y/Z}} = q_{\mathrm{Y/Z}} + \epsilon\frac{1}{2} q_{\mathrm{Y/Z}} r^{\mathrm{Y}}_{\mathrm{Y/Z}} \in \mathcal{L}_\infty$ *(where* $q_{\mathrm{Y/Z}}$ *is a unit quaternion), if and only if* $r^{\mathrm{Y}}_{\mathrm{Y/Z}} \in \mathcal{L}_\infty$.

Proof. If $\boldsymbol{q}_{\mathrm{Y/Z}} \in \mathcal{L}_\infty$, then $q_{\mathrm{Y/Z}} r^{\mathrm{Y}}_{\mathrm{Y/Z}} \in \mathcal{L}_\infty$. Note that the unit quaternion $q_{\mathrm{Y/Z}} \in \mathcal{L}_\infty$ by definition. Moreover, since $\|q_{\mathrm{Y/Z}} r^{\mathrm{Y}}_{\mathrm{Y/Z}}\| = \|r^{\mathrm{Y}}_{\mathrm{Y/Z}}\|$, this also implies that $r^{\mathrm{Y}}_{\mathrm{Y/Z}} \in \mathcal{L}_\infty$. On the other hand, it is trivial to see that if $q_{\mathrm{Y/Z}}, r^{\mathrm{Y}}_{\mathrm{Y/Z}} \in \mathcal{L}_\infty$, then $\boldsymbol{q}_{\mathrm{Y/Z}} = q_{\mathrm{Y/Z}} + \epsilon\frac{1}{2} q_{\mathrm{Y/Z}} r^{\mathrm{Y}}_{\mathrm{Y/Z}} \in \mathcal{L}_\infty$ as well. □

It can also be shown that the following properties hold for dual vector quaternions.

Lemma 54. *If* $\boldsymbol{a}, \boldsymbol{b}, \boldsymbol{c} \in \mathbb{H}_d^v$, *then* $\boldsymbol{a} \cdot (\boldsymbol{b} \times \boldsymbol{c}) = \boldsymbol{b} \cdot (\boldsymbol{c} \times \boldsymbol{a}) = \boldsymbol{c} \cdot (\boldsymbol{a} \times \boldsymbol{b})$.

Proof. If $\boldsymbol{a}, \boldsymbol{b}, \boldsymbol{c} \in \mathbb{H}_d^v$, then $\boldsymbol{a} \cdot (\boldsymbol{b} \times \boldsymbol{c}) = (a_r + \epsilon a_d) \cdot ((b_r \times c_r) + \epsilon(b_r \times c_d + b_d \times c_r)) = (a_r \cdot (b_r \times c_r)) + \epsilon(a_r \cdot (b_r \times c_d) + a_r \cdot (b_d \times c_r) + a_d \cdot (b_r \times c_r)) = (b_r \cdot (c_r \times a_r)) + \epsilon(b_r \cdot (c_d \times a_r) + b_d \cdot (c_r \times a_r) + b_r \cdot (c_r \times a_d)) = (b_r + \epsilon b_d) \cdot ((c_r \times a_r) + \epsilon(c_d \times a_r + c_r \times a_d)) = \boldsymbol{b} \cdot (\boldsymbol{c} \times \boldsymbol{a})$ and $\boldsymbol{a} \cdot (\boldsymbol{b} \times \boldsymbol{c}) = (a_r \cdot (b_r \times c_r)) + \epsilon(a_r \cdot (b_r \times c_d) + a_r \cdot (b_d \times c_r) + a_d \cdot (b_r \times c_r)) = (c_r \cdot (a_r \times b_r)) + \epsilon(c_d \cdot (a_r \times b_r) + c_r \cdot (a_r \times b_d) + c_r \cdot (a_d \times b_r)) = (c_r + \epsilon c_d) \cdot ((a_r \times b_r) + \epsilon(a_r \times b_d + a_d \times b_r)) = \boldsymbol{c} \cdot (\boldsymbol{a} \times \boldsymbol{b})$. □

Lemma 55. *If* $\boldsymbol{a}, \boldsymbol{b}, \boldsymbol{c} \in \mathbb{H}_d^v$, *then* $\boldsymbol{a} \circ (\boldsymbol{b} \times \boldsymbol{c}) = \boldsymbol{b}^{\mathsf{s}} \circ (\boldsymbol{c} \times \boldsymbol{a}^{\mathsf{s}}) = \boldsymbol{c}^{\mathsf{s}} \circ (\boldsymbol{a}^{\mathsf{s}} \times \boldsymbol{b})$.

Proof. If $\boldsymbol{a}, \boldsymbol{b}, \boldsymbol{c} \in \mathbb{H}_d^v$, then $\boldsymbol{a} \circ (\boldsymbol{b} \times \boldsymbol{c}) = (a_r + \epsilon a_d) \circ ((b_r \times c_r) + \epsilon(b_r \times c_d + b_d \times c_r)) = a_r \cdot (b_r \times c_r) + a_d \cdot (b_r \times c_d) + a_d \cdot (b_d \times c_r) = c_r \cdot (a_r \times b_r) + c_d \cdot (a_d \times b_r) + c_r \cdot (a_d \times b_d) = (c_d + \epsilon c_r) \otimes ((a_d \times b_r) + \epsilon(a_r \times b_r + a_d \times b_d)) = \boldsymbol{c}^{\mathsf{s}} \circ (\boldsymbol{a}^{\mathsf{s}} \times \boldsymbol{b})$ and $\boldsymbol{a} \circ (\boldsymbol{b} \times \boldsymbol{c}) = a_r \cdot (b_r \times c_r) + a_d \cdot (b_r \times c_d) + a_d \cdot (b_d \times c_r) = b_r \cdot (c_r \times a_r) + b_r \cdot (c_d \times a_d) + b_d \cdot (c_r \times a_d) = (b_d + \epsilon b_r) \otimes ((c_r \times a_d) + \epsilon(c_r \times a_r + c_d \times a_d)) = \boldsymbol{b}^{\mathsf{s}} \circ (\boldsymbol{c} \times \boldsymbol{a}^{\mathsf{s}})$. □

Lemma 56. *If* $\boldsymbol{a} \in \mathbb{H}_d^v$, *then* $\boldsymbol{a} \times \boldsymbol{a} = \boldsymbol{0}$.

Proof. If $\boldsymbol{a} \in \mathbb{H}_d^v$, then $\boldsymbol{a} \times \boldsymbol{a} = (a_r \times a_r) + \epsilon(a_r \times a_d + a_d \times a_r) = 0 + \epsilon(a_r \times a_d - a_r \times a_d) = \mathbf{0}$. □

Lemma 57. *If* $\boldsymbol{a}, \boldsymbol{b} \in \mathbb{H}_d^v$, *then* $\boldsymbol{a} \times \boldsymbol{b} = -\boldsymbol{b} \times \boldsymbol{a}$.

Proof. If $\boldsymbol{a}, \boldsymbol{b} \in \mathbb{H}_d^v$, then $\boldsymbol{a} \times \boldsymbol{b} = (a_r \times b_r) + \epsilon(a_r \times b_d + a_d \times b_r) = -((b_r \times a_r) + \epsilon((b_d \times a_r + b_r \times a_d))) = -\boldsymbol{b} \times \boldsymbol{a}$. □

2.2.1 Attitude and Position Representation with Unit Dual Quaternions

The position and orientation, i.e., *pose*, of a body frame with respect to an inertial frame can be represented by a unit quaternion and by a translation vector. Alternatively, the pose of a body frame with respect to an inertial frame can be represented more compactly by the *unit dual quaternion* [105]

$$\boldsymbol{q}_{\mathrm{B/I}} = q_{\mathrm{B/I},r} + \epsilon q_{\mathrm{B/I},d} = q_{\mathrm{B/I}} + \epsilon \tfrac{1}{2} r^{\mathrm{I}}_{\mathrm{B/I}} q_{\mathrm{B/I}} = q_{\mathrm{B/I}} + \epsilon \tfrac{1}{2} q_{\mathrm{B/I}} r^{\mathrm{B}}_{\mathrm{B/I}}, \tag{44}$$

where $r^{\mathrm{X}}_{\mathrm{Y/Z}} = (0, \bar{r}^{\mathrm{X}}_{\mathrm{Y/Z}})$ and $\bar{r}^{\mathrm{X}}_{\mathrm{Y/Z}} = [x^{\mathrm{X}}_{\mathrm{Y/Z}}, y^{\mathrm{X}}_{\mathrm{Y/Z}}, z^{\mathrm{X}}_{\mathrm{Y/Z}}]^{\intercal}$ is the translation vector from the origin of the Z-frame to the origin of the Y-frame expressed in the X-frame. Note that the dual part of $\boldsymbol{q}_{\mathrm{B/I}}$, i.e., $q_{\mathrm{B/I},d}$, is a representation of the position of the body frame with respect to the inertial frame that is neither expressed in the B-frame nor in the I-frame. Given the unit dual quaternion $\boldsymbol{q}_{\mathrm{B/I}} = q_{\mathrm{B/I},r} + \epsilon q_{\mathrm{B/I},d}$, $r^{\mathrm{B}}_{\mathrm{B/I}}$ and $r^{\mathrm{I}}_{\mathrm{B/I}}$ can be recovered through

$$r^{\mathrm{I}}_{\mathrm{B/I}} = 2 q_{\mathrm{B/I},d} q^*_{\mathrm{B/I},r} \quad \text{and} \quad r^{\mathrm{B}}_{\mathrm{B/I}} = 2 q^*_{\mathrm{B/I},r} q_{\mathrm{B/I},d}. \tag{45}$$

Figure 1 illustrates the relation between $r^{\mathrm{B}}_{\mathrm{B/I}}$, $q_{\mathrm{B/I},d}$, and $r^{\mathrm{I}}_{\mathrm{B/I}}$. Note that whereas the relation between $r^{\mathrm{B}}_{\mathrm{B/I}}$ and $r^{\mathrm{I}}_{\mathrm{B/I}}$ is quadratic in $q_{\mathrm{B/I}}$, the relation between $q_{\mathrm{B/I},d}$ and $r^{\mathrm{B}}_{\mathrm{B/I}}$ and between $q_{\mathrm{B/I},d}$ and $r^{\mathrm{I}}_{\mathrm{B/I}}$ is linear in $q_{\mathrm{B/I}}$.

Lemma 58. *The dual quaternion given by Eq.* (44) *is a unit dual quaternion, i.e.,* $\boldsymbol{q}_{\mathrm{B/I}} \in \mathbb{H}_d^u = \{\boldsymbol{q} \in \mathbb{H}_d : \ \boldsymbol{q} \cdot \boldsymbol{q} = \boldsymbol{q}\boldsymbol{q}^* = \boldsymbol{q}^*\boldsymbol{q} = \|\boldsymbol{q}\|_d = \mathbf{1}\}$.

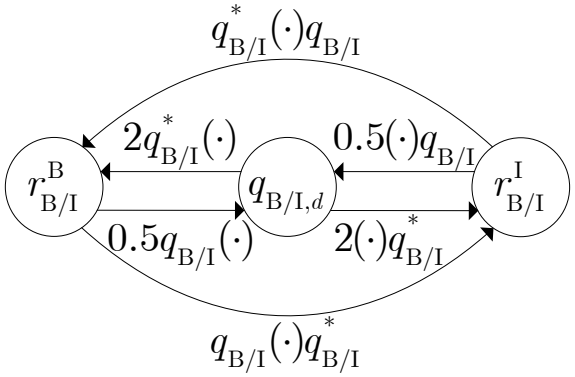

Figure 1: Relation between the different representations of position.

Proof. First, note that $\boldsymbol{q} \cdot \boldsymbol{q} = q_r \cdot q_r + \epsilon(q_r \cdot q_d + q_d \cdot q_r) = q_r \cdot q_r + \epsilon(2q_r \cdot q_d)$. Hence, for a dual quaternion to be a unit dual quaternion, it must satisfy two algebraic constraints,

$$q_r \cdot q_r = \mathtt{1} \quad \text{and} \quad q_r \cdot q_d = \mathtt{0}. \tag{46}$$

The dual quaternion given by Eq. (44) satisfies these two algebraic constraints since $q_r \cdot q_r = q_{\mathrm{B/I}} \cdot q_{\mathrm{B/I}} = \mathtt{1}$ and $q_r \cdot q_d = q_{\mathrm{B/I}} \cdot (\frac{1}{2} r^{\mathrm{I}}_{\mathrm{B/I}} q_{\mathrm{B/I}}) = (\frac{1}{2} r^{\mathrm{I}}_{\mathrm{B/I}}) \cdot (q_{\mathrm{B/I}} q^*_{\mathrm{B/I}}) = (\frac{1}{2} r^{\mathrm{I}}_{\mathrm{B/I}}) \cdot \mathtt{1} = \mathtt{0}$. □

Since only three elements are necessary to represent a rotation, a unit quaternion, which has four elements, must satisfy one algebraic constraint. Likewise, since only six elements are necessary to represent a pose, a unit dual quaternion, which has eight elements, must satisfy two algebraic constraints, given by Eq. (46). From these constraints and assuming that $-180 < \phi < 180$ deg, the scalar parts of the real and dual parts of a unit dual quaternion can be computed from their respective vector parts from

$$q_{r,0} = \sqrt{1 - \|\overline{q}_r\|^2} \quad \text{and} \quad q_{d,0} = \frac{-\overline{q_r}^{\mathsf{T}} \overline{q_d}}{q_{r,0}}. \tag{47}$$

In the same way as unit quaternions can be used to transform the coordinates of a vector quaternion between frames, unit dual quaternions can be used to transform the coordinates of a dual vector quaternion between frames, with a small caveat. This result is presented in the next lemma.

Lemma 59. *Given a dual vector quaternion expressed in frame Y, $\boldsymbol{v}^{\mathrm{Y}} = v_r^{\mathrm{Y}} + \epsilon v_d^{\mathrm{Y}}$, and the unit dual quaternion describing the pose of frame X with respect to frame Y, $\boldsymbol{q}_{\mathrm{X/Y}} = q_{\mathrm{X/Y}} + \epsilon\frac{1}{2} q_{\mathrm{X/Y}} r^{\mathrm{X}}_{\mathrm{X/Y}} = q_{\mathrm{X/Y}} + \epsilon\frac{1}{2} r^{\mathrm{Y}}_{\mathrm{X/Y}} q_{\mathrm{X/Y}}$, then*

$$\boldsymbol{v}^{\mathrm{X}} \triangleq \boldsymbol{q}^*_{\mathrm{X/Y}} \boldsymbol{v}^{\mathrm{Y}} \boldsymbol{q}_{\mathrm{X/Y}} = v_r^{\mathrm{X}} + \epsilon(v_d^{\mathrm{X}} + v_r^{\mathrm{X}} \times r^{\mathrm{X}}_{\mathrm{X/Y}}). \tag{48}$$

Likewise, given a dual vector quaternion expressed in frame X, $\boldsymbol{v}^{\mathrm{X}} = v_r^{\mathrm{X}} + \epsilon v_d^{\mathrm{X}}$, and $\boldsymbol{q}_{\mathrm{X/Y}}$, then

$$\boldsymbol{v}^{\mathrm{Y}} \triangleq \boldsymbol{q}_{\mathrm{X/Y}} \boldsymbol{v}^{\mathrm{X}} \boldsymbol{q}^*_{\mathrm{X/Y}} = v_r^{\mathrm{Y}} + \epsilon(v_d^{\mathrm{Y}} - v_r^{\mathrm{Y}} \times r^{\mathrm{Y}}_{\mathrm{X/Y}}). \tag{49}$$

Proof. By definition,

$$\begin{aligned}
\boldsymbol{q}^*_{\mathrm{X/Y}} \boldsymbol{v}^{\mathrm{Y}} \boldsymbol{q}_{\mathrm{X/Y}} &= (q_{\mathrm{X/Y}} + \epsilon\tfrac{1}{2} q_{\mathrm{X/Y}} r^{\mathrm{X}}_{\mathrm{X/Y}})^* (v_r^{\mathrm{Y}} + \epsilon v_d^{\mathrm{Y}})(q_{\mathrm{X/Y}} + \epsilon\tfrac{1}{2} q_{\mathrm{X/Y}} r^{\mathrm{X}}_{\mathrm{X/Y}}) \\
&= (q_{\mathrm{X/Y}} + \epsilon\tfrac{1}{2} q_{\mathrm{X/Y}} r^{\mathrm{X}}_{\mathrm{X/Y}})^* (v_r^{\mathrm{Y}} q_{\mathrm{X/Y}} + \epsilon(v_r^{\mathrm{Y}} \tfrac{1}{2} q_{\mathrm{X/Y}} r^{\mathrm{X}}_{\mathrm{X/Y}} + v_d^{\mathrm{Y}} q_{\mathrm{X/Y}})) \\
&= q^*_{\mathrm{X/Y}} v_r^{\mathrm{Y}} q_{\mathrm{X/Y}} + \epsilon(\tfrac{1}{2}(r^{\mathrm{X}}_{\mathrm{X/Y}})^* q^*_{\mathrm{X/Y}} v_r^{\mathrm{Y}} q_{\mathrm{X/Y}} + q^*_{\mathrm{X/Y}} v_r^{\mathrm{Y}} \tfrac{1}{2} q_{\mathrm{X/Y}} r^{\mathrm{X}}_{\mathrm{X/Y}} + q^*_{\mathrm{X/Y}} v_d^{\mathrm{Y}} q_{\mathrm{X/Y}}) \\
&= v_r^{\mathrm{X}} + \epsilon(\tfrac{1}{2}(r^{\mathrm{X}}_{\mathrm{X/Y}})^* v_r^{\mathrm{X}} + \tfrac{1}{2} v_r^{\mathrm{X}} r^{\mathrm{X}}_{\mathrm{X/Y}} + v_d^{\mathrm{X}}) \\
&= v_r^{\mathrm{X}} + \epsilon(v_d^{\mathrm{X}} + \tfrac{1}{2} v_r^{\mathrm{X}} r^{\mathrm{X}}_{\mathrm{X/Y}} - \tfrac{1}{2}(r^{\mathrm{X}}_{\mathrm{X/Y}})^* (v_r^{\mathrm{X}})^*) = v_r^{\mathrm{X}} + \epsilon(v_d^{\mathrm{X}} + v_r^{\mathrm{X}} \times r^{\mathrm{X}}_{\mathrm{X/Y}}),
\end{aligned}$$

$$\begin{aligned}
\boldsymbol{q}_{\mathrm{X/Y}} \boldsymbol{v}^{\mathrm{X}} \boldsymbol{q}^*_{\mathrm{X/Y}} &= (q_{\mathrm{X/Y}} + \epsilon\tfrac{1}{2} q_{\mathrm{X/Y}} r^{\mathrm{X}}_{\mathrm{X/Y}})(v_r^{\mathrm{X}} + \epsilon v_d^{\mathrm{X}})(q_{\mathrm{X/Y}} + \epsilon\tfrac{1}{2} q_{\mathrm{X/Y}} r^{\mathrm{X}}_{\mathrm{X/Y}})^* \\
&= (q_{\mathrm{X/Y}} + \epsilon\tfrac{1}{2} q_{\mathrm{X/Y}} r^{\mathrm{X}}_{\mathrm{X/Y}})(v_r^{\mathrm{X}} q^*_{\mathrm{X/Y}} + \epsilon(v_r^{\mathrm{X}} \tfrac{1}{2}(r^{\mathrm{X}}_{\mathrm{X/Y}})^* q^*_{\mathrm{X/Y}} + v_d^{\mathrm{X}} q^*_{\mathrm{X/Y}})) \\
&= q_{\mathrm{X/Y}} v_r^{\mathrm{X}} q^*_{\mathrm{X/Y}} + \epsilon(\tfrac{1}{2} q_{\mathrm{X/Y}} r^{\mathrm{X}}_{\mathrm{X/Y}} v_r^{\mathrm{X}} q^*_{\mathrm{X/Y}} + q_{\mathrm{X/Y}} v_r^{\mathrm{X}} \tfrac{1}{2}(r^{\mathrm{X}}_{\mathrm{X/Y}})^* q^*_{\mathrm{X/Y}} + q_{\mathrm{X/Y}} v_d^{\mathrm{X}} q^*_{\mathrm{X/Y}}) \\
&= v_r^{\mathrm{Y}} + \epsilon(\tfrac{1}{2} q_{\mathrm{X/Y}} r^{\mathrm{X}}_{\mathrm{X/Y}} q^*_{\mathrm{X/Y}} q_{\mathrm{X/Y}} v_r^{\mathrm{X}} q^*_{\mathrm{X/Y}} + q_{\mathrm{X/Y}} v_r^{\mathrm{X}} q^*_{\mathrm{X/Y}} q_{\mathrm{X/Y}} \tfrac{1}{2}(r^{\mathrm{X}}_{\mathrm{X/Y}})^* q^*_{\mathrm{X/Y}} + v_d^{\mathrm{Y}}) \\
&= v_r^{\mathrm{Y}} + \epsilon(v_d^{\mathrm{Y}} + \tfrac{1}{2} r^{\mathrm{Y}}_{\mathrm{X/Y}} v_r^{\mathrm{Y}} + \tfrac{1}{2} v_r^{\mathrm{Y}} (r^{\mathrm{Y}}_{\mathrm{X/Y}})^*) \\
&= v_r^{\mathrm{Y}} + \epsilon(v_d^{\mathrm{Y}} + \tfrac{1}{2} r^{\mathrm{Y}}_{\mathrm{X/Y}} v_r^{\mathrm{Y}} - \tfrac{1}{2}(v_r^{\mathrm{Y}})^* (r^{\mathrm{Y}}_{\mathrm{X/Y}})^*) \\
&= v_r^{\mathrm{Y}} + \epsilon(v_d^{\mathrm{Y}} + r^{\mathrm{Y}}_{\mathrm{X/Y}} \times v_r^{\mathrm{Y}}) = v_r^{\mathrm{Y}} + \epsilon(v_d^{\mathrm{Y}} - v_r^{\mathrm{Y}} \times r^{\mathrm{Y}}_{\mathrm{X/Y}}).
\end{aligned}$$

□

Note that whereas it might seem intuitive that $\boldsymbol{q}^*_{\mathrm{X/Y}} \boldsymbol{v}^{\mathrm{Y}} \boldsymbol{q}_{\mathrm{X/Y}} = v_r^{\mathrm{X}} + \epsilon v_d^{\mathrm{X}}$ and $\boldsymbol{q}_{\mathrm{X/Y}} \boldsymbol{v}^{\mathrm{X}} \boldsymbol{q}^*_{\mathrm{X/Y}} = v_r^{\mathrm{Y}} + \epsilon v_d^{\mathrm{Y}}$, Lemma 59 shows that this is not true. An extra term appears in the dual part of the transformed dual vector quaternion, as shown in Eq. (48) and Eq. (49).

The following lemma shows that in the same way as $q_{\mathrm{Y/Z}}$ and $-q_{\mathrm{Y/Z}}$ represent the same relative orientation between frames, $\boldsymbol{q}_{\mathrm{Y/Z}}$ and $-\boldsymbol{q}_{\mathrm{Y/Z}}$ represent the same relative pose between frames.

Lemma 60. *Let the relative pose of frame Y with respect to frame Z be given by the unit dual quaternion $\boldsymbol{q}_{\mathrm{Y/Z}}$. Then, $\boldsymbol{q}_{\mathrm{Y/Z}}$ and $-\boldsymbol{q}_{\mathrm{Y/Z}}$ represent the same relative pose between the two frames.*

Proof. According to Lemma 22, $q_{\mathrm{Y/Z}}$ and $-q_{\mathrm{Y/Z}}$ represent the same relative orientation between the two frames. Hence, $\boldsymbol{q}_{\mathrm{Y/Z}} = q_{\mathrm{Y/Z}} + \epsilon\frac{1}{2} r^{\mathrm{Z}}_{\mathrm{Y/Z}} q_{\mathrm{Y/Z}}$ and $(-q_{\mathrm{Y/Z}}) + \epsilon\frac{1}{2} r^{\mathrm{Z}}_{\mathrm{Y/Z}}(-q_{\mathrm{Y/Z}}) = -\boldsymbol{q}_{\mathrm{Y/Z}}$ represent the same relative pose between the two frames. □

In particular, when $\boldsymbol{q}_{\mathrm{Y/Z}} = \mathbf{1}$ and $\boldsymbol{q}_{\mathrm{Y/Z}} = -\mathbf{1}$, the two frames have the same pose.

2.2.2 Dual Quaternion Representation of the Relative Rotational and Translational Kinematic Equations

The following proposition shows that the combined rotational and translational kinematic equations written using dual quaternion algebra and the rotational-only kinematic equations written using quaternion algebra, given by Eq. (21), have the same form.

Proposition 1. *The combined rotational and translational kinematic equations of frame X with respect to frame Y written using dual quaternion algebra are [105]*

$$\dot{\boldsymbol{q}}_{\mathrm{X/Y}} = \tfrac{1}{2}\boldsymbol{\omega}^{\mathrm{Y}}_{\mathrm{X/Y}}\boldsymbol{q}_{\mathrm{X/Y}} = \tfrac{1}{2}\boldsymbol{q}_{\mathrm{X/Y}}\boldsymbol{\omega}^{\mathrm{X}}_{\mathrm{X/Y}}, \tag{50}$$

where $\boldsymbol{\omega}^{\mathrm{X}}_{\mathrm{Y/Z}}$ is the dual velocity of the Y-frame with respect to the Z-frame expressed in the X-frame, so that $\boldsymbol{\omega}^{\mathrm{X}}_{\mathrm{Y/Z}} = \omega^{\mathrm{X}}_{\mathrm{Y/Z}} + \epsilon(v^{\mathrm{X}}_{\mathrm{Y/Z}} + \omega^{\mathrm{X}}_{\mathrm{Y/Z}} \times r^{\mathrm{X}}_{\mathrm{X/Y}})$, $\omega^{\mathrm{X}}_{\mathrm{Y/Z}} = (0, \bar{\omega}^{\mathrm{X}}_{\mathrm{Y/Z}})$, $\bar{\omega}^{\mathrm{X}}_{\mathrm{Y/Z}} = [p^{\mathrm{X}}_{\mathrm{Y/Z}}, q^{\mathrm{X}}_{\mathrm{Y/Z}}, r^{\mathrm{X}}_{\mathrm{Y/Z}}]^{\intercal}$ is the angular velocity of the Y-frame with respect to the Z-frame expressed in the X-frame, $v^{\mathrm{X}}_{\mathrm{Y/Z}} = (0, \bar{v}^{\mathrm{X}}_{\mathrm{Y/Z}})$, and $\bar{v}^{\mathrm{X}}_{\mathrm{Y/Z}} = [u^{\mathrm{X}}_{\mathrm{Y/Z}}, v^{\mathrm{X}}_{\mathrm{Y/Z}}, w^{\mathrm{X}}_{\mathrm{Y/Z}}]^{\intercal}$ is the linear velocity of the origin of the Y-frame with respect to the Z-frame expressed in the X-frame.

Proof. The time derivative of $\boldsymbol{q}_{\mathrm{X/Y}} = q_{\mathrm{X/Y}} + \epsilon\frac{1}{2}r^{\mathrm{Y}}_{\mathrm{X/Y}}q_{\mathrm{X/Y}}$ is given by $\dot{\boldsymbol{q}}_{\mathrm{X/Y}} = \dot{q}_{\mathrm{X/Y}} + \epsilon\frac{1}{2}\dot{r}^{\mathrm{Y}}_{\mathrm{X/Y}}q_{\mathrm{X/Y}} + \epsilon\frac{1}{2}r^{\mathrm{Y}}_{\mathrm{X/Y}}\dot{q}_{\mathrm{X/Y}}$. Using Eq. (21) to substitute $\dot{q}_{\mathrm{X/Y}}$ yields $\dot{\boldsymbol{q}}_{\mathrm{X/Y}} = \frac{1}{2}\omega^{\mathrm{Y}}_{\mathrm{X/Y}}q_{\mathrm{X/Y}} + \epsilon\frac{1}{2}\dot{r}^{\mathrm{Y}}_{\mathrm{X/Y}}q_{\mathrm{X/Y}} + \epsilon\frac{1}{2}r^{\mathrm{Y}}_{\mathrm{X/Y}}\frac{1}{2}\omega^{\mathrm{Y}}_{\mathrm{X/Y}}q_{\mathrm{X/Y}}$. Note that $\dot{r}^{\mathrm{Y}}_{\mathrm{X/Y}} = v^{\mathrm{Y}}_{\mathrm{X/Y}}$ and $\frac{1}{2}r^{\mathrm{Y}}_{\mathrm{X/Y}}\omega^{\mathrm{Y}}_{\mathrm{X/Y}} = r^{\mathrm{Y}}_{\mathrm{X/Y}} \times \omega^{\mathrm{Y}}_{\mathrm{X/Y}} + \frac{1}{2}\omega^{\mathrm{Y}}_{\mathrm{X/Y}}r^{\mathrm{Y}}_{\mathrm{X/Y}}$. Hence, $\dot{\boldsymbol{q}}_{\mathrm{X/Y}} = \frac{1}{2}\omega^{\mathrm{Y}}_{\mathrm{X/Y}}q_{\mathrm{X/Y}} + \frac{1}{2}\epsilon(v^{\mathrm{Y}}_{\mathrm{X/Y}}q_{\mathrm{X/Y}} + (r^{\mathrm{Y}}_{\mathrm{X/Y}} \times \omega^{\mathrm{Y}}_{\mathrm{X/Y}})q_{\mathrm{X/Y}} + \frac{1}{2}\omega^{\mathrm{Y}}_{\mathrm{X/Y}}r^{\mathrm{Y}}_{\mathrm{X/Y}}q_{\mathrm{X/Y}})$, which can be factorized into $\dot{\boldsymbol{q}}_{\mathrm{X/Y}} = \frac{1}{2}(\omega^{\mathrm{Y}}_{\mathrm{X/Y}} + \epsilon(v^{\mathrm{Y}}_{\mathrm{X/Y}} + r^{\mathrm{Y}}_{\mathrm{X/Y}} \times \omega^{\mathrm{Y}}_{\mathrm{X/Y}}))(q_{\mathrm{X/Y}} + \epsilon\frac{1}{2}r^{\mathrm{Y}}_{\mathrm{X/Y}}q_{\mathrm{X/Y}})$. Thus, if $\omega^{\mathrm{Y}}_{\mathrm{X/Y}} = \omega^{\mathrm{Y}}_{\mathrm{X/Y}} + \epsilon(v^{\mathrm{Y}}_{\mathrm{X/Y}} + r^{\mathrm{Y}}_{\mathrm{X/Y}} \times \omega^{\mathrm{Y}}_{\mathrm{X/Y}})$, one obtains $\dot{\boldsymbol{q}}_{\mathrm{X/Y}} = \frac{1}{2}\boldsymbol{\omega}^{\mathrm{Y}}_{\mathrm{X/Y}}\boldsymbol{q}_{\mathrm{X/Y}}$. Finally, by applying Lemma 59 to this form of the kinematics yields $\dot{\boldsymbol{q}}_{\mathrm{X/Y}} = \frac{1}{2}(\boldsymbol{q}_{\mathrm{X/Y}}\boldsymbol{q}^{*}_{\mathrm{X/Y}})\boldsymbol{\omega}^{\mathrm{Y}}_{\mathrm{X/Y}}\boldsymbol{q}_{\mathrm{X/Y}} = \frac{1}{2}\boldsymbol{q}_{\mathrm{X/Y}}\boldsymbol{\omega}^{\mathrm{X}}_{\mathrm{X/Y}}$, where $\boldsymbol{\omega}^{\mathrm{X}}_{\mathrm{X/Y}} = \omega^{\mathrm{X}}_{\mathrm{X/Y}} + \epsilon v^{\mathrm{X}}_{\mathrm{X/Y}}$. □

Hence, based on Proposition 1, the rotational and translational kinematic equations of the pose of a body frame and of a desired frame with respect to an inertial frame, represented by the unit dual quaternions $\boldsymbol{q}_{\mathrm{B/I}}$ and $\boldsymbol{q}_{\mathrm{D/I}} = q_{\mathrm{D/I}} + \epsilon\frac{1}{2}r^{\mathrm{I}}_{\mathrm{D/I}}q_{\mathrm{D/I}} = q_{\mathrm{D/I}} + \epsilon\frac{1}{2}q_{\mathrm{D/I}}r^{\mathrm{D}}_{\mathrm{D/I}}$, respectively, are given by [105]

$$\dot{\boldsymbol{q}}_{\mathrm{B/I}} = \frac{1}{2}\boldsymbol{\omega}^{\mathrm{I}}_{\mathrm{B/I}}\boldsymbol{q}_{\mathrm{B/I}} = \frac{1}{2}\boldsymbol{q}_{\mathrm{B/I}}\boldsymbol{\omega}^{\mathrm{B}}_{\mathrm{B/I}} \quad \text{and} \quad \dot{\boldsymbol{q}}_{\mathrm{D/I}} = \frac{1}{2}\boldsymbol{\omega}^{\mathrm{I}}_{\mathrm{D/I}}\boldsymbol{q}_{\mathrm{D/I}} = \frac{1}{2}\boldsymbol{q}_{\mathrm{D/I}}\boldsymbol{\omega}^{\mathrm{D}}_{\mathrm{D/I}}, \tag{51}$$

where

$$\boldsymbol{\omega}^{\mathrm{B}}_{\mathrm{B/I}} = \omega^{\mathrm{B}}_{\mathrm{B/I}} + \epsilon v^{\mathrm{B}}_{\mathrm{B/I}}, \tag{52}$$

$$\boldsymbol{\omega}^{\mathrm{I}}_{\mathrm{B/I}} = \omega^{\mathrm{I}}_{\mathrm{B/I}} + \epsilon(v^{\mathrm{I}}_{\mathrm{B/I}} - \omega^{\mathrm{I}}_{\mathrm{B/I}} \times r^{\mathrm{I}}_{\mathrm{B/I}}). \tag{53}$$

By direct analogy to Eq. (22), the *error dual quaternion* [93, 44] is defined as

$$\boldsymbol{q}_{\mathrm{B/D}} \triangleq \boldsymbol{q}^{*}_{\mathrm{D/I}}\boldsymbol{q}_{\mathrm{B/I}}. \tag{54}$$

This definition has some desirable properties. First, $\boldsymbol{q}_{\mathrm{B/D}}$ is a unit dual quaternion. (In Ref. [75], the error dual quaternion is defined as $\boldsymbol{q}_{\mathrm{B/D}} = \boldsymbol{q}_{\mathrm{D/I}} - \boldsymbol{q}_{\mathrm{B/I}}$. In this case, $\boldsymbol{q}_{\mathrm{B/D}}$ is not a unit dual quaternion.)

Lemma 61. *The error dual quaternion given by Eq.* (54) *is a unit dual quaternion, i.e.,* $\boldsymbol{q}_{\mathrm{B/D}} \in \mathbb{H}^{u}_{d}$.

Proof. By definition, $\boldsymbol{q}_{\mathrm{B/D}} \cdot \boldsymbol{q}_{\mathrm{B/D}} = \boldsymbol{q}^{*}_{\mathrm{B/D}}\boldsymbol{q}_{\mathrm{B/D}} = \boldsymbol{q}^{*}_{\mathrm{B/I}}\boldsymbol{q}_{\mathrm{D/I}}\boldsymbol{q}^{*}_{\mathrm{D/I}}\boldsymbol{q}_{\mathrm{B/I}} = \mathbf{1}$. □

Moreover, $\boldsymbol{q}_{\mathrm{B/D}}$ can be shown to represent the relative pose of the body frame with respect to the desired frame.

Lemma 62. *The error dual quaternion given by Eq.* (54) *is equal to* $\boldsymbol{q}_{\mathrm{B/D}} = q_{\mathrm{B/D}} + \epsilon\frac{1}{2}q_{\mathrm{B/D}}r^{\mathrm{B}}_{\mathrm{B/D}} = q_{\mathrm{B/D}} + \epsilon\frac{1}{2}r^{\mathrm{D}}_{\mathrm{B/D}}q_{\mathrm{B/D}}$, *where* $r^{\mathrm{B}}_{\mathrm{B/D}} = r^{\mathrm{B}}_{\mathrm{B/I}} - r^{\mathrm{B}}_{\mathrm{D/I}}$.

Proof. By definition, $\boldsymbol{q}_{\mathrm{B/D}} \triangleq \boldsymbol{q}^*_{\mathrm{D/I}}\boldsymbol{q}_{\mathrm{B/I}} = (q_{\mathrm{D/I}}+\epsilon\frac{1}{2}q_{\mathrm{D/I}}r^{\mathrm{D}}_{\mathrm{D/I}})^*(q_{\mathrm{B/I}}+\epsilon\frac{1}{2}q_{\mathrm{B/I}}r^{\mathrm{B}}_{\mathrm{B/I}}) = q^*_{\mathrm{D/I}}q_{\mathrm{B/I}}+\epsilon(\frac{1}{2}(r^{\mathrm{D}}_{\mathrm{D/I}})^*q^*_{\mathrm{D/I}}q_{\mathrm{B/I}} + \frac{1}{2}q^*_{\mathrm{D/I}}q_{\mathrm{B/I}}r^{\mathrm{B}}_{\mathrm{B/I}})$. Using Eq. (22), $\boldsymbol{q}_{\mathrm{B/D}} = q_{\mathrm{B/D}} + \epsilon(\frac{1}{2}(r^{\mathrm{D}}_{\mathrm{D/I}})^*q_{\mathrm{B/D}} + \frac{1}{2}q_{\mathrm{B/D}}r^{\mathrm{B}}_{\mathrm{B/I}}) = q_{\mathrm{B/D}}+\epsilon(\frac{1}{2}q_{\mathrm{B/D}}q^*_{\mathrm{B/D}}(r^{\mathrm{D}}_{\mathrm{D/I}})^*q_{\mathrm{B/D}}+\frac{1}{2}q_{\mathrm{B/D}}r^{\mathrm{B}}_{\mathrm{B/I}}) = q_{\mathrm{B/D}}+\epsilon(-\frac{1}{2}q_{\mathrm{B/D}}(q^*_{\mathrm{B/D}}r^{\mathrm{D}}_{\mathrm{D/I}}q_{\mathrm{B/D}})+\frac{1}{2}q_{\mathrm{B/D}}r^{\mathrm{B}}_{\mathrm{B/I}}) = q_{\mathrm{B/D}} + \epsilon(-\frac{1}{2}q_{\mathrm{B/D}}r^{\mathrm{B}}_{\mathrm{D/I}} + \frac{1}{2}q_{\mathrm{B/D}}r^{\mathrm{B}}_{\mathrm{B/I}}) = q_{\mathrm{B/D}} + \epsilon\frac{1}{2}q_{\mathrm{B/D}}(r^{\mathrm{B}}_{\mathrm{B/I}} - r^{\mathrm{D}}_{\mathrm{D/I}}) = q_{\mathrm{B/D}} + \epsilon\frac{1}{2}q_{\mathrm{B/D}}r^{\mathrm{B}}_{\mathrm{B/D}} = q_{\mathrm{B/D}} + \epsilon\frac{1}{2}r^{\mathrm{D}}_{\mathrm{B/D}}q_{\mathrm{B/D}}$. □

Hence, the error dual quaternion represents the attitude ($q_{\mathrm{B/D}}$) and position ($r^{\mathrm{B}}_{\mathrm{B/D}}$) of the body frame with respect to the desired frame. This is illustrated in Figure 2.

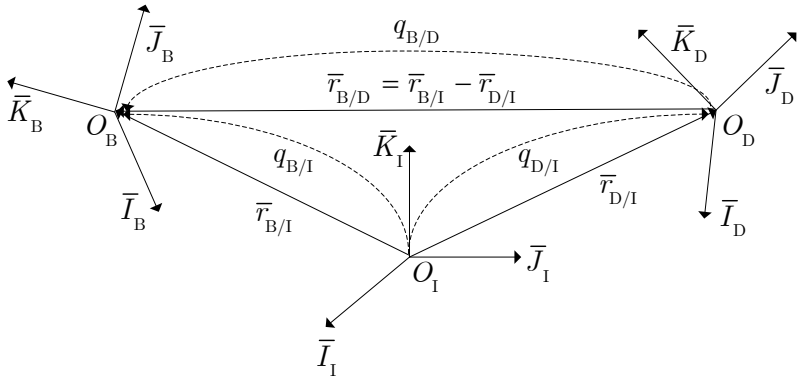

Figure 2: Relation between the desired, body, an inertial frames.

By direct application of Proposition 1, the dual quaternion representation of the relative rotational and translational kinematic equations is given by [93]

$$\dot{\boldsymbol{q}}_{\mathrm{B/D}} = \frac{1}{2}\boldsymbol{q}_{\mathrm{B/D}}\boldsymbol{\omega}^{\mathrm{B}}_{\mathrm{B/D}} = \frac{1}{2}\boldsymbol{\omega}^{\mathrm{D}}_{\mathrm{B/D}}\boldsymbol{q}_{\mathrm{B/D}}, \tag{55}$$

where $\boldsymbol{\omega}^{\mathrm{B}}_{\mathrm{B/D}} = \boldsymbol{\omega}^{\mathrm{B}}_{\mathrm{B/I}} - \boldsymbol{\omega}^{\mathrm{B}}_{\mathrm{D/I}}$, $\boldsymbol{\omega}^{\mathrm{B}}_{\mathrm{D/I}} = \boldsymbol{q}^*_{\mathrm{B/D}}\boldsymbol{\omega}^{\mathrm{D}}_{\mathrm{D/I}}\boldsymbol{q}_{\mathrm{B/D}}$, and $\boldsymbol{\omega}^{\mathrm{D}}_{\mathrm{B/I}} = \boldsymbol{q}_{\mathrm{B/D}}\boldsymbol{\omega}^{\mathrm{B}}_{\mathrm{B/I}}\boldsymbol{q}^*_{\mathrm{B/D}}$. Note that the kinematic equations of the dual error quaternion, Eq. (55), and of the error quaternion, Eq. (23), have the same form.

2.2.3 Dual Quaternion Representation of the Relative Rotational and Translational Dynamic Equations

Whereas much has been published about dual quaternions and rigid body kinematics [75, 43, 74, 105], the formulation of the rigid body dynamics in terms of dual quaternions has been given less attention.

In Ref. [44], the rigid body dynamics are written component-wise in terms of the real and dual parts of $\dot{\boldsymbol{\omega}}^{\mathrm{B}}_{\mathrm{B/I}}$, and not in dual quaternion algebra (as Eq. (51) for the rigid body kinematics). Moreover, as stated in Ref. [95], "the equations of motion are quite complicated and the physical significance of the variables is not intuitively apparent."

In Ref. [95], like in Ref. [44], the rigid body dynamics are written component-wise in terms of the real and dual parts of $\dot{\boldsymbol{\omega}}^{\mathrm{B}}_{\mathrm{B/I}}$. Moreover, the derivation of the dynamic equations in Ref. [95] is based on an incorrect form of the second law of Newton, namely $m\frac{^{\mathrm{B}}\mathrm{d}^2\bar{r}_{\mathrm{B/I}}}{\mathrm{d}t^2} = \bar{f}$, where m is the mass of the rigid body, $\bar{f}$ is the total external force vector applied to the body, and $\frac{^{\mathrm{B}}\mathrm{d}^2(.)}{\mathrm{d}t^2}$ is the second time derivative with respect to the body frame. Note that the correct form of Newton's second law is $m\frac{^{\mathrm{I}}\mathrm{d}^2\bar{r}_{\mathrm{B/I}}}{\mathrm{d}t^2} = \bar{f}$.

In Ref. [24], the rigid body dynamics are written in terms of the second derivative of the dual quaternion ($\ddot{\boldsymbol{q}}_{\mathrm{B/I}}$), i.e., the elements of the first derivative of the dual quaternion ($\dot{\boldsymbol{q}}_{\mathrm{B/I}}$) are chosen as generalized speeds. Even though mathematically there is nothing wrong with this formulation, it is easier to interpret the motion of a rigid body by looking at $\boldsymbol{\omega}^{\mathrm{B}}_{\mathrm{B/I}}$. Moreover, since in most cases $\bar{\omega}^{\mathrm{B}}_{\mathrm{B/I}}$ and $\bar{v}^{\mathrm{B}}_{\mathrm{B/I}}$ (i.e., the real and dual parts of $\boldsymbol{\omega}^{\mathrm{B}}_{\mathrm{B/I}}$) are directly measured by on-board sensors, it is also easier to implement feedback control laws based on $\boldsymbol{\omega}^{\mathrm{B}}_{\mathrm{B/I}}$ than on $\dot{\boldsymbol{q}}_{\mathrm{B/I}}$. Hence, the elements of $\boldsymbol{\omega}^{\mathrm{B}}_{\mathrm{B/I}}$ are a better choice for generalized speeds than the elements of $\dot{\boldsymbol{q}}_{\mathrm{B/I}}$. Finally, Ref. [24] does not take advantage of the properties of dual quaternion algebra. Instead, it uses vector-matrix algebra to develop the equations of motion.

In this work, an alternative representation of the rigid body dynamics based on

Refs. [93, 9, 106] is proposed. According to Ref. [9], the dual quaternion representation of the dynamic equations is analogous to the classical translational and rotational dynamic equations and is given by

$$\frac{\mathrm{d}\boldsymbol{H}^{\mathrm{B}}_{\mathrm{B/I}}}{\mathrm{d}t} + \boldsymbol{\omega}^{\mathrm{B}}_{\mathrm{B/I}} \times \boldsymbol{H}^{\mathrm{B}}_{\mathrm{B/I}} = \boldsymbol{f}^{\mathrm{B}}, \tag{56}$$

where $\boldsymbol{H}^{\mathrm{B}}_{\mathrm{B/I}}$ are the body coordinates of the *dual momentum* of the body with respect to the inertial frame about its center of mass and $\boldsymbol{f}^{B}$ are the body coordinates of the total external *dual force* applied to the body about its center of mass. In Ref. (56), $\boldsymbol{H}^{\mathrm{B}}_{\mathrm{B/I}}$ and $\boldsymbol{f}^{\mathrm{B}}$ are defined as

$$\boldsymbol{H}^{\mathrm{B}}_{\mathrm{B/I}} = mv^{\mathrm{B}}_{\mathrm{B/I}} + \epsilon(I^{\mathrm{B}} * \omega^{\mathrm{B}}_{\mathrm{B/I}}), \tag{57}$$

$$\boldsymbol{f}^{\mathrm{B}} = f^{\mathrm{B}} + \epsilon\tau^{\mathrm{B}}, \tag{58}$$

where $f^{\mathrm{B}} = (0, \bar{f}^{\mathrm{B}})$, and $\bar{f}^{\mathrm{B}} = [f^{\mathrm{B}}_1, f^{\mathrm{B}}_2, f^{\mathrm{B}}_3]^{\intercal}$ are the body coordinates of the total external force vector applied to the body. By substituting Eqs. (57), (58), and (52) in Eq. (56), the equivalence between Eq. (56) and the classical translational and rotational rigid body dynamic can be confirmed:

$$\frac{\mathrm{d}\boldsymbol{H}^{\mathrm{B}}_{\mathrm{B/I}}}{\mathrm{d}t} + \boldsymbol{\omega}^{\mathrm{B}}_{\mathrm{B/I}} \times \boldsymbol{H}^{\mathrm{B}}_{\mathrm{B/I}} = \boldsymbol{f}^{\mathrm{B}}$$

$$\frac{\mathrm{d}(mv^{\mathrm{B}}_{\mathrm{B/I}} + \epsilon(I^{\mathrm{B}} * \omega^{\mathrm{B}}_{\mathrm{B/I}}))}{\mathrm{d}t} + (\omega^{\mathrm{B}}_{\mathrm{B/I}} + \epsilon v^{\mathrm{B}}_{\mathrm{B/I}}) \times (mv^{\mathrm{B}}_{\mathrm{B/I}} + \epsilon(I^{\mathrm{B}} * \omega^{\mathrm{B}}_{\mathrm{B/I}})) = f^{\mathrm{B}} + \epsilon\tau^{\mathrm{B}}$$

$$m\dot{v}^{\mathrm{B}}_{\mathrm{B/I}} + \epsilon(I^{\mathrm{B}} * \dot{\omega}^{\mathrm{B}}_{\mathrm{B/I}}) + \omega^{\mathrm{B}}_{\mathrm{B/I}} \times (mv^{\mathrm{B}}_{\mathrm{B/I}}) + \epsilon(\omega^{\mathrm{B}}_{\mathrm{B/I}} \times (I^{\mathrm{B}} * \omega^{\mathrm{B}}_{\mathrm{B/I}}) + v^{\mathrm{B}}_{\mathrm{B/I}} \times (mv^{\mathrm{B}}_{\mathrm{B/I}})) = f^{\mathrm{B}} + \epsilon\tau^{\mathrm{B}}$$

$$(m\dot{v}^{\mathrm{B}}_{\mathrm{B/I}} + \omega^{\mathrm{B}}_{\mathrm{B/I}} \times (mv^{\mathrm{B}}_{\mathrm{B/I}})) + \epsilon(I^{\mathrm{B}} * \dot{\omega}^{\mathrm{B}}_{\mathrm{B/I}} + \omega^{\mathrm{B}}_{\mathrm{B/I}} \times (I^{\mathrm{B}} * \omega^{\mathrm{B}}_{\mathrm{B/I}})) = f^{\mathrm{B}} + \epsilon\tau^{\mathrm{B}}. \tag{59}$$

Comparing the real and dual parts of Eq. (59) yields $m\dot{v}^{\mathrm{B}}_{\mathrm{B/I}} + \omega^{\mathrm{B}}_{\mathrm{B/I}} \times (mv^{\mathrm{B}}_{\mathrm{B/I}}) = f^{\mathrm{B}}$ and $I^{\mathrm{B}} * \dot{\omega}^{\mathrm{B}}_{\mathrm{B/I}} + \omega^{\mathrm{B}}_{\mathrm{B/I}} \times (I^{\mathrm{B}} * \omega^{\mathrm{B}}_{\mathrm{B/I}}) = \tau^{\mathrm{B}}$, which are indeed the classical translational and rotational rigid body dynamic equations.

Note that Eq. (56) is expressed in the body frame. The dynamic equations can also be expressed in the inertial frame. To do that, it is convenient to introduce the following proposition.

Proposition 2. *Let a dual vector quaternion expressed in frame D, $\boldsymbol{v}^{\mathrm{D}}$, and the unit dual quaternion $\boldsymbol{q}_{\mathrm{B/D}}$ describing the pose of frame B with respect to frame D, such that $\boldsymbol{v}^{\mathrm{B}} = \boldsymbol{q}^{*}_{\mathrm{B/D}}\boldsymbol{v}^{\mathrm{D}}\boldsymbol{q}_{\mathrm{B/D}}$, be given. Then, the time derivative of $\boldsymbol{v}^{\mathrm{B}}$ is related to the time derivative of $\boldsymbol{v}^{\mathrm{D}}$ by $\dot{\boldsymbol{v}}^{\mathrm{B}} = \boldsymbol{q}^{*}_{\mathrm{B/D}}(\dot{\boldsymbol{v}}^{\mathrm{D}} + \boldsymbol{\omega}^{\mathrm{D}}_{\mathrm{D/B}} \times \boldsymbol{v}^{\mathrm{D}})\boldsymbol{q}_{\mathrm{B/D}}$.*

Proof. By definition,

$$\dot{\boldsymbol{v}}^{\mathrm{B}} = \frac{\mathrm{d}}{\mathrm{d}t}(\boldsymbol{q}^{*}_{\mathrm{B/D}}\boldsymbol{v}^{\mathrm{D}}\boldsymbol{q}_{\mathrm{B/D}}) = \dot{\boldsymbol{q}}^{*}_{\mathrm{B/D}}\boldsymbol{v}^{\mathrm{D}}\boldsymbol{q}_{\mathrm{B/D}} + \boldsymbol{q}^{*}_{\mathrm{B/D}}\dot{\boldsymbol{v}}^{\mathrm{D}}\boldsymbol{q}_{\mathrm{B/D}} + \boldsymbol{q}^{*}_{\mathrm{B/D}}\boldsymbol{v}^{\mathrm{D}}\dot{\boldsymbol{q}}_{\mathrm{B/D}}.$$

Replacing $\dot{\boldsymbol{q}}_{\mathrm{B/D}}$ by Eq. (55) yields

$$\begin{aligned}\dot{\boldsymbol{v}}^{\mathrm{B}} &= \tfrac{1}{2}\boldsymbol{q}^{*}_{\mathrm{B/D}}(\boldsymbol{\omega}^{\mathrm{D}}_{\mathrm{B/D}})^{*}\boldsymbol{v}^{\mathrm{D}}\boldsymbol{q}_{\mathrm{B/D}} + \boldsymbol{q}^{*}_{\mathrm{B/D}}\dot{\boldsymbol{v}}^{\mathrm{D}}\boldsymbol{q}_{\mathrm{B/D}} + \boldsymbol{q}^{*}_{\mathrm{B/D}}\boldsymbol{v}^{\mathrm{D}}\tfrac{1}{2}\boldsymbol{\omega}^{\mathrm{D}}_{\mathrm{B/D}}\boldsymbol{q}_{\mathrm{B/D}} \\ &= \boldsymbol{q}^{*}_{\mathrm{B/D}}(\tfrac{1}{2}(\boldsymbol{\omega}^{\mathrm{D}}_{\mathrm{B/D}})^{*}\boldsymbol{v}^{\mathrm{D}} + \dot{\boldsymbol{v}}^{\mathrm{D}} + \boldsymbol{v}^{\mathrm{D}}\tfrac{1}{2}\boldsymbol{\omega}^{\mathrm{D}}_{\mathrm{B/D}})\boldsymbol{q}_{\mathrm{B/D}}.\end{aligned}$$

Finally, since $\boldsymbol{v}^{\mathrm{D}}$ is a dual vector quaternion, $(\boldsymbol{v}^{\mathrm{D}})^{*} = -\boldsymbol{v}^{\mathrm{D}}$ and

$$\begin{aligned}\dot{\boldsymbol{v}}^{\mathrm{B}} = \boldsymbol{q}^{*}_{\mathrm{B/D}}(\dot{\boldsymbol{v}}^{\mathrm{D}} + \tfrac{1}{2}\boldsymbol{v}^{\mathrm{D}}\boldsymbol{\omega}^{\mathrm{D}}_{\mathrm{B/D}} - \tfrac{1}{2}(\boldsymbol{\omega}^{\mathrm{D}}_{\mathrm{B/D}})^{*}(\boldsymbol{v}^{\mathrm{D}})^{*})\boldsymbol{q}_{\mathrm{B/D}} &= \boldsymbol{q}^{*}_{\mathrm{B/D}}(\dot{\boldsymbol{v}}^{\mathrm{D}} + \boldsymbol{v}^{\mathrm{D}} \times \boldsymbol{\omega}^{\mathrm{D}}_{\mathrm{B/D}})\boldsymbol{q}_{\mathrm{B/D}} \\ &= \boldsymbol{q}^{*}_{\mathrm{B/D}}(\dot{\boldsymbol{v}}^{\mathrm{D}} + \boldsymbol{\omega}^{\mathrm{D}}_{\mathrm{D/B}} \times \boldsymbol{v}^{\mathrm{D}})\boldsymbol{q}_{\mathrm{B/D}}.\end{aligned}$$

□

Proposition 2 is the dual quaternion counterpart to the classical *transport theorem* used to compute the rate of change of a vector in a certain reference frame when observations are made about its rate of change in a different reference frame [76].

By applying Proposition 2 to Eq. (56), the dual quaternion representation of the rigid body dynamics expressed in the inertial frame can be calculated to be

$$\frac{\mathrm{d}\boldsymbol{H}^{\mathrm{I}}_{\mathrm{B/I}}}{\mathrm{d}t} = \boldsymbol{f}^{\mathrm{I}}, \tag{60}$$

where $\boldsymbol{H}^{\mathrm{I}}_{\mathrm{B/I}}$ are the inertial coordinates of the dual momentum of the body with respect to the inertial frame about its center of mass and $\boldsymbol{f}^{\mathrm{I}}$ are the inertial coordinates of the total external dual force applied to the body about its center of mass. From Lemma 59 and Eqs. (57) and (58), $\boldsymbol{H}^{\mathrm{I}}_{\mathrm{B/I}}$ and $\boldsymbol{f}^{\mathrm{I}}$ are given by

$$\boldsymbol{H}^{\mathrm{I}}_{\mathrm{B/I}} = \boldsymbol{q}_{\mathrm{B/D}}\boldsymbol{H}^{\mathrm{B}}_{\mathrm{B/I}}\boldsymbol{q}^{*}_{\mathrm{B/D}} = mv^{\mathrm{I}}_{\mathrm{B/I}} + \epsilon(q_{\mathrm{B/I}}(I^{B} * \omega^{B})q^{*}_{\mathrm{B/I}} + r^{\mathrm{I}}_{\mathrm{B/I}} \times (mv^{\mathrm{I}}_{\mathrm{B/I}})), \tag{61}$$

$$\boldsymbol{f}^{\mathrm{I}} = \boldsymbol{q}_{\mathrm{B/D}} \boldsymbol{f}^{\mathrm{B}} \boldsymbol{q}^{*}_{\mathrm{B/D}} = f^{\mathrm{I}} + \epsilon(\tau^{\mathrm{I}} + r^{\mathrm{I}}_{\mathrm{B/I}} \times f^{\mathrm{I}}). \tag{62}$$

Until this point, the dual quaternion representation of the rigid body dynamics used in this work matches the representation used in Refs. [93, 9, 106]. However, the representation used in this work differs from the representation used in Refs. [93, 9, 106] in the way the dual momentum $\boldsymbol{H}^{\mathrm{B}}_{\mathrm{B/I}}$ is written from the dual velocity $\boldsymbol{\omega}^{\mathrm{B}}_{\mathrm{B/I}}$. In Ref. [93], the authors write the dual momentum as $\boldsymbol{H}^{\mathrm{B}}_{\mathrm{B/I}} = \boldsymbol{M}^{\mathrm{B}} \boldsymbol{\omega}^{\mathrm{B}}_{\mathrm{B/I}}$, where $\boldsymbol{M}^{\mathrm{B}}$ is the *dual inertia operator* defined in Refs. [8, 9, 19] as $\boldsymbol{M}^{\mathrm{B}} = m\frac{\mathrm{d}}{\mathrm{d}\epsilon} I_{4\times 4} + \epsilon I^{\mathrm{B}}$. The operator $\frac{\mathrm{d}}{\mathrm{d}\epsilon}$ is defined by the properties $\frac{\mathrm{d}}{\mathrm{d}\epsilon}\boldsymbol{a} = \frac{\mathrm{d}}{\mathrm{d}\epsilon}(a_r + \epsilon a_d) = a_d$ and $\left(\frac{\mathrm{d}}{\mathrm{d}\epsilon}\right)^2 = 0$, where $\boldsymbol{a} = a_r + \epsilon a_d \in \mathbb{H}_d$. In this work, the dual inertia operator is replaced by the *dual inertia matrix*, which is defined as the following 8-by-8 symmetric positive-definite matrix

$$M^{\mathrm{B}} = \begin{bmatrix} 1 & 0_{1\times 3} & 0 & 0_{1\times 3} \\ 0_{3\times 1} & mI_{3\times 3} & 0_{3\times 1} & 0_{3\times 3} \\ 0 & 0_{1\times 3} & 1 & 0_{1\times 3} \\ 0_{3\times 1} & 0_{3\times 3} & 0_{3\times 1} & \bar{I}^{\mathrm{B}} \end{bmatrix}. \tag{63}$$

Then, the dual momentum $\boldsymbol{H}^{\mathrm{B}}_{\mathrm{B/I}}$ is written from the dual velocity $\boldsymbol{\omega}^{\mathrm{B}}_{\mathrm{B/I}}$ as

$$\boldsymbol{H}^{\mathrm{B}}_{\mathrm{B/I}} = M^{\mathrm{B}} \star (\boldsymbol{\omega}^{\mathrm{B}}_{\mathrm{B/I}})^{\mathsf{s}}. \tag{64}$$

Note that the dual inertia matrix has the same form as Eq. (42) in Lemma 52. As a result, from Eq. (64) and Eq. (56), the dual quaternion representation of the rigid body dynamics can be written as

$$M^{\mathrm{B}} \star (\dot{\boldsymbol{\omega}}^{\mathrm{B}}_{\mathrm{B/I}})^{\mathsf{s}} = \boldsymbol{f}^{\mathrm{B}} - \boldsymbol{\omega}^{\mathrm{B}}_{\mathrm{B/I}} \times (M^{\mathrm{B}} \star (\boldsymbol{\omega}^{\mathrm{B}}_{\mathrm{B/I}})^{\mathsf{s}}), \tag{65}$$

or equivalently,

$$(\dot{\boldsymbol{\omega}}^{\mathrm{B}}_{\mathrm{B/I}})^{\mathsf{s}} = (M^{\mathrm{B}})^{-1} \star (\boldsymbol{f}^{\mathrm{B}} - \boldsymbol{\omega}^{\mathrm{B}}_{\mathrm{B/I}} \times (M^{\mathrm{B}} \star (\boldsymbol{\omega}^{\mathrm{B}}_{\mathrm{B/I}})^{\mathsf{s}})), \tag{66}$$

where $(M^{\mathrm{B}})^{-1}$ is simply the matrix inverse of M^{B}. Recently, Ref. [56] has proposed rewriting Eq. (65) without the swap operation by defining the dual inertia matrix

as a block anti-diagonal matrix. Although this matrix is always invertible, it is no longer symmetric. Since the inertia matrix is symmetric and the results presented in this dissertation are based on existing attitude-only results, it is desirable to have a symmetric dual inertia matrix.

This formulation based on the dual inertia matrix has two advantages over the formulation used in Refs. [93, 9, 106]. First, the inverse of M^{B} is simply the matrix inverse of M^{B}. Thus, Eq. (66) can be obtained by simply multiplying Eq. (65) on the left by $(M^{\mathrm{B}})^{-1}$. However, using the dual inertia operator to go from

$$\boldsymbol{M}^{\mathrm{B}}\dot{\boldsymbol{\omega}}^{\mathrm{B}}_{\mathrm{B/I}} = \boldsymbol{f}^{\mathrm{B}} - \boldsymbol{\omega}^{\mathrm{B}}_{\mathrm{B/I}} \times (\boldsymbol{M}^{\mathrm{B}}\boldsymbol{\omega}^{\mathrm{B}}_{\mathrm{B/I}}) \tag{67}$$

to

$$\dot{\boldsymbol{\omega}}^{\mathrm{B}}_{\mathrm{B/I}} = (\boldsymbol{M}^{\mathrm{B}})^{-1}\left(\boldsymbol{f}^{\mathrm{B}} - \boldsymbol{\omega}^{\mathrm{B}}_{\mathrm{B/I}} \times (\boldsymbol{M}^{\mathrm{B}}\boldsymbol{\omega}^{\mathrm{B}}_{\mathrm{B/I}})\right), \tag{68}$$

requires defining the inverse of $\boldsymbol{M}^{\mathrm{B}}$ as $(\boldsymbol{M}^{\mathrm{B}})^{-1} = (I^{\mathrm{B}})^{-1}\frac{\mathrm{d}}{\mathrm{d}\epsilon} + \epsilon\frac{1}{m}I_{4\times 4}$ [93], which means that $\boldsymbol{M}^{\mathrm{B}}(\boldsymbol{M}^{\mathrm{B}})^{-1} = (\boldsymbol{M}^{\mathrm{B}})^{-1}\boldsymbol{M}^{\mathrm{B}} = 2I_{4\times 4}$. Thus, Eq. (68) cannot be calculated by simply multiplying Eq. (67) on the left by $(\boldsymbol{M}^{\mathrm{B}})^{-1}$. Moreover, the inverse of $\boldsymbol{M}^{\mathrm{B}}$ is not as straightforward to calculate as the inverse of M^{B}. Hence, it is more intuitive to operate with the dual inertia matrix than with the dual inertia operator.

Second, the multiplication of a 8-by-8 matrix with a dual quaternion is a more general operation than the multiplication of operator $\frac{\mathrm{d}}{\mathrm{d}\epsilon}$ with a dual quaternion. As an example, note that any dual quaternion $\boldsymbol{y}$ defined as $\boldsymbol{y} = \left(M_{12}\frac{\mathrm{d}}{\mathrm{d}\epsilon} + \epsilon M_{21}\right)\boldsymbol{x}$, where $M_{12}, M_{21} \in \mathbb{R}^{4\times 4}$ and $\boldsymbol{x} = x_r + \epsilon x_d \in \mathbb{H}_d$, can also be calculated as

$$\boldsymbol{y} = \begin{bmatrix} 0_{4\times 4} & M_{12} \\ M_{21} & 0_{4\times 4} \end{bmatrix} \star \boldsymbol{x}. \tag{69}$$

In both cases, $\boldsymbol{y} = M_{12}x_d + \epsilon M_{21}x_r$. However, the operation

$$\boldsymbol{y} = \begin{bmatrix} M_{11} & M_{12} \\ M_{21} & M_{22} \end{bmatrix} \star \boldsymbol{x} \tag{70}$$

cannot be performed using the operator $\frac{\mathrm{d}}{\mathrm{d}\epsilon}$. In particular, the multiplication of a 8-by-8 matrix with a dual quaternion is used in Chapter 3 to define a general Linear Time-Invariant (LTI) system, where the input, output, and state are dual quaternions. This could have not been done with the operator $\frac{\mathrm{d}}{\mathrm{d}\epsilon}$.

Finally, the following proposition gives the dual quaternion representation of the relative rotational and translational dynamic equations of motion of a rigid body. Equivalent equations have been used in Ref. [93].

Proposition 3. *The dual quaternion representation of the relative rotational and translational dynamic equations of motion of a rigid body is given by*

$$\begin{aligned}(\dot{\boldsymbol{\omega}}^{\mathrm{B}}_{\mathrm{B/D}})^{\mathsf{s}}=&(M^{\mathrm{B}})^{-1}\star\Big(\boldsymbol{f}^{\mathrm{B}}-(\boldsymbol{\omega}^{\mathrm{B}}_{\mathrm{B/D}}+\boldsymbol{\omega}^{\mathrm{B}}_{\mathrm{D/I}})\times\big(M^{\mathrm{B}}\star((\boldsymbol{\omega}^{\mathrm{B}}_{\mathrm{B/D}})^{\mathsf{s}}+(\boldsymbol{\omega}^{\mathrm{B}}_{\mathrm{D/I}})^{\mathsf{s}})\big)\\&-M^{\mathrm{B}}\star(\boldsymbol{q}^{*}_{\mathrm{B/D}}\dot{\boldsymbol{\omega}}^{\mathrm{D}}_{\mathrm{D/I}}\boldsymbol{q}_{\mathrm{B/D}})^{\mathsf{s}}-M^{\mathrm{B}}\star(\boldsymbol{\omega}^{\mathrm{B}}_{\mathrm{D/I}}\times\boldsymbol{\omega}^{\mathrm{B}}_{\mathrm{B/D}})^{\mathsf{s}}\Big).\end{aligned}\tag{71}$$

Proof. Differentiating $\boldsymbol{\omega}^{\mathrm{B}}_{\mathrm{B/D}}=\boldsymbol{\omega}^{\mathrm{B}}_{\mathrm{B/I}}-\boldsymbol{\omega}^{\mathrm{B}}_{\mathrm{D/I}}$ and noting that the swap of the addition is equal to the addition of the swaps (see Lemma 42) yields $(\dot{\boldsymbol{\omega}}^{\mathrm{B}}_{\mathrm{B/D}})^{\mathsf{s}}=(\dot{\boldsymbol{\omega}}^{\mathrm{B}}_{\mathrm{B/I}})^{\mathsf{s}}-(\dot{\boldsymbol{\omega}}^{\mathrm{B}}_{\mathrm{D/I}})^{\mathsf{s}}$. The first term is given by Eq. (66). Using Proposition 2, the second term can be written as $(\dot{\boldsymbol{\omega}}^{\mathrm{B}}_{\mathrm{D/I}})^{\mathsf{s}}=(\boldsymbol{q}^{*}_{\mathrm{B/D}}(\dot{\boldsymbol{\omega}}^{\mathrm{D}}_{\mathrm{D/I}}+\boldsymbol{\omega}^{\mathrm{D}}_{\mathrm{D/B}}\times\boldsymbol{\omega}^{\mathrm{D}}_{\mathrm{D/I}})\boldsymbol{q}_{\mathrm{B/D}})^{\mathsf{s}}=(\boldsymbol{q}^{*}_{\mathrm{B/D}}\dot{\boldsymbol{\omega}}^{\mathrm{D}}_{\mathrm{D/I}}\boldsymbol{q}_{\mathrm{B/D}})^{\mathsf{s}}+(\boldsymbol{\omega}^{\mathrm{B}}_{\mathrm{D/I}}\times\boldsymbol{\omega}^{\mathrm{B}}_{\mathrm{B/D}})^{\mathsf{s}}$. Finally, subtracting $(\dot{\boldsymbol{\omega}}^{\mathrm{B}}_{\mathrm{D/I}})^{\mathsf{s}}$ from $(\dot{\boldsymbol{\omega}}^{\mathrm{B}}_{\mathrm{B/I}})^{\mathsf{s}}$ yields Eq. (71). □

Note the similarity between the dual quaternion representation of the combined rotational and translational relative dynamic equations given by Eq. (71) and the quaternion representation of the rotational(-only) relative dynamic equations given by Eq. (24).

For the case of a spacecraft in Earth orbit, the total external dual force acting on the spacecraft is decomposed as

$$\boldsymbol{f}^{\mathrm{B}}=\boldsymbol{f}^{\mathrm{B}}_{g}+\boldsymbol{f}^{\mathrm{B}}_{\nabla g}+\boldsymbol{f}^{\mathrm{B}}_{J_2}+\boldsymbol{f}^{\mathrm{B}}_{d}+\boldsymbol{f}^{\mathrm{B}}_{c},\tag{72}$$

where $\boldsymbol{f}^{\mathrm{B}}_{g}=m\boldsymbol{a}^{\mathrm{B}}_{g}$, $\boldsymbol{a}^{\mathrm{B}}_{g}=a^{\mathrm{B}}_{g}+\epsilon\mathsf{0}$, $a^{\mathrm{B}}_{g}=(0,\bar{a}^{\mathrm{B}}_{g})$, $\bar{a}^{\mathrm{B}}_{g}$ is the gravitational acceleration given

by

$$\bar{a}_g^{\mathrm{B}} = -\mu \frac{\bar{r}_{\mathrm{B/I}}^{\mathrm{B}}}{\|\bar{r}_{\mathrm{B/I}}^{\mathrm{B}}\|^3}, \tag{73}$$

$\mu = 398600.4418$ km^3/s^2 is Earth's gravitational parameter [91], $\boldsymbol{f}_{\nabla g}^{\mathrm{B}} = \mathsf{0} + \epsilon \tau_{\nabla g}^{\mathrm{B}}$, $\tau_{\nabla g}^{\mathrm{B}} = (0, \bar{\tau}_{\nabla g}^{\mathrm{B}})$, $\bar{\tau}_{\nabla g}^{\mathrm{B}}$ is the gravity gradient torque given by [93]

$$\bar{\tau}_{\nabla g}^{\mathrm{B}} = 3\mu \frac{\bar{r}_{\mathrm{B/I}}^{\mathrm{B}} \times (\bar{I}^{\mathrm{B}} \bar{r}_{\mathrm{B/I}}^{\mathrm{B}})}{\|\bar{r}_{\mathrm{B/I}}^{\mathrm{B}}\|^5}, \tag{74}$$

$\boldsymbol{f}_{J_2}^{\mathrm{B}} = m\boldsymbol{a}_{J_2}^{\mathrm{B}}, \boldsymbol{a}_{J_2}^{\mathrm{B}} = a_{J_2}^{\mathrm{B}} + \epsilon \mathsf{0}$, $a_{J_2}^{\mathrm{B}} = (0, \bar{a}_{J_2}^{\mathrm{B}})$, $\bar{a}_{J_2}^{\mathrm{B}}$ is the perturbing acceleration due to J_2 [78] given by

$$\bar{a}_{J_2}^{\mathrm{I}} = -\frac{3}{2} \frac{\mu J_2 R_e^2}{\|\bar{r}_{\mathrm{B/I}}^{\mathrm{I}}\|^4} \begin{bmatrix} (1 - 5(\frac{z_{\mathrm{B/I}}^{\mathrm{I}}}{\|\bar{r}_{\mathrm{B/I}}^{\mathrm{I}}\|})^2) \frac{x_{\mathrm{B/I}}^{\mathrm{I}}}{\|\bar{r}_{\mathrm{B/I}}^{\mathrm{I}}\|} \\ (1 - 5(\frac{z_{\mathrm{B/I}}^{\mathrm{I}}}{\|\bar{r}_{\mathrm{B/I}}^{\mathrm{I}}\|})^2) \frac{y_{\mathrm{B/I}}^{\mathrm{I}}}{\|\bar{r}_{\mathrm{B/I}}^{\mathrm{I}}\|} \\ (3 - 5(\frac{z_{\mathrm{B/I}}^{\mathrm{I}}}{\|\bar{r}_{\mathrm{B/I}}^{\mathrm{I}}\|})^2) \frac{z_{\mathrm{B/I}}^{\mathrm{I}}}{\|\bar{r}_{\mathrm{B/I}}^{\mathrm{I}}\|} \end{bmatrix}, \tag{75}$$

$J_2 = 0.0010826267$, $R_e = 6378.137$ km is Earth's mean equatorial radius [91], $\boldsymbol{f}_d^{\mathrm{B}} = f_d^{\mathrm{B}} + \epsilon \tau_d^{\mathrm{B}}$ is the dual disturbance force, and $\boldsymbol{f}_c^{\mathrm{B}} = f_c^{\mathrm{B}} + \epsilon \tau_c^{\mathrm{B}}$ is the dual control force. This work does not explicitly take into account other disturbance forces and torques due to, for example, atmospheric drag, solar radiation, and third-bodies. Instead, this work assumes that $\boldsymbol{f}_d^{\mathrm{B}}$ is a constant (or slowly varying), but otherwise unknown, dual force that captures all neglected (but small) external forces and torques. For the sake of simplicity and compactness, it is convenient to write $\boldsymbol{f}_g^{\mathrm{B}}$, $\boldsymbol{f}_{\nabla g}^{\mathrm{B}}$, and $\boldsymbol{f}_{J_2}^{\mathrm{B}}$ in terms of the dual inertia matrix as follows:

$$\boldsymbol{f}_g^{\mathrm{B}} = M^{\mathrm{B}} \star \boldsymbol{a}_g^{\mathrm{B}}, \tag{76}$$

$$\boldsymbol{f}_{\nabla g}^{\mathrm{B}} = \frac{3\mu \boldsymbol{r}_{\mathrm{B/I}}^{\mathrm{B}}}{\|\boldsymbol{r}_{\mathrm{B/I}}^{\mathrm{B}}\|^5} \times (M^{\mathrm{B}} \star (\boldsymbol{r}_{\mathrm{B/I}}^{\mathrm{B}})^{\mathsf{s}}), \tag{77}$$

$$\boldsymbol{f}_{J_2}^{\mathrm{B}} = M^{\mathrm{B}} \star \boldsymbol{a}_{J_2}^{\mathrm{B}}, \tag{78}$$

where $\boldsymbol{r}_{\mathrm{B/I}}^{\mathrm{B}} = r_{\mathrm{B/I}}^{\mathrm{B}} + \epsilon \mathsf{0}$.

CHAPTER III

POSE-TRACKING WITHOUT RELATIVE LINEAR AND ANGULAR VELOCITY FEEDBACK

In this chapter, dual quaternions are used to design a pose-tracking controller without angular and linear velocity feedback.

Velocity-free pose-tracking controllers have been proposed by several authors. In particular, in Ref. [82], a velocity-free pose-tracking controller that does not require mass and inertia matrix information is proposed. However, as explained in Ref. [85], if the reference pose is not sufficiently exciting, the pose of the rigid body might not converge to the desired pose. In Ref. [104], another velocity-free pose-tracking controller is designed based on the vectrix formalism. This controller suffers from two problems. First, the attitude of the rigid body cannot be more than 180 deg away from the desired attitude. Second, the region of convergence is dependent on the gains chosen by the user. In other words, an infinitely large region of convergence requires infinitely large gains. In turn, high gains lead to actuator saturation and poor noise rejection. Finally, in Ref. [61], it is shown that a locally asymptotically stable closed-loop system can be obtained by combining an almost globally asymptotically stable attitude-only tracking controller with a locally exponentially convergent angular velocity observer. Although the theory presented in Ref. [61] can, in principle, be extended to combined attitude and position control, only attitude control is demonstrated.

Compared to existing literature, the velocity-free pose-tracking controller presented in this chapter is almost globally asymptotically stable. In particular, the

pose of the rigid body converges to the desired pose independently of the initial condition and, unlike in Ref. [82], the reference motion does not need to be exciting. Moreover, the region of convergence does not depend on the gains chosen by the user.

This chapter starts with the derivation of a pose-tracking controller that actually requires linear and angular velocity measurements (Section 3.1). Based on this velocity-feedback controller, the velocity-free controller is derived in Section 3.2. The chapter ends with the numerical verification of these controllers. Two examples are presented. In the first example, a rigid body subject to no external forces and moments is required to track a relatively demanding sinusoidal pose reference. In the second example, a chaser spacecraft is required to track a more realistic pose reference around a target spacecraft.

The following assumptions are made in this chapter.

i) The mass and inertia matrix of the rigid body are constant and known.

ii) The center of mass of the rigid body is known.

iii) The external forces and torques are known.

iv) There are no constraints on the control force and torque.

v) In the second example, the linear and angular velocity and acceleration of the target satellite with respect to the inertial frame are known.

3.1 Velocity-Feedback Pose-Tracking Controller

When the relative linear and angular velocities are known, the controller proposed in Theorem 1 can be used to track a time-varying reference pose.

Theorem 1. *Consider the rigid body relative kinematic and dynamic equations given by Eq.* (55) *and Eq.* (71)*, respectively. Let the total external dual force acting on the*

rigid body be defined by the feedback control law

$$\boldsymbol{f}^{\mathrm{B}} = -k_p \mathrm{vec}(\boldsymbol{q}^{*}_{\mathrm{B/D}}(\boldsymbol{q}^{\mathsf{s}}_{\mathrm{B/D}} - \mathbf{1}^{\mathsf{s}})) - k_d(\boldsymbol{\omega}^{\mathrm{B}}_{\mathrm{B/D}})^{\mathsf{s}} + M^{\mathrm{B}} \star (\boldsymbol{q}^{*}_{\mathrm{B/D}} \dot{\boldsymbol{\omega}}^{\mathrm{D}}_{\mathrm{D/I}} \boldsymbol{q}_{\mathrm{B/D}})^{\mathsf{s}} + \boldsymbol{\omega}^{\mathrm{B}}_{\mathrm{D/I}} \times (M^{\mathrm{B}} \star (\boldsymbol{\omega}^{\mathrm{B}}_{\mathrm{D/I}})^{\mathsf{s}}), \quad k_p, k_d > 0, \tag{79}$$

and assume that $\dot{\boldsymbol{\omega}}^{\mathrm{D}}_{\mathrm{D/I}}, \boldsymbol{\omega}^{\mathrm{D}}_{\mathrm{D/I}} \in \mathcal{L}_\infty$. *Then,* $\boldsymbol{q}_{\mathrm{B/D}} \to \pm\mathbf{1}$ *(i.e.,* $q_{\mathrm{B/D}} \to \pm 1$ *and* $r^{\mathrm{B}}_{\mathrm{B/D}} \to 0$*)* *and* $\boldsymbol{\omega}^{\mathrm{B}}_{\mathrm{B/D}} \to \mathbf{0}$ *(i.e.,* $\omega^{\mathrm{B}}_{\mathrm{B/D}} \to 0$ *and* $v^{\mathrm{B}}_{\mathrm{B/D}} \to 0$*) as* $t \to +\infty$ *for all initial conditions.*

Proof. First, note that $\boldsymbol{q}_{\mathrm{B/D}} = \pm\mathbf{1}$ and $\boldsymbol{\omega}^{\mathrm{B}}_{\mathrm{B/D}} = \mathbf{0}$ are in fact the equilibrium conditions for the closed-loop system formed by Eqs. (71), (55), and (79). Consider now the following candidate Lyapunov function for the equilibrium point $\boldsymbol{q}_{\mathrm{B/D}} = +\mathbf{1}$ and $\boldsymbol{\omega}^{\mathrm{B}}_{\mathrm{B/D}} = \mathbf{0}$:

$$V(\boldsymbol{q}_{\mathrm{B/D}}, \boldsymbol{\omega}^{\mathrm{B}}_{\mathrm{B/D}}) = k_p(\boldsymbol{q}_{\mathrm{B/D}} - \mathbf{1}) \circ (\boldsymbol{q}_{\mathrm{B/D}} - \mathbf{1}) + \tfrac{1}{2}(\boldsymbol{\omega}^{\mathrm{B}}_{\mathrm{B/D}})^{\mathsf{s}} \circ (M^{\mathrm{B}} \star (\boldsymbol{\omega}^{\mathrm{B}}_{\mathrm{B/D}})^{\mathsf{s}}).$$

Note that V is a valid candidate Lyapunov function since $V(\boldsymbol{q}_{\mathrm{B/D}} = \mathbf{1}, \boldsymbol{\omega}^{\mathrm{B}}_{\mathrm{B/D}} = \mathbf{0}) = 0$ and $V(\boldsymbol{q}_{\mathrm{B/D}}, \boldsymbol{\omega}^{\mathrm{B}}_{\mathrm{B/D}}) > 0$ for all $(\boldsymbol{q}_{\mathrm{B/D}}, \boldsymbol{\omega}^{\mathrm{B}}_{\mathrm{B/D}}) \in \mathbb{H}^u_d \times \mathbb{H}^v_d \backslash \{\mathbf{1}, \mathbf{0}\}$, according to Lemma 52. The time derivative of V is equal to $\dot{V} = 2k_p(\boldsymbol{q}_{\mathrm{B/D}} - \mathbf{1}) \circ \dot{\boldsymbol{q}}_{\mathrm{B/D}} + (\boldsymbol{\omega}^{\mathrm{B}}_{\mathrm{B/D}})^{\mathsf{s}} \circ (M^{\mathrm{B}} \star (\dot{\boldsymbol{\omega}}^{\mathrm{B}}_{\mathrm{B/D}})^{\mathsf{s}})$. Then, by plugging in Eqs. (71) and (55) and using Lemma 33, it follows that

$$\dot{V} = (\boldsymbol{\omega}^{\mathrm{B}}_{\mathrm{B/D}})^{\mathsf{s}} \circ (k_p \boldsymbol{q}^{*}_{\mathrm{B/D}}(\boldsymbol{q}^{\mathsf{s}}_{\mathrm{B/D}} - \mathbf{1}^{\mathsf{s}}) + \boldsymbol{f}^{\mathrm{B}} - (\boldsymbol{\omega}^{\mathrm{B}}_{\mathrm{B/D}} + \boldsymbol{\omega}^{\mathrm{B}}_{\mathrm{D/I}}) \times (M^{\mathrm{B}} \star ((\boldsymbol{\omega}^{\mathrm{B}}_{\mathrm{B/D}})^{\mathsf{s}} + (\boldsymbol{\omega}^{\mathrm{B}}_{\mathrm{D/I}}))^{\mathsf{s}} - M^{\mathrm{B}} \star (\boldsymbol{q}^{*}_{\mathrm{B/D}} \dot{\boldsymbol{\omega}}^{\mathrm{D}}_{\mathrm{D/I}} \boldsymbol{q}_{\mathrm{B/D}})^{\mathsf{s}} - M^{\mathrm{B}} \star (\boldsymbol{\omega}^{\mathrm{B}}_{\mathrm{D/I}} \times \boldsymbol{\omega}^{\mathrm{B}}_{\mathrm{B/D}})^{\mathsf{s}}).$$

Introducing the feedback control law given by Eq. (79) yields

$$\dot{V} = (\boldsymbol{\omega}^{\mathrm{B}}_{\mathrm{B/D}})^{\mathsf{s}} \circ (-k_d(\boldsymbol{\omega}^{\mathrm{B}}_{\mathrm{B/D}})^{\mathsf{s}}) + (\boldsymbol{\omega}^{\mathrm{B}}_{\mathrm{B/D}})^{\mathsf{s}} \circ \left(k_p \boldsymbol{q}^{*}_{\mathrm{B/D}}(\boldsymbol{q}^{\mathsf{s}}_{\mathrm{B/D}} - \mathbf{1}^{\mathsf{s}}) - k_p \mathrm{vec}(\boldsymbol{q}^{*}_{\mathrm{B/D}}(\boldsymbol{q}^{\mathsf{s}}_{\mathrm{B/D}} - \mathbf{1}^{\mathsf{s}}))\right) + (\boldsymbol{\omega}^{\mathrm{B}}_{\mathrm{B/D}})^{\mathsf{s}} \circ (-(\boldsymbol{\omega}^{\mathrm{B}}_{\mathrm{B/D}} + \boldsymbol{\omega}^{\mathrm{B}}_{\mathrm{D/I}}) \times (M^{\mathrm{B}} \star ((\boldsymbol{\omega}^{\mathrm{B}}_{\mathrm{B/D}})^{\mathsf{s}} + (\boldsymbol{\omega}^{\mathrm{B}}_{\mathrm{D/I}}))^{\mathsf{s}}) - M^{\mathrm{B}} \star (\boldsymbol{\omega}^{\mathrm{B}}_{\mathrm{D/I}} \times \boldsymbol{\omega}^{\mathrm{B}}_{\mathrm{B/D}})^{\mathsf{s}} + \boldsymbol{\omega}^{\mathrm{B}}_{\mathrm{D/I}} \times (M^{\mathrm{B}} \star (\boldsymbol{\omega}^{\mathrm{B}}_{\mathrm{D/I}})^{\mathsf{s}})).$$

Note that the second term is zero because it is the circle product of a dual vector quaternion with a dual scalar quaternion. Moreover, the third term can be shown to be equal to zero as follows:

$$(\boldsymbol{\omega}^{\mathrm{B}}_{\mathrm{B/D}})^{\mathsf{s}} \circ (-(\boldsymbol{\omega}^{\mathrm{B}}_{\mathrm{B/D}} + \boldsymbol{\omega}^{\mathrm{B}}_{\mathrm{D/I}}) \times (M^{\mathrm{B}} \star ((\boldsymbol{\omega}^{\mathrm{B}}_{\mathrm{B/D}})^{\mathsf{s}} + (\boldsymbol{\omega}^{\mathrm{B}}_{\mathrm{D/I}}))^{\mathsf{s}}) - M^{\mathrm{B}} \star (\boldsymbol{\omega}^{\mathrm{B}}_{\mathrm{D/I}} \times \boldsymbol{\omega}^{\mathrm{B}}_{\mathrm{B/D}})^{\mathsf{s}}$$

$$+\boldsymbol{\omega}^{\mathrm{B}}_{\mathrm{D/I}} \times (M^{\mathrm{B}} \star (\boldsymbol{\omega}^{\mathrm{B}}_{\mathrm{D/I}})^{\mathsf{s}})) = ((\boldsymbol{\omega}^{\mathrm{B}}_{\mathrm{B/I}})^{\mathsf{s}} - (\boldsymbol{\omega}^{\mathrm{B}}_{\mathrm{D/I}})^{\mathsf{s}}) \circ (-\boldsymbol{\omega}^{\mathrm{B}}_{\mathrm{B/I}} \times (M^{\mathrm{B}} \star (\boldsymbol{\omega}^{\mathrm{B}}_{\mathrm{B/I}})^{\mathsf{s}})$$

$$-M^{\mathrm{B}} \star (\boldsymbol{\omega}^{\mathrm{B}}_{\mathrm{D/I}} \times (\boldsymbol{\omega}^{\mathrm{B}}_{\mathrm{B/I}} - \boldsymbol{\omega}^{\mathrm{B}}_{\mathrm{D/I}}))^{\mathsf{s}} + \boldsymbol{\omega}^{\mathrm{B}}_{\mathrm{D/I}} \times (M^{\mathrm{B}} \star (\boldsymbol{\omega}^{\mathrm{B}}_{\mathrm{D/I}})^{\mathsf{s}}))$$

$$= (\boldsymbol{\omega}^{\mathrm{B}}_{\mathrm{B/I}})^{\mathsf{s}} \circ (-\boldsymbol{\omega}^{\mathrm{B}}_{\mathrm{B/I}} \times (M^{\mathrm{B}} \star (\boldsymbol{\omega}^{\mathrm{B}}_{\mathrm{B/I}})^{\mathsf{s}}) - M^{\mathrm{B}} \star (\boldsymbol{\omega}^{\mathrm{B}}_{\mathrm{D/I}} \times \boldsymbol{\omega}^{\mathrm{B}}_{\mathrm{B/I}})^{\mathsf{s}} + \boldsymbol{\omega}^{\mathrm{B}}_{\mathrm{D/I}} \times (M^{\mathrm{B}} \star (\boldsymbol{\omega}^{\mathrm{B}}_{\mathrm{D/I}})^{\mathsf{s}}))$$

$$-(\boldsymbol{\omega}^{\mathrm{B}}_{\mathrm{D/I}})^{\mathsf{s}} \circ (-\boldsymbol{\omega}^{\mathrm{B}}_{\mathrm{B/I}} \times (M^{\mathrm{B}} \star (\boldsymbol{\omega}^{\mathrm{B}}_{\mathrm{B/I}})^{\mathsf{s}}) - M^{\mathrm{B}} \star (\boldsymbol{\omega}^{\mathrm{B}}_{\mathrm{D/I}} \times \boldsymbol{\omega}^{\mathrm{B}}_{\mathrm{B/I}})^{\mathsf{s}} + \boldsymbol{\omega}^{\mathrm{B}}_{\mathrm{D/I}} \times (M^{\mathrm{B}} \star (\boldsymbol{\omega}^{\mathrm{B}}_{\mathrm{D/I}})^{\mathsf{s}}))$$

$$= -(\boldsymbol{\omega}^{\mathrm{B}}_{\mathrm{B/I}})^{\mathsf{s}} \circ (\boldsymbol{\omega}^{\mathrm{B}}_{\mathrm{B/I}} \times (M^{\mathrm{B}} \star (\boldsymbol{\omega}^{\mathrm{B}}_{\mathrm{B/I}})^{\mathsf{s}})) - (\boldsymbol{\omega}^{\mathrm{B}}_{\mathrm{B/I}})^{\mathsf{s}} \circ (M^{\mathrm{B}} \star (\boldsymbol{\omega}^{\mathrm{B}}_{\mathrm{D/I}} \times \boldsymbol{\omega}^{\mathrm{B}}_{\mathrm{B/I}})^{\mathsf{s}})$$

$$+(\boldsymbol{\omega}^{\mathrm{B}}_{\mathrm{B/I}})^{\mathsf{s}} \circ (\boldsymbol{\omega}^{\mathrm{B}}_{\mathrm{D/I}} \times (M^{\mathrm{B}} \star (\boldsymbol{\omega}^{\mathrm{B}}_{\mathrm{D/I}})^{\mathsf{s}})) + (\boldsymbol{\omega}^{\mathrm{B}}_{\mathrm{D/I}})^{\mathsf{s}} \circ (\boldsymbol{\omega}^{\mathrm{B}}_{\mathrm{B/I}} \times (M^{\mathrm{B}} \star (\boldsymbol{\omega}^{\mathrm{B}}_{\mathrm{B/I}})^{\mathsf{s}}))$$

$$+(\boldsymbol{\omega}^{\mathrm{B}}_{\mathrm{D/I}})^{\mathsf{s}} \circ (M^{\mathrm{B}} \star (\boldsymbol{\omega}^{\mathrm{B}}_{\mathrm{D/I}} \times \boldsymbol{\omega}^{\mathrm{B}}_{\mathrm{B/I}})^{\mathsf{s}}) - (\boldsymbol{\omega}^{\mathrm{B}}_{\mathrm{D/I}})^{\mathsf{s}} \circ (\boldsymbol{\omega}^{\mathrm{B}}_{\mathrm{D/I}} \times (M^{\mathrm{B}} \star (\boldsymbol{\omega}^{\mathrm{B}}_{\mathrm{D/I}})^{\mathsf{s}})).$$

Note that the first and last terms are zero due to Lemmas 55 and 56. Moreover, using Lemmas 39 and 37, the second and fifth terms can be rewritten as

$$-(M^{\mathrm{B}} \star (\boldsymbol{\omega}^{\mathrm{B}}_{\mathrm{B/I}})^{\mathsf{s}})^{\mathsf{s}} \circ (\boldsymbol{\omega}^{\mathrm{B}}_{\mathrm{D/I}} \times \boldsymbol{\omega}^{\mathrm{B}}_{\mathrm{B/I}}) + (\boldsymbol{\omega}^{\mathrm{B}}_{\mathrm{B/I}})^{\mathsf{s}} \circ (\boldsymbol{\omega}^{\mathrm{B}}_{\mathrm{D/I}} \times (M^{\mathrm{B}} \star (\boldsymbol{\omega}^{\mathrm{B}}_{\mathrm{D/I}})^{\mathsf{s}}))$$

$$+(\boldsymbol{\omega}^{\mathrm{B}}_{\mathrm{D/I}})^{\mathsf{s}} \circ (\boldsymbol{\omega}^{\mathrm{B}}_{\mathrm{B/I}} \times (M^{\mathrm{B}} \star (\boldsymbol{\omega}^{\mathrm{B}}_{\mathrm{B/I}})^{\mathsf{s}})) + (M^{\mathrm{B}} \star (\boldsymbol{\omega}^{\mathrm{B}}_{\mathrm{D/I}})^{\mathsf{s}})^{\mathsf{s}} \circ (\boldsymbol{\omega}^{\mathrm{B}}_{\mathrm{D/I}} \times \boldsymbol{\omega}^{\mathrm{B}}_{\mathrm{B/I}}).$$

Finally, applying Lemmas 55 and 57 to the first and last terms of the previous expression yields

$$-(\boldsymbol{\omega}^{\mathrm{B}}_{\mathrm{D/I}})^{\mathsf{s}} \circ (\boldsymbol{\omega}^{\mathrm{B}}_{\mathrm{B/I}} \times (M^{\mathrm{B}} \star (\boldsymbol{\omega}^{\mathrm{B}}_{\mathrm{B/I}})^{\mathsf{s}})) + (\boldsymbol{\omega}^{\mathrm{B}}_{\mathrm{B/I}})^{\mathsf{s}} \circ (\boldsymbol{\omega}^{\mathrm{B}}_{\mathrm{D/I}} \times (M^{\mathrm{B}} \star (\boldsymbol{\omega}^{\mathrm{B}}_{\mathrm{D/I}})^{\mathsf{s}}))$$

$$+(\boldsymbol{\omega}^{\mathrm{B}}_{\mathrm{D/I}})^{\mathsf{s}} \circ (\boldsymbol{\omega}^{\mathrm{B}}_{\mathrm{B/I}} \times (M^{\mathrm{B}} \star (\boldsymbol{\omega}^{\mathrm{B}}_{\mathrm{B/I}})^{\mathsf{s}})) - (\boldsymbol{\omega}^{\mathrm{B}}_{\mathrm{B/I}})^{\mathsf{s}} \circ (\boldsymbol{\omega}^{\mathrm{B}}_{\mathrm{D/I}} \times (M^{\mathrm{B}} \star (\boldsymbol{\omega}^{\mathrm{B}}_{\mathrm{D/I}})^{\mathsf{s}})) = \mathbf{0}.$$

Therefore, the time derivative of the Lyapunov function is equal to $\dot{V} = -k_d(\boldsymbol{\omega}^{\mathrm{B}}_{\mathrm{B/D}})^{\mathsf{s}} \circ (\boldsymbol{\omega}^{\mathrm{B}}_{\mathrm{B/D}})^{\mathsf{s}} \leq 0$, for all $(\boldsymbol{q}_{\mathrm{B/D}}, \boldsymbol{\omega}^{\mathrm{B}}_{\mathrm{B/D}}) \in \mathbb{H}^u_d \times \mathbb{H}^v_d \backslash \{\mathbf{1}, \mathbf{0}\}$. Hence, $\boldsymbol{q}_{\mathrm{B/D}}$ and $\boldsymbol{\omega}^{\mathrm{B}}_{\mathrm{B/D}}$ are uniformly bounded, i.e., $\boldsymbol{q}_{\mathrm{B/D}}, \boldsymbol{\omega}^{\mathrm{B}}_{\mathrm{B/D}} \in \mathcal{L}_\infty$.

Since $V \geq 0$ and $\dot{V} \leq 0$, $\lim_{t\to\infty} V(t)$ exists and is finite. By integrating both sides of $\dot{V} = -k_d(\boldsymbol{\omega}^{\mathrm{B}}_{\mathrm{B/D}})^{\mathsf{s}} \circ (\boldsymbol{\omega}^{\mathrm{B}}_{\mathrm{B/D}})^{\mathsf{s}} \leq 0$, one obtains $\lim_{t\to\infty} \int_0^t \dot{V}(\tau)\,\mathrm{d}\tau = \lim_{t\to\infty} V(t) - V(0) = -\lim_{t\to\infty} \int_0^t k_d(\boldsymbol{\omega}^{\mathrm{B}}_{\mathrm{B/D}}(\tau))^{\mathsf{s}} \circ (\boldsymbol{\omega}^{\mathrm{B}}_{\mathrm{B/D}}(\tau))^{\mathsf{s}} \mathrm{d}\tau$ or

$$\lim_{t\to\infty} \int_0^t k_d(\boldsymbol{\omega}^{\mathrm{B}}_{\mathrm{B/D}}(\tau))^{\mathsf{s}} \circ (\boldsymbol{\omega}^{\mathrm{B}}_{\mathrm{B/D}}(\tau))^{\mathsf{s}}\,\mathrm{d}\tau \leq V(0). \tag{80}$$

Since $\boldsymbol{q}_{\mathrm{B/D}}, \boldsymbol{\omega}^{\mathrm{B}}_{\mathrm{B/D}} \in \mathcal{L}_\infty$ and $\dot{\boldsymbol{\omega}}^{\mathrm{D}}_{\mathrm{D/I}}, \boldsymbol{\omega}^{\mathrm{D}}_{\mathrm{D/I}} \in \mathcal{L}_\infty$ by assumption, from Eq. (79) it follows

that $\boldsymbol{f}^{\mathrm{B}} \in \mathcal{L}_\infty$ as well. Then, from Eq. (71) it also follows that $\dot{\boldsymbol{\omega}}^{\mathrm{B}}_{\mathrm{B/D}} \in \mathcal{L}_\infty$. Along with Eq. (80), this implies that $\boldsymbol{\omega}^{\mathrm{B}}_{\mathrm{B/D}} \to \mathbf{0}$ as $t \to \infty$, according to Barbalat's lemma [41].

It can also be shown that $\dot{\boldsymbol{\omega}}^{\mathrm{B}}_{\mathrm{B/D}} \to \mathbf{0}$ as $t \to \infty$. First, note that

$$\lim_{t\to\infty} \int_0^t \dot{\boldsymbol{\omega}}^{\mathrm{B}}_{\mathrm{B/D}}(\tau)\,\mathrm{d}\tau = \lim_{t\to\infty} \boldsymbol{\omega}^{\mathrm{B}}_{\mathrm{B/D}}(t) - \boldsymbol{\omega}^{\mathrm{B}}_{\mathrm{B/D}}(0) = -\boldsymbol{\omega}^{\mathrm{B}}_{\mathrm{B/D}}(0)$$

exits and is finite. Now note that $\ddot{\boldsymbol{\omega}}^{\mathrm{B}}_{\mathrm{B/D}} \in \mathcal{L}_\infty$ since $\dot{\boldsymbol{\omega}}^{\mathrm{D}}_{\mathrm{D/I}}, \boldsymbol{\omega}^{\mathrm{D}}_{\mathrm{D/I}}, \dot{\boldsymbol{\omega}}^{\mathrm{B}}_{\mathrm{B/D}}, \boldsymbol{\omega}^{\mathrm{B}}_{\mathrm{B/D}}, \boldsymbol{q}_{\mathrm{B/D}}, \dot{\boldsymbol{q}}_{\mathrm{B/D}} \in \mathcal{L}_\infty$. Hence, by Barbalat's lemma, $\dot{\boldsymbol{\omega}}^{\mathrm{B}}_{\mathrm{B/D}} \to \mathbf{0}$ as $t \to \infty$.

Finally, calculating the limit as $t \to \infty$ of both sides of Eq. (71) yields

$$\mathrm{vec}(\boldsymbol{q}^*_{\mathrm{B/D}}(\boldsymbol{q}^{\mathsf{s}}_{\mathrm{B/D}} - \mathbf{1}^{\mathsf{s}})) \to \mathbf{0} \text{ as } t \to \infty. \tag{81}$$

Note that

$$\begin{aligned}\mathrm{vec}(\boldsymbol{q}^*_{\mathrm{B/D}}(\boldsymbol{q}^{\mathsf{s}}_{\mathrm{B/D}} - \mathbf{1}^{\mathsf{s}})) &= \mathrm{vec}((q^*_{\mathrm{B/I}} + \epsilon\tfrac{1}{2}(r^{\mathrm{B}}_{\mathrm{B/I}})^* q^*_{\mathrm{B/I}})(\tfrac{1}{2} q_{\mathrm{B/I}} r^{\mathrm{B}}_{\mathrm{B/I}} + \epsilon(q_{\mathrm{B/I}} - 1)) \\ &= \mathrm{vec}(\tfrac{1}{2} r^{\mathrm{B}}_{\mathrm{B/I}} + \epsilon(1 - q^*_{\mathrm{B/I}} + \tfrac{1}{4}(r^{\mathrm{B}}_{\mathrm{B/I}})^* r^{\mathrm{B}}_{\mathrm{B/I}})) = \mathrm{vec}(\tfrac{1}{2} r^{\mathrm{B}}_{\mathrm{B/I}} - \epsilon q^*_{\mathrm{B/I}}) \to \mathbf{0}\end{aligned}$$

is equivalent to $\boldsymbol{q}_{\mathrm{B/D}} \to \pm\mathbf{1}$. □

The closed-loop system created with the feedback law derived in Theorem 1 is illustrated in Figure 3.

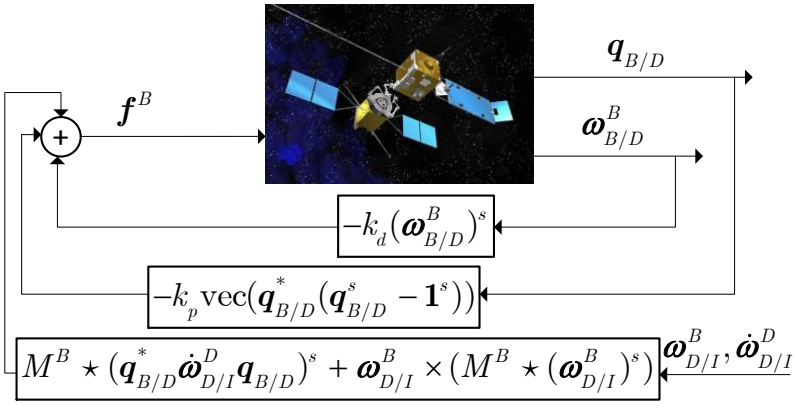

Figure 3: Closed-loop system with velocity feedback.

3.2 Velocity-Free Pose-Tracking Controller

The pose-tracking controller presented in Section 3.1 is almost globally asymptotically stable, but requires measurements of $\boldsymbol{\omega}^{\mathrm{B}}_{\mathrm{B/D}}$. The next theorem shows that it is still possible to obtain an almost globally asymptotically stable pose-tracking controller without measurements of $\boldsymbol{\omega}^{\mathrm{B}}_{\mathrm{B/D}}$.

Theorem 2. *Consider the rigid body relative kinematic and dynamic equations given by Eq.* (55) *and Eq.* (71)*, respectively. Let the total external dual force acting on the rigid body be defined by the feedback control law*

$$\begin{aligned}\boldsymbol{f}^{\mathrm{B}} = &-k_p \mathrm{vec}(\boldsymbol{q}^{*}_{\mathrm{B/D}}(\boldsymbol{q}^{\mathsf{s}}_{\mathrm{B/D}} - \mathbf{1}^{\mathsf{s}})) - 2\mathrm{vec}(\boldsymbol{q}^{*}_{\mathrm{B/D}}\boldsymbol{z}^{\mathsf{s}}) + M^{\mathrm{B}} \star (\boldsymbol{q}^{*}_{\mathrm{B/D}} \dot{\boldsymbol{\omega}}^{\mathrm{D}}_{\mathrm{D/I}} \boldsymbol{q}_{\mathrm{B/D}})^{\mathsf{s}} \\ &+ \boldsymbol{\omega}^{\mathrm{B}}_{\mathrm{D/I}} \times (M^{\mathrm{B}} \star (\boldsymbol{\omega}^{\mathrm{B}}_{\mathrm{D/I}})^{\mathsf{s}}), \quad k_p > 0, \end{aligned} \tag{82}$$

where $\boldsymbol{z}$ *is the output of the LTI system* $\dot{\boldsymbol{x}}_{\mathrm{p}} = A \star \boldsymbol{x}_{\mathrm{p}} + B \star \boldsymbol{q}_{\mathrm{B/D}}$ *and* $\boldsymbol{z} = (CA) \star \boldsymbol{x}_{\mathrm{p}} + (CB) \star \boldsymbol{q}_{\mathrm{B/D}}$*,* (A, B, C) *is a minimal realization of a strictly positive real transfer matrix* $C_{\mathrm{sp}}(s)$*, and* B *is a full rank matrix. Assume that* $\dot{\boldsymbol{\omega}}^{\mathrm{D}}_{\mathrm{D/I}}, \boldsymbol{\omega}^{\mathrm{D}}_{\mathrm{D/I}} \in \mathcal{L}_\infty$*. Then,* $\boldsymbol{q}_{\mathrm{B/D}} \to \pm\mathbf{1}$*,* $\boldsymbol{\omega}^{\mathrm{B}}_{\mathrm{B/D}} \to \mathbf{0}$*, and* $\boldsymbol{x}_{\mathrm{sp}} = \dot{\boldsymbol{x}}_{\mathrm{p}} \to \mathbf{0}$ *as* $t \to +\infty$ *for all initial conditions.*

Proof. First, rewrite the LTI system as follows:

$$\dot{\boldsymbol{x}}_{\mathrm{sp}} = A \star \boldsymbol{x}_{\mathrm{sp}} + B \star \dot{\boldsymbol{q}}_{\mathrm{B/D}} \quad \text{and} \quad \boldsymbol{z} = C \star \boldsymbol{x}_{\mathrm{sp}}. \tag{83}$$

Note that $\boldsymbol{q}_{\mathrm{B/D}} = \pm\mathbf{1}$, $\boldsymbol{\omega}^{\mathrm{B}}_{\mathrm{B/D}} = \mathbf{0}$, and $\boldsymbol{x}_{\mathrm{sp}} = \mathbf{0}$ is the equilibrium condition of the closed-loop system formed by Eqs. (71), (55), (83), and (82). Consider the candidate Lyapunov function

$$V(\boldsymbol{q}_{\mathrm{B/D}}, \boldsymbol{\omega}^{\mathrm{B}}_{\mathrm{B/D}}, \boldsymbol{x}_{\mathrm{sp}}) = k_p(\boldsymbol{q}_{\mathrm{B/D}} - \mathbf{1}) \circ (\boldsymbol{q}_{\mathrm{B/D}} - \mathbf{1}) + \tfrac{1}{2}(\boldsymbol{\omega}^{\mathrm{B}}_{\mathrm{B/D}})^{\mathsf{s}} \circ (M^{\mathrm{B}} \star (\boldsymbol{\omega}^{\mathrm{B}}_{\mathrm{B/D}})^{\mathsf{s}}) + 2\boldsymbol{x}_{\mathrm{sp}} \circ (P \star \boldsymbol{x}_{\mathrm{sp}})$$

for the equilibrium point $\boldsymbol{q}_{\mathrm{B/D}} = \mathbf{1}$, $\boldsymbol{\omega}^{\mathrm{B}}_{\mathrm{B/D}} = \mathbf{0}$, and $\boldsymbol{x}_{\mathrm{sp}} = \mathbf{0}$, where $P = P^{\mathsf{T}} > 0$ satisfies $A^{\mathsf{T}}P + PA = -Q$, $PB = C^{\mathsf{T}}$, and $Q = Q^{\mathsf{T}} > 0$. By the *Kalman-Yakubovich-Popov* (KYP) conditions [41], there always exist matrices P and Q satisfying these

conditions, since (A, B, C) is a minimal realization of a strictly positive real transfer matrix $C_{\rm sp}(s)$. Note that V is a valid candidate Lyapunov function since $V(\boldsymbol{q}_{\rm B/D} = \mathbf{1}, \boldsymbol{\omega}^{\rm B}_{\rm B/D} = \mathbf{0}, \boldsymbol{x}_{\rm sp} = \mathbf{0}) = 0$ and $V(\boldsymbol{q}_{\rm B/D}, \boldsymbol{\omega}^{\rm B}_{\rm B/D}, \boldsymbol{x}_{\rm sp}) > 0$ for all $(\boldsymbol{q}_{\rm B/D}, \boldsymbol{\omega}^{\rm B}_{\rm B/D}, \boldsymbol{x}_{\rm sp}) \in \mathbb{H}^u_d \times \mathbb{H}^v_d \times \mathbb{H}_d \backslash \{\mathbf{1}, \mathbf{0}, \mathbf{0}\}$. The time derivative of V is equal to $\dot{V} = 2k_p(\boldsymbol{q}_{\rm B/D} - \mathbf{1}) \circ \dot{\boldsymbol{q}}_{\rm B/D} + (\boldsymbol{\omega}^{\rm B}_{\rm B/D})^{\mathsf{s}} \circ (M^{\rm B} \star (\dot{\boldsymbol{\omega}}^{\rm B}_{\rm B/D})^{\mathsf{s}}) + 4\dot{\boldsymbol{x}}_{\rm sp} \circ (P \star \boldsymbol{x}_{\rm sp})$. By plugging in Eqs. (55) and (71) and applying Lemma 33 and the KYP conditions, it follows that

$$\dot{V} = (\boldsymbol{\omega}^{\rm B}_{\rm B/D})^{\mathsf{s}} \circ (k_p \boldsymbol{q}^*_{\rm B/D}(\boldsymbol{q}^{\mathsf{s}}_{\rm B/D} - \mathbf{1}^{\mathsf{s}}) + \boldsymbol{f}^{\rm B} - (\boldsymbol{\omega}^{\rm B}_{\rm B/D} + \boldsymbol{\omega}^{\rm B}_{\rm D/I}) \times (M^{\rm B} \star ((\boldsymbol{\omega}^{\rm B}_{\rm B/D})^{\mathsf{s}} + (\boldsymbol{\omega}^{\rm B}_{\rm D/I})^{\mathsf{s}}))$$
$$-M^{\rm B} \star (\boldsymbol{q}^*_{\rm B/D} \dot{\boldsymbol{\omega}}^{\rm D}_{\rm D/I} \boldsymbol{q}_{\rm B/D})^{\mathsf{s}} - M^{\rm B} \star (\boldsymbol{\omega}^{\rm B}_{\rm D/I} \times \boldsymbol{\omega}^{\rm B}_{\rm B/D})^{\mathsf{s}}) + 4(A \star \boldsymbol{x}_{\rm sp} + B \star \dot{\boldsymbol{q}}_{\rm B/D}) \circ (P \star \boldsymbol{x}_{\rm sp}).$$

Introducing the feedback control law given by Eq. (82) yields

$$\dot{V} = (\boldsymbol{\omega}^{\rm B}_{\rm B/D})^{\mathsf{s}} \circ (-2\mathrm{vec}(\boldsymbol{q}^*_{\rm B/D} \boldsymbol{z}^{\mathsf{s}})) + (\boldsymbol{\omega}^{\rm B}_{\rm B/D})^{\mathsf{s}} \circ (k_p \boldsymbol{q}^*_{\rm B/D}(\boldsymbol{q}^{\mathsf{s}}_{\rm B/D} - \mathbf{1}^{\mathsf{s}})$$
$$-k_p \mathrm{vec}(\boldsymbol{q}^*_{\rm B/D}(\boldsymbol{q}^{\mathsf{s}}_{\rm B/D} - \mathbf{1}^{\mathsf{s}}))) + (\boldsymbol{\omega}^{\rm B}_{\rm B/D})^{\mathsf{s}} \circ (-(\boldsymbol{\omega}^{\rm B}_{\rm B/D} + \boldsymbol{\omega}^{\rm B}_{\rm D/I}) \times (M^{\rm B} \star ((\boldsymbol{\omega}^{\rm B}_{\rm B/D})^{\mathsf{s}} + (\boldsymbol{\omega}^{\rm B}_{\rm D/I})^{\mathsf{s}}))$$
$$-M^{\rm B} \star (\boldsymbol{\omega}^{\rm B}_{\rm D/I} \times \boldsymbol{\omega}^{\rm B}_{\rm B/D})^{\mathsf{s}} + \boldsymbol{\omega}^{\rm B}_{\rm D/I} \times (M^{\rm B} \star (\boldsymbol{\omega}^{\rm B}_{\rm D/I})^{\mathsf{s}})) + 4(A \star \boldsymbol{x}_{\rm sp} + B \star \dot{\boldsymbol{q}}_{\rm B/D}) \circ (P \star \boldsymbol{x}_{\rm sp}).$$

Again, note that the second term is zero because it is the circle product of a dual vector quaternion with a dual scalar quaternion. Moreover, the third term has been shown to be equal to zero in the proof of Theorem 1. As for the fourth term, it can be simplified as follows:

$$\dot{V} = (\boldsymbol{\omega}^{\rm B}_{\rm B/D})^{\mathsf{s}} \circ (-2\mathrm{vec}(\boldsymbol{q}^*_{\rm B/D} \boldsymbol{z}^{\mathsf{s}})) + 4(A \star \boldsymbol{x}_{\rm sp}) \circ (P \star \boldsymbol{x}_{\rm sp}) + 4(B \star \dot{\boldsymbol{q}}_{\rm B/D}) \circ (P \star \boldsymbol{x}_{\rm sp})$$
$$= (\boldsymbol{\omega}^{\rm B}_{\rm B/D})^{\mathsf{s}} \circ (-2\mathrm{vec}(\boldsymbol{q}^*_{\rm B/D} \boldsymbol{z}^{\mathsf{s}})) + 2((A^{\mathsf{T}} P + PA) \star \boldsymbol{x}_{\rm sp}) \circ \boldsymbol{x}_{\rm sp} + 4\dot{\boldsymbol{q}}_{\rm B/D} \circ ((B^T P) \star \boldsymbol{x}_{\rm sp})$$
$$= (\boldsymbol{\omega}^{\rm B}_{\rm B/D})^{\mathsf{s}} \circ (-2\mathrm{vec}(\boldsymbol{q}^*_{\rm B/D} \boldsymbol{z}^{\mathsf{s}})) - 2\boldsymbol{x}_{\rm sp} \circ (Q \star \boldsymbol{x}_{\rm sp}) + 2(\boldsymbol{q}_{\rm B/D} \boldsymbol{\omega}^{\rm B}_{\rm B/D}) \circ (C \star \boldsymbol{x}_{\rm sp})$$
$$= (\boldsymbol{\omega}^{\rm B}_{\rm B/D})^{\mathsf{s}} \circ (2\boldsymbol{q}^*_{\rm B/D} \boldsymbol{z}^{\mathsf{s}} - 2\mathrm{vec}(\boldsymbol{q}^*_{\rm B/D} \boldsymbol{z}^{\mathsf{s}})) - 2\boldsymbol{x}_{\rm sp} \circ (Q \star \boldsymbol{x}_{\rm sp}) = -2\boldsymbol{x}_{\rm sp} \circ (Q \star \boldsymbol{x}_{\rm sp}) \leq 0$$

for all $(\boldsymbol{q}_{\rm B/D}, \boldsymbol{\omega}^{\rm B}_{\rm B/D}, \boldsymbol{x}_{\rm sp}) \in \mathbb{H}^u_d \times \mathbb{H}^v_d \times \mathbb{H}_d \backslash \{\mathbf{1}, \mathbf{0}, \mathbf{0}\}$. Hence, $\boldsymbol{q}_{\rm B/D}$, $\boldsymbol{\omega}^{\rm B}_{\rm B/D}$, and $\boldsymbol{x}_{\rm sp}$ are uniformly bounded, i.e., $\boldsymbol{q}_{\rm B/D}, \boldsymbol{\omega}^{\rm B}_{\rm B/D}, \boldsymbol{x}_{\rm sp} \in \mathcal{L}_\infty$.

It is now shown that $\boldsymbol{x}_{\rm sp} \to \mathbf{0}$ as $t \to \infty$. Since $V \geq 0$ and $\dot{V} \leq 0$, $\lim_{t\to\infty} V(t)$ exists and is finite. By integrating both sides of $\dot{V} = -2\boldsymbol{x}_{\rm sp} \circ (Q \star \boldsymbol{x}_{\rm sp}) \leq 0$, one obtains

$\lim_{t\to\infty}\int_0^t \dot{V}(\tau)\,\mathrm{d}\tau = \lim_{t\to\infty} V(t) - V(0) = -\lim_{t\to\infty}\int_0^t 2\boldsymbol{x}_{\mathrm{sp}}(\tau)\circ(Q\star\boldsymbol{x}_{\mathrm{sp}}(\tau))\mathrm{d}\tau$ or

$$\lim_{t\to\infty}\int_0^t 2\boldsymbol{x}_{\mathrm{sp}}(\tau)\circ(Q\star\boldsymbol{x}_{\mathrm{sp}}(\tau))\,\mathrm{d}\tau \leq V(0). \tag{84}$$

Since $\boldsymbol{q}_{\mathrm{B/D}}, \boldsymbol{\omega}^{\mathrm{B}}_{\mathrm{B/D}}, \boldsymbol{x}_{\mathrm{sp}} \in \mathcal{L}_\infty$, it follows that $\dot{\boldsymbol{q}}_{\mathrm{B/D}} \in \mathcal{L}_\infty$ and $\dot{\boldsymbol{x}}_{\mathrm{sp}} \in \mathcal{L}_\infty$. Along with Eq. (84), this implies that $\boldsymbol{x}_{\mathrm{sp}} \to \mathbf{0}$ as $t \to \infty$, according to Barbalat's lemma. This, in turn, implies that $\boldsymbol{z} \to \mathbf{0}$ as $t \to \infty$ from Eq. (83).

It can also be shown that $\dot{\boldsymbol{x}}_{\mathrm{sp}} \to \mathbf{0}$ as $t \to \infty$. First, note that

$$\lim_{t\to\infty}\int_0^t \dot{\boldsymbol{x}}_{\mathrm{sp}}(\tau)\,\mathrm{d}\tau = \lim_{t\to\infty}\boldsymbol{x}_{\mathrm{sp}}(t) - \boldsymbol{x}_{\mathrm{sp}}(0) = -\boldsymbol{x}_{\mathrm{sp}}(0)$$

exits and is finite. Since $\ddot{\boldsymbol{x}}_{\mathrm{sp}} = A\star\dot{\boldsymbol{x}}_{\mathrm{sp}} + B\star\ddot{\boldsymbol{q}}_{\mathrm{B/D}}$ and

$$\boldsymbol{q}_{\mathrm{B/D}}, \boldsymbol{\omega}^{\mathrm{B}}_{\mathrm{B/D}}, \boldsymbol{x}_{\mathrm{sp}}, \dot{\boldsymbol{q}}_{\mathrm{B/D}}, \dot{\boldsymbol{x}}_{\mathrm{sp}}, \dot{\boldsymbol{\omega}}^{\mathrm{D}}_{\mathrm{D/I}}, \boldsymbol{\omega}^{\mathrm{D}}_{\mathrm{D/I}}, \boldsymbol{z}, \dot{\boldsymbol{\omega}}^{\mathrm{B}}_{\mathrm{B/D}}, \ddot{\boldsymbol{q}}_{\mathrm{B/D}} \in \mathcal{L}_\infty,$$

it follows that $\ddot{\boldsymbol{x}}_{\mathrm{sp}} \in \mathcal{L}_\infty$. Hence, by Barbalat's lemma, $\dot{\boldsymbol{x}}_{\mathrm{sp}} \to \mathbf{0}$ as $t \to \infty$.

Thus, calculating the limit as $t \to \infty$ of both sides of Eq. (83) yields $\dot{\boldsymbol{q}}_{\mathrm{B/D}} \to \mathbf{0}$ as $t \to \infty$, since B is assumed to be full rank. Given that Eq. (55) can be rewritten as $\boldsymbol{\omega}^{\mathrm{B}}_{\mathrm{B/D}} = 2\boldsymbol{q}^*_{\mathrm{B/D}}\dot{\boldsymbol{q}}_{\mathrm{B/D}}$, this implies that $\boldsymbol{\omega}^{\mathrm{B}}_{\mathrm{B/D}} \to \mathbf{0}$ as $t \to \infty$.

Now, it is shown that $\dot{\boldsymbol{\omega}}^{\mathrm{B}}_{\mathrm{B/D}} \to \mathbf{0}$ as $t \to \infty$. First, note that $\lim_{t\to\infty}\int_0^t \dot{\boldsymbol{\omega}}^{\mathrm{B}}_{\mathrm{B/D}}(\tau)\,\mathrm{d}\tau = \lim_{t\to\infty}\boldsymbol{\omega}^{\mathrm{B}}_{\mathrm{B/D}}(t) - \boldsymbol{\omega}^{\mathrm{B}}_{\mathrm{B/D}}(0) = -\boldsymbol{\omega}^{\mathrm{B}}_{\mathrm{B/D}}(0)$ exits and is finite. Since

$$\begin{aligned}(\ddot{\boldsymbol{\omega}}^{\mathrm{B}}_{\mathrm{B/D}})^{\mathsf{s}} = (M^{\mathrm{B}})^{-1}\star(-k_p\mathrm{vec}(\dot{\boldsymbol{q}}^*_{\mathrm{B/D}}(\boldsymbol{q}^{\mathsf{s}}_{\mathrm{B/D}} - \mathbf{1}^{\mathsf{s}})) - k_p\mathrm{vec}(\boldsymbol{q}^*_{\mathrm{B/D}}(\dot{\boldsymbol{q}}^{\mathsf{s}}_{\mathrm{B/D}}))-2\mathrm{vec}(\dot{\boldsymbol{q}}^*_{\mathrm{B/D}}\boldsymbol{z}^{\mathsf{s}})\\ -2\mathrm{vec}(\boldsymbol{q}^*_{\mathrm{B/D}}(\dot{\boldsymbol{z}})^{\mathsf{s}})+\dot{\boldsymbol{\omega}}^{\mathrm{B}}_{\mathrm{D/I}}\times(M^{\mathrm{B}}\star(\boldsymbol{\omega}^{\mathrm{B}}_{\mathrm{D/I}})^{\mathsf{s}})+\boldsymbol{\omega}^{\mathrm{B}}_{\mathrm{D/I}}\times(M^{\mathrm{B}}\star(\dot{\boldsymbol{\omega}}^{\mathrm{B}}_{\mathrm{D/I}})^{\mathsf{s}})-\dot{\boldsymbol{\omega}}^{\mathrm{B}}_{\mathrm{B/I}}\times(M^{\mathrm{B}}\star(\boldsymbol{\omega}^{\mathrm{B}}_{\mathrm{B/I}})^{\mathsf{s}})\\ -\boldsymbol{\omega}^{\mathrm{B}}_{\mathrm{B/I}}\times(M^{\mathrm{B}}\star(\dot{\boldsymbol{\omega}}^{\mathrm{B}}_{\mathrm{B/I}})^{\mathsf{s}}) - M^{\mathrm{B}}\star(\dot{\boldsymbol{\omega}}^{\mathrm{B}}_{\mathrm{D/I}}\times\boldsymbol{\omega}^{\mathrm{B}}_{\mathrm{B/D}})^{\mathsf{s}} - M^{\mathrm{B}}\star(\boldsymbol{\omega}^{\mathrm{B}}_{\mathrm{D/I}}\times\dot{\boldsymbol{\omega}}^{\mathrm{B}}_{\mathrm{B/D}})^{\mathsf{s}})\end{aligned}$$

and $\dot{\boldsymbol{\omega}}^{\mathrm{B}}_{\mathrm{B/D}}, \boldsymbol{\omega}^{\mathrm{B}}_{\mathrm{B/D}}, \dot{\boldsymbol{\omega}}^{\mathrm{B}}_{\mathrm{B/I}}, \boldsymbol{\omega}^{\mathrm{B}}_{\mathrm{B/I}}, \boldsymbol{q}_{\mathrm{B/D}}, \dot{\boldsymbol{q}}_{\mathrm{B/D}}, \boldsymbol{z}, \dot{\boldsymbol{z}} \in \mathcal{L}_\infty$, it follows that $\ddot{\boldsymbol{\omega}}^{\mathrm{B}}_{\mathrm{B/D}} \in \mathcal{L}_\infty$. Hence, by Barbalat's lemma, $\dot{\boldsymbol{\omega}}^{\mathrm{B}}_{\mathrm{B/D}} \to \mathbf{0}$ as $t \to \infty$.

Finally, calculating the limit as $t \to \infty$ of both sides of Eq. (71) yields Eq. (81), which is equivalent to $\boldsymbol{q}_{\mathrm{B/D}} \to \pm\mathbf{1}$ (as shown in the proof of Theorem 1). □

Remark 1. Theorems 1 and 2 state that $\boldsymbol{q}_{\mathrm{B/D}}$ converges to either $+\mathbf{1}$ or $-\mathbf{1}$. Note that $\boldsymbol{q}_{\mathrm{B/D}} = +\mathbf{1}$ and $\boldsymbol{q}_{\mathrm{B/D}} = -\mathbf{1}$ represent the same pose. Therefore, either equilibrium

is acceptable. However, this can lead to the so-called *unwinding phenomenon*, where a large rotation (greater than 180 deg) is performed despite the fact that a smaller rotation (less than 180 deg) exits. This problem of quaternions is well documented and possible solutions exist in literature [43, 7, 63, 93].

Remark 2. If the reference pose is constant, i.e., $\boldsymbol{\omega}^{\mathrm{D}}_{\mathrm{D/I}} = 0$, then the pose-tracking controllers suggested in Theorems 1 and 2 become pose-stabilization controllers. Note that in this special case, the feedback control laws given by Eqs. (79) and (82) do not depend on M^{B}, i.e., they do not depend on the mass and inertia matrix of the rigid body.

Remark 3. The closed-loop system created with the feedback law derived in Theorem 2 is illustrated in Figure 4 in state space form. By choosing A and B as $-k_f I_8$

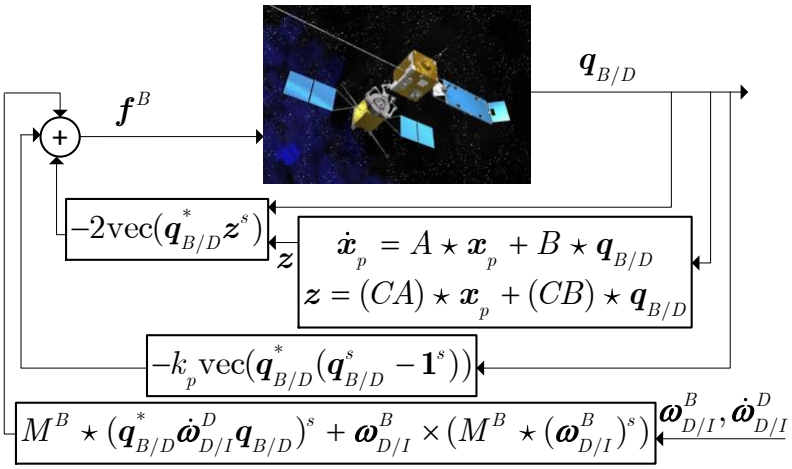

Figure 4: Closed-loop system without velocity feedback in state-space form.

and $k_f I_8$, respectively, where $k_f > 0$, and by defining $Q = -k_d(B^{-\intercal}A + A^{\intercal}B^{-\intercal})$ as in Ref. [60], the KYP conditions yield $P = k_d B^{-\intercal}$ and $C = k_d I_8$. Then, the closed-loop system represented in Figure 4 in state space form can be represented in transfer matrix form as shown in Figure 5, where $d = k_d k_f$ and $a = k_f$. In this case, $\boldsymbol{z}$ is obtained by differentiating $\boldsymbol{q}_{\mathrm{B/D}}$ and passing $\dot{\boldsymbol{q}}_{\mathrm{B/D}}$ through a low-pass filter. Theorem 2 proves that in the absence of measurement noise, the cut-off frequency of the

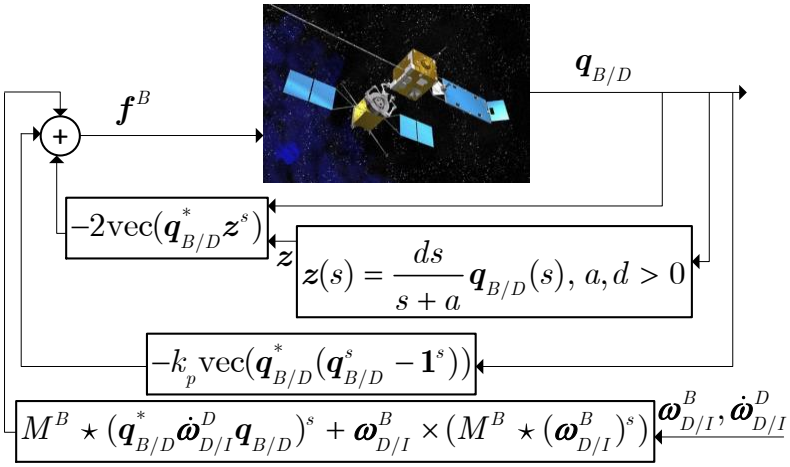

Figure 5: Closed-loop system without velocity feedback in transfer matrix form.

low-pass filter can be chosen arbitrarily. In practice, in the presence of measurement noise, the cut-off frequency of the low-pass filter has to be chosen low enough to reject high-frequency noise.

3.3 Simulation Results

The velocity-free pose-tracking controllers given by Eqs. (79) and (82) are numerically verified and compared in this section via two examples.

3.3.1 Rigid Body Example

The first example consist of a rigid body subject to no external forces and torques that is required to track a relatively demanding sinusoidal pose reference.

The inertia matrix and mass of the rigid body are assumed to be

$$\bar{I}^{\mathrm{B}} = \begin{bmatrix} 1 & 0 & 0 \\ 0 & 0.63 & 0 \\ 0 & 0 & 0.85 \end{bmatrix} \ \mathrm{kg}\cdot\mathrm{m}^2$$

and $m = 1$ kg. The initial conditions for this example are $\bar{r}^{\mathrm{B}}_{\mathrm{B/D}}(0) = [20, 20, 10]^{\intercal}$ m, $[q_{\mathrm{B/D}}(0)] = [0.3320, 0.4618, 0.1917, 0.7999]^{\intercal}$, $\bar{v}^{\mathrm{B}}_{\mathrm{B/D}}(0) = [0.1, -0.2, 0.3]^{\intercal}$ m/s, $\bar{\omega}^{\mathrm{B}}_{\mathrm{B/D}}(0) = [-0.1, 0.2, -0.3]^{\intercal}$ rad/s, and $[\boldsymbol{x}_{\mathrm{p}}(0)] = 0_{8\times 1}$.

The reference pose is given by $\bar{v}^{\mathrm{D}}_{\mathrm{D/I}} = -[0.1, 0.2, 0.3]^{\intercal} \cos(2\pi[10^{-1}, 10^{-1}, 10^{-1}]^{\intercal} + \frac{\pi}{180}[30, 60, 90]^{\intercal})$ m/s and $\bar{\omega}^{\mathrm{D}}_{\mathrm{D/I}} = [0.1, 0.2, 0.3]^{\intercal} \cos(2\pi[10^{-1}, 10^{-1}, 10^{-1}]^{\intercal} + \frac{\pi}{180}[0, 45, 90]^{\intercal})$ rad/s. It is illustrated in Figure 6.

The control gains are chosen as $k_p = 0.2$ (both in Eq. (79) and Eq. (82)) and $k_d = 0.4$ (in Eq. (79)). The matrices of the LTI system are chosen as in Remark 3.

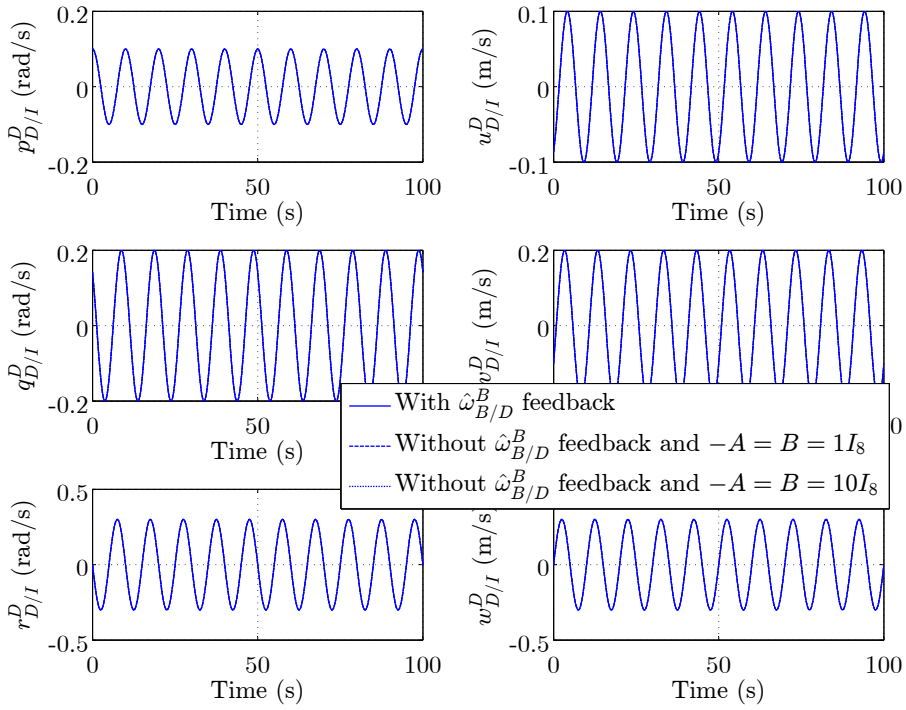

Figure 6: Desired linear and angular velocity expressed in the desired frame.

The pose of the body frame with respect to the desired frame obtained with the controller given by Eq. (79) (with velocity feedback) and with the controller given by Eq. (82) (without velocity feedback) for $k_f = 1$ and $k_f = 10$ is shown in Figure 7. In all three cases, $q_{\mathrm{B/D}} \to \mathtt{1}$ and $r^{\mathrm{B}}_{\mathrm{B/D}} \to \mathtt{0}$ as $t \to \infty$, as expected. Figure 8 shows the linear and angular velocity of the body frame with respect to the desired frame for the same three cases studied in Figure 7. As expected, $\omega^{\mathrm{B}}_{\mathrm{B/D}} \to \mathtt{0}$ and $v^{\mathrm{B}}_{\mathrm{B/D}} \to \mathtt{0}$ as $t \to \infty$. Finally, Figure 9 shows the control force and torque for the same three cases.

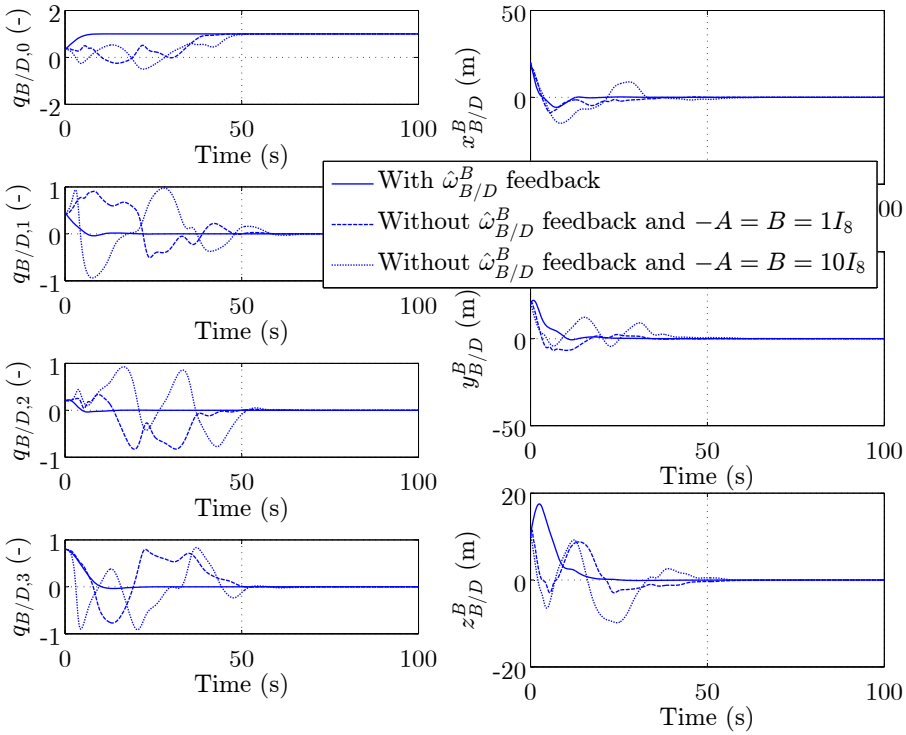

Figure 7: Pose of the body frame with respect to the desired frame.

3.3.2 Satellite Proximity Operations Example

The second example consists of a satellite proximity operations scenario where a chaser satellite is required to track an elliptical motion around a target satellite while pointing at it.

Four reference frames are defined: the inertial frame, the target frame, the desired frame, and the body frame. The inertial frame is the *Earth-Centered-Inertial* (ECI) frame. The body frame is some frame fixed to the chaser satellite and centered at its center of mass. The target frame and the desired frame are defined as

$$\bar{I}_{\mathrm{T}} = \frac{\bar{r}_{\mathrm{T/I}}}{\|\bar{r}_{\mathrm{T/I}}\|}, \qquad \bar{J}_{\mathrm{T}} = \bar{K}_{\mathrm{T}} \times \bar{I}_{\mathrm{T}}, \qquad \bar{K}_{\mathrm{T}} = \frac{\bar{\omega}_{\mathrm{T/I}}}{\|\bar{\omega}_{\mathrm{T/I}}\|}$$

and

$$\bar{I}_{\mathrm{D}} = \frac{\bar{r}_{\mathrm{D/T}}}{\|\bar{r}_{\mathrm{D/T}}\|}, \qquad \bar{J}_{\mathrm{D}} = \bar{K}_{\mathrm{D}} \times \bar{I}_{\mathrm{D}}, \qquad \bar{K}_{\mathrm{D}} \parallel \bar{K}_{\mathrm{T}},$$

respectively, where $\bar{\omega}_{\mathrm{T/I}} = \frac{\bar{r}_{\mathrm{T/I}} \times \bar{v}_{\mathrm{T/I}}}{\|\bar{r}_{\mathrm{T/I}}\|^2}$ is calculated from the orbital angular momentum

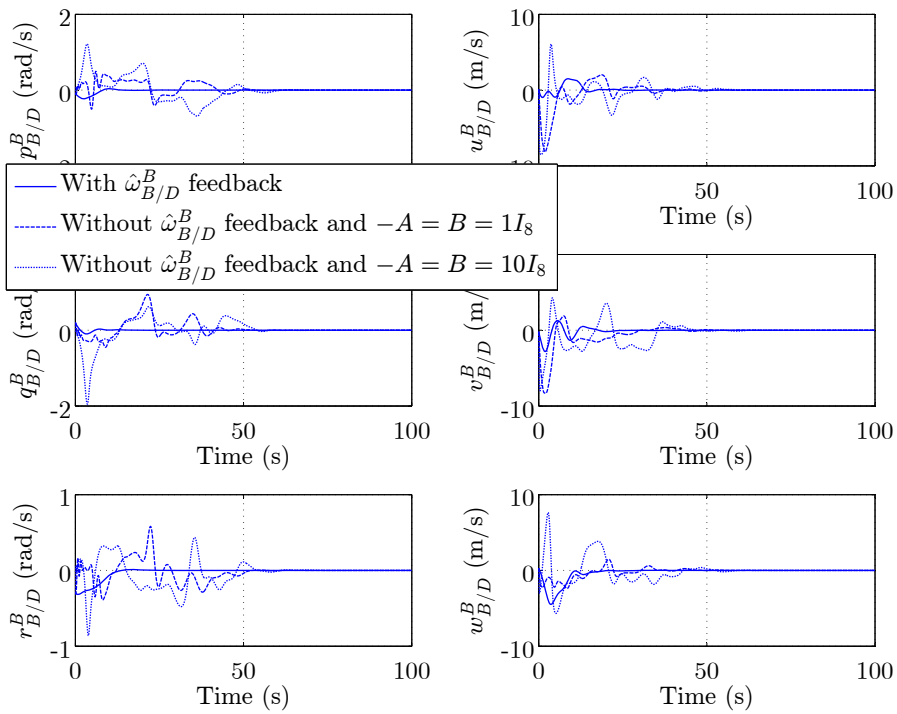

Figure 8: Linear and angular velocity of the body frame with respect to the desired frame expressed in the body frame.

vector of the target spacecraft with respect to the inertial frame given by $\bar{H}_{\mathrm{T/I}} = m\|\bar{r}_{\mathrm{T/I}}\|^2\bar{\omega}_{\mathrm{T/I}} = \bar{r}_{\mathrm{T/I}} \times (m\bar{v}_{\mathrm{T/I}})$. The target satellite is assumed to be fixed to the target frame. The different frames are illustrated in Figure 10. The control objective is to superimpose the body frame onto the desired frame.

The target spacecraft is assumed to be in a highly eccentric Molniya orbit with initial orbital elements given in Table 2 and nadir pointing. The relative motion of the desired frame with respect to the target frame is defined as an ellipse in the $\bar{I}_{\mathrm{T}}$-$\bar{J}_{\mathrm{T}}$ plane with semi-major axis equal to 20 m along $\bar{J}_{\mathrm{T}}$ and semi-minor axis equal to 10 m along $\bar{I}_{\mathrm{T}}$. The relative motion has constant angular speed equal to the mean motion of the target satellite. More precisely, during this phase, $\bar{\omega}^{\mathrm{T}}_{\mathrm{D/T}} = [0, 0, n]^\intercal$ rad/s and $\bar{v}^{\mathrm{T}}_{\mathrm{D/T}} = [-a_e n \sin(nt), b_e n \cos(nt), 0]^\intercal$ m/s, where $a_e = 10$ m, $b_e = 20$ m, $n = \sqrt{\mu/a^3}$ is the mean motion of the target satellite (assuming no J_2-perturbation), and a is the semi-major axis of the target satellite (assuming no J_2-perturbation).

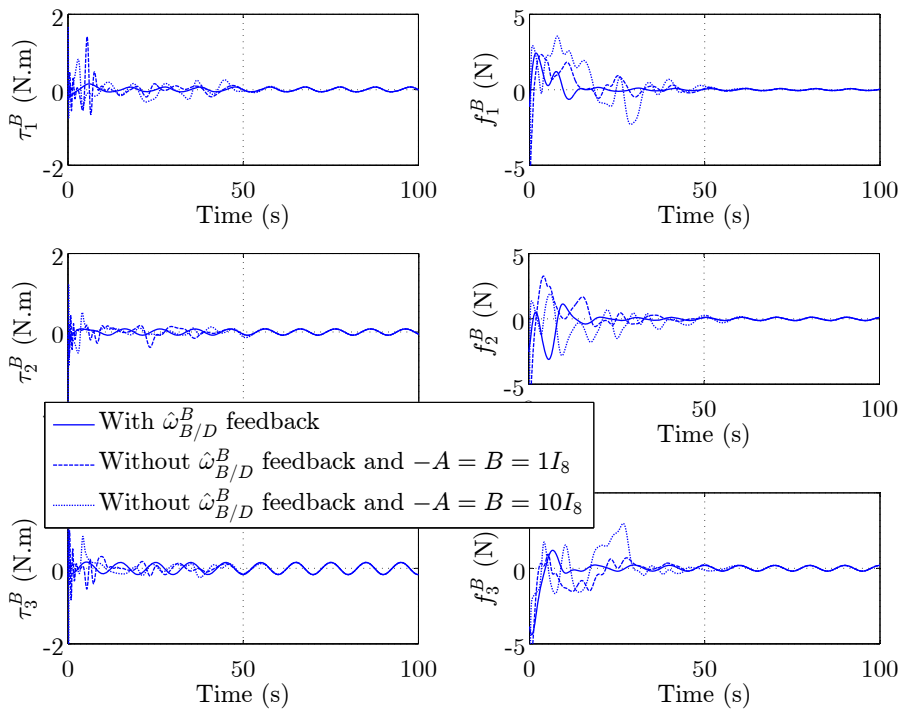

Figure 9: Control force and torque expressed in the body frame.

The linear velocity of the target satellite with respect to the inertial frame is calculated by numerically integrating the gravitational acceleration and also the perturbing acceleration due to Earth's oblateness. On the other hand, the angular acceleration of the target satellite with respect to the inertial frame is calculated analytically through

$$\alpha_{\mathrm{T/I}}^{\mathrm{I}} = \dot{\omega}_{\mathrm{T/I}}^{\mathrm{I}} = \frac{(r_{\mathrm{T/I}}^{\mathrm{I}} \times a_{\mathrm{T/I}}^{\mathrm{I}})\|r_{\mathrm{T/I}}^{\mathrm{I}}\|^2 - (r_{\mathrm{T/I}}^{\mathrm{I}} \times v_{\mathrm{T/I}}^{\mathrm{I}})2(r_{\mathrm{T/I}}^{\mathrm{I}} \cdot v_{\mathrm{T/I}}^{\mathrm{I}})}{\|r_{\mathrm{T/I}}^{\mathrm{I}}\|^4}. \tag{85}$$

Note that the J_2-perturbation changes the direction of the target's angular velocity

Table 2: Initial orbital elements of the target satellite.

	Molniya orbit	GEO
Perigee altitude (km)	813.2	35786
Eccentricity (-)	0.7	0
Inclination (deg)	63.4	0
Argument of perigee (deg)	270	0
RAAN (deg)	329.6	0
True anomaly (deg)	180	0

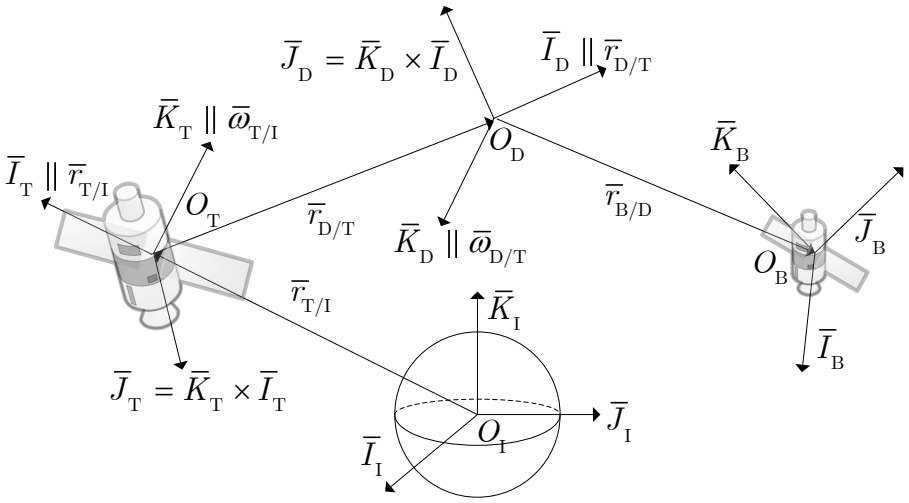

Figure 10: Reference frames.

with respect to the inertial frame. However, this change is relatively small in this scenario due to the critical inclination of the Molniya orbit. The rotational and translational kinematic equations of the target frame with respect to the inertial frame and of the desired frame with respect to the target frame are calculated through Eq. (50).

The pose-tracking controllers given by Eqs. (79) and (82) are functions of $\boldsymbol{\omega}^{\mathrm{D}}_{\mathrm{D/I}}$ and $\dot{\boldsymbol{\omega}}^{\mathrm{D}}_{\mathrm{D/I}}$. These variables are calculated using dual quaternion algebra as follows:

$$\boldsymbol{\omega}^{\mathrm{D}}_{\mathrm{D/I}} = \boldsymbol{\omega}^{\mathrm{D}}_{\mathrm{T/I}} + \boldsymbol{\omega}^{\mathrm{D}}_{\mathrm{D/T}} = \boldsymbol{q}^{*}_{\mathrm{D/I}} \boldsymbol{\omega}^{\mathrm{I}}_{\mathrm{T/I}} \boldsymbol{q}_{\mathrm{D/I}} + \boldsymbol{q}^{*}_{\mathrm{D/T}} \boldsymbol{\omega}^{\mathrm{T}}_{\mathrm{D/T}} \boldsymbol{q}_{\mathrm{D/T}}, \tag{86}$$

$$\dot{\boldsymbol{\omega}}^{\mathrm{D}}_{\mathrm{D/I}} = \boldsymbol{q}^{*}_{\mathrm{D/I}} \boldsymbol{\alpha}^{\mathrm{I}}_{\mathrm{T/I}} \boldsymbol{q}_{\mathrm{D/I}} - \boldsymbol{\omega}^{\mathrm{D}}_{\mathrm{D/I}} \times \boldsymbol{\omega}^{\mathrm{D}}_{\mathrm{T/I}} + \boldsymbol{q}^{*}_{\mathrm{D/T}} \boldsymbol{\alpha}^{\mathrm{T}}_{\mathrm{D/T}} \boldsymbol{q}_{\mathrm{D/T}}, \tag{87}$$

where $\boldsymbol{\alpha}^{\mathrm{T}}_{\mathrm{D/T}} = \dot{\boldsymbol{\omega}}^{\mathrm{T}}_{\mathrm{D/T}} = \alpha^{\mathrm{T}}_{\mathrm{D/T}} + \epsilon(a^{\mathrm{T}}_{\mathrm{D/T}} - \alpha^{\mathrm{T}}_{\mathrm{D/T}} \times r^{\mathrm{T}}_{\mathrm{D/T}} - \omega^{\mathrm{T}}_{\mathrm{D/T}} \times v^{\mathrm{T}}_{\mathrm{D/T}})$ and $\boldsymbol{\alpha}^{\mathrm{I}}_{\mathrm{T/I}} = \dot{\boldsymbol{\omega}}^{\mathrm{I}}_{\mathrm{T/I}} = \alpha^{\mathrm{I}}_{\mathrm{T/I}} + \epsilon(a^{\mathrm{I}}_{\mathrm{T/I}} - \alpha^{\mathrm{I}}_{\mathrm{T/I}} \times r^{\mathrm{I}}_{\mathrm{T/I}} - \omega^{\mathrm{I}}_{\mathrm{T/I}} \times v^{\mathrm{I}}_{\mathrm{T/I}})$. Equation (87) is calculated by differentiating Eq. (86) and using Proposition 2. Note that instead of using dual quaternion algebra to calculate $\boldsymbol{\omega}^{\mathrm{D}}_{\mathrm{D/I}}$ and $\dot{\boldsymbol{\omega}}^{\mathrm{D}}_{\mathrm{D/I}}$, one could instead calculate $\omega^{\mathrm{D}}_{\mathrm{D/I}}$, $\dot{\omega}^{\mathrm{D}}_{\mathrm{D/I}}$, $v^{\mathrm{D}}_{\mathrm{D/I}}$, and $\dot{v}^{\mathrm{D}}_{\mathrm{D/I}}$ using the traditional equations for a point moving with respect to a rotating frame. However, this would require the calculation of four parameters instead of just two and significant more work to calculate $v^{\mathrm{D}}_{\mathrm{D/I}}$ and $\dot{v}^{\mathrm{D}}_{\mathrm{D/I}}$, whose expressions are coupled with the rotational

motion. Thus, Eqs. (86) and (87) are another good example of the benefits in terms of compactness and simplicity of using dual quaternions.

The inertia matrix and mass of the chaser satellite are assumed to be [93]

$$\bar{I}^{\mathrm{B}} = \begin{bmatrix} 22 & 0.2 & 0.5 \\ 0.2 & 20 & 0.4 \\ 0.5 & 0.4 & 23 \end{bmatrix} \ \mathrm{kg} \cdot \mathrm{m}^2$$

and $m = 100$ kg. The initial conditions for this example are $\bar{r}^{\mathrm{B}}_{\mathrm{B/D}}(0)=[5,5,5]^{\intercal}$ m, $q_{\mathrm{B/D}}(0) = [0.3320, 0.4618, 0.1917, 0.7999]^{\intercal}$, $\bar{v}^{\mathrm{B}}_{\mathrm{B/D}}(0) = [0.1, 0.1, 0.1]^{\intercal}$ m/s, $\bar{\omega}^{\mathrm{B}}_{\mathrm{B/D}}(0) = [0.1, 0.1, 0.1]^{\intercal}$ rad/s, and $\boldsymbol{x}_{\mathrm{p}}(0) = \boldsymbol{q}_{\mathrm{B/D}}(0)$. The constant disturbance force and torque acting on the chaser satellite are set to $\bar{f}^{\mathrm{B}}_{d} = [0.005, 0.005, 0.005]^{\intercal}$ N and $\bar{\tau}^{\mathrm{B}}_{d} = [0.005, 0.005, 0.005]^{\intercal}$ N $\cdot$ m, respectively.

The control gains are chosen as $k_p = 0.2$ (both in Eq. (79) and Eq. (82)) and $k_d = 4$ (in Eq. (79)). The matrices of the LTI system are chosen as in Remark 3 with $k_f = 10$.

Figure 11 shows the linear and angular velocity of the desired frame with respect to the inertial frame expressed in the desired frame for the complete maneuver. These signals define the desired motion.

Figure 12 shows the initial transient response of the pose of the body frame with respect to the desired frame obtained with Eq. (79) (feedback law with velocity feedback) and with Eq. (82) (feedback law without velocity feedback). Both controllers are able to superimpose the body frame onto the desired frame after the initial transient response.

Figure 13 shows the linear and angular velocity of the body frame with respect to the desired frame obtained with Eqs. (79) and (82). Again, after the initial transient response, both controllers cancel the relative linear and angular velocity of the body frame with respect to the desired frame.

Figure 14 shows the control force and control torque during the initial transient

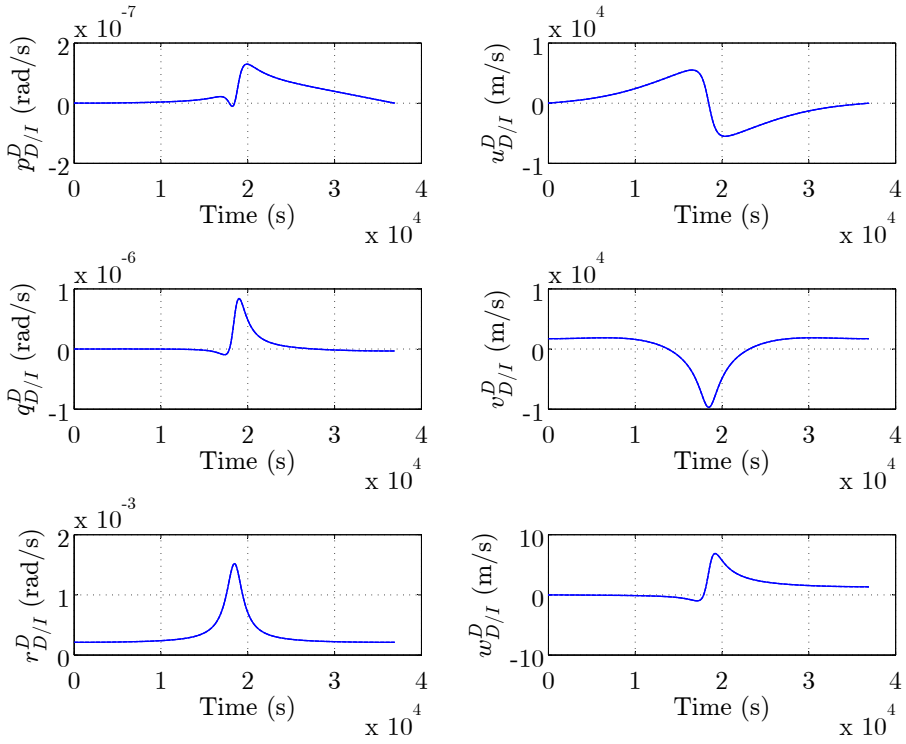

Figure 11: Reference motion.

response produced by Eqs. (79) and (82). For completeness, Figure 15 shows the control force and torque for the complete maneuver. As a comparison, the complete maneuver requires a ΔV of 3.7614 m/s if done with Eq. (79) (with velocity feedback) and 0.0196 m/s more if done with Eq. (82) (without velocity feedback).

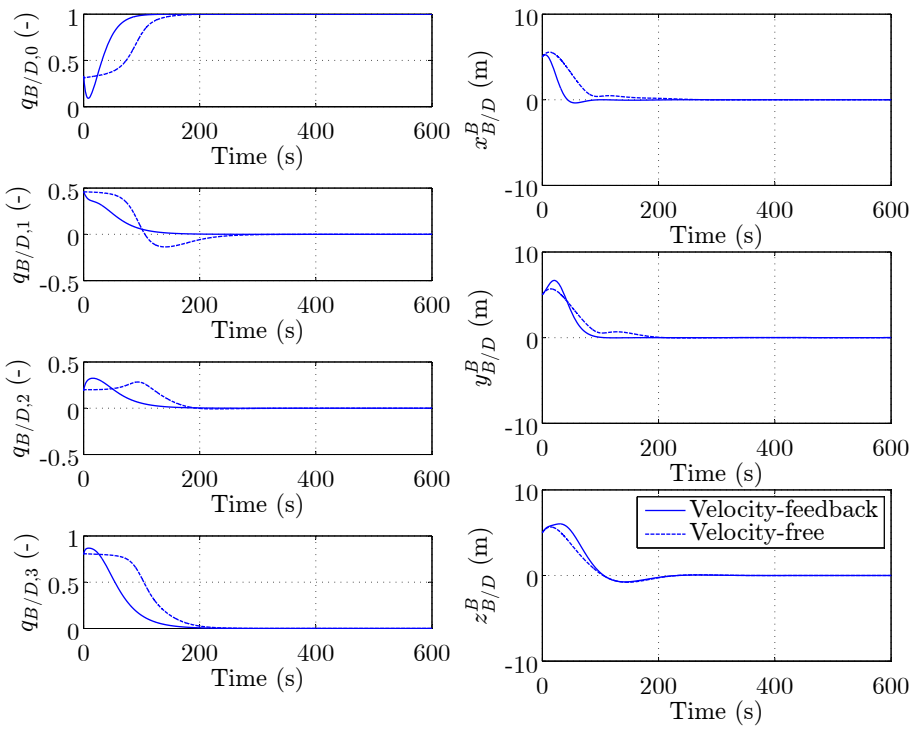

Figure 12: Pose of the body frame with respect to the desired frame.

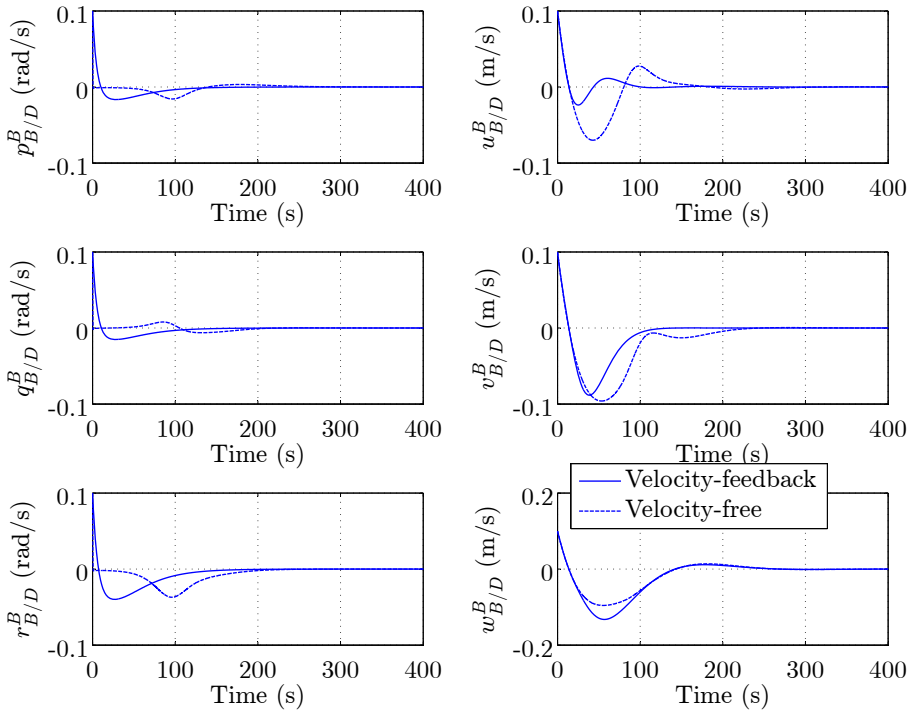

Figure 13: Linear and angular velocity of the body frame with respect to the desired frame.

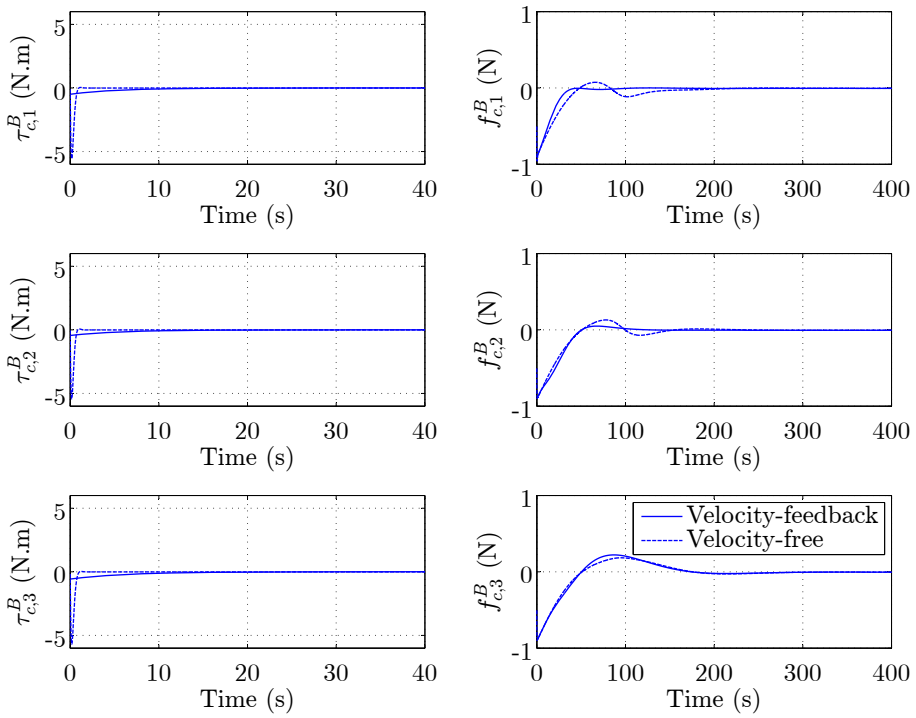

Figure 14: Control force and torque during the initial transient response.

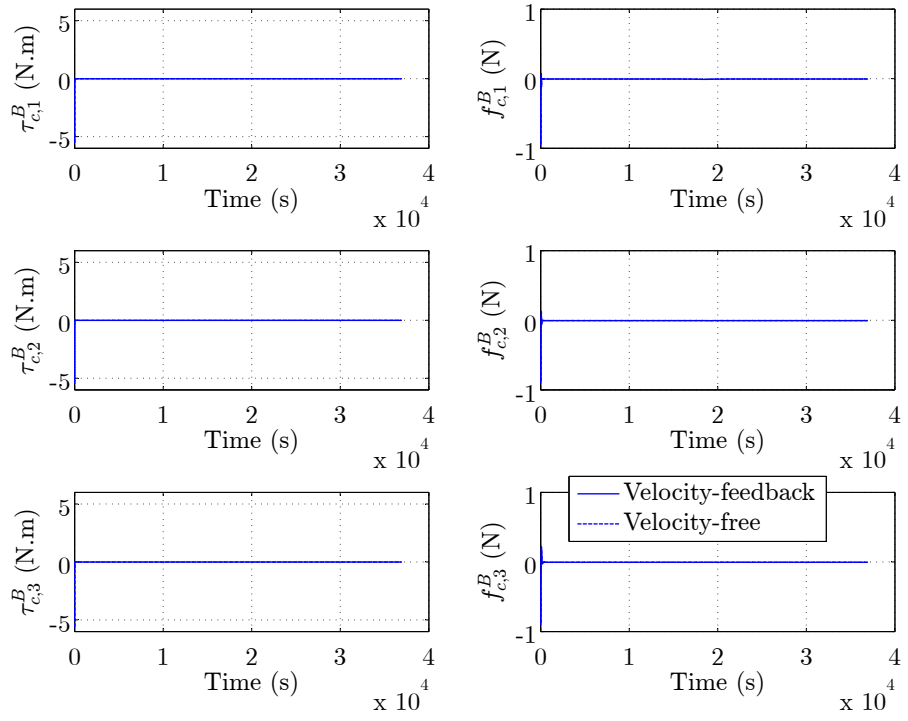

Figure 15: Control force and torque during the complete maneuver.

CHAPTER IV

DUAL QUATERNION MULTIPLICATIVE EXTENDED KALMAN FILTER (DQ-MEFK) FOR SPACECRAFT POSE ESTIMATION

The highly successful Quaternion Multiplicative Extended Kalman Filter (Q-MEKF) based on unit quaternions for spacecraft attitude estimation, described in detail in Section XI of Ref. [57], has been used extensively in several NASA spacecraft [21]. It has been analyzed in great detail throughout the years [109, 62]. Part of its success lies on the fact that unit quaternions provide a global non-singular representation of attitude with the minimum number of parameters. Moreover, they appear linearly in the kinematic equations of motion, unlike Euler angles which require the calculation of computationally expensive trigonometric functions. Another reason for the success of the Q-MEKF is that it does not rely on a model of the system dynamics. In fact, the lack of success of Kalman filtering before 1967 is attributed to the inability to model the system dynamics accurately enough [57]. Although newer approaches, such as nonlinear observers, have been shown to have some advantages over the classical EKF, a comprehensive survey of nonlinear attitude estimation methods [21] concluded that the classical EKF is still the most useful and practical solution.

An additional major advantage of the Q-MEKF described in Ref. [57] is that the 4-by-4 covariance matrix of the four elements of the unit quaternion does not need to be computed. As stated in Ref. [57], propagating the state covariance matrix is the largest computational burden in any Kalman filter implementation. By rewriting the state of the EKF in terms of the three elements of the vector part of the unit *error* quaternion between the true unit quaternion and its estimate, only a 3-by-3 covariance

matrix needs to be computed. The unavoidable drawback of this approach is that with just three elements, it is impossible to represent the attitude error globally. Indeed, by construction, the Q-MEKF will fail if the attitude error between the true attitude and its estimate is larger than 180 deg. However, unlike the true attitude of the body which can vary arbitrarily, the attitude error between the true attitude of the body and its estimate is expected to be close to zero, especially after the Q-MEFK has converged. Hence, in the Q-MEKF described in Ref. [57], whereas the attitude covariance matrix is only 3-by-3, the body can still have any arbitrary attitude. This is one of the most appealing properties of the Q-MEKF.

Based on the analogies between quaternions and dual quaternions, a Dual Quaternion Multiplicative EKF (DQ-MEKF) for spacecraft pose estimation based on the classical Q-MEKF for attitude estimation is derived in this chapter. As far as the author knowns, this is the first multiplicative EKF for combined position and attitude estimation.

The traditional approach to estimate the pose of a body consists on developing separate estimators for attitude and position. For example, Ref. [77] suggests two discrete-time linear Kalman filters to estimate the relative attitude and position separately. Since the translation Kalman filter requires the attitude estimated by the rotation Kalman filter, the former is only switched on after the latter as converged. Because of this inherent coupling between rotation and translation, several authors have proposed estimating the attitude and position simultaneously. For example, in Ref. [68], a lander's terrain-relative position and attitude are estimated simultaneously using an EKF. The state of the EKF contains the vector part of the unit error quaternion (like in the Q-MEKF) and the position vector of the lander with respect to the inertial frame expressed in the inertial frame. Also in Ref. [50], the relative position and attitude of two satellites are estimated simultaneously using an EKF. In this case, the state of the EKF contains the vector part of the unit error quaternion

(like the Q-MEKF) and the position vector of the chaser satellite with respect to the target satellite expressed in a reference frame attached to the target satellite. The approach described in Ref. [50] is cooperative, in the sense that the two satellites share their angular velocity measurements. Finally, Ref. [40] also estimates the position and attitude between two frames simultaneously using a discrete-time EKF. In Ref. [40], the state contains the position vector of a body with respect to some reference frame expressed in that reference frame and the four elements of the true quaternion describing the orientation of the body. Hence, Reference [40] does not take advantage of the concept of unit error quaternion. Moreover, in Ref. [40], the optimal Kalman state update is added to, and not multiplied with, the current best unit quaternion estimate, making the EKF presented in Ref. [40] additive and not multiplicative. However, Ref. [40] takes advantage of the compactness of dual quaternions to represent 3-D lines and their relative pose to develop the measurement update of the EKF.

As far as the author knows, the only previous EKF formulations where the state includes a unit dual quaternion are given in Refs. [6, 112]. However, these EKF formulations include the true unit dual quaternion describing the pose of the body and not the error unit dual quaternion between the true unit dual quaternion and its best estimate. Therefore, the state of the EKF formulations presented in Refs. [6, 112] contains all eight elements of a unit dual quaternion. Moreover, the EKF formulations proposed in Refs. [6, 112] are additive EKF formulations, i.e., the optimal Kalman state update is added to and not multiplied with the current best unit dual quaternion estimate. As a consequence, the predicted value of the unit dual quaternion immediately after a measurement update does not fulfill the two algebraic constraints that a unit dual quaternion must satisfy. Hence, in Ref. [6], this predicted value after a measurement update is further modified to satisfy these constraints through a process that includes parameters that must be tuned by the user. On the other hand, in

Ref. [112], these two algebraic constraints are simply not enforced after a measurement update, which can lead to numerical problems. Finally, it should be mentioned that the discrete-time EKF formulations in Refs. [6, 112] are designed to take only measurements from a camera.

Compared to the existing literature, the main contributions of this chapter are:

1) By using the concept of error unit dual quaternion defined analogously to the concept of error unit quaternion of the Q-MEKF, this chapter proposes, as far as the author knows, the first multiplicative EKF for pose estimation. As a consequence, the predicted value of the unit dual quaternion immediately after a measurement update automatically satisfies the two algebraic constraints of a unit dual quaternion. Unlike in Ref. [6], no additional parameters need to be tuned by the user.
2) By using the error unit dual quaternion instead of the true unit dual quaternion, the state of the DQ-MEKF is reduced from eight elements (as in Refs. [6, 112]) to just six. As a consequence, the associated computational cost is reduced. Moreover, the state estimate of the DQ-MEKF can be directly used by the pose controllers given in Refs. [28, 30] without additional conversions.
3) Similarly to the Q-MEKF, the DQ-MEKF is a *continuous-discrete Kalman filter* [59], i.e., the state and its covariance matrix are propagated continuously between discrete-time measurements. One of the advantages of this approach is that the discrete-time measurements do not need to be equally spaced in time, making irregular or intermittent measurements easy to handle. Moreover, this structure eases the integration of different sensors with different update rates. In particular, the DQ-MEKF described in this chapter is designed to take continuous-time linear and angular velocity measurements with noise and bias and discrete-time pose measurements with noise. This work also proposes two extensions of this standard DQ-MEKF. The first extension is designed to

take only discrete-time pose measurements with noise and estimate the linear and angular velocities. This version is suitable for uncooperative satellite proximity operation scenarios where the chaser satellite has only access to measurements of the relative pose (e.g., from a camera), but requires the relative linear and angular velocities for control. In the second extension, the linear velocity measurements of the standard DQ-MEKF are replaced with linear acceleration measurements with bias and noise. This version is suitable for a satellite equipped with an accelerometer and having no means of directly measuring linear velocity.

4) Finally, the two extensions of the standard DQ-MEKF are validated experimentally on a 5-DOF air-bearing platform. Moreover, the first extension is compared with two alternative EKF formulations, similar to the ones used in Refs. [68, 50, 40].

This chapter is organized as follows. In Section 4.1, the main equations of an EKF are reviewed. Then, the linear and angular velocity measurement model is defined in Section 4.2. The standard DQ-MEKF is derived in Section 4.3, whereas its two extensions are derived in Sections 4.4 and 4.5. In Section 4.6, the two extensions of the DQ-MEKF are validated experimentally and the first extension is compared with two alternative EKF formulations. Finally, two alternative solutions to the problem of pose-tracking without relative linear and angular velocity feedback are compared in Section 4.7. The first consists on using directly the velocity-free controller derived in Theorem 2, whereas the second consists on using the velocity-feedback controller derived in Theorem 1 while estimating the relative linear and angular velocities using the DQ-MEKF described in Section 4.4.

4.1 The Extended Kalman Filter

The main equations of the EKF are first reviewed in order to introduce the necessary notation for the remaining sections. The review is based on a similar review provided in Ref. [57] and serves as the starting point of the DQ-MEKF formulation.

The state equation of the EKF can be written as

$$\dot{x}_n(t) = f_n(x_n(t), t) + g_{n\times p}(x_n(t), t)w_p(t), \tag{88}$$

where $x_n(t) \in \mathbb{R}^n$ is the state and $w_p(t) \in \mathbb{R}^p$ is the process noise. The process noise is assumed to be a Gaussian white-noise process, whose mean and covariance function are given by $E\{w_p(t)\} = 0_{p\times 1}$ and $E\left\{w_p(t)w_p^\intercal(\tau)\right\} = Q_{p\times p}(t)\delta(t-\tau)$, where $Q_{p\times p}(t) \in \mathbb{R}^{p\times p}$ is a symmetric positive semidefinite matrix. The initial mean and covariance of the state are given by $E\{x_n(t_0)\} \triangleq \hat{x}_n(t_0) = x_{n,0} \in \mathbb{R}^n$ and $E\{(x_n(t_0) - x_{n,0})(x_n(t_0) - x_{n,0})^\intercal\} \triangleq P_{n\times n}(t_0) = P_{n\times n,0} \in \mathbb{R}^{n\times n}$ and are assumed to be known. (Note that in Refs. [6, 112], $p = n$ and $g_{n\times p}(x_n(t), t) = I_{n\times n}$.)

4.1.1 Time Update

Given the initial mean of the state, the minimum covariance estimate of the state at a future time t in the absence of measurements is given by the conditional expectation $\hat{x}_n(t) = E\{x_n(t)|\hat{x}_n(t_0) = x_{n,0}\}$. This estimate satisfies the differential equation $\dot{\hat{x}}_n(t) = E\{f_n(x_n(t), t)\}$, which is typically approximated as

$$\dot{\hat{x}}_n(t) \approx f_n(\hat{x}_n(t), t). \tag{89}$$

Hence, in the absence of measurements, the state estimate is propagated using Eq. (89).

In addition to the state estimate, also the covariance matrix of the state needs to be propagated. The covariance matrix of the state is given by

$$P_{n\times n}(t) = E\{\Delta x_n(t)\Delta x_n^\intercal(t)\} \in \mathbb{R}^{n\times n}, \tag{90}$$

where $\Delta x_n(t) = x_n(t) - \hat{x}_n(t) \in \mathbb{R}^n$ is the state error. As a first-order approximation, the derivative of the state error is given by

$$\frac{\mathrm{d}}{\mathrm{d}t}\Delta x_n(t) = F_{n\times n}(t)\Delta x_n(t) + G_{n\times p}(t)w_p(t) \tag{91}$$

and the covariance matrix of the state satisfies the Riccati equation

$$\dot{P}_{n\times n}(t) = F_{n\times n}(t)P_{n\times n}(t) + P_{n\times n}(t)F_{n\times n}^{\mathsf{T}}(t) + G_{n\times p}(t)Q_{p\times p}(t)G_{n\times p}^{\mathsf{T}}(t), \tag{92}$$

where

$$F_{n\times n}(t) \triangleq \left.\frac{\partial f_n(x_n,t)}{\partial x_n}\right|_{\hat{x}_n(t)} \in \mathbb{R}^{n\times n} \quad \text{and} \quad G_{n\times p}(t) \triangleq g_{n\times p}(\hat{x}_n(t),t) \in \mathbb{R}^{n\times p}. \tag{93}$$

Hence, in the absence of measurements, the covariance matrix of the state is propagated using Eq. (92).

4.1.2 Measurement Update

Assume that a measurement is taken at time t_k that is related with the state of the EKF through the nonlinear output equation

$$z_m(t_k) = h_m(x_n(t_k)) + v_m(t_k) \in \mathbb{R}^m, \tag{94}$$

where $v_m(t_k) \in \mathbb{R}^m$ is the measurement noise assumed to be a discrete Gaussian white-noise process whose mean and covariance function are given by $E\{v_m(t_k)\} = 0_{m\times 1}$ and $E\{v_m(t_k)v_m^{\mathsf{T}}(t_\ell)\} = R_{m\times m}(t_k)\delta_{t_k t_\ell}$, where $R_{m\times m}(t_k) \in \mathbb{R}^{m\times m}$ is a symmetric positive-definite matrix.

Immediately following the measurement at time t_k, the minimum variance estimate of $x_n(t_k)$ is given by

$$\hat{x}_n^+(t_k) = \hat{x}_n^-(t_k) + \Delta^\star\hat{x}_n(t_k), \tag{95}$$

where

$$\Delta^\star\hat{x}_n(t_k) = K_{n\times m}(t_k)\nu_m(t_k), \tag{96}$$

$$\nu_m(t_k) = z_m(t_k) - \hat{z}_m(t_k), \tag{97}$$

$\Delta^\star \hat{x}_n(t_k)$ is the optimal Kalman state update, $\nu_m(t_k)$ is termed the innovation or residual [25], $\hat{z}_m(t_k) = E\{z_m(t_k)\} \approx h_m(\hat{x}_n^-(t_k))$, $\hat{x}_n^-(t_k)$ and $\hat{x}_n^+(t_k)$ are the predicted values of the state immediately before and after the measurement, and $K_{n\times m}(t_k)$ is the Kalman gain. The Kalman gain is given by

$$K_{n\times m}(t_k) = P^-_{n\times n}(t_k) H^\intercal_{m\times n}(t_k) [H_{m\times n}(t_k) P^-_{n\times n}(t_k) H^\intercal_{m\times n}(t_k) + R_{m\times m}(t_k)]^{-1}, \tag{98}$$

where $P^-_{n\times n}(t_k)$ is the predicted state covariance matrix immediately before the measurement and

$$H_{m\times n}(t_k) = \left.\frac{\partial h_m(x_n)}{\partial x_n}\right|_{\hat{x}_n^-(t_k)} \in \mathbb{R}^{m\times n} \tag{99}$$

is the measurement sensitivity matrix.

Immediately after the measurement, the state covariance matrix is given by

$$\begin{aligned} P^+_{n\times n}(t_k) &= (I_{n\times n} - K_{n\times m}(t_k) H_{m\times n}(t_k)) P^-_{n\times n}(t_k) && (100)\\ &= (I_{n\times n} - K_{n\times m}(t_k) H_{m\times n}(t_k)) P^-_{n\times n}(t_k) (I_{n\times n} - K_{n\times m}(t_k) H_{m\times n}(t_k))^\intercal \\ &\quad + K_{n\times m}(t_k) R_{m\times m}(t_k) K_{n\times m}(t_k)^\intercal, && (101) \end{aligned}$$

where Eq. (101) is numerically more stable than Eq. (100).

Finally, the covariance matrix of the innovation is given by [25]

$$S_{m\times m}(t_k) = E\{\nu_m(t_k)\nu_m^\intercal(t_k)\} = R_{m\times m}(t_k) + H_{m\times n}(t_k) P^-_{n\times n}(t_k) H^\intercal_{m\times n}(t_k). \tag{102}$$

4.2 Angular and Linear Velocity Measurement Model

The dual velocity measurement model is defined analogously to the angular velocity measurement model typically used in literature [57, 21] as follows:

$$\boldsymbol{\omega}^{\mathrm{B}}_{\mathrm{B/I},m} = \boldsymbol{\omega}^{\mathrm{B}}_{\mathrm{B/I}} + \boldsymbol{b}_{\boldsymbol{\omega}} + \boldsymbol{\eta}_{\boldsymbol{\omega}}, \tag{103}$$

where $\boldsymbol{\omega}^{\mathrm{B}}_{\mathrm{B/I},m} = \omega^{\mathrm{B}}_{\mathrm{B/I},m} + \epsilon v^{\mathrm{B}}_{\mathrm{B/I},m} \in \mathbb{H}^v_d$, $\omega^{\mathrm{B}}_{\mathrm{B/I},m} = (0, \overline{\omega}^{\mathrm{B}}_{\mathrm{B/I},m})$, $\overline{\omega}^{\mathrm{B}}_{\mathrm{B/I},m}$ is a measurement of $\overline{\omega}^{\mathrm{B}}_{\mathrm{B/I}}$, $v^{\mathrm{B}}_{\mathrm{B/I},m} = (0, \overline{v}^{\mathrm{B}}_{\mathrm{B/I},m})$, $\overline{v}^{\mathrm{B}}_{\mathrm{B/I},m}$ is a measurement of $\overline{v}^{\mathrm{B}}_{\mathrm{B/I}}$, $\boldsymbol{b}_{\boldsymbol{\omega}} = b_\omega + \epsilon b_v$ is the *dual bias*,

$b_\omega = (0, \overline{b}_\omega)$, $\overline{b}_\omega \in \mathbb{R}^3$ is the bias of the angular velocity measurement, $b_v = (0, \overline{b}_v)$, $\overline{b}_v \in \mathbb{R}^3$ is the bias of the linear velocity measurement, $\boldsymbol{\eta_\omega} = \eta_\omega + \epsilon\eta_v$ is the *dual noise*, $\eta_\omega = (0, \overline{\eta}_\omega)$, $\overline{\eta}_\omega \in \mathbb{R}^3$ is the noise of the angular velocity measurement assumed to be a Gaussian white-noise process, $\eta_v = (0, \overline{\eta}_v)$, $\overline{\eta}_v \in \mathbb{R}^3$ is the noise of the linear velocity measurement assumed to be a Gaussian white-noise process, $E\left\{\overline{\boldsymbol{\eta}}_{\boldsymbol{\omega}}\right\} = 0_{6\times 1}$,

$$E\left\{\overline{\boldsymbol{\eta}}_{\boldsymbol{\omega}}(t)\overline{\boldsymbol{\eta}}_{\boldsymbol{\omega}}^{\mathrm{T}}(\tau)\right\} = \overline{Q}_{\boldsymbol{\omega}}(t)\delta(t-\tau) = \begin{bmatrix} \overline{Q}_\omega(t) & \overline{Q}_{\omega v}(t) \\ \overline{Q}_{\omega v}(t) & \overline{Q}_v(t) \end{bmatrix} \delta(t-\tau), \tag{104}$$

and $\overline{Q}_{\boldsymbol{\omega}}(t) \in \mathbb{R}^{6\times 6}$ is a symmetric positive semidefinite matrix. The dual bias is not constant, but assumed to be driven by another Gaussian white-noise process as follows:

$$\dot{\boldsymbol{b}}_{\boldsymbol{\omega}} = \boldsymbol{\eta}_{\boldsymbol{b}_{\boldsymbol{\omega}}}, \tag{105}$$

where $\boldsymbol{\eta}_{\boldsymbol{b}_{\boldsymbol{\omega}}} = (0, \overline{\eta}_{b_\omega}) + \epsilon(0, \overline{\eta}_{b_v})$, $E\left\{\overline{\boldsymbol{\eta}}_{\boldsymbol{b}_{\boldsymbol{\omega}}}\right\} = 0_{6\times 1}$,

$$E\left\{\overline{\boldsymbol{\eta}}_{\boldsymbol{b}_{\boldsymbol{\omega}}}(t)\overline{\boldsymbol{\eta}}_{\boldsymbol{b}_{\boldsymbol{\omega}}}^{\mathrm{T}}(\tau)\right\} = \overline{Q}_{\boldsymbol{b}_{\boldsymbol{\omega}}}(t)\delta(t-\tau) = \begin{bmatrix} \overline{Q}_{b_\omega}(t) & \overline{Q}_{b_\omega b_v}(t) \\ \overline{Q}_{b_\omega b_v}(t) & \overline{Q}_{b_v}(t) \end{bmatrix} \delta(t-\tau), \tag{106}$$

and $\overline{Q}_{\boldsymbol{b}_{\boldsymbol{\omega}}}(t) \in \mathbb{R}^{6\times 6}$ is a symmetric positive semidefinite matrix.

In this chapter, the I-frame denotes a general frame, not necessary inertial. If the I-frame is inertial, $\boldsymbol{\omega}_{\mathrm{B/I}}^{\mathrm{B}}$ should be interpreted as the inertial angular and linear velocities of the satellite. In that case, $\boldsymbol{\omega}_{\mathrm{B/I}}^{\mathrm{B}}$ can be measured from a combination of, for example, rate-gyros, Doppler radar, and GPS. On the other hand, if the I-frame is not inertial, $\boldsymbol{\omega}_{\mathrm{B/I}}^{\mathrm{B}}$ should be interpreted as the relative angular and linear velocities of the satellite with respect to a moving frame, for example, a frame attached to another satellite. In that case, $\boldsymbol{\omega}_{\mathrm{B/I}}^{\mathrm{B}}$ can be measured from a combination of, for example, rate-gyros on both satellites [50], Doppler radar, differential GPS, and LIDAR.

4.3 Derivation of the DQ-MEKF

In this section, the DQ-MEKF for pose estimation is derived. The state and process noise of the DQ-MEKF are initially selected as

$$x_{16} = \begin{bmatrix} [\delta \boldsymbol{q}_{\mathrm{B/I}}] \\ [\boldsymbol{b}_{\boldsymbol{\omega}}] \end{bmatrix} \in \mathbb{R}^{16} \quad \text{and} \quad w_{16} = \begin{bmatrix} [\boldsymbol{\eta}_{\boldsymbol{\omega}}] \\ [\boldsymbol{\eta}_{\boldsymbol{b}_{\boldsymbol{\omega}}}] \end{bmatrix} \in \mathbb{R}^{16}, \tag{107}$$

where the *unit dual error quaternion* $\delta \boldsymbol{q}_{\mathrm{B/I}} \in \mathbb{H}_d^u$ is defined analogously to the *unit error quaternion* $\delta q_{\mathrm{B/I}} = \hat{q}_{\mathrm{B/I}}^* q_{\mathrm{B/I}} \in \mathbb{H}^u$ defined in Ref. [57] as follows

$$\delta \boldsymbol{q}_{\mathrm{B/I}} = \hat{\boldsymbol{q}}_{\mathrm{B/I}}^* \boldsymbol{q}_{\mathrm{B/I}} \in \mathbb{H}_d^u, \tag{108}$$

i.e., $\delta \boldsymbol{q}_{\mathrm{B/I}}$ is the unit dual quaternion between the actual dual quaternion $\boldsymbol{q}_{\mathrm{B/I}}$ and its estimate $\hat{\boldsymbol{q}}_{\mathrm{B/I}} \triangleq E\left\{\boldsymbol{q}_{\mathrm{B/I}}\right\}$. Note that $E\left\{\delta \boldsymbol{q}_{\mathrm{B/I}}\right\} = \mathbf{1}$. Similarly to the typical EKF approximation given by Eq. (89), given $E\left\{q_{\mathrm{B/I}}\right\} \triangleq \hat{q}_{\mathrm{B/I}}$ and $E\left\{r_{\mathrm{B/I}}^{\mathrm{I}}\right\} \triangleq \hat{r}_{\mathrm{B/I}}^{\mathrm{I}}$, it is assumed that $\hat{\boldsymbol{q}}_{\mathrm{B/I}}$ can be constructed from

$$\hat{\boldsymbol{q}}_{\mathrm{B/I}} = E\left\{q_{\mathrm{B/I}} + \epsilon \tfrac{1}{2} r_{\mathrm{B/I}}^{\mathrm{I}} q_{\mathrm{B/I}}\right\} = E\left\{q_{\mathrm{B/I}}\right\} + \epsilon \tfrac{1}{2} E\left\{r_{\mathrm{B/I}}^{\mathrm{I}} q_{\mathrm{B/I}}\right\} \approx \hat{q}_{\mathrm{B/I}} + \epsilon \tfrac{1}{2} \hat{r}_{\mathrm{B/I}}^{\mathrm{I}} \hat{q}_{\mathrm{B/I}}. \tag{109}$$

Similarly, given $\hat{q}_{\mathrm{B/I}}$ and $E\left\{r_{\mathrm{B/I}}^{\mathrm{B}}\right\} = E\left\{\delta q_{\mathrm{B/I}}^* r_{\mathrm{B/I}}^{\hat{\mathrm{B}}} \delta q_{\mathrm{B/I}}\right\} \approx E\left\{r_{\mathrm{B/I}}^{\hat{\mathrm{B}}}\right\} \triangleq \hat{r}_{\mathrm{B/I}}^{\hat{\mathrm{B}}}$, it is assumed that $\hat{\boldsymbol{q}}_{\mathrm{B/I}}$ can be constructed from

$$\hat{\boldsymbol{q}}_{\mathrm{B/I}} = E\left\{q_{\mathrm{B/I}} + \epsilon \tfrac{1}{2} q_{\mathrm{B/I}} r_{\mathrm{B/I}}^{\mathrm{B}}\right\} = E\left\{q_{\mathrm{B/I}}\right\} + \epsilon \tfrac{1}{2} E\left\{q_{\mathrm{B/I}} r_{\mathrm{B/I}}^{\mathrm{B}}\right\} \approx \hat{q}_{\mathrm{B/I}} + \epsilon \tfrac{1}{2} \hat{q}_{\mathrm{B/I}} \hat{r}_{\mathrm{B/I}}^{\hat{\mathrm{B}}}, \tag{110}$$

where the $\hat{\mathrm{B}}$-frame is defined as a frame with orientation and position with respect to the I-frame given by $\hat{q}_{\mathrm{B/I}}$ and $\hat{\overline{r}}_{\mathrm{B/I}}$, respectively. Note that $\hat{\overline{r}}_{\mathrm{B/I}}$ denotes the expected value of $\overline{r}_{\mathrm{B/I}}$, i.e., the expected value of the translation vector from the origin of the I-frame to the origin of the B-frame (not expressed in any specific reference frame). Note also that, if $q_{\mathrm{B/I}}$ and $r_{\mathrm{B/I}}^{\mathrm{I}}$ can be assumed to be independent random variables, then Eqs. (109) and (110) are equalities.

A geometric interpretation of the dual error quaternion $\delta \boldsymbol{q}_{\mathrm{B/I}}$ is given in Figure 16. It shows that $\delta \boldsymbol{q}_{\mathrm{B/I}}$ is the unit dual quaternion that represents the pose of the B-

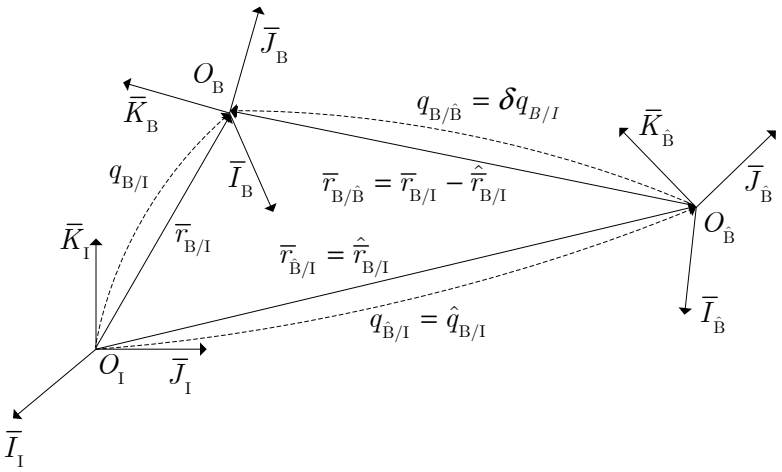

Figure 16: Interpretation of the dual error quaternion.

frame with respect to the $\hat{\mathrm{B}}$-frame. This can be seen from expanding Eq. (108) using Eq. (109) as follows

$$\begin{aligned}
\delta\boldsymbol{q}_{\mathrm{B/I}} &= \hat{\boldsymbol{q}}^{*}_{\mathrm{B/I}}\boldsymbol{q}_{\mathrm{B/I}} = \delta q_{\mathrm{B/I},r} + \epsilon\delta q_{\mathrm{B/I},d} = (\hat{q}_{\mathrm{B/I}} + \epsilon\tfrac{1}{2}\hat{r}^{\mathrm{I}}_{\mathrm{B/I}}\hat{q}_{\mathrm{B/I}})^{*}(q_{\mathrm{B/I}} + \epsilon\tfrac{1}{2}r^{\mathrm{I}}_{\mathrm{B/I}}q_{\mathrm{B/I}}) \\
&= \hat{q}^{*}_{\mathrm{B/I}}q_{\mathrm{B/I}} + \epsilon(\tfrac{1}{2}\hat{q}^{*}_{\mathrm{B/I}}r^{\mathrm{I}}_{\mathrm{B/I}}q_{\mathrm{B/I}} + \tfrac{1}{2}\hat{q}^{*}_{\mathrm{B/I}}(\hat{r}^{\mathrm{I}}_{\mathrm{B/I}})^{*}q_{\mathrm{B/I}}) \\
&= \delta q_{\mathrm{B/I}} + \epsilon(\tfrac{1}{2}\hat{q}^{*}_{\mathrm{B/I}}q_{\mathrm{B/I}}q^{*}_{\mathrm{B/I}}r^{\mathrm{I}}_{\mathrm{B/I}}q_{\mathrm{B/I}} - \tfrac{1}{2}\hat{q}^{*}_{\mathrm{B/I}}q_{\mathrm{B/I}}q^{*}_{\mathrm{B/I}}\hat{r}^{\mathrm{I}}_{\mathrm{B/I}}q_{\mathrm{B/I}}) \\
&= \delta q_{\mathrm{B/I}} + \epsilon(\tfrac{1}{2}\delta q_{\mathrm{B/I}}r^{\mathrm{B}}_{\mathrm{B/I}} - \tfrac{1}{2}\delta q_{\mathrm{B/I}}\hat{r}^{\mathrm{B}}_{\mathrm{B/I}}) \\
&= \delta q_{\mathrm{B/I}} + \epsilon\tfrac{1}{2}\delta q_{\mathrm{B/I}}r^{\mathrm{B}}_{\mathrm{B}/\hat{\mathrm{B}}} = \delta q_{\mathrm{B/I}} + \epsilon\tfrac{1}{2}r^{\hat{\mathrm{B}}}_{\mathrm{B}/\hat{\mathrm{B}}}\delta q_{\mathrm{B/I}}.
\end{aligned} \tag{111}$$

Note that from Eq. (111), $r^{\mathrm{B}}_{\mathrm{B/I}}$ can be written in terms of $\delta q_{\mathrm{B/I},r}$ and $\delta q_{\mathrm{B/I},d}$ as follows

$$r^{\mathrm{B}}_{\mathrm{B/I}} = 2\delta q^{*}_{\mathrm{B/I},r}\delta q_{\mathrm{B/I},d} + \hat{r}^{\mathrm{B}}_{\mathrm{B/I}} = 2\delta q^{*}_{\mathrm{B/I},r}\delta q_{\mathrm{B/I},d} + \delta q^{*}_{\mathrm{B/I},r}\hat{r}^{\hat{\mathrm{B}}}_{\mathrm{B/I}}\delta q_{\mathrm{B/I},r}, \tag{112}$$

whereas $r^{\mathrm{I}}_{\mathrm{B/I}}$ can be written in terms of $\delta q_{\mathrm{B/I},r}$ and $\delta q_{\mathrm{B/I},d}$ from Eq. (112) as

$$\begin{aligned}
r^{\mathrm{I}}_{\mathrm{B/I}} &= q_{\mathrm{B/I}}r^{\mathrm{B}}_{\mathrm{B/I}}q^{*}_{\mathrm{B/I}} = q_{\mathrm{B/I}}(2\delta q^{*}_{\mathrm{B/I},r}\delta q_{\mathrm{B/I},d} + \delta q^{*}_{\mathrm{B/I},r}\hat{r}^{\hat{\mathrm{B}}}_{\mathrm{B/I}}\delta q_{\mathrm{B/I},r})q^{*}_{\mathrm{B/I}} \\
&= 2\hat{q}_{\mathrm{B/I}}\delta q_{\mathrm{B/I},d}\delta q^{*}_{\mathrm{B/I},r}\hat{q}^{*}_{\mathrm{B/I}} + \hat{q}_{\mathrm{B/I}}\hat{r}^{\hat{\mathrm{B}}}_{\mathrm{B/I}}\hat{q}^{*}_{\mathrm{B/I}}.
\end{aligned} \tag{113}$$

To determine the state equation of the DQ-MEKF, the time derivative of $\delta\boldsymbol{q}_{\mathrm{B/I}}$ needs to be calculated. Taking the time derivative of Eq. (108) yields

$$\frac{\mathrm{d}}{\mathrm{d}t}(\delta\boldsymbol{q}_{\mathrm{B/I}}) = \frac{\mathrm{d}}{\mathrm{d}t}(\hat{\boldsymbol{q}}^{*}_{\mathrm{B/I}})\boldsymbol{q}_{\mathrm{B/I}} + \hat{\boldsymbol{q}}^{*}_{\mathrm{B/I}}\frac{\mathrm{d}}{\mathrm{d}t}(\boldsymbol{q}_{\mathrm{B/I}}). \tag{114}$$

Whereas $\frac{\mathrm{d}}{\mathrm{d}t}(\boldsymbol{q}_{\mathrm{B/I}})$ is given by Eq. (51), $\frac{\mathrm{d}}{\mathrm{d}t}(\hat{\boldsymbol{q}}^{*}_{\mathrm{B/I}})$ is approximated according to Eq. (89) by

$$\frac{\mathrm{d}}{\mathrm{d}t}(\hat{\boldsymbol{q}}_{\mathrm{B/I}}) = \frac{\mathrm{d}(E\left\{\boldsymbol{q}_{\mathrm{B/I}}\right\})}{\mathrm{d}t} = E\left\{\dot{\boldsymbol{q}}_{\mathrm{B/I}}\right\} = E\left\{\tfrac{1}{2}\boldsymbol{q}_{\mathrm{B/I}}\boldsymbol{\omega}^{\mathrm{B}}_{\mathrm{B/I}}\right\} \approx \tfrac{1}{2}\hat{\boldsymbol{q}}_{\mathrm{B/I}}\hat{\boldsymbol{\omega}}^{\hat{\mathrm{B}}}_{\mathrm{B/I}}, \tag{115}$$

where, from Eq. (103),

$$\begin{aligned}\hat{\boldsymbol{\omega}}^{\hat{\mathrm{B}}}_{\mathrm{B/I}} &\triangleq E\left\{\boldsymbol{\omega}^{\hat{\mathrm{B}}}_{\mathrm{B/I}}\right\} = E\left\{\delta q_{\mathrm{B/I}}\boldsymbol{\omega}^{\mathrm{B}}_{\mathrm{B/I}}\delta q^{*}_{\mathrm{B/I}}\right\} \approx E\left\{\boldsymbol{\omega}^{\mathrm{B}}_{\mathrm{B/I}}\right\} = E\left\{\boldsymbol{\omega}^{\mathrm{B}}_{\mathrm{B/I},m} - \boldsymbol{b}_{\boldsymbol{\omega}} - \boldsymbol{\eta}_{\boldsymbol{\omega}}\right\} \\ &= \boldsymbol{\omega}^{\mathrm{B}}_{\mathrm{B/I},m} - \hat{\boldsymbol{b}}_{\boldsymbol{\omega}},\end{aligned} \tag{116}$$

with $\hat{\boldsymbol{b}}_{\boldsymbol{\omega}} \triangleq E\left\{\boldsymbol{b}_{\boldsymbol{\omega}}\right\}$. Likewise,

$$\frac{\mathrm{d}}{\mathrm{d}t}\left(\hat{\boldsymbol{b}}_{\boldsymbol{\omega}}\right) = \frac{\mathrm{d}}{\mathrm{d}t}E\left\{\boldsymbol{b}_{\boldsymbol{\omega}}\right\} = E\left\{\dot{\boldsymbol{b}}_{\boldsymbol{\omega}}\right\} = E\left\{\boldsymbol{\eta}_{\boldsymbol{b}_{\boldsymbol{\omega}}}\right\} = \mathbf{0}. \tag{117}$$

Substituting Eqs. (51) and (115) in Eq. (114) yields

$$\frac{\mathrm{d}}{\mathrm{d}t}(\delta\boldsymbol{q}_{\mathrm{B/I}}) \approx \tfrac{1}{2}(\hat{\boldsymbol{\omega}}^{\hat{\mathrm{B}}}_{\mathrm{B/I}})^{*}\hat{\boldsymbol{q}}^{*}_{\mathrm{B/I}}\boldsymbol{q}_{\mathrm{B/I}} + \tfrac{1}{2}\hat{\boldsymbol{q}}^{*}_{\mathrm{B/I}}\boldsymbol{q}_{\mathrm{B/I}}\boldsymbol{\omega}^{\mathrm{B}}_{\mathrm{B/I}} = -\tfrac{1}{2}\hat{\boldsymbol{\omega}}^{\hat{\mathrm{B}}}_{\mathrm{B/I}}\delta\boldsymbol{q}_{\mathrm{B/I}} + \tfrac{1}{2}\delta\boldsymbol{q}_{\mathrm{B/I}}\boldsymbol{\omega}^{\mathrm{B}}_{\mathrm{B/I}}. \tag{118}$$

Combining Eqs. (116) and (103) yields

$$\boldsymbol{\omega}^{\mathrm{B}}_{\mathrm{B/I}} \approx \hat{\boldsymbol{\omega}}^{\hat{\mathrm{B}}}_{\mathrm{B/I}} + \hat{\boldsymbol{b}}_{\boldsymbol{\omega}} - \boldsymbol{b}_{\boldsymbol{\omega}} - \boldsymbol{\eta}_{\boldsymbol{\omega}}. \tag{119}$$

Finally, inserting Eq. (119) in Eq. (118) results in

$$\frac{\mathrm{d}}{\mathrm{d}t}(\delta\boldsymbol{q}_{\mathrm{B/I}}) \approx -\tfrac{1}{2}\hat{\boldsymbol{\omega}}^{\hat{\mathrm{B}}}_{\mathrm{B/I}}\delta\boldsymbol{q}_{\mathrm{B/I}} + \tfrac{1}{2}\delta\boldsymbol{q}_{\mathrm{B/I}}\hat{\boldsymbol{\omega}}^{\hat{\mathrm{B}}}_{\mathrm{B/I}} + \tfrac{1}{2}\delta\boldsymbol{q}_{\mathrm{B/I}}\hat{\boldsymbol{b}}_{\boldsymbol{\omega}} - \tfrac{1}{2}\delta\boldsymbol{q}_{\mathrm{B/I}}\boldsymbol{b}_{\boldsymbol{\omega}} - \tfrac{1}{2}\delta\boldsymbol{q}_{\mathrm{B/I}}\boldsymbol{\eta}_{\boldsymbol{\omega}}. \tag{120}$$

The state equations of the DQ-MEKF are then given by Eq. (120) and Eq. (105), yielding

$$f_{16}(x_{16}(t),t) = \begin{bmatrix} [-\tfrac{1}{2}\hat{\boldsymbol{\omega}}^{\hat{\mathrm{B}}}_{\mathrm{B/I}}\delta\boldsymbol{q}_{\mathrm{B/I}} + \tfrac{1}{2}\delta\boldsymbol{q}_{\mathrm{B/I}}\hat{\boldsymbol{\omega}}^{\hat{\mathrm{B}}}_{\mathrm{B/I}} + \tfrac{1}{2}\delta\boldsymbol{q}_{\mathrm{B/I}}\hat{\boldsymbol{b}}_{\boldsymbol{\omega}} - \tfrac{1}{2}\delta\boldsymbol{q}_{\mathrm{B/I}}\boldsymbol{b}_{\boldsymbol{\omega}}] \\ 0_{8\times 1} \end{bmatrix}, \tag{121}$$

$$g_{16\times 16}(x_{16}(t),t) = \begin{bmatrix} -\tfrac{1}{2}[\delta\boldsymbol{q}_{\mathrm{B/I}}]^{\mathrm{L}} & 0_{8\times 8} \\ 0_{8\times 8} & I_{8\times 8} \end{bmatrix}. \tag{122}$$

At this point, as in the derivation of the Q-MEKF, reduced state and process noise vectors are selected, namely

$$x_{12} = \begin{bmatrix} \overline{\delta \boldsymbol{q}_{\mathrm{B/I}}} \\ \overline{\boldsymbol{b}}_{\boldsymbol{\omega}} \end{bmatrix} \in \mathbb{R}^{12} \quad \text{and} \quad w_{12} = \begin{bmatrix} \overline{\boldsymbol{\eta}}_{\boldsymbol{\omega}} \\ \overline{\boldsymbol{\eta}}_{\boldsymbol{b}_{\boldsymbol{\omega}}} \end{bmatrix} \in \mathbb{R}^{12}, \tag{123}$$

where $\overline{\delta \boldsymbol{q}_{\mathrm{B/I}}}$ and $\overline{\boldsymbol{b}}_{\boldsymbol{\omega}}$ are the vector parts of $\delta \boldsymbol{q}_{\mathrm{B/I}}$ and $\boldsymbol{b}_{\boldsymbol{\omega}}$, respectively. By replacing $\delta q_{\mathrm{B/I},r,0}$ and $\delta q_{\mathrm{B/I},d,0}$ through Eq. (47) in Eqs. (121) and (122) and using Eq. (93), $F_{12\times12}(t)$ and $G_{12\times12}(t)$ can be determined to be

$$F_{12\times12}(t) = \begin{bmatrix} -[\overline{\hat{\boldsymbol{\omega}}^{\hat{\mathrm{B}}}_{\mathrm{B/I}}}]^{\times} & -\frac{1}{2} I_{6\times6} \\ 0_{6\times6} & 0_{6\times6} \end{bmatrix} \quad \text{and} \quad G_{12\times12}(t) = \begin{bmatrix} -\frac{1}{2} I_{6\times6} & 0_{6\times6} \\ 0_{6\times6} & I_{6\times6} \end{bmatrix}. \tag{124}$$

4.3.1 Time Update

For the time update of the DQ-MEKF, the estimates of $\boldsymbol{q}_{\mathrm{B/I}}$, $\boldsymbol{\omega}^{\mathrm{B}}_{\mathrm{B/I}}$, and $\boldsymbol{b}_{\boldsymbol{\omega}}$ are propagated using Eqs. (115), (116), and (117), respectively, given $\hat{\boldsymbol{q}}_{\mathrm{B/I}}(t_0)$ and $\hat{\boldsymbol{b}}_{\boldsymbol{\omega}}(t_0)$.

Numerical errors in the propagation of $\boldsymbol{q}_{\mathrm{B/I}}$ through Eq. (115) can result in the violation of the algebraic constraints that define a unit dual quaternion, given by Eq. (46). Hence, after each integration step, these algebraic constraints are enforced by calculating

$$[q_{\mathrm{B/I},r}] = \frac{[q_{\mathrm{B/I},r}]}{\|[q_{\mathrm{B/I},r}]\|} \quad \text{and} \quad [q_{\mathrm{B/I},d}] = \left(I_{4\times4} - \frac{[q_{\mathrm{B/I},r}][q_{\mathrm{B/I},r}]^{\mathsf{T}}}{\|[q_{\mathrm{B/I},r}]\|^2} \right) [q_{\mathrm{B/I},d}]. \tag{125}$$

As for the covariance matrix of x_{12}, i.e.,

$$\begin{aligned} P_{12\times12}(t) &\triangleq E\left\{\Delta x_{12}(t) \Delta x_{12}(t)^{\mathsf{T}}\right\}] \\ &\triangleq E\left\{ \left(\begin{bmatrix} \overline{\delta \boldsymbol{q}_{\mathrm{B/I}}}(t) \\ \overline{\boldsymbol{b}}_{\boldsymbol{\omega}}(t) \end{bmatrix} - \begin{bmatrix} 0_{6\times6} \\ \overline{\hat{\boldsymbol{b}}}_{\boldsymbol{\omega}}(t) \end{bmatrix} \right) \left(\begin{bmatrix} \overline{\delta \boldsymbol{q}_{\mathrm{B/I}}}(t) \\ \overline{\boldsymbol{b}}_{\boldsymbol{\omega}}(t) \end{bmatrix} - \begin{bmatrix} 0_{6\times6} \\ \overline{\hat{\boldsymbol{b}}}_{\boldsymbol{\omega}}(t) \end{bmatrix} \right)^{\mathsf{T}} \right\}, \end{aligned} \tag{126}$$

it is propagated according to Eq. (92) given $P_{12\times12}(t_0)$ and where

$$Q_{12\times12}(t) = \begin{bmatrix} \overline{Q}_{\boldsymbol{\omega}}(t) & 0_{6\times6} \\ 0_{6\times6} & \overline{Q}_{\boldsymbol{b}_{\boldsymbol{\omega}}}(t) \end{bmatrix}. \tag{127}$$

Note that it is not very intuitive to define $P_{12\times12}(t_0)$. It is more intuitive to define the covariance matrix

$$\tilde{P}_{16\times16}(t_0) \triangleq E\left\{\left(\begin{bmatrix}[\boldsymbol{q}_{\mathrm{B/I}}(t_0)]\\ [\boldsymbol{b}_{\boldsymbol{\omega}}(t_0)]\end{bmatrix} - \begin{bmatrix}[\hat{\boldsymbol{q}}_{\mathrm{B/I}}(t_0)]\\ [\hat{\boldsymbol{b}}_{\boldsymbol{\omega}}(t_0)]\end{bmatrix}\right)\left(\begin{bmatrix}[\boldsymbol{q}_{\mathrm{B/I}}(t_0)]\\ [\boldsymbol{b}_{\boldsymbol{\omega}}(t_0)]\end{bmatrix} - \begin{bmatrix}[\hat{\boldsymbol{q}}_{\mathrm{B/I}}(t_0)]\\ [\hat{\boldsymbol{b}}_{\boldsymbol{\omega}}(t_0)]\end{bmatrix}\right)^{\mathsf{T}}\right\}.$$

Given $\tilde{P}_{16\times16}(t_0)$, $P_{12\times12}(t_0)$ can be calculated by first computing

$$\begin{aligned}P_{16\times16}(t_0) &\triangleq E\left\{\left(\begin{bmatrix}[\delta\boldsymbol{q}_{\mathrm{B/I}}(t_0)]\\ [\boldsymbol{b}_{\boldsymbol{\omega}}(t_0)]\end{bmatrix} - \begin{bmatrix}[\mathbf{1}]\\ [\hat{\boldsymbol{b}}_{\boldsymbol{\omega}}(t_0)]\end{bmatrix}\right)\left(\begin{bmatrix}[\delta\boldsymbol{q}_{\mathrm{B/I}}(t_0)]\\ [\boldsymbol{b}_{\boldsymbol{\omega}}(t_0)]\end{bmatrix} - \begin{bmatrix}[\mathbf{1}]\\ [\hat{\boldsymbol{b}}_{\boldsymbol{\omega}}(t_0)]\end{bmatrix}\right)^{\mathsf{T}}\right\}\\ &= S\tilde{P}_{16\times16}(t_0)S^{\mathsf{T}},\end{aligned} \tag{128}$$

where

$$S = \begin{bmatrix}[\hat{\boldsymbol{q}}^{*}_{\mathrm{B/I}}]^{\mathrm{L}} & 0_{8\times8}\\ 0_{8\times8} & I_{8\times8}\end{bmatrix}. \tag{129}$$

Then, $P_{12\times12}(t_0)$ can be obtained from $P_{16\times16}(t_0)$ by removing the first, fifth, ninth, and thirteenth rows and columns of $P_{16\times16}(t_0)$.

4.3.2 Measurement Update

In this section, it is assumed that a direct measurement of $\boldsymbol{q}_{\mathrm{B/I}}$ corrupted by additive white Gaussian noise is available. If the I-frame is a moving frame, this measurement can come, for example, from a vision-based system. If the I-frame is an inertial frame, this measurement can come, for example, from a combination of a star sensor and a GPS. If the pose measurement is available in terms of a quaternion and a translation vector, then the corresponding dual quaternion can be computed from Eq. (44). Under this assumption, the output equation that relates a measurement taken at time t_k with the state x_{12} at time t_k is given by

$$[\boldsymbol{q}_{\mathrm{B/I},m}(t_k)] = [\hat{\boldsymbol{q}}_{\mathrm{B/I}}(t_k)\delta\boldsymbol{q}_{\mathrm{B/I}}(t_k)] + v_8(t_k), \tag{130}$$

where, in accordance with Eq. (94), $z_8(t_k) = [\boldsymbol{q}_{\mathrm{B/I},m}(t_k)]$ is the measurement at time t_k of $\boldsymbol{q}_{\mathrm{B/I}}(t_k)$ and $h_8(x_{12}(t_k)) = [\hat{\boldsymbol{q}}_{\mathrm{B/I}}(t_k)\delta\boldsymbol{q}_{\mathrm{B/I}}(t_k)]$.

Replacing $\delta q_{\mathrm{B/I},r,0}$ and $\delta q_{\mathrm{B/I},d,0}$ through Eq. (47) in Eq. (130) and calculating the measurement sensitivity matrix using Eq. (99) yields

$$H_{8\times 12}(t_k) = \left[[\hat{\boldsymbol{q}}_{\mathrm{B/I}}]^{\mathrm{L}}_{8\times 6} \quad 0_{8\times 6} \right]. \tag{131}$$

In summary, for the measurement update of the DQ-MEKF, the Kalman gain is calculated from Eq. (98), whereas the optimal Kalman state update is calculated from Eq. (96) as

$$\Delta^\star \hat{x}_{12}(t_k) \triangleq \begin{bmatrix} \Delta^\star \overline{\delta \hat{\boldsymbol{q}}_{\mathrm{B/I}}}(t_k) \\ \Delta^\star \bar{\hat{\boldsymbol{b}}}_{\boldsymbol{\omega}}(t_k) \end{bmatrix} = K_{12\times 8}(t_k)(z_8(t_k) - \hat{z}_8(t_k)). \tag{132}$$

The estimate of the state at time t_k after the measurement is then calculated from

$$\hat{\boldsymbol{q}}^+_{\mathrm{B/I}}(t_k) = \hat{\boldsymbol{q}}^-_{\mathrm{B/I}}(t_k) \Delta^\star \delta \hat{\boldsymbol{q}}_{\mathrm{B/I}}(t_k), \tag{133}$$

$$\bar{\hat{\boldsymbol{b}}}^+_{\boldsymbol{\omega}}(t_k) = \bar{\hat{\boldsymbol{b}}}^-_{\boldsymbol{\omega}}(t_k) + \Delta^\star \bar{\hat{\boldsymbol{b}}}_{\boldsymbol{\omega}}(t_k), \tag{134}$$

where $\Delta^\star \delta \hat{\boldsymbol{q}}_{\mathrm{B/I}}$ is defined as the unit dual quaternion

$$\left(\sqrt{1 - \|\Delta^\star \overline{\delta \hat{q}_{\mathrm{B/I},r}}\|^2}, \Delta^\star \overline{\delta \hat{q}_{\mathrm{B/I},r}} \right) + \epsilon \left(\frac{-\Delta^\star \overline{\delta \hat{q}_{\mathrm{B/I},r}}^{\mathsf{T}} \Delta^\star \overline{\delta \hat{q}_{\mathrm{B/I},d}}}{\sqrt{1 - \|\Delta^\star \overline{\delta \hat{q}_{\mathrm{B/I},r}}\|^2}}, \Delta^\star \overline{\delta \hat{q}_{\mathrm{B/I},d}} \right). \tag{135}$$

If the initial guess of the state is not close enough to the real state, the norm of $\Delta^\star \overline{\delta \hat{q}_{\mathrm{B/I},r}}$ can become larger than one, which will make the scalar part of the quaternions in Eq. (135) complex. Hence, if the norm of $\Delta^\star \overline{\delta \hat{q}_{\mathrm{B/I},r}}$ is larger than one, Eq. (135) is replaced by

$$\left(\frac{1}{\sqrt{1 + \|\Delta^\star \overline{\delta \hat{q}_{\mathrm{B/I},r}}\|^2}}, \frac{\Delta^\star \overline{\delta \hat{q}_{\mathrm{B/I},r}}}{\sqrt{1 + \|\Delta^\star \overline{\delta \hat{q}_{\mathrm{B/I},r}}\|^2}} \right) + \epsilon \left(\frac{-\Delta^\star \overline{\delta \hat{q}_{\mathrm{B/I},r}}^{\mathsf{T}} \Delta^\star \overline{\delta \hat{q}_{\mathrm{B/I},d}}}{1 \Big/ \sqrt{1 + \|\Delta^\star \overline{\delta \hat{q}_{\mathrm{B/I},r}}\|^2}}, \Delta^\star \overline{\delta \hat{q}_{\mathrm{B/I},d}} \right). \tag{136}$$

Note that whereas Eq. (134) is a direct application of Eq. (95), Eq. (133) is not. Since $\Delta^\star \delta \hat{\boldsymbol{q}}_{\mathrm{B/I}}(t_k)$ is a unit dual quaternion, $\hat{\boldsymbol{q}}^+_{\mathrm{B/I}}(t_k)$ is calculated using the dual quaternion multiplication, making the proposed EKF multiplicative. Finally, the

covariance matrix of the state immediately after the measurement at t_k is computed from Eq. (101).

Note that any measurement that is a nonlinear function of the state of the DQ-MEKF, i.e., any measurement that satisfies Eq. (94), can be used in the measurement update. If another measurement is used, only the measurement sensitivity matrix given by Eq. (131) needs to be recalculated. For example, if it is assumed that direct measurements of $q_{\mathrm{B/I}}$ and $r^{\mathrm{I}}_{\mathrm{B/I}}$ corrupted by additive white Gaussian noise are available, then, by using Eq. (113), the output equation becomes

$$\begin{bmatrix} [q_{\mathrm{B/I},m}(t_k)] \\ \overline{r}^{\mathrm{I}}_{\mathrm{B/I},m}(t_k) \end{bmatrix} = \begin{bmatrix} [\hat{q}_{\mathrm{B/I},r}(t_k)\delta q_{\mathrm{B/I},r}(t_k)] \\ \hline 2\hat{q}_{\mathrm{B/I},r}(t_k)\delta q_{\mathrm{B/I},d}(t_k)\delta q^{*}_{\mathrm{B/I},r}(t_k)\hat{q}^{*}_{\mathrm{B/I},r}(t_k)+\hat{q}_{\mathrm{B/I},r}(t_k)\hat{r}^{\hat{\mathrm{B}}}_{\mathrm{B/I}}(t_k)\hat{q}^{*}_{\mathrm{B/I},r}(t_k) \end{bmatrix} + v_7(t_k), \tag{137}$$

and the new sensitivity matrix is given by

$$H_{7\times 12}(t_k) = \begin{bmatrix} [\hat{q}_{\mathrm{B/I}}]^{\mathrm{L}}_{4\times 3} & 0_{4\times 3} & 0_{4\times 3} & 0_{4\times 3} \\ 0_{3\times 3} & 2\hat{R}^{\mathrm{I}\leftarrow\mathrm{B}} & 0_{3\times 3} & 0_{3\times 3} \end{bmatrix}, \tag{138}$$

where $\hat{R}^{\mathrm{I}\leftarrow\mathrm{B}}$ is the estimated value of $R^{\mathrm{I}\leftarrow\mathrm{B}}$, which can be formed from $\hat{q}_{\mathrm{B/I}}$.

4.3.3 Summary

For the convenience of the reader, a step-by-step breakdown of the DQ-MEKF is provided here, assuming that the output equation is given by Eq. (130).

1. Initialization:

   1.1. If $\hat{\boldsymbol{q}}_{\mathrm{B/I}}(t_0)$ is given in terms of $\hat{q}_{\mathrm{B/I}}(t_0)$ and $\hat{r}^{\mathrm{I}}_{\mathrm{B/I}}(t_0)$ (or $\hat{r}^{\hat{\mathrm{B}}}_{\mathrm{B/I}}(t_0)$), construct $\hat{\boldsymbol{q}}_{\mathrm{B/I}}(t_0)$ using Eq. (109) (or Eq. (110)).

   1.2. If $\hat{\boldsymbol{b}}_{\boldsymbol{\omega}}(t_0)$ is given in terms of $\hat{b}_{\omega}(t_0)$ and $\hat{b}_{v}(t_0)$, construct $\hat{\boldsymbol{b}}_{\boldsymbol{\omega}}(t_0)$ using $\hat{\boldsymbol{b}}_{\boldsymbol{\omega}}(t_0) = \hat{b}_{\omega}(t_0) + \epsilon\hat{b}_{v}(t_0)$.

1.3. If $P_{12\times12}(t_0)$ is given in terms of $\tilde{P}_{16\times16}(t_0)$, calculate $P_{16\times16}(t_0)$ from Eq. (128) and remove the first, fifth, ninth, and thirteenth rows and columns of $P_{16\times16}(t_0)$ to obtain $P_{12\times12}(t_0)$.

1.4. Perform step 2.

2. Time Update:

2.1. Let t_k be the current time. Normalize $\hat{q}_{\mathrm{B/I}}(t_k)$ using Eq. (125).

2.2. If a new measurement of $\boldsymbol{q}_{\mathrm{B/I},m}$ is available at time t_k, perform step 3.

2.3. If $\boldsymbol{\omega}^{\mathrm{B}}_{\mathrm{B/I},m}(t_k)$ is given in terms of $\omega^{\mathrm{B}}_{\mathrm{B/I},m}(t_k)$ and $v^{\mathrm{B}}_{\mathrm{B/I},m}(t_k)$, construct $\boldsymbol{\omega}^{\mathrm{B}}_{\mathrm{B/I},m}(t_k)$ using $\boldsymbol{\omega}^{\mathrm{B}}_{\mathrm{B/I},m}(t_k) = \omega^{\mathrm{B}}_{\mathrm{B/I},m}(t_k) + \epsilon v^{\mathrm{B}}_{\mathrm{B/I},m}(t_k)$.

2.4. Given $\boldsymbol{\omega}^{\mathrm{B}}_{\mathrm{B/I},m}(t_k)$ and $\hat{\boldsymbol{b}}_{\boldsymbol{\omega}}(t_k)$, calculate $\hat{\boldsymbol{\omega}}^{\hat{\mathrm{B}}}_{\mathrm{B/I}}(t_k)$ using Eq. (116).

2.5. Output $\hat{\boldsymbol{q}}_{\mathrm{B/I}}(t_k)$ and $\hat{\boldsymbol{\omega}}^{\hat{\mathrm{B}}}_{\mathrm{B/I}}(t_k)$.

2.6. Given $\hat{\boldsymbol{\omega}}^{\hat{\mathrm{B}}}_{\mathrm{B/I}}(t_k)$, calculate $F_{12\times12}(t_k)$ and $G_{12\times12}(t_k)$ using Eq. (124).

2.7. Given $\hat{\boldsymbol{\omega}}^{\hat{\mathrm{B}}}_{\mathrm{B/I}}(t_k)$, $\hat{\boldsymbol{q}}_{\mathrm{B/I}}(t_k)$, $P_{12\times12}(t_k)$, $F_{12\times12}(t_k)$, $G_{12\times12}(t_k)$, and $Q_{12\times12}(t_k)$, calculate $\boldsymbol{q}_{\mathrm{B/I}}(t_{k+1})$, $\boldsymbol{b}_{\boldsymbol{\omega}}(t_{k+1})$, and $P_{12\times12}(t_{k+1})$ by propagating Eqs. (115), (117), and (92), respectively, where t_{k+1} is the time after one time step of the clock. Note that since $P_{12\times12}$ is a symmetric matrix, only the upper triangular part of $P_{12\times12}$ needs to be propagated.

2.8. Repeat step 2 with $t_k = t_{k+1}$.

3. Measurement Update:

3.1. Let t_k be the current time. Given $\hat{\boldsymbol{q}}_{\mathrm{B/I}}(t_k)$, calculate $H_{8\times12}(t_k)$ using Eq. (131).

3.2. Given $H_{8\times12}(t_k)$, $P_{12\times12}(t_k)$, and $R_{8\times8}(t_k)$, calculate $K_{12\times8}(t_k)$.

3.3. If $\boldsymbol{q}_{\mathrm{B/I},m}(t_k)$ is given in terms of $q_{\mathrm{B/I},m}(t_k)$ and $r^{\mathrm{I}}_{\mathrm{B/I},m}(t_k)$ (or $r^{\mathrm{B}}_{\mathrm{B/I},m}(t_k)$), construct $\boldsymbol{q}_{\mathrm{B/I},m}(t_k)$ using $\boldsymbol{q}_{\mathrm{B/I},m}(t_k) = q_{\mathrm{B/I},m}(t_k) + \epsilon\frac{1}{2}r^{\mathrm{I}}_{\mathrm{B/I},m}(t_k)q_{\mathrm{B/I},m}(t_k) = q_{\mathrm{B/I},m}(t_k) + \epsilon\frac{1}{2}q_{\mathrm{B/I},m}(t_k)r^{\mathrm{B}}_{\mathrm{B/I},m}(t_k)$.

3.4. Given $K_{12\times 8}(t_k)$, $\boldsymbol{q}_{\mathrm{B/I},m}(t_k)$, and $\hat{\boldsymbol{q}}_{\mathrm{B/I}}(t_k)$, calculate $\Delta^{\star}\overline{\delta\hat{\boldsymbol{q}}_{\mathrm{B/I}}}(t_k)$ and $\Delta^{\star}\overline{\hat{\boldsymbol{b}}}_{\boldsymbol{\omega}}(t_k)$ using Eq. (132).

3.5. Given $\Delta^{\star}\overline{\delta\hat{\boldsymbol{q}}_{\mathrm{B/I}}}(t_k)$, if the norm of $\Delta^{\star}\overline{\delta\hat{q}_{\mathrm{B/I},r}}(t_k)$ is smaller or equal to one, calculate $\Delta^{\star}\delta\hat{\boldsymbol{q}}_{\mathrm{B/I}}$ using Eq. (135). Otherwise, calculate $\Delta^{\star}\delta\hat{\boldsymbol{q}}_{\mathrm{B/I}}$ using Eq. (136).

3.6. Given $\Delta^{\star}\delta\hat{\boldsymbol{q}}_{\mathrm{B/I}}$, $\hat{\boldsymbol{q}}_{\mathrm{B/I}}(t_k)$, $\Delta^{\star}\overline{\hat{\boldsymbol{b}}}_{\boldsymbol{\omega}}(t_k)$, and $\overline{\hat{\boldsymbol{b}}}_{\boldsymbol{\omega}}(t_k)$, update $\hat{\boldsymbol{q}}_{\mathrm{B/I}}(t_k)$ and $\hat{\boldsymbol{b}}_{\boldsymbol{\omega}}(t_k)$ using Eqs. (133) and (134).

3.7. Given $K_{12\times 8}(t_k)$, $H_{8\times 12}(t_k)$, $P_{12\times 12}(t_k)$, and $R_{8\times 8}(t_k)$, update $P_{12\times 12}(t_k)$ using Eq. (101).

3.8. Perform step 2.3.

4.4 Special Case: No Angular and Linear Velocity Measurements

A special case of particular interest is when pose measurements are available, but angular and linear velocity measurements are not. Although angular and linear velocity measurements are not available, angular and linear velocity estimates might be required for pose stabilization/tracking, as in Theorem 1. In this section, it is shown how this special case can be handled by modifying the inputs and parameters of the DQ-MEKF algorithm, without any modifications to the structure and basic equations of the DQ-MEKF algorithm.

As before, the I-frame may or many not be inertial. However, this version of the DQ-MEKF is specially suited for satellite proximity operations where the relative pose is measured using vision-based systems, which typically do not provide relative velocity measurements [15]. In this scenario, the I-frame is the moving frame of the

target satellite.

If angular and linear velocity measurements are not available, but estimates are required, $\boldsymbol{\omega}^{\mathrm{B}}_{\mathrm{B/I},m}$ and $\boldsymbol{\eta}_{\boldsymbol{\omega}}$ are set to zero in Eq. (103). This results in

$$\boldsymbol{b}_{\boldsymbol{\omega}} = -\boldsymbol{\omega}^{\mathrm{B}}_{\mathrm{B/I}} \tag{139}$$

and $\overline{Q}_{\boldsymbol{\omega}} = 0_{6\times 6}$. The dual velocity estimate is still given by Eq. (116), which now has the form $\hat{\boldsymbol{\omega}}^{\hat{\mathrm{B}}}_{\mathrm{B/I}} \approx -\hat{\boldsymbol{b}}_{\boldsymbol{\omega}}$. The time derivative of $\boldsymbol{b}_{\boldsymbol{\omega}}$ is still calculated as in Eq. (105). However, since $\boldsymbol{b}_{\boldsymbol{\omega}}$ is now expected to be time-varying and not constant, the noise $\boldsymbol{\eta}_{\boldsymbol{b}_{\boldsymbol{\omega}}}$ might have to be increased by increasing $\overline{Q}_{\boldsymbol{b}_{\boldsymbol{\omega}}}$.

In summary, this special case can be handled by just setting $\boldsymbol{\omega}^{\mathrm{B}}_{\mathrm{B/I},m}$ and $\overline{Q}_{\boldsymbol{\omega}}$ to zero and, if necessary, by increasing $\overline{Q}_{\boldsymbol{b}_{\boldsymbol{\omega}}}$.

4.5 Special Case: Linear Acceleration Measurements

Unlike in Section 4.4, the structure of the DQ-MEKF algorithm described in Section 4.3 needs to be modified for the case of a satellite having no means of directly measuring linear velocity, but with the ability to measure linear acceleration using an accelerometer or an Inertial Measurement Unit (IMU). Since an accelerometer measures accelerations with respect to an inertial frame, in this section, the I-frame should be interpreted as an inertial frame. The main modifications compared to the algorithm described in Section 4.3 are the addition of the bias of the accelerometer to the state of the DQ-MEKF and a new expression for the time derivative of b_v, which in this case is not calculated from Eq. (105). Since angular (but not linear) velocity measurements and linear (but not angular) acceleration measurements are assumed to be available, the duality between the linear and angular motion is broken in this case. Hence, the equations of the DQ-MEKF for this particular case cannot be written compactly in terms of dual quaternions as in Sections 4.3 and 4.4.

First, similarly to the angular and linear velocity measurement model, the linear

acceleration measurement model is defined as [68]

$$n^{\mathrm{B}}_{\mathrm{A/I},m} = n^{\mathrm{B}}_{\mathrm{A/I}} + b_n + \eta_n, \tag{140}$$

where $n^{\mathrm{B}}_{\mathrm{A/I}} = (0, \overline{n}^{\mathrm{B}}_{\mathrm{A/I}})$, $\overline{n}^{\mathrm{B}}_{\mathrm{A/I}}$ is the non-dimensional specific force at the location of the accelerometer with respect to the inertial frame expressed in the body frame, $n^{\mathrm{B}}_{\mathrm{A/I},m} = (0, \overline{n}^{\mathrm{B}}_{\mathrm{A/I},m})$, $\overline{n}^{\mathrm{B}}_{\mathrm{A/I},m}$ is a measurement of $\overline{n}^{\mathrm{B}}_{\mathrm{A/I}}$ produced by the accelerometer/IMU, $b_n = (0, \overline{b}_n)$, $\overline{b}_n$ is the bias of the specific force measurement, $\eta_n = (0, \overline{\eta}_n)$, $\overline{\eta}_n$ is the noise of the specific force measurement assumed to be a Gaussian white-noise process, $E\{\overline{\eta}_n\} = 0_{3\times1}$, $E\{\overline{\eta}_n(t)\overline{\eta}_n^{\mathsf{T}}(\tau)\} = \overline{Q}_n(t)\delta(t-\tau)$, and $\overline{Q}_n(t) \in \mathbb{R}^{3\times3}$ is a symmetric positive semidefinite matrix. The bias is not constant, but assumed to be driven by another Gaussian white-noise process as follows:

$$\dot{b}_n = \eta_{b_n}, \tag{141}$$

where $\eta_{b_n} = (0, \overline{\eta}_{b_n})$, $E\left\{\overline{\eta}_{b_n}\right\} = 0_{3\times1}$, $E\left\{\overline{\eta}_{b_n}(t)\overline{\eta}_{b_n}^{\mathsf{T}}(\tau)\right\} = \overline{Q}_{b_n}(t)\delta(t-\tau)$, and $\overline{Q}_{b_n}(t) \in \mathbb{R}^{3\times3}$ is a symmetric positive semidefinite matrix. From Eq. (140), the expected value of $n^{\mathrm{B}}_{\mathrm{A/I}}$ is given by

$$\hat{n}^{\hat{\mathrm{B}}}_{\mathrm{A/I}} \triangleq E\left\{n^{\hat{\mathrm{B}}}_{\mathrm{A/I}}\right\} = E\left\{\delta q_{\mathrm{B/I}} n^{\mathrm{B}}_{\mathrm{A/I}} \delta q^{*}_{\mathrm{B/I}}\right\} \approx E\left\{n^{\mathrm{B}}_{\mathrm{A/I}}\right\} = n^{\mathrm{B}}_{\mathrm{A/I},m} - \hat{b}_n, \tag{142}$$

where $\hat{b}_n \triangleq E\{b_n\}$. Likewise,

$$\frac{\mathrm{d}}{\mathrm{d}t}\left(\hat{b}_n\right) = \frac{\mathrm{d}}{\mathrm{d}t}E\{b_n\} = E\left\{\dot{b}_n\right\} = E\{\eta_{b_n}\} = 0. \tag{143}$$

Moreover, combining Eqs. (140) and (142) yields

$$n^{\mathrm{B}}_{\mathrm{A/I}} \approx \hat{n}^{\hat{\mathrm{B}}}_{\mathrm{A/I}} + \hat{b}_n - b_n - \eta_n. \tag{144}$$

The state and process noise of the DQ-MEKF are now initially selected as

$$x_{20}=[[\delta\boldsymbol{q}_{\mathrm{B/I}}]^{\mathsf{T}}\ [\boldsymbol{b}_{\boldsymbol{\omega}}]^{\mathsf{T}}\ [b_n]^{\mathsf{T}}]^{\mathsf{T}} \in \mathbb{R}^{20} \text{ and } w_{20}=[[\boldsymbol{\eta}_{\boldsymbol{\omega}}]^{\mathsf{T}}\ [\eta_{b_\omega}]^{\mathsf{T}}\ [\eta_n]^{\mathsf{T}}\ [\eta_{b_n}]^{\mathsf{T}}]^{\mathsf{T}} \in \mathbb{R}^{20}, \tag{145}$$

where the state equation for $\delta \boldsymbol{q}_{\mathrm{B/I}}$ is given by Eq. (120) and the state equation for b_ω, i.e., the real part of $\boldsymbol{b_\omega}$, is given as in Eq. (105) by $\dot{b}_\omega = \eta_{b_\omega}$, which implies that

$$\frac{\mathrm{d}}{\mathrm{d}t}\left(\hat{b}_\omega\right) = \frac{\mathrm{d}}{\mathrm{d}t}E\left\{b_\omega\right\} = E\left\{\dot{b}_\omega\right\} = E\left\{\eta_{b_\omega}\right\} = 0. \tag{146}$$

Whereas in Section 4.3 the time derivative of b_v was also calculated from Eq. (105), here the time derivative of b_v is calculated as follows. Since there are no linear velocity measurements, $v^{\mathrm{B}}_{\mathrm{B/I},m}$ and η_v are set to zero (as in Section 4.4) in Eq. (103), resulting in $b_v = -v^{\mathrm{B}}_{\mathrm{B/I}}$ and $\overline{Q}_v = \overline{Q}_{\omega v} = 0_{3\times 3}$. This in turn implies that

$$\hat{v}^{\hat{\mathrm{B}}}_{\mathrm{B/I}} \approx -\hat{b}_v. \tag{147}$$

Taking the time derivative of both sides of $b_v = -v^{\mathrm{B}}_{\mathrm{B/I}}$ leads to $\dot{b}_v = -\dot{v}^{\mathrm{B}}_{\mathrm{B/I}}$. Note that $\dot{v}^{\mathrm{B}}_{\mathrm{B/I}}$ is related to $n^{\mathrm{B}}_{\mathrm{A/I}}$ through

$$\dot{v}^{\mathrm{B}}_{\mathrm{B/I}} = -\omega^{\mathrm{B}}_{\mathrm{B/I}} \times v^{\mathrm{B}}_{\mathrm{B/I}} + c n^{\mathrm{B}}_{\mathrm{A/I}} - q^*_{\mathrm{B/I}} g^{\mathrm{I}} q_{\mathrm{B/I}} - \alpha^{\mathrm{B}}_{\mathrm{B/I}} \times r^{\mathrm{B}}_{\mathrm{A/B}} - \omega^{\mathrm{B}}_{\mathrm{B/I}} \times (\omega^{\mathrm{B}}_{\mathrm{B/I}} \times r^{\mathrm{B}}_{\mathrm{A/B}}), \tag{148}$$

where $c \in \mathbb{R}$ is a scaling constant specific to each accelerometer, $g^{\mathrm{I}} = (0, \overline{g}^{\mathrm{I}})$, $\overline{g}^{\mathrm{I}}$ is the local gravity acceleration vector expressed in the inertial frame (assumed to be known), $\alpha^{\mathrm{B}}_{\mathrm{B/I}} = (0, \overline{\alpha}^{\mathrm{B}}_{\mathrm{B/I}})$, $\overline{\alpha}^{\mathrm{B}}_{\mathrm{B/I}}$ is the angular acceleration of the body frame with respect to the inertial frame expressed in the body frame, $r^{\mathrm{B}}_{\mathrm{A/B}} = (0, \overline{r}^{\mathrm{B}}_{\mathrm{A/B}})$, and $\overline{r}^{\mathrm{B}}_{\mathrm{A/B}}$ is the translation vector from the origin of the body frame to the accelerometer expressed in the body frame (assumed to be known). Hence, $\dot{b}_v = -\dot{v}^{\mathrm{B}}_{\mathrm{B/I}} = -\omega^{\mathrm{B}}_{\mathrm{B/I}} \times b_v - c n^{\mathrm{B}}_{\mathrm{A/I}} + q^*_{\mathrm{B/I}} g^{\mathrm{I}} q_{\mathrm{B/I}} + \alpha^{\mathrm{B}}_{\mathrm{B/I}} \times r^{\mathrm{B}}_{\mathrm{A/B}} + \omega^{\mathrm{B}}_{\mathrm{B/I}} \times (\omega^{\mathrm{B}}_{\mathrm{B/I}} \times r^{\mathrm{B}}_{\mathrm{A/B}})$. Finally, neglecting $\alpha^{\mathrm{B}}_{\mathrm{B/I}}$, which is assumed to be unknown, and using Eq. (144) and the real parts of Eqs. (108) and (119), results in

$$\begin{aligned}
\dot{b}_v = -\dot{v}^{\mathrm{B}}_{\mathrm{B/I}} \approx & -(\hat{\omega}^{\hat{\mathrm{B}}}_{\mathrm{B/I}} + \hat{b}_\omega - b_\omega - \eta_\omega) \times b_v - c(\hat{n}^{\hat{\mathrm{B}}}_{\mathrm{A/I}} + \hat{b}_n - b_n - \eta_n) + \delta q^*_{\mathrm{B/I}} \hat{q}^*_{\mathrm{B/I}} g^{\mathrm{I}} \hat{q}_{\mathrm{B/I}} \delta q_{\mathrm{B/I}} \\
& + (\hat{\omega}^{\hat{\mathrm{B}}}_{\mathrm{B/I}} + \hat{b}_\omega - b_\omega - \eta_\omega) \times ((\hat{\omega}^{\hat{\mathrm{B}}}_{\mathrm{B/I}} + \hat{b}_\omega - b_\omega - \eta_\omega) \times r^{\mathrm{B}}_{\mathrm{A/B}}) \\
= & -(\hat{\omega}^{\hat{\mathrm{B}}}_{\mathrm{B/I}} + \hat{b}_\omega - b_\omega) \times b_v - c(\hat{n}^{\hat{\mathrm{B}}}_{\mathrm{A/I}} + \hat{b}_n - b_n) + \delta q^*_{\mathrm{B/I}} \hat{q}^*_{\mathrm{B/I}} g^{\mathrm{I}} \hat{q}_{\mathrm{B/I}} \delta q_{\mathrm{B/I}} \\
& + (\hat{\omega}^{\hat{\mathrm{B}}}_{\mathrm{B/I}} + \hat{b}_\omega - b_\omega) \times ((\hat{\omega}^{\hat{\mathrm{B}}}_{\mathrm{B/I}} + \hat{b}_\omega - b_\omega) \times r^{\mathrm{B}}_{\mathrm{A/B}})
\end{aligned}$$

$$-b_v\times\eta_\omega+c\eta_n-\eta_\omega\times((\hat{\omega}^{\hat{\mathrm{B}}}_{\mathrm{B/I}}+\hat{b}_\omega-b_\omega)\times r^{\mathrm{B}}_{\mathrm{A/B}})+(\hat{\omega}^{\hat{\mathrm{B}}}_{\mathrm{B/I}}+\hat{b}_\omega-b_\omega)\times(-\eta_\omega\times r^{\mathrm{B}}_{\mathrm{A/B}})$$
$$+(-\eta_\omega)\times(-\eta_\omega\times r^{\mathrm{B}}_{\mathrm{A/B}}). \tag{149}$$

Since the last term in Eq. (149) is quadratic in η_ω and, thus, does not have the same form as Eq. (88), it is ignored.

Note that by using the typical approximation given by Eq. (89), the time derivative of $\hat{b}_v$ can be calculated from Eq. (149) to be

$$\dot{\hat{b}}_v\approx-\hat{\omega}^{\hat{\mathrm{B}}}_{\mathrm{B/I}}\times\hat{b}_v-c\hat{n}^{\hat{\mathrm{B}}}_{\mathrm{A/I}}+\hat{q}^*_{\mathrm{B/I}}g^{\mathrm{I}}\hat{q}_{\mathrm{B/I}}+\hat{\omega}^{\hat{\mathrm{B}}}_{\mathrm{B/I}}\times(\hat{\omega}^{\hat{\mathrm{B}}}_{\mathrm{B/I}}\times r^{\mathrm{B}}_{\mathrm{A/B}}). \tag{150}$$

Hence, in summary, the state equations of the DQ-MEKF when linear acceleration measurements are available are defined by $f_{20}(x_{20}(t),t)$ and $g_{20\times20}(x_{20}(t),t)$ given by, respectively,

$$\begin{bmatrix} [-\frac{1}{2}\hat{\boldsymbol{\omega}}^{\hat{\mathrm{B}}}_{\mathrm{B/I}}\delta\boldsymbol{q}_{\mathrm{B/I}}+\frac{1}{2}\delta\boldsymbol{q}_{\mathrm{B/I}}\hat{\boldsymbol{\omega}}^{\hat{\mathrm{B}}}_{\mathrm{B/I}}+\frac{1}{2}\delta\boldsymbol{q}_{\mathrm{B/I}}\hat{\boldsymbol{b}}_{\boldsymbol{\omega}}-\frac{1}{2}\delta\boldsymbol{q}_{\mathrm{B/I}}\boldsymbol{b}_{\boldsymbol{\omega}}] \\ 0_{4\times1} \\ [-(\hat{\omega}^{\hat{\mathrm{B}}}_{\mathrm{B/I}}+\hat{b}_\omega-b_\omega)\times b_v-c(\hat{n}^{\hat{\mathrm{B}}}_{\mathrm{A/I}}+\hat{b}_n-b_n)+\delta q^*_{\mathrm{B/I}}\hat{q}^*_{\mathrm{B/I}}g^{\mathrm{I}}\hat{q}_{\mathrm{B/I}}\delta q_{\mathrm{B/I}}+(\hat{\omega}^{\hat{\mathrm{B}}}_{\mathrm{B/I}}+\hat{b}_\omega-b_\omega)\times((\hat{\omega}^{\hat{\mathrm{B}}}_{\mathrm{B/I}}+\hat{b}_\omega-b_\omega)\times r^{\mathrm{B}}_{\mathrm{A/B}})] \\ 0_{4\times1} \end{bmatrix},$$

$$\begin{bmatrix} -\frac{1}{2}[\delta\boldsymbol{q}_{\mathrm{B/I},r}]^{\mathrm{L}} & 0_{4\times4} & 0_{4\times4} & 0_{4\times4} & 0_{4\times4} \\ -\frac{1}{2}[\delta\boldsymbol{q}_{\mathrm{B/I},d}]^{\mathrm{L}} & -\frac{1}{2}[\delta\boldsymbol{q}_{\mathrm{B/I},r}]^{\mathrm{L}} & 0_{4\times4} & 0_{4\times4} & 0_{4\times4} \\ 0_{4\times4} & 0_{4\times4} & I_{4\times4} & 0_{4\times4} & 0_{4\times4} \\ -[b_v]^\times+[(\hat{\omega}^{\hat{\mathrm{B}}}_{\mathrm{B/I}}+\hat{b}_\omega-b_\omega)\times r^{\mathrm{B}}_{\mathrm{A/B}}]^\times+[\hat{\omega}^{\hat{\mathrm{B}}}_{\mathrm{B/I}}+\hat{b}_\omega-b_\omega]^\times[r^{\mathrm{B}}_{\mathrm{A/B}}]^\times & 0_{4\times4} & 0_{4\times4} & cI_{4\times4} & 0_{4\times4} \\ 0_{4\times4} & 0_{4\times4} & 0_{4\times4} & 0_{4\times4} & I_{4\times4} \end{bmatrix}.$$

At this point, as before, reduced state and process noise vectors are selected, namely

$$x_{15}=[\overline{\delta\boldsymbol{q}_{\mathrm{B/I}}}^{\mathsf{T}}\ \overline{\boldsymbol{b}}^{\mathsf{T}}_{\boldsymbol{\omega}}\ \overline{b}^{\mathsf{T}}_n]^{\mathsf{T}}\in\mathbb{R}^{15}\text{ and }w_{15}=[\overline{\boldsymbol{\eta}}^{\mathsf{T}}_{\boldsymbol{\omega}}\ \overline{\eta}^{\mathsf{T}}_{b_\omega}\ \overline{\eta}^{\mathsf{T}}_n\ \overline{\eta}^{\mathsf{T}}_{b_n}]^{\mathsf{T}}\in\mathbb{R}^{15}. \tag{151}$$

By replacing $\delta q_{\mathrm{B/I},r,0}$ and $\delta q_{\mathrm{B/I},d,0}$ through Eq. (47) in $f_{20}(x_{20},t)$ and $g_{20\times20}(x_{20},t)$ and

using Eq. (93), $F_{15\times15}(t)$ and $G_{15\times15}(t)$ can be determined to be, respectively,

$$\begin{bmatrix} -[\overline{\hat{\omega}^{\hat{\mathrm{B}}}_{\mathrm{B/I}}}]^\times & 0_{3\times3} & -\frac{1}{2}I_{3\times3} & 0_{3\times3} & 0_{3\times3} \\ -[\overline{\hat{v}^{\hat{\mathrm{B}}}_{\mathrm{B/I}}}]^\times & -[\overline{\hat{\omega}^{\hat{\mathrm{B}}}_{\mathrm{B/I}}}]^\times & 0_{3\times3} & -\frac{1}{2}I_{3\times3} & 0_{3\times3} \\ 0_{3\times3} & 0_{3\times3} & 0_{3\times3} & 0_{3\times3} & 0_{3\times3} \\ 2[\overline{\hat{q}^*_{\mathrm{B/I}}g^{\mathrm{I}}\hat{q}_{\mathrm{B/I}}}]^\times & 0_{3\times3} & -[\overline{\hat{b}_v}]^\times+[\overline{[\hat{\omega}^{\hat{\mathrm{B}}}_{\mathrm{B/I}}\times r^{\mathrm{B}}_{\mathrm{A/B}}]}]^\times+[\overline{\hat{\omega}^{\hat{\mathrm{B}}}_{\mathrm{B/I}}}]^\times[\overline{r^{\mathrm{B}}_{\mathrm{A/B}}}]^\times & -[\overline{\hat{\omega}^{\hat{\mathrm{B}}}_{\mathrm{B/I}}}]^\times & cI_{3\times3} \\ 0_{3\times3} & 0_{3\times3} & 0_{3\times3} & 0_{3\times3} & 0_{3\times3} \end{bmatrix},$$

$$\begin{bmatrix} -\frac{1}{2}I_{3\times3} & 0_{3\times3} & 0_{3\times3} & 0_{3\times3} & 0_{3\times3} \\ 0_{3\times3} & -\frac{1}{2}I_{3\times3} & 0_{3\times3} & 0_{3\times3} & 0_{3\times3} \\ 0_{3\times3} & 0_{3\times3} & I_{3\times3} & 0_{3\times3} & 0_{3\times3} \\ -[\overline{\hat{b}_v}]^\times+[\overline{[\hat{\omega}^{\hat{\mathrm{B}}}_{\mathrm{B/I}}\times r^{\mathrm{B}}_{\mathrm{A/B}}]}]^\times+[\overline{\hat{\omega}^{\hat{\mathrm{B}}}_{\mathrm{B/I}}}]^\times[\overline{r^{\mathrm{B}}_{\mathrm{A/B}}}]^\times & 0_{3\times3} & 0_{3\times3} & cI_{3\times3} & 0_{3\times3} \\ 0_{3\times3} & 0_{3\times3} & 0_{3\times3} & 0_{3\times3} & I_{3\times3} \end{bmatrix}.$$

4.5.1 Time Update

When acceleration measurements are available, for the time update of the DQ-MEKF, the estimates of $\boldsymbol{q}_{\mathrm{B/I}}$, b_ω, b_v, b_n, $v^{\mathrm{B}}_{\mathrm{B/I}}$, $\omega^{\mathrm{B}}_{\mathrm{B/I}}$ are propagated using Eqs. (115), (146), (150), (143), (147), and the real part of Eq. (116), i.e., $\hat{\omega}^{\hat{\mathrm{B}}}_{\mathrm{B/I}} \approx \omega^{\mathrm{B}}_{\mathrm{B/I},m} - \hat{b}_\omega$, respectively, given $\hat{\boldsymbol{q}}_{\mathrm{B/I}}(t_0)$, $\hat{\boldsymbol{b}}_{\boldsymbol{\omega}}(t_0)$, and $\hat{b}_n(t_0)$. As for the covariance matrix of x_{15}, i.e., $P_{15\times15}(t) \triangleq E\left\{\Delta x_{15}(t)\Delta x_{15}(t)^\intercal\right\}$ or

$$P_{15\times15}(t) = E\left\{\left(\begin{bmatrix}\overline{\delta\boldsymbol{q}_{\mathrm{B/I}}}(t)\\ \overline{\boldsymbol{b}}_{\boldsymbol{\omega}}(t)\\ \overline{b}_n(t)\end{bmatrix} - \begin{bmatrix}0_{6\times6}\\ \overline{\hat{\boldsymbol{b}}}_{\boldsymbol{\omega}}(t)\\ \overline{\hat{b}}_n(t)\end{bmatrix}\right)\left(\begin{bmatrix}\overline{\delta\boldsymbol{q}_{\mathrm{B/I}}}(t)\\ \overline{\boldsymbol{b}}_{\boldsymbol{\omega}}(t)\\ \overline{b}_n(t)\end{bmatrix} - \begin{bmatrix}0_{6\times6}\\ \overline{\hat{\boldsymbol{b}}}_{\boldsymbol{\omega}}(t)\\ \overline{\hat{b}}_n(t)\end{bmatrix}\right)^\intercal\right\}, \quad (152)$$

it is propagated according to Eq. (92) given $P_{15\times15}(t_0)$ and where

$$Q_{15\times15}(t) = \begin{bmatrix} \overline{Q}_\omega(t) & 0_{3\times3} & 0_{3\times3} & 0_{3\times3} & 0_{3\times3} \\ 0_{3\times3} & 0_{3\times3} & 0_{3\times3} & 0_{3\times3} & 0_{3\times3} \\ 0_{3\times3} & 0_{3\times3} & \overline{Q}_{b_\omega}(t) & 0_{3\times3} & 0_{3\times3} \\ 0_{3\times3} & 0_{3\times3} & 0_{3\times3} & \overline{Q}_n(t) & 0_{3\times3} \\ 0_{3\times3} & 0_{3\times3} & 0_{3\times3} & 0_{3\times3} & \overline{Q}_{b_n}(t) \end{bmatrix}. \quad (153)$$

Given

$$\tilde{P}_{20\times 20}(t_0) \triangleq E\left\{\left(\begin{bmatrix}[\boldsymbol{q}_{\mathrm{B/I}}(t_0)]\\ [\boldsymbol{b}_{\boldsymbol{\omega}}(t_0)]\\ [b_n(t)]\end{bmatrix} - \begin{bmatrix}[\hat{\boldsymbol{q}}_{\mathrm{B/I}}(t_0)]\\ [\hat{\boldsymbol{b}}_{\boldsymbol{\omega}}(t_0)]\\ [\hat{b}_n(t)]\end{bmatrix}\right)\left(\begin{bmatrix}[\boldsymbol{q}_{\mathrm{B/I}}(t_0)]\\ [\boldsymbol{b}_{\boldsymbol{\omega}}(t_0)]\\ [b_n(t)]\end{bmatrix} - \begin{bmatrix}[\hat{\boldsymbol{q}}_{\mathrm{B/I}}(t_0)]\\ [\hat{\boldsymbol{b}}_{\boldsymbol{\omega}}(t_0)]\\ [\hat{b}_n(t)]\end{bmatrix}\right)^{\mathsf{T}}\right\},$$

$P_{15\times 15}(t_0)$ can be calculated by first computing

$$\begin{aligned} P_{20\times 20}(t_0) &\triangleq E\left\{\left(\begin{bmatrix}[\delta\boldsymbol{q}_{\mathrm{B/I}}(t_0)]\\ [\boldsymbol{b}_{\boldsymbol{\omega}}(t_0)]\\ [b_n(t)]\end{bmatrix} - \begin{bmatrix}[\mathbf{1}]\\ [\hat{\boldsymbol{b}}_{\boldsymbol{\omega}}(t_0)]\\ [\hat{b}_n(t)]\end{bmatrix}\right)\left(\begin{bmatrix}[\delta\boldsymbol{q}_{\mathrm{B/I}}(t_0)]\\ [\boldsymbol{b}_{\boldsymbol{\omega}}(t_0)]\\ [b_n(t)]\end{bmatrix} - \begin{bmatrix}[\mathbf{1}]\\ [\hat{\boldsymbol{b}}_{\boldsymbol{\omega}}(t_0)]\\ [\hat{b}_n(t)]\end{bmatrix}\right)^{\mathsf{T}}\right\} \\ &= S\tilde{P}_{20\times 20}(t_0)S^{\mathsf{T}}, \end{aligned} \tag{154}$$

where

$$S = \begin{bmatrix}[\hat{\boldsymbol{q}}^{*}_{\mathrm{B/I}}]^{\mathrm{L}} & 0_{8\times 8} & 0_{8\times 4}\\ 0_{8\times 8} & I_{8\times 8} & 0_{8\times 4}\\ 0_{4\times 8} & 0_{4\times 8} & I_{4\times 4}\end{bmatrix}. \tag{155}$$

Then, $P_{15\times 15}(t_0)$ can be obtained from $P_{20\times 20}(t_0)$ by removing the first, fifth, ninth, thirteenth, and seventeenth rows and columns of $P_{20\times 20}(t_0)$.

4.5.2 Measurement Update

When acceleration measurements are available, the measurement update is performed as in Section 4.3 with the measurement sensitivity matrix now given by

$$H_{8\times 15}(t_k) = \begin{bmatrix}[\hat{\boldsymbol{q}}_{\mathrm{B/I}}]^{\mathrm{L}}_{8\times 6} & 0_{8\times 6} & 0_{8\times 3}\end{bmatrix}. \tag{156}$$

The optimal Kalman state update is now calculated from Eq. (96) as follows

$$\Delta^{\star}\hat{x}_{15}(t_k) \triangleq \begin{bmatrix}\Delta^{\star}\overline{\delta\hat{\boldsymbol{q}}_{\mathrm{B/I}}}(t_k)\\ \Delta^{\star}\overline{\hat{\boldsymbol{b}}}_{\boldsymbol{\omega}}(t_k)\\ \Delta^{\star}\overline{\hat{b}}_n(t_k)\end{bmatrix} = K_{15\times 8}(t_k)(z_8(t_k) - \hat{z}_8(t_k)). \tag{157}$$

Finally, the estimate of the state at time t_k after the measurement is calculated from Eqs. (133) and (134) and from $\overline{\hat{b}}^{+}_n(t_k) = \overline{\hat{b}}^{-}_n(t_k) + \Delta^{\star}\overline{\hat{b}}_n(t_k)$.

4.6 Experimental Results

In this section, the two special cases of the DQ-MEKF are validated experimentally on the *Autonomous Spacecraft Testing of Robotic Operations in Space* (ASTROS) facility at the School of Aerospace Engineering of Georgia Tech. This experimental facility includes a 5-DOF platform supported on hemispherical and linear air-bearings moving over a flat epoxy floor in order to simulate as best as possible the frictionless environment of space. It also includes a VICON motion capture system mounted on an aluminum grid above the experimental area. The VICON system measures the attitude and position of the platform with respect to a reference frame fixed to the room. These measurements are then transmitted wirelessly to the platform. A picture of the platform is shown in Figure 17. More information about the ASTROS facility and its 5-DOF platform can be found in Refs. [87, 14]. The most relevant characteristics of the sensors used in the experiments are summarized in Table 3, where SD stands for Standard Deviation. The scaling constant of the IMU is $c = 9.8$ m/s^2 and it is located at $\bar{r}^{\mathrm{B}}_{\mathrm{A/B}} = [0.113, -0.016, -0.089]^{\intercal}$ m.

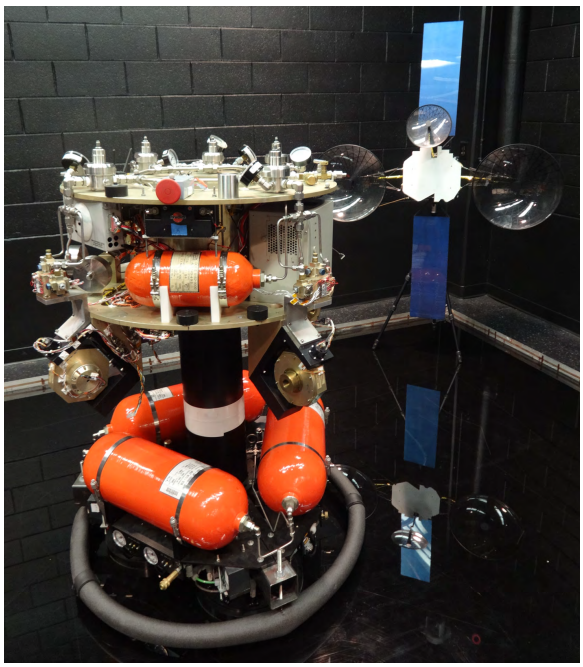

Figure 17: The 5-DOF experimental platform of the ASTROS facility.

Table 3: Characteristics of the sensors.

Meas.	Sensor	Noise SD	Bias	Refresh Rate
$\bar{\omega}^{\mathrm{B}}_{\mathrm{B/I},m}$	Humphrey RG02-3227-1 rate-gyro	0.027 deg/s	<2 deg/s	100 Hz
$\bar{n}^{\mathrm{B}}_{\mathrm{A/I},m}$	Crossbow AHRS400CC-100 IMU	1.5 mg	<8.5 mg	100 Hz
$q_{\mathrm{B/I},m}$	8 VICON Bonita B10 cameras	$< 7 \times 10^{-5}$	-	Variable ($\leq$ 250 Hz)
$\bar{r}^{\mathrm{I}}_{\mathrm{B/I},m}$	8 VICON Bonita B10 cameras	$<$ 1 mm	-	Variable ($\leq$ 250 Hz)

The ground truth for attitude and position was obtained from VICON measurements at 100 Hz. The ground truth for linear velocity was obtained by passing these position measurements through a LTI system with transfer matrix $H(s) = \frac{3s}{s+3} I_{3\times 3}$. The position of the pole was chosen by trial-and-error to minimize noise and lag. Finally, the ground truth for angular velocity was obtained by passing the quaternion measurements through a LTI system with transfer matrix $H(s) = \frac{3s}{s+3} I_{4\times 4}$ and by using the relation $\omega^{\mathrm{B}}_{\mathrm{B/I}} = 2q^{*}_{\mathrm{B/I}}\dot{q}_{\mathrm{B/I}}$. Note that whereas the LTI filters can reduce the noise at the cost of lag, they cannot totally eliminate it.

4.6.1 DQ-MEKF With No Angular and Linear Velocity Measurements

For this experiment, the DQ-MEKF was fed attitude and position measurements from the VICON system at 10 Hz modeled through the output equation given by Eq. (137). The initial estimate of the state is given in Table 4. The same table also shows an a posteriori guess of the initial state based on the measurements. The DQ-MEKF was initialized with the covariance matrices given in Table 5.

The pose estimated by the DQ-MEKF is compared with the ground truth in Figure 18. The two appear almost superimposed. This is to be expected due to the relatively high update rate of the pose measurements in this case. Note that the motion only starts around 20 sec after the beginning of the experiment.

Table 4: Case 1: Initial estimate and a posteriori guess of the state.

Variable	Initial Estimate	A Posteriori Guess
$q_{\mathrm{B/I}}(0)$	$[0.7071, 0, 0, 0.7071]^\intercal$ (-)	$[0.7987, -0.0221, -0.0195, 0.6009]^\intercal$ (-)
$\bar{r}^{\mathrm{I}}_{\mathrm{B/I}}(0)$	$[0, 0, -1.4]^\intercal$ (m)	$[-0.5256, 2.0425, -0.9887]^\intercal$ (m)
$b_\omega(0)$	$[0, 0, 0]^\intercal$ (deg/s)	$[0, 0, 0]^\intercal$ (deg/s)
$b_v(0)$	$[0, 0, 0]^\intercal$ (m/s)	$[0, 0, 0]^\intercal$ (m/s)

Table 5: Case 1: Covariance matrices.

$\tilde{P}_{16\times16}(0)$	$\mathrm{diag}([0.0069, 0.0069, 0.0069, 0.0069, 0.69, 0.69, 0.69, 0.69, 0, 1\times10^{-9}, 1\times10^{-9}, 1\times10^{-9}, 0, 1\times10^{-9}, 1\times10^{-9}, 1\times10^{-9}])$
$Q_{12\times12}$	$\mathrm{diag}([0, 0, 0, 0, 0, 0, 1\times10^{-4}, 1\times10^{-4}, 1\times10^{-4}, 1\times10^{-4}, 1\times10^{-4}, 1\times10^{-4}])$
$R_{7\times7}$	$\mathrm{diag}([1\times10^{-6}, 1\times10^{-6}, 1\times10^{-6}, 1\times10^{-6}, 2.5\times10^{-6}, 2.5\times10^{-6}, 2.5\times10^{-6}])$

The pose estimation error obtained with the DQ-MEKF is plotted in Figure 19. Note that the pose error increases at around 20 sec, when the motion starts. The same figure also shows the pose estimation error obtained with two alternative EKF formulations.

This first alternative EKF formulation, hereby referred to as the *QV-AEKF*, is an additive EKF where the state contains the vector part of the unit error quaternion (like in the Q-MEKF) and the position vector of the body with respect to the inertial frame expressed in the body frame. The QV-AEKF is derived in detail in Appendix A. The biggest differences between the DQ-MEKF and the QV-AEKF are that in the former the position is represented by the dual part of the dual quaternion and the position measurement update is performed using the dual quaternion multiplication, whereas in the latter the position is represented by the body coordinates of the position vector and the position measurement update is performed by adding the optimal correction to the current best estimate.

The second alternative EKF formulation, hereby referred to as the *SQV-AEKF*,

is essentially the QV-AEKF split into two additive EKFs, one for the attitude and another one for the position. The SQV-AEKF is derived in detail in Appendix B.

For the comparison between the DQ-MEKF, the QV-AEKF, and the SQV-AEKF to be fair, the three filters were fed the same measurements, were initialized with the same initial estimate of the state (given in Table 4), and were tuned with the same noise covariance matrices (given in Table 5).

Figure 20 shows the linear and angular velocity estimation errors obtained with the three filters.

The Root-Mean-Square (RMS) attitude, position, angular velocity, and linear velocity estimation errors after 20 sec obtained with the three filters are given in Table 6. Note that the RMS attitude and angular velocity estimation errors obtained with the three filters are the same. This is not surprising since the DQ-MEKF, the QV-AEKF, and the SQV-AEKF represent and update the attitude in the same way and the attitude is independent from the position. However, whereas the RMS position and linear velocity estimation errors obtained with the DQ-MEKF and the QV-AEKF are the same, the RMS position and linear velocity estimation errors obtained with the SQV-AEKF are higher. This is understandable since whereas the DQ-MEKF and the QV-AEKF take into consideration that the position vector of the body with respect to the inertial frame expressed in the body frame depends on the attitude of the body, the SQV-AEKF does not. Another way to see this is to realize that some of the elements of Eqs. (248), (249), and (255) do not appear in Eqs. (261), (262), (272), (273), (268), and (277).

The consistency of the DQ-MEKF is checked in two ways. First, in Figure 21, $\overline{\delta \boldsymbol{q}_{\mathrm{B/I}}}$ is plotted against its 3σ bounds obtained from $P_{12\times 12}$. Whereas the state of the DQ-MEKF is composed by $\overline{\delta \boldsymbol{q}_{\mathrm{B/I}}}$ and $\overline{\boldsymbol{b}}_{\boldsymbol{\omega}}$, only the consistency of $\overline{\delta \boldsymbol{q}_{\mathrm{B/I}}}$ is checked, since a direct measurement of the ground truth of $\overline{\boldsymbol{b}}_{\boldsymbol{\omega}}$ is not available. From Figure 21, it is possible to calculate that the probability that each element of $\overline{\delta \boldsymbol{q}_{\mathrm{B/I}}}$ is inside its

Table 6: Case 1: RMS estimation errors after 20 sec obtained with the three filters (pose measurements at 10 Hz).

RMS Estimation Error	DQ-MEKF	QV-AEKF	SQV-AEKF
Attitude (deg)	0.16	0.16	0.16
Position (mm)	5.2	5.2	5.7
Angular Velocity (deg/s)	0.36	0.36	0.36
Linear Velocity (mm/s)	3.5	3.5	19.1

respective 3σ bounds is no less than 96.7%. Second, in Figure 22, the innovation is plotted against its 3σ bounds obtained from $S_{7\times7}$, given by Eq. (102). It is possible to calculate that the probability that each element of ν_7 is inside its respective 3σ bounds is no less than 98.8%.

To compare the filters in a more demanding scenario, the same experimental data was fed into the DQ-MEKF, QV-AEKF, and SQV-AEKF, but now with an update rate of 0.5 Hz. All other parameters were kept the same. The pose estimated by the DQ-MEKF is compared with the ground truth in Figure 23. As expected, the pose estimation error in this case is visibly higher than in Figure 18.

The attitude, position, angular velocity, and linear velocity estimation errors obtained with the DQ-MEKF, the QV-AEKF, and the SQV-AEKF are compared in Figures 24 and 25 and in Table 7. Like in Table 6, the RMS attitude and angular velocity estimation errors obtained with the three filters are the same and the SQV-AEKF exhibits the highest RMS position and linear velocity estimation errors. However, unlike in Table 6, the RMS position and linear velocity estimation errors obtained with the DQ-MEKF are smaller than the ones obtained with the QV-AEKF. In other words, as the update rate of the pose measurements decreases, the DQ-MEKF starts producing better position and linear velocity estimates than the QV-AEKF. This can be justified in part by Figure 1. Since the relation between $r^{\mathrm{B}}_{\mathrm{B/I}}$ and $r^{\mathrm{I}}_{\mathrm{B/I}}$ is quadratic in $q_{\mathrm{B/I}}$, whereas the relation between $q_{\mathrm{B/I},d}$ and $r^{\mathrm{I}}_{\mathrm{B/I}}$ is linear in $q_{\mathrm{B/I}}$, the

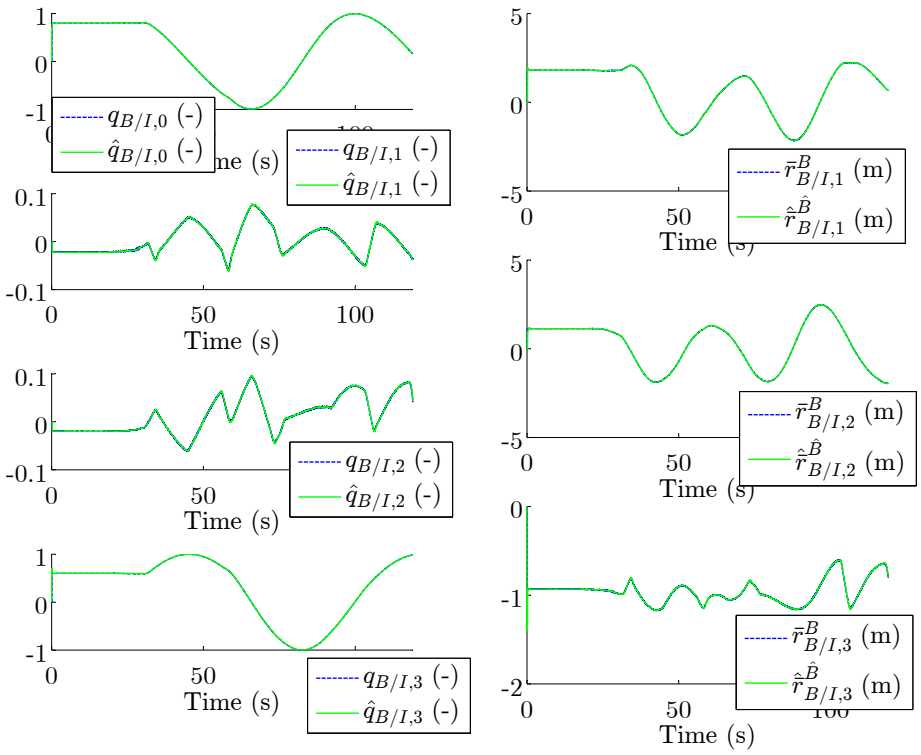

Figure 18: Case 1: estimated and true pose (pose measurements at 10 Hz).

linearization error committed when linearizing the output equations of the QV-AEKF and of the DQ-MEKF (i.e., Eq. (254) and Eq. (137), respectively) with respect to $\delta q_{\mathrm{B/I}}$ is smaller in the DQ-MEKF case.

Table 7: Case 1: RMS estimation errors after 20 sec obtained with the three filters (pose measurements at 0.5 Hz).

RMS Estimation Error	DQ-MEKF	QV-AEKF	SQV-AEKF
Attitude (deg)	2.20	2.20	2.20
Position (mm)	68.8	70.2	124.2
Angular Velocity (deg/s)	1.90	1.90	1.90
Linear Velocity (mm/s)	21.8	22.2	83.8

4.6.2 DQ-MEKF With Linear Acceleration Measurements

For this experiment, the DQ-MEKF was fed attitude and position measurements from the VICON system at 1 Hz, linear acceleration measurements from the IMU at

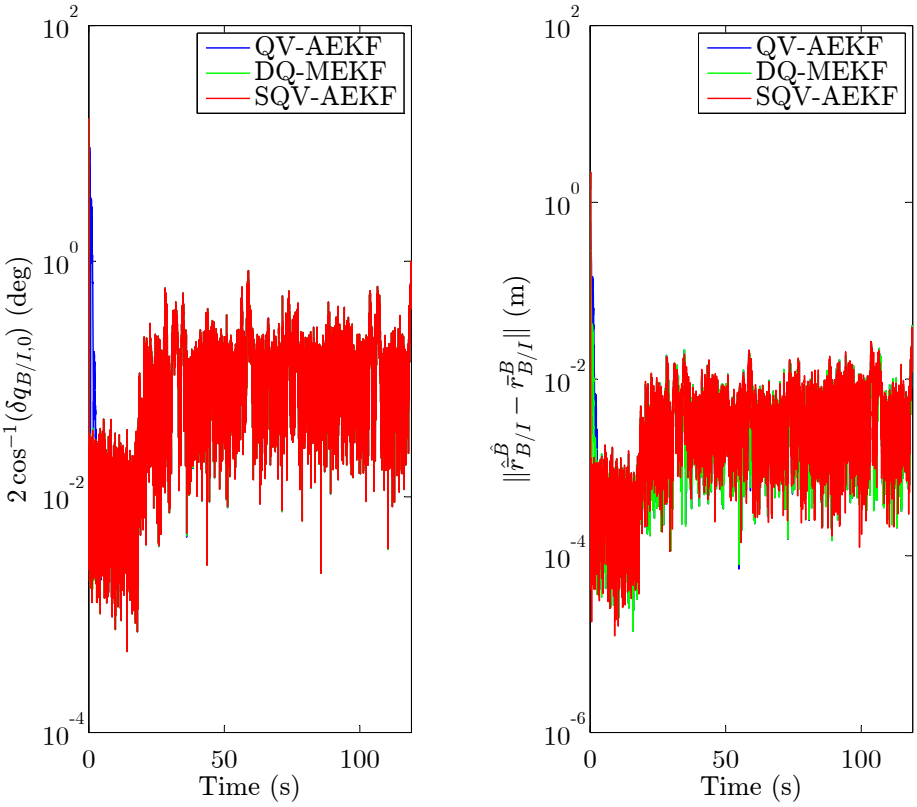

Figure 19: Case 1: pose estimation error (pose measurements at 10 Hz).

100 Hz, and angular velocity measurements from the rate-gyro at 100 Hz. The initial estimate of the state is given in Table 8. The same table also shows an a posteriori guess of the initial state based on the measurements. The DQ-MEKF was initialized with the covariance matrices given in Table 9.

Table 8: Case 2: Initial estimate and a posteriori guess of the state.

Variable	Initial Estimate	A Posteriori Guess
$q_{\mathrm{B/I}}(0)$	$[0.6947, -0.0004, 0.0247, 0.7189]^\intercal$	$[0.7987, -0.0221, -0.0195, 0.6009]^\intercal$
$\bar{r}^{\mathrm{I}}_{\mathrm{B/I}}(0)$	$[0, 0, 0]^\intercal$ (m)	$[-0.5256, 2.0425, -0.9887]^\intercal$ (m)
$\bar{b}_\omega(0)$	$[-1, 1, 1]^\intercal$ (deg/s)	$[-0.7583, 1.044, 0.6717]^\intercal$ (deg/s)
$\bar{b}_v(0)$	$[0, 0, 0]^\intercal$ (m/s)	$[0, 0, 0]^\intercal$ (m/s)
$\bar{b}_n(0)$	$[0, 0, 0]^\intercal$ (-)	$[0.0251, 0.0160, 0.0005]^\intercal$ (-)

The measured and estimated (i.e., without bias) non-dimensional specific force captured by the accelerometer are plotted in Figure 26. The difference between them

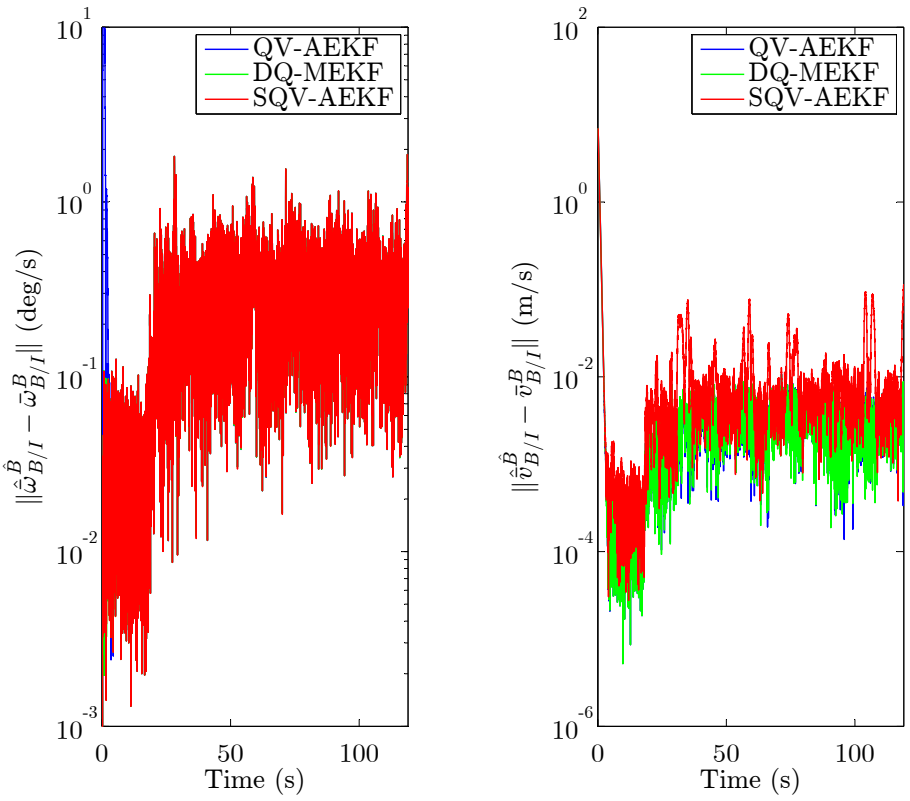

Figure 20: Case 1: angular and linear velocity estimation errors (pose measurements at 10 Hz).

is the estimated bias of the accelerometer. This estimated bias is higher than the expected bias listed in the accelerometer's datasheet given in Table 3. In addition, the estimated bias varies with time when the platform is moving. These two phenomena can be interpreted as the DQ-MEKF trying to compensate for errors in the determination of the center of rotation of the upper stage of the 5-DOF platform, errors in the determination of the position of the accelerometer, and errors due to the assumption of zero angular acceleration in Eq. (149).

The measured and estimated (i.e., without bias) angular velocity captured by the rate-gyro are compared in Figure 27. The difference between them is the estimated bias of the rate-gyro. This estimated bias is within the expected bias listed in Table 3 and, compared with Figure 26, does not show any signification variation with time. This is expected as the errors that effect the bias of the accelerometer do not affect

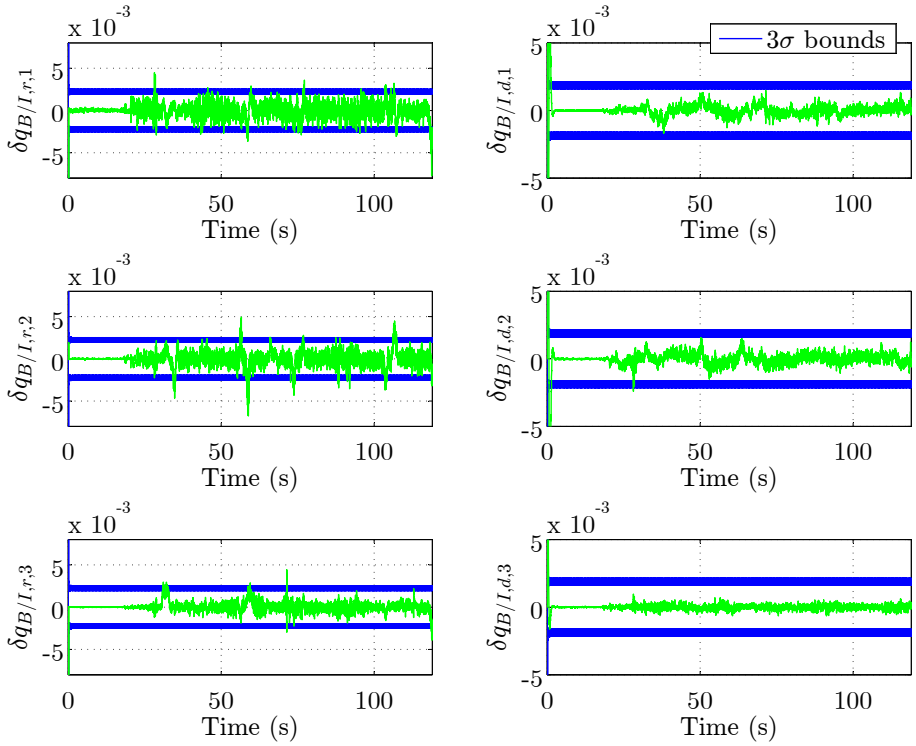

Figure 21: Case 1: consistency check of the DQ-MEKF using the pose estimation error.

the bias of the rate-gyro.

The estimated pose is compared with the ground truth in Figure 28 and the pose estimation error is plotted in Figure 29. After 80 sec, the RMS attitude estimation error is 0.20 deg and the RMS position estimation error is 1.6 cm.

Finally, Figure 30 shows the linear and angular velocity estimation errors for this case. Whereas after 80 sec the RMS angular velocity estimation error is 0.70 deg/s, the RMS linear velocity estimation error is 3.3 cm/s.

4.7 Comparison between the Velocity-Free Pose-Tracking Controller and the Velocity-Feedback Pose-Tracking Controller in conjunction with the DQ-MEKF

Until now, two alternative solutions to the problem of pose-tracking without relative linear and angular velocity feedback, i.e., without $\boldsymbol{\omega}^{\mathrm{B}}_{\mathrm{B/D}}$ feedback, have been proposed. The first consist of using directly the velocity-free controller derived in Theorem 2.

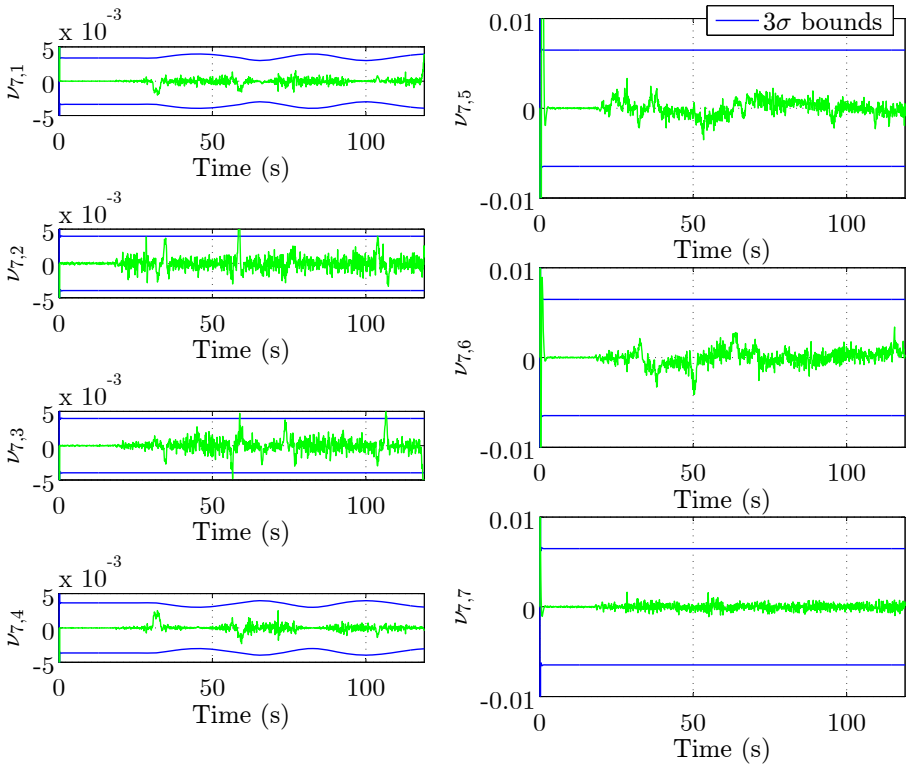

Figure 22: Case 1: consistency check of the DQ-MEKF using the innovation.

The second consists of using the velocity-feedback controller derived in Theorem 1 and the DQ-MEKF described in Section 4.4 to estimate the unmeasured relative linear and angular velocities. Both solutions have theoretical and numerical pros and cos, which are analyzed in this section.

The first solution has three main advantages over the second solution. The first main advantage is that under the conditions specified in Theorem 2, pose-tracking is guaranteed (i.e., $\boldsymbol{q}_{\mathrm{B/D}} \to \pm\mathbf{1}$ and $\boldsymbol{\omega}^{\mathrm{B}}_{\mathrm{B/D}} \to \mathbf{0}$ as $t \to +\infty$) independently of the initial condition chosen for $\boldsymbol{x}_{\mathrm{p}}$. On the other hand, because the DQ-MEKF is based on first-order approximations, if the initial guess of the state is not close enough to the true state, the DQ-MEKF may diverge, causing the velocity-feedback controller to fail. The second main advantage of the velocity-free controller is that Theorem 2 essentially establishes a *separation principle*, by which the LTI system in the feedback-loop can be designed independently of the value of k_p. On the other hand, there is

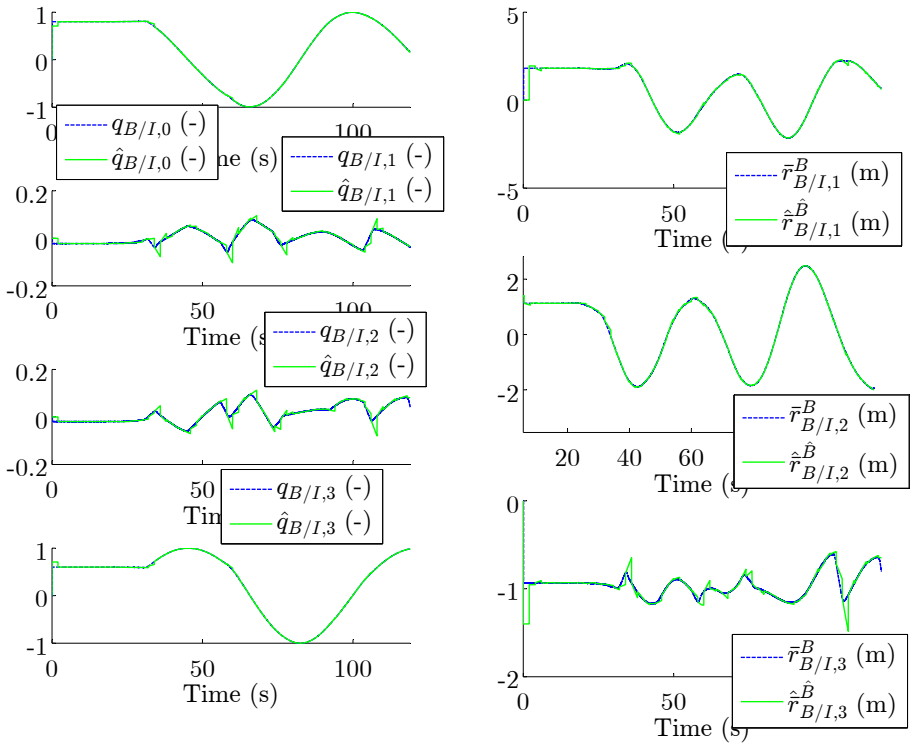

Figure 23: Case 1: estimated and true pose (pose measurements at 0.5 Hz).

no theoretical guarantee that the connection between the velocity-feedback controller derived in Theorem 1 and the DQ-MEKF will ensure pose-tracking. The third and final main advantage of the velocity-free controller is the fewer number of states. Whereas the velocity-free controller requires the propagation of 8 states, the DQ-MEKF requires the propagation of 92 states (mostly due to the propagation of the state covariance matrix). This might make the DQ-MEKF unsuitable for satellites with limited computational resources.

On the other hand, the solution based on the velocity-feedback controller and the DQ-MEKF has three important advantages over the velocity-free controller. First, the DQ-MEKF is specifically designed to handle measurement noise, whereas the velocity-free controller described in Theorem 2 assumes no noise. In particular, the DQ-MEKF filters out measurement noise (albeit, at the cost of lag), whereas the velocity-free controller does not. Second, the DQ-MEKF is specifically designed to

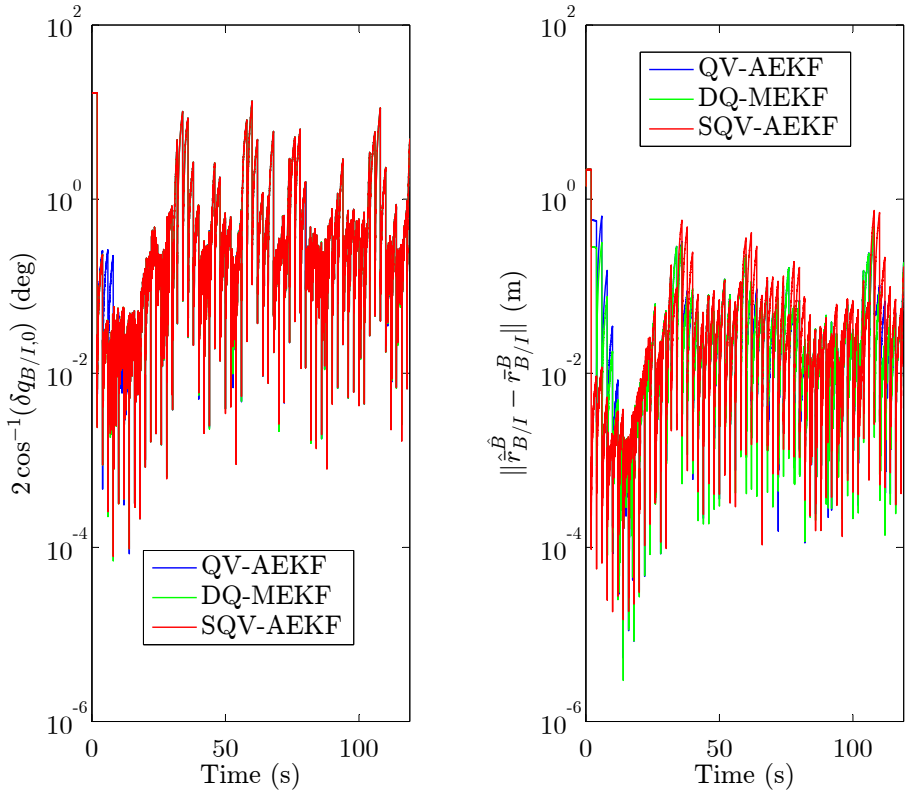

Figure 24: Case 1: pose estimation error (pose measurements at 0.5 Hz).

handle discrete-time measurements, whereas the velocity-free controller described in Theorem 2 assumes continuous-time measurements. Finally, the DQ-MEKF produces a direct estimate of $\boldsymbol{\omega}^{\mathrm{B}}_{\mathrm{B/D}}$, whereas the velocity-free controller does not. This estimate can be used to estimate $\boldsymbol{\omega}^{\mathrm{B}}_{\mathrm{D/I}} = \boldsymbol{\omega}^{\mathrm{B}}_{\mathrm{B/I}} - \boldsymbol{\omega}^{\mathrm{B}}_{\mathrm{B/D}}$, which in turn is used in both Eqs. (79) and (82). In an uncooperative satellite proximity operations scenario, where $\boldsymbol{\omega}^{\mathrm{B}}_{\mathrm{D/I}}$ is unknown, and assuming that the chaser satellite can measure its own linear and angular velocities with respect to the inertial frame, i.e., $\boldsymbol{\omega}^{\mathrm{B}}_{\mathrm{B/I}}$, this provides a method to estimate $\boldsymbol{\omega}^{\mathrm{B}}_{\mathrm{D/I}}$, which is not available with the velocity-free controller. Note also that the DQ-MEKF provides a measure of the uncertainty associated with the estimate of $\boldsymbol{\omega}^{\mathrm{B}}_{\mathrm{B/D}}$ through the state covariance matrix.

To compare the two solutions numerically, both controllers are applied to the

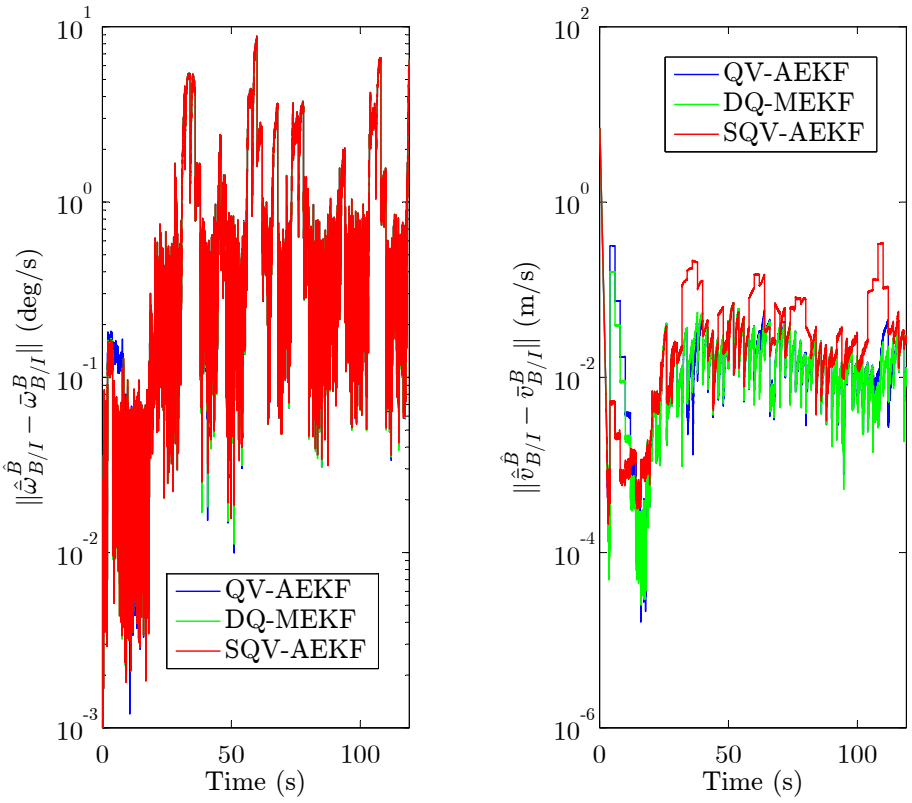

Figure 25: Case 1: angular and linear velocity estimation errors (pose measurements at 0.5 Hz).

same satellite proximity operations scenario described in Section 3.3.2, but now under more realistic conditions. Instead of continuous-time measurements, both controllers are now fed pose measurements at 10 Hz. Since the velocity-free controller requires continuous-time measurements, a *Zero-Order-Hold* (ZOH) is used to convert the discrete-time measurements into continuous-time signals. Note that the DQ-MEKF can deal with the discrete-time measurements directly. Moreover, zero-mean *Additive White Gaussian Noise* (AWGN) is added to the measurements of $q_{\mathrm{B/D}}$ and $r^{\mathrm{B}}_{\mathrm{B/D}}$, with standard deviation of 1×10^{-4} (-) and 1.7×10^{-3} m, respectively. After the AWGN is added to $q_{\mathrm{B/D}}$, $q_{\mathrm{B/D}}$ is re-normalized through $[q_{\mathrm{B/D}}] = [q_{\mathrm{B/D}}]/\|[q_{\mathrm{B/D}}]\|$. Additionally, each element of the control torque and force is saturated at ± 5 N$\cdot$m and ± 5 N, respectively. Finally, the controllers are run at 100 Hz to simulate a satellite with limited computational resources.

Table 9: Case 2: Covariance matrices.

$\tilde{P}_{20\times20}(0)$	$\text{diag}([0.0069, 0.0069, 0.0069, 0.0069, 0.69, 0.69, 0.69, 0.69, 0, 2\times10^{-6}, 2\times10^{-6}, 2\times10^{-6}, 0, 1\times10^{-9}, 1\times10^{-9}, 1\times10^{-9}, 0, 1.6\times10^{-5}, 1.6\times10^{-5}, 1.6\times10^{-5}])$
$Q_{15\times15}$	$\text{diag}([7\times10^{-7}, 7\times10^{-7}, 7\times10^{-7}, 0, 0, 0,\ 2\times10^{-6}, 2\times10^{-6}, 2\times10^{-6}, 1.9\times10^{-5}, 1.9\times10^{-5}, 1.9\times10^{-5}, 1.6\times10^{-5}, 1.6\times10^{-5}, 1.6\times10^{-5}])$
$R_{8\times8}$	$\text{diag}([1\times10^{-9}, 1\times10^{-9}, 1\times10^{-9}, 1\times10^{-9}, 2.5\times10^{-7}, 2.5\times10^{-7}, 2.5\times10^{-7}, 2.5\times10^{-7}])$

The measurement update of the DQ-MEKF is based on Eq. (130). Moreover, the DQ-MEKF is initialized with the covariance matrices given in Table 10 and the initial guess given in Table 11. The true initial state is also given in Table 11. All the other parameters of the scenario are identical to the parameters specified in Section 3.3.2. In particular, to make the comparison as fair as possible, the controls gains are chosen as $k_p = 0.2$ and $k_d = 0.4$ in both Eq. (79) and Eq. (82). Note that the steady-state output value of the lead-compensator illustrated in Figure 5 to a unit ramp input is k_d.

Table 10: Covariance matrices.

$\tilde{P}_{16\times16}(0)$	$\text{diag}([0.0069, 0.0069, 0.0069, 0.0069, 0.69, 0.69, 0.69, 0.69, 0, 1\times10^{-9}, 1\times10^{-9}, 1\times10^{-9}, 0, 1\times10^{-9}, 1\times10^{-9}, 1\times10^{-9}])$
$Q_{12\times12}$	$\text{diag}([0, 0, 0, 0, 0, 0, 1\times10^{-6}, 1\times10^{-6}, 1\times10^{-6}, 1\times10^{-4}, 1\times10^{-4}, 1\times10^{-4}])$
$R_{8\times8}$	$\text{diag}([1\times10^{-8}, 1\times10^{-8}, 1\times10^{-8}, 1\times10^{-8}, 2.5\times10^{-6}, 2.5\times10^{-6}, 2.5\times10^{-6}, 2.5\times10^{-6}])$

Figure 31 shows the initial transient response of the true (i.e., continuous-time and noise-free) pose of the body frame with respect to the desired frame obtained with the velocity-free controller and with the velocity-feedback controller in series with the DQ-MEKF. It demonstrates that, even under these more realistic conditions, both solutions succeed in tracking the desired pose. In fact, Figure 31 is relatively similar to

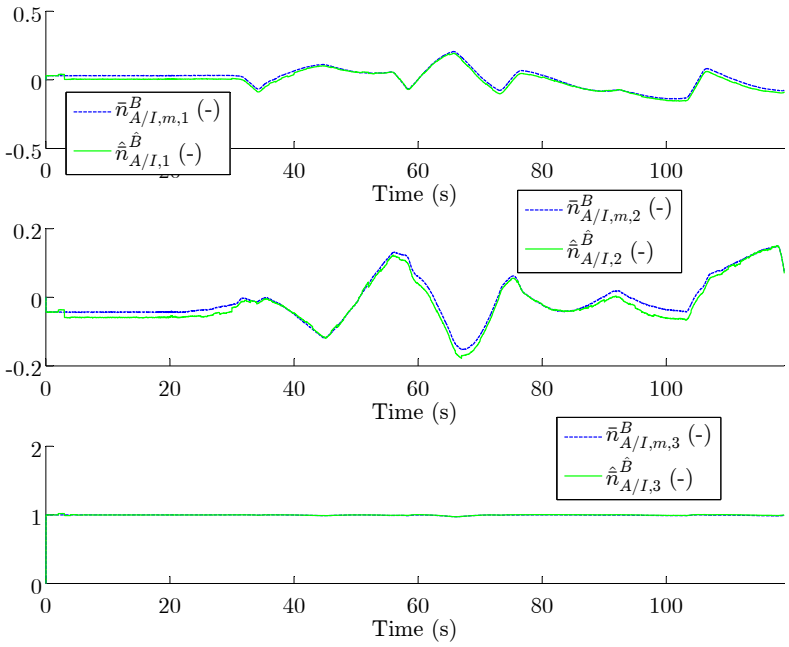

Figure 26: Case 2: estimated and measured non-dimensional specific force.

Table 11: Initial guess and true initial state.

Variable	Initial Guess	True State
$q_{\mathrm{B/D}}(0)$	$[0.3320, 0.4618, 0.1917, 0.7999]^\intercal$	$[0.3320, 0.4618, 0.1917, 0.7999]^\intercal$
$\bar{r}^{\mathrm{B}}_{\mathrm{B/D}}(0)$	$[5, 5, 5]^\intercal$ (m)	$[5, 5, 5]^\intercal$ (m)
$\bar{b}_\omega(0)$	$[0, 0, 0]^\intercal$ (rad/s)	$[-0.1, -0.1, -0.1]^\intercal$ (rad/s)
$\bar{b}_v(0)$	$[0, 0, 0]^\intercal$ (m/s)	$[-0.1, -0.1, -0.1]^\intercal$ (m/s)

Figure 12, obtained under ideal conditions. The pose-tracking error is shown in more detail in Figure 32. Whereas the pose-tracking error during the transient response is smaller with the velocity-feedback controller and the DQ-MEKF, both controllers achieve similar steady-state errors.

Figure 33 shows the true (i.e., continuous-time and noise-free) linear and angular velocity of the body frame with respect to the desired frame obtained with both solutions under these more realistic conditions. Both controllers succeed in tracking the desired velocities. Moreover, Figure 33 is relatively similar to Figure 13, obtained under ideal conditions.

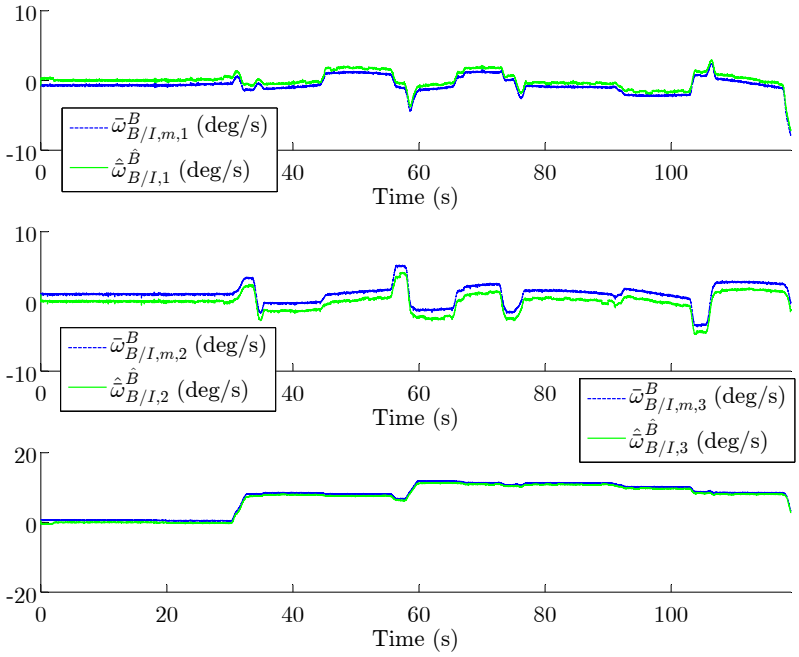

Figure 27: Case 2: estimated and measured angular velocity.

Finally, Figure 34 shows the control force and torque produced by both controllers under these more realistic conditions. The control force and torque produced by the velocity-free controller exhibits noise and oscillations that are not visible in the control force and torque produced by the velocity-feedback controller with the DQ-MEKF. They also do not appear in Figure 14 under ideal conditions. This is expected since, unlike the DQ-MEKF, the velocity-free controller does not filter out the measurement noise nor is designed to take discrete-time measurements.

Hence, in this particular scenario, and assuming the computational resources allow it, the velocity-feedback controller in series with the DQ-MEKF seems to be the more robust solution to the pose-tracking problem without relative linear and angular velocity measurements.

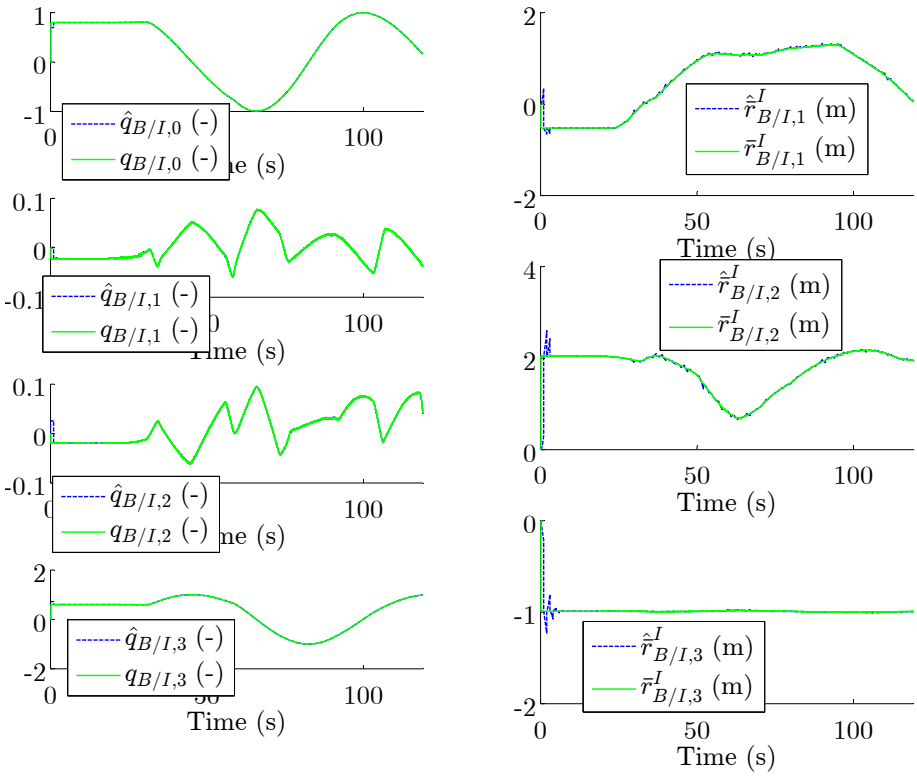

Figure 28: Case 2: estimated and true pose.

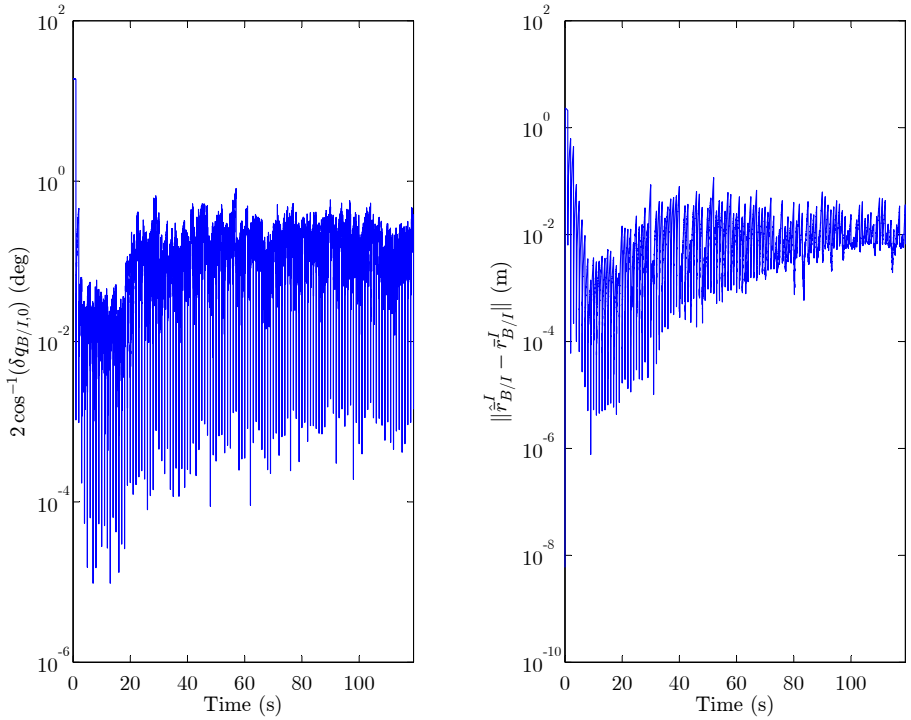

Figure 29: Case 2: pose estimation error.

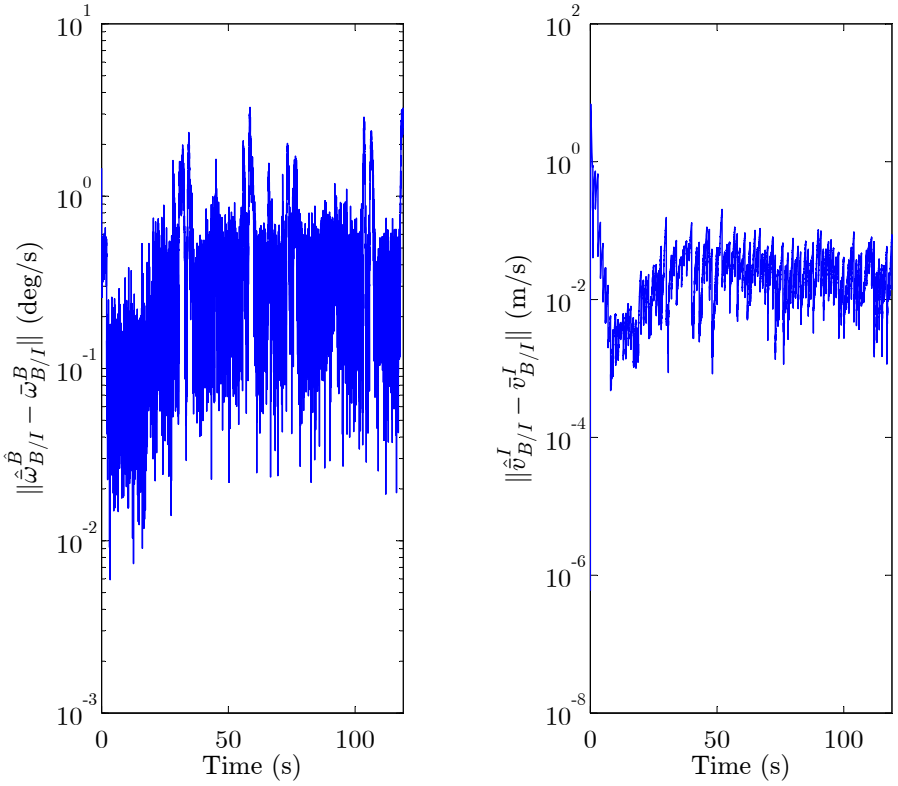

Figure 30: Case 2: angular and linear velocity estimation errors.

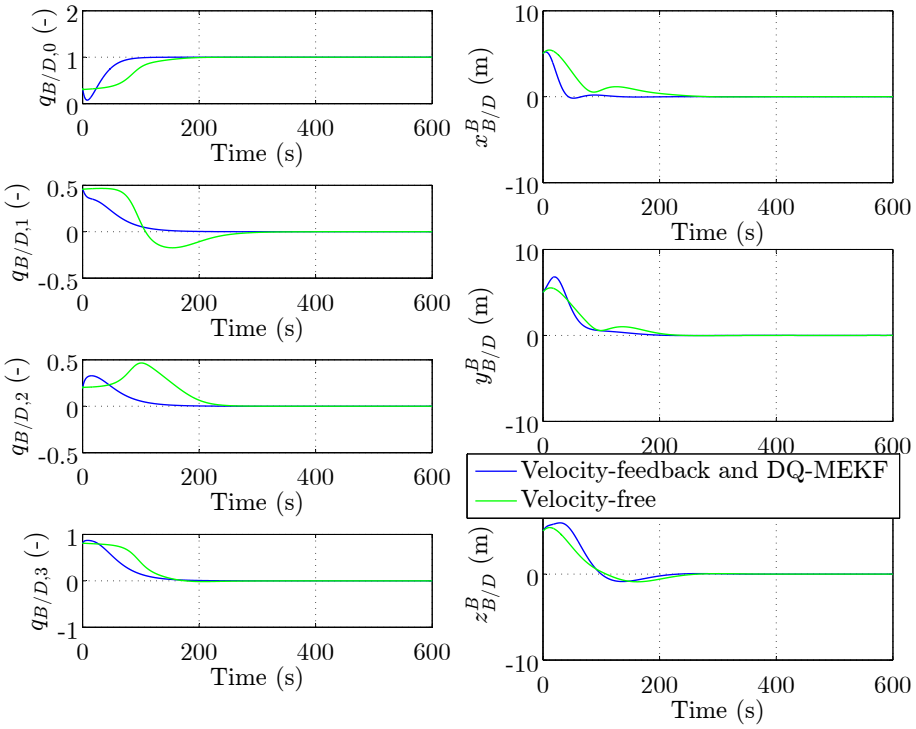

Figure 31: Pose-tracking using the velocity-free controller and the velocity-feedback controller with the DQ-MEKF.

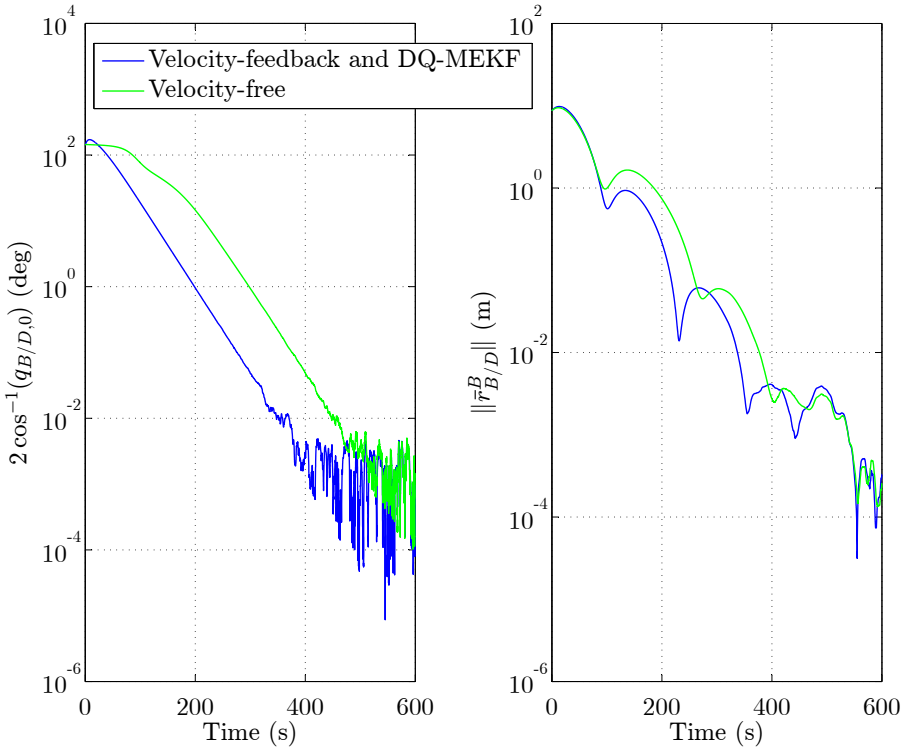

Figure 32: Pose-tracking error using the velocity-free controller and the velocity-feedback controller with the DQ-MEKF.

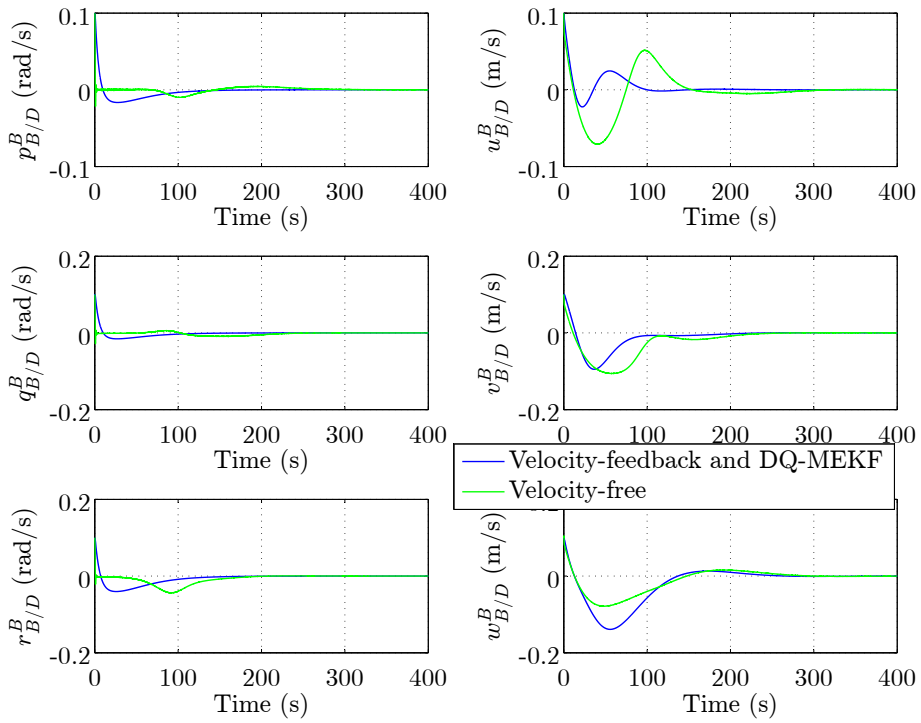

Figure 33: Relative linear and angular velocity using the velocity-free controller and the velocity-feedback controller with the DQ-MEKF.

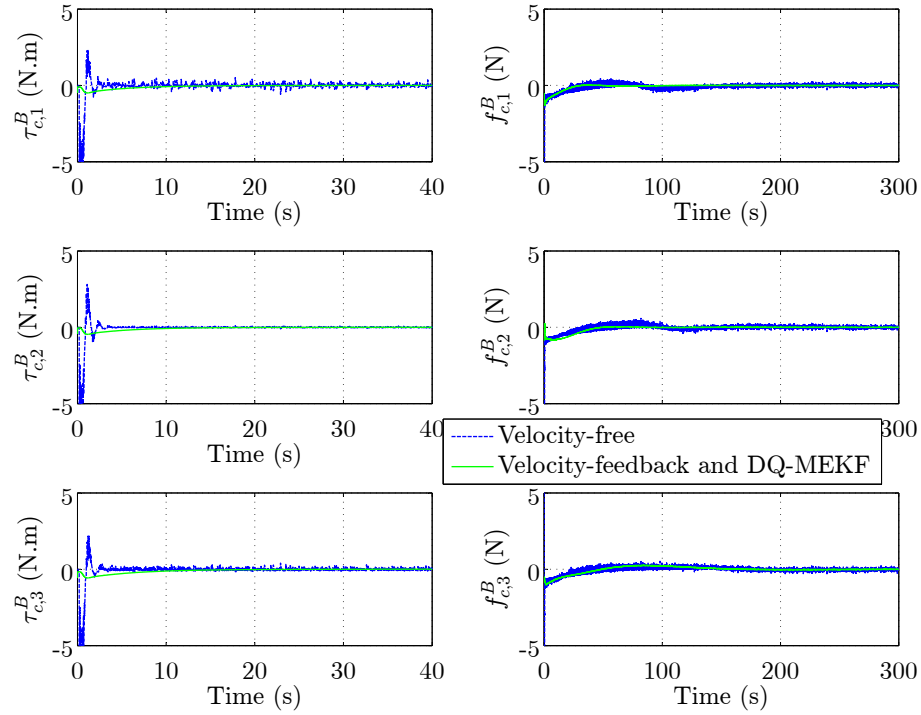

Figure 34: Control force and torque using the velocity-free controller and the velocity-feedback controller with the DQ-MEKF.

CHAPTER V

POSE-TRACKING WITHOUT MASS AND INERTIA MATRIX INFORMATION

The problem of deriving control laws for satellite proximity operations when the mass and/or inertia matrix of the chaser satellite are unknown has a long history. For example, in Ref. [73], nonlinear control and adaptation laws are designed using the vectrix formalism ensuring almost global asymptotic convergence of the pose error, despite the presence of unknown mass and inertia parameters. However, the controller in Ref. [73] is a very high-order dynamic compensator, which limits its applicability, especially for satellites with limited on-board computational resources. In Ref. [82], a relative pose-tracking controller that requires no linear and angular velocity measurements and no mass and inertia matrix information is presented. As explained in Ref. [85], if the reference trajectory is not sufficiently exciting, this controller cannot guarantee that the relative pose error will converge to zero. In Ref. [93], an adaptive terminal sliding-mode pose-tracking controller is proposed, based on dual quaternions, that does not require full knowledge of the mass and inertia matrix of the spacecraft. This controller takes into account the gravitational acceleration, the gravity-gradient torque, constant – but otherwise unknown – disturbance forces and torques, but not the perturbing acceleration due to Earth's oblateness. In addition, the convergence region of the controller is not specified in Ref. [93] and no conditions for identifying the mass and inertia matrix of the spacecraft are given. Moreover, this controller requires a priori knowledge of upper bounds on the mass, on the maximum eigenvalue of the inertia matrix, on the constant but otherwise unknown disturbance forces and torques, on the desired relative linear and angular velocity between the spacecraft

and their first derivative, on the linear and angular velocity of the chaser spacecraft with respect to the inertial frame, and on the position of the chaser spacecraft with respect to the inertial frame.

This chapter proposes an adaptive pose-tracking controller based on dual quaternions. In particular, this chapter extends the results presented in Ref. [1] to include position-tracking and mass identification. Unlike Ref. [93], the controller proposed in this chapter does not require a priori knowledge of any upper bounds on the system parameters or states. Another contribution of this work with respect to Ref. [93] is the consideration of the perturbing acceleration due to Earth's oblateness, which is typically the largest perturbing acceleration on a satellite below GEO [92]. Moreover, unlike Ref. [93], the controller proposed in this chapter is proven to ensure almost global asymptotical stability of the linear and angular position and velocity tracking errors. In regards to Ref. [73], the controller proposed in this chapter has only as many states as unknown parameters and, hence, requires less computational resources. A final contribution of this work with respect to existing literature is the definition of sufficient conditions for both mass and inertia matrix identification. Although these conditions are not needed for tracking, they can be useful to design maneuvers to identify these parameters, if needed (e.g., after a docking maneuver, after the deployment of antennas or solar panels, etc).

The chapter is organized as follows. In Section 5.1, the inertia-free pose-tracking controller for satellite proximity operations is deduced and proved to ensure almost global asymptotical stability of the linear and angular position and velocity tracking errors. Then, sufficient conditions on the reference motion are given that ensure mass and inertia matrix identification in Section 5.2. Finally, the results of two numerical examples are presented and analyzed in Section 5.3.

The following assumptions are made in this chapter.

i) The mass and inertia matrix of the chaser satellite are constant but unknown.

ii) The center of mass of the chaser satellite is known.

iii) The chaser satellite knowns its position with respect to the inertial frame, its relative pose with respect to the target satellite, and its relative linear and angular velocity with respect to the target satellite.

iv) There are no constraints on the control force and torque.

v) The linear and angular velocity and acceleration of the target satellite with respect to the inertial frame are known.

vi) The disturbance forces and torques acting on the chaser satellite are constant but unknown.

5.1 Inertia-Free Pose-Tracking Controller

The next theorem presents the inertia-free pose-tracking controller for satellite proximity operations and shows that it ensures almost global asymptotic stability of the linear and angular position and velocity tracking errors.

Theorem 3. *Consider the rigid body relative kinematic and dynamic equations given by Eq.* (55) *and Eq.* (71)*, respectively. Let the dual control force be defined by the feedback control law*

$$\begin{aligned}\boldsymbol{f}_c^{\mathrm{B}} =& -\widehat{M^{\mathrm{B}}} \star \boldsymbol{a}_g^{\mathrm{B}} - \frac{3\mu \boldsymbol{r}_{\mathrm{B/I}}^{\mathrm{B}}}{\|\boldsymbol{r}_{\mathrm{B/I}}^{\mathrm{B}}\|^5} \times (\widehat{M^{\mathrm{B}}} \star (\boldsymbol{r}_{\mathrm{B/I}}^{\mathrm{B}})^{\mathsf{s}}) - \widehat{M^{\mathrm{B}}} \star \boldsymbol{a}_{J_2}^{\mathrm{B}} - \widehat{\boldsymbol{f}_d^{\mathrm{B}}} \\ & - \mathrm{vec}(\boldsymbol{q}_{\mathrm{B/D}}^{*}(\boldsymbol{q}_{\mathrm{B/D}}^{\mathsf{s}} - \mathbf{1}^{\mathsf{s}})) - K_d \star \boldsymbol{s}^{\mathsf{s}} + \boldsymbol{\omega}_{\mathrm{B/I}}^{\mathrm{B}} \times (\widehat{M^{\mathrm{B}}} \star (\boldsymbol{\omega}_{\mathrm{B/I}}^{\mathrm{B}})^{\mathsf{s}}) \\ & + \widehat{M^{\mathrm{B}}} \star (\boldsymbol{q}_{\mathrm{B/D}}^{*} \dot{\boldsymbol{\omega}}_{\mathrm{D/I}}^{\mathrm{D}} \boldsymbol{q}_{\mathrm{B/D}})^{\mathsf{s}} + \widehat{M^{\mathrm{B}}} \star (\boldsymbol{\omega}_{\mathrm{D/I}}^{\mathrm{B}} \times \boldsymbol{\omega}_{\mathrm{B/D}}^{\mathrm{B}})^{\mathsf{s}} - \widehat{M^{\mathrm{B}}} \star (K_p \star \frac{\mathrm{d}}{\mathrm{d}t}(\boldsymbol{q}_{\mathrm{B/D}}^{*}(\boldsymbol{q}_{\mathrm{B/D}}^{\mathsf{s}} - \mathbf{1}^{\mathsf{s}}))),\end{aligned} \tag{158}$$

where

$$\boldsymbol{s} = \boldsymbol{\omega}_{\mathrm{B/D}}^{\mathrm{B}} + (K_p \star (\boldsymbol{q}_{\mathrm{B/D}}^{*}(\boldsymbol{q}_{\mathrm{B/D}}^{\mathsf{s}} - \mathbf{1}^{\mathsf{s}})))^{\mathsf{s}}, \tag{159}$$

$$K_p = \begin{bmatrix} K_r & 0_{4\times 4} \\ 0_{4\times 4} & K_q \end{bmatrix}, \quad K_d = \begin{bmatrix} K_v & 0_{4\times 4} \\ 0_{4\times 4} & K_\omega \end{bmatrix},$$

$$K_r = \begin{bmatrix} 0 & 0_{1\times 3} \\ 0_{3\times 1} & \bar{K}_r \end{bmatrix}, K_q = \begin{bmatrix} 0 & 0_{1\times 3} \\ 0_{3\times 1} & \bar{K}_q \end{bmatrix}, K_v = \begin{bmatrix} 0 & 0_{1\times 3} \\ 0_{3\times 1} & \bar{K}_v \end{bmatrix}, K_\omega = \begin{bmatrix} 0 & 0_{1\times 3} \\ 0_{3\times 1} & \bar{K}_\omega \end{bmatrix},$$

$\bar{K}_r, \bar{K}_q, \bar{K}_v, \bar{K}_\omega \in \mathbb{R}^{3\times 3}$ *are symmetric positive-definite matrices,* $\widehat{M^{\mathrm{B}}}$ *is an estimate of the dual inertia matrix updated according to*

$$\frac{\mathrm{d}}{\mathrm{d}t}\mathrm{v}(\widehat{M^{\mathrm{B}}}) = K_i\big[-\mathrm{h}((\boldsymbol{s}\times\boldsymbol{\omega}^{\mathrm{B}}_{\mathrm{B/I}})^{\mathsf{s}}, (\boldsymbol{\omega}^{\mathrm{B}}_{\mathrm{B/I}})^{\mathsf{s}}) + \mathrm{h}((\boldsymbol{s}\times\frac{3\mu\boldsymbol{r}^{\mathrm{B}}_{\mathrm{B/I}}}{\|\boldsymbol{r}^{\mathrm{B}}_{\mathrm{B/I}}\|^5})^{\mathsf{s}}, (\boldsymbol{r}^{\mathrm{B}}_{\mathrm{B/I}})^{\mathsf{s}})$$
$$+\mathrm{h}(\boldsymbol{s}^{\mathsf{s}}, -(\boldsymbol{q}^{*}_{\mathrm{B/D}}\dot{\boldsymbol{\omega}}^{\mathrm{D}}_{\mathrm{D/I}}\boldsymbol{q}_{\mathrm{B/D}})^{\mathsf{s}} - (\boldsymbol{\omega}^{\mathrm{B}}_{\mathrm{D/I}}\times\boldsymbol{\omega}^{\mathrm{B}}_{\mathrm{B/D}})^{\mathsf{s}} + K_p\star\frac{\mathrm{d}(\boldsymbol{q}^{*}_{\mathrm{B/D}}(\boldsymbol{q}^{\mathsf{s}}_{\mathrm{B/D}}-\mathbf{1}^{\mathsf{s}}))}{\mathrm{d}t} + \boldsymbol{a}^{\mathrm{B}}_{g} + \boldsymbol{a}^{\mathrm{B}}_{J_2})\big], \quad (160)$$

$K_i \in \mathbb{R}^{7\times 7}$ *is a symmetric positive-definite matrix,* $\mathrm{v}(M^{\mathrm{B}}) = [I_{11}\ I_{12}\ I_{13}\ I_{22}\ I_{23}\ I_{33}\ m]^{\mathsf{T}}$ *is a vectorized version of the dual inertia matrix* M^{B}*, the function* $\mathrm{h} : \mathbb{H}^v_d \times \mathbb{H}^v_d \to \mathbb{R}^7$ *is defined as* $\boldsymbol{a}\circ(M^{\mathrm{B}}\star\boldsymbol{b}) = \mathrm{h}(\boldsymbol{a},\boldsymbol{b})^{\mathsf{T}}\mathrm{v}(M^{\mathrm{B}}) = \mathrm{v}(M^{\mathrm{B}})^{\mathsf{T}}\mathrm{h}(\boldsymbol{a},\boldsymbol{b})$ *or, equivalently,* $\mathrm{h}(\boldsymbol{a},\boldsymbol{b}) = [a_{d,1}b_{d,1},\ a_{d,2}b_{d,1}+a_{d,1}b_{d,2},\ a_{d,3}b_{d,1}+a_{d,1}b_{d,3},\ a_{d,2}b_{d,2},\ a_{d,3}b_{d,2}+a_{d,2}b_{d,3},\ a_{d,3}b_{d,3},\ a_{r,1}b_{r,1}+a_{r,2}b_{r,2}+a_{r,3}b_{r,3}]^{\mathsf{T}}$*,* $\widehat{\boldsymbol{f}^{\mathrm{B}}_{d}}$ *is an estimate of the dual disturbance force updated according to*

$$\frac{\mathrm{d}}{\mathrm{d}t}\widehat{\boldsymbol{f}^{\mathrm{B}}_{d}} = K_j\star\boldsymbol{s}^{\mathsf{s}}, \quad (161)$$

$$K_j = \begin{bmatrix} K_f & 0_{4\times 4} \\ 0_{4\times 4} & K_\tau \end{bmatrix}, \quad K_f = \begin{bmatrix} 1 & 0_{1\times 3} \\ 0_{3\times 1} & \bar{K}_f \end{bmatrix}, \quad K_\tau = \begin{bmatrix} 1 & 0_{1\times 3} \\ 0_{3\times 1} & \bar{K}_\tau \end{bmatrix}, \quad (162)$$

and $\bar{K}_f, \bar{K}_\tau \in \mathbb{R}^{3\times 3}$ *are symmetric positive-definite matrices. Assume that* $\boldsymbol{q}_{\mathrm{D/I}}$,$\boldsymbol{\omega}^{\mathrm{D}}_{\mathrm{D/I}}$, $\dot{\boldsymbol{\omega}}^{\mathrm{D}}_{\mathrm{D/I}} \in \mathcal{L}_\infty$ *and* $\boldsymbol{r}^{\mathrm{B}}_{\mathrm{B/I}} \neq \mathbf{0}$*. Then, for all initial conditions,* $\lim_{t\to\infty}\boldsymbol{q}_{\mathrm{B/D}} = \pm\mathbf{1}$ *(i.e.,* $\lim_{t\to\infty} q_{\mathrm{B/D}} = \pm 1$ *and* $\lim_{t\to\infty} r^{\mathrm{B}}_{\mathrm{B/D}} = 0$*),* $\lim_{t\to\infty}\boldsymbol{\omega}^{\mathrm{B}}_{\mathrm{B/D}} = \mathbf{0}$ *(i.e.,* $\lim_{t\to\infty}\omega^{\mathrm{B}}_{\mathrm{B/D}} = 0$ *and* $\lim_{t\to\infty} v^{\mathrm{B}}_{\mathrm{B/D}} = 0$*), and* $\mathrm{v}(\widehat{M^{\mathrm{B}}}), \widehat{\boldsymbol{f}^{\mathrm{B}}_{d}} \in \mathcal{L}_\infty$*.*

Proof. First, define the dual inertia matrix and dual disturbance force estimation errors as

$$\Delta M^{\mathrm{B}} = \widehat{M^{\mathrm{B}}} - M^{\mathrm{B}} \quad \text{and} \quad \Delta\boldsymbol{f}^{\mathrm{B}}_{d} = \widehat{\boldsymbol{f}^{\mathrm{B}}_{d}} - \boldsymbol{f}^{\mathrm{B}}_{d}, \quad (163)$$

respectively. Note that $\boldsymbol{q}_{\mathrm{B/D}} = \pm\mathbf{1}$, $\boldsymbol{s} = \mathbf{0}$, $\mathrm{v}(\Delta M^{\mathrm{B}}) = 0_{7\times 1}$, and $\Delta\boldsymbol{f}^{\mathrm{B}}_{d} = \mathbf{0}$ are the equilibrium conditions of the closed-loop system formed by Eqs. (71), (72), (55),

(160), and (161). Consider now the following candidate Lyapunov function for the equilibrium point $(\boldsymbol{q}_{\mathrm{B/D}}, \boldsymbol{s}, \mathrm{v}(\Delta M^{\mathrm{B}}), \Delta \boldsymbol{f}_d^{\mathrm{B}}) = (+\mathbf{1}, \mathbf{0}, 0_{7\times 1}, \mathbf{0})$:

$$\begin{aligned} V(\boldsymbol{q}_{\mathrm{B/D}}, \boldsymbol{s}, \mathrm{v}(\Delta M^{\mathrm{B}}), \Delta \boldsymbol{f}_d^{\mathrm{B}}) = (\boldsymbol{q}_{\mathrm{B/D}} - \mathbf{1}) \circ (\boldsymbol{q}_{\mathrm{B/D}} - \mathbf{1}) + \tfrac{1}{2}\boldsymbol{s}^{\mathsf{s}} \circ (M^{\mathrm{B}} \star \boldsymbol{s}^{\mathsf{s}}) \\ + \tfrac{1}{2}\mathrm{v}(\Delta M^{\mathrm{B}})^{\intercal} K_i^{-1} \mathrm{v}(\Delta M^{\mathrm{B}}) + \tfrac{1}{2}\Delta \boldsymbol{f}_d^{\mathrm{B}} \circ (K_j^{-1} \star \Delta \boldsymbol{f}_d^{\mathrm{B}}). \end{aligned} \tag{164}$$

Note that V is a valid candidate Lyapunov function since

$$V(\boldsymbol{q}_{\mathrm{B/D}} = \mathbf{1}, \boldsymbol{s} = \mathbf{0}, \mathrm{v}(\Delta M^{\mathrm{B}}) = 0_{7\times 1}, \Delta \boldsymbol{f}_d^{\mathrm{B}} = \mathbf{0}) = 0$$

and

$$V(\boldsymbol{q}_{\mathrm{B/D}}, \boldsymbol{s}, \mathrm{v}(\Delta M^{\mathrm{B}}), \Delta \boldsymbol{f}_d^{\mathrm{B}}) > 0$$

for all $(\boldsymbol{q}_{\mathrm{B/D}}, \boldsymbol{s}, \mathrm{v}(\Delta M^{\mathrm{B}}), \Delta \boldsymbol{f}_d^{\mathrm{B}}) \in \mathbb{H}_d^u \times \mathbb{H}_d^v \times \mathbb{R}^7 \times \mathbb{H}_d^v \backslash \{\mathbf{1}, \mathbf{0}, 0_{7\times 1}, \mathbf{0}\}$. Note also that the real part of the first three terms of Eq. (164) is equal to the Lyapunov function used in Ref. [1]. The time derivative of V is equal to

$$\dot{V} = 2(\boldsymbol{q}_{\mathrm{B/D}} - \mathbf{1}) \circ \dot{\boldsymbol{q}}_{\mathrm{B/D}} + \boldsymbol{s}^{\mathsf{s}} \circ (M^{\mathrm{B}} \star \dot{\boldsymbol{s}}^{\mathsf{s}}) + \mathrm{v}(\Delta M^{\mathrm{B}})^{\intercal} K_i^{-1} \frac{\mathrm{d}}{\mathrm{d}t} \mathrm{v}(\Delta M^{\mathrm{B}}) + \Delta \boldsymbol{f}_d^{\mathrm{B}} \circ (K_j^{-1} \star \frac{\mathrm{d}}{\mathrm{d}t} \Delta \boldsymbol{f}_d^{\mathrm{B}}).$$

Then, since from Eq. (55), $\boldsymbol{\omega}_{\mathrm{B/D}}^{\mathrm{B}} = 2\boldsymbol{q}_{\mathrm{B/D}}^{*} \dot{\boldsymbol{q}}_{\mathrm{B/D}}$, Eq. (159) can be rewritten as $\dot{\boldsymbol{q}}_{\mathrm{B/D}} = \frac{1}{2}\boldsymbol{q}_{\mathrm{B/D}} \boldsymbol{s} - \frac{1}{2}\boldsymbol{q}_{\mathrm{B/D}} (K_p \star (\boldsymbol{q}_{\mathrm{B/D}}^{*} (\boldsymbol{q}_{\mathrm{B/D}}^{\mathsf{s}} - \mathbf{1}^{\mathsf{s}})))^{\mathsf{s}}$, which can then be plugged into $\dot{V}$, together with the time derivative of Eq. (159), to yield

$$\begin{aligned} \dot{V} = &(\boldsymbol{q}_{\mathrm{B/D}} - \mathbf{1}) \circ (\boldsymbol{q}_{\mathrm{B/D}} \boldsymbol{s} - \boldsymbol{q}_{\mathrm{B/D}} (K_p \star (\boldsymbol{q}_{\mathrm{B/D}}^{*} (\boldsymbol{q}_{\mathrm{B/D}}^{\mathsf{s}} - \mathbf{1}^{\mathsf{s}})))^{\mathsf{s}}) + \boldsymbol{s}^{\mathsf{s}} \circ (M^{\mathrm{B}} \star (\dot{\boldsymbol{\omega}}_{\mathrm{B/D}}^{\mathrm{B}})^{\mathsf{s}}) \\ &+ \boldsymbol{s}^{\mathsf{s}} \circ (M^{\mathrm{B}} \star (K_p \star \frac{\mathrm{d}(\boldsymbol{q}_{\mathrm{B/D}}^{*} (\boldsymbol{q}_{\mathrm{B/D}}^{\mathsf{s}} - \mathbf{1}^{\mathsf{s}}))}{\mathrm{d}t})) + \mathrm{v}(\Delta M^{\mathrm{B}})^{\intercal} K_i^{-1} \frac{\mathrm{d}}{\mathrm{d}t} \mathrm{v}(\Delta M^{\mathrm{B}}) + \Delta \boldsymbol{f}_d^{\mathrm{B}} \circ (K_j^{-1} \star \frac{\mathrm{d}}{\mathrm{d}t} \Delta \boldsymbol{f}_d^{\mathrm{B}}). \end{aligned}$$

Applying Lemma 33, inserting Eq. (71), and using $\boldsymbol{\omega}_{\mathrm{B/D}}^{\mathrm{B}} + \boldsymbol{\omega}_{\mathrm{D/I}}^{\mathrm{B}} = \boldsymbol{\omega}_{\mathrm{B/I}}^{\mathrm{B}}$ yields

$$\begin{aligned} \dot{V} = &\boldsymbol{s}^{\mathsf{s}} \circ (\boldsymbol{q}_{\mathrm{B/D}}^{*} (\boldsymbol{q}_{\mathrm{B/D}}^{\mathsf{s}} - \mathbf{1}^{\mathsf{s}})) - (K_p \star (\boldsymbol{q}_{\mathrm{B/D}}^{*} (\boldsymbol{q}_{\mathrm{B/D}}^{\mathsf{s}} - \mathbf{1}^{\mathsf{s}}))) \circ (\boldsymbol{q}_{\mathrm{B/D}}^{*} (\boldsymbol{q}_{\mathrm{B/D}}^{\mathsf{s}} - \mathbf{1}^{\mathsf{s}})) + \boldsymbol{s}^{\mathsf{s}} \circ (\boldsymbol{f}^{\mathrm{B}} \\ &- \boldsymbol{\omega}_{\mathrm{B/I}}^{\mathrm{B}} \times (M^{\mathrm{B}} \star (\boldsymbol{\omega}_{\mathrm{B/I}}^{\mathrm{B}})^{\mathsf{s}}) - M^{\mathrm{B}} \star (\boldsymbol{q}_{\mathrm{B/D}}^{*} \dot{\boldsymbol{\omega}}_{\mathrm{D/I}}^{\mathrm{D}} \boldsymbol{q}_{\mathrm{B/D}})^{\mathsf{s}} - M^{\mathrm{B}} \star (\boldsymbol{\omega}_{\mathrm{D/I}}^{\mathrm{B}} \times \boldsymbol{\omega}_{\mathrm{B/D}}^{\mathrm{B}})^{\mathsf{s}}) \\ &+ \boldsymbol{s}^{\mathsf{s}} \circ (M^{\mathrm{B}} \star (K_p \star \frac{\mathrm{d}(\boldsymbol{q}_{\mathrm{B/D}}^{*} (\boldsymbol{q}_{\mathrm{B/D}}^{\mathsf{s}} - \mathbf{1}^{\mathsf{s}}))}{\mathrm{d}t})) + \mathrm{v}(\Delta M^{\mathrm{B}})^{\intercal} K_i^{-1} \frac{\mathrm{d}}{\mathrm{d}t} \mathrm{v}(\Delta M^{\mathrm{B}}) + \Delta \boldsymbol{f}_d^{\mathrm{B}} \circ (K_j^{-1} \star \frac{\mathrm{d}}{\mathrm{d}t} \Delta \boldsymbol{f}_d^{\mathrm{B}}). \end{aligned}$$

Introducing the control law given by Eq. (158) and using Lemmas 55, 37, and 24

yields

$$\dot{V}=-(\boldsymbol{q}^{*}_{\mathrm{B/D}}(\boldsymbol{q}^{\mathsf{s}}_{\mathrm{B/D}}-\mathbf{1}^{\mathsf{s}}))\circ(K_p\star(\boldsymbol{q}^{*}_{\mathrm{B/D}}(\boldsymbol{q}^{\mathsf{s}}_{\mathrm{B/D}}-\mathbf{1}^{\mathsf{s}})))+\boldsymbol{s}^{\mathsf{s}}\circ(\boldsymbol{\omega}^{\mathrm{B}}_{\mathrm{B/I}}\times\big(\Delta M^{\mathrm{B}}\star(\boldsymbol{\omega}^{\mathrm{B}}_{\mathrm{B/I}})^{\mathsf{s}}\big)$$
$$+\Delta M^{\mathrm{B}}\star(\boldsymbol{q}^{*}_{\mathrm{B/D}}\dot{\boldsymbol{\omega}}^{\mathrm{D}}_{\mathrm{D/I}}\boldsymbol{q}_{\mathrm{B/D}})^{\mathsf{s}}+\Delta M^{\mathrm{B}}\star(\boldsymbol{\omega}^{\mathrm{B}}_{\mathrm{D/I}}\times\boldsymbol{\omega}^{\mathrm{B}}_{\mathrm{B/D}})^{\mathsf{s}}$$
$$-\Delta M^{\mathrm{B}}\star(K_p\star\frac{\mathrm{d}(\boldsymbol{q}^{*}_{\mathrm{B/D}}(\boldsymbol{q}^{\mathsf{s}}_{\mathrm{B/D}}-\mathbf{1}^{\mathsf{s}}))}{\mathrm{d}t})-\Delta M^{\mathrm{B}}\star\boldsymbol{a}^{\mathrm{B}}_{g}-\frac{3\mu\boldsymbol{r}^{\mathrm{B}}_{\mathrm{B/I}}}{\|\boldsymbol{r}^{\mathrm{B}}_{\mathrm{B/I}}\|^{5}}\times(\Delta M^{\mathrm{B}}\star(\boldsymbol{r}^{\mathrm{B}}_{\mathrm{B/I}})^{\mathsf{s}})$$
$$-\Delta M^{\mathrm{B}}\star\boldsymbol{a}^{\mathrm{B}}_{J_2}-\Delta\boldsymbol{f}^{\mathrm{B}}_{d})-\boldsymbol{s}^{\mathsf{s}}\circ(K_d\star\boldsymbol{s}^{\mathsf{s}})+\mathrm{v}(\Delta M^{\mathrm{B}})^{\mathsf{T}}K_i^{-1}\frac{\mathrm{d}}{\mathrm{d}t}\mathrm{v}(\Delta M^{\mathrm{B}})+\Delta\boldsymbol{f}^{\mathrm{B}}_{d}\circ(K_j^{-1}\star\frac{\mathrm{d}}{\mathrm{d}t}\Delta\boldsymbol{f}^{\mathrm{B}}_{d})$$

or

$$\dot{V}=-(\boldsymbol{q}^{*}_{\mathrm{B/D}}(\boldsymbol{q}^{\mathsf{s}}_{\mathrm{B/D}}-\mathbf{1}^{\mathsf{s}}))\circ(K_p\star(\boldsymbol{q}^{*}_{\mathrm{B/D}}(\boldsymbol{q}^{\mathsf{s}}_{\mathrm{B/D}}-\mathbf{1}^{\mathsf{s}})))+(\boldsymbol{s}\times\boldsymbol{\omega}^{\mathrm{B}}_{\mathrm{B/I}})^{\mathsf{s}}\circ(\Delta M^{\mathrm{B}}\star(\boldsymbol{\omega}^{\mathrm{B}}_{\mathrm{B/I}})^{\mathsf{s}})$$
$$+\boldsymbol{s}^{\mathsf{s}}\circ(\Delta M^{\mathrm{B}}\star(\boldsymbol{q}^{*}_{\mathrm{B/D}}\dot{\boldsymbol{\omega}}^{\mathrm{D}}_{\mathrm{D/I}}\boldsymbol{q}_{\mathrm{B/D}})^{\mathsf{s}}+\Delta M^{\mathrm{B}}\star(\boldsymbol{\omega}^{\mathrm{B}}_{\mathrm{D/I}}\times\boldsymbol{\omega}^{\mathrm{B}}_{\mathrm{B/D}})^{\mathsf{s}}$$
$$-\Delta M^{\mathrm{B}}\star(K_p\star\frac{\mathrm{d}(\boldsymbol{q}^{*}_{\mathrm{B/D}}(\boldsymbol{q}^{\mathsf{s}}_{\mathrm{B/D}}-\mathbf{1}^{\mathsf{s}}))}{\mathrm{d}t})-\Delta M^{\mathrm{B}}\star\boldsymbol{a}^{\mathrm{B}}_{g}-\Delta M^{\mathrm{B}}\star\boldsymbol{a}^{\mathrm{B}}_{J_2}-\Delta\boldsymbol{f}^{\mathrm{B}}_{d})$$
$$-(\boldsymbol{s}\times\frac{3\mu\boldsymbol{r}^{\mathrm{B}}_{\mathrm{B/I}}}{\|\boldsymbol{r}^{\mathrm{B}}_{\mathrm{B/I}}\|^{5}})^{\mathsf{s}}\circ(\Delta M^{\mathrm{B}}\star(\boldsymbol{r}^{\mathrm{B}}_{\mathrm{B/I}})^{\mathsf{s}})-\boldsymbol{s}^{\mathsf{s}}\circ(K_d\star\boldsymbol{s}^{\mathsf{s}})+\mathrm{v}(\Delta M^{\mathrm{B}})^{\mathsf{T}}K_i^{-1}\frac{\mathrm{d}}{\mathrm{d}t}\mathrm{v}(\Delta M^{\mathrm{B}})$$
$$+\Delta\boldsymbol{f}^{\mathrm{B}}_{d}\circ(K_j^{-1}\star\frac{\mathrm{d}}{\mathrm{d}t}\Delta\boldsymbol{f}^{\mathrm{B}}_{d}).$$

Therefore, if $\frac{\mathrm{d}}{\mathrm{d}t}\mathrm{v}(\Delta M^{\mathrm{B}})$ is defined as in Eq. (160) and $\frac{\mathrm{d}}{\mathrm{d}t}\Delta\boldsymbol{f}^{\mathrm{B}}_{d}$ is defined as in Eq. (161), it follows that $\dot{V}=-(\boldsymbol{q}^{*}_{\mathrm{B/D}}(\boldsymbol{q}^{\mathsf{s}}_{\mathrm{B/D}}-\mathbf{1}^{\mathsf{s}}))\circ(K_p\star(\boldsymbol{q}^{*}_{\mathrm{B/D}}(\boldsymbol{q}^{\mathsf{s}}_{\mathrm{B/D}}-\mathbf{1}^{\mathsf{s}})))-\boldsymbol{s}^{\mathsf{s}}\circ(K_d\star\boldsymbol{s}^{\mathsf{s}})\leq 0$, for all $(\boldsymbol{q}_{\mathrm{B/D}},\boldsymbol{s},\mathrm{v}(\Delta M^{\mathrm{B}}),\Delta\boldsymbol{f}^{\mathrm{B}}_{d})\in\mathbb{H}^{u}_{d}\times\mathbb{H}^{v}_{d}\times\mathbb{R}^{7}\times\mathbb{H}^{v}_{d}\backslash\{\mathbf{1},\mathbf{0},0_{7\times 1},\mathbf{0}\}$. Hence, the equilibrium point $(\boldsymbol{q}_{\mathrm{B/D}},\boldsymbol{s},\mathrm{v}(\Delta M^{\mathrm{B}}),\Delta\boldsymbol{f}^{\mathrm{B}}_{d})=(+\mathbf{1},\mathbf{0},0_{7\times 1},\mathbf{0})$ is uniformly stable and uniformly bounded, i.e., $\boldsymbol{q}_{\mathrm{B/D}}$, $\boldsymbol{s}$, $\mathrm{v}(\Delta M^{\mathrm{B}})$, $\Delta\boldsymbol{f}^{\mathrm{B}}_{d}\in\mathcal{L}_{\infty}$. Moreover, from Eqs. (159) and (163), this also means that $\boldsymbol{\omega}^{\mathrm{B}}_{\mathrm{B/D}},\mathrm{v}(\widehat{M^{\mathrm{B}}}),\widehat{\boldsymbol{f}^{\mathrm{B}}_{d}}\in\mathcal{L}_{\infty}$. Since $V\geq 0$ and $\dot{V}\leq 0$, $\lim_{t\to\infty}V(t)$ exists and is finite. Hence, $\lim_{t\to\infty}\int_0^t\dot{V}(\tau)\,\mathrm{d}\tau=\lim_{t\to\infty}V(t)-V(0)$ also exists and is finite. Since $\boldsymbol{q}_{\mathrm{B/D}},\boldsymbol{s},\mathrm{v}(\Delta M^{\mathrm{B}}),\Delta\boldsymbol{f}^{\mathrm{B}}_{d},\boldsymbol{\omega}^{\mathrm{B}}_{\mathrm{B/D}},\mathrm{v}(\widehat{M^{\mathrm{B}}}),\widehat{\boldsymbol{f}^{\mathrm{B}}_{d}},\dot{\boldsymbol{\omega}}^{\mathrm{D}}_{\mathrm{D/I}},\boldsymbol{\omega}^{\mathrm{B}}_{\mathrm{D/I}},\boldsymbol{q}_{\mathrm{D/I}}\in\mathcal{L}_{\infty}$ and $\boldsymbol{r}^{\mathrm{B}}_{\mathrm{B/I}}\neq\mathbf{0}$, then from Eqs. (55), (158), and (71) and from Lemma 53, $\boldsymbol{r}^{\mathrm{B}}_{\mathrm{B/I}},\dot{\boldsymbol{q}}_{\mathrm{B/D}},\boldsymbol{f}^{\mathrm{B}},\dot{\boldsymbol{\omega}}^{\mathrm{B}}_{\mathrm{B/D}},\dot{\boldsymbol{s}}\in\mathcal{L}_{\infty}$. Hence, by Barbalat's lemma, $\mathrm{vec}(\boldsymbol{q}^{*}_{\mathrm{B/D}}(\boldsymbol{q}^{\mathsf{s}}_{\mathrm{B/D}}-\mathbf{1}^{\mathsf{s}}))\to\mathbf{0}$ and $\boldsymbol{s}\to\mathbf{0}$ as $t\to\infty$. In the proof of Theorem 1, it is shown that $\mathrm{vec}(\boldsymbol{q}^{*}_{\mathrm{B/D}}(\boldsymbol{q}^{\mathsf{s}}_{\mathrm{B/D}}-\mathbf{1}^{\mathsf{s}}))\to\mathbf{0}$ is equivalent to $\boldsymbol{q}_{\mathrm{B/D}}\to\pm\mathbf{1}$. Finally, calculating the limit as $t\to\infty$ of both sides of Eq. (159) yields $\boldsymbol{\omega}^{\mathrm{B}}_{\mathrm{B/D}}\to\mathbf{0}$. □

In addition to Remark 1, the following remarks are in order.

Remark 4. The terms $\widehat{M^{\mathrm{B}}} \star \boldsymbol{a}_g^{\mathrm{B}}$, $\frac{3\mu \boldsymbol{r}_{\mathrm{B/I}}^{\mathrm{B}}}{\|\boldsymbol{r}_{\mathrm{B/I}}^{\mathrm{B}}\|^5} \times (\widehat{M^{\mathrm{B}}} \star (\boldsymbol{r}_{\mathrm{B/I}}^{\mathrm{B}})^{\mathsf{s}})$, $\widehat{M^{\mathrm{B}}} \star \boldsymbol{a}_{J_2}^{\mathrm{B}}$, and $\widehat{\boldsymbol{f}_d^{\mathrm{B}}}$ of the control law given by Eq. (158) are estimates of the gravitational force, gravity-gradient torque, perturbing force due to Earth's oblateness, and dual disturbance force calculated using the estimated mass and inertia matrix. These terms can be thought of as approximate cancellations of these forces and torques. The remaining terms of the control law are a result of the rigid body dynamics [27]. As shown in the proof of Theorem 1, the term $\mathrm{vec}(\boldsymbol{q}_{\mathrm{B/D}}^{*}(\boldsymbol{q}_{\mathrm{B/D}}^{\mathsf{s}} - \mathbf{1}^{\mathsf{s}}))$ is equal to $\frac{1}{2} r_{\mathrm{B/D}}^{\mathrm{B}} + \epsilon \mathrm{vec}(q_{\mathrm{B/D}})$ and, hence, is the feedback of the relative position vector and of the vector part of the relative quaternion. The term $K_d \star \boldsymbol{s}^{\mathsf{s}}$ can be thought of as a damping term, where $\boldsymbol{s}$ takes the place of $\boldsymbol{\omega}_{\mathrm{B/D}}^{\mathrm{B}}$. The terms $\boldsymbol{\omega}_{\mathrm{B/I}}^{\mathrm{B}} \times (\widehat{M^{\mathrm{B}}} \star (\boldsymbol{\omega}_{\mathrm{B/I}}^{\mathrm{B}})^{\mathsf{s}})$, $\widehat{M^{\mathrm{B}}} \star (\boldsymbol{q}_{\mathrm{B/D}}^{*} \dot{\boldsymbol{\omega}}_{\mathrm{D/I}}^{\mathrm{D}} \boldsymbol{q}_{\mathrm{B/D}})^{\mathsf{s}}$, and $\widehat{M^{\mathrm{B}}} \star (\boldsymbol{\omega}_{\mathrm{D/I}}^{\mathrm{B}} \times \boldsymbol{\omega}_{\mathrm{B/D}}^{\mathrm{B}})^{\mathsf{s}}$ are a direct cancellation of identical terms in Eq. (71) with the true mass and inertia matrix replaced by their estimates. Finally, the term $\widehat{M^{\mathrm{B}}} \star (K_p \star \frac{\mathrm{d}}{\mathrm{d}t}(\boldsymbol{q}_{\mathrm{B/D}}^{*}(\boldsymbol{q}_{\mathrm{B/D}}^{\mathsf{s}} - \mathbf{1}^{\mathsf{s}})))$ is a result of using $\boldsymbol{s}$ instead of $\boldsymbol{\omega}_{\mathrm{B/D}}^{\mathrm{B}}$ in the damping term and, ultimately, guarantees that the pose error will converge to zero even if the reference motion is not sufficiently exciting, unlike in Ref. [82].

Remark 5. Apart from the terms due to the gravitational field, the dual part of the control law given by Eq. (158) is

$$\begin{aligned}\tau^{\mathrm{B}} = &-\mathrm{vec}(q_{\mathrm{B/D}}) - K_\omega * \omega_{\mathrm{B/D}}^{\mathrm{B}} - (K_\omega K_q) * q_{\mathrm{B/D}} + \omega_{\mathrm{B/I}}^{\mathrm{B}} \times (\widehat{I^{\mathrm{B}}} * \omega_{\mathrm{B/I}}^{\mathrm{B}}) + \widehat{I^{\mathrm{B}}} * (q_{\mathrm{B/D}}^{*} \dot{\omega}_{\mathrm{D/I}}^{\mathrm{D}} q_{\mathrm{B/D}}) \\ &+ \widehat{I^{\mathrm{B}}} * (\omega_{\mathrm{D/I}}^{\mathrm{B}} \times \omega_{\mathrm{B/D}}^{\mathrm{B}}) - (\widehat{I^{\mathrm{B}}} K_q) * \frac{\mathrm{d}}{\mathrm{d}t}(q_{\mathrm{B/D}}),\end{aligned} \tag{165}$$

where $\widehat{I^{\mathrm{B}}}$ is an estimate of the inertia matrix. This control law is identical to the attitude(-only) control law proposed in Ref. [1].

Remark 6. It can be easily shown that the nonadaptive version of the control law

given by Eq. (158), where the estimates of the dual inertia matrix and dual disturbance force are replaced by their true values, i.e.,

$$\begin{aligned}\boldsymbol{f}_c^{\mathrm{B}} = & -M^{\mathrm{B}} \star \boldsymbol{a}_g^{\mathrm{B}} - \frac{3\mu \boldsymbol{r}_{\mathrm{B/I}}^{\mathrm{B}}}{\|\boldsymbol{r}_{\mathrm{B/I}}^{\mathrm{B}}\|^5} \times (M^{\mathrm{B}} \star (\boldsymbol{r}_{\mathrm{B/I}}^{\mathrm{B}})^{\mathsf{s}}) - M^{\mathrm{B}} \star \boldsymbol{a}_{J_2}^{\mathrm{B}} - \boldsymbol{f}_d^{\mathrm{B}} \\ & - \mathrm{vec}(\boldsymbol{q}_{\mathrm{B/D}}^* (\boldsymbol{q}_{\mathrm{B/D}}^{\mathsf{s}} - \mathbf{1}^{\mathsf{s}})) - K_d \star \boldsymbol{s}^{\mathsf{s}} + \boldsymbol{\omega}_{\mathrm{B/I}}^{\mathrm{B}} \times (M^{\mathrm{B}} \star (\boldsymbol{\omega}_{\mathrm{B/I}}^{\mathrm{B}})^{\mathsf{s}}) \\ & + M^{\mathrm{B}} \star (\boldsymbol{q}_{\mathrm{B/D}}^* \dot{\boldsymbol{\omega}}_{\mathrm{D/I}}^{\mathrm{D}} \boldsymbol{q}_{\mathrm{B/D}})^{\mathsf{s}} + M^{\mathrm{B}} \star (\boldsymbol{\omega}_{\mathrm{D/I}}^{\mathrm{B}} \times \boldsymbol{\omega}_{\mathrm{B/D}}^{\mathrm{B}})^{\mathsf{s}} - M^{\mathrm{B}} \star (K_p \star \frac{\mathrm{d}}{\mathrm{d}t} (\boldsymbol{q}_{\mathrm{B/D}}^* (\boldsymbol{q}_{\mathrm{B/D}}^{\mathsf{s}} - \mathbf{1}^{\mathsf{s}}))),\end{aligned} \tag{166}$$

still guarantees that, for all initial conditions, $\lim_{t\to\infty} \boldsymbol{q}_{\mathrm{B/D}} = \pm\mathbf{1}$ and $\lim_{t\to\infty} \boldsymbol{\omega}_{\mathrm{B/D}}^{\mathrm{B}} = \mathbf{0}$.

Remark 7. Even though the control law given by Eq. (158) requires no information about the mass and inertia matrix of the chaser spacecraft, it still requires the center of mass of the chaser spacecraft to be known. This is because Eq. (71) is only valid if the origin of the body frame coincides with the center of mass of the spacecraft.

5.2 Sufficient Conditions for Mass and Inertia Matrix Identification

In this section, sufficient conditions on the reference pose are given that guarantee that the estimate of the dual inertia matrix will converge to the true dual inertia matrix. Note however that the result presented in Theorem 3 does not depend on the convergence of this estimate. In other words, the controller proposed in Theorem 3 guarantees almost global asymptotical stability of the linear and angular position and velocity tracking errors even if the true mass and inertia matrix are not identified. Nevertheless, identification of the mass and inertia matrix of the satellite might be important, for example, for fuel consumption estimation, for calculation of re-entry trajectories and terminal velocities, for state estimation, for fault-detecting-and-isolation systems, or for docking/undocking scenarios.

Proposition 4. *Let the dual disturbance force be exactly known or estimated so that* $\widehat{\boldsymbol{f}_d^{\mathrm{B}}}$ *can be replaced by* $\boldsymbol{f}_d^{\mathrm{B}}$ *in Eq.* (158)*. Moreover, assume that* $\boldsymbol{q}_{\mathrm{D/I}}, \boldsymbol{\omega}_{\mathrm{D/I}}^{\mathrm{D}}, \dot{\boldsymbol{\omega}}_{\mathrm{D/I}}^{\mathrm{D}}, \ddot{\boldsymbol{\omega}}_{\mathrm{D/I}}^{\mathrm{D}} \in$

$\mathcal{L}_\infty$, $\boldsymbol{r}^{\mathrm{B}}_{\mathrm{B/I}} \neq \mathbf{0}$, *and* $\boldsymbol{q}_{\mathrm{D/I}}$ *is periodic. Furthermore, let* $\mathrm{W} : [0,\infty) \to \mathbb{R}^{8\times 7}$ *be defined as*

$$\begin{aligned}\mathrm{W}(t)\mathrm{v}(\Delta M^{\mathrm{B}}) = [&\boldsymbol{\omega}^{\mathrm{D}}_{\mathrm{D/I}}(t) \times (\Delta M^{\mathrm{B}} \star (\boldsymbol{\omega}^{\mathrm{D}}_{\mathrm{D/I}}(t))^{\mathsf{s}}) + \Delta M^{\mathrm{B}} \star (\dot{\boldsymbol{\omega}}^{\mathrm{D}}_{\mathrm{D/I}}(t))^{\mathsf{s}} - \Delta M^{\mathrm{B}} \star \boldsymbol{a}^{\mathrm{D}}_{g} \\ &- \frac{3\mu \boldsymbol{r}^{\mathrm{D}}_{\mathrm{D/I}}}{\|\boldsymbol{r}^{\mathrm{D}}_{\mathrm{D/I}}\|^5} \times (\Delta M^{\mathrm{B}} \star (\boldsymbol{r}^{\mathrm{D}}_{\mathrm{D/I}})^{\mathsf{s}}) - \Delta M^{\mathrm{B}} \star \boldsymbol{a}^{\mathrm{D}}_{J_2}] \end{aligned} \tag{167}$$

or, equivalently, $\mathrm{W}(t) = \mathrm{W}_{rb}(t) + \mathrm{W}_{g}(t) + \mathrm{W}_{\nabla g}(t) + \mathrm{W}_{J_2}(t)$, *where*

$$\mathrm{W}_{rb}(t) = \begin{bmatrix} 0_{4\times 6} & [\dot{v}^{\mathrm{D}}_{\mathrm{D/I}} + \omega^{\mathrm{D}}_{\mathrm{D/I}} \times v^{\mathrm{D}}_{\mathrm{D/I}}] \\ \mathrm{W}_{rb,I}(t) & 0_{4\times 1} \end{bmatrix}, \quad \mathrm{W}_{\nabla g}(t) = \begin{bmatrix} 0_{4\times 6} & 0_{4\times 1} \\ \frac{3\mu}{\|\bar{r}^{\mathrm{D}}_{\mathrm{D/I}}\|^5}\mathrm{W}_{\nabla g,I}(t) & 0_{4\times 1} \end{bmatrix},$$

$$\mathrm{W}_{rb,I}(t)=\begin{bmatrix} 0 & 0 & 0 & 0 & 0 & 0 \\ \dot{p}^{\mathrm{D}}_{\mathrm{D/I}} & \dot{q}^{\mathrm{D}}_{\mathrm{D/I}} - p^{\mathrm{D}}_{\mathrm{D/I}} r^{\mathrm{D}}_{\mathrm{D/I}} & \dot{r}^{\mathrm{D}}_{\mathrm{D/I}} + p^{\mathrm{D}}_{\mathrm{D/I}} q^{\mathrm{D}}_{\mathrm{D/I}} & -q^{\mathrm{D}}_{\mathrm{D/I}} r^{\mathrm{D}}_{\mathrm{D/I}} & (q^{\mathrm{D}}_{\mathrm{D/I}})^2 - (r^{\mathrm{D}}_{\mathrm{D/I}})^2 & q^{\mathrm{D}}_{\mathrm{D/I}} r^{\mathrm{D}}_{\mathrm{D/I}} \\ p^{\mathrm{D}}_{\mathrm{D/I}} r^{\mathrm{D}}_{\mathrm{D/I}} & \dot{p}^{\mathrm{D}}_{\mathrm{D/I}} + q^{\mathrm{D}}_{\mathrm{D/I}} r^{\mathrm{D}}_{\mathrm{D/I}} & (r^{\mathrm{D}}_{\mathrm{D/I}})^2 - (p^{\mathrm{D}}_{\mathrm{D/I}})^2 & \dot{q}^{\mathrm{D}}_{\mathrm{D/I}} & \dot{r}^{\mathrm{D}}_{\mathrm{D/I}} - p^{\mathrm{D}}_{\mathrm{D/I}} q^{\mathrm{D}}_{\mathrm{D/I}} & -p^{\mathrm{D}}_{\mathrm{D/I}} r^{\mathrm{D}}_{\mathrm{D/I}} \\ -p^{\mathrm{D}}_{\mathrm{D/I}} q^{\mathrm{D}}_{\mathrm{D/I}} & (p^{\mathrm{D}}_{\mathrm{D/I}})^2 - (q^{\mathrm{D}}_{\mathrm{D/I}})^2 & \dot{p}^{\mathrm{D}}_{\mathrm{D/I}} - q^{\mathrm{D}}_{\mathrm{D/I}} r^{\mathrm{D}}_{\mathrm{D/I}} & p^{\mathrm{D}}_{\mathrm{D/I}} q^{\mathrm{D}}_{\mathrm{D/I}} & \dot{q}^{\mathrm{D}}_{\mathrm{D/I}} + p^{\mathrm{D}}_{\mathrm{D/I}} r^{\mathrm{D}}_{\mathrm{D/I}} & \dot{r}^{\mathrm{D}}_{\mathrm{D/I}} \end{bmatrix},$$

$$\mathrm{W}_{\nabla g,I}(t)=\begin{bmatrix} 0 & 0 & 0 & 0 & 0 & 0 \\ 0 & x^{\mathrm{D}}_{\mathrm{D/I}} z^{\mathrm{D}}_{\mathrm{D/I}} & -x^{\mathrm{D}}_{\mathrm{D/I}} y^{\mathrm{D}}_{\mathrm{D/I}} & y^{\mathrm{D}}_{\mathrm{D/I}} z^{\mathrm{D}}_{\mathrm{D/I}} & (z^{\mathrm{D}}_{\mathrm{D/I}})^2 - (y^{\mathrm{D}}_{\mathrm{D/I}})^2 & -y^{\mathrm{D}}_{\mathrm{D/I}} z^{\mathrm{D}}_{\mathrm{D/I}} \\ -x^{\mathrm{D}}_{\mathrm{D/I}} z^{\mathrm{D}}_{\mathrm{D/I}} & -y^{\mathrm{D}}_{\mathrm{D/I}} z^{\mathrm{D}}_{\mathrm{D/I}} & (x^{\mathrm{D}}_{\mathrm{D/I}})^2 - (z^{\mathrm{D}}_{\mathrm{D/I}})^2 & 0 & x^{\mathrm{D}}_{\mathrm{D/I}} y^{\mathrm{D}}_{\mathrm{D/I}} & x^{\mathrm{D}}_{\mathrm{D/I}} z^{\mathrm{D}}_{\mathrm{D/I}} \\ x^{\mathrm{D}}_{\mathrm{D/I}} y^{\mathrm{D}}_{\mathrm{D/I}} & (y^{\mathrm{D}}_{\mathrm{D/I}})^2 - (x^{\mathrm{D}}_{\mathrm{D/I}})^2 & y^{\mathrm{D}}_{\mathrm{D/I}} z^{\mathrm{D}}_{\mathrm{D/I}} & -x^{\mathrm{D}}_{\mathrm{D/I}} y^{\mathrm{D}}_{\mathrm{D/I}} & -x^{\mathrm{D}}_{\mathrm{D/I}} z^{\mathrm{D}}_{\mathrm{D/I}} & 0 \end{bmatrix},$$

$$\mathrm{W}_{g}(t) = \begin{bmatrix} 0_{4\times 6} & [a^{\mathrm{D}}_{g,\mathrm{D/I}}] \\ 0_{4\times 6} & 0_{4\times 1} \end{bmatrix}, \quad \mathrm{W}_{J_2}(t) = \begin{bmatrix} 0_{4\times 6} & [a^{\mathrm{D}}_{J_2,\mathrm{D/I}}] \\ 0_{4\times 6} & 0_{4\times 1} \end{bmatrix},$$

$$a^{\mathrm{D}}_{g,\mathrm{D/I}}=\frac{\mu r^{\mathrm{D}}_{\mathrm{D/I}}}{\|\bar{r}^{\mathrm{D}}_{\mathrm{D/I}}\|^3}, \quad a^{\mathrm{D}}_{J_2,\mathrm{D/I}}=q^{*}_{\mathrm{D/I}} a^{\mathrm{I}}_{J_2,\mathrm{D/I}} q_{\mathrm{D/I}}, \quad [a^{\mathrm{I}}_{J_2,\mathrm{D/I}}]=-\frac{3}{2}\frac{\mu J_2 R_e^2}{\|\bar{r}^{\mathrm{I}}_{\mathrm{D/I}}\|^5}\begin{bmatrix} 0 \\ (1-5(\frac{z^{\mathrm{I}}_{\mathrm{D/I}}}{\|\bar{r}^{\mathrm{I}}_{\mathrm{D/I}}\|})^2)x^{\mathrm{I}}_{\mathrm{D/I}} \\ (1-5(\frac{z^{\mathrm{I}}_{\mathrm{D/I}}}{\|\bar{r}^{\mathrm{I}}_{\mathrm{D/I}}\|})^2)y^{\mathrm{I}}_{\mathrm{D/I}} \\ (3-5(\frac{z^{\mathrm{I}}_{\mathrm{D/I}}}{\|\bar{r}^{\mathrm{I}}_{\mathrm{D/I}}\|})^2)z^{\mathrm{I}}_{\mathrm{D/I}} \end{bmatrix}.$$

Let also $0 \leq t_1 \leq t_2 \leq \ldots \leq t_n$ *be such that*

$$\operatorname{rank}\begin{bmatrix} \mathrm{W}(t_1) \\ \vdots \\ \mathrm{W}(t_n) \end{bmatrix} = 7. \tag{168}$$

Then, under the control law given by Eq. (158), $\lim_{t\to\infty} \widehat{M^{\mathrm{B}}} = M^{\mathrm{B}}$.

Proof. The first step is to prove that $\lim_{t\to\infty} \dot{\boldsymbol{\omega}}^{\mathrm{B}}_{\mathrm{B/D}} = \mathbf{0}$. (Note that $\lim_{t\to\infty} \boldsymbol{\omega}^{\mathrm{B}}_{\mathrm{B/D}} = \mathbf{0}$ does not imply that $\lim_{t\to\infty} \dot{\boldsymbol{\omega}}^{\mathrm{B}}_{\mathrm{B/D}} = \mathbf{0}$.) Note that

$$\lim_{t\to\infty} \int_0^t \dot{\boldsymbol{\omega}}^{\mathrm{B}}_{\mathrm{B/D}}(\tau)\,\mathrm{d}\tau = \lim_{t\to\infty} \boldsymbol{\omega}^{\mathrm{B}}_{\mathrm{B/D}}(t) - \boldsymbol{\omega}^{\mathrm{B}}_{\mathrm{B/D}}(0) = -\boldsymbol{\omega}^{\mathrm{B}}_{\mathrm{B/D}}(0)$$

exits and is finite. Furthermore, since

$$\boldsymbol{q}_{\mathrm{D/I}}, \boldsymbol{\omega}^{\mathrm{D}}_{\mathrm{D/I}}, \dot{\boldsymbol{\omega}}^{\mathrm{D}}_{\mathrm{D/I}}, \ddot{\boldsymbol{\omega}}^{\mathrm{D}}_{\mathrm{D/I}}, \dot{\boldsymbol{q}}_{\mathrm{B/D}}, \ddot{\boldsymbol{q}}_{\mathrm{B/D}}, \dot{\boldsymbol{\omega}}^{\mathrm{B}}_{\mathrm{B/D}}, \frac{\mathrm{dv}(\widehat{M^{\mathrm{B}}})}{\mathrm{d}t}, \frac{\mathrm{d}\widehat{f^{\mathrm{B}}_d}}{\mathrm{d}t} \in \mathcal{L}_\infty$$

and $\boldsymbol{r}^{\mathrm{B}}_{\mathrm{B/I}} \neq \mathbf{0}$, it follows that $\ddot{\boldsymbol{\omega}}^{\mathrm{B}}_{\mathrm{B/D}} \in \mathcal{L}_\infty$ by differentiating Eq. (71). Hence, by Barbalat's lemma, $\lim_{t\to\infty} \dot{\boldsymbol{\omega}}^{\mathrm{B}}_{\mathrm{B/D}} = \mathbf{0}$. Now, calculate the limit as $t \to \infty$ of both sides of Eq. (71). Next, substitute in the control law given by Eq. (158) and replace $\widehat{\boldsymbol{f}^{\mathrm{B}}_d}$ by $\boldsymbol{f}^{\mathrm{B}}_d$ in Eq. (158) (note that $\boldsymbol{f}^{\mathrm{B}}_d$ is assumed to be known). Finally, using the fact that, according to Theorem 3, $\lim_{t\to\infty} \boldsymbol{\omega}^{\mathrm{B}}_{\mathrm{B/D}} = \mathbf{0}$ and $\lim_{t\to\infty} \boldsymbol{q}_{\mathrm{B/D}} = \pm\mathbf{1}$ (in other words, in the limit the body frame and the desired frame have the same pose) yields

$$\begin{aligned}\lim_{t\to\infty} (\boldsymbol{\omega}^{\mathrm{D}}_{\mathrm{D/I}} \times (\Delta M^{\mathrm{B}} \star (\boldsymbol{\omega}^{\mathrm{D}}_{\mathrm{D/I}})^{\mathsf{s}}) + \Delta M^{\mathrm{B}} \star (\dot{\boldsymbol{\omega}}^{\mathrm{D}}_{\mathrm{D/I}})^{\mathsf{s}} - \Delta M^{\mathrm{B}} \star \boldsymbol{a}^{\mathrm{D}}_{g,\mathrm{D/I}} \\ - \frac{3\mu \boldsymbol{r}^{\mathrm{D}}_{\mathrm{D/I}}}{\|\boldsymbol{r}^{\mathrm{D}}_{\mathrm{D/I}}\|^5} \times (\Delta M^{\mathrm{B}} \star (\boldsymbol{r}^{\mathrm{D}}_{\mathrm{D/I}})^{\mathsf{s}}) - \Delta M^{\mathrm{B}} \star \boldsymbol{a}^{\mathrm{D}}_{J_2,\mathrm{D/I}}) = \mathbf{0}, \end{aligned} \tag{169}$$

where $\boldsymbol{a}^{\mathrm{D}}_{g,\mathrm{D/I}} = a^{\mathrm{D}}_{g,\mathrm{D/I}} + \epsilon\mathsf{0}$ and $\boldsymbol{a}^{\mathrm{D}}_{J_2,\mathrm{D/I}} = a^{\mathrm{D}}_{J_2,\mathrm{D/I}} + \epsilon\mathsf{0}$. Moreover, note that if $\boldsymbol{q}_{\mathrm{D/I}}$ is periodic with period T, so are $\dot{\boldsymbol{q}}_{\mathrm{D/I}}$, $\boldsymbol{\omega}^{\mathrm{D}}_{\mathrm{D/I}}$, $\dot{\boldsymbol{\omega}}^{\mathrm{D}}_{\mathrm{D/I}}$, $\boldsymbol{r}^{\mathrm{D}}_{\mathrm{D/I}}$, $\boldsymbol{a}^{\mathrm{D}}_{g,\mathrm{D/I}}$, $\boldsymbol{a}^{\mathrm{D}}_{J_2,\mathrm{D/I}}$, and $\mathrm{W}(t)$. Finally, noting that $\lim_{t\to\infty} \frac{\mathrm{d}}{\mathrm{d}t}\mathrm{v}(\widehat{M^{\mathrm{B}}}) = 0_{7\times 1}$ from Eq. (160) and Theorem 3, under the conditions of Proposition 4, Eq. (169) implies that $\lim_{t\to\infty} \mathrm{v}(\Delta M^{\mathrm{B}}) = 0_{7\times 1}$ or, equivalently, $\lim_{t\to\infty} \widehat{M^{\mathrm{B}}} = M^{\mathrm{B}}$. □

Remark 8. In practice, the true dual disturbance force $\boldsymbol{f}^{\mathrm{B}}_d$ may not be known. Moreover, there is no guarantee that the estimate of the dual disturbance force will converge to its true value. Hence, in practice, the estimate of the mass and inertia matrix of the spacecraft will only be as good as the estimate of the dual disturbance force.

Remark 9. An alternative, and more general, sufficient condition than Eq. (168) for mass and inertia matrix identification, which does not require $\boldsymbol{q}_{\mathrm{D/I}}$ to be periodic, is that the 7×7 symmetric matrix $\int_t^{t+T_2} \mathrm{W}^\intercal(t)\mathrm{W}(t)\,\mathrm{d}t$ is positive-definite for all $t \geq T_1$ for some $T_1 \geq 0$ and $T_2 > 0$ [86, 83].

5.3 Simulation Results

In this section, two examples are considered. In the first example, the inertia-free pose-tracking controller is applied to a conceivable satellite proximity operations scenario, where a chaser satellite approaches, circumnavigates, and docks with a target satellite. In the second example, the same controller is used to identify the mass and inertia matrix of a satellite in GEO.

5.3.1 Satellite Proximity Operations

In this example, the versatility of the controller is demonstrated by using it, in sequence, to approach, circumnavigate, and dock with a target satellite, while always pointing at it.

The inertial frame, the target frame, the desired frame, and the body frame are defined as in Section 3.3.2 and represented in Figure 10. The target spacecraft is assumed to be in a Molniya orbit with initial orbital elements given in Table 2 and nadir pointing. The relative motion of the desired frame with respect to the target frame is divided into the following three phases.

- Phase #1: Straight line approach along $\bar{J}_{\mathrm{T}}$ from -30 m to -20 m at a constant speed of 0.025 m/s. In other words, during this phase, $\bar{\omega}^{\mathrm{T}}_{\mathrm{D/T}} = [0, 0, 0]^\intercal$ rad/s and $\bar{v}^{\mathrm{T}}_{\mathrm{D/T}} = [0, 0.025, 0]^\intercal$ m/s, with initial condition $\bar{r}^{\mathrm{T}}_{\mathrm{D/T}} = [0, -30, 0]^\intercal$ m.

- Phase #2: Circular circumnavigation around the target satellite with a radius of 20 m in the $\bar{J}_{\mathrm{T}}$-$\bar{K}_{\mathrm{T}}$ plane (so that chaser satellite does not cross the nadir direction of the target satellite) and with constant angular speed equal to the

mean motion of the target satellite. In other words, during this phase, $\bar{\omega}^{\mathrm{T}}_{\mathrm{D/T}} = [-n, 0, 0]^{\intercal}$ rad/s, $\bar{v}^{\mathrm{T}}_{\mathrm{D/T}} = [0, -a_e n \sin(nt), b_e n \cos(nt)]^{\intercal}$ m/s, and $a_e = b_e = 20$ m, where $n = \sqrt{\mu/a^3}$ is the mean motion of the target satellite (assuming no J_2-perturbation) and a is the semi-major axis of the target satellite (assuming no J_2-perturbation).

- Phase #3: Straight-line docking along $\bar{J}_{\mathrm{T}}$ from -20 m to contact at a constant speed of 0.025 m/s. In other words, during this phase, $\bar{\omega}^{\mathrm{T}}_{\mathrm{D/T}} = [0,\ 0,\ 0]^{\intercal}$ rad/s and $\bar{v}^{\mathrm{T}}_{\mathrm{D/T}} = [0,\ 0.025,\ 0]^{\intercal}$ m/s.

The linear velocity of the target satellite with respect to the inertial frame is calculated by numerically integrating the gravitational acceleration and also the perturbing acceleration due to Earth's oblateness. On the other hand, the angular acceleration of the target satellite with respect to the inertial frame is calculated analytically through Eq. (85). Moreover, $\boldsymbol{q}_{\mathrm{T/I}}$ and $\boldsymbol{q}_{\mathrm{D/I}}$ are propagated according to Eq. (50). Finally, $\boldsymbol{\omega}^{\mathrm{D}}_{\mathrm{D/I}}$ and $\dot{\boldsymbol{\omega}}^{\mathrm{D}}_{\mathrm{D/I}}$ are calculated from Eqs. (86) and (87).

As in Section 3.3.2, the inertia matrix and mass of the chaser satellite are assumed to be [93]

$$\bar{I}^{\mathrm{B}} = \begin{bmatrix} 22 & 0.2 & 0.5 \\ 0.2 & 20 & 0.4 \\ 0.5 & 0.4 & 23 \end{bmatrix} \ \mathrm{kg} \cdot \mathrm{m}^2$$

and $m = 100$ kg. The initial conditions for this simulation are $\bar{r}^{\mathrm{B}}_{\mathrm{B/D}}(0)$=$[2, 2, 2]^{\intercal}$ m, $q_{\mathrm{B/D}}(0) = [0.3320, 0.4618, 0.1917, 0.7999]^{\intercal}$, $\bar{v}^{\mathrm{B}}_{\mathrm{B/D}}(0) = [0.1, 0.1, 0.1]^{\intercal}$ m/s, $\bar{\omega}^{\mathrm{B}}_{\mathrm{B/D}}(0) = [0.1, 0.1, 0.1]^{\intercal}$ rad/s. The initial estimates for the mass, inertia matrix, and dual disturbance force are set to zero. The constant disturbance force and torque acting on the chaser satellite are set to $\bar{f}^{\mathrm{B}}_d = [0.005, 0.005, 0.005]^{\intercal}$ N and $\bar{\tau}^{\mathrm{B}}_d = [0.005, 0.005, 0.005]^{\intercal}$ N $\cdot$ m, respectively.

The control gains are chosen to be $\bar{K}_r = 0.1 I_{3\times3}$, $\bar{K}_q = 0.25 I_{3\times3}$, $\bar{K}_v = 15 I_{3\times3}$, $\bar{K}_\omega = 15 I_{3\times3}$, $K_i = 100 I_{7\times7}$, $\bar{K}_f = 0.8 I_{3\times3}$, and $\bar{K}_\tau = 0.8 I_{3\times3}$.

Figure 35 shows the linear and angular velocity of the desired frame with respect to the inertial frame expressed in the desired frame for the complete maneuver. These signals form the reference for the controller.

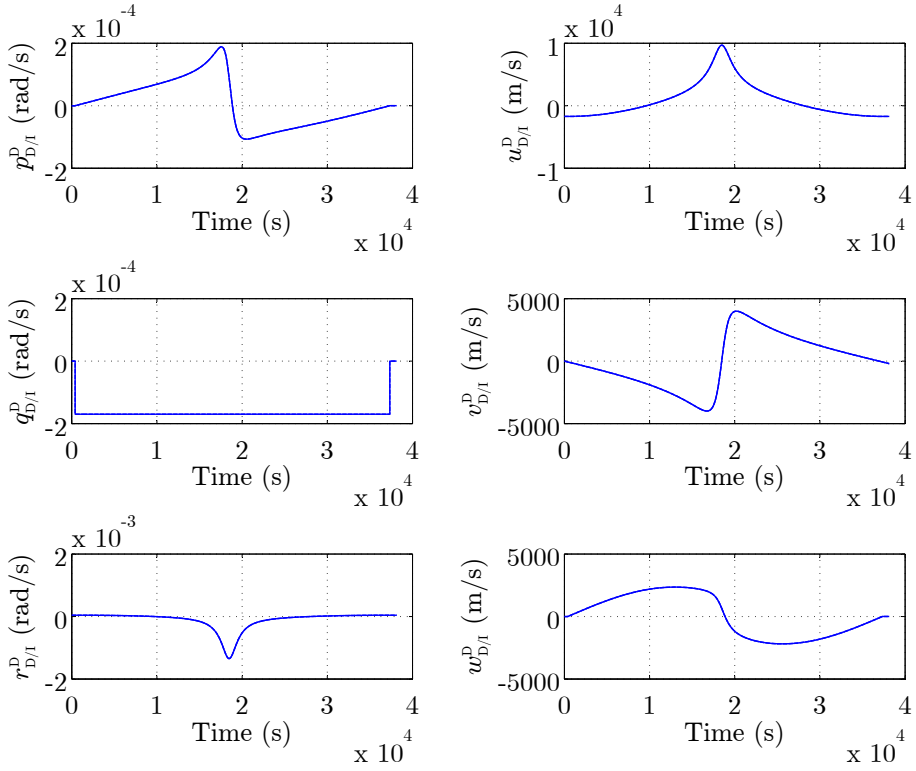

Figure 35: Reference motion.

Figure 36 shows the initial transient response and the transient response between phases #1 and #2 of the pose of the body frame with respect to the desired frame using the controller given by Eq. (158) (adaptive) and the controller given by Eq. (166) (nonadaptive). Note that the transition between phases #1 and #2 occurs at 400 s. The transient response between phases #2 and #3 is similar and, thus, not shown here. Both controllers successfully cancel the relative pose error at the beginning of the maneuver and between phases. These latter are due to the fact that $\bar{\omega}^{\mathrm{T}}_{\mathrm{D/T}}$ and $\bar{v}^{\mathrm{T}}_{\mathrm{D/T}}$ are discontinuous between phases. In other words, between phases $\boldsymbol{\omega}^{\mathrm{D}}_{\mathrm{D/I}} \notin \mathcal{L}_\infty$, which instantaneously violates the conditions of Theorem 3.

Figure 37 shows the relative linear and angular velocity of the body frame with

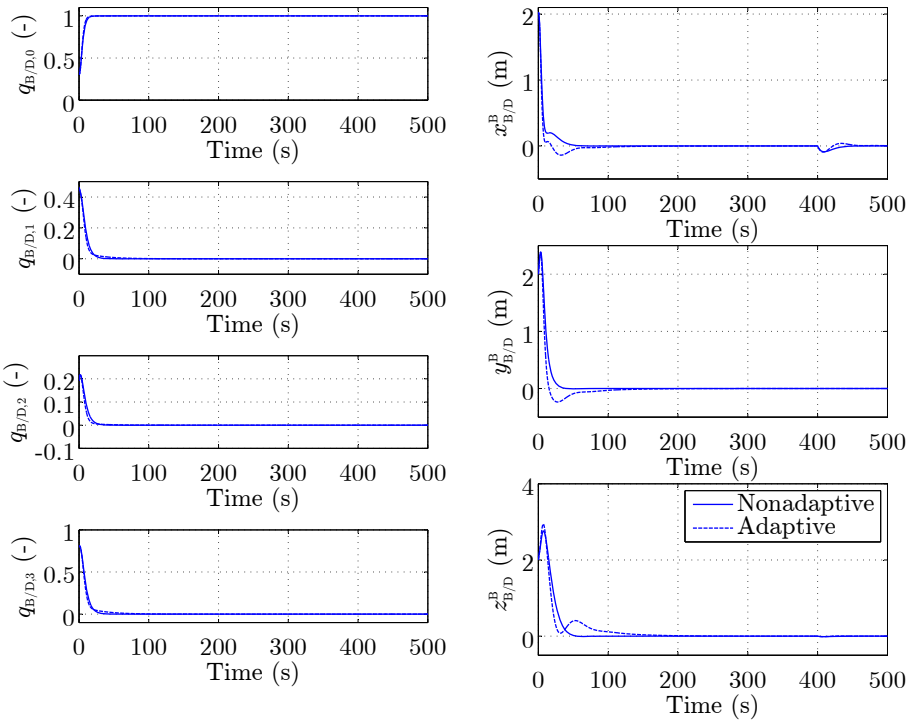

Figure 36: Relative pose expressed in the body frame.

respect to the desired frame for the same two cases studied in Figure 36. Again, both controllers successfully cancel the relative linear and angular velocity errors at the beginning of the maneuver and between phases.

Figure 38 shows that even though the adaptive controller is not able to identify the true mass and inertia matrix of the chaser satellite, it is still able to track the reference motion. As a matter of fact, the similarities between the responses obtained with the adaptive controller (which has no information about the true mass, inertia matrix, and dual disturbance force) and the nonadaptive controller (which knowns the true mass, inertia matrix, and dual disturbance force) are quite remarkable. For this reference motion, the minimum singular value of the matrix in Eq. (168) for $t_1 = 0$, $t_2 \approx 3.4e^{-2}$, ..., $t_{32847} \approx 3.8e^{4}$ s is $1.5e^{-6}$.

Figure 39 shows that the estimates of the disturbance force and torque converge to values of the same order of magnitude as the true disturbance force and torque. Note that Theorem 3 only guarantees that these estimates will be uniformly bounded.

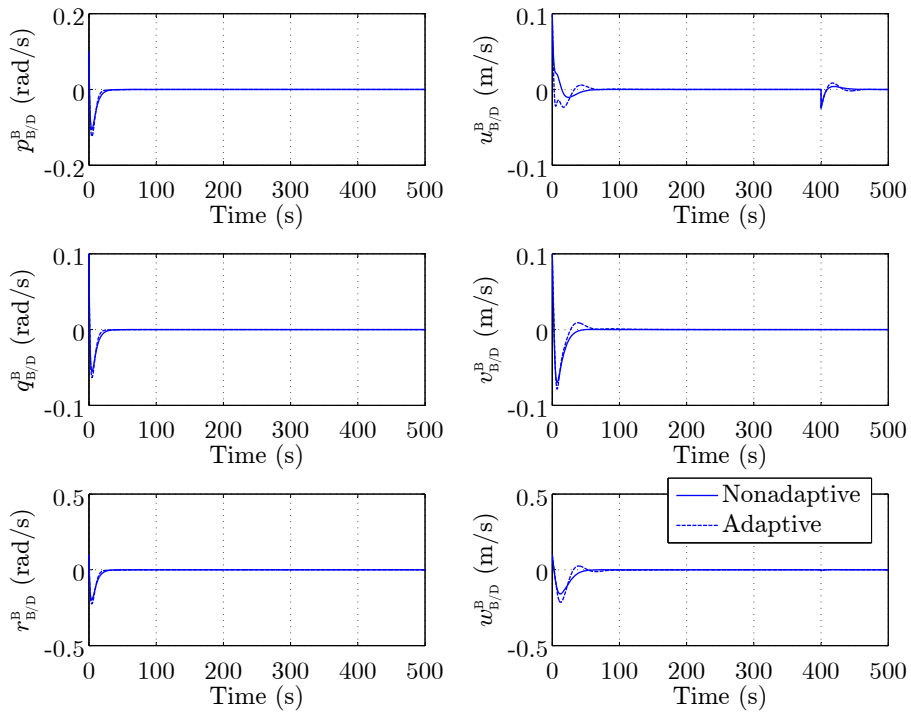

Figure 37: Relative linear and angular velocity expressed in the body frame.

Relatively small oscillations in the estimates can be seen between phases as a result of the discontinuities in $\boldsymbol{\omega}^{D}_{D/I}$.

Finally, Figure 40 shows the control force and torque produced by the adaptive and nonadaptive controllers during the initial transient response and between phases #1 and #2. The relatively high values of control force and torque during the initial transient response are required to eliminate the initial linear and angular position and velocity errors that were arbitrarily set between the body frame and the desired frame. As a comparison, the complete maneuver requires a ΔV of 3.9211 m/s if done with Eq. (166) (nonadaptive) and 0.1722 m/s more if done with Eq. (158) (adaptive).

5.3.2 Identification of the Mass and Inertia Matrix of a Satellite in GEO

In this example, the adaptive control law is used to identify the mass and inertia matrix of a satellite in a *Geosynchronous Earth Orbit* (GEO) with initial orbital

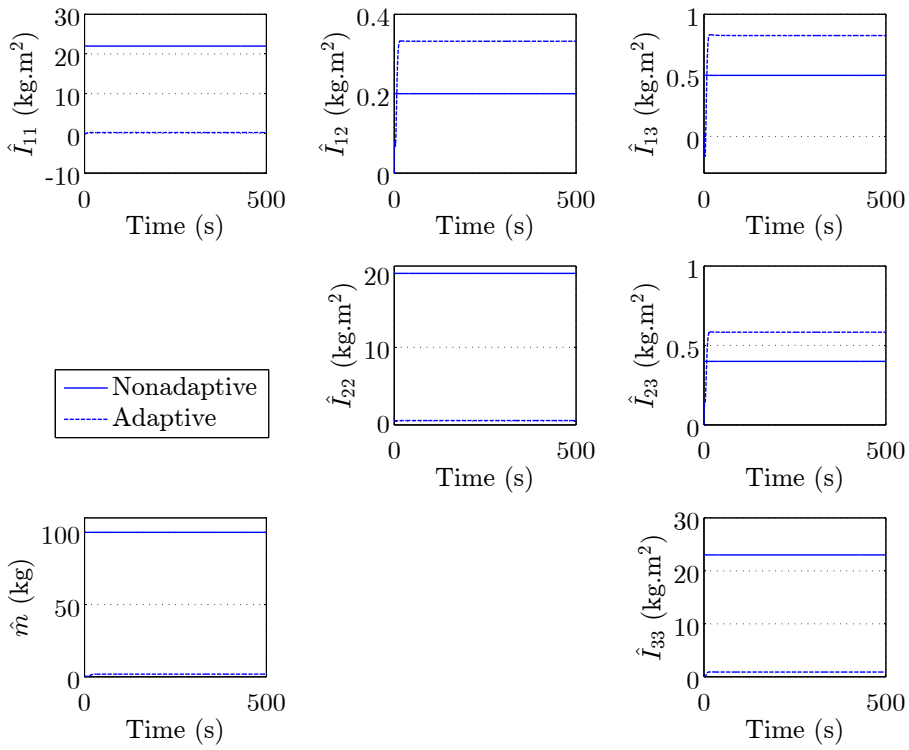

Figure 38: Mass and inertia matrix estimation for low-exciting reference motion.

elements given in Table 2.

In this scenario, the target frame is the unperturbed Hill frame [52] of the satellite. Note that in this case there is not a physical spacecraft attached to the target frame. The desired frame is defined to have the same position and orientation as the target frame at the beginning of the simulation. The inertial frame and the body frame are defined as in Section 3.3.2.

The satellite has the same mass and inertia matrix as the chaser satellite in the previous example. As assumed in Proposition 4, the dual disturbance force is assumed to be known and, in this example, equal to zero. The body frame is assumed to have the same position, attitude, linear velocity, and angular velocity as the desired frame at the beginning of the simulation. The initial estimates for the mass and inertia matrix are set to zero. The control gains are the same as in Section 3.3.2.

The relative motion of the desired frame with respect to the target frame is defined

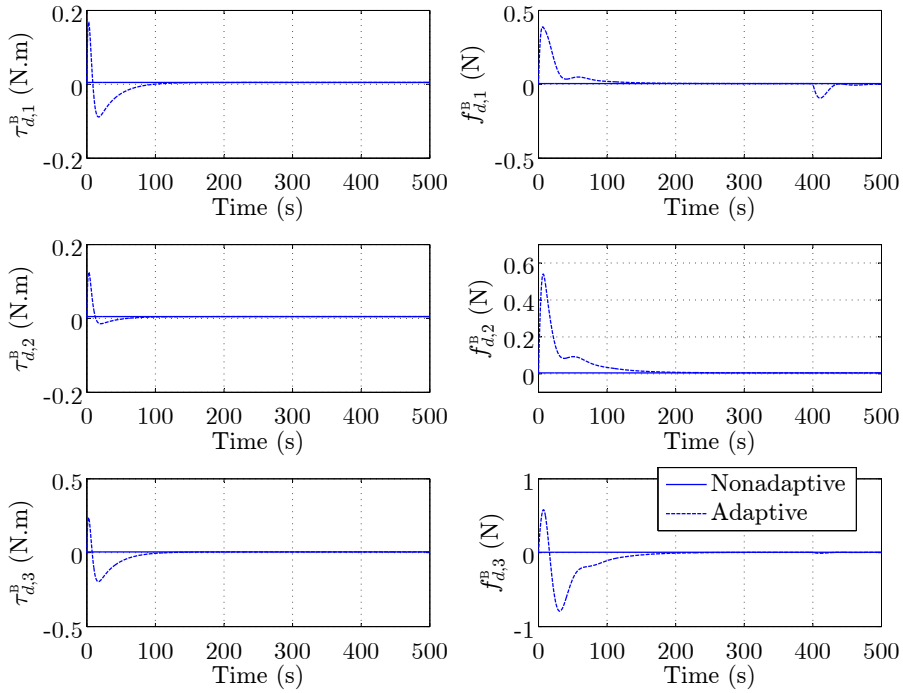

Figure 39: Dual disturbance force estimation.

in Figure 41. It is composed by a pure translation and several pure rotations designed to identify the mass and the elements of the inertia matrix in sequence, while keeping the control forces and torques within reasonable values. This reference motion was created by taking into consideration the structure of matrix $\mathrm{W}(t)$ and the results presented in Ref. [1]. For this reference motion, the minimum singular value of the matrix in Eq. (168) for $t_1 = 0$, $t_2 \approx 1.0e^{-5}$, ..., $t_{14030} = 900$ s is 1.15.

The mass and inertia matrix identification is shown in Figure 42. Note that the mass and inertia matrix are identified even though their initial estimates are zero. They are identified in sequence: m is identified during the first triangle waveform (on $v^{\mathrm{D}}_{\mathrm{D/T}}$), I_{12}, I_{22}, and I_{23} are identified during the second triangle waveform (on $q^{\mathrm{D}}_{\mathrm{D/T}}$), I_{11} and I_{13} are identified during the third triangle waveform (on $p^{\mathrm{D}}_{\mathrm{D/T}}$), and I_{33} is identified during the fourth and last triangle waveform (on $r^{\mathrm{D}}_{\mathrm{D/T}}$). The associated control forces and torques are shown in Figure 43. As a comparison, the complete maneuver requires a ΔV of 16.0103 m/s if done with Eq. (166) (nonadaptive) and

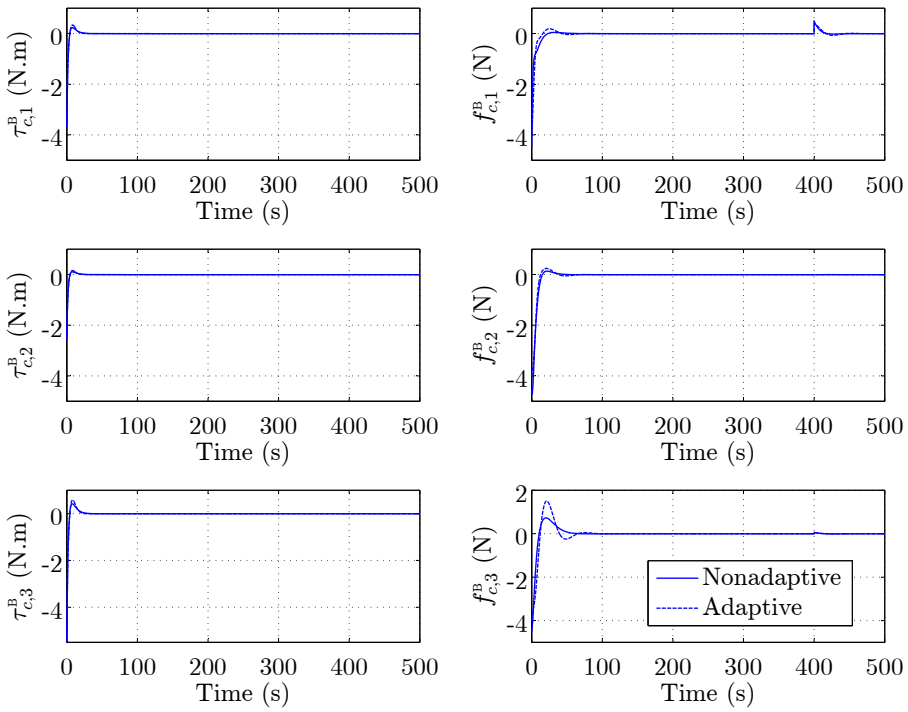

Figure 40: Control force and torque.

0.1143 m/s more if done with Eq. (158) (adaptive).

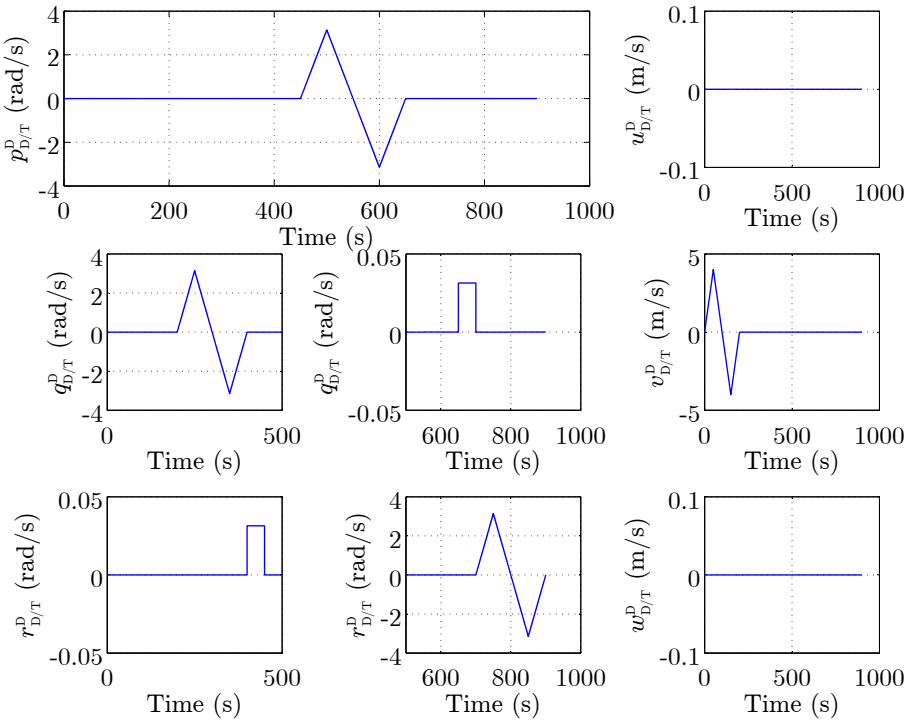

Figure 41: Reference motion for identification.

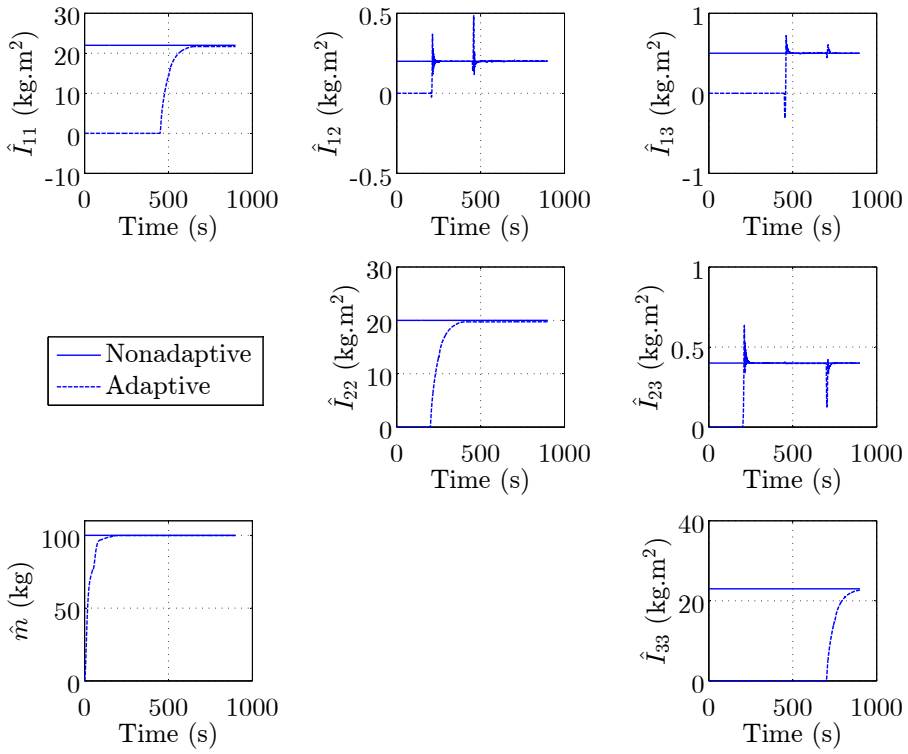

Figure 42: Mass and inertia matrix identification.

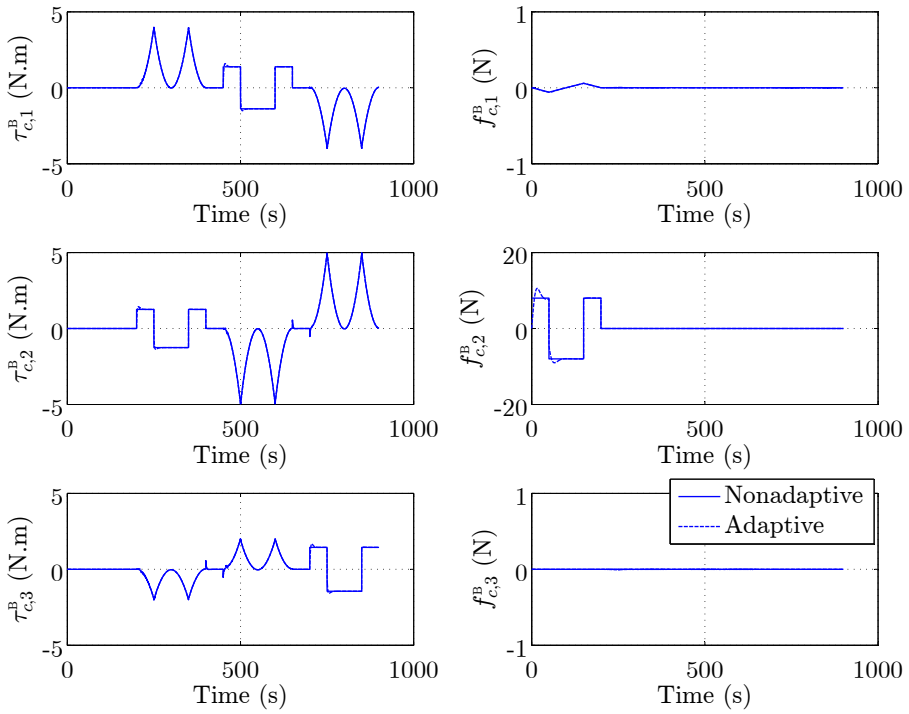

Figure 43: Control force and torque during identification.

CHAPTER VI

HIGH-FIDELITY SIMULATION AND EXPERIMENTAL RESULTS

In this chapter, the inertia-free pose-tracking controller described in Chapter 5 and the DQ-MEKF described in Chapter 4 are tested on a high-fidelity simulation of the 5-DOF platform of the ASTROS facility and also experimentally validated on the actual platform.

The high-fidelity simulation is implemented as a Simulink model, which is shown in Figure 44. One of the biggest advantages of this implementation is that the exact same control software used in the simulations is used in the experiments, thanks to Simulink's xPC Target environment. After a certain piece of code has been tested in simulation, only the block that simulates the dynamics of the platform needs to be replaced by an existing xPC Target block that takes care of all communications between the control software and the sensors and actuators on the platform. After this, a single button wirelessly uploads the control software to the on-board computer and the same piece of code tested in simulation is ready to be tested on the platform. This process substantially reduces the time between simulation and experiment.

The outputs of the Simulink model also drive a virtual-reality environment that provides a relatively realistic 3D visualization of the platform's motion.

This chapter starts with the derivation of the equations of motion of the 5-DOF platform, on which the high-fidelity simulation is based. Then, in Section 6.2 the real-world effects (e.g., noise and bias of the sensors, deadzone of the actuators) included in the high-fidelity simulation are detailed. The allocation of the control moment to the *Variable-Speed Control Moment Gyros* (VSCMGs) and the allocation of the control

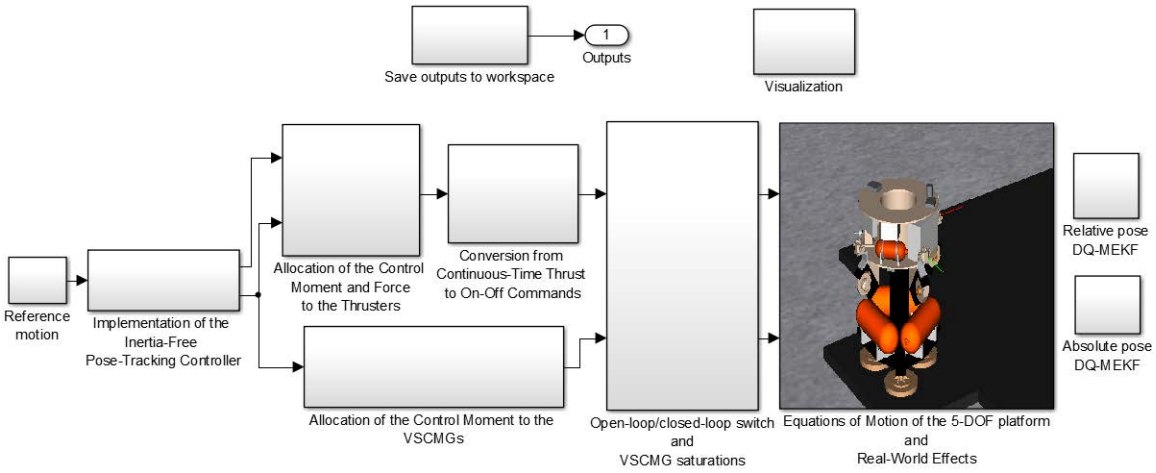

Figure 44: High-fidelity Simulink model of the 5-DOF platform.

moment and force to the thrusters is explained in Sections 6.3 and 6.4, respectively. Since the thrusters on the platform only accept on-off commands, the continuous-time signals generated by the controller need to be converted. This conversation is explained in Section 6.5. A few comments about the coding of the controller are given in Section 6.6. Finally, the results of four experiments are presented in Section 6.7 and used to validate the high-fidelity 5-DOF simulation, the inertia-free pose-tracking controller, and the DQ-MEKF.

6.1 Derivation of the Equations of Motion of the 5-DOF Platform

The equations of motion of the 5-DOF platform are derived in this section using classical Newton/Euler dynamics. Three cases are considered.

1) 3-DOF case: pure rotation of the upper stage.

2) (2+1)-DOF case: rotation and translation of the upper stage when rigidly connected to the lower stage.

3) 5-DOF case: rotation and translation of the upper stage when levitated with respect to the lower stage.

To validate this derivation, the equations of motion of the 5-DOF platform were also derived using analytical dynamics, in particular, using Eqs. (4.166) and (4.167) of Ref. [65]. In analytical dynamics, these equations are the equations of motion with respect to an arbitrary system of axes, not necessarily centered at the center of mass. The two derivations yielded the same equations of motion. Only the first derivation is shown here.

The derivation of the equations of motion is organized as follows. In Section 6.1.1, the angular momentum of a system of N particles with respect to the inertial frame about an arbitrary moving point P is derived. This result is used in the subsequent sections. In Section 6.1.2, the reference frames used in the derivation of the equations of motion are defined. In Section 6.1.3, the assumptions made in the derivation of the equations of motion are summarized. In Sections 6.1.4 and 6.1.5, the rotational and translational dynamic equations of the upper stage and of the lower stage are deduced. The free-body diagrams are also presented. In Section 6.1.6, the equations of motion for the 3-DOF case are deduced based on the results shown in Sections 6.1.4 and 6.1.5. Likewise, in Sections 6.1.7 and 6.1.8, the equations of motion for the (2+1)-DOF case and for the 5-DOF case, respectively, are derived.

6.1.1 Angular Momentum of Two Groups of Particles with respect to a Moving Point

By definition, the angular momentum of a system of N particles with respect to an inertial frame about an arbitrary moving point P is given by

$$ {}^{P}\bar{H}_{\text{system/I}} = \sum_{i=1}^{N} \bar{r}_{m_i/P} \times m_i \frac{{}^{\text{I}}\mathrm{d}\bar{r}_{m_i/P}}{\mathrm{d}t}, \tag{170} $$

where $\bar{r}_{\text{Y/X}}$ is the vector that goes from point X to point Y, $\frac{{}^{\text{X}}\mathrm{d}\bar{y}}{\mathrm{d}t}$ is the time derivative of vector $\bar{y}$ with respect to the X-frame, m_i is the mass of particle i, and ${}^{P}\bar{H}_{\text{Y/Z}}$ is the angular momentum vector of system Y with respect to reference frame Z about point P. This system of particles is divided into two groups of particles, one with N_1

particles and another one with N_2 particles, as represented in Figure 45. The particles

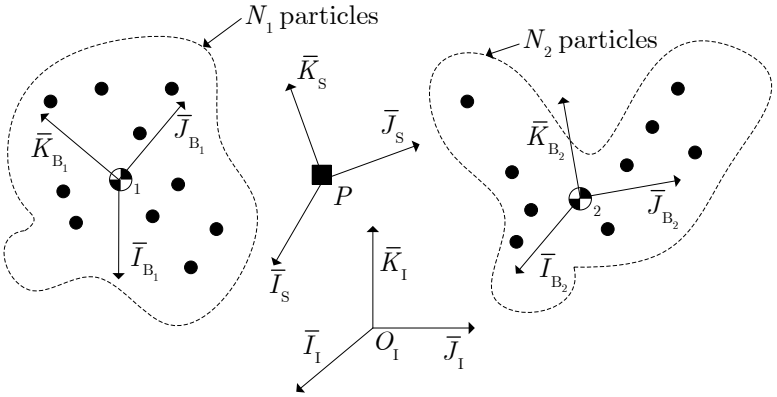

Figure 45: System of particles.

of each group are assumed to be rigidly fixed to each other. In other words, each group of particles behaves like a rigid body. Each group of particles has its own center of mass and these centers of mass might be moving with respect to each other and with respect to point P. The objective in this section is to calculate the contribution to ${}^{P}\bar{H}_{\mathrm{system/I}}$ of each group of particles. First, the summation in Eq. (170) is divided into two terms as follows

$$ {}^{P}\bar{H}_{\mathrm{system/I}} = \sum_{i=1}^{N_1} \bar{r}_{m_i/P} \times m_i \frac{{}^{\mathrm{I}}\mathrm{d}\bar{r}_{m_i/P}}{\mathrm{d}t} + \sum_{i=1}^{N_2} \bar{r}_{m_i/P} \times m_i \frac{{}^{\mathrm{I}}\mathrm{d}\bar{r}_{m_i/P}}{\mathrm{d}t}. \tag{171} $$

The first term is now analyzed. Note that the analysis of the second term is analogous. By writing $\bar{r}_{m_i/P} = \bar{r}_{\bullet_1/P} + \bar{r}_{m_i/\bullet_1}$, Eq. (171) can be rewritten as

$$ \sum_{i=1}^{N_1} \bar{r}_{m_i/P} \times m_i \frac{{}^{\mathrm{I}}\mathrm{d}\bar{r}_{m_i/P}}{\mathrm{d}t} = \sum_{i=1}^{N_1} (\bar{r}_{\bullet_1/P} + \bar{r}_{m_i/\bullet_1}) \times m_i (\frac{{}^{\mathrm{I}}\mathrm{d}\bar{r}_{\bullet_1/P}}{\mathrm{d}t} + \frac{{}^{\mathrm{I}}\mathrm{d}\bar{r}_{m_i/\bullet_1}}{\mathrm{d}t}), \tag{172} $$

where $\bullet_1$ denotes the center of mass of the N_1 particles. The S-frame is defined as a frame with an arbitrary orientation and with origin coincident with point P. Moreover, frame B_1 is defined as a frame fixed to the N_1 particles and with origin coincident with the center of mass of the N_1 particles. Then, $\frac{{}^{\mathrm{I}}\mathrm{d}\bar{r}_{\bullet_1/P}}{\mathrm{d}t} = \frac{{}^{\mathrm{S}}\mathrm{d}\bar{r}_{\bullet_1/P}}{\mathrm{d}t} + \bar{\omega}_{\mathrm{S/I}} \times \bar{r}_{\bullet_1/P} = \bar{v}_{\bullet_1/\mathrm{S}} + \bar{\omega}_{\mathrm{S/I}} \times \bar{r}_{\bullet_1/P}$ and $\frac{{}^{\mathrm{I}}\mathrm{d}\bar{r}_{m_i/\bullet_1}}{\mathrm{d}t} = \frac{{}^{\mathrm{B}_1}\mathrm{d}\bar{r}_{m_i/\bullet_1}}{\mathrm{d}t} + \bar{\omega}_{\mathrm{B}_1/\mathrm{I}} \times \bar{r}_{m_i/\bullet_1}$, where $\bar{\omega}_{\mathrm{X/Y}}$ is the angular velocity vector of the X-frame with respect to the Y-frame. Since the N_1

particles are assumed to be rigidly fixed to each other, $\frac{^{\mathrm{B}_1}\mathrm{d}\bar{r}_{m_i/\mathfrak{B}_1}}{\mathrm{d}t} = 0$. Substituting $\frac{^{\mathrm{I}}\mathrm{d}\bar{r}_{\mathfrak{B}_1/P}}{\mathrm{d}t}$ and $\frac{^{\mathrm{I}}\mathrm{d}\bar{r}_{m_i/\mathfrak{B}_1}}{\mathrm{d}t}$ into Eq. (172) and expanding yields

$$\sum_{i=1}^{N_1} (\bar{r}_{\mathfrak{B}_1/P}+\bar{r}_{m_i/\mathfrak{B}_1})\times m_i(\frac{^{\mathrm{I}}\mathrm{d}\bar{r}_{\mathfrak{B}_1/P}}{\mathrm{d}t}+\frac{^{\mathrm{I}}\mathrm{d}\bar{r}_{m_i/\mathfrak{B}_1}}{\mathrm{d}t})$$

$$=\sum_{i=1}^{N_1} (\bar{r}_{\mathfrak{B}_1/P}+\bar{r}_{m_i/\mathfrak{B}_1})\times m_i(\bar{v}_{\mathfrak{B}_1/\mathrm{S}}+\bar{\omega}_{\mathrm{S/I}}\times\bar{r}_{\mathfrak{B}_1/P}+\bar{\omega}_{\mathrm{B}_1/\mathrm{I}}\times\bar{r}_{m_i/\mathfrak{B}_1})$$

$$=\sum_{i=1}^{N_1} \bar{r}_{\mathfrak{B}_1/P}\times m_i\bar{v}_{\mathfrak{B}_1/\mathrm{S}}+\sum_{i=1}^{N_1} \bar{r}_{\mathfrak{B}_1/P}\times m_i(\bar{\omega}_{\mathrm{S/I}}\times\bar{r}_{\mathfrak{B}_1/P})+\sum_{i=1}^{N_1} \bar{r}_{\mathfrak{B}_1/P}\times m_i(\bar{\omega}_{\mathrm{B}_1/\mathrm{I}}\times\bar{r}_{m_i/\mathfrak{B}_1})$$

$$+\sum_{i=1}^{N_1} \bar{r}_{m_i/\mathfrak{B}_1}\times m_i\bar{v}_{\mathfrak{B}_1/\mathrm{S}}+\sum_{i=1}^{N_1} \bar{r}_{m_i/\mathfrak{B}_1}\times m_i(\bar{\omega}_{\mathrm{S/I}}\times\bar{r}_{\mathfrak{B}_1/P})+\sum_{i=1}^{N_1} \bar{r}_{m_i/\mathfrak{B}_1}\times m_i(\bar{\omega}_{\mathrm{B}_1/\mathrm{I}}\times\bar{r}_{m_i/\mathfrak{B}_1})$$

$$=\bar{r}_{\mathfrak{B}_1/P}\times m_1\bar{v}_{\mathfrak{B}_1/\mathrm{S}}-m_1\bar{r}_{\mathfrak{B}_1/P}\times(\bar{r}_{\mathfrak{B}_1/P}\times\bar{\omega}_{\mathrm{S/I}})+\bar{r}_{\mathfrak{B}_1/P}\times(\bar{\omega}_{\mathrm{B}_1/\mathrm{I}}\times\sum_{i=1}^{N_1} m_i\bar{r}_{m_i/\mathfrak{B}_1})$$

$$+\sum_{i=1}^{N_1} m_i\bar{r}_{m_i/\mathfrak{B}_1}\times\bar{v}_{\mathfrak{B}_1/\mathrm{S}}+\sum_{i=1}^{N_1} m_i\bar{r}_{m_i/\mathfrak{B}_1}\times(\bar{\omega}_{\mathrm{S/I}}\times\bar{r}_{\mathfrak{B}_1/P})-\sum_{i=1}^{N_1} m_i\bar{r}_{m_i/\mathfrak{B}_1}\times(\bar{r}_{m_i/\mathfrak{B}_1}\times\bar{\omega}_{\mathrm{B}_1/\mathrm{I}}),$$

where m_1 is the total mass of the N_1 particles. Note that the third, fourth, and fifth terms are zero because $\sum_{i=1}^{N_1} m_i\bar{r}_{m_i/\mathfrak{B}_1} = 0$. Using the identity $\bar{\omega}_{\mathrm{B}_1/\mathrm{I}} = \bar{\omega}_{\mathrm{B}_1/\mathrm{S}} + \omega_{\mathrm{S/I}}$ yields

$$\sum_{i=1}^{N_1} (\bar{r}_{\mathfrak{B}_1/P} + \bar{r}_{m_i/\mathfrak{B}_1}) \times m_i(\frac{^{\mathrm{I}}\mathrm{d}\bar{r}_{\mathfrak{B}_1/P}}{\mathrm{d}t} + \frac{^{\mathrm{I}}\mathrm{d}\bar{r}_{m_i/\mathfrak{B}_1}}{\mathrm{d}t})$$

$$= \bar{r}_{\mathfrak{B}_1/P} \times m_1\bar{v}_{\mathfrak{B}_1/\mathrm{S}} - m_1\bar{r}_{\mathfrak{B}_1/P} \times (\bar{r}_{\mathfrak{B}_1/P} \times \bar{\omega}_{\mathrm{S/I}}) - \sum_{i=1}^{N_1} m_i\bar{r}_{m_i/\mathfrak{B}_1} \times (\bar{r}_{m_i/\mathfrak{B}_1} \times \bar{\omega}_{\mathrm{B}_1/\mathrm{S}})$$

$$- \sum_{i=1}^{N_1} m_i\bar{r}_{m_i/\mathfrak{B}_1} \times (\bar{r}_{m_i/\mathfrak{B}_1} \times \bar{\omega}_{\mathrm{S/I}})$$

$$= \bar{r}_{\mathfrak{B}_1/P} \times m_1\bar{v}_{\mathfrak{B}_1/\mathrm{S}} - m_1\bar{r}_{\mathfrak{B}_1/P} \times (\bar{r}_{\mathfrak{B}_1/P} \times \bar{\omega}_{\mathrm{S/I}}) + {}^{\mathfrak{B}_1}\bar{I}_{\mathrm{B}_1}\bar{\omega}_{\mathrm{B}_1/\mathrm{S}} + {}^{\mathfrak{B}_1}\bar{I}_{\mathrm{B}_1}\bar{\omega}_{\mathrm{S/I}}$$

where ${}^{Y}\bar{I}_{\mathrm{X}}$ is the inertia matrix of body X about point Y. Thus, using the *Parallel Axis Theorem*, ${}^{\mathfrak{B}_1}\bar{I}_{\mathrm{B}_1}\bar{\omega}_{\mathrm{S/I}} - m_1\bar{r}_{\mathfrak{B}_1/P} \times (\bar{r}_{\mathfrak{B}_1/P} \times \bar{\omega}_{\mathrm{S/I}}) = {}^{P}\bar{I}_{\mathrm{B}_1}\bar{\omega}_{\mathrm{S/I}}$ and

$$\sum_{i=1}^{N_1} \bar{r}_{m_i/P} \times m_i\frac{^{\mathrm{I}}\mathrm{d}\bar{r}_{m_i/P}}{\mathrm{d}t} = {}^{P}\bar{I}_{\mathrm{B}_1}\bar{\omega}_{\mathrm{S/I}} + {}^{\mathfrak{B}_1}\bar{I}_{\mathrm{B}_1}\bar{\omega}_{\mathrm{B}_1/\mathrm{S}} + \bar{r}_{\mathfrak{B}_1/P} \times m_1\bar{v}_{\mathfrak{B}_1/\mathrm{S}}. \tag{173}$$

Note that the same analysis for the N_2 particles would have yielded

$$\sum_{i=1}^{N_2} \bar{r}_{m_i/P} \times m_i\frac{^{\mathrm{I}}\mathrm{d}\bar{r}_{m_i/P}}{\mathrm{d}t} = {}^{P}\bar{I}_{\mathrm{B}_2}\bar{\omega}_{\mathrm{S/I}} + {}^{\mathfrak{B}_2}\bar{I}_{\mathrm{B}_2}\bar{\omega}_{\mathrm{B}_2/\mathrm{S}} + \bar{r}_{\mathfrak{B}_2/P} \times m_2\bar{v}_{\mathfrak{B}_2/\mathrm{S}}. \tag{174}$$

Finally, Eq. (171) is equal to the sum of Eqs. (173) and (174), i.e.,

$$
\begin{aligned}
{}^{P}\bar{H}_{\text{system/I}} &= {}^{P}\bar{I}_{\text{B}_1}\bar{\omega}_{\text{S/I}} + {}^{\spadesuit_1}\bar{I}_{\text{B}_1}\bar{\omega}_{\text{B}_1/\text{S}} + \bar{r}_{\spadesuit_1/P}\times m_1\bar{v}_{\spadesuit_1/\text{S}} + {}^{P}\bar{I}_{\text{B}_2}\bar{\omega}_{\text{S/I}} + {}^{\spadesuit_2}\bar{I}_{\text{B}_2}\bar{\omega}_{\text{B}_2/\text{S}} + \bar{r}_{\spadesuit_2/P}\times m_2\bar{v}_{\spadesuit_2/\text{S}} \\
&= {}^{P}\bar{I}_{\text{B}_1+\text{B}_2}\bar{\omega}_{\text{S/I}} + {}^{\spadesuit_1}\bar{I}_{\text{B}_1}\bar{\omega}_{\text{B}_1/\text{S}} + {}^{\spadesuit_2}\bar{I}_{\text{B}_2}\bar{\omega}_{\text{B}_2/\text{S}} + \bar{r}_{\spadesuit_1/P}\times m_1\bar{v}_{\spadesuit_1/\text{S}} + \bar{r}_{\spadesuit_2/P}\times m_2\bar{v}_{\spadesuit_2/\text{S}}. \qquad (175)
\end{aligned}
$$

Note that is rather trivial to extend this result to a system with more than two groups of particles.

6.1.2 Reference Frames

The following reference frames are defined for the 5-DOF platform:

- Inertial reference frame or I-frame: reference frame with $\bar{K}_{\text{I}}$ aligned with the gravity acceleration vector $\bar{g}$, $\bar{I}_{\text{I}}$ and $\bar{J}_{\text{I}}$ aligned as shown in Figure 46, and origin at the point of the epoxy floor shown in Figure 46.

- Upper stage reference frame or S-frame: reference frame with $\bar{I}_{\text{S}}$ parallel to the surface of the upper stage bus and pointing in the direction of VSCMG 1, $\bar{J}_{\text{S}}$ parallel to the surface of the upper stage bus and pointing in the direction of VSCMG 2, $\bar{K}_{\text{S}}$ completing the right-hand frame, and origin at the center of rotation (illustrated in Figure 47).

- Upper stage bus reference frame or F-frame: reference frame with the same orientation as the S-frame and origin at the center of mass of the upper stage bus (does not include the gimbals and the wheels of the VSCMGs) (illustrated in Figure 48).

- Lower stage reference frame or L-frame: reference frame with $\bar{K}_{\text{L}}$ parallel to the vertical column of the lower stage and pointing down, $\bar{I}_{\text{L}}$ fixed to a certain point of the lower stage, $\bar{J}_{\text{L}}$ completing the right-hand frame, and origin at the center of rotation (illustrated in Figure 49).

- Ground reference frame or G-frame: reference frame with $\bar{K}_{\mathrm{G}}$ orthogonal to the floor at point Q (point along $\bar{K}_{\mathrm{L}}$) and pointing down, $\bar{I}_{\mathrm{G}}$ tangent to the floor and in the $\bar{I}_{\mathrm{I}} - \bar{K}_{\mathrm{I}}$ plane, $\bar{J}_{\mathrm{G}}$ tangent to the floor and in the $\bar{J}_{\mathrm{I}} - \bar{K}_{\mathrm{I}}$ plane, and origin at point Q (illustrated in Figure 49).

- Gimbal i reference frame or G_i-frame: reference frame with $\bar{I}_{\mathrm{G}_i}$ along the axis of rotation of gimbal i, $\bar{J}_{\mathrm{G}_i}$ along the axis of rotation of wheel i (inside gimbal i), $\bar{K}_{\mathrm{G}_i}$ completing the right-hand frame, and origin at the center of mass of gimbal i (illustrated in Figure 48).

- Wheel i reference frame or W_i-frame: reference frame with $\bar{J}_{\mathrm{W}_i}$ along the axis of rotation of wheel i, $\bar{I}_{\mathrm{W}_i}$ fixed to a certain point of wheel i, $\bar{K}_{\mathrm{W}_i}$ completing the right-hand frame, and origin at the center of mass of wheel i (illustrated in Figure 48).

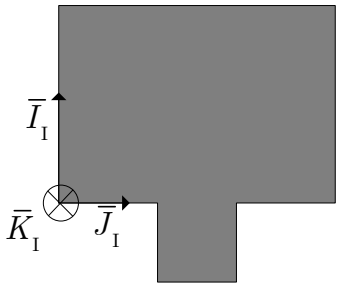

Figure 46: Definition of the I-frame with respect to the epoxy floor.

6.1.3 Assumptions

The following assumptions are made in the derivation of the equations of motion.

1) The bus of the upper stage (not including the gimbals and the wheels of the VSCMGs), the gimbals of the VSCMGs (not including the wheels of the VSCMGs), the wheels of the VSCMGs, and the lower stage are assumed to be rigid bodies.

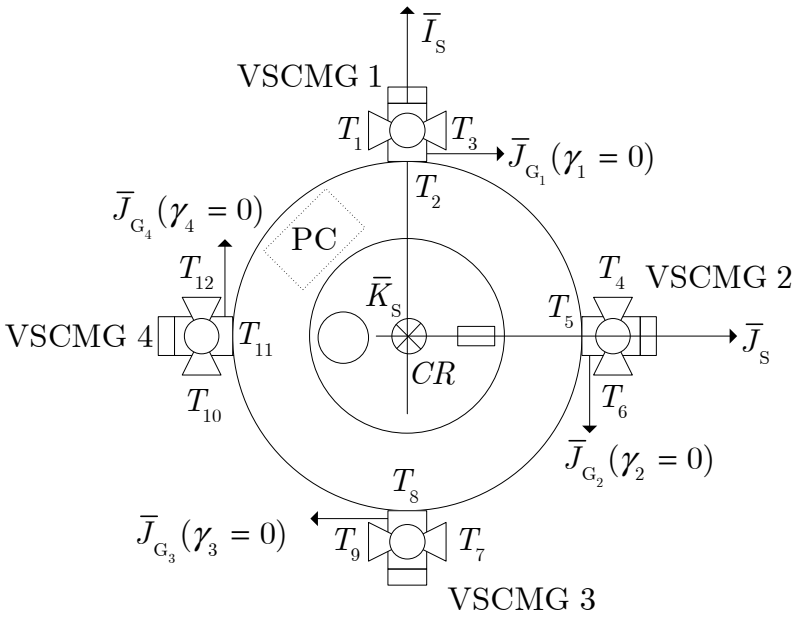

Figure 47: Definition of the S-frame with respect to the upper stage.

2) The mass of the bus of the upper stage (not including the gimbals and the wheels of the VSCMGs), the mass of the gimbals of the VSCMGs (not including the wheels of the VSCMGs), the mass of the wheels of the VSCMGs, and the mass of the lower stage are assumed to be constant. Note that assuming that the masses of the upper stage bus and of the lower stage are constant implies assuming that the change in mass due to the depletion of the air-bottles is negligible. Table 12 shows the maximum air-mass that the air-bottles of the upper stage bus and lower stage can take. This mass is deemed small when compared to the mass

Table 12: Maximum air-mass that the air-bottles of the upper stage bus and lower stage can take, assuming ideal gas and an air temperature of 298.15 K.

	Lower Stage	Upper Stage
Volume (in^3)	3×1000	2×225
Maximum Pressure (psi)	3300	2500
Maximum Air-Mass (kg)	13.1	1.5

of the upper stage bus and of the lower stage.

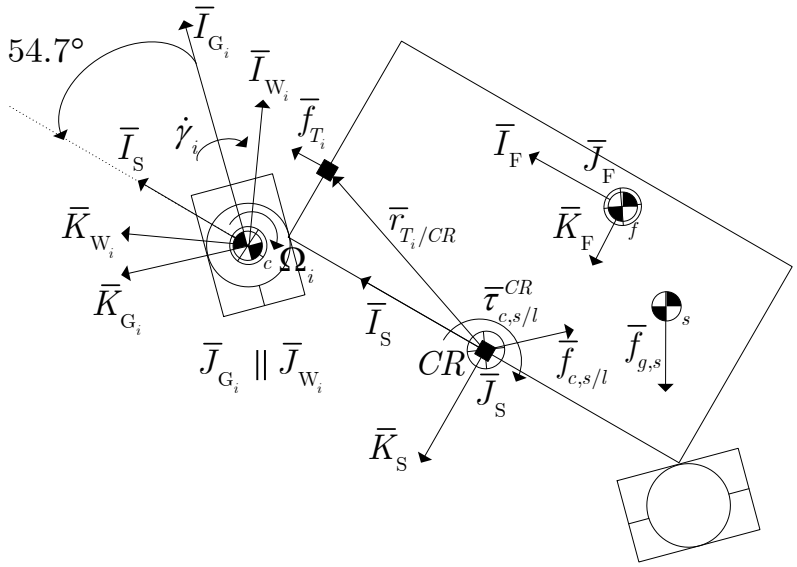

Figure 48: Free-body diagram of the upper stage.

3) The centers of mass of the gimbals and wheels of the VSCMGs cannot move with respect to the center of rotation.

4) The center of mass of gimbal i and the center of mass of wheel i have the same position.

5) The vector perpendicular to the floor at point Q is always parallel to the vertical column of the lower stage. In particular, this implies that $\bar{K}_{\mathrm{L}}$ and $\bar{K}_{\mathrm{G}}$ are parallel.

6) The angular velocity of the G-frame with respect to the I-frame can be neglected. In particular, this implies that the angular velocity of the L-frame with respect to the I-frame is equal to the angular velocity of the L-frame with respect to the G-frame.

7) The contact force between the lower stage and the floor is applied at point Q.

8) The epoxy floor is frictionless (This assumption can be easily removed if a model for the friction of the epoxy floor is available.) In particular, this assumption

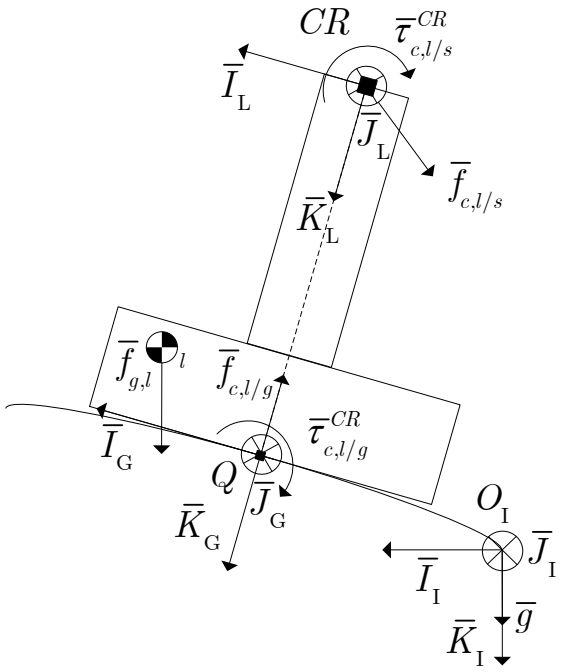

Figure 49: Free-body diagram of the lower stage.

implies that the contact force between the lower stage and the floor has no components along $\bar{I}_{\mathrm{L}}$ and $\bar{J}_{\mathrm{L}}$ and that the contact moment between the lower stage and the floor has no component along $\bar{K}_{\mathrm{L}}$

9) The axes of the G_i-frame are principal axes of gimbal i.

10) The axes of the W_i-frame are principal axes of wheel i.

11) The inertia matrix of the upper stage bus (does not include the gimbals and the wheels of the VSCMGs) about the center of rotation expressed in the S-frame does not change with time (this assumption can be easily removed if a model for this time variation is available).

12) The inertia matrix of the lower stage about the center of rotation expressed in the L-frame does not change with time (this assumption can be easily removed if a model for this time variation is available).

13) In the 3-DOF case and in the 5-DOF case, the contact moments between the

upper stage and the lower stage are assumed to be zero. (However, the contact forces are NOT assumed to be zero.)

14) The center of rotation is a point of both the upper stage and the lower stage. (In particular, this implies that the upper stage cannot move in a direction perpendicular to the floor with respect to the lower stage.)

15) When coding the equations of motion and in the control allocation block, the forces due to the thrusters are assumed to be parallel to the axes of the S-frame. This assumption is only made when coding the equations of motion and in the control allocation block. It is not used in the derivation of the equations of motion.

16) The closed-loop dynamics of the control systems that drive the wheels and gimbals of the VSCMGs are not modeled.

Note that the equations of motion take into account the following effects.

1) The center of mass of the upper stage bus (does not include the gimbals and the wheels of the VSCMGs) and therefore the center of mass of the upper stage (includes the gimbals and the wheels of the VSCMGs) can move with respect to the center of rotation.

2) The center of mass of the lower stage can move with respect to the center of rotation.

3) The epoxy floor is NOT perfectly flat.

6.1.4 Equations of Motion of the Upper Stage

6.1.4.1 Translational Motion

From classical Newton/Euler dynamics, the translational dynamic equations of the center of mass of the upper stage (including the gimbals and the wheels of the

VSCMGs) are given by

$$m_s \bar{a}_{\mathbf{o}_s/\mathrm{I}} = \bar{f}_{g,s} + \bar{f}_{c,s/l} + \sum_{i=1}^{12} \bar{f}_{T_i}, \tag{176}$$

where $\bar{a}_{Y/\mathrm{X}}$ is the acceleration vector of point Y with respect to reference frame X, m_* is the mass of $*$, $\mathbf{o}_*$ is the center of mass of $*$, $\bar{f}_{g,*}$ is the gravitational force acting on $*$, $\bar{f}_{c,*/\#}$ is the contact force acting on $*$ due to $\#$, and $\bar{f}_{T_i}$ is the force due to thruster i. The symbols $*$ and $\#$ will be replaced by the symbols s, f, l, g, w_i, g_i, c_i when representing the upper stage (including the gimbals and wheels of the VSCMGs), the upper stage bus (which does not include the gimbals and the wheels of the VSCMGs), the lower stage, the ground, the wheel of VSCMG i, the gimbal of VSCMG i (without the wheel), and the wheel and gimbal of VSCMG i together. The acceleration of the center of mass of the upper stage with respect to the inertial frame can be rewritten in terms of the acceleration of the center of rotation, point CR, with respect to the inertial frame as follows:

$$\begin{aligned} & m_s(\bar{a}_{CR/\mathrm{I}} + \bar{a}_{\mathbf{o}_s/\mathrm{S}} + \frac{{}^{\mathrm{S}}\mathrm{d}\bar{\omega}_{\mathrm{S/I}}}{\mathrm{d}t} \times \bar{r}_{\mathbf{o}_s/CR} + 2(\bar{\omega}_{\mathrm{S/I}} \times \bar{v}_{\mathbf{o}_s/\mathrm{S}}) + \bar{\omega}_{\mathrm{S/I}} \times (\bar{\omega}_{\mathrm{S/I}} \times \bar{r}_{\mathbf{o}_s/CR})) \\ & = \bar{f}_{g,s} + \bar{f}_{c,s/l} + \sum_{i=1}^{12} \bar{f}_{T_i}. \end{aligned} \tag{177}$$

6.1.4.2 Rotational Motion

From classical Newton/Euler dynamics, the rotational dynamic equations of the system composed by the upper stage bus (not including the gimbals and wheels of the VSCMGs) and the gimbals and the wheels of the VSCMGs about the center of rotation (which moves with respect to the inertial frame) are given by

$$\frac{{}^{\mathrm{I}}\mathrm{d}^{CR}\bar{H}_{\mathrm{system/I}}}{\mathrm{d}t} + \bar{r}_{\mathbf{o}_s/CR} \times m_s \bar{a}_{CR/\mathrm{I}} = \bar{r}_{\mathbf{o}_s/CR} \times \bar{f}_{g,s} + \sum_{i=1}^{12} \bar{r}_{T_i/CR} \times \bar{f}_{T_i} + {}^{CR}\bar{\tau}_{c,s/l}, \tag{178}$$

where ${}^{P}\bar{\tau}_{c,*/\#}$ is the contact moment vector on $*$ due to $\#$ about point P. Note that ${}^{CR}\bar{\tau}_{c,s/l}$ is assumed to be zero in the 5-DOF case and in the 3-DOF case, but not in

the (2+1)-DOF case. Using Eq. (175), ${}^{CR}\bar{H}_{\text{system/I}}$ can be calculated as follows:

$$
\begin{aligned}
{}^{CR}\bar{H}_{\text{system/I}} = {}^{CR}\bar{I}_s\bar{\omega}_{\text{S/I}} + {}^{\bullet_f}\bar{I}_f\bar{\omega}_{\text{F/S}} + \sum_{i=1}^{4} {}^{\bullet_{w_i}}\bar{I}_{w_i}\bar{\omega}_{\text{W}_i\text{/S}} + \sum_{i=1}^{4} {}^{\bullet_{g_i}}\bar{I}_{g_i}\bar{\omega}_{\text{G}_i\text{/S}} \\
+ \bar{r}_{\bullet_f/CR} \times (m_f\bar{v}_{\bullet_f\text{/S}}) + \sum_{i=1}^{4} \bar{r}_{\bullet_{w_i}/CR} \times (m_{w_i}\bar{v}_{\bullet_{w_i}\text{/S}}) + \sum_{i=1}^{4} \bar{r}_{\bullet_{g_i}/CR} \times (m_{g_i}\bar{v}_{\bullet_{g_i}\text{/S}}),
\end{aligned}
$$

where ${}^{P}\bar{I}_*$ is the inertia matrix of $*$ about point P. This equation can be simplified by noting that $\bar{\omega}_{\text{F/S}} = 0$ and $\bar{\omega}_{\text{W}_i\text{/S}} = \bar{\omega}_{\text{W}_i\text{/G}_i} + \bar{\omega}_{\text{G}_i\text{/S}}$ and assuming that the centers of mass of the gimbals coincide with the centers of mass of the wheels and that the centers of mass of the wheels and of the gimbals do not move with respect to the S-frame (which implies that $m_f\bar{v}_{\bullet_f\text{/S}} = m_s\bar{v}_{\bullet_s\text{/S}}$). This yields

$$
{}^{CR}\bar{H}_{\text{system/I}} = {}^{CR}\bar{I}_s\bar{\omega}_{\text{S/I}} + \sum_{i=1}^{4} {}^{\bullet_{c_i}}\bar{I}_{w_i}\bar{\omega}_{\text{W}_i\text{/G}_i} + \sum_{i=1}^{4} {}^{\bullet_{c_i}}\bar{I}_{c_i}\bar{\omega}_{\text{G}_i\text{/S}} + \bar{r}_{\bullet_f/CR} \times (m_s\bar{v}_{\bullet_s\text{/S}}). \quad (179)
$$

The I-frame time derivative of the previous equation is given by

$$
\begin{aligned}
&\frac{{}^{\text{I}}\text{d}\,{}^{CR}\bar{H}_{\text{system/I}}}{\text{d}t} = \frac{{}^{\text{S}}\text{d}\,{}^{CR}\bar{H}_{\text{system/I}}}{\text{d}t} + \bar{\omega}_{\text{S/I}} \times {}^{CR}\bar{H}_{\text{system/I}} \\
&= \frac{{}^{\text{S}}\text{d}\,{}^{CR}\bar{I}_s}{\text{d}t}\bar{\omega}_{\text{S/I}} + {}^{CR}\bar{I}_s\frac{{}^{\text{S}}\text{d}\bar{\omega}_{\text{S/I}}}{\text{d}t} + \frac{{}^{\text{S}}\text{d}}{\text{d}t}\sum_{i=1}^{4} {}^{\bullet_{c_i}}\bar{I}_{w_i}\bar{\omega}_{\text{W}_i\text{/G}_i} + \frac{{}^{\text{S}}\text{d}}{\text{d}t}\sum_{i=1}^{4} {}^{\bullet_{c_i}}\bar{I}_{c_i}\bar{\omega}_{\text{G}_i\text{/S}} + \bar{r}_{\bullet_f/CR} \times (m_s\bar{a}_{\bullet_s\text{/S}}) \\
&+ \bar{\omega}_{\text{S/I}} \times \Big({}^{CR}\bar{I}_s\bar{\omega}_{\text{S/I}} + \sum_{i=1}^{4} {}^{\bullet_{c_i}}\bar{I}_{w_i}\bar{\omega}_{\text{W}_i\text{/G}_i} + \sum_{i=1}^{4} {}^{\bullet_{c_i}}\bar{I}_{c_i}\bar{\omega}_{\text{G}_i\text{/S}} + \bar{r}_{\bullet_f/CR} \times (m_s\bar{v}_{\bullet_s\text{/S}})\Big). \quad (180)
\end{aligned}
$$

Finally, combining Eq. (180) with Eq. (178) yields

$$
\begin{aligned}
&\frac{{}^{\text{S}}\text{d}\,{}^{CR}\bar{I}_s}{\text{d}t}\bar{\omega}_{\text{S/I}} + {}^{CR}\bar{I}_s\frac{{}^{\text{S}}\text{d}\bar{\omega}_{\text{S/I}}}{\text{d}t} + \frac{{}^{\text{S}}\text{d}}{\text{d}t}\sum_{i=1}^{4} {}^{\bullet_{c_i}}\bar{I}_{w_i}\bar{\omega}_{\text{W}_i\text{/G}_i} + \frac{{}^{\text{S}}\text{d}}{\text{d}t}\sum_{i=1}^{4} {}^{\bullet_{c_i}}\bar{I}_{c_i}\bar{\omega}_{\text{G}_i\text{/S}} + \bar{r}_{\bullet_f/CR} \times (m_s\bar{a}_{\bullet_s\text{/S}}) \\
&+ \bar{\omega}_{\text{S/I}} \times ({}^{CR}\bar{I}_s\bar{\omega}_{\text{S/I}} + \sum_{i=1}^{4} {}^{\bullet_{c_i}}\bar{I}_{w_i}\bar{\omega}_{\text{W}_i\text{/G}_i} + \sum_{i=1}^{4} {}^{\bullet_{c_i}}\bar{I}_{c_i}\bar{\omega}_{\text{G}_i\text{/S}} + \bar{r}_{\bullet_f/CR} \times (m_s\bar{v}_{\bullet_s\text{/S}})) + \bar{r}_{\bullet_s/CR} \times m_s\bar{a}_{CR/\text{I}} \\
&= \bar{r}_{\bullet_s/CR} \times \bar{f}_{g,s} + \sum_{i=1}^{12} \bar{r}_{T_i/CR} \times \bar{f}_{T_i} + {}^{CR}\bar{\tau}_{c,s/l}. \quad (181)
\end{aligned}
$$

6.1.5 Equations of Motion of the Lower Stage

6.1.5.1 Translational Motion

From classical Newton/Euler dynamics, the translational dynamic equations of the center of mass of the lower stage are given by

$$m_l \bar{a}_{\mathfrak{o}_l/\mathrm{I}} = \bar{f}_{g,l} + \bar{f}_{c,l/s} + \bar{f}_{c,l/g}. \tag{182}$$

The acceleration of the center of mass of the lower stage with respect to the inertial frame can be rewritten in terms of the acceleration of the center of rotation, point CR, with respect to the inertial frame as follows (using $\bar{f}_{c,l/s} = -\bar{f}_{c,s/l}$)

$$\begin{aligned} &m_l(\bar{a}_{CR/\mathrm{I}} + \bar{a}_{\mathfrak{o}_l/\mathrm{L}} + \frac{{}^{\mathrm{L}}\mathrm{d}\bar{\omega}_{\mathrm{L/I}}}{\mathrm{d}t} \times \bar{r}_{\mathfrak{o}_l/CR} + 2(\bar{\omega}_{\mathrm{L/I}} \times \bar{v}_{\mathfrak{o}_l/\mathrm{L}}) + \bar{\omega}_{\mathrm{L/I}} \times (\bar{\omega}_{\mathrm{L/I}} \times \bar{r}_{\mathfrak{o}_l/CR})) \\ &= \bar{f}_{g,l} - \bar{f}_{c,s/l} + \bar{f}_{c,l/g}. \end{aligned} \tag{183}$$

6.1.5.2 Rotational Motion

From classical Newton/Euler dynamics, the rotational dynamic equations of the lower stage about the center of rotation (which moves with respect to the inertial frame) are given by

$$\frac{{}^{\mathrm{I}}\mathrm{d}{}^{CR}\bar{H}_{l/\mathrm{I}}}{\mathrm{d}t} + \bar{r}_{\mathfrak{o}_l/CR} \times m_l \bar{a}_{CR/\mathrm{I}} = \bar{r}_{\mathfrak{o}_l/CR} \times \bar{f}_{g,l} + {}^{CR}\bar{\tau}_{c,l/s} + {}^{CR}\bar{\tau}_{c,l/g} + \bar{r}_{Q/CR} \times \bar{f}_{c,l/g}. \tag{184}$$

Note that ${}^{CR}\bar{\tau}_{c,l/s} = -{}^{CR}\bar{\tau}_{c,s/l}$. Moreover, the epoxy floor is assumed to be frictionless. Hence, the only non-zero component of $\bar{f}_{c,l/g}$ is along $\bar{K}_{\mathrm{L}}$ and, thus, $\bar{r}_{Q/CR} \times \bar{f}_{c,l/g} = 0$. Using Eq. (175), ${}^{CR}\bar{H}_{l/\mathrm{I}}$ can be calculated as follows:

$${}^{CR}\bar{H}_{l/\mathrm{I}} = {}^{CR}\bar{I}_l \bar{\omega}_{\mathrm{L/I}} + \bar{r}_{\mathfrak{o}_l/CR} \times (m_l \bar{v}_{\mathfrak{o}_l/\mathrm{L}}). \tag{185}$$

Its I-frame time derivative is equal to

$$\begin{aligned} &\frac{{}^{\mathrm{I}}\mathrm{d}{}^{CR}\bar{H}_{l/\mathrm{I}}}{\mathrm{d}t} = \frac{{}^{\mathrm{L}}\mathrm{d}{}^{CR}\bar{H}_{l/\mathrm{I}}}{\mathrm{d}t} + \bar{\omega}_{\mathrm{L/I}} \times {}^{CR}\bar{H}_{l/\mathrm{I}} \\ &= \frac{{}^{\mathrm{L}}\mathrm{d}{}^{CR}\bar{I}_l}{\mathrm{d}t}\bar{\omega}_{\mathrm{L/I}} + {}^{CR}\bar{I}_l \frac{{}^{\mathrm{L}}\mathrm{d}\bar{\omega}_{\mathrm{L/I}}}{\mathrm{d}t} + \bar{r}_{\mathfrak{o}_l/CR} \times (m_l \bar{a}_{\mathfrak{o}_l/\mathrm{L}}) + \bar{\omega}_{\mathrm{L/I}} \times \big({}^{CR}\bar{I}_l \bar{\omega}_{\mathrm{L/I}} + \bar{r}_{\mathfrak{o}_l/CR} \times (m_l \bar{v}_{\mathfrak{o}_l/\mathrm{L}})\big). \end{aligned}$$

Finally, combining the previous equation with Eq. (184) and assuming that $\frac{^{\mathrm{L}}\mathrm{d}}{\mathrm{d}t}({}^{CR}\bar{I}_l) = 0$ yields

$$
\begin{aligned}
&{}^{CR}\bar{I}_l \frac{^{\mathrm{L}}\mathrm{d}\bar{\omega}_{\mathrm{L/I}}}{\mathrm{d}t} + \bar{r}_{\bullet_l/CR} \times (m_l \bar{a}_{\bullet_l/\mathrm{L}}) + \bar{\omega}_{\mathrm{L/I}} \times \left({}^{CR}\bar{I}_l \bar{\omega}_{\mathrm{L/I}} + \bar{r}_{\bullet_l/CR} \times (m_l \bar{v}_{\bullet_l/\mathrm{L}}) \right) \\
&+ \bar{r}_{\bullet_l/CR} \times m_l \bar{a}_{CR/\mathrm{I}} = \bar{r}_{\bullet_l/CR} \times \bar{f}_{g,l} - {}^{CR}\bar{\tau}_{c,s/l} + {}^{CR}\bar{\tau}_{c,l/g}. \qquad (186)
\end{aligned}
$$

6.1.6 Equations of Motion for the 3-DOF case

The equations of motion when the lower stage is fixed with respect to the inertial frame and only the upper stage is allowed to rotate with respect to the inertial frame are given by Eq. (181). In this case, $\bar{a}_{CR/\mathrm{I}} = 0$. Moreover, the connection between the upper stage and the lower stage is assumed to be frictionless, i.e., ${}^{CR}\bar{\tau}_{c,s/l} = 0$. With this simplifications, Eq. (181) becomes

$$
\begin{aligned}
&\frac{^{\mathrm{S}}\mathrm{d}{}^{CR}\bar{I}_s}{\mathrm{d}t}\bar{\omega}_{\mathrm{S/I}} + {}^{CR}\bar{I}_s \frac{^{\mathrm{S}}\mathrm{d}\bar{\omega}_{\mathrm{S/I}}}{\mathrm{d}t} + \frac{^{\mathrm{S}}\mathrm{d}}{\mathrm{d}t} \sum_{i=1}^{4} {}^{\bullet_{c_i}}\bar{I}_{w_i} \bar{\omega}_{\mathrm{W}_i/\mathrm{G}_i} + \frac{^{\mathrm{S}}\mathrm{d}}{\mathrm{d}t} \sum_{i=1}^{4} {}^{\bullet_{c_i}}\bar{I}_{c_i} \bar{\omega}_{\mathrm{G}_i/\mathrm{S}} + \bar{r}_{\bullet_f/CR} \times (m_s \bar{a}_{\bullet_s/\mathrm{S}}) \\
&+ \bar{\omega}_{\mathrm{S/I}} \times \left({}^{CR}\bar{I}_s \bar{\omega}_{\mathrm{S/I}} + \sum_{i=1}^{4} {}^{\bullet_{c_i}}\bar{I}_{w_i} \bar{\omega}_{\mathrm{W}_i/\mathrm{G}_i} + \sum_{i=1}^{4} {}^{\bullet_{c_i}}\bar{I}_{c_i} \bar{\omega}_{\mathrm{G}_i/\mathrm{S}} + \bar{r}_{\bullet_f/CR} \times (m_s \bar{v}_{\bullet_s/\mathrm{S}}) \right) \\
&= \bar{r}_{\bullet_s/CR} \times \bar{f}_{g,s} + \sum_{i=1}^{12} \bar{r}_{T_i/CR} \times \bar{f}_{T_i}. \qquad (187)
\end{aligned}
$$

Note that the previous equation is in a vector form. For numerical implementation, it will be rewritten in the S-frame. In what follows, $\bar{y}^{\mathrm{X}}$ denotes the vector $\bar{y}$ expressed in the X-frame and $\bar{I}^{\mathrm{X}}$ denotes the inertia matrix $\bar{I}$ expressed in the X-frame. First, note that

$$
\sum_{i=1}^{4} {}^{\bullet_{c_i}}\bar{I}^{\mathrm{S}}_{c_i} \bar{\omega}^{\mathrm{S}}_{\mathrm{G}_i/\mathrm{S}} = A_g I_{cg} \dot{\gamma}, \qquad (188)
$$

where $A_g = [\bar{I}^{\mathrm{S}}_{\mathrm{G}_1}, \bar{I}^{\mathrm{S}}_{\mathrm{G}_2}, \bar{I}^{\mathrm{S}}_{\mathrm{G}_3}, \bar{I}^{\mathrm{S}}_{\mathrm{G}_4}]$, $I_{cg} = \mathrm{diag}([{}^{\bullet_{c_1}}I^{\mathrm{G}_1}_{c_1,11}, {}^{\bullet_{c_2}}I^{\mathrm{G}_2}_{c_2,11}, {}^{\bullet_{c_3}}I^{\mathrm{G}_3}_{c_3,11}, {}^{\bullet_{c_4}}I^{\mathrm{G}_4}_{c_4,11}])$, $\dot{\gamma} = [\dot{\gamma}_1, \dot{\gamma}_2, \dot{\gamma}_3, \dot{\gamma}_4]^{\mathsf{T}}$, $\bar{I}^{\mathrm{S}}_{\mathrm{G}_i}$ is the unit vector $\bar{I}_{\mathrm{G}_i}$ expressed in the S-frame, $\dot{\gamma}_i$ is the angular speed of gimbal i, and

$$
{}^{\bullet_{c_i}}\bar{I}^{\mathrm{G}_i}_{c_i} = \begin{bmatrix} {}^{\bullet_{c_i}}I^{\mathrm{G}_i}_{c_i,11} & 0 & 0 \\ 0 & {}^{\bullet_{c_i}}I^{\mathrm{G}_i}_{c_i,22} & 0 \\ 0 & 0 & {}^{\bullet_{c_i}}I^{\mathrm{G}_i}_{c_i,33} \end{bmatrix} \qquad (189)
$$

is the inertia matrix of gimbal i and wheel i with respect to their (common) center of mass expressed in the G_i-frame. Note that the G_i-frame axes are assumed to be principal axes of gimbal i and wheel i. Moreover, note that

$$\sum_{i=1}^{4} {}^{\bullet_{c_i}}\bar{I}^{\mathrm{S}}_{w_i}\bar{\omega}^{\mathrm{S}}_{\mathrm{W}_i/\mathrm{G}_i} = A_s(\gamma) I_{ws}\Omega, \tag{190}$$

where $A_s(\gamma) = [\bar{J}^{\mathrm{S}}_{\mathrm{G}_1}(\gamma_1), \bar{J}^{\mathrm{S}}_{\mathrm{G}_2}(\gamma_2), \bar{J}^{\mathrm{S}}_{\mathrm{G}_3}(\gamma_3), \bar{J}^{\mathrm{S}}_{\mathrm{G}_4}(\gamma_4)]$, $\Omega = [\Omega_1, \Omega_2, \Omega_3, \Omega_4]^{\mathsf{T}}$, $\bar{J}^{\mathrm{S}}_{\mathrm{G}_i}$ is the unit vector $\bar{J}_{\mathrm{G}_i}$ expressed in the S-frame (which is a function of γ_i), Ω_i is the angular speed of wheel i, $I_{ws} = \mathrm{diag}([{}^{\bullet_{c_1}}I^{\mathrm{G}_1}_{w_1,22}, {}^{\bullet_{c_2}}I^{\mathrm{G}_2}_{w_2,22}, {}^{\bullet_{c_3}}I^{\mathrm{G}_3}_{w_3,22}, {}^{\bullet_{c_4}}I^{\mathrm{G}_4}_{w_4,22}])$, and

$${}^{\bullet_{c_i}}\bar{I}^{\mathrm{G}_i}_{w_i} = \begin{bmatrix} {}^{\bullet_{c_i}}I^{\mathrm{G}_i}_{w_i,11} & 0 & 0 \\ 0 & {}^{\bullet_{c_i}}I^{\mathrm{G}_i}_{w_i,22} & 0 \\ 0 & 0 & {}^{\bullet_{c_i}}I^{\mathrm{G}_i}_{w_i,33} \end{bmatrix} \tag{191}$$

is the inertia matrix of wheel i with respect to its center of mass expressed in the G_i-frame. Note that the G_i-frame axes are assumed to be principal axes of wheel i. Finally, note that

$$\begin{aligned} {}^{CR}\bar{I}^{\mathrm{S}}_{s} &= {}^{CR}\bar{I}^{\mathrm{S}}_{f} + \sum_{i=1}^{4} {}^{CR}\bar{I}^{\mathrm{S}}_{c_i} = {}^{CR}\bar{I}^{\mathrm{S}}_{f} + \sum_{i=1}^{4} {}^{\bullet_{c_i}}\bar{I}^{\mathrm{S}}_{c_i} - \sum_{i=1}^{4} m_{c_i}[\bar{r}^{\mathrm{S}}_{\bullet_{c_i}/CR}]^{\times}[\bar{r}^{\mathrm{S}}_{\bullet_{c_i}/CR}]^{\times} \\ &= {}^{CR}\bar{I}^{\mathrm{S}}_{f} + A_g I_{cg} A_g^{\mathsf{T}} + A_s(\gamma) I_{cs} A_s(\gamma)^{\mathsf{T}} + A_t(\gamma) I_{ct} A_t(\gamma)^{\mathsf{T}} - \sum_{i=1}^{4} m_{c_i}[\bar{r}^{\mathrm{S}}_{\bullet_{c_i}/CR}]^{\times}[\bar{r}^{\mathrm{S}}_{\bullet_{c_i}/CR}]^{\times} \\ &= {}^{CR}\bar{I}^{\mathrm{S}}_{f+m_{c_i}} + A_g I_{cg} A_g^{\mathsf{T}} + A_s(\gamma) I_{cs} A_s(\gamma)^{\mathsf{T}} + A_t(\gamma) I_{ct} A_t(\gamma)^{\mathsf{T}}, \end{aligned} \tag{192}$$

where

$${}^{CR}\bar{I}^{\mathrm{S}}_{f+m_{c_i}} = {}^{CR}\bar{I}^{\mathrm{S}}_{f} - \sum_{i=1}^{4} m_{c_i}[\bar{r}^{\mathrm{S}}_{\bullet_{c_i}/CR}]^{\times}[\bar{r}^{\mathrm{S}}_{\bullet_{c_i}/CR}]^{\times},$$

$A_t(\gamma) = [\bar{K}^{\mathrm{S}}_{\mathrm{G}_1}(\gamma_1),\ \bar{K}^{\mathrm{S}}_{\mathrm{G}_2}(\gamma_2),\ \bar{K}^{\mathrm{S}}_{\mathrm{G}_3}(\gamma_3),\ \bar{K}^{\mathrm{S}}_{\mathrm{G}_4}(\gamma_4)]$, $I_{cs} = \mathrm{diag}([{}^{\bullet_{c_1}}I^{\mathrm{G}_1}_{c_1,22},\ {}^{\bullet_{c_2}}I^{\mathrm{G}_2}_{c_2,22},\ {}^{\bullet_{c_3}}I^{\mathrm{G}_3}_{c_3,22},\ {}^{\bullet_{c_4}}I^{\mathrm{G}_4}_{c_4,22}])$, $I_{ct} = \mathrm{diag}([{}^{\bullet_{c_1}}I^{\mathrm{G}_1}_{c_1,33},\ {}^{\bullet_{c_2}}I^{\mathrm{G}_2}_{c_2,33},\ {}^{\bullet_{c_3}}I^{\mathrm{G}_3}_{c_3,33},\ {}^{\bullet_{c_4}}I^{\mathrm{G}_4}_{c_4,33}])$, and $\bar{K}^{\mathrm{S}}_{\mathrm{G}_i}$ is the unit vector $\bar{K}_{\mathrm{G}_i}$ expressed in the S-frame (which is a function of γ_i).

Calculating the time derivative of Eqs. (188), (190), and (192) using [107]

$$\dot{A}_s = A_t\,\mathrm{diag}\,(\dot{\gamma}) \text{ and } \dot{A}_t = -A_s\,\mathrm{diag}\,(\dot{\gamma}),$$

assuming that $\frac{\mathrm{d}}{\mathrm{d}t}({}^{CR}\bar{I}_f^{\mathrm{S}}) = 0$, and substituting the results into Eq. (187) expressed in the S-frame yields

$$\begin{aligned}
&\big(A_t\,\mathrm{diag}(\dot{\gamma})(I_{cs}-I_{ct})A_s^{\mathsf{T}}+A_s\,\mathrm{diag}(\dot{\gamma})(I_{cs}-I_{ct})A_t^{\mathsf{T}}\big)\bar{\omega}_{\mathrm{S/I}}^{\mathrm{S}}+{}^{CR}\bar{I}_s^{\mathrm{S}}\frac{\mathrm{d}\bar{\omega}_{\mathrm{S/I}}^{\mathrm{S}}}{\mathrm{d}t}+A_t(\gamma)I_{ws}\,\mathrm{diag}(\Omega)\dot{\gamma}\\
&+A_s(\gamma)I_{ws}\dot{\Omega}+A_gI_{cg}\ddot{\gamma}+\bar{r}_{\mathfrak{o}_f/CR}^{\mathrm{S}}\times(m_s\bar{a}_{\mathfrak{o}_s/\mathrm{S}}^{\mathrm{S}})+\bar{\omega}_{\mathrm{S/I}}^{\mathrm{S}}\times({}^{CR}\bar{I}_s^{\mathrm{S}}\bar{\omega}_{\mathrm{S/I}}^{\mathrm{S}}+A_s(\gamma)I_{ws}\Omega\\
&+A_gI_{cg}\dot{\gamma}+\bar{r}_{\mathfrak{o}_f/CR}^{\mathrm{S}}\times(m_s\bar{v}_{\mathfrak{o}_s/\mathrm{S}}^{\mathrm{S}}))=\bar{r}_{\mathfrak{o}_s/CR}^{\mathrm{S}}\times\bar{f}_{g,s}^{\mathrm{S}}+\sum_{i=1}^{12}\bar{r}_{T_i/CR}^{\mathrm{S}}\times\bar{f}_{T_i}^{\mathrm{S}},
\end{aligned}\tag{193}$$

where $\bar{f}_{g,s}^{\mathrm{S}} = m_sR^{\mathrm{S}\leftarrow\mathrm{I}}[0,0,g]^{\mathsf{T}}$, $R^{\mathrm{X}\leftarrow\mathrm{Y}}$ is the rotation matrix that transforms the coordinates of a vector from the Y-frame to the X-frame, and

$${}^{CR}\dot{\bar{I}}_s^{\mathrm{S}}(\dot{\gamma}) = A_t\,\mathrm{diag}(\dot{\gamma})(I_{cs}-I_{ct})A_s^{\mathsf{T}}+A_s\,\mathrm{diag}(\dot{\gamma})(I_{cs}-I_{ct})A_t^{\mathsf{T}}.\tag{194}$$

Note that Eq. (193) matches Eq. (9) of Ref. [107] assuming that $\bar{r}_{\mathfrak{o}_s/CR}^{\mathrm{S}} = 0$ and $\bar{f}_{T_i}^{\mathrm{S}} = 0$. Moreover, note that A_g, $A_s(\gamma)$, and $A_t(\gamma)$ can be calculated from $A_{g0} \triangleq A_g(\gamma = 0)$, $A_{s0} \triangleq A_s(\gamma = 0)$, and $A_{t0} \triangleq A_t(\gamma = 0)$ as follows [107]

$$A_g = A_{g0},\tag{195}$$

$$A_s(\gamma) = A_{s0}\,\mathrm{diag}(\cos(\gamma)) + A_{t0}\,\mathrm{diag}(\sin(\gamma)),\tag{196}$$

$$A_t(\gamma) = A_{t0}\,\mathrm{diag}(\cos(\gamma)) - A_{s0}\,\mathrm{diag}(\sin(\gamma)).\tag{197}$$

6.1.6.1 Kinematics

The quaternion representation of the kinematic equations for this case is given by

$$\dot{q}_{\mathrm{S/I}} = \tfrac{1}{2}q_{\mathrm{S/I}}\omega_{\mathrm{S/I}}^{\mathrm{S}},\tag{198}$$

where $\omega_{\mathrm{S/I}}^{\mathrm{S}} = (0, \bar{\omega}_{\mathrm{S/I}}^{\mathrm{S}})$.

6.1.7 Equations of Motion for the 5-DOF case

The equations of motion for the 5-DOF case describe the rotation of the upper stage with respect to the inertial frame and the translation of the center of rotation with respect to the inertial frame. Like in Section 6.1.6, the connection between the upper

stage and the lower stage is assumed to be frictionless, i.e., ${}^{CR}\bar{\tau}_{c,s/l} = 0$, but now $\bar{a}_{CR/\mathrm{I}} \neq 0$. From Eq. (181), the rotational motion is then described by

$$\frac{{}^{\mathrm{S}}\mathrm{d}{}^{CR}\bar{I}_s}{\mathrm{d}t}\bar{\omega}_{\mathrm{S/I}} + {}^{CR}\bar{I}_s\frac{{}^{\mathrm{S}}\mathrm{d}\bar{\omega}_{\mathrm{S/I}}}{\mathrm{d}t} + \frac{{}^{\mathrm{S}}\mathrm{d}}{\mathrm{d}t}\sum_{i=1}^{4}{}^{\bullet_{c_i}}\bar{I}_{w_i}\bar{\omega}_{\mathrm{W}_i/\mathrm{G}_i} + \frac{{}^{\mathrm{S}}\mathrm{d}}{\mathrm{d}t}\sum_{i=1}^{4}{}^{\bullet_{c_i}}\bar{I}_{c_i}\bar{\omega}_{\mathrm{G}_i/\mathrm{S}} + \bar{r}_{\bullet_f/CR}\times(m_s\bar{a}_{\bullet_s/\mathrm{S}})$$
$$+\bar{\omega}_{\mathrm{S/I}}\times\Big({}^{CR}\bar{I}_s\bar{\omega}_{\mathrm{S/I}} + \sum_{i=1}^{4}{}^{\bullet_{c_i}}\bar{I}_{w_i}\bar{\omega}_{\mathrm{W}_i/\mathrm{G}_i} + \sum_{i=1}^{4}{}^{\bullet_{c_i}}\bar{I}_{c_i}\bar{\omega}_{\mathrm{G}_i/\mathrm{S}} + \bar{r}_{\bullet_f/CR}\times(m_s\bar{v}_{\bullet_s/\mathrm{S}})\Big) + \bar{r}_{\bullet_s/CR}\times m_s\bar{a}_{CR/\mathrm{I}}$$
$$= \bar{r}_{\bullet_s/CR}\times\bar{f}_{g,s} + \sum_{i=1}^{12}\bar{r}_{T_i/CR}\times\bar{f}_{T_i}. \tag{199}$$

Note that, alternatively, Eq. (199) can be written using the time derivative with respect to the inertial frame (instead of the time derivative with respect to the S-frame) as follows:

$$\frac{{}^{\mathrm{I}}\mathrm{d}}{\mathrm{d}t}({}^{CR}\bar{I}_s\bar{\omega}_{\mathrm{S/I}}) + \frac{{}^{\mathrm{I}}\mathrm{d}}{\mathrm{d}t}(\sum_{i=1}^{4}{}^{\bullet_{c_i}}\bar{I}_{w_i}\bar{\omega}_{\mathrm{W}_i/\mathrm{G}_i}) + \frac{{}^{\mathrm{I}}\mathrm{d}}{\mathrm{d}t}(\sum_{i=1}^{4}{}^{\bullet_{c_i}}\bar{I}_{c_i}\bar{\omega}_{\mathrm{G}_i/\mathrm{S}}) + \frac{{}^{\mathrm{I}}\mathrm{d}}{\mathrm{d}t}(\bar{r}_{\bullet_f/CR}\times(m_s\bar{v}_{\bullet_s/\mathrm{S}}))$$
$$+\,\bar{r}_{\bullet_s/CR}\times m_s\bar{a}_{CR/\mathrm{I}} = \bar{r}_{\bullet_s/CR}\times\bar{f}_{g,s} + \sum_{i=1}^{12}\bar{r}_{T_i/CR}\times\bar{f}_{T_i}, \tag{200}$$

which makes it easier to compare with Eq. (1) of Ref. [14].[1]

---

[1] A different version of Eq. (200) is given in Ref. [14]. In the notation used in this document, Eq. (1) of Ref. [14] can be written as (neglecting terms due to the proof-masses considered in Ref. [14])

$$\frac{{}^{\mathrm{I}}\mathrm{d}}{\mathrm{d}t}({}^{CR}\bar{I}_s\bar{\omega}_{\mathrm{S/I}}) + \sum_{i=1}^{4}{}^{CR}\bar{I}_{w_i}\frac{{}^{\mathrm{I}}\mathrm{d}}{\mathrm{d}t}(\bar{\omega}_{\mathrm{W}_i/\mathrm{G}_i}) + \sum_{i=1}^{4}{}^{CR}\bar{I}_{c_i}\frac{{}^{\mathrm{I}}\mathrm{d}}{\mathrm{d}t}(\bar{\omega}_{\mathrm{G}_i/\mathrm{S}}) + \bar{r}_{\bullet_s/CR}\times m_s\bar{a}_{CR/\mathrm{I}}$$
$$+\,\bar{v}_{\bullet_s/\mathrm{S}}\times(m_s\bar{v}_{CR/\mathrm{I}}) + \bar{\omega}_{\mathrm{S/I}}\times(\bar{r}_{\bullet_s/CR}\times(m_s\bar{v}_{CR/\mathrm{I}})) = \bar{r}_{\bullet_s/CR}\times\bar{f}_{g,s} + \sum_{i=1}^{12}\bar{r}_{T_i/CR}\times\bar{f}_{T_i}. \tag{201}$$

The differences between Eq. (201) and Eq. (200) are:

i) In Eq. (201), $\bar{I}_{w_i}$ and $\bar{I}_{c_i}$ are inertia matrices about the center of rotation and not about the center of mass of the gimbals/wheels. This is considered to be a typo.

ii) In Eq. (201), $\frac{{}^{\mathrm{I}}\mathrm{d}({}^{CR}\bar{I}_{w_i})}{\mathrm{d}t}$ and $\frac{{}^{\mathrm{I}}\mathrm{d}({}^{CR}\bar{I}_{c_i})}{\mathrm{d}t}$ are neglected.

iii) In Eq. (201), the term $\frac{{}^{\mathrm{I}}\mathrm{d}}{\mathrm{d}t}(\bar{r}_{\bullet_f/CR}\times(m_s\bar{v}_{\bullet_s/\mathrm{S}}))$ does not appear. This can be traced to the fact that the total kinetic energy calculated in Ref. [14] does not account for terms due to $\bar{v}_{\bullet_f/\mathrm{S}}$ and $\bar{v}_{\bullet_l/\mathrm{L}}$.

iv) Two additional terms appear in Eq. (201), $\bar{v}_{\bullet_s/\mathrm{S}}\times(m_s\bar{v}_{CR/\mathrm{I}})$ and $\bar{\omega}_{\mathrm{S/I}}\times(\bar{r}_{\bullet_s/CR}\times(m_s\bar{v}_{CR/\mathrm{I}}))$. If the term $\bar{\omega}_{\mathrm{S/I}}\times(\bar{r}_{\bullet_s/CR}\times(m_s\bar{v}_{CR/\mathrm{I}}))$ is assumed to be mistyped, where the correct term should be $(\bar{\omega}_{\mathrm{S/I}}\times\bar{r}_{\bullet_s/CR})\times(m_s\bar{v}_{CR/\mathrm{I}})$, then these two additional terms can be traced to the fact that Eq. (4.157) of Ref. [65] was used to calculate Eq. (201), whereas Eq. (4.167) should have been used.

Following the same steps used in Section 6.1.6, Eq. (199) can be expressed in the S-frame as follows:

$$
\begin{aligned}
&{}^{CR}\dot{\bar{I}}^{\mathrm{S}}_{s}(\dot{\gamma})\bar{\omega}^{\mathrm{S}}_{\mathrm{S/I}}+{}^{CR}\bar{I}^{\mathrm{S}}_{s}\dot{\bar{\omega}}^{\mathrm{S}}_{\mathrm{S/I}}+A_t(\gamma)I_{ws}\,\mathrm{diag}(\Omega)\dot{\gamma}+A_s(\gamma)I_{ws}\dot{\Omega}\\
&+A_gI_{cg}\ddot{\gamma}+\bar{r}^{\mathrm{S}}_{\mathbf{o}_f/CR}\times(m_s\bar{a}^{\mathrm{S}}_{\mathbf{o}_s/\mathrm{S}})+\bar{\omega}^{\mathrm{S}}_{\mathrm{S/I}}\times\big({}^{CR}\bar{I}^{\mathrm{S}}_{s}\bar{\omega}^{\mathrm{S}}_{\mathrm{S/I}}+A_s(\gamma)I_{ws}\Omega+A_gI_{cg}\dot{\gamma}+\bar{r}^{\mathrm{S}}_{\mathbf{o}_f/CR}\times(m_s\bar{v}^{\mathrm{S}}_{\mathbf{o}_s/\mathrm{S}})\big)\\
&=\bar{r}^{\mathrm{S}}_{\mathbf{o}_s/CR}\times\bar{f}^{\mathrm{S}}_{g,s}+\sum_{i=1}^{12}\bar{r}^{\mathrm{S}}_{T_i/CR}\times\bar{f}^{\mathrm{S}}_{T_i}-\bar{r}^{\mathrm{S}}_{\mathbf{o}_s/CR}\times m_s(R^{\mathrm{S}\leftarrow\mathrm{L}}\dot{\bar{v}}^{\mathrm{L}}_{CR/\mathrm{I}})-\bar{r}^{\mathrm{S}}_{\mathbf{o}_s/CR}\times m_s(\bar{\omega}^{\mathrm{S}}_{\mathrm{L/I}}\times\bar{v}^{\mathrm{S}}_{CR/\mathrm{I}}),
\end{aligned}
\tag{202}
$$

where $R^{\mathrm{S}\leftarrow\mathrm{L}}=R^{\mathrm{S}\leftarrow\mathrm{I}}(R^{\mathrm{L}\leftarrow\mathrm{I}})^{\intercal}$.

Moreover, assuming that ${}^{CR}\bar{\tau}_{c,s/l}=0$ and expressing Eq. (186) in the L-frame results in

$$
\begin{aligned}
&{}^{CR}\bar{I}^{\mathrm{L}}_{l}\dot{\bar{\omega}}^{\mathrm{L}}_{\mathrm{L/I}}+\bar{r}^{\mathrm{L}}_{\mathbf{o}_l/CR}\times(m_l\bar{a}^{\mathrm{L}}_{\mathbf{o}_l/\mathrm{L}})+\bar{\omega}^{\mathrm{L}}_{\mathrm{L/I}}\times\big({}^{CR}\bar{I}^{\mathrm{L}}_{l}\bar{\omega}^{\mathrm{L}}_{\mathrm{L/I}}+\bar{r}^{\mathrm{L}}_{\mathbf{o}_l/CR}\times(m_l\bar{v}^{\mathrm{L}}_{\mathbf{o}_l/\mathrm{L}})\big)\\
&+\bar{r}^{\mathrm{L}}_{\mathbf{o}_l/CR}\times m_l(\dot{\bar{v}}^{\mathrm{L}}_{CR/\mathrm{I}}+\bar{\omega}^{\mathrm{L}}_{\mathrm{L/I}}\times\bar{v}^{\mathrm{L}}_{CR/\mathrm{I}})=\bar{r}^{\mathrm{L}}_{\mathbf{o}_l/CR}\times\bar{f}^{\mathrm{L}}_{g,l}+{}^{CR}\bar{\tau}^{\mathrm{L}}_{c,l/g}.
\end{aligned}
\tag{203}
$$

Finally, the translational dynamic equations of the center of rotation of the platform are composed by first rewriting Eq. (183) in terms of $\bar{f}_{c,s/l}$ and then substituting the result in Eq. (177). This yields

$$
\begin{aligned}
&m_t\bar{a}_{CR/\mathrm{I}}+m_s(\bar{a}_{\mathbf{o}_s/\mathrm{S}}+\frac{{}^{\mathrm{S}}\mathrm{d}\bar{\omega}_{\mathrm{S/I}}}{\mathrm{d}t}\times\bar{r}_{\mathbf{o}_s/CR}+2(\bar{\omega}_{\mathrm{S/I}}\times\bar{v}_{\mathbf{o}_s/\mathrm{S}})+\bar{\omega}_{\mathrm{S/I}}\times(\bar{\omega}_{\mathrm{S/I}}\times\bar{r}_{\mathbf{o}_s/CR}))\\
&+m_l(\bar{a}_{\mathbf{o}_l/\mathrm{L}}+\frac{{}^{\mathrm{L}}\mathrm{d}\bar{\omega}_{\mathrm{L/I}}}{\mathrm{d}t}\times\bar{r}_{\mathbf{o}_l/CR}+2(\bar{\omega}_{\mathrm{L/I}}\times\bar{v}_{\mathbf{o}_l/\mathrm{L}})+\bar{\omega}_{\mathrm{L/I}}\times(\bar{\omega}_{\mathrm{L/I}}\times\bar{r}_{\mathbf{o}_l/CR}))\\
&=\bar{f}_{g,s}+\bar{f}_{g,l}+\bar{f}_{c,l/g}+\sum_{i=1}^{12}\bar{f}_{T_i},
\end{aligned}
\tag{204}
$$

where $m_t=m_s+m_l$ is the total mass of the platform.[2] Expressing the previous

[2]A different version of Eq. (204) is given in Ref. [14]. In the notation used in this document, the equation given in Ref. [14] is (neglecting terms due to the proof-masses considered in Ref. [14])

$$
\begin{aligned}
&m_t\bar{a}_{CR/\mathrm{I}}+m_s(\frac{{}^{\mathrm{S}}\mathrm{d}\bar{\omega}_{\mathrm{S/I}}}{\mathrm{d}t}\times\bar{r}_{\mathbf{o}_s/CR}+(\bar{\omega}_{\mathrm{S/I}}\times\bar{v}_{\mathbf{o}_s/\mathrm{S}})+\bar{\omega}_{\mathrm{S/I}}\times(\bar{\omega}_{\mathrm{S/I}}\times\bar{r}_{\mathbf{o}_s/CR}))\\
&+m_l(\frac{{}^{\mathrm{L}}\mathrm{d}\bar{\omega}_{\mathrm{L/I}}}{\mathrm{d}t}\times\bar{r}_{\mathbf{o}_l/CR}+\bar{\omega}_{\mathrm{L/I}}\times(\bar{\omega}_{\mathrm{L/I}}\times\bar{r}_{\mathbf{o}_l/CR}))=\sum_{i=1}^{12}\bar{f}_{T_i}.
\end{aligned}
\tag{205}
$$

The differences between Eq. (205) and Eq. (204) are:

i) In Eq. (205), the terms $\bar{a}_{\mathbf{o}_s/\mathrm{S}}$, $\bar{a}_{\mathbf{o}_l/\mathrm{L}}$, and $\bar{v}_{\mathbf{o}_l/\mathrm{L}}$ are neglected.

equation in the L-frame yields

$$m_t(\dot{\bar{v}}^{\mathrm{L}}_{CR/\mathrm{I}}+\bar{\omega}^{\mathrm{L}}_{\mathrm{L/I}}\times\bar{v}^{\mathrm{L}}_{CR/\mathrm{I}})+m_s(\bar{a}^{\mathrm{L}}_{\mathbf{o}_s/\mathrm{S}}+R^{\mathrm{L}\leftarrow\mathrm{S}}\dot{\bar{\omega}}^{\mathrm{S}}_{\mathrm{S/I}}\times\bar{r}^{\mathrm{L}}_{\mathbf{o}_s/CR}+2(\bar{\omega}^{\mathrm{L}}_{\mathrm{S/I}}\times\bar{v}^{\mathrm{L}}_{\mathbf{o}_s/\mathrm{S}})+\bar{\omega}^{\mathrm{L}}_{\mathrm{S/I}}\times(\bar{\omega}^{\mathrm{L}}_{\mathrm{S/I}}\times\bar{r}^{\mathrm{L}}_{\mathbf{o}_s/CR}))$$
$$+m_l(\bar{a}^{\mathrm{L}}_{\mathbf{o}_l/\mathrm{L}}+\dot{\bar{\omega}}^{\mathrm{L}}_{\mathrm{L/I}}\times\bar{r}^{\mathrm{L}}_{\mathbf{o}_l/CR}+2(\bar{\omega}^{\mathrm{L}}_{\mathrm{L/I}}\times\bar{v}^{\mathrm{L}}_{\mathbf{o}_l/\mathrm{L}})+\bar{\omega}^{\mathrm{L}}_{\mathrm{L/I}}\times(\bar{\omega}^{\mathrm{L}}_{\mathrm{L/I}}\times\bar{r}^{\mathrm{L}}_{\mathbf{o}_l/CR}))$$
$$=\bar{f}^{\mathrm{L}}_{g,s}+\bar{f}^{\mathrm{L}}_{g,l}+\bar{f}^{\mathrm{L}}_{c,l/g}+\sum_{i=1}^{12}\bar{f}^{\mathrm{L}}_{T_i}. \tag{206}$$

If the connection between lower stage and the epoxy floor is frictionless, then the contact moment due to the floor on the lower stage is zero along $\bar{K}_{\mathrm{L}}$, i.e., ${}^{CR}\bar{\tau}^{\mathrm{L}}_{c,l/g} = [{}^{CR}\bar{\tau}^{\mathrm{L}}_{c,l/g,1}, {}^{CR}\bar{\tau}^{\mathrm{L}}_{c,l/g,2}, 0]^{\intercal}$. Under the same assumption, the contact force due to the floor on the lower stage is only nonzero along $\bar{K}_{\mathrm{L}}$, i.e., $\bar{f}^{\mathrm{L}}_{c,l/g} = [0, 0, \bar{f}^{\mathrm{L}}_{c,l/g,3}]^{\intercal}$.

Moreover, the floor constrains the angular velocity of the lower platform with respect to the G-frame to be along $\bar{K}_{\mathrm{L}}$. Since it is assumed that $\bar{\omega}_{\mathrm{G/I}} = 0$, then $\bar{\omega}^{\mathrm{L}}_{\mathrm{L/I}} = \bar{\omega}^{\mathrm{L}}_{\mathrm{L/G}} + \bar{\omega}^{\mathrm{L}}_{\mathrm{G/I}} = \bar{\omega}^{\mathrm{L}}_{\mathrm{L/G}} = [0, 0, r^{\mathrm{L}}_{\mathrm{L/I}}]^{\intercal}$. In addition, the floor constrains the velocity of the center of rotation with respect to the inertial frame to be zero along $\bar{K}_{\mathrm{L}}$, i.e., $\bar{v}^{\mathrm{L}}_{CR/\mathrm{I}} = [u^{\mathrm{L}}_{CR/\mathrm{I}}, v^{\mathrm{L}}_{CR/\mathrm{I}}, 0]^{\intercal}$.

Hence, the three coordinates of Eq. (202), the third coordinate of Eq. (203), and the first and second coordinates of Eq. (206) form a system of 6 equations and 6 unknowns: $\dot{p}^{\mathrm{S}}_{\mathrm{S/I}}$, $\dot{q}^{\mathrm{S}}_{\mathrm{S/I}}$, $\dot{r}^{\mathrm{S}}_{\mathrm{S/I}}$, $\dot{u}^{\mathrm{L}}_{CR/\mathrm{I}}$, $\dot{v}^{\mathrm{L}}_{CR/\mathrm{I}}$, and $\dot{r}^{\mathrm{L}}_{\mathrm{L/I}}$, where $\dot{\bar{\omega}}^{\mathrm{S}}_{\mathrm{S/I}} = [\dot{p}^{\mathrm{S}}_{\mathrm{S/I}}, \dot{q}^{\mathrm{S}}_{\mathrm{S/I}}, \dot{r}^{\mathrm{S}}_{\mathrm{S/I}}]^{\intercal}$, $\dot{\bar{v}}^{\mathrm{L}}_{CR/\mathrm{I}} = [\dot{u}^{\mathrm{L}}_{CR/\mathrm{I}}, \dot{v}^{\mathrm{L}}_{CR/\mathrm{I}}, 0]^{\intercal}$, and $\dot{\bar{\omega}}^{\mathrm{L}}_{\mathrm{L/I}} = [0, 0, \dot{r}^{\mathrm{L}}_{\mathrm{L/I}}]^{\intercal}$. These equations are the dynamic equations for this case.

6.1.7.1 Kinematics

The kinematic equations for the rotation of the upper stage are given by Eq. (198).

Assuming that $\bar{\omega}_{\mathrm{G/I}} = 0$, the kinematic equations for the rotation of the lower

ii) In Eq. (205), the term $(\bar{\omega}_{\mathrm{S/I}} \times \bar{v}_{\mathbf{o}_s/\mathrm{S}})$ should be multiplied by two.

iii) In Eq. (205), the floor is assumed to be perfectly flat. Since $\bar{f}_{c,l/g}$, $\bar{f}_{g,s}$, and $\bar{f}_{g,l}$ are perpendicular to the direction of motion, they are neglected in Eq. (205).

stage are given by $\bar{\omega}^{\mathrm{L}}_{\mathrm{L/I}} = \bar{\omega}^{\mathrm{L}}_{\mathrm{L/G}} + \bar{\omega}^{\mathrm{L}}_{\mathrm{G/I}} = \bar{\omega}^{\mathrm{L}}_{\mathrm{L/G}} = [0, 0, r^{\mathrm{L}}_{\mathrm{L/I}}]^{\intercal} = [0, 0, \dot{\psi}_{\mathrm{L/I}}]^{\intercal}$, or simply,

$$\dot{\psi}_{\mathrm{L/I}} = r^{\mathrm{L}}_{\mathrm{L/I}}, \tag{207}$$

where $\psi_{\mathrm{L/I}}$ is the angle from $\bar{I}_{\mathrm{G}}$ to $\bar{I}_{\mathrm{L}}$ (or from $\bar{J}_{\mathrm{G}}$ to $\bar{J}_{\mathrm{L}}$). Then, the orientation of the L-frame with respect to the I-frame can be calculated from $R^{\mathrm{L}\leftarrow\mathrm{I}} = R^{\mathrm{L}\leftarrow\mathrm{G}} R^{\mathrm{G}\leftarrow\mathrm{I}}$, where

$$R^{\mathrm{L}\leftarrow\mathrm{G}} = \begin{bmatrix} \cos(\psi_{\mathrm{L/I}}) & \sin(\psi_{\mathrm{L/I}}) & 0 \\ -\sin(\psi_{\mathrm{L/I}}) & \cos(\psi_{\mathrm{L/I}}) & 0 \\ 0 & 0 & 1 \end{bmatrix}. \tag{208}$$

If the position of point Q (the contact point between the epoxy floor and the lower stage) with respect to the origin of the inertial frame can be expressed in the inertial frame as $\bar{r}^{\mathrm{I}}_{Q/O_{\mathrm{I}}} = [x^{\mathrm{I}}_{Q/O_{\mathrm{I}}}, y^{\mathrm{I}}_{Q/O_{\mathrm{I}}}, z^{\mathrm{I}}_{Q/O_{\mathrm{I}}} = f(x^{\mathrm{I}}_{Q/O_{\mathrm{I}}}, y^{\mathrm{I}}_{Q/O_{\mathrm{I}}})]^{\intercal}$, for some function $f(x^{\mathrm{I}}_{Q/O_{\mathrm{I}}}, y^{\mathrm{I}}_{Q/O_{\mathrm{I}}})$, then the rotation matrix $R^{\mathrm{G}\leftarrow\mathrm{I}}$ is given by

$$R^{\mathrm{G}\leftarrow\mathrm{I}} = (R^{\mathrm{I}\leftarrow\mathrm{G}})^{\intercal} = \begin{bmatrix} (\bar{I}^{I}_{\mathrm{G}})^{\intercal} \\ (\bar{J}^{I}_{\mathrm{G}})^{\intercal} \\ (\bar{K}^{I}_{\mathrm{G}})^{\intercal} \end{bmatrix}, \tag{209}$$

where

$$\bar{I}^{I}_{\mathrm{G}} = \frac{[1, 0, \frac{\partial f(x^{\mathrm{I}}_{Q/O_{\mathrm{I}}}, y^{\mathrm{I}}_{Q/O_{\mathrm{I}}})}{\partial x^{\mathrm{I}}_{Q/O_{\mathrm{I}}}}\big|_{Q}]^{\intercal}}{||[1, 0, \frac{\partial f(x^{\mathrm{I}}_{Q/O_{\mathrm{I}}}, y^{\mathrm{I}}_{Q/O_{\mathrm{I}}})}{\partial x^{\mathrm{I}}_{Q/O_{\mathrm{I}}}}\big|_{Q}]^{\intercal}||}, \quad \bar{J}^{I}_{\mathrm{G}} = \frac{[0, 1, \frac{\partial f(x^{\mathrm{I}}_{Q/O_{\mathrm{I}}}, y^{\mathrm{I}}_{Q/O_{\mathrm{I}}})}{\partial y^{\mathrm{I}}_{Q/O_{\mathrm{I}}}}\big|_{Q}]^{\intercal}}{||[0, 1, \frac{\partial f(x^{\mathrm{I}}_{Q/O_{\mathrm{I}}}, y^{\mathrm{I}}_{Q/O_{\mathrm{I}}})}{\partial y^{\mathrm{I}}_{Q/O_{\mathrm{I}}}}\big|_{Q}]^{\intercal}||}, \quad \bar{K}^{I}_{\mathrm{G}} = \bar{I}^{I}_{\mathrm{G}} \times \bar{J}^{I}_{\mathrm{G}}.$$

The partial derivatives $\frac{\partial f(x^{\mathrm{I}}_{Q/O_{\mathrm{I}}}, y^{\mathrm{I}}_{Q/O_{\mathrm{I}}})}{\partial x^{\mathrm{I}}_{Q/O_{\mathrm{I}}}}\big|_{Q}$ and $\frac{\partial f(x^{\mathrm{I}}_{Q/O_{\mathrm{I}}}, y^{\mathrm{I}}_{Q/O_{\mathrm{I}}})}{\partial y^{\mathrm{I}}_{Q/O_{\mathrm{I}}}}\big|_{Q}$ have been measured at different points of the epoxy floor. In the main file of the simulation, the user can choose to linearly interpolate these measurements during the simulation or assign constant values to $\frac{\partial f(x^{\mathrm{I}}_{Q/O_{\mathrm{I}}}, y^{\mathrm{I}}_{Q/O_{\mathrm{I}}})}{\partial x^{\mathrm{I}}_{Q/O_{\mathrm{I}}}}\big|_{Q}$ and $\frac{\partial f(x^{\mathrm{I}}_{Q/O_{\mathrm{I}}}, y^{\mathrm{I}}_{Q/O_{\mathrm{I}}})}{\partial y^{\mathrm{I}}_{Q/O_{\mathrm{I}}}}\big|_{Q}$.

Finally, the kinematic equations for the translation of the center of rotation with respect to the inertial frame are given by $\dot{\bar{r}}^{\mathrm{I}}_{CR/O_{\mathrm{I}}} = R^{\mathrm{I}\leftarrow\mathrm{L}} \bar{v}^{\mathrm{L}}_{CR/\mathrm{I}}$, or equivalently,

$$\dot{\bar{r}}^{\mathrm{I}}_{Q/O_{\mathrm{I}}} = R^{\mathrm{I}\leftarrow\mathrm{L}} \bar{v}^{\mathrm{L}}_{CR/\mathrm{I}}, \tag{210}$$

since $\dot{\bar{r}}^{\mathrm{I}}_{CR/O_{\mathrm{I}}} = \bar{v}^{\mathrm{I}}_{CR/\mathrm{I}} = \bar{v}^{\mathrm{I}}_{Q/\mathrm{I}} + \bar{v}^{\mathrm{I}}_{CR/\mathrm{G}} + \bar{\omega}^{\mathrm{I}}_{\mathrm{G/I}} \times \bar{r}^{\mathrm{I}}_{CR/Q} = \bar{v}^{\mathrm{I}}_{Q/\mathrm{I}} = \dot{\bar{r}}^{\mathrm{I}}_{Q/O_{\mathrm{I}}}$, where $\bar{\omega}_{\mathrm{G/I}} = 0$ is an assumption and $\bar{v}_{CR/\mathrm{G}} = 0$.

6.1.8 Equations of Motion for the (2+1)-DOF case

The translational dynamic equations for the (2+1)-DOF case are given by Eq. (204). Note that in this case, $\bar{\omega}_{\mathrm{L/I}} = \bar{\omega}_{\mathrm{S/I}}$ and $\frac{{}^{\mathrm{S}}\mathrm{d}\bar{\omega}_{\mathrm{S/I}}}{\mathrm{d}t} = \frac{{}^{\mathrm{S}}\mathrm{d}\bar{\omega}_{\mathrm{L/I}}}{\mathrm{d}t} = \frac{{}^{\mathrm{L}}\mathrm{d}\bar{\omega}_{\mathrm{L/I}}}{\mathrm{d}t} + \bar{\omega}_{\mathrm{L/S}} \times \bar{\omega}_{\mathrm{L/I}} = \frac{{}^{\mathrm{L}}\mathrm{d}\bar{\omega}_{\mathrm{L/I}}}{\mathrm{d}t}$, since $\bar{\omega}_{\mathrm{L/S}} = 0$. Using these results in Eq. (204) and expressing it in the L-frame yields

$$
\begin{aligned}
&m_t(\dot{\bar{v}}^{\mathrm{L}}_{CR/\mathrm{I}} + \bar{\omega}^{\mathrm{L}}_{\mathrm{L/I}} \times \bar{v}^{\mathrm{L}}_{CR/\mathrm{I}}) + m_s(\bar{a}^{\mathrm{L}}_{\mathbf{o}_s/\mathrm{S}} + \dot{\bar{\omega}}^{\mathrm{L}}_{\mathrm{L/I}} \times \bar{r}^{\mathrm{L}}_{\mathbf{o}_s/CR} + 2(\bar{\omega}^{\mathrm{L}}_{\mathrm{L/I}} \times \bar{v}^{\mathrm{L}}_{\mathbf{o}_s/\mathrm{S}}) + \bar{\omega}^{\mathrm{L}}_{\mathrm{L/I}} \times (\bar{\omega}^{\mathrm{L}}_{\mathrm{L/I}} \times \bar{r}^{\mathrm{L}}_{\mathbf{o}_s/CR})) \\
&+ m_l(\bar{a}^{\mathrm{L}}_{\mathbf{o}_l/\mathrm{L}} + \dot{\bar{\omega}}^{\mathrm{L}}_{\mathrm{L/I}} \times \bar{r}^{\mathrm{L}}_{\mathbf{o}_l/CR} + 2(\bar{\omega}^{\mathrm{L}}_{\mathrm{L/I}} \times \bar{v}^{\mathrm{L}}_{\mathbf{o}_l/\mathrm{L}}) + \bar{\omega}^{\mathrm{L}}_{\mathrm{L/I}} \times (\bar{\omega}^{\mathrm{L}}_{\mathrm{L/I}} \times \bar{r}^{\mathrm{L}}_{\mathbf{o}_l/CR})) \\
&= \bar{f}^{\mathrm{L}}_{g,s} + \bar{f}^{\mathrm{L}}_{g,l} + \bar{f}^{\mathrm{L}}_{c,l/g} + \sum_{i=1}^{12} \bar{f}^{\mathrm{L}}_{T_i}.
\end{aligned} \tag{211}
$$

As for the rotational dynamic equations, note that now ${}^{CR}\bar{\tau}_{c,s/l} \neq 0$. Hence, writing Eq. (186) in terms of ${}^{CR}\bar{\tau}_{c,s/l}$ and substituting it in Eq. (181) yields

$$
\begin{aligned}
&\frac{{}^{\mathrm{S}}\mathrm{d}\,{}^{CR}\bar{I}_s}{\mathrm{d}t}\bar{\omega}_{\mathrm{S/I}} + {}^{CR}\bar{I}_l \frac{{}^{\mathrm{L}}\mathrm{d}\bar{\omega}_{\mathrm{L/I}}}{\mathrm{d}t} + {}^{CR}\bar{I}_s \frac{{}^{\mathrm{S}}\mathrm{d}\bar{\omega}_{\mathrm{S/I}}}{\mathrm{d}t} + \frac{{}^{\mathrm{S}}\mathrm{d}}{\mathrm{d}t}\sum_{i=1}^{4} {}^{\mathbf{o}_{c_i}}\bar{I}_{w_i}\bar{\omega}_{\mathrm{W}_i/\mathrm{G}_i} + \frac{{}^{\mathrm{S}}\mathrm{d}}{\mathrm{d}t}\sum_{i=1}^{4} {}^{\mathbf{o}_{c_i}}\bar{I}_{c_i}\bar{\omega}_{\mathrm{G}_i/\mathrm{S}} \\
&+ \bar{r}_{\mathbf{o}_f/CR} \times (m_s \bar{a}_{\mathbf{o}_s/\mathrm{S}}) + \bar{r}_{\mathbf{o}_l/CR} \times (m_l \bar{a}_{\mathbf{o}_l/\mathrm{L}}) + \bar{\omega}_{\mathrm{S/I}} \times ({}^{CR}\bar{I}_s\bar{\omega}_{\mathrm{S/I}} + \sum_{i=1}^{4} {}^{\mathbf{o}_{c_i}}\bar{I}_{w_i}\bar{\omega}_{\mathrm{W}_i/\mathrm{G}_i} \\
&+ \sum_{i=1}^{4} {}^{\mathbf{o}_{c_i}}\bar{I}_{c_i}\bar{\omega}_{\mathrm{G}_i/\mathrm{S}} + \bar{r}_{\mathbf{o}_f/CR} \times (m_s \bar{v}_{\mathbf{o}_s/\mathrm{S}})) + \bar{\omega}_{\mathrm{L/I}} \times \left({}^{CR}\bar{I}_l\bar{\omega}_{\mathrm{L/I}} + \bar{r}_{\mathbf{o}_l/CR} \times (m_l \bar{v}_{\mathbf{o}_l/\mathrm{L}})\right) \\
&+ \bar{r}_{\mathbf{o}_s/CR} \times m_s \bar{a}_{CR/\mathrm{I}} + \bar{r}_{\mathbf{o}_l/CR} \times m_l \bar{a}_{CR/\mathrm{I}} = \bar{r}_{\mathbf{o}_s/CR} \times \bar{f}_{g,s} + \sum_{i=1}^{12} \bar{r}_{T_i/CR} \times \bar{f}_{T_i} + \bar{r}_{\mathbf{o}_l/CR} \times \bar{f}_{g,l} \\
&+ {}^{CR}\bar{\tau}_{c,l/g}.
\end{aligned} \tag{212}
$$

Finally, expressing Eq. (212) in the L-frame and using $\bar{\omega}_{\mathrm{L/I}} = \bar{\omega}_{\mathrm{S/I}}$, $\frac{{}^{\mathrm{S}}\mathrm{d}\bar{\omega}_{\mathrm{S/I}}}{\mathrm{d}t} = \frac{{}^{\mathrm{L}}\mathrm{d}\bar{\omega}_{\mathrm{L/I}}}{\mathrm{d}t}$, and Eqs. (192), (190), and (188) and their time derivatives yields

$$
\begin{aligned}
&R^{\mathrm{L}\leftarrow\mathrm{S}}\left(A_t\,\mathrm{diag}(\dot{\gamma})(I_{cs} - I_{ct})A_s^{\mathsf{T}} + A_s\,\mathrm{diag}(\dot{\gamma})(I_{cs} - I_{ct})A_t^{\mathsf{T}}\right)R^{\mathrm{S}\leftarrow\mathrm{L}}\bar{\omega}^{\mathrm{L}}_{\mathrm{L/I}} + {}^{CR}\bar{I}^{\mathrm{L}}_l\dot{\bar{\omega}}^{\mathrm{L}}_{\mathrm{L/I}} \\
&+ R^{\mathrm{L}\leftarrow\mathrm{S}}({}^{CR}\bar{I}^{\mathrm{S}}_s)R^{\mathrm{S}\leftarrow\mathrm{L}}\dot{\bar{\omega}}^{\mathrm{L}}_{\mathrm{L/I}} + R^{\mathrm{L}\leftarrow\mathrm{S}}(A_t(\gamma)I_{ws}\,\mathrm{diag}(\Omega)\dot{\gamma} + A_s(\gamma)I_{ws}\dot{\Omega}) + R^{\mathrm{L}\leftarrow\mathrm{S}}(A_g I_{cg}\ddot{\gamma}) \\
&+ \bar{r}^{\mathrm{L}}_{\mathbf{o}_f/CR} \times (m_s \bar{a}^{\mathrm{L}}_{\mathbf{o}_s/\mathrm{S}}) + \bar{r}^{\mathrm{L}}_{\mathbf{o}_l/CR} \times (m_l \bar{a}^{\mathrm{L}}_{\mathbf{o}_l/\mathrm{L}}) + \bar{\omega}^{\mathrm{L}}_{\mathrm{L/I}} \times \left(R^{\mathrm{L}\leftarrow\mathrm{S}}({}^{CR}\bar{I}^{\mathrm{S}}_s)R^{\mathrm{S}\leftarrow\mathrm{L}}\bar{\omega}^{\mathrm{L}}_{\mathrm{L/I}} + {}^{CR}\bar{I}^{\mathrm{L}}_l\bar{\omega}^{\mathrm{L}}_{\mathrm{L/I}}\right. \\
&\left. + R^{\mathrm{L}\leftarrow\mathrm{S}}(A_s(\gamma)I_{ws}\Omega) + R^{\mathrm{L}\leftarrow\mathrm{S}}(A_g I_{cg}\dot{\gamma}) + \bar{r}^{\mathrm{L}}_{\mathbf{o}_f/CR} \times (m_s \bar{v}^{\mathrm{L}}_{\mathbf{o}_s/\mathrm{S}}) + \bar{r}^{\mathrm{L}}_{\mathbf{o}_l/CR} \times (m_l \bar{v}^{\mathrm{L}}_{\mathbf{o}_l/\mathrm{L}})\right) \\
&+ \bar{r}^{\mathrm{L}}_{\mathbf{o}_s/CR} \times m_s(\dot{\bar{v}}^{\mathrm{L}}_{CR/\mathrm{I}} + \bar{\omega}^{\mathrm{L}}_{\mathrm{L/I}} \times \bar{v}^{\mathrm{L}}_{CR/\mathrm{I}}) + \bar{r}^{\mathrm{L}}_{\mathbf{o}_l/CR} \times m_l(\dot{\bar{v}}^{\mathrm{L}}_{CR/\mathrm{I}} + \bar{\omega}^{\mathrm{L}}_{\mathrm{L/I}} \times \bar{v}^{\mathrm{L}}_{CR/\mathrm{I}}) = \bar{r}^{\mathrm{L}}_{\mathbf{o}_s/CR} \times \bar{f}^{\mathrm{L}}_{g,s}
\end{aligned}
$$

$$+\bar{r}^{\mathrm{L}}_{\mathfrak{o}_l/CR} \times \bar{f}^{\mathrm{L}}_{g,l} + \sum_{i=1}^{12} \bar{r}^{\mathrm{L}}_{T_i/CR} \times \bar{f}^{\mathrm{L}}_{T_i} + {}^{CR}\bar{\tau}^{\mathrm{L}}_{c,l/g}. \tag{213}$$

If the connection between lower stage and the epoxy floor is frictionless, then the contact moment due to the floor on the lower stage is zero along $\bar{K}_{\mathrm{L}}$, i.e., ${}^{CR}\bar{\tau}^{\mathrm{L}}_{c,l/g} = [{}^{CR}\bar{\tau}^{\mathrm{L}}_{c,l/g,1}, {}^{CR}\bar{\tau}^{\mathrm{L}}_{c,l/g,2}, 0]^{\intercal}$. Under the same assumption, the contact force due to the floor on the lower stage is only nonzero along $\bar{K}_{\mathrm{L}}$, i.e., $\bar{f}^{\mathrm{L}}_{c,l/g} = [0, 0, \bar{f}^{\mathrm{L}}_{c,l/g,3}]^{\intercal}$.

Moreover, the floor constrains the angular velocity of the lower platform with respect to the G-frame to be along $\bar{K}_{\mathrm{L}}$. Since it is assumed that $\bar{\omega}_{\mathrm{G/I}} = 0$, then $\bar{\omega}^{\mathrm{L}}_{\mathrm{L/I}} = \bar{\omega}^{\mathrm{L}}_{\mathrm{L/G}} + \bar{\omega}^{\mathrm{L}}_{\mathrm{G/I}} = \bar{\omega}^{\mathrm{L}}_{\mathrm{L/G}} = [0, 0, r^{\mathrm{L}}_{\mathrm{L/I}}]^{\intercal}$. In addition, the floor constrains the velocity of the center of rotation with respect to the inertial frame to be zero along $\bar{K}_{\mathrm{L}}$, i.e., $\bar{v}^{\mathrm{L}}_{CR/\mathrm{I}} = [u^{\mathrm{L}}_{CR/\mathrm{I}}, v^{\mathrm{L}}_{CR/\mathrm{I}}, 0]^{\intercal}$.

Hence, the third coordinate of Eq. (213) and the first and second coordinates of Eq. (211) form a system of 3 equations and 3 unknowns: $\dot{u}^{\mathrm{L}}_{CR/\mathrm{I}}$, $\dot{v}^{\mathrm{L}}_{CR/\mathrm{I}}$, and $\dot{r}^{\mathrm{L}}_{\mathrm{L/I}}$, where $\dot{\bar{v}}^{\mathrm{L}}_{CR/\mathrm{I}} = [\dot{u}^{\mathrm{L}}_{CR/\mathrm{I}}, \dot{v}^{\mathrm{L}}_{CR/\mathrm{I}}, 0]^{\intercal}$ and $\dot{\bar{\omega}}^{\mathrm{L}}_{\mathrm{L/I}} = [0, 0, \dot{r}^{\mathrm{L}}_{\mathrm{L/I}}]^{\intercal}$. These equations are the dynamic equations for this case.

6.1.8.1 Kinematics

The kinematic equations of motion for this case are given by Eq. (207) and Eq. (210).

Note that, in this case, the orientation of the S-frame with respect to the I-frame can be calculated from

$$R^{\mathrm{S}\leftarrow\mathrm{I}}(t) = R^{\mathrm{S}\leftarrow\mathrm{L}}(0) R^{\mathrm{L}\leftarrow\mathrm{I}}(t),$$

where $R^{\mathrm{S}\leftarrow\mathrm{L}}(0) = R^{\mathrm{S}\leftarrow\mathrm{I}}(0)(R^{\mathrm{L}\leftarrow\mathrm{I}}(0))^{\intercal}$, since in the (2+1)-DOF case, $R^{\mathrm{S}\leftarrow\mathrm{L}}$ does not change with time.

6.2 Real-World Effects

In addition to the equations of motion, the high-fidelity simulation of the platform takes into consideration the following real-world effects. The default values presented here are defined and can be easily changed in the input file of the simulation.

1) The opening and closing of the solenoid valves of the cold-gas thrusters is modeled as a first-order system with transfer function $H(s) = \frac{1/\tau}{s+1/\tau}$. The value of τ was measured experimentally for each thruster. From thruster 1 to thruster 12, τ is given by 6.7, 20.0, 6.7, 6.7, 13.3, 6.7, 6.7, 33.3, 6.7, 6.7, 6.7, and 6.7 ms.

2) The angular velocity measurement produced by the IMU (after being filtered by a 4-th order discrete-time Butterworth filter) is simulated by adding noise, bias, and drift to the true angular velocity. The default values for these parameters, based on experimental data, are $[0.14, 0.14, 0.14]^\intercal$ deg/s (standard deviation of AWGN), $[0, 0, 0]^\intercal$ deg/s, and $[0, 0, 0]^\intercal$ deg/s^2, respectively. Moreover, the measurement of $q_{\mathrm{S/I}}$ produced by the IMU (after being filtered by a 4-th order discrete-time Butterworth filter) is simulated by adding AWGN to the true value of $q_{\mathrm{S/I}}$. The default value of the standard deviation of this AWGN is $[0, 0, 0, 0]^\intercal$, based on experimental data. After the AWGN is added to $q_{\mathrm{S/I}}$, $q_{\mathrm{S/I}}$ is re-normalized through $[q_{\mathrm{S/I}}] = \frac{[q_{\mathrm{S/I}}]}{\|[q_{\mathrm{S/I}}]\|}$.

3) The non-dimensional specific force measurement produced by the IMU is simulated by calculating $\bar{n}^{\mathrm{S}}_{\mathrm{A/I},m} = (\bar{a}^{\mathrm{S}}_{\mathrm{A/I}} + R^{\mathrm{S}\leftarrow\mathrm{I}} R^{\mathrm{I}\leftarrow\mathrm{I_{true}}}[0, 0, g]^\intercal)/c$, where $\bar{a}^{\mathrm{S}}_{\mathrm{A/I}}$ is the true linear acceleration at the location of the IMU with respect to the inertial frame, $c = 9.8$ m/s^2 is a scaling constant defined in the user manual of the IMU, g is assumed to be 9.8 m/s^2, and $R^{\mathrm{I}\leftarrow\mathrm{I_{true}}}$ is a rotation matrix used to simulate the misalignment between $\bar{K}_{\mathrm{I}}$ (defined experimentally) and the true direction of the local gravity acceleration vector. By default, $R^{\mathrm{I}\leftarrow\mathrm{I_{true}}} = I_{3\times3}$. Noise and bias is also added to $\bar{n}^{\mathrm{S}}_{\mathrm{A/I},m}$. The default values for these parameters, based on experimental data, are $[4.3e^{-4}, 4.3e^{-4}, 4.3e^{-4}]^\intercal$ (standard deviation of AWGN) and $[0.014, 0.021, -0.0006]^\intercal$ s^{-1}.

4) The angular velocity measurement produced by the rate-gyros is simulated by adding noise, bias, and drift to the true angular velocity. The default values for

these parameters, based on experimental data, are $[0.05, 0.05, 0.05]^\intercal$ deg/s (standard deviation of AWGN), $[-0.9, 1.1, 0.8]^\intercal$ deg/s, and $[1.2e^{-3}, -2.3e^{-3}, -1.0e^{-3}]^\intercal$ deg/s^2, respectively.

5) The measurement of $q_{\mathrm{S/I}}$ produced by the VICON system is simulated by adding AWGN to the true $q_{\mathrm{S/I}}$, with standard deviation $[1.2e^{-3}, 1.2e^{-3}, 1.2e^{-3}, 1.2e^{-3}]^\intercal$. After the AWGN is added to $q_{\mathrm{S/I}}$, $q_{\mathrm{S/I}}$ is re-normalized through $[q_{\mathrm{S/I}}] = \frac{[q_{\mathrm{S/I}}]}{\|[q_{\mathrm{S/I}}]\|}$. Similarly, the measurement of $\bar{r}^{\mathrm{I}}_{CR/O_{\mathrm{I}}}$ produced by the VICON system is simulated by adding AWGN to the true $\bar{r}^{\mathrm{I}}_{CR/O_{\mathrm{I}}}$, with standard deviation $[1.5, 1.5, 1.5]^\intercal$ mm.

6) The measurement of $q_{\mathrm{S/T}}$ produced by the vision-based pose estimation algorithm described in Ref. [111], where the T-frame is a frame fixed to the target object, is simulated by adding AWGN to the true $q_{\mathrm{S/T}}$, with standard deviation $[1e^{-4}, 1e^{-4}, 1e^{-4}, 1e^{-4}]^\intercal$. After the AWGN is added to $q_{\mathrm{S/T}}$, $q_{\mathrm{S/T}}$ is re-normalized through $[q_{\mathrm{S/T}}] = \frac{[q_{\mathrm{S/T}}]}{\|[q_{\mathrm{S/T}}]\|}$. In the current implementation of the code, the true value of $q_{\mathrm{S/T}}$ is calculated from the true value of $q_{\mathrm{S/I}}$ and from the (constant) value of $q_{\mathrm{T/I}}$ specified in the input file of the simulation. Similarly, the measurement of $\bar{r}^{\mathrm{T}}_{CR/O_{\mathrm{T}}}$ produced by the vision system is simulated by adding AWGN to the true $\bar{r}^{\mathrm{T}}_{CR/O_{\mathrm{T}}}$, with standard deviation $[1.7, 1.7, 1.7]^\intercal$ mm. In the current implementation of the code, the true value of $\bar{r}^{\mathrm{T}}_{CR/O_{\mathrm{T}}}$ is calculated from the true value of $\bar{r}^{\mathrm{I}}_{CR/O_{\mathrm{I}}}$ and from the (constant) values of $q_{\mathrm{T/I}}$ and $\bar{r}^{\mathrm{I}}_{O_{\mathrm{T}}/O_{\mathrm{I}}}$ specified in the input file. The update rate of the vision system is defined in the input file and is 10 Hz by default.

7) The measurement of γ produced by US Digital MA3 miniature absolute magnetic shaft encoders is simulated by adding AWGN to the true γ, with standard deviation $[0.3, 0.3, 0.3, 0]^\intercal$ deg.

8) The measurement of Ω produced by Hall sensors is simulated by adding AWGN

to the true Ω, with standard deviation $[5, 5, 5, 0]^{\mathrm{T}}$ rpm.

9) Experimental tests have shown that the motors that control the gimbals of the VSCMGs cannot produce angular rates smaller than approximately 4 deg/s in absolute value. This deadzone is included in the high-fidelity simulation.

10) The maximum thrust produced by each thruster has been measured experimentally. These measurements are used *as is* in Section 6.5 to convert continuous-time thrust into on-off commands. However, the actual maximum thrust produced by each thruster during an experiment is expected to differ significantly from these measurements. Hence, to simulate this mismatch, the maximum thrust of each thruster is currently simulated to be 10% higher than the measured maximum thrust.

6.3 Allocation of the Control Moment to the Variable-Speed Control Moment Gyros

Note that whereas the control force calculated by the controller can only be allocated to the cold-gas thrusters, the control moment can be allocated to the cold-gas thrusters and/or the *Variable-Speed Control Moment Gyros* (VSCMGs). The current implementation of the control software allows the user to choose either to allocate the control moment to the cold-gas thrusters or to the VSCMGs. This section addresses the allocation of the control moment to the latter.

6.3.1 Assumptions

The following assumptions are made in the allocation of the control moment to the VSCMGs:

1) In all cases, the term $A_g I_{cg} \ddot{\gamma}$ is assumed to be zero.

2) In the (2+1)-DOF case only, the epoxy floor is assumed to be perfectly flat.

6.3.2 Control Moment Allocation in the 3-DOF and 5-DOF cases

Since the 3-DOF case is similar to the 5-DOF case (note that Eq. (202) is identical to Eq. (193), apart from two additional terms resulting from the translation of the center of rotation), the control moment allocation for these two cases can be analyzed at the same time. First, the attitude dynamic equations for the 5-DOF case, given by Eq. (202), are rearranged as follows

$$\begin{aligned}
&{}^{CR}\bar{I}_s^{\mathrm{S}}\dot{\bar{\omega}}_{\mathrm{S/I}}^{\mathrm{S}}+\bar{\omega}_{\mathrm{S/I}}^{\mathrm{S}}\times({}^{CR}\bar{I}_s^{\mathrm{S}}\bar{\omega}_{\mathrm{S/I}}^{\mathrm{S}})\\
=&-{}^{CR}\dot{\bar{I}}_s^{\mathrm{S}}(\dot{\gamma})\bar{\omega}_{\mathrm{S/I}}^{\mathrm{S}}-A_t(\gamma)I_{ws}\,\mathrm{diag}(\Omega)\dot{\gamma}-A_s(\gamma)I_{ws}\dot{\Omega}-A_gI_{cg}\ddot{\gamma}-\bar{\omega}_{\mathrm{S/I}}^{\mathrm{S}}\times\big(A_s(\gamma)I_{ws}\Omega+A_gI_{cg}\dot{\gamma}\big)\\
&+\bar{r}_{\bullet_s/CR}^{\mathrm{S}}\times\bar{f}_{g,s}^{\mathrm{S}}-\bar{r}_{\bullet_s/CR}^{\mathrm{S}}\times m_s(R^{\mathrm{S}\leftarrow\mathrm{L}}\dot{\bar{v}}_{CR/\mathrm{I}}^{\mathrm{L}})-\bar{r}_{\bullet_s/CR}^{\mathrm{S}}\times m_s(\bar{\omega}_{\mathrm{L/I}}^{\mathrm{S}}\times\bar{v}_{CR/\mathrm{I}}^{\mathrm{S}})\\
&-\bar{\omega}_{\mathrm{S/I}}^{\mathrm{S}}\times\big(\bar{r}_{\bullet_f/CR}^{\mathrm{S}}\times(m_s\bar{v}_{\bullet_s/\mathrm{S}}^{\mathrm{S}})\big)-\bar{r}_{\bullet_f/CR}^{\mathrm{S}}\times(m_s\bar{a}_{\bullet_s/\mathrm{S}}^{\mathrm{S}})\\
&+\sum_{i=1}^{12}\bar{r}_{T_i/CR}^{\mathrm{S}}\times\bar{f}_{T_i}^{\mathrm{S}}.
\end{aligned}\tag{214}$$

The first line corresponds to terms coming from the rigid body dynamics. They cannot be used to control the platform. The second line corresponds to terms coming from the dynamics of the VSCMGs. These terms can be used to control the platform. The third and fourth lines correspond to unwanted terms coming from having the centers of mass not coincident with the center of rotation. Finally, if the cold-gas thrusters are used exclusively for control force allocation (and not for control moment allocation), the fifth line corresponds to unwanted moments created by the cold-gas thrusters due to, for example, misalignments.

Denote the desired control moment with respect to the center of rotation expressed in the S-frame by $\bar{\tau}_c^{\mathrm{S}}$. This moment should be equal to the terms of Eq. (214) coming from the dynamics of the VCCMGs, i.e.,

$$\begin{aligned}
\bar{\tau}_c^{\mathrm{S}}=&-{}^{CR}\dot{\bar{I}}_s^{\mathrm{S}}(\dot{\gamma})\bar{\omega}_{\mathrm{S/I}}^{\mathrm{S}}-A_t(\gamma)I_{ws}\,\mathrm{diag}(\Omega)\dot{\gamma}-A_s(\gamma)I_{ws}\dot{\Omega}-A_gI_{cg}\ddot{\gamma}\\
&-\bar{\omega}_{\mathrm{S/I}}^{\mathrm{S}}\times\big(A_s(\gamma)I_{ws}\Omega+A_gI_{cg}\dot{\gamma}\big).
\end{aligned}\tag{215}$$

The problem is now to choose $\dot{\gamma}$ and $\dot{\Omega}$ so that the right-side of Eq. (214) matches

$\bar{\tau}_c^{\mathrm{S}}$. A common assumption [107, 108, 47, 48] is to consider the term $A_g I_{cg}\ddot{\gamma}$ equal to zero, since it is relatively small compared to the other terms. Under this assumption, Eq. (215) can be rewritten as

$$\bar{\tau}_c^{\mathrm{S}}+\bar{\omega}_{\mathrm{S/I}}^{\mathrm{S}}\times(A_s(\gamma)I_{ws}\Omega)=-{}^{CR}\dot{\bar{I}}_s^{\mathrm{S}}(\dot{\gamma})\bar{\omega}_{\mathrm{S/I}}^{\mathrm{S}}-A_t(\gamma)I_{ws}\,\mathrm{diag}(\Omega)\dot{\gamma}-A_s(\gamma)I_{ws}\dot{\Omega}-\bar{\omega}_{\mathrm{S/I}}^{\mathrm{S}}\times(A_g I_{cg}\dot{\gamma})$$

or

$$\begin{bmatrix} C & D \end{bmatrix} \begin{bmatrix} \dot{\gamma} \\ \dot{\Omega} \end{bmatrix} = L_\tau, \tag{216}$$

where

$$C \triangleq -A_t(\gamma)I_{ws}\,\mathrm{diag}(\Omega) - [\bar{\omega}_{\mathrm{S/I}}^{\mathrm{S}}]^{\times} A_g I_{cg} - V(I_{cs}-I_{ct}), \tag{217}$$

$$V \triangleq [\big(\bar{J}_{\mathrm{G}_1}^{\mathrm{S}}(\bar{K}_{\mathrm{G}_1}^{\mathrm{S}})^{\mathsf{T}} + \bar{K}_{\mathrm{G}_1}^{\mathrm{S}}(\bar{J}_{\mathrm{G}_1}^{\mathrm{S}})^{\mathsf{T}}\big)\bar{\omega}_{\mathrm{S/I}}^{\mathrm{S}}, ..., (\bar{J}_{\mathrm{G}_4}^{\mathrm{S}}(\bar{K}_{\mathrm{G}_4}^{\mathrm{S}})^{\mathsf{T}} + \bar{K}_{\mathrm{G}_4}^{\mathrm{S}}(\bar{J}_{\mathrm{G}_4}^{\mathrm{S}})^{\mathsf{T}})\bar{\omega}_{\mathrm{S/I}}^{\mathrm{S}}], \tag{218}$$

$$D \triangleq -A_s(\gamma)I_{ws}, \tag{219}$$

$$L_\tau \triangleq \bar{\tau}_c^{\mathrm{S}} + \bar{\omega}_{\mathrm{S/I}}^{\mathrm{S}} \times (A_s(\gamma)I_{ws}\Omega). \tag{220}$$

The VSCMGs can be run in three modes:

1) *Reaction Wheel* (RW) mode: $\dot{\gamma} = 0_{4\times 1}$ and $\dot{\Omega} \in \mathbb{R}^4$.

2) *Control Moment Gyro* (CMG) mode: $\dot{\gamma} \in \mathbb{R}^4$ and $\dot{\Omega} = 0_{4\times 1}$.

3) *Variable-Speed Control Moment Gyro* (VSCMG) mode: $\dot{\gamma} \in \mathbb{R}^4$ and $\dot{\Omega} \in \mathbb{R}^4$.

When the VSCMGs are run in VSCMG mode or RW mode, the control moment allocation problem is solved by solving the following minimization problem [107]

$$y^* = \arg\min_y \tfrac{1}{2} y^{\mathsf{T}} W^{-1} y, \text{ subject to } Qy = L, \tag{221}$$

where

$$y = [\dot{\gamma}, \dot{\Omega}]^{\mathsf{T}}, \tag{222}$$

$Q = [C, D]$, $L = L_\tau$, and W is a weighting matrix. Depending on how this weighting matrix is defined, the VSCMGs can operate in VSCMG mode, RW mode, or even CMG mode. (However, in the current implementation, a different optimization problem is solved in CMG mode. More details follow.) In particular, if this weighting matrix is defined as

$$W = \begin{bmatrix} w_1 e^{-w_2 \sigma_c} I_{N_{\mathrm{ON}} \times N_{\mathrm{ON}}} & 0_{N_{\mathrm{ON}} \times N_{\mathrm{ON}}} \\ 0_{N_{\mathrm{ON}} \times N_{\mathrm{ON}}} & I_{N_{\mathrm{ON}} \times N_{\mathrm{ON}}} \end{bmatrix}, \tag{223}$$

$$W = \begin{bmatrix} 0_{N_{\mathrm{ON}} \times N_{\mathrm{ON}}} & 0_{N_{\mathrm{ON}} \times N_{\mathrm{ON}}} \\ 0_{N_{\mathrm{ON}} \times N_{\mathrm{ON}}} & I_{N_{\mathrm{ON}} \times N_{\mathrm{ON}}} \end{bmatrix}, \tag{224}$$

$$W = \begin{bmatrix} I_{N_{\mathrm{ON}} \times N_{\mathrm{ON}}} & 0_{N_{\mathrm{ON}} \times N_{\mathrm{ON}}} \\ 0_{N_{\mathrm{ON}} \times N_{\mathrm{ON}}} & 0_{N_{\mathrm{ON}} \times N_{\mathrm{ON}}} \end{bmatrix}, \tag{225}$$

the VSCMGs will operate in VSCMG mode, RW mode, or CMG mode, respectively. In Eqs. (223)-(225), w_1 and w_2 are positive gains, σ_c is the condition number of matrix C (i.e., the ratio between its largest and smallest singular value), and N_{ON} is the number of operational VSCMGs. The solution to the minimization problem defined by Eq. (221) is given by [107]

$$y^* = W^{\frac{1}{2}} (Q W^{\frac{1}{2}})^\dagger L, \tag{226}$$

where † denotes the Moore-Penrose pseudoinverse.

In VSCMG mode, depending on the condition number of matrix C, the VSCMGs can operate either as reaction wheels (close to a singularity, i.e., when σ_c is large) or as regular CMGs (away from a singularity, i.e., when σ_c is small) [107]. As a singularity is approached, the VSCMGs will smoothly switch to RW mode. As a result, this method can handle temporary rank deficiencies in matrix C.

When the VSCMGs are run in CMG mode, in order to escape or avoid singularities, the steering logic suggested in Refs. [102] and [47] is employed. This steering

logic consists on solving the following minimization problem:

$$\dot{\gamma}^* = \arg\min_{\dot{\gamma}} (C\dot{\gamma} - L_\tau)^\intercal V^{-1} (C\dot{\gamma} - L_\tau) + \dot{\gamma}^\intercal W^{-1} \dot{\gamma}, \text{ subject to } C\dot{\gamma} = L_\tau, \tag{227}$$

where

$$V = \alpha \begin{bmatrix} 1 & \epsilon_3 & \epsilon_2 \\ \epsilon_3 & 1 & \epsilon_1 \\ \epsilon_2 & \epsilon_1 & 1 \end{bmatrix} > 0, \tag{228}$$

W is a N_{ON}-by-N_{ON} positive-definite matrix with diagonal elements W_{11},...,$W_{N_{\text{ON}}N_{\text{ON}}}$ and non-diagonal elements equal to α,

$$\alpha = \alpha_0 \exp(-\mu \det(CC^\intercal)),$$

$$\epsilon_k = \epsilon_0 \sin(\omega t + \phi_k),$$

and α_0, μ, ϵ_0, ω, ϕ_k, and W_{ii} are constants to be properly selected. The solution to the minimization problem defined by Eq. (227) is given by

$$\dot{\gamma}^* = C^\# L_\tau, \tag{229}$$

where

$$C^\# = (C^\intercal V^{-1} C + W^{-1})^{-1} C^\intercal V^{-1} = W C^\intercal (CWC^\intercal + V)^{-1}. \tag{230}$$

To simulate the limitations of the VSCMGs and to protect them during experiments, $\dot{\gamma}_i$ and $\dot{\Omega}_i$ are limited to ± 25 deg/s and ± 74 rad/s^2, respectively, for $i = 1, 2, 3, 4$. Likewise, the simulation/experiment is automatically stopped if Ω_i reaches ± 3500 rpm. These values are specified and can be changed in the input file of the simulation.

6.3.3 Wheel Speed Equalization

When the VSCMGs are running in VSCMG mode, if the spin rate of some wheels becomes too small, it may not be possible to generate the required torque by changing

the gimbal angles [107]. If this is the case, the remaining degrees of freedom may not be enough to achieve attitude-tracking. Moreover, if the spin rate of some wheels becomes too high, they might saturate. Hence, in VSCMG mode, it is desirable to equalize the spin rates of the wheels of all operational VSCMGs, whenever possible.

Two methods for wheel speed equalization are proposed in Ref. [107]. The first one guarantees exact equalization of the wheel speeds, but requires an additional degree of freedom. The second method shows a tendency for wheel speed equalization, but does not guarantee it. However, this method does not require an additional degree of freedom.

The first method was chosen for implementation. This method introduces the performance index

$$J_{w_1} = \tfrac{1}{2}\sum_{i=1}^{N_{\mathrm{ON}}} (\Omega_i - \bar{\Omega})^2 = \tfrac{1}{2}(\Omega_e)^{\intercal}\Omega_e, \tag{231}$$

where $\bar{\Omega} = \frac{1}{N_{\mathrm{ON}}}\sum_{i=1}^{N_{\mathrm{ON}}} \Omega_i$,

$$\Omega_e = \Omega - \bar{\Omega} 1_{N_{\mathrm{ON}}\times 1} = (I_{N_{\mathrm{ON}}\times N_{\mathrm{ON}}} - \frac{1}{N_{\mathrm{ON}}} 1_{N_{\mathrm{ON}}\times N_{\mathrm{ON}}})\Omega, \tag{232}$$

and $1_{m\times n}$ is a m-by-n matrix of ones. The wheel speed equalization requirement is enforced by requiring J_{w_1} to exponentially decay, that is,

$$\frac{\mathrm{d}}{\mathrm{d}t} J_{w_1} = (\Omega_e)^{\intercal}\dot{\Omega}_e = (\Omega_e)^{\intercal}(I_{N_{\mathrm{ON}}\times N_{\mathrm{ON}}} - \frac{1}{N_{\mathrm{ON}}} 1_{N_{\mathrm{ON}}\times N_{\mathrm{ON}}})\dot{\Omega} = -k_2 J_{w_1}, \tag{233}$$

where $k_2 > 0$. This condition is added to the minimization problem given by Eq. (221), where now

$$Q = \begin{bmatrix} C & D \\ 0_{1\times N_{\mathrm{ON}}} & E \end{bmatrix}, \tag{234}$$

$L = [L_\tau, -k_2 J_{w_1}]^{\intercal}$, and $E = (\Omega_e)^{\intercal}(I_{N_{\mathrm{ON}}\times N_{\mathrm{ON}}} - \frac{1}{N_{\mathrm{ON}}} 1_{N_{\mathrm{ON}}\times N_{\mathrm{ON}}})$.

6.3.4 Control Moment Allocation in the (2+1)-DOF case

This section shows that the control moment allocation to the VSCMGs in the (2+1)-DOF case can be done as in the other two cases. First, the attitude dynamic equations

for the (2+1)-DOF case, given by Eq. (202), are rearranged as follows (ignoring the term ${}^{CR}\bar{\tau}^{\mathrm{L}}_{c,l/g}$, since only the third coordinate of Eq. (202) is of interest):

$$
\begin{aligned}
&(R^{\mathrm{L}\leftarrow\mathrm{S}}({}^{CR}\bar{I}^{\mathrm{S}}_{s})R^{\mathrm{S}\leftarrow\mathrm{L}} + {}^{CR}\bar{I}^{\mathrm{L}}_{l})\dot{\bar{\omega}}^{\mathrm{L}}_{\mathrm{L/I}} + \bar{\omega}^{\mathrm{L}}_{\mathrm{L/I}} \times ((R^{\mathrm{L}\leftarrow\mathrm{S}}({}^{CR}\bar{I}^{\mathrm{S}}_{s})R^{\mathrm{S}\leftarrow\mathrm{L}} + {}^{CR}\bar{I}^{\mathrm{L}}_{l})\bar{\omega}^{\mathrm{L}}_{\mathrm{L/I}}) \\
&= -R^{\mathrm{L}\leftarrow\mathrm{S}\,CR}\dot{\bar{I}}^{\mathrm{S}}_{s}R^{\mathrm{S}\leftarrow\mathrm{L}}\bar{\omega}^{\mathrm{L}}_{\mathrm{L/I}} - R^{\mathrm{L}\leftarrow\mathrm{S}}A_t(\gamma)I_{ws}\,\mathrm{diag}(\Omega)\dot{\gamma} - R^{\mathrm{L}\leftarrow\mathrm{S}}A_s(\gamma)I_{ws}\dot{\Omega} \\
&\quad - R^{\mathrm{L}\leftarrow\mathrm{S}}A_g I_{cg}\ddot{\gamma} - \bar{\omega}^{\mathrm{L}}_{\mathrm{L/I}} \times \left(R^{\mathrm{L}\leftarrow\mathrm{S}}A_s(\gamma)I_{ws}\Omega + R^{\mathrm{L}\leftarrow\mathrm{S}}A_g I_{cg}\dot{\gamma}\right) \\
&+ \bar{r}^{\mathrm{L}}_{\mathfrak{o}_s/CR} \times \bar{f}^{\mathrm{L}}_{g,s} + \bar{r}^{\mathrm{L}}_{\mathfrak{o}_l/CR} \times \bar{f}^{\mathrm{L}}_{g,l} - \bar{r}^{\mathrm{L}}_{\mathfrak{o}_f/CR} \times (m_s\bar{a}^{\mathrm{L}}_{\mathfrak{o}_s/\mathrm{S}}) - \bar{r}^{\mathrm{L}}_{\mathfrak{o}_l/CR} \times (m_l\bar{a}^{\mathrm{L}}_{\mathfrak{o}_l/\mathrm{L}}) \\
&\quad - \bar{\omega}^{\mathrm{L}}_{\mathrm{L/I}} \times \left(\bar{r}^{\mathrm{L}}_{\mathfrak{o}_f/CR} \times (m_s\bar{v}^{\mathrm{L}}_{\mathfrak{o}_s/\mathrm{S}}) + \bar{r}^{\mathrm{L}}_{\mathfrak{o}_l/CR} \times (m_l\bar{v}^{\mathrm{L}}_{\mathfrak{o}_l/\mathrm{L}})\right) \\
&- \bar{r}^{\mathrm{L}}_{\mathfrak{o}_s/CR} \times m_s(\dot{\bar{v}}^{\mathrm{L}}_{CR/\mathrm{I}} + \bar{\omega}^{\mathrm{L}}_{\mathrm{L/I}} \times \bar{v}^{\mathrm{L}}_{CR/\mathrm{I}}) - \bar{r}^{\mathrm{L}}_{\mathfrak{o}_l/CR} \times m_l(\dot{\bar{v}}^{\mathrm{L}}_{CR/\mathrm{I}} + \bar{\omega}^{\mathrm{L}}_{\mathrm{L/I}} \times \bar{v}^{\mathrm{L}}_{CR/\mathrm{I}}) \\
&\quad + \sum_{i=1}^{12} \bar{r}^{\mathrm{L}}_{T_i/CR} \times \bar{f}^{\mathrm{L}}_{T_i}.
\end{aligned}
\tag{235}
$$

The first line corresponds to terms coming from the rigid body dynamics. They cannot be used to control the platform. The second and third lines correspond to terms coming from the dynamics of the VSCMGs. These terms can be used to control the platform. The fourth, fifth, and sixth lines correspond to unwanted terms coming from having the centers of mass not coincident with the center of rotation. Finally, if the cold-gas thrusters are used exclusively for control force allocation (and not for control moment allocation), the seventh line corresponds to unwanted moments created by the cold-gas thrusters due to, for example, misalignments.

Denote the desired control moment with respect to the center of rotation expressed in the L-frame by $\bar{\tau}^{\mathrm{L}}_{c}$. This moment should be equal to the terms of Eq. (235) coming from the dynamics of the VCCMGs, i.e.,

$$
\begin{aligned}
\bar{\tau}^{\mathrm{L}}_{c} &= -R^{\mathrm{L}\leftarrow\mathrm{S}\,CR}\dot{\bar{I}}^{\mathrm{S}}_{s}R^{\mathrm{S}\leftarrow\mathrm{L}}\bar{\omega}^{\mathrm{L}}_{\mathrm{L/I}} - R^{\mathrm{L}\leftarrow\mathrm{S}}A_t(\gamma)I_{ws}\,\mathrm{diag}(\Omega)\dot{\gamma} - R^{\mathrm{L}\leftarrow\mathrm{S}}A_s(\gamma)I_{ws}\dot{\Omega} \\
&\quad - R^{\mathrm{L}\leftarrow\mathrm{S}}A_g I_{cg}\ddot{\gamma} - \bar{\omega}^{\mathrm{L}}_{\mathrm{L/I}} \times \left(R^{\mathrm{L}\leftarrow\mathrm{S}}A_s(\gamma)I_{ws}\Omega + R^{\mathrm{L}\leftarrow\mathrm{S}}A_g I_{cg}\dot{\gamma}\right).
\end{aligned}
\tag{236}
$$

By multiplying Eq. (236) on the left by $R^{\mathrm{S}\leftarrow\mathrm{L}}$ and noting that in the (2+1)-DOF case $\bar{\omega}^{\mathrm{S}}_{\mathrm{S/I}} = \bar{\omega}^{\mathrm{S}}_{\mathrm{L/I}}$, one obtains Eq. (215). Hence, the control moment allocation in the (2+1)-DOF case can be done as in the other two cases.

The only difference between the control moment allocation in the (2+1)-DOF case and the other two cases is that the first two inertial coordinates of the control moment supplied by the controller block to the control moment allocation block, i.e., $\bar{\tau}_{c,1}^{\mathrm{I}}$ and $\bar{\tau}_{c,2}^{\mathrm{I}}$ in $\bar{\tau}_c^{\mathrm{I}} = [\bar{\tau}_{c,1}^{\mathrm{I}}, \bar{\tau}_{c,2}^{\mathrm{I}}, \bar{\tau}_{c,3}^{\mathrm{I}}]^{\mathsf{T}}$, are set to zero in the control moment allocation block. This is done to protect the epoxy floor from damage since in the (2+1)-DOF case and assuming that the epoxy floor is perfectly flat, these two coordinates would just press the lower stage against the epoxy floor, without producing any motion.

6.3.5 Control Moment Allocation With Less Than Four VSCMGs

The control moment allocation to the VSCMGs can still be realized with less than four operational VSCMGs. An nonoperational VSCMG is defined as a VSCMG that cannot be commanded, in other words, a VSCMG with $\dot{\Omega}_i \equiv 0$ and $\dot{\gamma}_i \equiv 0$, but possibly with $\Omega_i \neq 0$.

The algorithms described in Sections 6.3.2, 6.3.3, and 6.3.4 can be easily adapted to handle nonoperational VSCMGs. Let N_{ON} be the number of operational VSCMGs and $i(j)$ the indexes of the operational VSCMGs for $j = 1, ..., N_{\mathrm{ON}}$. Then, redefine

$$A_t(\gamma) = [\bar{K}^{\mathrm{S}}_{\mathrm{G}_{i(1)}}(\gamma_{i(1)}), ..., \bar{K}^{\mathrm{S}}_{\mathrm{G}_{i(N_{\mathrm{ON}})}}(\gamma_{i(N_{\mathrm{ON}})})],$$

$$I_{ws} = \mathrm{diag}([{}^{\mathcal{C}_{i(1)}}I^{\mathrm{G}_{i(1)}}_{w_{i(1)},22}, ..., {}^{\mathcal{C}_{i(N_{\mathrm{ON}})}}I^{\mathrm{G}_{i(N_{\mathrm{ON}})}}_{w_{i(N_{\mathrm{ON}})},22}]),$$

$$\Omega = [\Omega_{i(1)}, ..., \Omega_{i(N_{\mathrm{ON}})}]^{\mathsf{T}}, \tag{237}$$

$$A_g = [\bar{I}^{\mathrm{S}}_{\mathrm{G}_{i(1)}}, ..., \bar{I}^{\mathrm{S}}_{\mathrm{G}_{i(N_{\mathrm{ON}})}}],$$

$$I_{cg} = \mathrm{diag}([{}^{\mathcal{C}_{i(1)}}I^{\mathrm{G}_{i(1)}}_{c_{i(1)},11}, ..., {}^{\mathcal{C}_{i(N_{\mathrm{ON}})}}I^{\mathrm{G}_{i(N_{\mathrm{ON}})}}_{c_{i(N_{\mathrm{ON}})},11}]),$$

$$V = \begin{bmatrix} [\big(\bar{J}^{\mathrm{S}}_{\mathrm{G}_{i(1)}}(\bar{K}^{\mathrm{S}}_{\mathrm{G}_{i(1)}})^{\mathsf{T}} + \bar{K}^{\mathrm{S}}_{\mathrm{G}_{i(1)}}(\bar{J}^{\mathrm{S}}_{\mathrm{G}_{i(1)}})^{\mathsf{T}}\big)\bar{\omega}^{\mathrm{S}}_{\mathrm{S/I}}]^{\mathsf{T}} \\ ... \\ [(\bar{J}^{\mathrm{S}}_{\mathrm{G}_{i(N_{\mathrm{ON}})}}(\bar{K}^{\mathrm{S}}_{\mathrm{G}_{i(N_{\mathrm{ON}})}})^{\mathsf{T}} + \bar{K}^{\mathrm{S}}_{\mathrm{G}_{i(N_{\mathrm{ON}})}}(\bar{J}^{\mathrm{S}}_{\mathrm{G}_{i(N_{\mathrm{ON}})}})^{\mathsf{T}})\bar{\omega}^{\mathrm{S}}_{\mathrm{S/I}}]^{\mathsf{T}} \end{bmatrix}^{\mathsf{T}},$$

$$I_{cs} = \text{diag}([{}^{\mathcal{B}_{c_{i(1)}}} I^{\mathrm{G}_{i(1)}}_{c_{i(1)},22}, ..., {}^{\mathcal{B}_{c_{i(N_{\mathrm{ON}})}}} I^{\mathrm{G}_{i(N_{\mathrm{ON}})}}_{c_{i(N_{\mathrm{ON}})},22}]),$$

$$I_{ct} = \text{diag}([{}^{\mathcal{B}_{c_{i(1)}}} I^{\mathrm{G}_{i(1)}}_{c_{i(1)},33}, ..., {}^{\mathcal{B}_{c_{i(N_{\mathrm{ON}})}}} I^{\mathrm{G}_{i(N_{\mathrm{ON}})}}_{c_{i(N_{\mathrm{ON}})},33}]),$$

$$A_s(\gamma) = [\bar{J}^{\mathrm{S}}_{\mathrm{G}_{i(1)}}(\gamma_{i(1)}), ..., \bar{J}^{\mathrm{S}}_{\mathrm{G}_{i(N_{\mathrm{ON}})}}(\gamma_{i(N_{\mathrm{ON}})})],$$

$$\dot{\gamma} = [\dot{\gamma}_{i(1)}, ..., \dot{\gamma}_{i(N_{\mathrm{ON}})}]^{\mathsf{T}},$$

in Eqs. (217), (219), (222), and (227), while keeping the original definitions of $A_s(\gamma)$, I_{ws}, and Ω in Eq. (220). Then, the new minimization problems are still described by Eq. (221) and Eq. (227) and their solutions are still given by Eq. (226) and Eq. (229), respectively. Moreover, the wheel speeds of the operational VSCMGs can still be equalized as described in Section 6.3.3 by replacing the definition of Ω in Eqs. (232) and (233) by Eq. (237).

6.4 Allocation of the Control Moment and Force to the Thrusters

This section addresses the allocation of the control force and moment to the cold-gas thrusters. In the current implementation, the user can choose to allocate the control moment to the cold-gas thrusters or to the VSCMGs.

6.4.1 Assumptions

The following assumptions are made in the allocation of the control force and moment to the cold-gas thrusters:

1) The forces due to the thrusters are assumed to be parallel to the axes of the S-frame.

2) The exact location of each thruster with respect to the center of rotation expressed in the S-frame is known.

3) The epoxy floor is assumed to be perfectly flat.

4) The total force produced by the thrusters is insufficient to levitate the upper stage with respect to the lower stage.

6.4.2 Control Allocation in the 5-DOF Case

Denote the desired control force and the desired control moment expressed in the S-frame by $\bar{f}_c^{\mathrm{S}}$ and $\bar{\tau}_c^{\mathrm{S}}$. Since the forces due to the thrusters are assumed to be parallel to the axes of the S-frame, they can be written as $\bar{f}_{T_1}^{\mathrm{S}} = [0, T_1, 0]^\intercal$, $\bar{f}_{T_2}^{\mathrm{S}} = [0, 0, T_2]^\intercal$, $\bar{f}_{T_3}^{\mathrm{S}} = [0, -T_3, 0]^\intercal$, $\bar{f}_{T_4}^{\mathrm{S}} = [-T_4, 0, 0]^\intercal$, $\bar{f}_{T_5}^{\mathrm{S}} = [0, 0, T_5]^\intercal$, $\bar{f}_{T_6}^{\mathrm{S}} = [T_6, 0, 0]^\intercal$, $\bar{f}_{T_7}^{\mathrm{S}} = [0, -T_7, 0]^\intercal$, $\bar{f}_{T_8}^{\mathrm{S}} = [0, 0, T_8]^\intercal$, $\bar{f}_{T_9}^{\mathrm{S}} = [0, T_9, 0]^\intercal$, $\bar{f}_{T_{10}}^{\mathrm{S}} = [T_{10}, 0, 0]^\intercal$, $\bar{f}_{T_{11}}^{\mathrm{S}} = [0, 0, T_{11}]^\intercal$, and $\bar{f}_{T_{12}}^{\mathrm{S}} = [-T_{12}, 0, 0]^\intercal$ from Figure 47. Then, the control allocation problem consists on finding appropriate T_i, $i = 1, 2, ..., 12$, to produce $\bar{f}_c^{\mathrm{S}}$ and $\bar{\tau}_c^{\mathrm{S}}$.

Note that due to the geometry of the problem and assuming that the epoxy floor is perfectly flat, if the desired control force is expressed in the I-frame as $\bar{f}_c^{\mathrm{I}} = [\bar{f}_{c,1}^{\mathrm{I}}, \bar{f}_{c,2}^{\mathrm{I}}, \bar{f}_{c,3}^{\mathrm{I}}]^\intercal$, only $\bar{f}_{c,1}^{\mathrm{I}}$ and $\bar{f}_{c,2}^{\mathrm{I}}$ need to be produced by the thrusters. Note that the coordinate $\bar{f}_{c,3}^{\mathrm{I}}$ does not produce any translational motion due to the contact force on the upper stage due to the floor and assuming that the thrusters cannot levitate the upper stage with respect to the lower stage. However, to produce the desired control moment $\bar{\tau}_c^{\mathrm{S}}$, the total force produced by the thrusters might have to have a component perpendicular to the epoxy floor. This is because the upper stage cannot generate pure moments along $\bar{I}_{\mathrm{S}}$ and $\bar{J}_{\mathrm{S}}$, since it cannot generate forces along the $-\bar{K}_{\mathrm{S}}$ axis.

With this in mind, the control allocation problem is formally defined as the following minimization problem:

$$T^* = \arg\min_T w^\intercal T \tag{238}$$

subject to

$$0 \leq T_i \leq T_{i,\max,\text{LP}}, \quad i = 1, 2, ..., 12, \tag{239}$$

$$u = PT, \tag{240}$$

where $T = [T_1, T_2, ..., T_{12}]^\intercal$, $w = [w_1, w_2, ..., w_{12}]^\intercal$ is an array of weights specified by the user, $T_{i,\max,\text{LP}}$ is the maximum value of T_i allowed by the user, $u = [\bar{f}^{\text{I}}_{c,1},\ \bar{f}^{\text{I}}_{c,2},\ \bar{\tau}^{\text{S}}_{c,1},\ \bar{\tau}^{\text{S}}_{c,2},\ \bar{\tau}^{\text{S}}_{c,3}]^\intercal$, and $P = [P_f^\intercal, P_\tau^\intercal]^\intercal$, with $P_f \in \mathbb{R}^{2\times 12}$ and $P_\tau \in \mathbb{R}^{3\times 12}$. The matrix P_f is defined as

$$\begin{bmatrix} \bar{f}^{\text{I}}_{c,1} \\ \bar{f}^{\text{I}}_{c,2} \\ 0 \end{bmatrix} = \begin{bmatrix} P_f \\ 0_{1\times 12} \end{bmatrix} T = \begin{bmatrix} I_2 & 0_{2\times 1} \\ 0_{1\times 2} & 0 \end{bmatrix} R^{\text{I}\leftarrow\text{S}} \sum_{i=1}^{12} \bar{f}^{\text{S}}_{T_i} \tag{241}$$

or, equivalently,

$$P_f^\intercal = \begin{bmatrix} -(2q_{\text{S/I},0}q_{\text{S/I},3} - 2q_{\text{S/I},1}q_{\text{S/I},2}) & -(2q^2_{\text{S/I},1} + 2q^2_{\text{S/I},3} - 1) \\ (2q_{\text{S/I},0}q_{\text{S/I},2} + 2q_{\text{S/I},1}q_{\text{S/I},3}) & -(2q_{\text{S/I},0}q_{\text{S/I},1} - 2q_{\text{S/I},2}q_{\text{S/I},3}) \\ (2q_{\text{S/I},0}q_{\text{S/I},3} - 2q_{\text{S/I},1}q_{\text{S/I},2}) & (2q^2_{\text{S/I},1} + 2q^2_{\text{S/I},3} - 1) \\ (2q^2_{\text{S/I},2} + 2q^2_{\text{S/I},3} - 1) & -(2q_{\text{S/I},0}q_{\text{S/I},3} + 2q_{\text{S/I},1}q_{\text{S/I},2}) \\ (2q_{\text{S/I},0}q_{\text{S/I},2} + 2q_{\text{S/I},1}q_{\text{S/I},3}) & -(2q_{\text{S/I},0}q_{\text{S/I},1} - 2q_{\text{S/I},2}q_{\text{S/I},3}) \\ -(2q^2_{\text{S/I},2} + 2q^2_{\text{S/I},3} - 1) & (2q_{\text{S/I},0}q_{\text{S/I},3} + 2q_{\text{S/I},1}q_{\text{S/I},2}) \\ (2q_{\text{S/I},0}q_{\text{S/I},3} - 2q_{\text{S/I},1}q_{\text{S/I},2}) & (2q^2_{\text{S/I},1} + 2q^2_{\text{S/I},3} - 1) \\ (2q_{\text{S/I},0}q_{\text{S/I},2} + 2q_{\text{S/I},1}q_{\text{S/I},3}) & -(2q_{\text{S/I},0}q_{\text{S/I},1} - 2q_{\text{S/I},2}q_{\text{S/I},3}) \\ -(2q_{\text{S/I},0}q_{\text{S/I},3} - 2q_{\text{S/I},1}q_{\text{S/I},2}) & -(2q^2_{\text{S/I},1} + 2q^2_{\text{S/I},3} - 1) \\ -(2q^2_{\text{S/I},2} + 2q^2_{\text{S/I},3} - 1) & (2q_{\text{S/I},0}q_{\text{S/I},3} + 2q_{\text{S/I},1}q_{\text{S/I},2}) \\ (2q_{\text{S/I},0}q_{\text{S/I},2} + 2q_{\text{S/I},1}q_{\text{S/I},3}) & -(2q_{\text{S/I},0}q_{\text{S/I},1} - 2q_{\text{S/I},2}q_{\text{S/I},3}) \\ (2q^2_{\text{S/I},2} + 2q^2_{\text{S/I},3} - 1) & -(2q_{\text{S/I},0}q_{\text{S/I},3} + 2q_{\text{S/I},1}q_{\text{S/I},2}) \end{bmatrix}, \tag{242}$$

where $q_{\text{S/I}} = (q_{\text{S/I},0}, \bar{q}_{\text{S/I}})$. On the other hand, the matrix P_τ is defined as

$$\bar{\tau}^{\text{S}}_c = P_\tau T = \sum_{i=1}^{12} \bar{r}^{\text{S}}_{T_i/CR} \times \bar{f}^{\text{S}}_{T_i} \tag{243}$$

or, equivalently,

$$P_\tau^{\mathsf{T}} = \begin{bmatrix} -z^{\mathrm{S}}_{T_1/CR} & 0 & x^{\mathrm{S}}_{T_1/CR} \\ y^{\mathrm{S}}_{T_2/CR} & -x^{\mathrm{S}}_{T_2/CR} & 0 \\ z^{\mathrm{S}}_{T_3/CR} & 0 & -x^{\mathrm{S}}_{T_3/CR} \\ 0 & -z^{\mathrm{S}}_{T_4/CR} & y^{\mathrm{S}}_{T_4/CR} \\ y^{\mathrm{S}}_{T_5/CR} & -x^{\mathrm{S}}_{T_5/CR} & 0 \\ 0 & z^{\mathrm{S}}_{T_6/CR} & -y^{\mathrm{S}}_{T_6/CR} \\ z^{\mathrm{S}}_{T_7/CR} & 0 & -x^{\mathrm{S}}_{T_7/CR} \\ y^{\mathrm{S}}_{T_8/CR} & -x^{\mathrm{S}}_{T_8/CR} & 0 \\ -z^{\mathrm{S}}_{T_9/CR} & 0 & x^{\mathrm{S}}_{T_9/CR} \\ 0 & z^{\mathrm{S}}_{T_{10}/CR} & -y^{\mathrm{S}}_{T_{10}/CR} \\ y^{\mathrm{S}}_{T_{11}/CR} & -x^{\mathrm{S}}_{T_{11}/CR} & 0 \\ 0 & -z^{\mathrm{S}}_{T_{12}/CR} & y^{\mathrm{S}}_{T_{12}/CR} \end{bmatrix}, \tag{244}$$

where $\bar{r}^{\mathrm{S}}_{T_i/CR} = [x^{\mathrm{S}}_{T_i/CR}, y^{\mathrm{S}}_{T_i/CR}, z^{\mathrm{S}}_{T_i/CR}]^{\mathsf{T}}$. (The position vectors $\bar{r}^{\mathrm{S}}_{T_i/CR}$ were experimentally determined using the VICON system.)

The minimization problem specified by Eqs. (238), (239), and (240) is a *Linear Programming* (LP) problem. This problem is solved numerically using the *GNU Linear Programming Kit* (GLPK).

In the current implementation of the code, $T_{i,\max,\mathrm{LP}}$ is 50% higher than $T_{i,\max}$, where $T_{i,\max}$ is the maximum thrust of thruster i measured experimentally. This is to allow T_i to momentarily exceed $T_{i,\max}$ without leading to an infeasible LP problem. However, it is important that T_i does not exceed $T_{i,\max}$ for too long, as this can lead to an unstable closed-loop system. In addition, in the current implementation of the code, the user is given the choice to stop the simulation/experiment if the GLPK package cannot find an optimal feasible solution to the LP problem, e.g., because the norm of $\bar{f}^{\mathrm{S}}_c$ is too high.

6.4.3 Control Allocation in the (2+1)-Case

In the current implementation, the control allocation in the (2+1)-case is identical to the control allocation in the 5-DOF case. The only difference is that the first two inertial coordinates of the control moment supplied by the controller block to the control allocation block, i.e., $\bar{\tau}_{c,1}^{\mathrm{I}}$ and $\bar{\tau}_{c,2}^{\mathrm{I}}$ in $\bar{\tau}_c^{\mathrm{I}} = [\bar{\tau}_{c,1}^{\mathrm{I}}, \bar{\tau}_{c,2}^{\mathrm{I}}, \bar{\tau}_{c,3}^{\mathrm{I}}]^{\mathrm{T}}$, are set to zero in the controller block (in the current implementation, they are set to zero in the controller block and not in the control allocation block). This is done to protect the epoxy floor from damage since in the (2+1)-DOF case and assuming that the epoxy floor is perfectly flat, these two coordinates would just press the lower stage against the epoxy floor, without producing any motion.

6.4.4 Control Allocation in the 3-DOF Case

In the current implementation, the control allocation in the 3-DOF case is identical to the control allocation in the 5-DOF case. The only difference is that, in 3-DOF case, the desired control force supplied by the controller block is set to zero in the controller block.

6.5 Conversion from Continuous-Time Thrust to On-Off Commands

The thrust values T_i, $i = 1, 2, ..., 12$, calculated by the linear programming package cannot be implemented directly by the on-board cold-gas thrusters. Whereas T_i is a continuous-time signal bounded between 0 and $T_{i,\mathrm{max,LP}}$, the on-board thrusters only accept on-off commands. To make this conversion, a scheme based on a *Pulse-Width-Modulator* (PWM) [101] and a *Schmitt trigger* [4, 101] is employed. The PWM creates a linear mapping between the value of T_i and the *duty cycle* of a rectangular waveform with a certain frequency. In particular, if $T_i = 0$, the duty cycle of the rectangular waveform is 0%. If $T_{i,\max} \leq T_i \leq T_{i,\mathrm{max,LP}}$, the duty cycle of the rectangular waveform is 100%. This relation is illustrated in Figure 50. Moreover, to avoid chattering and

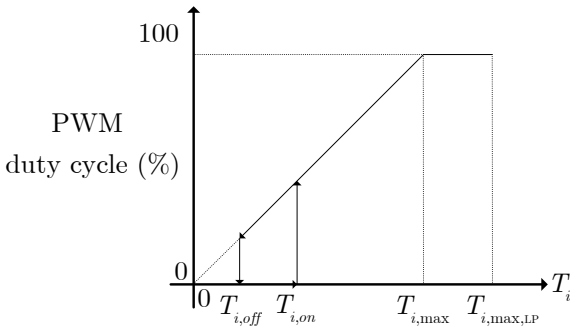

Figure 50: Relation between the duty cycle of the PWM and the desired continuous thrust.

waste of fuel near the reference pose (at the cost of pose-tracking error), a Schmitt trigger (i.e., a deadzone and hysteresis) is superposed to the PWM mapping. Finally, when the rectangular waveform is at its maximum value, thruster i is open. When the rectangular waveform is at its minimum value, thruster i is closed.

In the current implementation, the rectangular waveform has a frequency of 10 Hz. Note that the opening and closing time of the solenoid valves of the cold-gas thrusters imposes an upper limit on this frequency.

6.6 Implementation of the Inertia-Free Pose-Tracking Controller

The high-fidelity simulation of the 5-DOF platform includes an implementation of the adaptive and nonadaptive pose-tracking controllers given by Eq. (158) and Eq. (166), respectively. Since the 5-DOF platform operates in a 1-g environment, the terms due to the gravitational field in Eq. (158) and Eq. (166) are disregarded, as in Ref. [27]. Since these controllers were developed for 6-DOF motion, a few notes are in order about their implementation in the 3-DOF, (2+1)-DOF, and 5-DOF cases. From the point of view of the controller, in the 5-DOF and (2+1)-DOF cases, the epoxy floor is assumed to be perfectly flat.

In all cases, the third coordinate of $\bar{r}^{\mathrm{I}}_{CR/O_{\mathrm{I}}}$, $\bar{r}^{\mathrm{I}}_{O_{\mathrm{D}}/O_{\mathrm{I}}}$, $\bar{v}^{\mathrm{I}}_{CR/\mathrm{I}}$, $\bar{v}^{\mathrm{I}}_{\mathrm{D/I}}$, and $\dot{\bar{v}}^{\mathrm{I}}_{\mathrm{D/I}}$ are set zero and $m = m_t$ in Eq. (166).

In the 3-DOF case, $\bar{f}_c^{\mathrm{B}}$ is set to zero and $\bar{I}^{\mathrm{B}} = {}^{CR}\bar{I}_s^{\mathrm{S}}$ in Eq. (166).

In the 5-DOF case, $\bar{I}^{\mathrm{B}} = {}^{CR}\bar{I}_s^{\mathrm{S}}$ in Eq. (166) and the third coordinate of $\bar{f}_c^{\mathrm{I}}$ is set to zero.

In the (2+1)-DOF case, $\bar{I}^{\mathrm{B}} = {}^{CR}\bar{I}_s^{\mathrm{S}} + R^{\mathrm{S}\leftarrow\mathrm{L}}({}^{CR}\bar{I}_l^{\mathrm{L}})R^{\mathrm{L}\leftarrow\mathrm{S}}$ in Eq. (166), the third coordinate of $\bar{f}_c^{\mathrm{I}}$ is set to zero, and the first and second coordinates of $\bar{\tau}_c^{\mathrm{I}}$ are set to zero.

6.7 Experimental Results and Validation of the High-Fidelity Simulation

To experimentally validate the derivation of the equations of motion, the allocation of the control moment to the VSCMGs, the allocation of the control moment and force to the thrusters, the conversion from continuous-time thrust to on-off commands, and the implementation of the inertia-free pose-tracking controller and of the DQ-MEKF, four experiments were run in real-time on the 5-DOF platform. In the first, a sinusoidal reference attitude with respect to the inertial frame is tracked using the VSCMGs and measurements from the IMU. In the second, a constant reference attitude is maintained with respect to a target object using the VSCMGs and measurements from the rate-gyros and a camera. In the third, the same sinusoidal reference attitude with respect to the inertial frame tracked in the first experiment is now tracked using the cold-gas thrusters and measurements from the VICON system, rate-gyros, and IMU merged with the DQ-MEKF. Finally, in the fourth experiment, a time-varying reference pose with respect to the inertial frame is tracked using the cold-gas thrusters and measurements from the VICON system, rate-gyros, and IMU merged with DQ-MEKF.

6.7.1 Attitude-Tracking using the IMU and the VSCMGs

In the first experiment, three VSCMGs were used to track a time-varying attitude reference. The angular velocity and attitude of the upper stage with respect to the

inertial frame were measured with the IMU at 100 Hz. These measurements were passed through a 4-th order discrete-time Butterworth filter to reduce their noise and fed directly into the pose-tracking controller and into the control moment allocation block. The on-board computer was run at 100 Hz. The VSCMGs were run in VSCMG mode with no wheel speed equalization, $w_1 = 0.01$ and $w_2 = 0.01$ in Eq. (223), and

$$I_{ws} = \text{diag}([0.004224, 0.004224, 0.004224, 0.004224]) \text{ kg} \cdot \text{m}^2,$$
$$I_{cs} = \text{diag}([0.01456, 0.01456, 0.01456, 0.01456]) \text{ kg} \cdot \text{m}^2,$$
$$I_{cg} = \text{diag}([0.0082, 0.0082, 0.0082, 0.0082]) \text{ kg} \cdot \text{m}^2,$$
$$I_{ct} = \text{diag}([0.0121, 0.0121, 0.0121, 0.0121]) \text{ kg} \cdot \text{m}^2.$$

Only VSCMGs #1, #2, and #3 were operational.

The reference attitude is given by $\psi_{\text{D/I}} = 30 \sin(\frac{2\pi}{100} t)$ deg, $\theta_{\text{D/I}} = 0$ deg, and $\phi_{\text{D/I}} = 5 \sin(\frac{2\pi}{50} t)$ deg, as in Ref. [48], where $\psi_{\text{D/I}}$, $\theta_{\text{D/I}}$, and $\phi_{\text{D/I}}$ are the Euler angles (aerospace sequence) that describe the desired orientation of the S-frame with respect to the I-frame.

The control gains are chosen to be $\bar{K}_r = 0.1 I_{3\times3}$, $\bar{K}_q = 0.1 I_{3\times3}$, $\bar{K}_v = 15 I_{3\times3}$, $\bar{K}_\omega = 15 I_{3\times3}$, and $K_i = 1e^4 I_{7\times7}$. At the beginning of the experiment, the initial state of the inertia-free pose-tracking controller is

$$\text{v}(\widehat{M^{\text{B}}}) = [12.0534, 0.5348, 2.1950, 13.0253, 1.5343, 25.5473, 525.6481]^{\intercal}.$$

The initial state of the platform at the beginning of the experiment is given by $\bar{\omega}^{\text{S}}_{\text{S/I}}(0) = [0.0161, -0.0020, -0.0045]^{\intercal}$ rad/s, $\psi_{\text{S/I}}(0) = -6.1477$ deg, $\theta_{\text{S/I}}(0) = 0.3568$ deg, $\phi_{\text{S/I}}(0) = 1.4642$ deg, $\gamma(0) = [183.25, 359.37, 124.90, 0]^{\intercal}$ deg, and $\Omega(0) = [1797, 1775, 1791, 0]^{\intercal}$ rpm.

Figure 51 compares the desired attitude and angular velocity with the attitude and angular velocity measured with the IMU. The error between them is shown in Figure 52. After the initial transient response, each desired Euler angle is tracked

within ±2 deg and each desired angular velocity coordinate is tracked within ±1 deg/s. According to a posteriori high-fidelity simulations, the attitude-tracking error can be attributed to the measurement noise (by itself, responsible for an attitude-tracking error of ∼0.6 deg), to the ±4 deg/s deadzone on $\dot{\gamma}$ (by itself, responsible for an attitude-tracking error of ∼0.5 deg), and to the misalignment between the center of mass of the upper stage and the center of rotation (by itself, responsible for an attitude-tracking error of ∼1 deg).

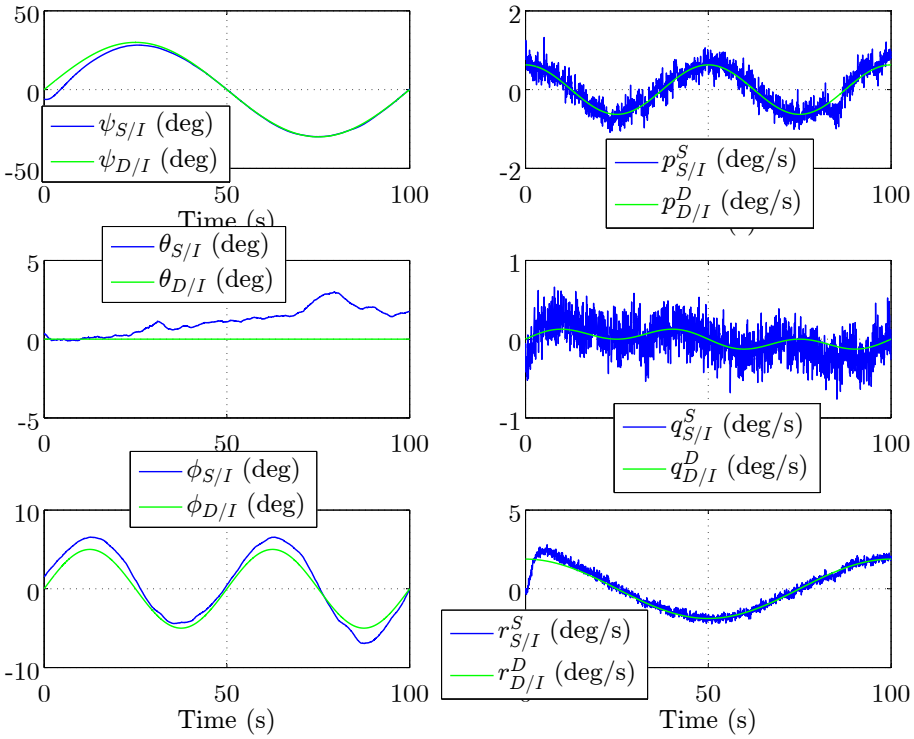

Figure 51: Data from attitude-tracking experiment with VSCMGs: desired attitude and angular velocity versus actual attitude and angular velocity.

Figure 53 shows the angular speeds and the commanded angular accelerations of the wheels of the VSCMGs. As explained in Section 6.3.2, when σ_c is large, i.e., when the VSCMGs are close to a singularity, the VSCMGs are operated as reaction wheels in order to avoid or escape the singularity. Otherwise, they are run as regular CMGs, i.e., $\dot{\Omega}$ is zero. Two such transitions from CMG mode to RW mode are visible in Figure 53, one at around 29 sec and another one at around 93 sec. The

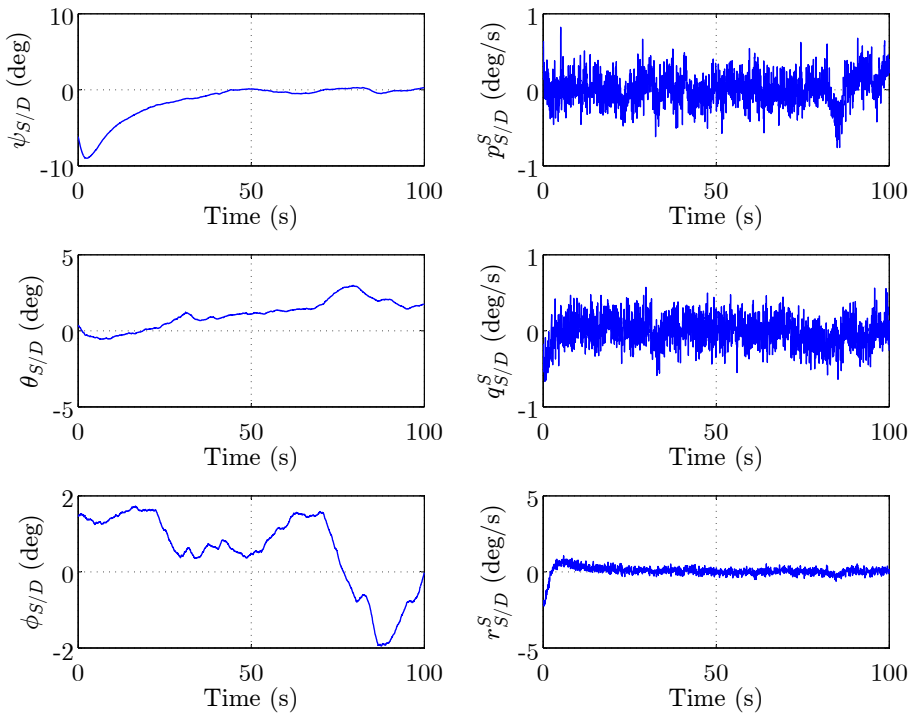

Figure 52: Data from attitude-tracking experiment with VSCMGs: attitude-tracking error and angular velocity tracking error.

condition numbers of matrices C and D defined in Eq. (216) are given in Figure 54. As expected, the transitions from CMG mode to RW mode occur when σ_c peaks. A posteriori high-fidelity simulations have shown that these singularities are mainly a result of using only three VSCMGs.

The angles and the angular speeds of the gimbals of the VSCMGs, as measured by the on-board sensors, are presented in Figure 54. The deadzone in $\dot{\gamma}$ is visible.

Finally, Figure 56 compares the states of the inertia-free pose-tracking controller with the best guess of the true inertia matrix of the upper stage. According to a posteriori high-fidelity simulations, the controller was not expected to be able to identify the inertia matrix in this experiment, mainly due to the many real-word effects that violate the conditions of Proposition 5.2.

The same 3-DOF case, with the same conditions, parameters and initial state, was run on the high-fidelity simulator to validate the simulated results against the

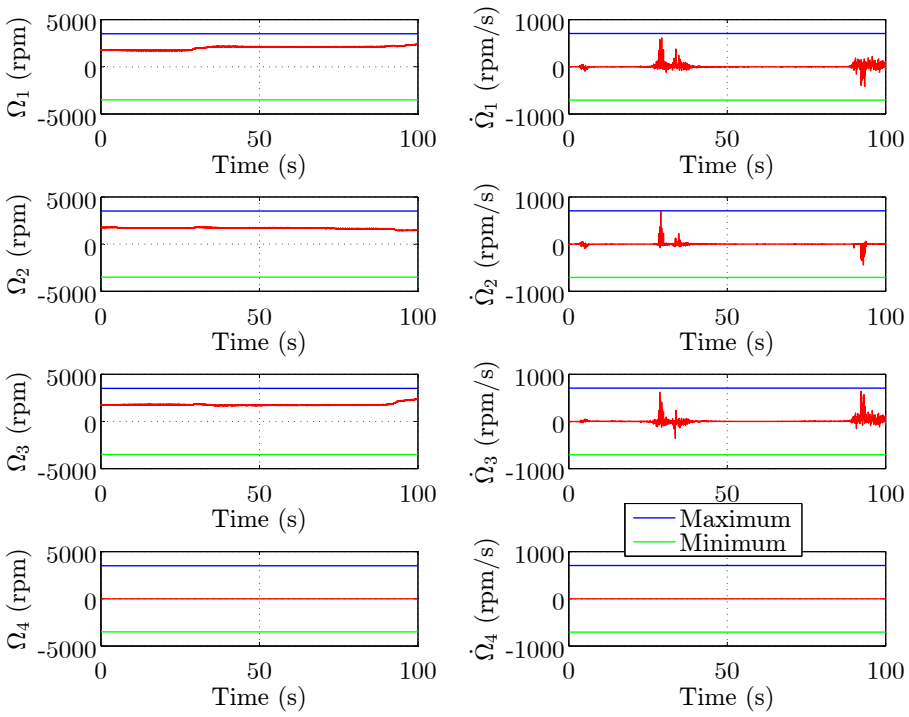

Figure 53: Data from attitude-tracking experiment with VSCMGs: wheel speeds and accelerations.

experimental results shown above. The real-world effects specified in Section 6.2 were applied and the following parameters were defined in the input file of the simulation:

$$T_{1,\max} = 3.65 \text{ N},\ T_{2,\max} = 1.10 \text{ N},\ T_{3,\max} = 3.86 \text{ N},\ T_{4,\max} = 4.99 \text{ N},$$

$$T_{5,\max} = 1.00 \text{ N},\ T_{6,\max} = 4.68 \text{ N},\ T_{7,\max} = 2.32 \text{ N},\ T_{8,\max} = 0.97 \text{ N},$$

$$T_{9,\max} = 3.11 \text{ N},\ T_{10,\max} = 3.04 \text{ N}, T_{11,\max} = 0.88 \text{ N},\ T_{12,\max} = 5.23 \text{ N},$$

$$w = 1_{12\times 1},\ T_{i,off} = 0.075 \text{ N},\ T_{i,on} = 0.1 \text{ N},\ m_t = 410 \text{ kg},\ m_s = 134 \text{ kg},$$

$$\bar{r}^{\mathrm{S}}_{\mathcal{B}_s/CR} = [5e^{-6}, 5e^{-6}, 0]^{\mathsf{T}} \text{ m},\ \bar{r}^{\mathrm{S}}_{\mathcal{B}_f/CR} = [0,0,0]^{\mathsf{T}} \text{ m},\ \bar{r}^{\mathrm{L}}_{\mathcal{B}_l/CR} = [0,0,1]^{\mathsf{T}} \text{ m},$$

$$\bar{a}^{\mathrm{S}}_{\mathcal{B}_s/\mathrm{S}} = [0,0,0]^{\mathsf{T}} \text{ m/s}^2,\ \bar{v}^{\mathrm{S}}_{\mathcal{B}_s/\mathrm{S}} = [0,0,0]^{\mathsf{T}} \text{ m/s},\ \bar{a}^{\mathrm{L}}_{\mathcal{B}_l/\mathrm{L}} = [0,0,0]^{\mathsf{T}} \text{ m/s}^2,$$

$$\bar{v}^{\mathrm{L}}_{\mathcal{B}_l/\mathrm{L}} = [0,0,0]^{\mathsf{T}} \text{ m/s},\ \bar{r}^{\mathrm{S}}_{A/CR} = [0.113, -0.016, -0.089]^{\mathsf{T}} \text{ m},$$

$${}^{CR}\bar{I}^{\mathrm{S}}_{f+m_{c_i}} = \begin{bmatrix} 12.2012 & -0.0899 & -0.0469 \\ -0.0899 & 12.9943 & -0.4187 \\ -0.0469 & -0.4187 & 16.2764 \end{bmatrix} \text{ kg}\cdot\text{m}^2,\ {}^{CR}\bar{I}^{\mathrm{L}}_{l} = \begin{bmatrix} 20 & 0 & 0 \\ 0 & 20 & 0 \\ 0 & 0 & 10 \end{bmatrix} \text{ kg}\cdot\text{m}^2,$$

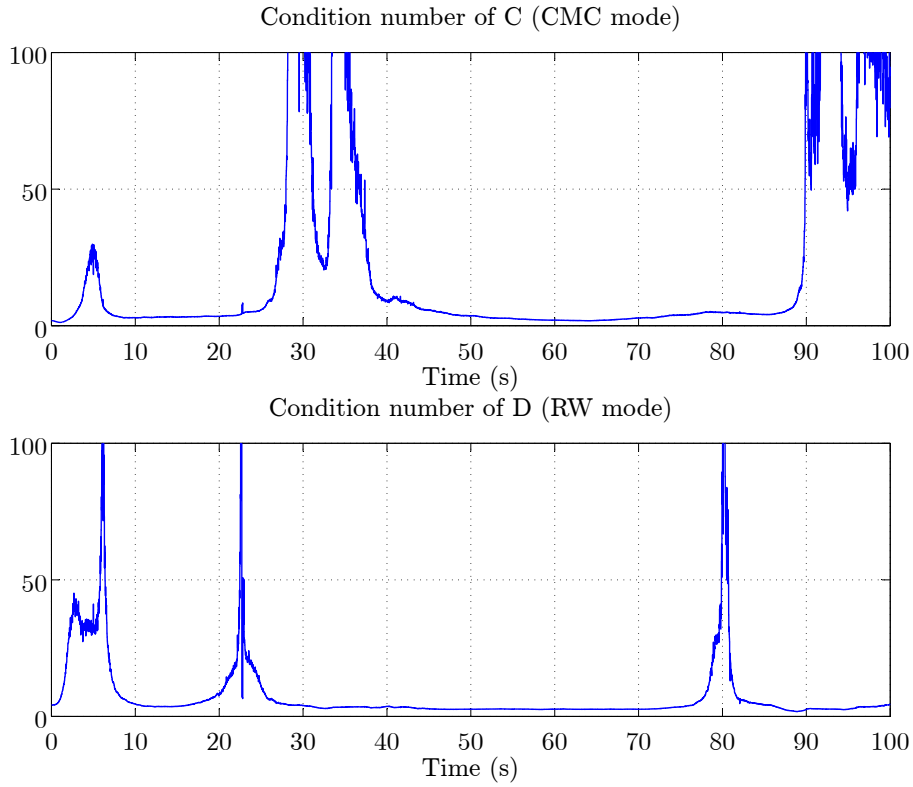

Figure 54: Data from attitude-tracking experiment with VSCMGs: condition numbers.

$$r^{\mathrm{S}}_{T_1/CR} = [0.482, -0.078, -0.017]^{\mathsf{T}} \text{ m}, \; r^{\mathrm{S}}_{T_2/CR} = [0.483, 0.002, -0.106]^{\mathsf{T}} \text{ m},$$

$$r^{\mathrm{S}}_{T_3/CR} = [0.484, 0.080, -0.018]^{\mathsf{T}} \text{ m}, \; r^{\mathrm{S}}_{T_4/CR} = [0.077, 0.483, -0.015]^{\mathsf{T}} \text{ m},$$

$$r^{\mathrm{S}}_{T_5/CR} = [-0.001, 0.483, -0.107]^{\mathsf{T}} \text{ m}, \; r^{\mathrm{S}}_{T_6/CR} = [-0.080, 0.482, -0.013]^{\mathsf{T}} \text{ m},$$

$$r^{\mathrm{S}}_{T_7/CR} = [-0.481, 0.081, -0.022]^{\mathsf{T}} \text{ m}, \; r^{\mathrm{S}}_{T_8/CR} = [-0.483, -0.002, -0.116]^{\mathsf{T}} \text{ m},$$

$$r^{\mathrm{S}}_{T_9/CR} = [-0.486, -0.091, -0.035]^{\mathsf{T}} \text{ m}, \; r^{\mathrm{S}}_{T_{10}/CR} = [-0.078, -0.484, -0.026]^{\mathsf{T}} \text{ m},$$

$$r^{\mathrm{S}}_{T_{11}/CR} = [0.001, -0.483, -0.117]^{\mathsf{T}} \text{ m}, \; r^{\mathrm{S}}_{T_{12}/CR} = [0.086, -0.485, -0.036]^{\mathsf{T}} \text{ m}.$$

Figure 57 compares the desired attitude and angular velocity with the attitude and angular velocity measured by the IMU in simulation. The error between them is shown in Figure 58. Whereas each desired Euler angle is tracked within ± 2 deg in Figure 52, here each desired Euler angle is tracked within ± 1 deg. Moreover, whereas each desired angular velocity coordinate is tracked within ± 1 deg/s in Figure 52,

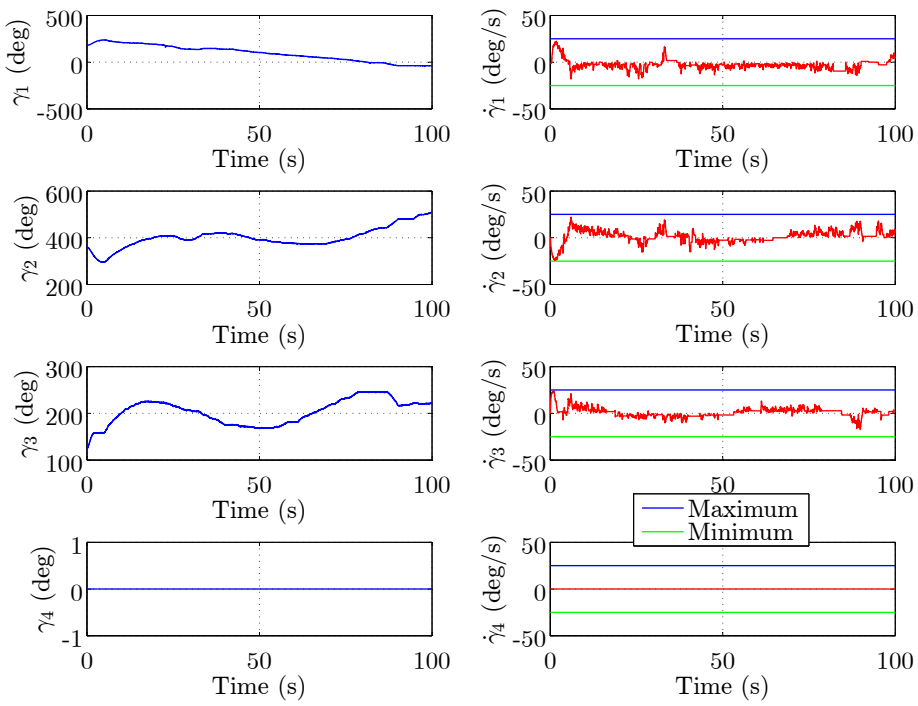

Figure 55: Data from attitude-tracking experiment with VSCMGs: gimbal angles and speeds.

here each desired angular velocity coordinate is tracked within ± 0.5 deg/s. Hence, the simulation with the current parameters slightly overestimates the performance of the hardware. However, the transient response of $\psi_{\text{S/D}}$ (note that the amplitude of $\psi_{\text{D/I}}$ is the highest of the three desired Euler angles) obtained in simulation is relatively similar to one obtained experimentally. Comparing Figure 58 with Figure 52 also shows that the experimental measurement noise of the IMU is not perfect AWGN as in the simulation.

Figure 60 gives the condition numbers of matrices C and D defined in Eq. (216) throughout the simulation. Compared to Figure 54, it is obvious that the number and location of the singularities in the simulation and in the experiment do not match. However, the simulation predicts the existence of singularities and the effectiveness of the algorithm in escaping them. Since the angular speeds and the commanded angular accelerations of the wheels of the VSCMGs depend on these singularities, Figure 59

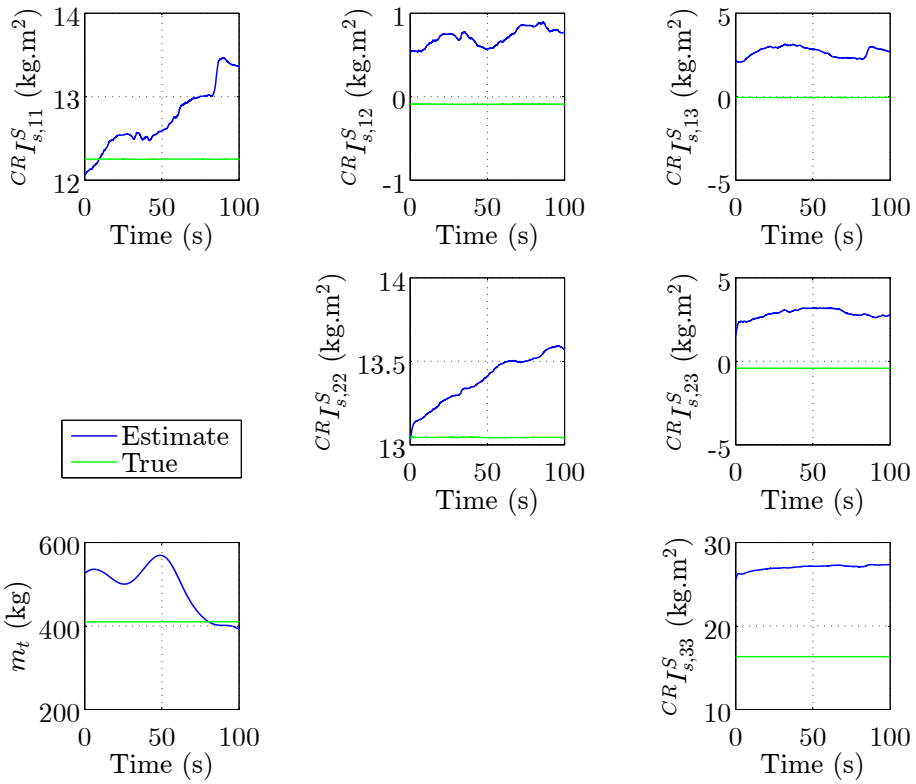

Figure 56: Data from attitude-tracking experiment with VSCMGs: mass and inertia matrix estimates.

and Figure 53 are necessarily different. A posteriori simulations have shown that moving the center of mass of the upper stage by as little as $5e^{-6}$ m will result in a completely different pattern of singularities. Since the true location of the center of mass is unknown and moves every time the upper stage of the platform is balanced (each happens at the beginning of every experiment), it is not reasonable to expect the simulation to accurately predict the location of these singularities.

The simulated angles and angular speeds of the gimbals of the VSCMGs are presented in Figure 61. Compared to Figure 54, the gimbals of the VSCMGs achieve much higher angular accelerations in the simulation. This is not surprising since the closed-loop dynamics of the control systems that drive the gimbals are not modeled in the simulation. Hence, the angular speeds of the gimbals can vary instantaneously in the simulation. The inertia of the gimbals prevents this from happening in real

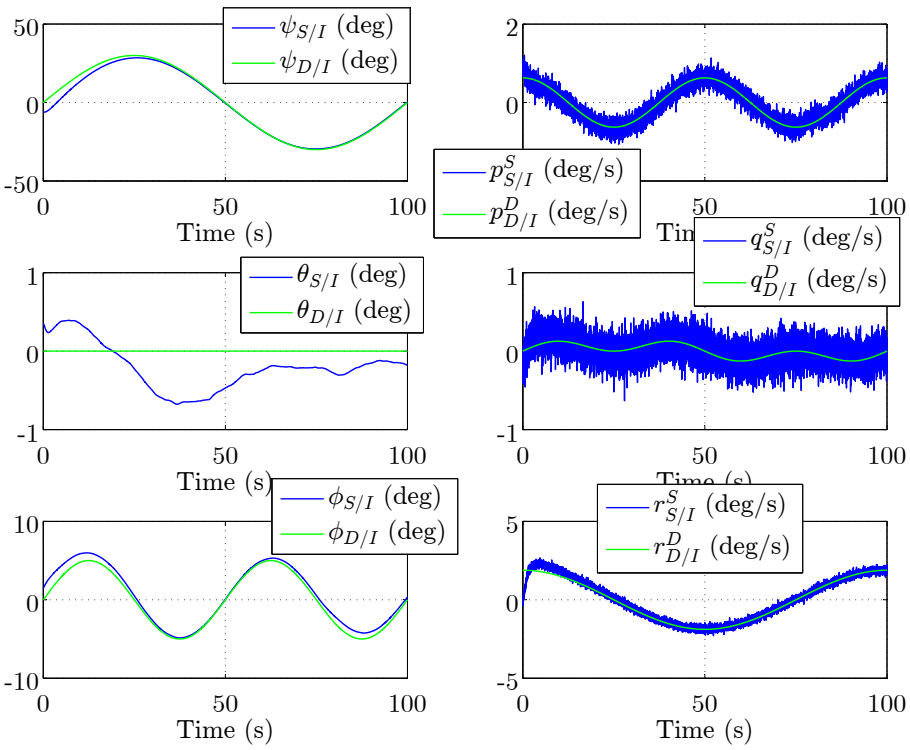

Figure 57: Data from attitude-tracking simulation with VSCMGs: desired attitude and angular velocity versus actual attitude and angular velocity.

life.

Finally, Figure 62 shows that the simulation predicts the order of magnitude and overall behavior of the states of the adaptive controller.

6.7.2 Attitude-Regulation using the Camera and the VSCMGs

Another 3-DOF experiment using three VSCMGs was run on the platform in combination with the vision-based pose estimation algorithm described in Ref. [111]. This algorithm estimates the pose of the S-frame with respect to a frame fixed to a known pattern on a target object, hereafter denoted as the T-frame. A PC-104 Meteor II-Morphis frame grabber (MOR+/2VD/J2K by Matrox Imaging) is used to grab images obtained from an analog CCD camera (TMS-730p by Pulnix) with a resolution of 640 $\times$ 480 pixels. The pose estimate is updated asynchronously, at approximately

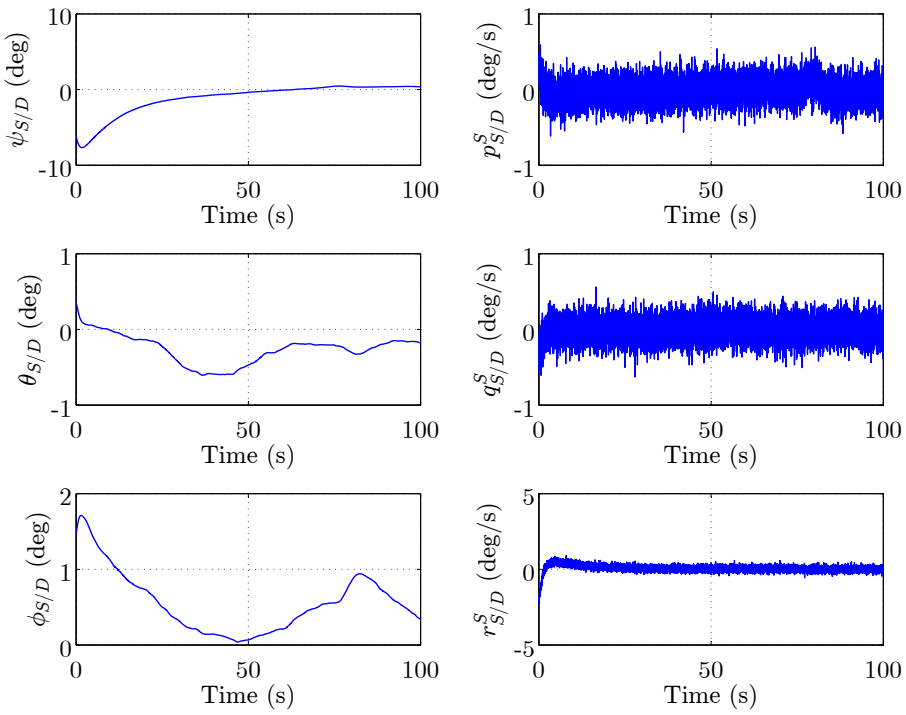

Figure 58: Data from attitude-tracking simulation with VSCMGs: attitude-tracking error and angular velocity tracking error.

10 Hz. Measurements of $\bar{\omega}^{\mathrm{S}}_{\mathrm{S/I}}$ are obtained from the rate-gyros at 100 Hz. These measurements are passed through a 4-th order discrete-time Butterworth filter to reduce their noise. It is assumed that the angular velocity of the T-frame with respect to the inertial frame is zero, i.e., $\bar{\omega}^{\mathrm{S}}_{\mathrm{T/I}} = 0$. Under this assumption, the rate-gyros on the platform give a direct measurement of the relative angular velocity between the S-frame and the T-frame, since $\bar{\omega}^{\mathrm{S}}_{\mathrm{S/T}} = \bar{\omega}^{\mathrm{S}}_{\mathrm{S/I}} - \bar{\omega}^{\mathrm{S}}_{\mathrm{T/I}} = \bar{\omega}^{\mathrm{S}}_{\mathrm{S/I}}$. The measurements of $\bar{q}_{\mathrm{S/T}}$ and $\bar{\omega}^{\mathrm{S}}_{\mathrm{S/T}}$ are merged in a Q-MEKF. The Q-MEKF is described in detail in Ref. [57] and is the real part of the DQ-MEKF algorithm described in Section 4.3. The output of the Q-MEKF is fed into the inertia-free pose-tracking controller and into the control moment allocation block. The initial estimate of the state of the Q-MEKF is given in Table 13. The same table also shows an a posteriori guess of the initial state based on the measurements. The Q-MEKF was initialized with the covariance matrices given in Table 14.

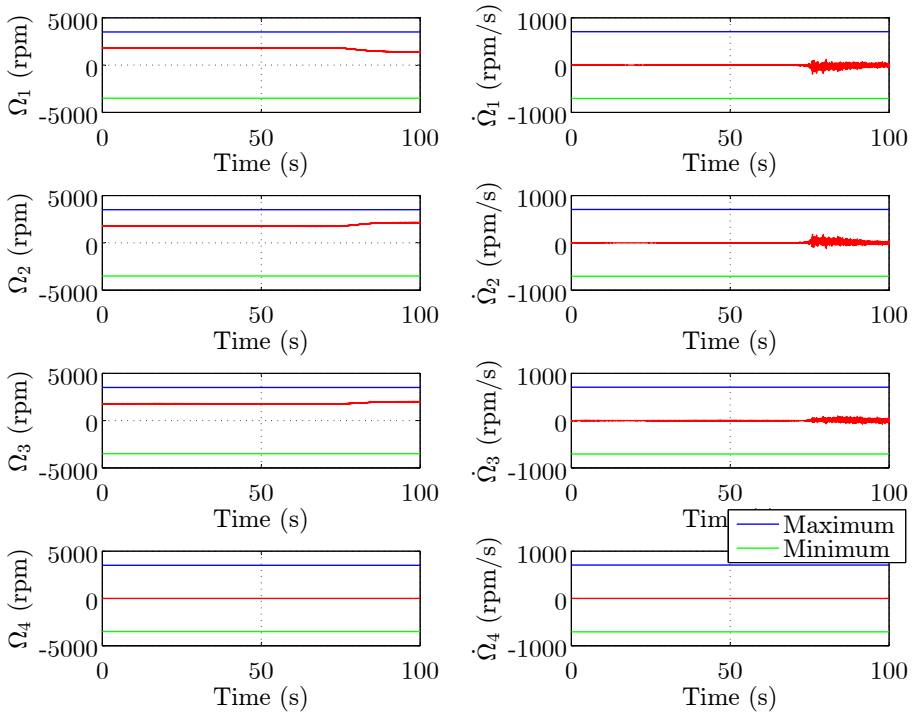

Figure 59: Data from attitude-tracking simulation with VSCMGs: wheel speeds and accelerations.

Table 13: Initial estimate and a posteriori guess of the state of the Q-MEKF.

Variable	Initial Estimate	A Posteriori Guess
$q_{\text{S/T}}(0)$	$[0.7061, -0.7044, 0.0616, 0.0370]^\intercal$	$[0.7090, -0.7018, 0.0570, 0.0385]^\intercal$
$b_\omega(0)$	$[-1, 1, 1]^\intercal$ (deg/s)	$[-1.5, 1.6, 1.3]^\intercal$ (deg/s)

The VSCMGs were run in VSCMG mode with no wheel speed equalization, $w_1 = 0.01$ and $w_2 = 0.01$ in Eq. (223), and I_{ws}, I_{cs}, I_{cg}, and I_{ct} defined as in Section 6.7.1. Only VSCMGs #1, #2, and #3 were operational.

During the first 20 sec, no control commands were issued and the Q-MEKF was allowed to converge. After 20 sec, the reference attitude is given by $\psi_{\text{D/T}} \equiv -2$ deg, $\theta_{\text{D/T}} \equiv 8$ deg, and $\phi_{\text{D/T}} \equiv -90$ deg. The upper stage is levitated at around 16 sec.

The control gains are chosen to be $\bar{K}_r = 0.3I_{3\times3}$, $\bar{K}_q = 0.1I_{3\times3}$, $\bar{K}_v = 25I_{3\times3}$, $\bar{K}_\omega = 15I_{3\times3}$, and $K_i = 1e^5 I_{7\times7}$. At the beginning of the experiment, the initial state

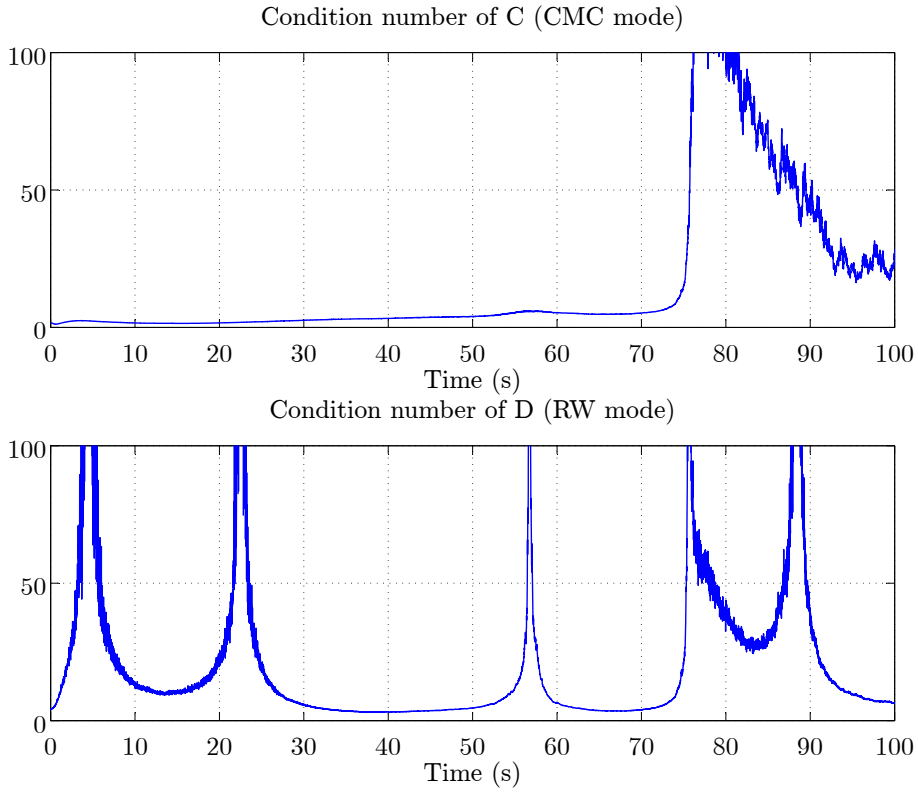

Figure 60: Data from attitude-tracking simulation with VSCMGs: condition numbers.

Table 14: Covariance matrices of the Q-MEKF.

$\tilde{P}_{8\times8}(0)$	$\text{diag}([0, 0.0069, 0.0069, 0.0069, 0, 2\times10^{-6}, 2\times10^{-6}, 2\times10^{-6}])$
$Q_{6\times6}$	$\text{diag}([7\times10^{-7}, 7\times10^{-7}, 7\times10^{-7}, 2\times10^{-9}, 2\times10^{-9}, 2\times10^{-9}])$
$R_{3\times3}$	$\text{diag}([1\times10^{-6}, 1\times10^{-6}, 1\times10^{-6}])$

of the inertia-free pose-tracking controller is

$$\text{v}(\widehat{M^{\text{B}}}) = [8.5408, -0.0629, -0.0328, 9.0960, -0.2931, 11.3935, 287]^{\intercal}.$$

The initial state of the platform at the beginning of the experiment is given by $\bar{\omega}^{\text{S}}_{\text{S/T}}(0) = [0, 0, 0]^{\intercal}$ rad/s, $\psi_{\text{S/T}}(0) = -1.5$ deg, $\theta_{\text{S/T}}(0) = 7.8$ deg, $\phi_{\text{S/T}}(0) = -89.5$ deg, $\gamma(0) = [3.57, 359.82, 124.76, 0]^{\intercal}$ deg, and $\Omega(0) = [0, 0, 0, 0]^{\intercal}$ rpm. During the first 20 sec, the wheels of the operational VSCMGs were accelerated up to 1800 rpm.

Figure 63 compares the attitude and angular velocity of the S-frame with respect

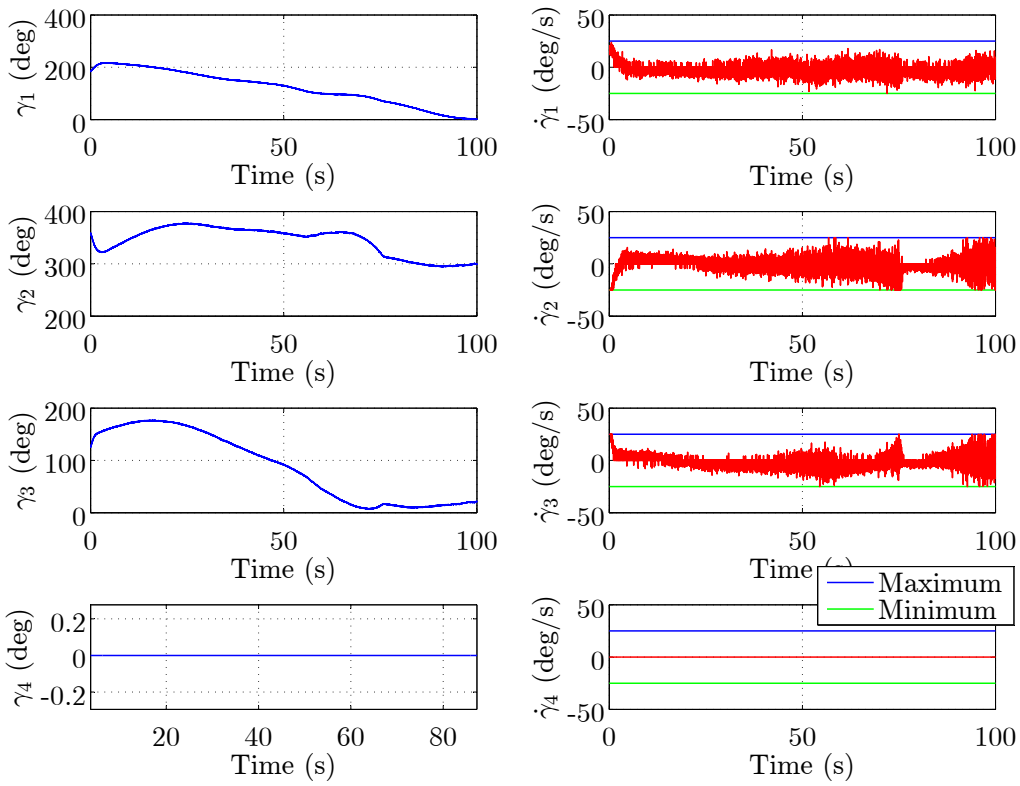

Figure 61: Data from attitude-tracking simulation with VSCMGs: gimbal angles and speeds.

to the T-frame measured by the vision algorithm and by the rate-gyros, respectively, with the estimates produced by the Q-MEKF. The Q-MEKF is used to smooth out the discrete-time attitude measurements, to bridge the gap between them, and to remove the biases of the rate-gyros (which are clearly visible in Figure 63).

Figure 64 compares the desired attitude and angular velocity of the S-frame with respect to the T-frame (constant in this experiment) with the best guess of the state of the platform (given by the outputs of the Q-MEKF). The error between them is presented in Figure 65. At approximately 42 sec after the beginning of the experiment, the target was slowly rotated, leading to a decrease of approximately 3 deg in $\psi_{\mathrm{S/T}}$ and $\theta_{\mathrm{S/T}}$. At approximately 68 sec after the beginning of the experiment, the target was slowly rotated to its original orientation, leading to an increase of approximately 3 deg in $\psi_{\mathrm{S/T}}$ and $\theta_{\mathrm{S/T}}$. Finally, at approximately 92 sec after the beginning of the

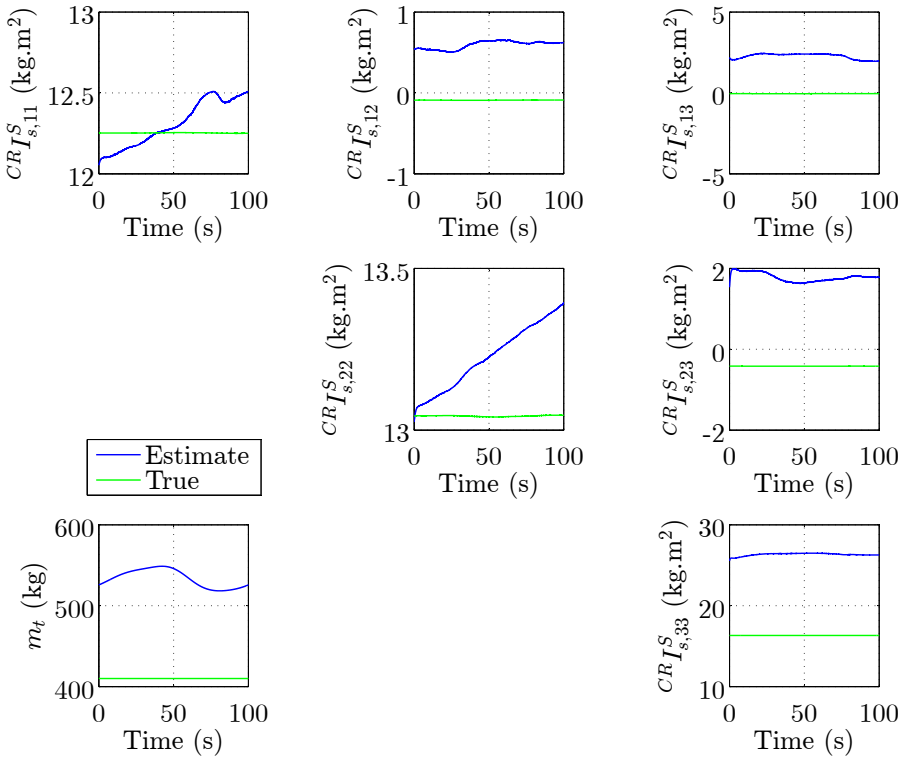

Figure 62: Data from attitude-tracking simulation with VSCMGs: mass and inertia matrix estimates.

experiment, the target was rotated again, leading again to a decrease of approximately 3 deg in $\psi_{\mathrm{S/T}}$ and $\theta_{\mathrm{S/T}}$. The third Euler angle remained approximately constant throughout the experiment. After each rotation of the target, each desired Euler angle was matched within ± 2 deg and each desired angular velocity coordinate was matched within ± 1 deg/s. This is approximately the same closed-loop performance observed in Section 6.7.1.

Figure 66 shows the angular speeds and the commanded angular accelerations of the wheels of the VSCMGs. Compared to Figure 53, the angular speeds remained approximately constant and no angular acceleration commands were issued. This is explained by Figure 68, which shows that no singularities were traversed. Hence, the VSCMGs remained in CMG mode throughout the experiment. Note that the singularity at the very beginning of the experiment is due to the fact that the wheels

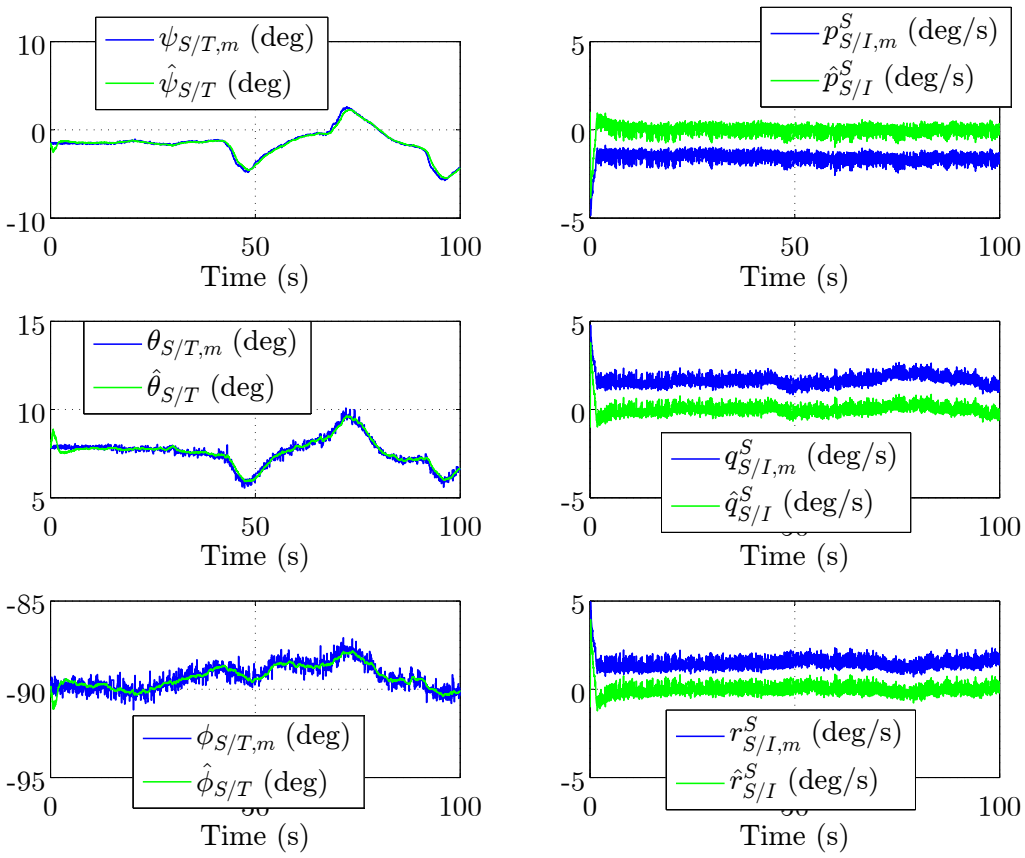

Figure 63: Data from attitude-regulation experiment with VSCMGs: attitude measured by the vision algorithm and angular velocity measured by the rate-gyros versus attitude and angular velocity estimated by the Q-MEKF.

were not spinning at this point and, thus, the VSCMGs could not produce any torque in CMG mode at this point. Note also that it is easier to avoid singularities in this experiment because the desired attitude is time-invariant, unlike in Section 6.7.1.

The angles and the angular speeds of the gimbals of the VSCMGs, as measured by the on-board sensors, are presented in Figure 68. The deadzone in $\dot{\gamma}$ is again visible.

Finally, Figure 69 shows the states of the adaptive controller. In this experiment, these states were propagated from the very beginning, even though the first control commands were only issued 20 sec into the experiment. Because of this and because of the adaptive controller was fed bad data while the Q-MEKF was converging, the states of the adaptive controller associated with the inertia matrix varied substantially

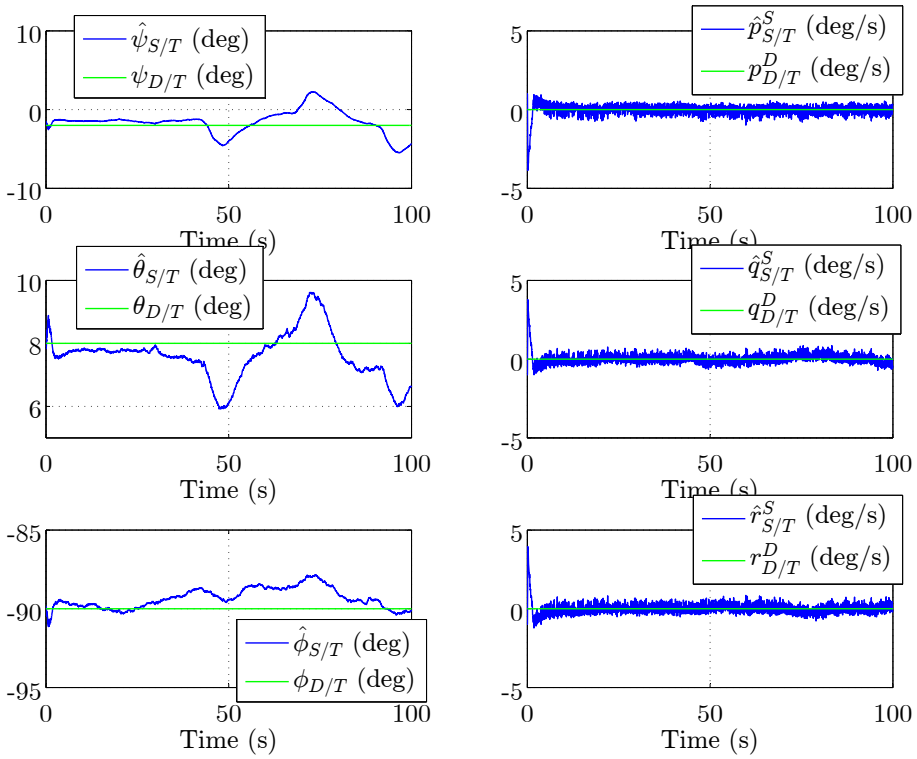

Figure 64: Data from attitude-regulation experiment with VSCMGs: desired attitude and angular velocity versus attitude and angular velocity estimated by the Q-MEKF.

during the first instants of the experiment. This can be avoided by not propagating the states of the adaptive controller while the navigation filters are converging. This has already been modified in the latest version of the code, as can be seen from Figures 76 and 96.

6.7.3 Attitude-Tracking using the VICON System and the Thrusters

In this experiment, the thrusters were used to track the same time-varying attitude reference tracked in Section 6.7.1 using three VSCMGs. The DQ-MEKF described in Section 4.5 was used to estimate the attitude and angular velocity of the upper stage with respect to the inertial frame. The DQ-MEKF was fed pose measurements at 1 Hz from the VICON system, angular velocity measurements at 100 Hz from the rate-gyros, and linear acceleration measurements at 100 Hz from the IMU. The

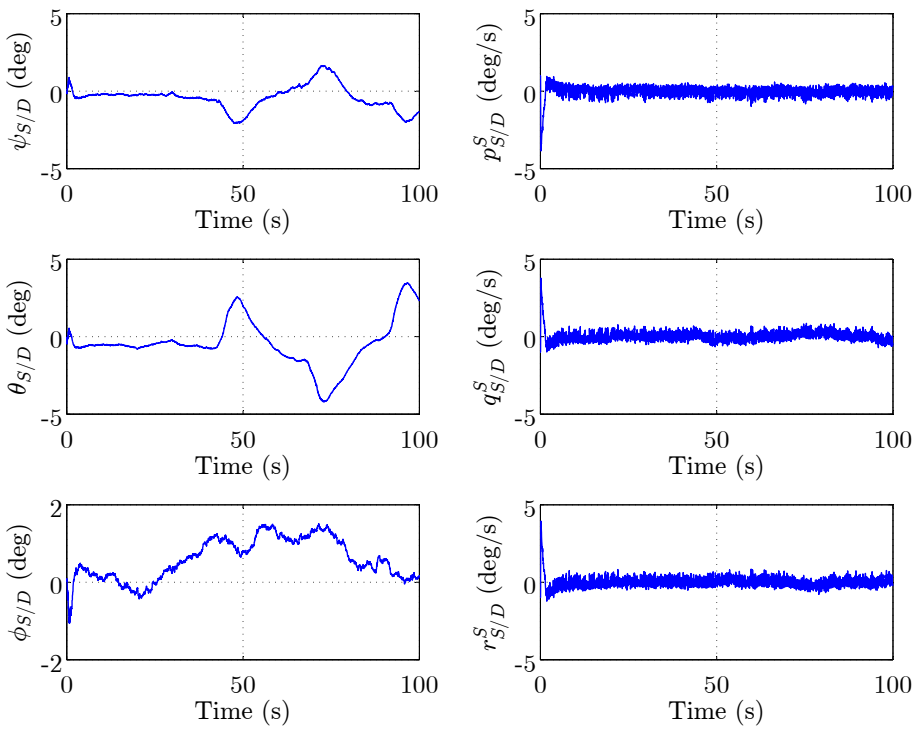

Figure 65: Data from attitude-regulation experiment with VSCMGs: attitude and angular velocity regulation error.

initial estimate of the state of the DQ-MEKF is given in Table 15. The same table also shows an a posteriori guess of the initial state based on the measurements. The DQ-MEKF was initialized with the covariance matrices given in Table 16.

Table 15: Initial estimate and a posteriori guess of the state of the DQ-MEKF in the 3-DOF experiment.

Variable	Initial Estimate	A Posteriori Guess
$q_{\mathrm{S/I}}(0)$	$[1,0,0,0]^\intercal$	$[0.9997,-0.0124,-0.0026,-0.0193]^\intercal$
$\bar{r}^{\mathrm{I}}_{CR/O_{\mathrm{I}}}(0)$	$[0.6,2.125,0]^\intercal$ (m)	$[-0.4714,2.2190,-0.9960]^\intercal$ (m)
$b_\omega(0)$	$[-1,1,1]^\intercal$ (deg/s)	$[-1.0800,1.397,0.9648]^\intercal$ (deg/s)
$b_v(0)$	$[0,0,0]^\intercal$ (m/s)	$[0,0,0]^\intercal$ (m/s)
$b_n(0)$	$[0,0,0]^\intercal$ (-)	$[0.0012,0.0257,0.0009]^\intercal$ (-)

The control gains are chosen to be $\bar{K}_r = 0.3I_{3\times3}$, $\bar{K}_q = 0.1I_{3\times3}$, $\bar{K}_v = 25I_{3\times3}$, $\bar{K}_\omega = 15I_{3\times3}$, and $K_i = 1e^5 I_{7\times7}$. At the beginning of the experiment, the initial state

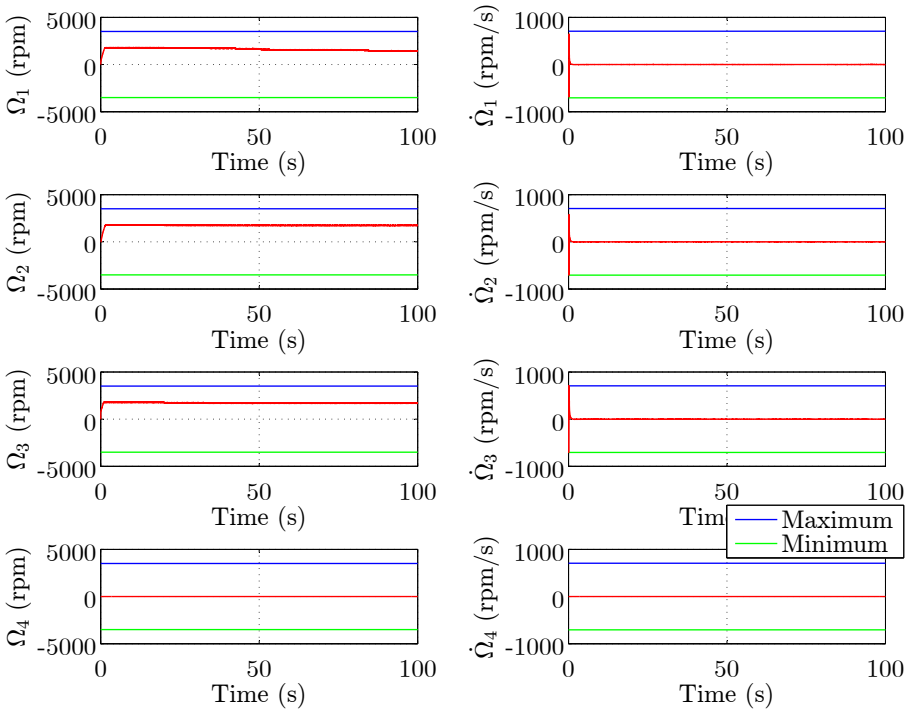

Figure 66: Data from attitude-regulation experiment with VSCMGs: wheel speeds and accelerations.

of the inertia-free pose-tracking controller is given by

$$\mathrm{v}(\widehat{M^{\mathrm{B}}}) = [12.2012, -0.0899, -0.0469, 12.9943, -0.4187, 16.2764, 410]^{\mathsf{T}}.$$

All other parameters required by the control software were defined as in the simulation presented in Section 6.7.1.

During the first 20 sec, the controller is off and the DQ-MEKF is allowed to converge. During the next 20 sec, the controller is turned on and the reference attitude is given by $\psi_{\mathrm{D/I}} = 0$ deg, $\theta_{\mathrm{D/I}} = 0$ deg, and $\phi_{\mathrm{D/I}} = 0$ deg. Finally, 40 sec after the beginning of the experiment, the reference attitude turns into the same sinusoidal reference tracked in Section 6.7.1.

The upper stage was levitated approximately 13.10 sec after the beginning of the experiment. At that instant, the state of the platform is approximately given by $\bar{\omega}^{\mathrm{S}}_{\mathrm{S/I}} = [0, 0, 0]^{\mathsf{T}}$ rad/s, $\bar{v}^{\mathrm{I}}_{CR/\mathrm{I}} = [0, 0, 0]^{\mathsf{T}}$ m/s, $\psi_{\mathrm{S/I}} = -2.3268$ deg, $\theta_{\mathrm{S/I}} = 0.0838$ deg, $\phi_{\mathrm{S/I}} = -1.2606$ deg, and $\bar{r}^{\mathrm{I}}_{CR/O_{\mathrm{I}}} = [-0.4686, 2.2191, -0.9931]^{\mathsf{T}}$ m. At the same time

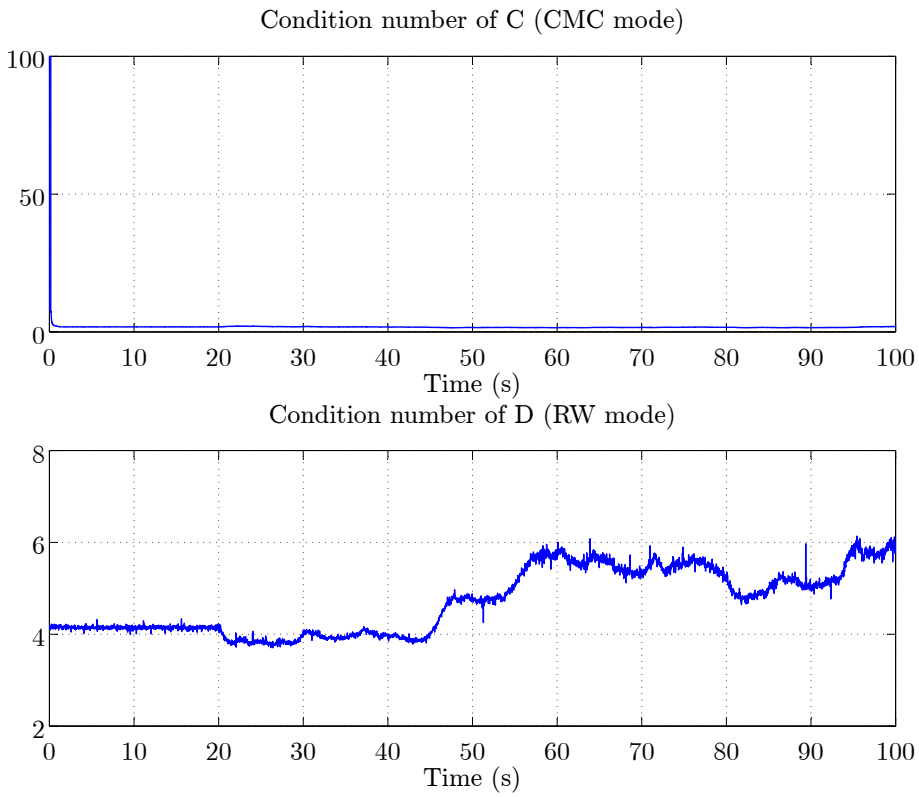

Figure 67: Data from attitude-regulation experiment with VSCMGs: condition numbers.

instant, the state of the DQ-MEKF (apart from the state covariance matrix) was $\hat{\bar{\omega}}^{\mathrm{S}}_{\mathrm{S/I}} = [0.0035, 0.0002, -0.0008]^{\intercal}$ rad/s, $\hat{\bar{v}}^{\mathrm{I}}_{CR/\mathrm{I}} = [0.0020, 0.0007, -0.0006]^{\intercal}$ m/s, $\hat{\psi}_{\mathrm{S/I}} = -2.2239$ deg, $\hat{\theta}_{\mathrm{S/I}} = -0.2760$ deg, $\hat{\phi}_{\mathrm{S/I}} = -1.4014$ deg, $\hat{\bar{r}}^{\mathrm{I}}_{CR/O_{\mathrm{I}}} = [-0.4711, 2.2191, -0.9959]^{\intercal}$ m, $\hat{\bar{b}}_{\omega} = [-0.9896, 1.3004, 0.9493]^{\intercal}$ deg/s, and $\hat{\bar{b}}_{n} = [0.0014, 0.0261, 0.0005]^{\intercal}$.

Figure 70 compares the attitude and angular velocity estimated by the DQ-MEKF with the ground truth. The error between them is shown in Figure 71. The ground truth was obtained as in Section 4.6. After 20 sec, the RMS attitude estimation error is 0.35 deg and the RMS angular velocity estimation error is 0.58 deg/s.

Figure 72 shows the real-time solution to the LP problem calculated by the GLPK package throughout the experiment. It can be seen that the maximum thrust of each thruster is not exceeded. Figure 73 shows the resulting on-off commands produced from this solution. During the experiment, the small thrusters were fired more times

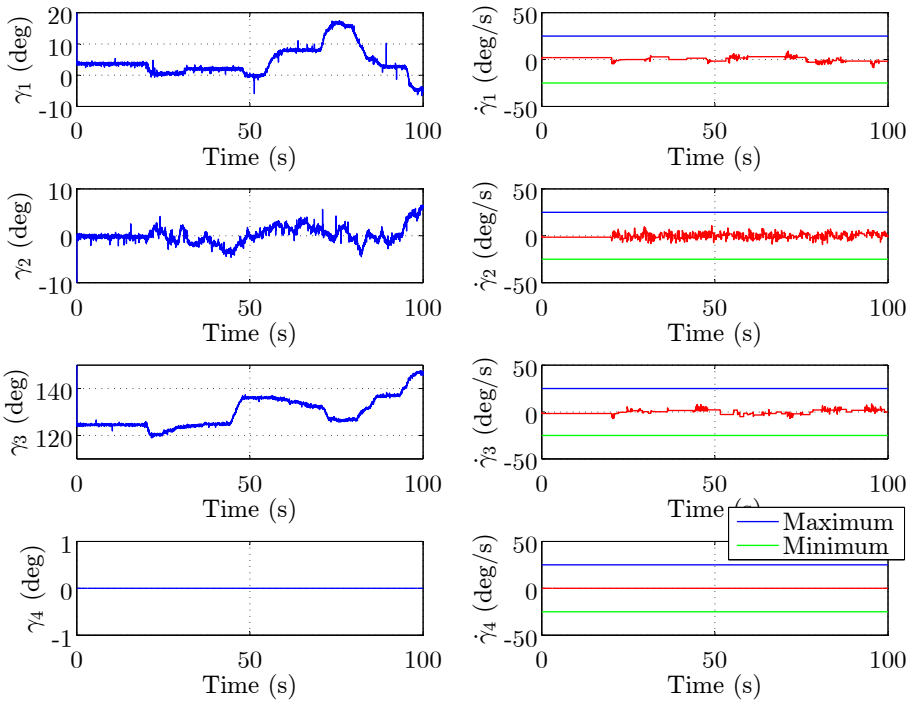

Figure 68: Data from attitude-regulation experiment with VSCMGs: gimbal angles and speeds.

than the large thrusters. Note that the disturbance torque created by the misalignment between the center of rotation and the center of mass of the upper stage is compensated primarily with the small thrusters.

Figure 74 compares the desired attitude and angular velocity with the attitude and angular velocity estimated by the DQ-MEKF. The error between them is shown in Figure 75. After the initial transient response, the yaw angle is tracked within ± 2 deg, whereas the pitch and roll angles are tracked within ± 1 deg (apart from a peak in the pitch error around 127 sec, most probably due to a thruster not firing when commanded). After the initial transient response, each desired angular velocity coordinate is tracked within ± 1 deg/s (apart from the peak at 127 sec).

Finally, Figure 76 compares the states of the inertia-free pose-tracking controller with the best guess of the true inertia matrix. As in Section 6.7.1, the controller was not expected to be able to identify the inertia matrix in this experiment, mainly

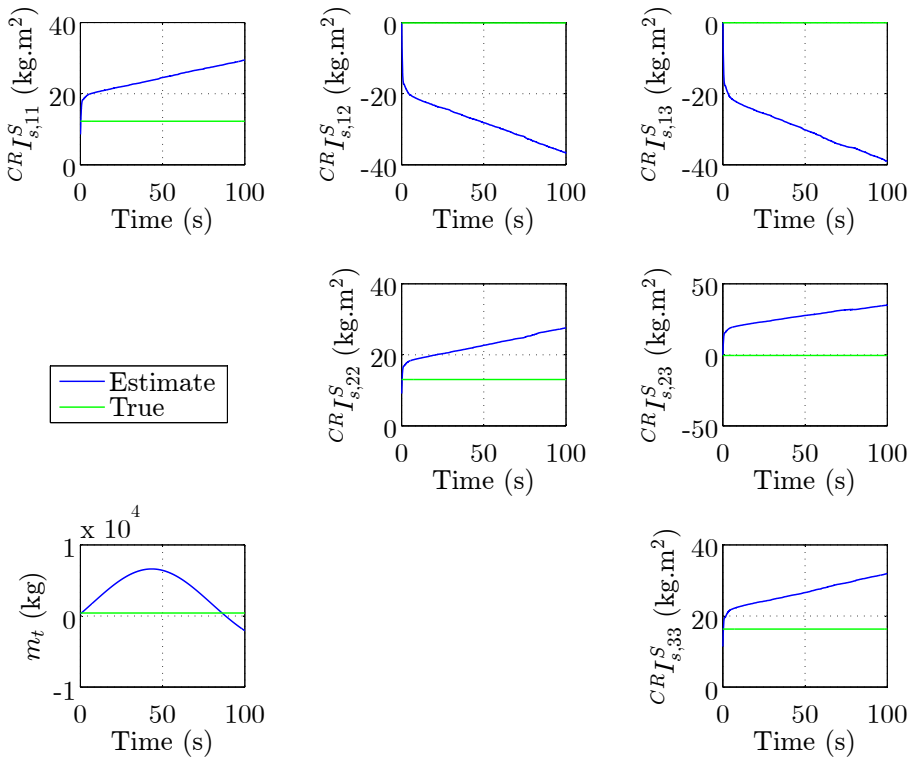

Figure 69: Data from attitude-regulation experiment with VSCMGs: mass and inertia matrix estimates.

due to the many real-word effects that violate the conditions of Proposition 5.2. The rapid increase of m_t is due to the fact that, even though the controller is calculating control force commands, the platform cannot translate, since the lower stage is not levitated.

The same 3-DOF case, with the same conditions and parameters, was run on the high-fidelity simulator to validate the simulated results against the experimental results. In particular, the position of the center of mass of the upper stage with respect to the center of rotation in the simulation is given by $\bar{r}^{S}_{\bullet_{s/CR}} = [5e^{-6}, 5e^{-6}, 0]^{\intercal}$ m. The initial state of the simulation was defined as the state of the experiment at 13.10 sec, i.e., at the instant the upper stage was levitated. The real-world effects specified in Section 6.2 were applied.

Figure 77 compares the attitude and angular velocity estimated by the DQ-MEKF with the true attitude and angular velocity, which is available in the simulation. The

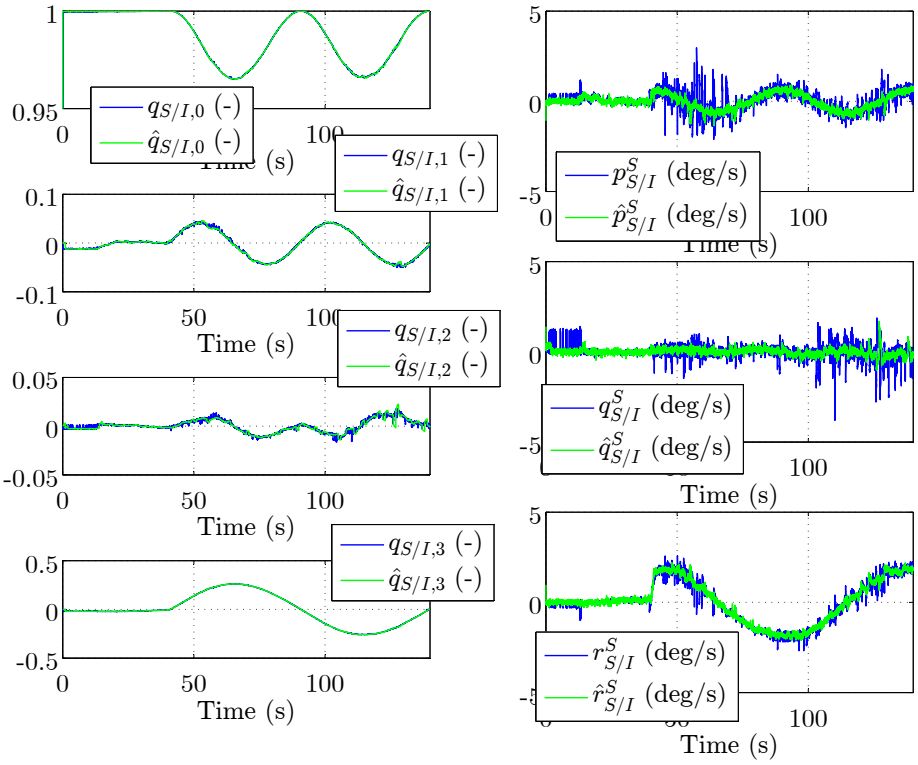

Figure 70: Data from attitude-tracking experiment with thrusters: attitude and angular velocity estimated by the DQ-MEKF versus ground truth.

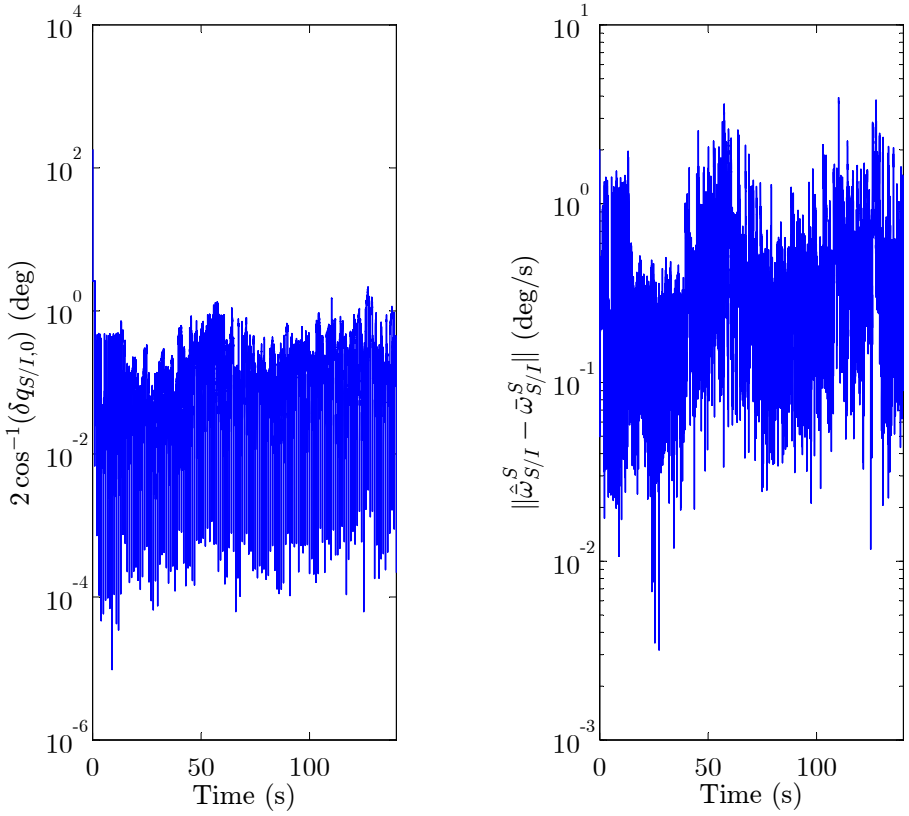

Figure 71: Data from attitude-tracking experiment with thrusters: attitude and angular velocity estimation error.

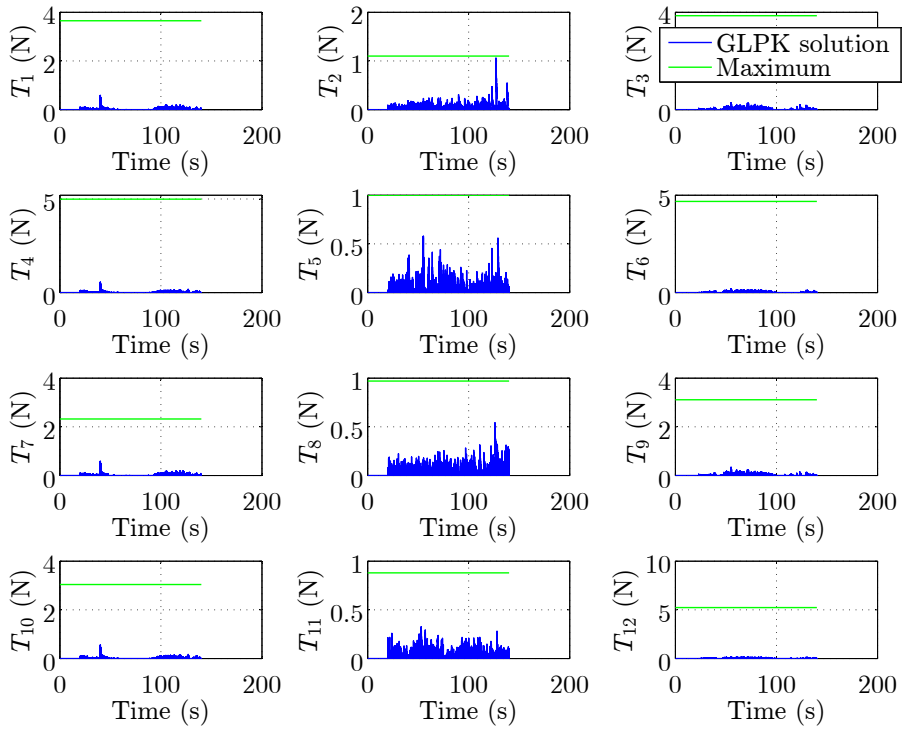

Figure 72: Data from attitude-tracking experiment with thrusters: solution of the LP problem calculated by the GLPK package.

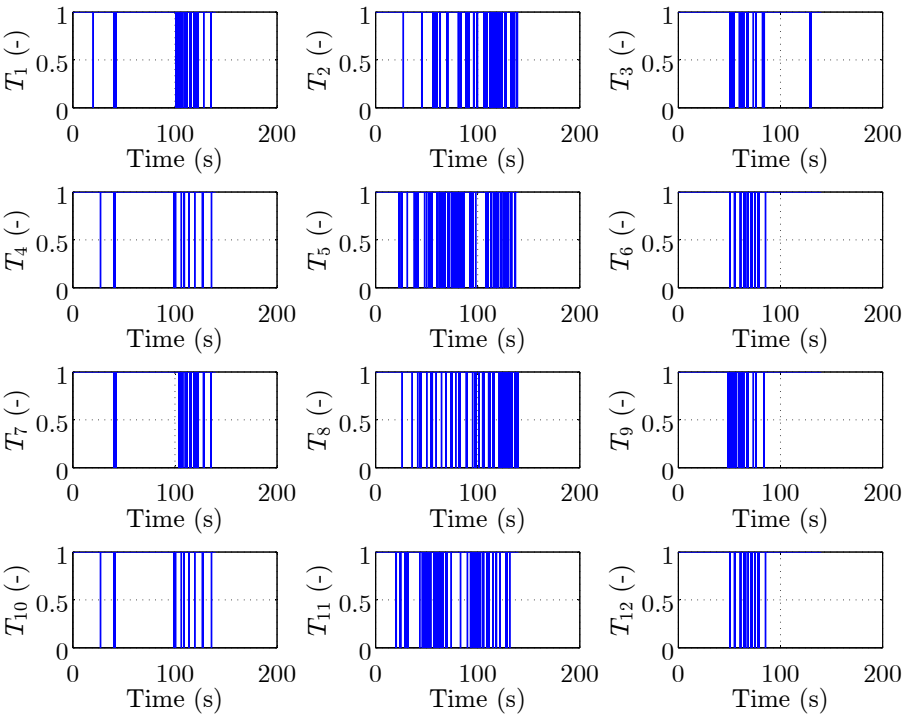

Figure 73: Data from attitude-tracking experiment with thrusters: on-off commands issued to the thrusters. The thrusters are open at 0 and closed at 1.

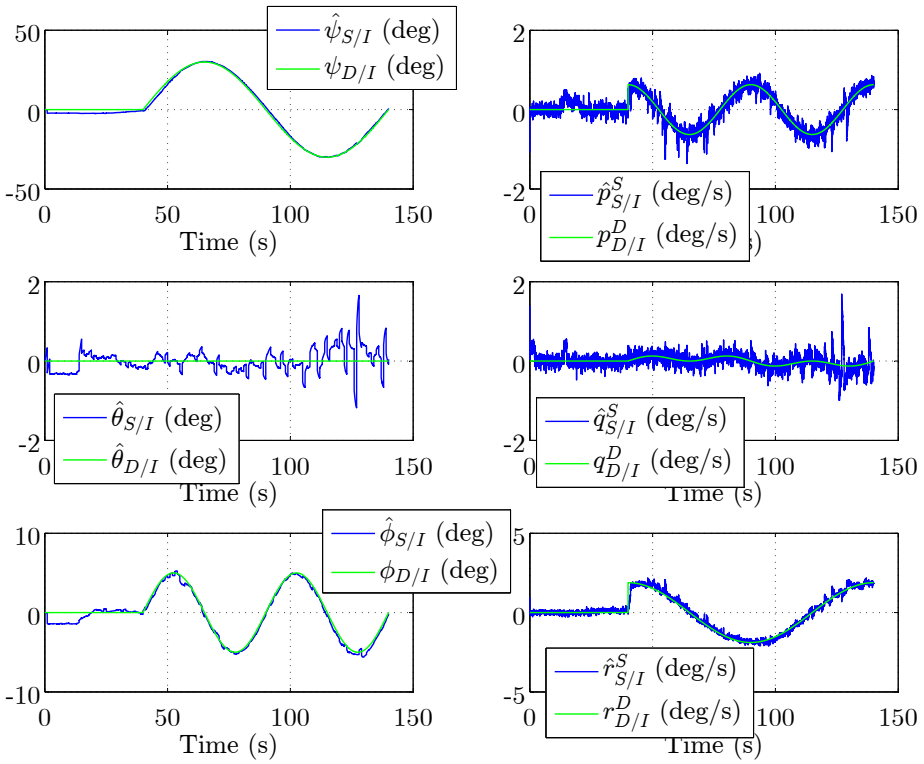

Figure 74: Data from attitude-tracking experiment with thrusters: desired attitude and angular velocity versus attitude and angular velocity estimated by the DQ-MEKF.

Table 16: Covariance matrices of the DQ-MEKF.

$\tilde{P}_{20\times20}(0)$	$\text{diag}([0.0069, 0.0069, 0.0069, 0.0069, 0.69, 0.69, 0.69, 0.69, 0, 2\times10^{-6}, 2\times10^{-6}, 2\times10^{-6}, 0, 1\times10^{-9}, 1\times10^{-9}, 1\times10^{-9}, 0, 1.6\times10^{-5}, 1.6\times10^{-5}, 1.6\times10^{-5}])$
$Q_{15\times15}$	$\text{diag}([7\times10^{-7}, 7\times10^{-7}, 7\times10^{-7}, 0, 0, 0, \ 2\times10^{-6}, 2\times10^{-6}, 2\times10^{-6}, 2\times10^{-7}, 2\times10^{-7}, 2\times10^{-7}, 1.6\times10^{-5}, 1.6\times10^{-5}, 1.6\times10^{-5}])$
$R_{8\times8}$	$\text{diag}([1\times10^{-9}, 1\times10^{-9}, 1\times10^{-9}, 1\times10^{-9}, 2.5\times10^{-7}, 2.5\times10^{-7}, 2.5\times10^{-7}, 2.5\times10^{-7}])$

error between them is shown in Figure 78. After 20 sec, the RMS attitude estimation error is 0.35 deg and the RMS angular velocity estimation error is 0.27 deg/s. Hence, the same RMS attitude estimation error obtained in the experiment was obtained in the simulation, whereas the RMS angular velocity estimation error obtained in the experiment is approximately two times the one obtained in the simulation. A better match can potentially be achieved by fine-tuning the simulated measurement noise specified in Section 6.2. However, this difference can also be a consequence of the extra noise introduced by differentiating the ground truth for the attitude when computing the ground truth for the angular velocity in the experiment.

Figure 79 shows the solution to the LP problem calculated by the GLPK package throughout the simulation. The simulation correctly predicts that the maximum thrust of each thruster is not violated. Figure 80 shows the corresponding on-off commands issued to the thrusters in the simulation. As in the experiment, the small thrusters are fired more times than the large thrusters. The differences between Figures 80 and 73 can be attributed to residual friction between the upper and lower stages of the platform and to small changes in the position of the center of mass with the respect to the center of rotation during the experiment. Neither one of these effects was considered in this simulation.

Figure 81 compares the desired attitude and angular velocity with the attitude and

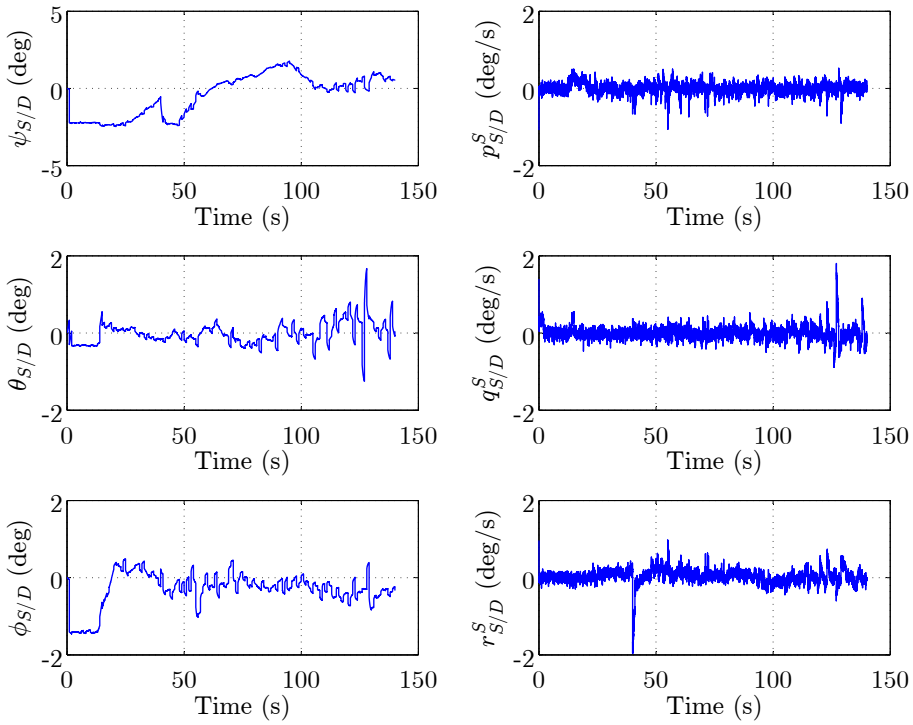

Figure 75: Data from attitude-tracking experiment with thrusters: attitude and angular velocity tracking error.

angular velocity estimated by the DQ-MEKF in the simulation. The error between them is shown in Figure 82. After the initial transient response, the yaw angle is tracked within ± 2 deg, whereas the pitch and roll angles are tracked within ± 1 deg. After the initial transient response, each desired angular velocity coordinate is tracked within ± 1 deg/s. Hence, the simulation correctly predicts the tracking error obtained in the experiment. Note however that the simulation does not account for thruster misfires and, therefore, cannot reproduce the peak in pitch error shown in Figure 75.

Finally, Figure 83 shows that the simulation predicts the order of magnitude and overall behavior of the states of the adaptive controller.

6.7.4 Pose-Tracking using the VICON System and the Thrusters

In this final experiment, the thrusters were used to track a time-varying attitude and position reference. The DQ-MEKF described in Section 4.5 was used to estimate the

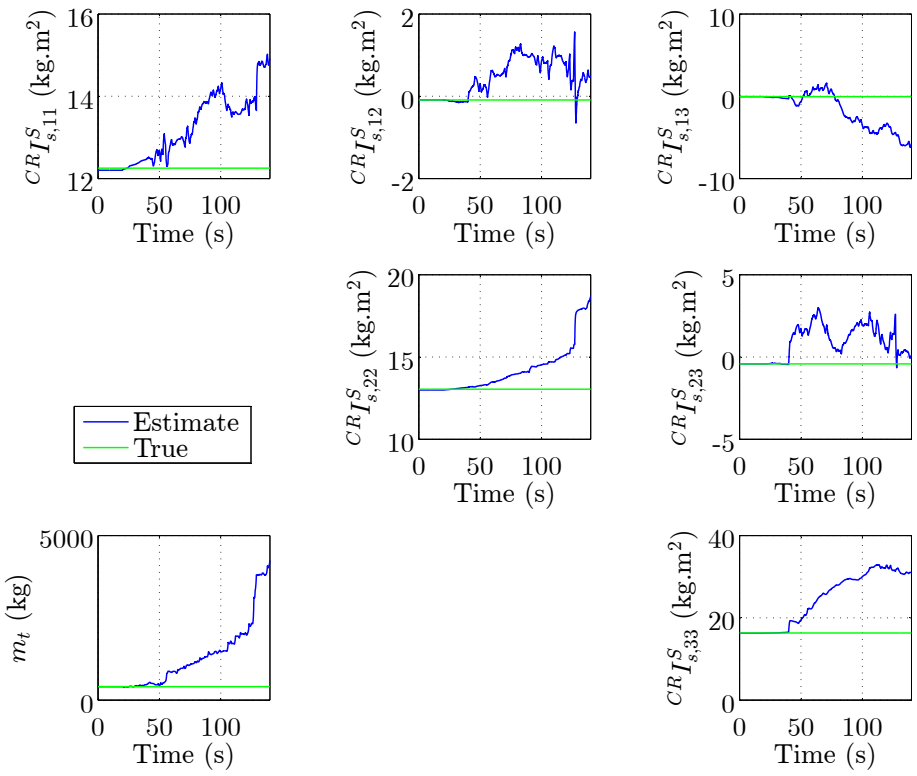

Figure 76: Data from attitude-tracking experiment with thrusters: mass and inertia matrix estimates.

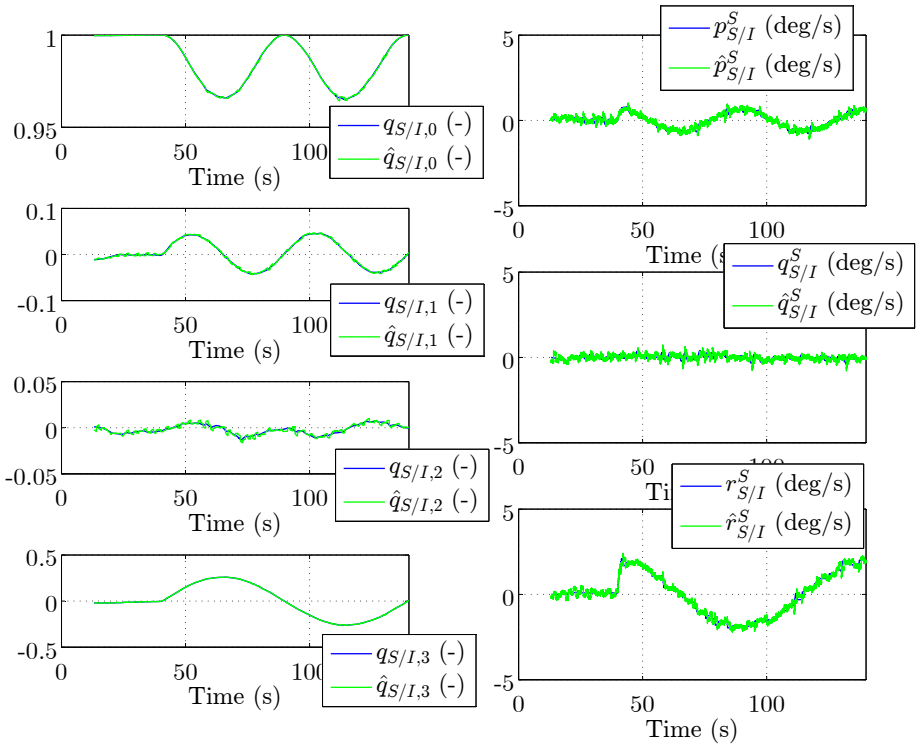

Figure 77: Data from attitude-tracking simulation with thrusters: attitude and angular velocity estimated by the DQ-MEKF versus ground truth.

pose and velocities of the upper stage with respect to the inertial frame. The DQ-MEKF was fed pose measurements at 10 Hz from the VICON system, angular velocity measurements at 100 Hz from the rate-gyros, and linear acceleration measurements at 100 Hz from the IMU. The initial estimate of the state of the DQ-MEKF is given in Table 17. The same table also shows an a posteriori guess of the initial state based on the measurements. The DQ-MEKF was initialized with the covariance matrices given in Table 16.

The control gains are chosen to be $\bar{K}_r = 0.74 I_{3\times3}$, $\bar{K}_q = 0.2 I_{3\times3}$, $\bar{K}_v = 84.37 I_{3\times3}$, $\bar{K}_\omega = 15 I_{3\times3}$, and $K_i = 500 I_{7\times7}$. At the beginning of the experiment, the initial state of the inertia-free pose-tracking controller is set to zero. All other parameters required by the control software were defined as in the simulation presented in Section 6.7.1.

The reference pose is illustrated in Figure 84 and is split in five phases:

- Phase #1: During the first 20 sec, the controller is off and the DQ-MEKF is

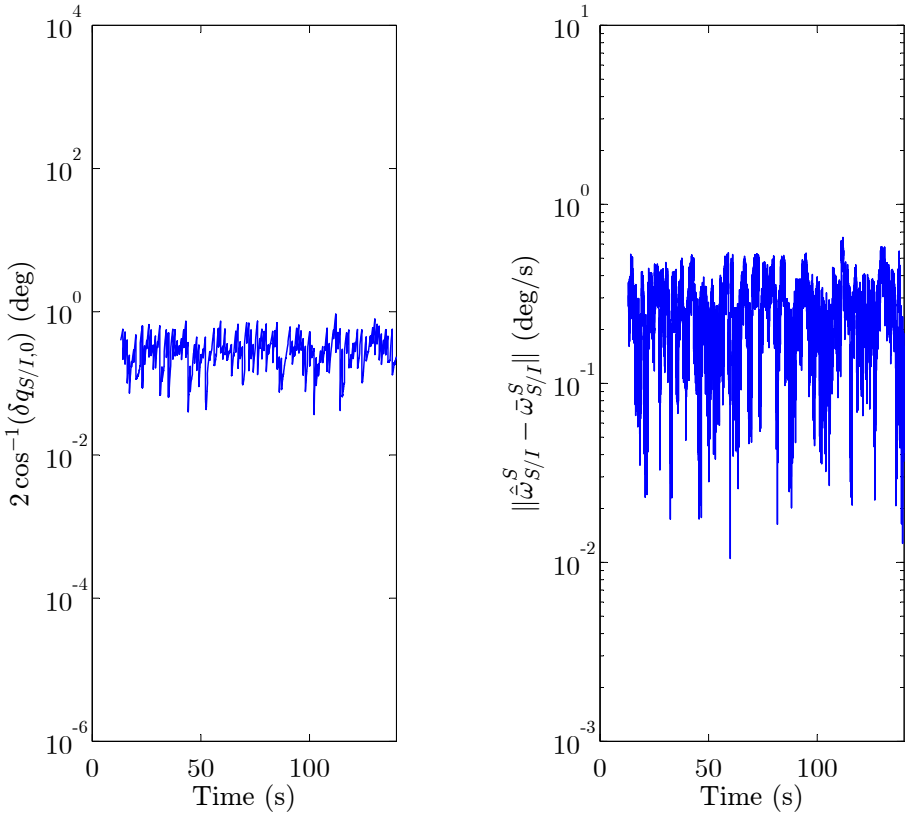

Figure 78: Data from attitude-tracking simulation with thrusters: attitude and angular velocity estimation error.

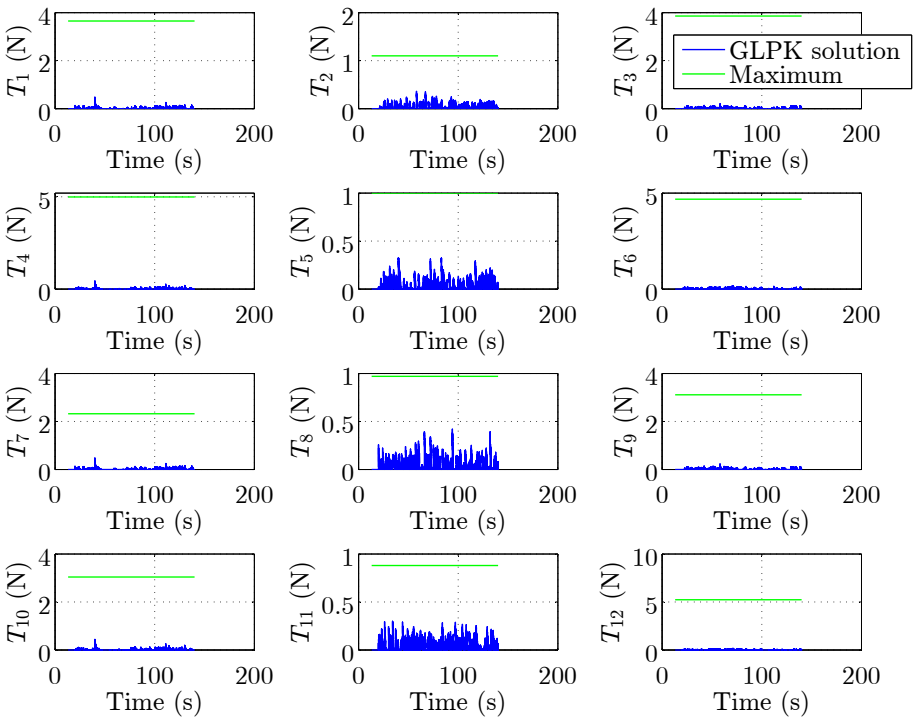

Figure 79: Data from attitude-tracking simulation with thrusters: solution of the LP problem calculated by the GLPK package.

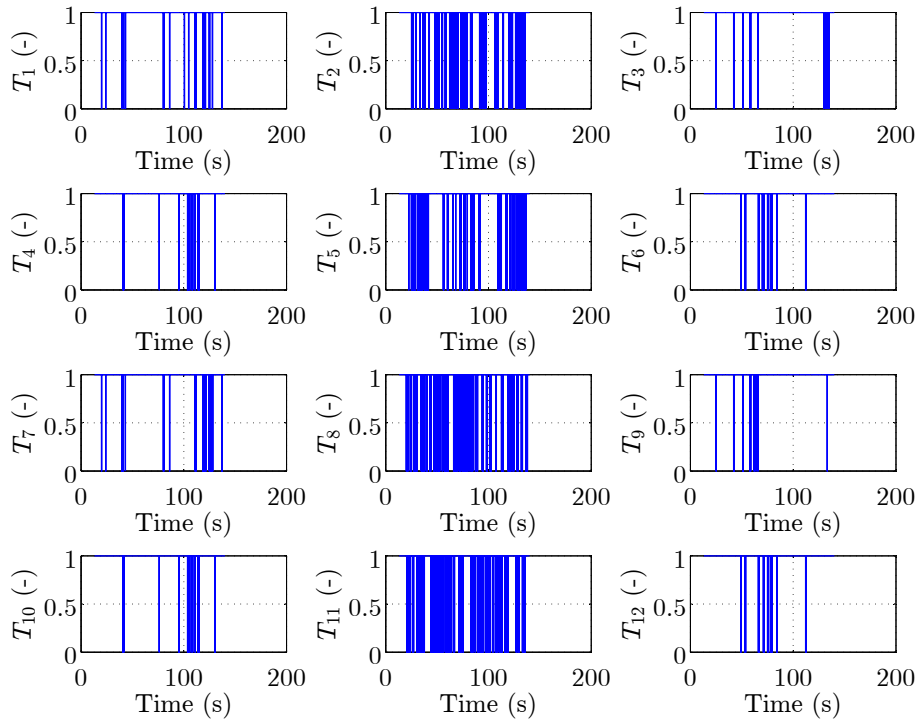

Figure 80: Data from attitude-tracking simulation with thrusters: on-off commands issued to the thrusters. The thrusters are open at 0 and closed at 1.

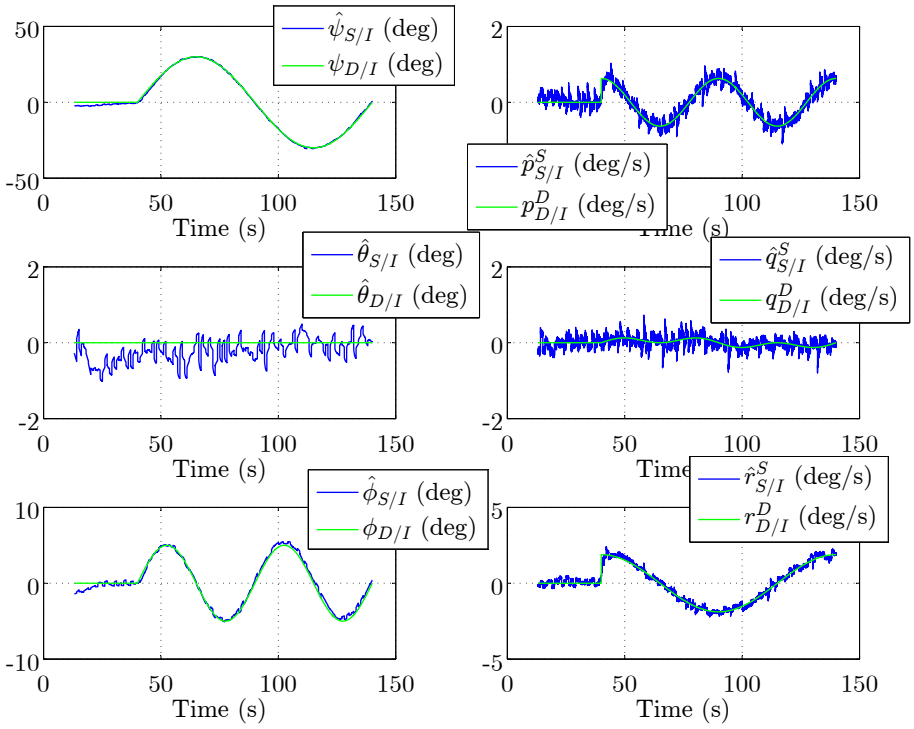

Figure 81: Data from attitude-tracking simulation with thrusters: desired attitude and angular velocity versus attitude and angular velocity estimated by the DQ-MEKF.

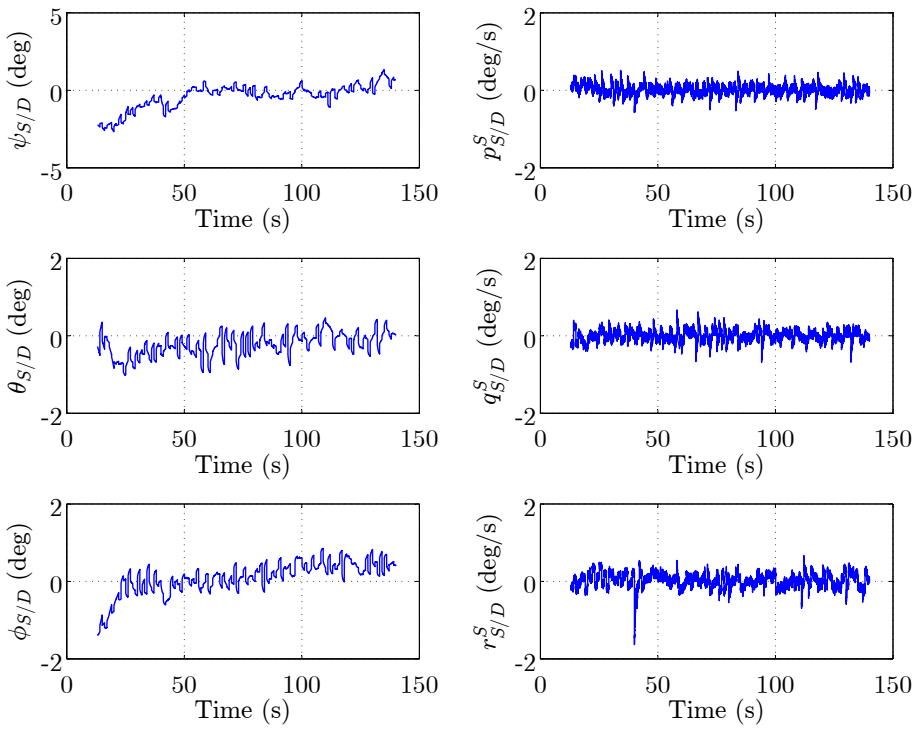

Figure 82: Data from attitude-tracking simulation with thrusters: attitude and angular velocity tracking error.

allowed to converge.

- Phase #2: During the next 20 sec, the controller is turned on. During this phase, the desired position of the center of rotation of the platform with respect to the inertial frame is given by $(x^{\mathrm{I}}_{O_{\mathrm{D}}/O_{\mathrm{I}}}, y^{\mathrm{I}}_{O_{\mathrm{D}}/O_{\mathrm{I}}}) = (3.003, 2.151)$ m and the desired orientation of the S-frame with respect to the I-frame is given by $\psi_{\mathrm{D/I}} = -90$ deg, $\theta_{\mathrm{D/I}} = 0$, and $\phi_{\mathrm{D/I}} = 0$.

- Phase #3: During the next 60 sec, the center of rotation of the platform should describe a quarter of a circle with a radius of 1.2 m around the center of the floor with constant angular speed. The upper stage should remain leveled and $-\bar{J}_{\mathrm{S}}$ should point to the center of the circle. In other words, during this phase, $(x^{\mathrm{I}}_{O_{\mathrm{D}}/O_{\mathrm{I}}}, y^{\mathrm{I}}_{O_{\mathrm{D}}/O_{\mathrm{I}}}) = (1.803 + 1.2\cos(\frac{2\pi}{240}t), 2.151 + 1.2\sin(\frac{2\pi}{240}t))$ m, $\psi_{\mathrm{D/I}} = -\frac{\pi}{2} + \frac{2\pi}{240}t$ rad, $\theta_{\mathrm{D/I}} = 0$, $\phi_{\mathrm{D/I}} = 0$, and t is the elapsed time since the beginning of the

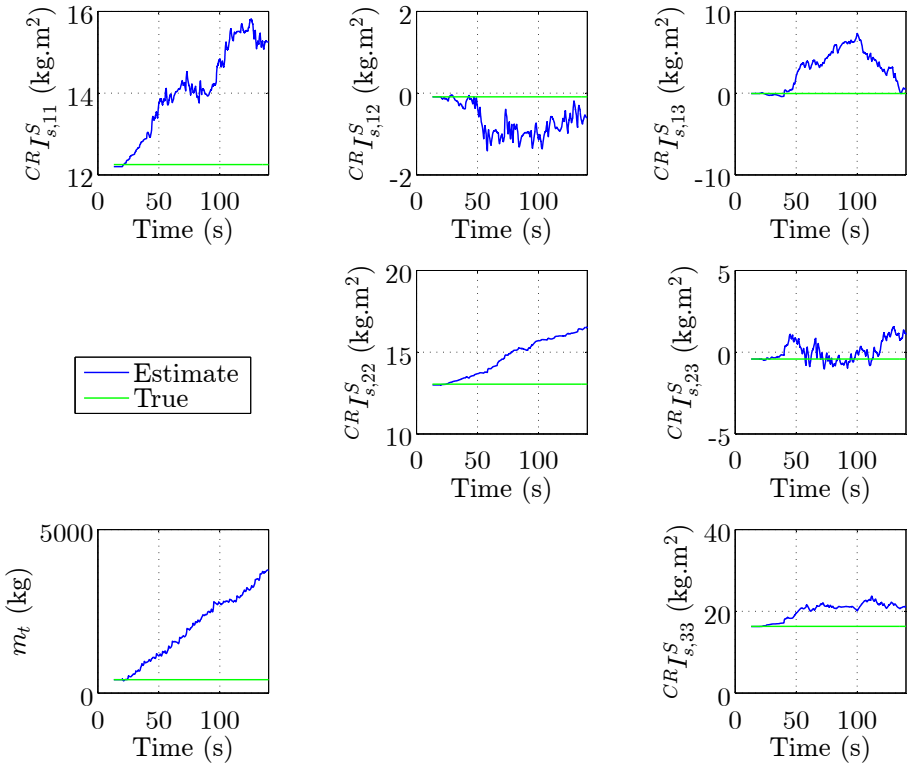

Figure 83: Data from attitude-tracking simulation with thrusters: mass and inertia matrix estimates.

Table 17: Initial estimate and a posteriori guess of the state of the DQ-MEKF in the 5-DOF experiment.

Variable	Initial Estimate	A Posteriori Guess
$q_{\mathrm{S/I}}(0)$	$[0.7071, 0, 0, -0.7071]^\intercal$	$[0.7036, -0.0032, 0.0113, -0.7105]^\intercal$
$\bar{r}^{\mathrm{I}}_{CR/O_{\mathrm{I}}}(0)$	$[2.903, 2.051, 0]^\intercal$ (m)	$[3.004, 2.151, -1.006]^\intercal$ (m)
$\bar{b}_\omega(0)$	$[-1, 1, 1]^\intercal$ (deg/s)	$[-1.022, 1.309, 0.7889]^\intercal$ (deg/s)
$\bar{b}_v(0)$	$[0, 0, 0]^\intercal$ (m/s)	$[0, 0, 0]^\intercal$ (m/s)
$\bar{b}_n(0)$	$[0, 0, 0]^\intercal$ (-)	$[0.0002, 0.0170, -0.0002]^\intercal$ (-)

phase.

- Phase #4: During the next 60 sec, the center of rotation of the platform should describe a straight-line along the $-\bar{J}_{\mathrm{I}}$ direction with constant linear speed. The upper stage should remain leveled and $-\bar{J}_{\mathrm{S}}$ should point to the center of the circle. In other words, during this phase, $(x^{\mathrm{I}}_{O_{\mathrm{D}}/O_{\mathrm{I}}}, y^{\mathrm{I}}_{O_{\mathrm{D}}/O_{\mathrm{I}}}) = (1.803, 3.351 - \frac{1.2}{60}t)$ m, $\psi_{\mathrm{D/I}} = 0$, $\theta_{\mathrm{D/I}} = 0$, $\phi_{\mathrm{D/I}} = 0$, and t is the elapsed time since the beginning of the phase.

- Phase #5: During the next 20 sec, the upper stage should maintain the desired position and attitude reached at the end of phase #4. In other words, during this phase, $(x^{\mathrm{I}}_{O_{\mathrm{D}}/O_{\mathrm{I}}}, y^{\mathrm{I}}_{O_{\mathrm{D}}/O_{\mathrm{I}}}) = (1.803, 2.151)$ m, $\psi_{\mathrm{D/I}} = 0$, $\theta_{\mathrm{D/I}} = 0$, and $\phi_{\mathrm{D/I}} = 0$.

The upper stage and the lower stage were levitated approximately 13.01 sec and 17.50 sec after the beginning of the experiment, respectively. The state of the platform 17.50 sec after the beginning of the experiment is approximately given by $\bar{\omega}^{\mathrm{S}}_{\mathrm{S/I}} = [0.3462, 0.1096, 0.1624]^\intercal$ deg/s, $\bar{v}^{\mathrm{I}}_{CR/\mathrm{I}} = [0, 0, 0]^\intercal$ m/s, $\psi_{\mathrm{S/I}} = -90.4911$ deg, $\theta_{\mathrm{S/I}} = 1.4355$ deg, $\phi_{\mathrm{S/I}} = -0.3164$ deg, and $\bar{r}^{\mathrm{I}}_{CR/O_{\mathrm{I}}} = [3.0043, 2.1512, -1.0060]^\intercal$ m. At the same time instant, the state of the DQ-MEKF (apart from the state covariance matrix) was $\hat{\bar{\omega}}^{\mathrm{S}}_{\mathrm{S/I}} = [0.1445, 0.6120, 0.1319]^\intercal$ deg/s, $\hat{\bar{v}}^{\mathrm{I}}_{CR/\mathrm{I}} = [-0.0012, -0.0122, 0.0028]^\intercal$ m/s, $\hat{\psi}_{\mathrm{S/I}} = -90.4954$ deg, $\hat{\theta}_{\mathrm{S/I}} = 1.4158$ deg, $\hat{\phi}_{\mathrm{S/I}} = -0.3118$ deg, $\hat{\bar{r}}^{\mathrm{I}}_{CR/O_{\mathrm{I}}} = [3.0040, 2.1523, -1.0066]^\intercal$ m, $\hat{\bar{b}}_\omega = [-0.9027, 0.8736, 0.7450]^\intercal$ deg/s, and $\hat{\bar{b}}_n = [-0.0096, 0.0171,$

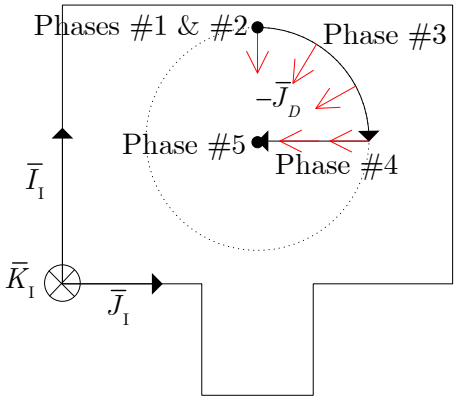

Figure 84: Reference pose. The desired trajectory of the center of rotation is illustrated in black, whereas the desired orientation of the upper stage is illustrated in red.

$-0.0015]^\intercal$.

Figure 85 compares the attitude and angular velocity estimated by the DQ-MEKF with the ground truth. The error between them is shown in Figure 86. The ground truth was obtained as in Section 4.6. After 20 sec, the RMS attitude estimation error is 0.13 deg and the RMS angular velocity estimation error is 0.41 deg/s. Likewise, Figure 87 compares the position and linear velocity estimated by the DQ-MEKF with the ground truth, obtained as in Section 4.6. The error between them is shown in Figure 88. After 20 sec, the RMS position estimation error is 1.0 mm and the RMS linear velocity estimation error is 6.3 mm/s. Note that the apparent vertical motion of the center of rotation is not only due to the slope of the epoxy floor, but also to errors in the experimental determination of the center of rotation.

Figure 89 shows the real-time solution to the LP problem calculated by the GLPK package throughout the experiment. Unlike in Figure 72, the maximum thrust of thrusters 7 and 8 is momentarily exceeded. Note that this is possible since $T_{i,\max,\mathrm{LP}}$ is set 50% higher than $T_{i,\max}$, as explained in Section 6.4.2. The control gains used in this experiment were tuned in simulation in order to prevent T_i from exceeding $T_{i,\max}$ for too long, as this could have led to an unstable closed-loop. Figure 90 shows the on-off commands produced from the solution of the LP problem. In Figure 90, the

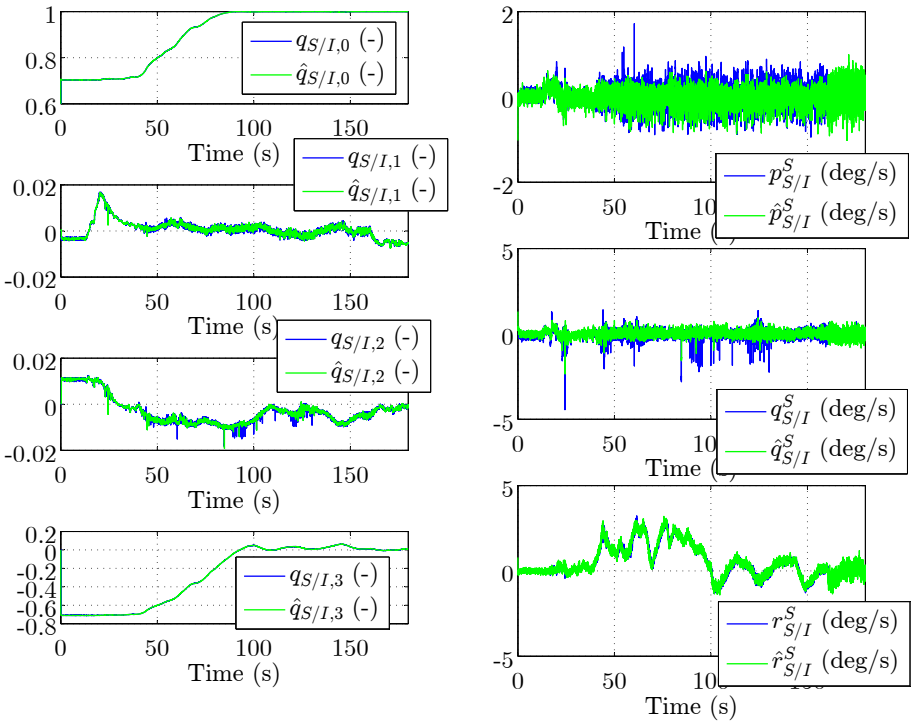

Figure 85: Data from pose-tracking experiment with thrusters: attitude and angular velocity estimated by the DQ-MEKF versus ground truth.

large thrusters are fired more times than in Figure 73. This is not surprising since now the large thrusters are required to track not only the desired attitude, but also the desired position. Because the epoxy floor is not perfectly flat, the large thrusters must also counteract gravity, which acts as a continuous disturbance force. As a result, the large thrusters must fire almost continuously in order to keep the position-tracking error within the values shown in Figure 95.

Figure 91 compares the desired attitude and angular velocity with the attitude and angular velocity estimated by the DQ-MEKF. The error between them is shown in Figure 92. The desired pitch and roll angles were tracked within approximately ± 1 deg. However, during phase #3, the yaw-tracking error reached approximately 11 deg, although during phase #5 it did not exceed ± 2 deg. The large yaw-tracking error during phase #3 is believed to have been caused by thruster 12 momentarily not firing when commanded. (In the mean time, thruster 12 has been serviced and

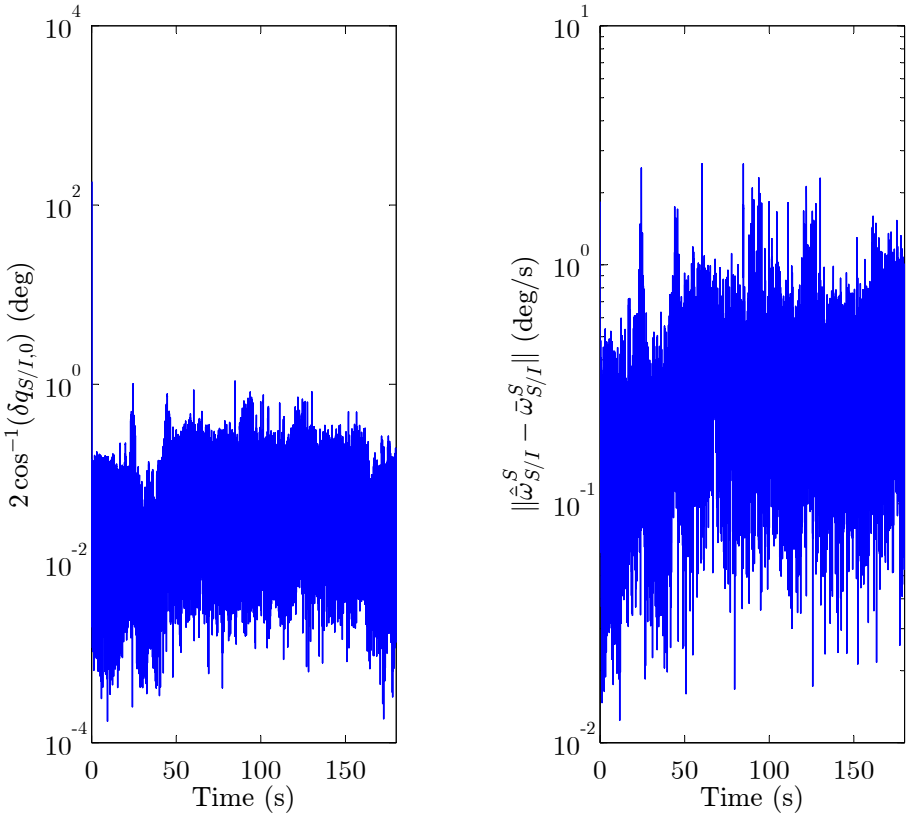

Figure 86: Data from pose-tracking experiment with thrusters: attitude and angular velocity estimation error.

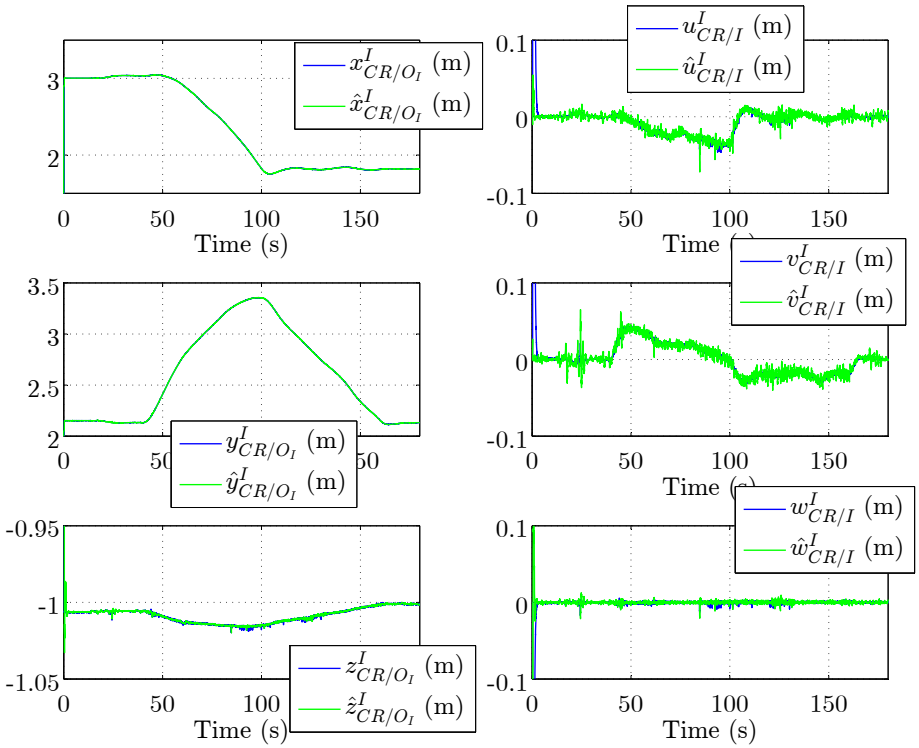

Figure 87: Data from pose-tracking experiment with thrusters: position and linear velocity estimated by the DQ-MEKF versus ground truth.

should operate normally in future experiments.) Similarly, the first and second coordinates of the desired angular velocity were tracked within ±1 deg/s, whereas the third coordinate was tracked within ±2 deg/s.

Figure 93 compares the desired position and linear velocity with the position and linear velocity estimated by the DQ-MEKF. The error between them is shown in Figure 95. Moreover, the desired position and the position estimated by the DQ-MEKF are projected onto the $\bar{I}_{\mathrm{I}}$-$\bar{J}_{\mathrm{I}}$ plane in Figure 94. After the transient response between phases #2 and #3 and phases #3 and #4, $x^{\mathrm{I}}_{CR/O_{\mathrm{D}}}$ is kept within ±6 cm and ±4 cm, respectively. Likewise, after the transient response between phases #2 and #3 and phases #3 and #4, $y^{\mathrm{I}}_{CR/O_{\mathrm{D}}}$ is kept within ±3 cm and ±4 cm, respectively. Moreover, at the end of the experiment, $x^{\mathrm{I}}_{CR/O_{\mathrm{D}}}$ and $y^{\mathrm{I}}_{CR/O_{\mathrm{D}}}$ are 1.3 cm and -1.9 cm, respectively. As for the desired linear velocity coordinates, they were tracked within ±0.05 m/s. A posteriori simulations have shown that the biggest contributor for the

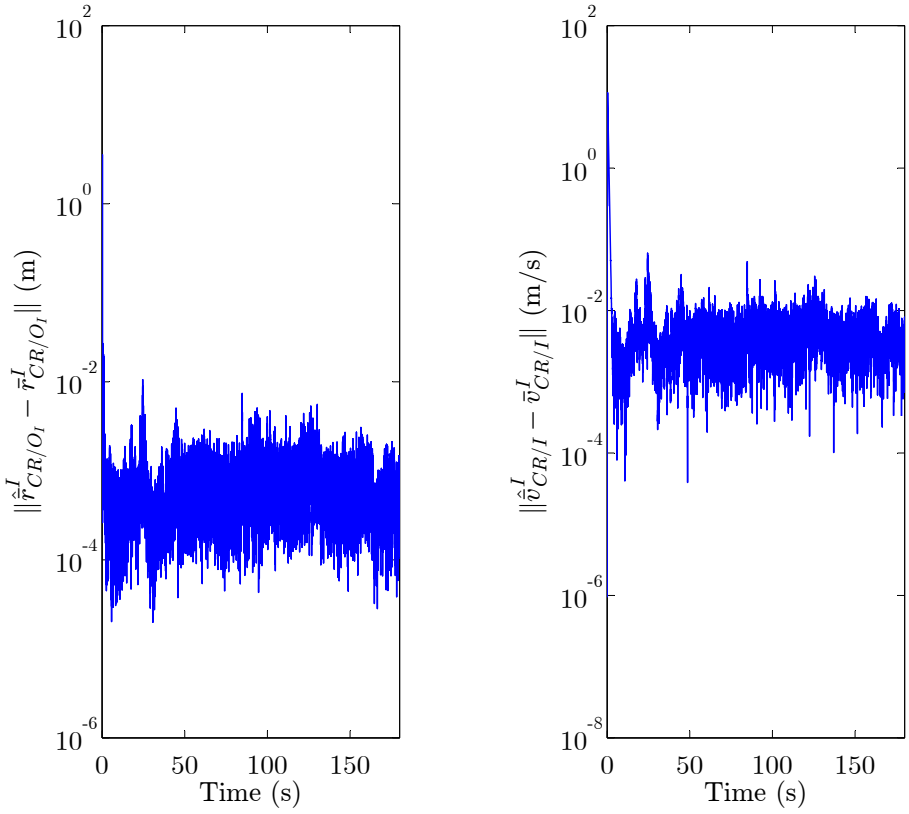

Figure 88: Data from pose-tracking experiment with thrusters: position and linear velocity estimation error.

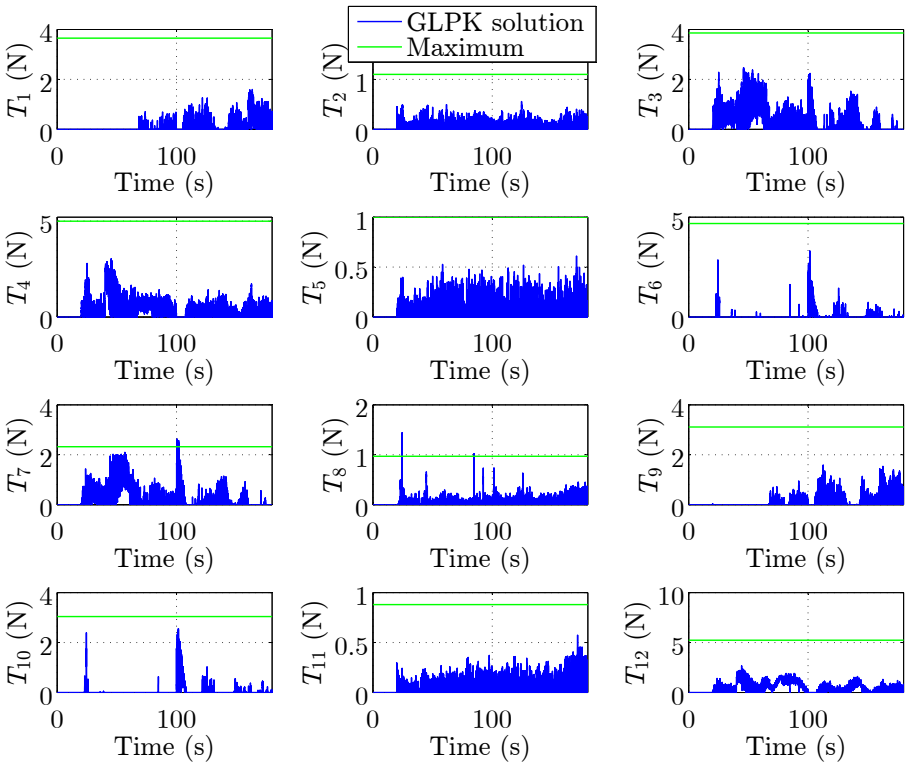

Figure 89: Data from pose-tracking experiment with thrusters: solution of the LP problem calculated by the GLPK package.

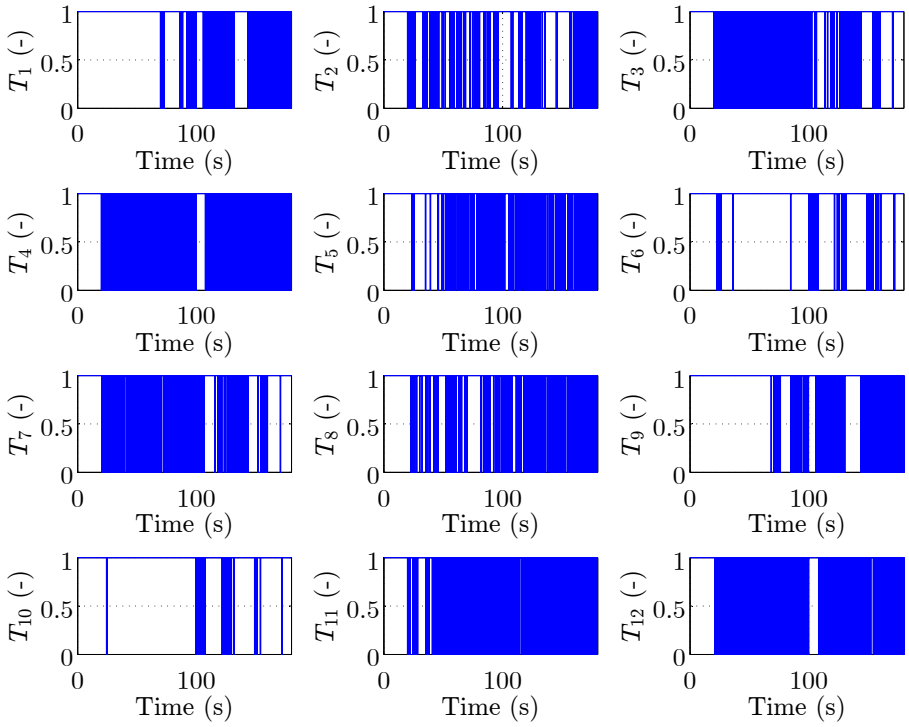

Figure 90: Data from pose-tracking experiment with thrusters: on-off commands issued to the thrusters. The thrusters are open at 0 and closed at 1.

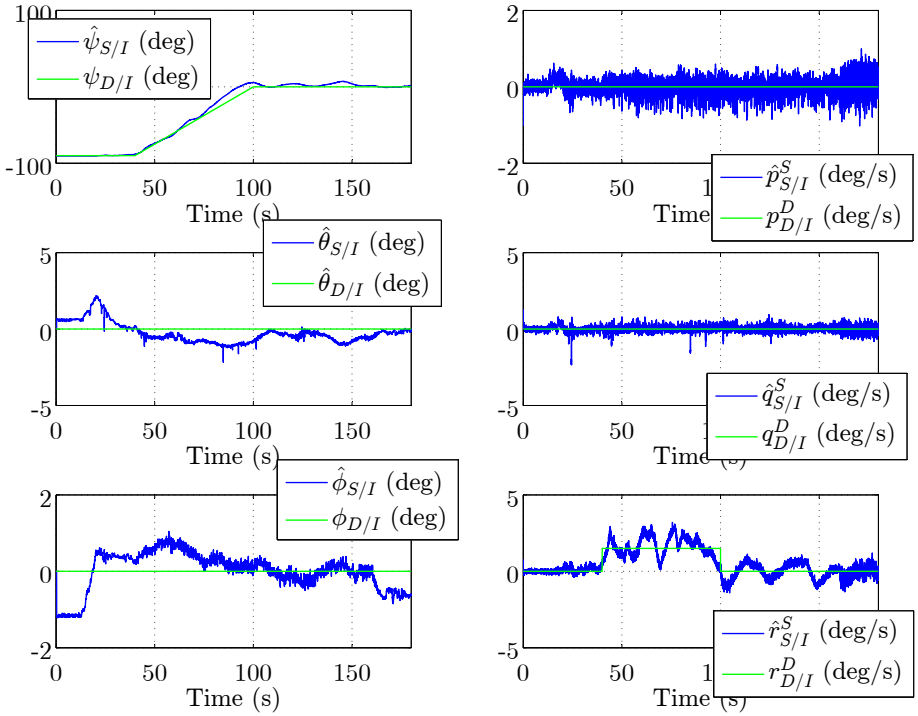

Figure 91: Data from pose-tracking experiment with thrusters: desired attitude and angular velocity versus attitude and angular velocity estimated by the DQ-MEKF.

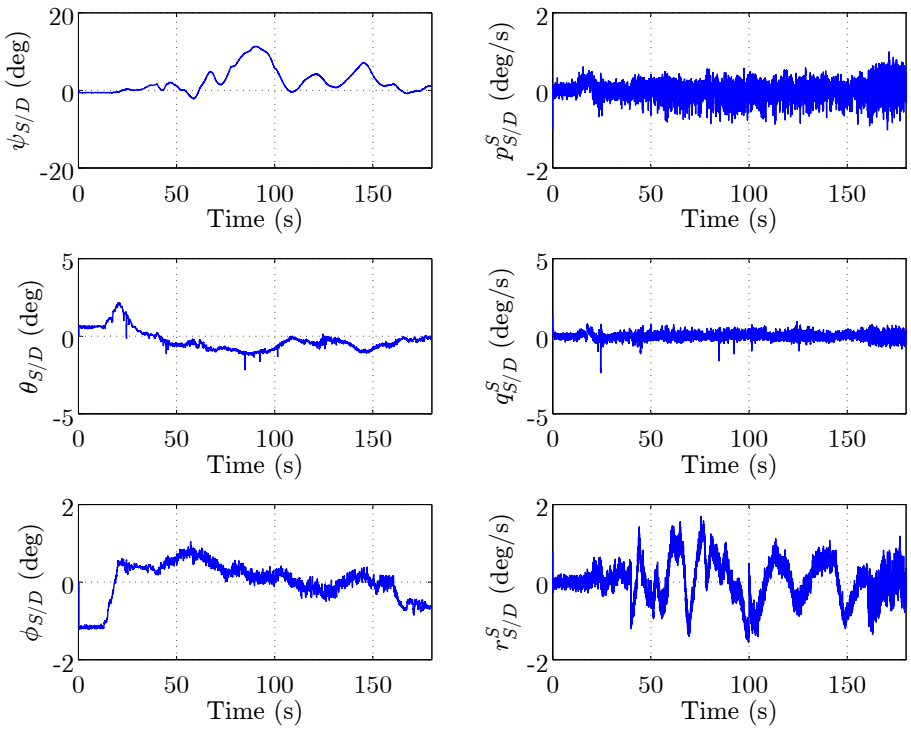

Figure 92: Data from pose-tracking experiment with thrusters: attitude and angular velocity tracking error.

position-tracking error is the slope of the epoxy floor.

Finally, Figure 96 compares the states of the inertia-free pose-tracking controller, which were started at zero, with the best available guess of m_t and ${}^{CR}\bar{I}^{\mathrm{S}}_s$. Again, the controller was not expected to be able to identify the mass and inertia matrix in this experiment, due to the many real world effects that violate the conditions of Proposition 5.2.

The same 5-DOF case, with the same conditions and parameters, was run on the high-fidelity simulator to validate the simulated results against the experimental results. In particular, in the simulation, the position of the center of mass of the upper stage with respect to the center of rotation is given by $\bar{r}^{\mathrm{S}}_{\bullet_s/CR} = [5e^{-6}, 5e^{-6}, 0]^{\mathrm{T}}$ m and the slope of the epoxy floor is linearly interpolated from a finite set of measurements, as explained in Section 6.1.7.1. The initial state of the simulation was defined as the state of the experiment at 17.50 sec, i.e., at the instant the lower stage was levitated.

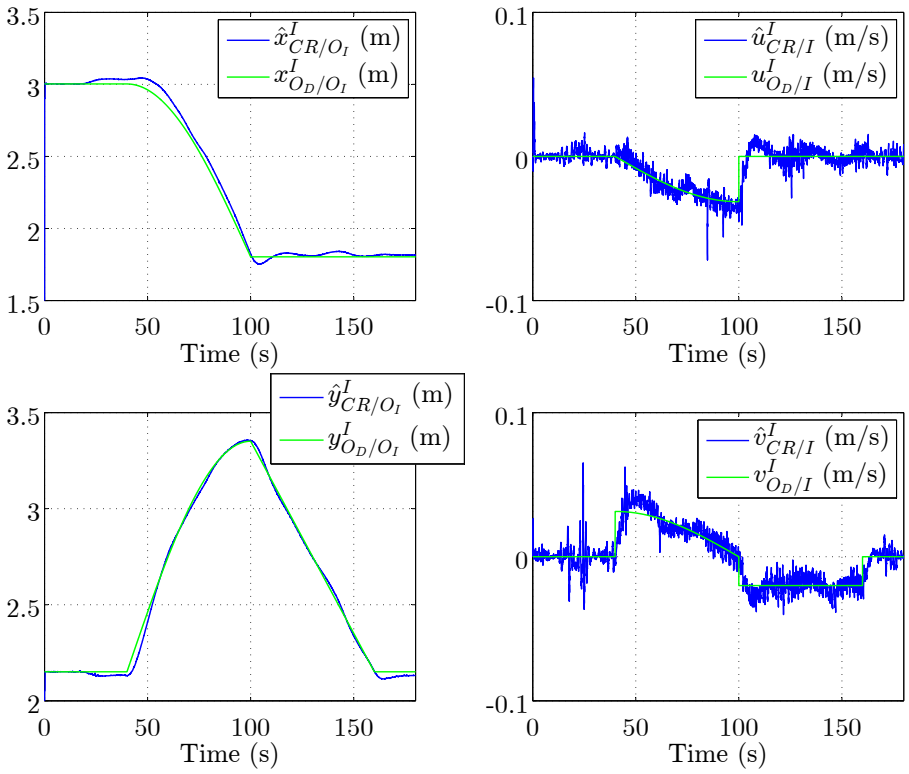

Figure 93: Data from pose-tracking experiment with thrusters: desired position and linear velocity versus position and linear velocity estimated by the DQ-MEKF.

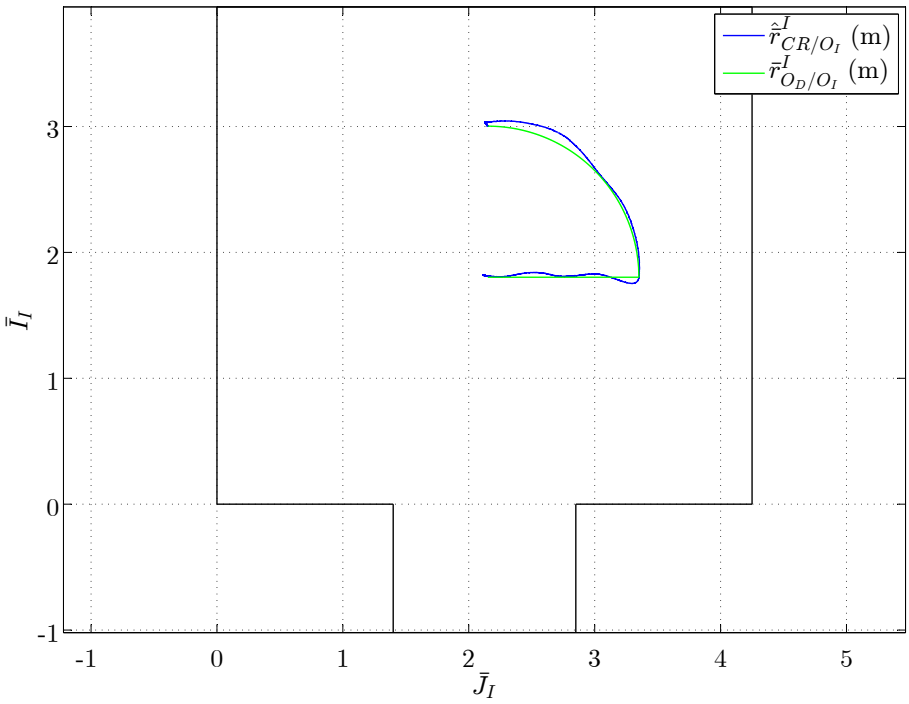

Figure 94: Data from pose-tracking experiment with thrusters: desired position versus position estimated by the DQ-MEKF within the limits of the epoxy floor.

The real-world effects specified in Section 6.2 were applied.

Figure 97 compares the attitude and angular velocity estimated by the DQ-MEKF with the true attitude and angular velocity, which is available in the simulation. The error between them is shown in Figure 98. After 20 sec, the RMS attitude estimation error is 0.24 deg (compared to 0.13 deg in the experiment) and the RMS angular velocity estimation error is 0.37 deg/s (compared to 0.41 deg/s in the experiment). Unlike in the experiment, in the simulation the measurement noise is perfect AWGN and the true attitude and angular velocity are known. Hence, the RMS attitude and angular velocity estimation errors in the simulation and in the experiment are not expected to be exactly the same. The current match is deemed acceptable.

Likewise, Figure 99 compares the position and linear velocity estimated by the DQ-MEKF with the true position and linear velocity, which is available in the simulation. The error between them is shown in Figure 100. After 20 sec, the RMS

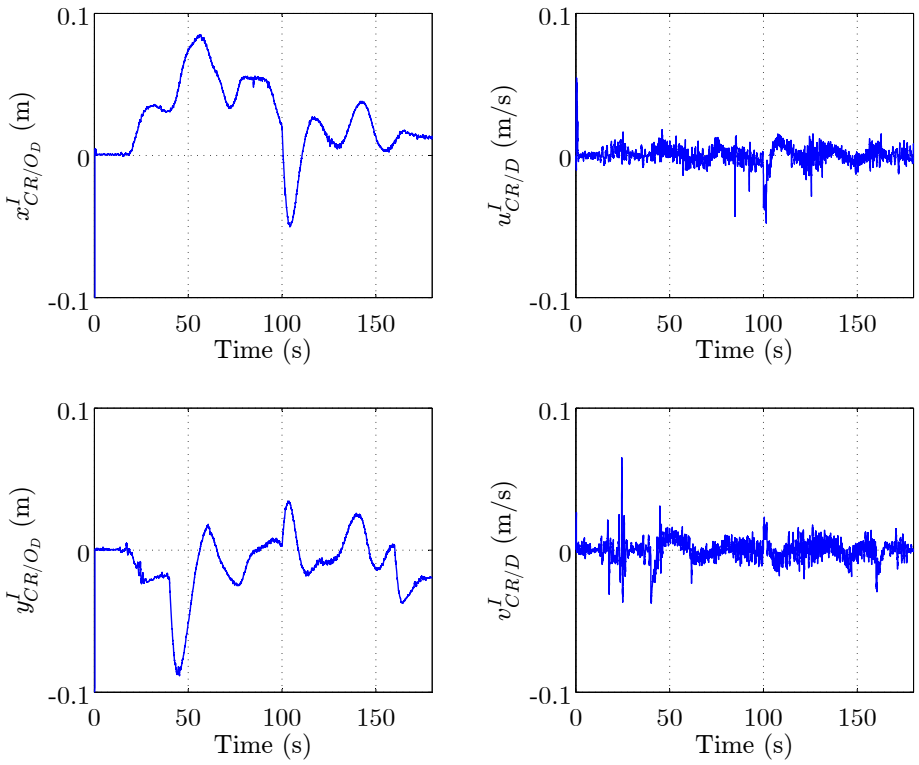

Figure 95: Data from pose-tracking experiment with thrusters: position and linear velocity tracking error.

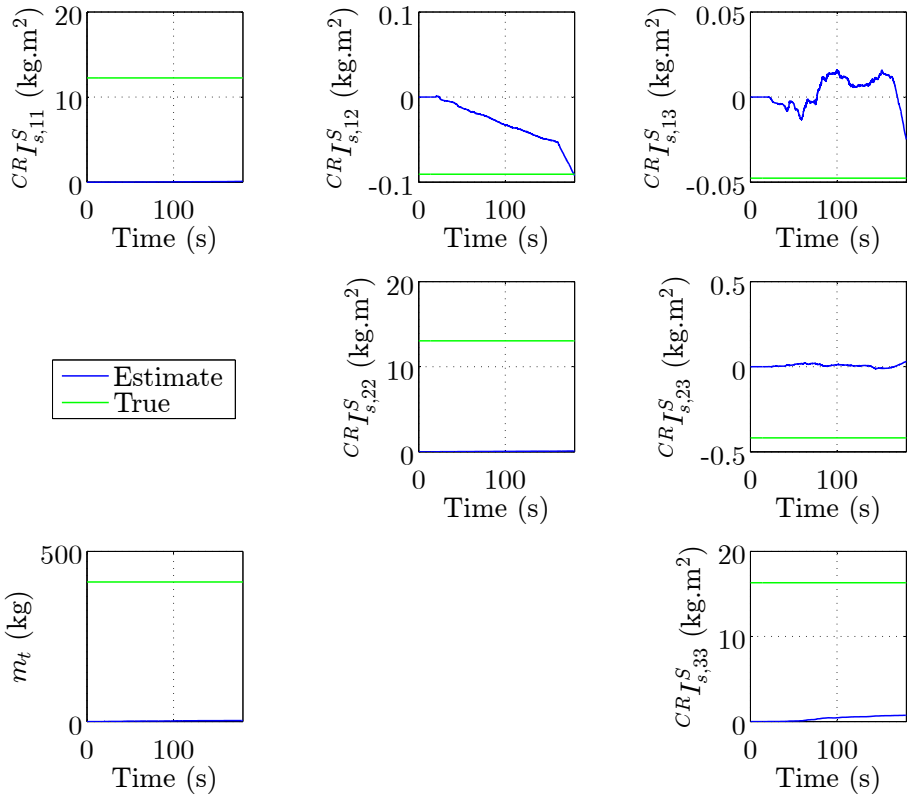

Figure 96: Data from pose-tracking experiment with thrusters: mass and inertia matrix estimates.

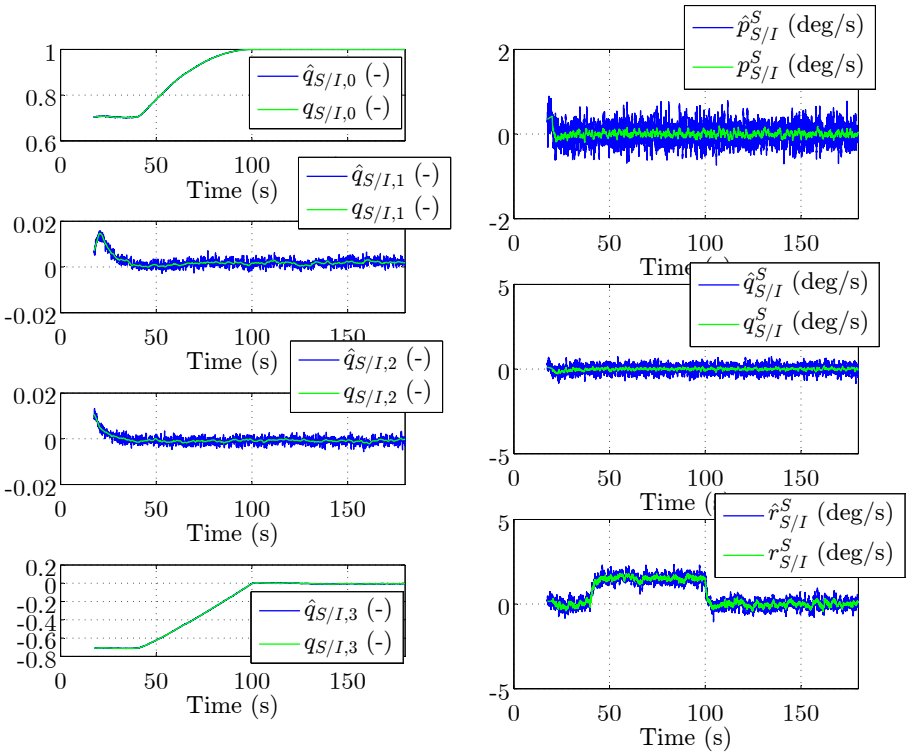

Figure 97: Data from pose-tracking simulation with thrusters: attitude and angular velocity estimated by the DQ-MEKF versus ground truth.

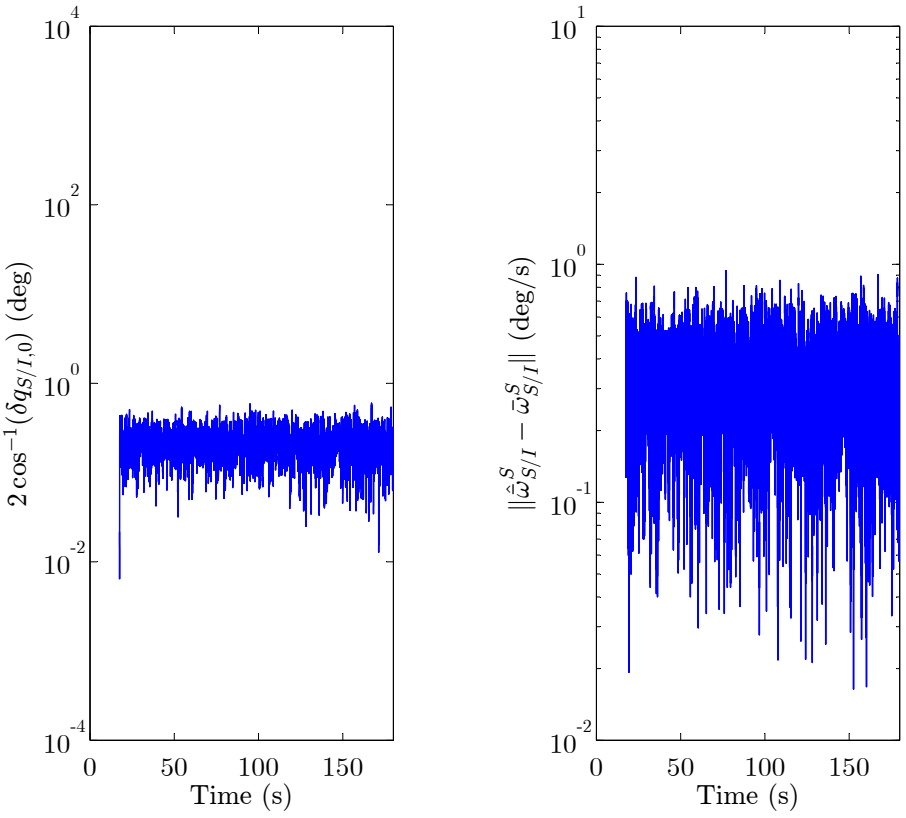

Figure 98: Data from pose-tracking simulation with thrusters: attitude and angular velocity estimation error.

position estimation error is 2.4 mm (compared to 1.0 mm in the experiment) and the RMS linear velocity estimation error is 12.5 mm/s (compared to 6.3 mm/s in the experiment). Hence, the simulation is currently overestimating the RMS position and linear velocity estimation errors by a factor of two, approximately. A better match can potentially be achieved by fine-tuning the simulated measurement noise specified in Section 6.2.

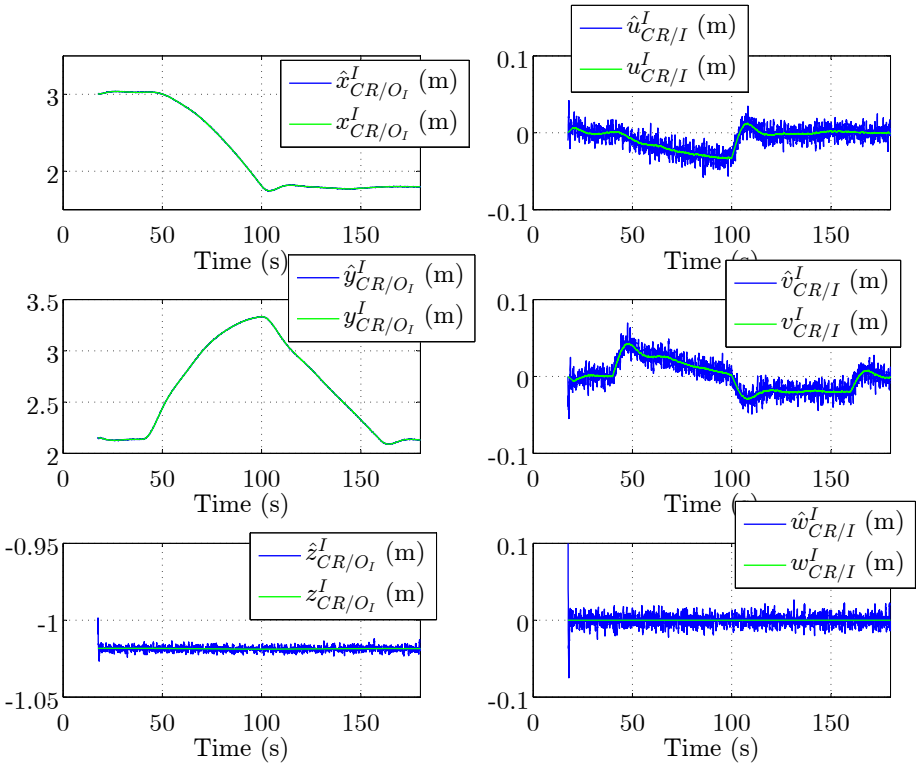

Figure 99: Data from pose-tracking simulation with thrusters: position and linear velocity estimated by the DQ-MEKF versus ground truth.

Figure 101 shows the solution to the LP problem calculated by the GLPK package throughout the simulation. By comparing Figure 101 with Figure 89, one can conclude that the simulation predicted that the maximum thrust of thruster 7 would be exceeded. In fact, the simulation provides a relatively good estimate of the maximum thrust that each thruster had to produce. This is probably one of the most

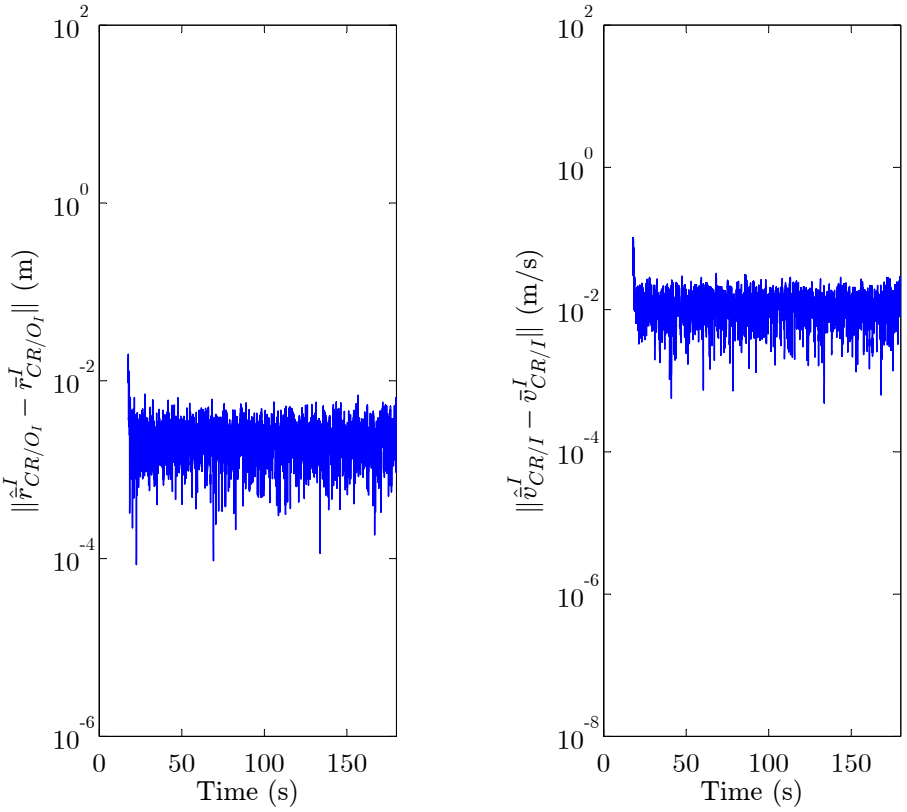

Figure 100: Data from pose-tracking simulation with thrusters: position and linear velocity estimation error.

important features of the simulation, as it allows the gains of the inertia-free pose-tracking controller to be properly tuned in the simulation before running an experiment. Figure 102 shows the corresponding on-off commands issued to the thrusters in the simulation. As in Figure 90, the large thrusters must fire almost continuously in order to counteract gravity and keep the position-tracking error within the values shown in Figure 107.

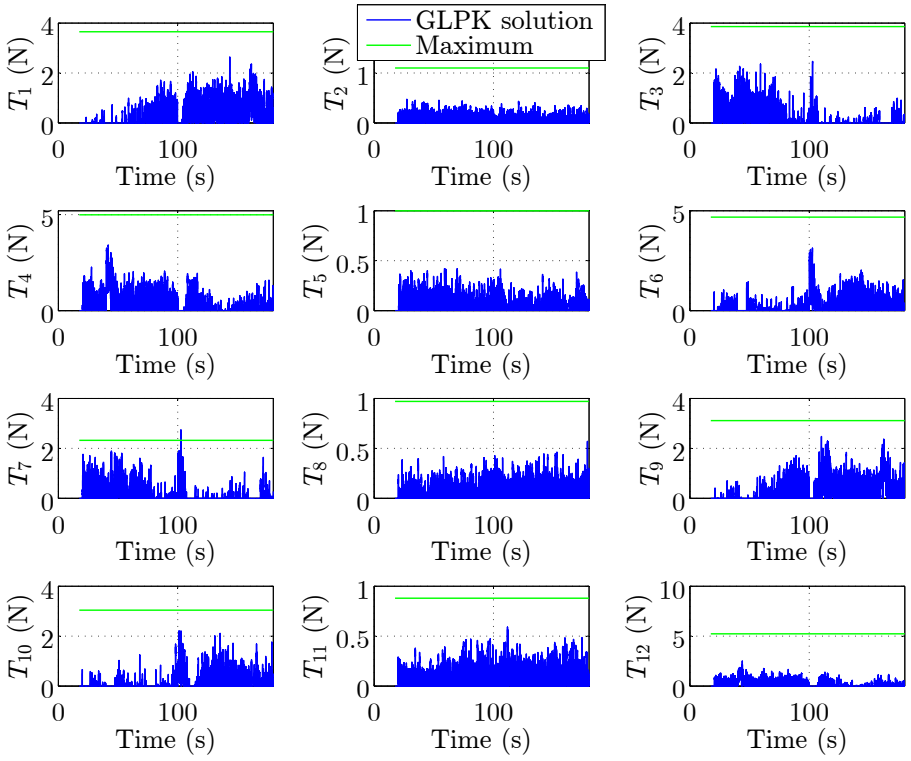

Figure 101: Data from pose-tracking simulation with thrusters: solution of the LP problem calculated by the GLPK package.

Figure 103 compares the desired attitude and angular velocity with the attitude and angular velocity estimated by the DQ-MEKF in the simulation. The error between them is shown in Figure 104. As in Figure 92, the desired pitch and roll angles are tracked within ± 1 deg. However, unlike in Figure 92, apart from the transient response between phases #2 and #3, the desired yaw angle is tracked within ± 2 deg. Hence, the simulation correctly predicted the pitch- and roll-tracking errors, but not

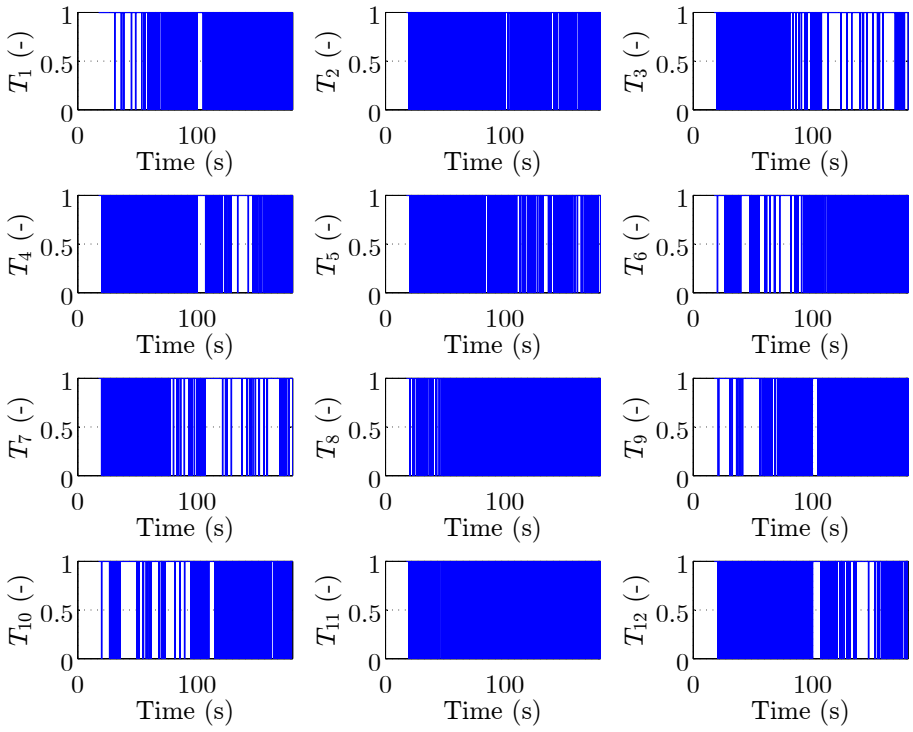

Figure 102: Data from pose-tracking simulation with thrusters: on-off commands issued to the thrusters. The thrusters are open at 0 and closed at 1.

the yaw-tracking error. As mentioned before, the large yaw-tracking error shown in Figure 92 is believed to have been caused by a momentarily malfunction of thruster 12. Since the simulation does not account for thrusters misfires, this large yaw-tracking error does not appear in Figure 104. Thus, the results shown in Figure 104 represent the best attitude-tracking error that can be expected if all thrusters operate as intended. Likewise, the first and second coordinates of the desired angular velocity are tracked within ± 1 deg/s in the simulation (same as in the experiment), whereas the third coordinate is tracked within ± 1 deg/s in the simulation (± 2 deg/s in the experiment), apart from the transitions between phases #2 and #3 and between phases #3 and #4.

Figure 105 compares the desired position and linear velocity with the position and linear velocity estimated by the DQ-MEKF in the simulation. The error between them is shown in Figure 107. Moreover, the desired position and the position estimated

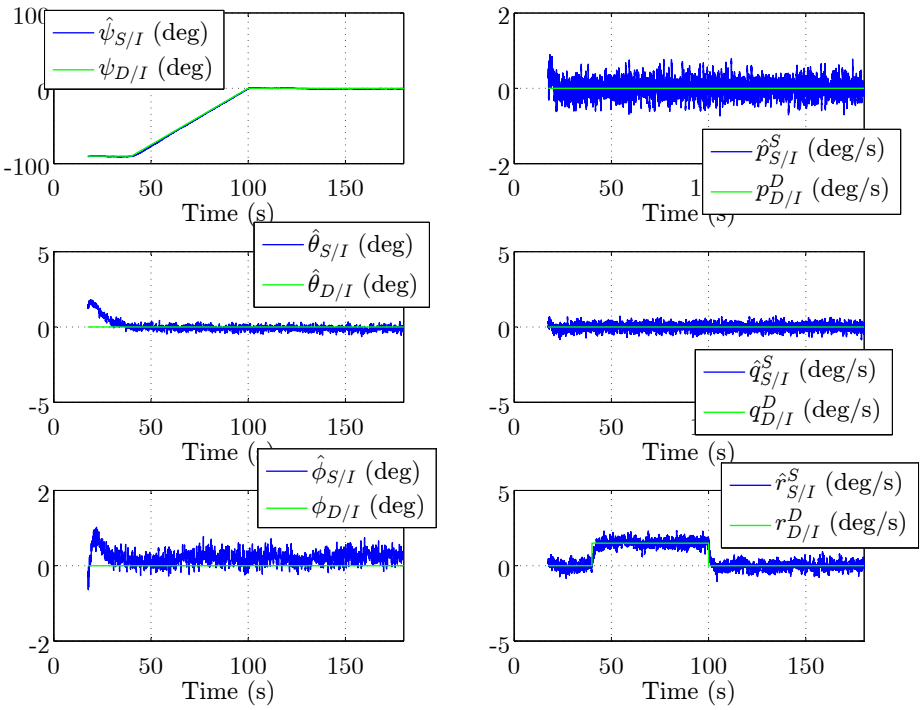

Figure 103: Data from pose-tracking simulation with thrusters: desired attitude and angular velocity versus attitude and angular velocity estimated by the DQ-MEKF.

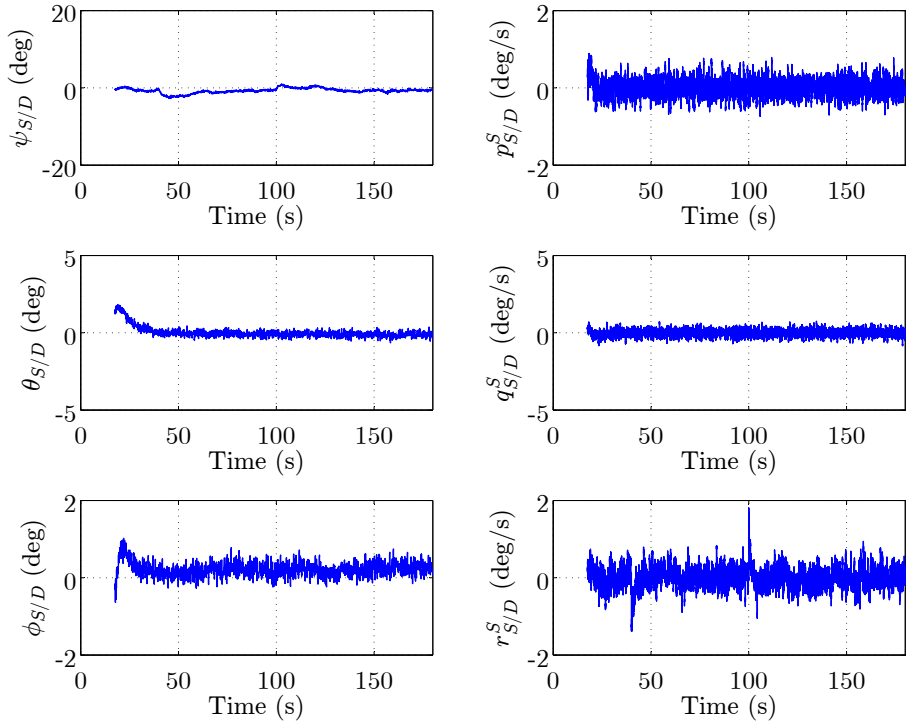

Figure 104: Data from pose-tracking simulation with thrusters: attitude and angular velocity tracking error.

by the DQ-MEKF in the simulation are projected onto the $\bar{I}_{\mathrm{I}}$-$\bar{J}_{\mathrm{I}}$ plane in Figure 106. After the transient response between phases #2 and #3 and phases #3 and #4, $x^{\mathrm{I}}_{CR/O_{\mathrm{D}}}$ is kept within ±3 cm (±6 cm in the experiment) and ±4 cm (±4 cm in the experiment), respectively. Likewise, after the transient response between phases #2 and #3 and phases #3 and #4, $y^{\mathrm{I}}_{CR/O_{\mathrm{D}}}$ is kept within ±3 cm (±3 cm in the experiment) and ±4 cm (±5 cm in the experiment), respectively. Moreover, at the end of the simulation, $x^{\mathrm{I}}_{CR/O_{\mathrm{D}}}$ and $y^{\mathrm{I}}_{CR/O_{\mathrm{D}}}$ are -0.4 cm (1.3 cm in the experiment) and -2.2 cm (-1.9 cm in the experiment), respectively. As for the desired linear velocity coordinates, they were tracked within ±0.05 m/s (±0.05 m/s in the experiment). The current match between the simulation and the experiment is deemed acceptable.

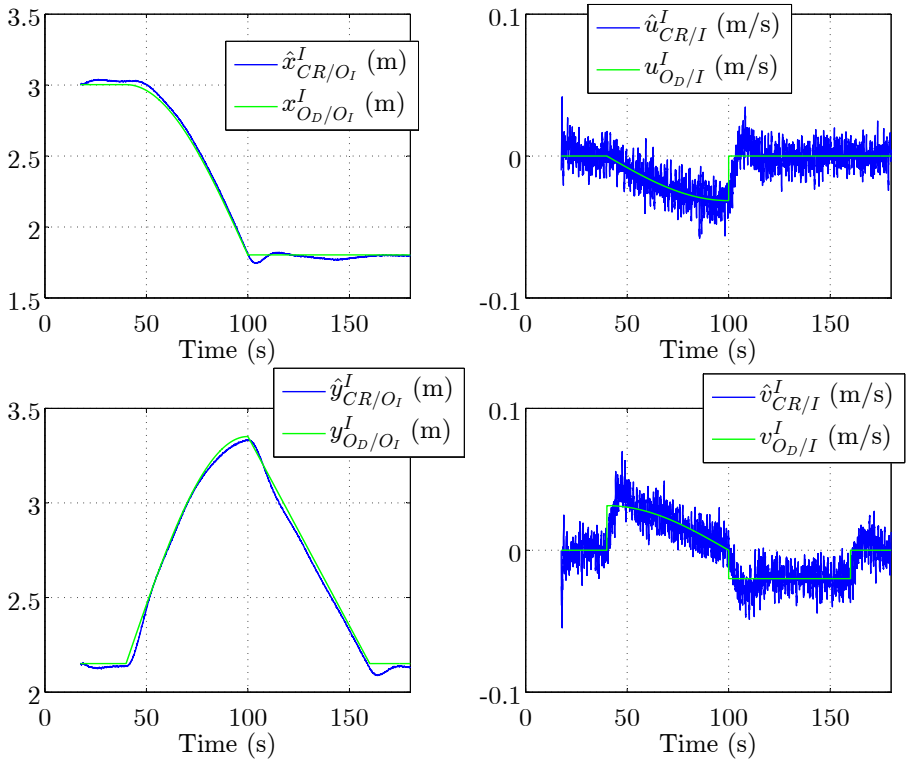

Figure 105: Data from pose-tracking simulation with thrusters: desired position and linear velocity versus position and linear velocity estimated by the DQ-MEKF.

Finally, Figure 108 shows that the simulation predicts the order of magnitude and overall behavior of the states of the adaptive controller.

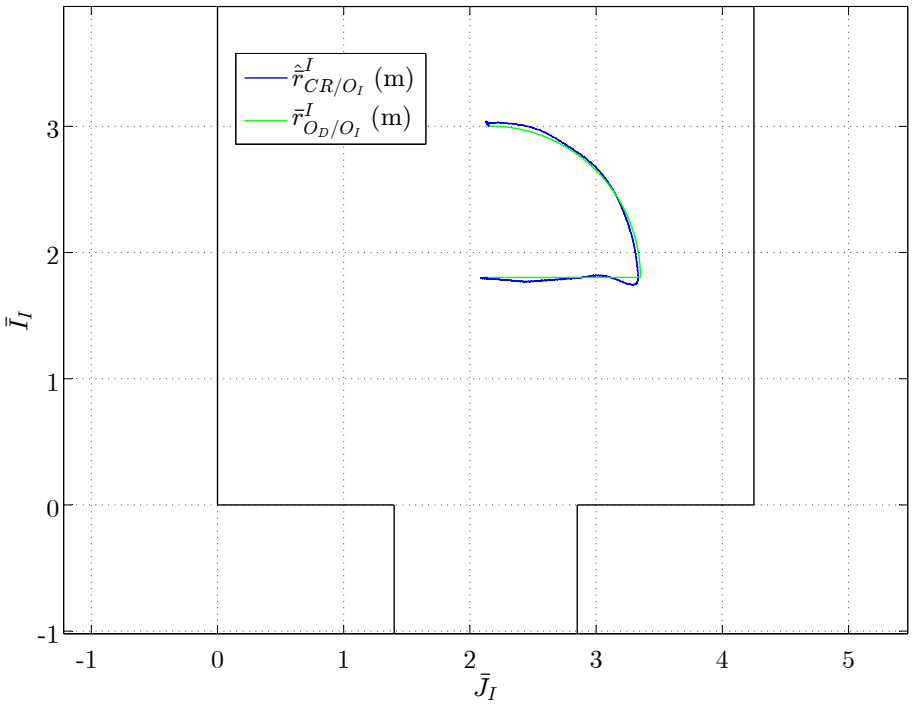

Figure 106: Data from pose-tracking simulation with thrusters: desired position versus position estimated by the DQ-MEKF within the limits of the epoxy floor.

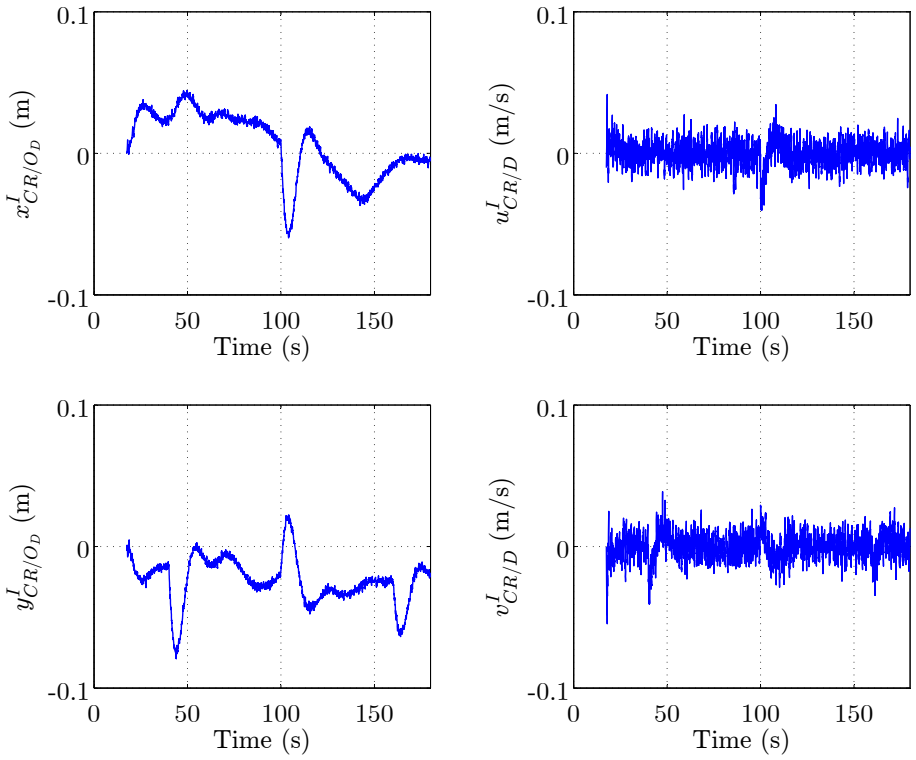

Figure 107: Data from pose-tracking simulation with thrusters: position and linear velocity tracking error.

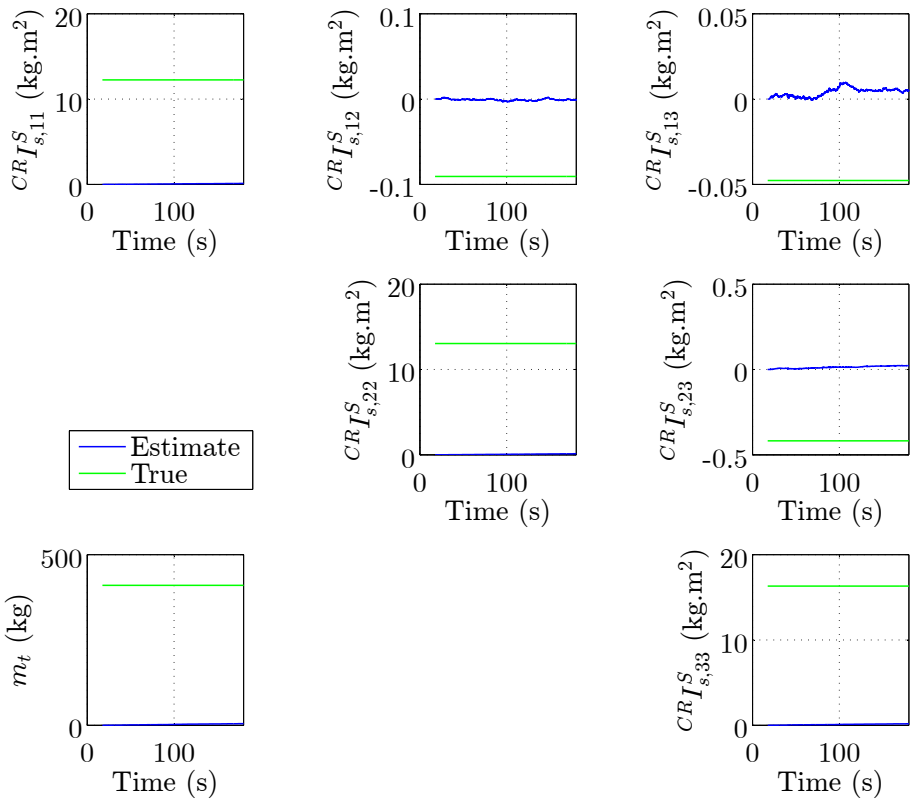

Figure 108: Data from pose-tracking simulation with thrusters: mass and inertia matrix estimates.

CHAPTER VII

CONCLUSION

One of the most common questions asked at the end of a technical presentation about dual quaternions is: apart from providing a compact representation of pose, why are dual quaternions relevant? In other words, why should anyone bother to learn dual quaternions? In the author's opinion, this is a very good question that, at least until now, was not easy to answer. The truth is, people have being solving position and attitude control and estimation problems for many years with relative success. Most solutions, at least in aerospace, are based on quaternions and translation vectors. However, this requires solving two separate problems, one for the rotational motion and another one for the translational motion. The latter problem is particularly hard since the translational motion depends on the rotational motion. Dual quaternions provide a way to solve both problems at the same time. Even more important than that, dual quaternions serve as a bridge between the rich literature on attitude control and estimation (with quaternions) and the harder problems of pose control and estimation. This dissertation shows that results that otherwise would have been hard to obtain are more or less simple to derive from existing attitude-only results via the use of dual quaternions. In the author's opinion, this is the most important property of dual quaternions and the main reason why people should look at them.

In space, the attitude of a satellite is typically controlled and estimated separately from its position. This makes sense since, whereas the attitude of a satellite needs to be controlled/estimated continuously, e.g., to point at Earth or at the Sun, position/orbital corrections are expensive and thus only performed when required. However, with the advent of space proximity operations for spacecraft servicing and

inspection, a real need for combined position and attitude controllers and estimators is starting to emerge in space. Dual quaternions and the results presented in this dissertation are especially suitable for these applications.

The first main contribution of this dissertation is Proposition 3, where the relative rotational and translational dynamic equations are written in dual quaternion algebra in the same form as the relative rotational-only dynamic equations are written in quaternion algebra. In particular, these equations are based on the dual inertia matrix. Like an inertia matrix, the dual inertia matrix is symmetric and positive-definite. Proposition 3 is the foundation on which the controllers proposed in Chapters 3 and 5 are built on.

The first demonstration of the usefulness of dual quaternions to extend existing attitude-only results is given in Chapter 3, where a velocity-free pose-tracking controller is derived from a velocity-free attitude-tracking controller presented in Ref. [3]. This pose controller requires only relative pose measurements, which can be provided by a vision-based sensor. This controller is also useful in the case of a velocity-sensor malfunction. Like all the controllers derived in this dissertation, this controller is based on the nonlinear 6-DOF equations of motion. Hence, it can handle, for example, elliptical orbits, tumbling targets, and long-range proximity operations.

An alternative way to perform pose-tracking with no velocity measurements is given in Chapter 4. It is based on a Dual Quaternion Multiplicative Extended Kalman Filter (DQ-MEKF) derived from the popular Quaternion Multiplicative Extended Kalman Filter (Q-MEKF) given in Ref. [57]. By using the Q-MEKF as a starting point, the DQ-MEKF is able to improve on other existing dual quaternion EKF formulations, which otherwise would be hard. In particular, the DQ-MEKF uses the concept of dual error quaternion, defined analogously to the concept of error quaternion in the Q-MEKF, to automatically satisfy the two algebraic constraints that unit dual quaternions must satisfy and to reduce the number of states from

eight to six. Three different formulations of the DQ-MEKF are presented, each with a different application in mind. The experimental results run on the ASTROS facility show that the DQ-MEKF does not encounter singularities and is accurate, precise, and fast enough for operational use. Whereas the derivations presented in Chapter 4 do not account for the system dynamics, as they can be hard to model accurately enough, it should be relatively straightforward to account for them if desired.

The two methods to perform pose-tracking without velocity measurements suggested in this dissertation are compared theoretically and numerically in the last section of Chapter 4. Although both methods have advantages and disadvantages, if the computational resources allow it, two points tilt the scale in favor of the formulation based on the DQ-MEKF. First, under the same circumstances, the transient responses obtained with the DQ-MEKF are less sensitive to noise, discrete-time measurements, and discrete-time implementation. Second, the DQ-MEKF produces direct estimates of the relative linear and angular velocities between the spacecraft, whereas the velocity-free controller presented in Chapter 3 does not. In an uncooperative satellite proximity operations scenario and assuming that the chaser satellite can measure its own linear and angular velocities with respect to the inertial frame, these estimates can be used to estimate the linear and angular velocity of the target spacecraft with respect to the inertial frame. Like most other pose-tracking controllers suggested in literature, the controllers presented in this dissertation require these velocities.

Another pose-tracking controller with unique properties is developed in Chapter 4 using dual quaternions, based on an existing attitude-tracking controller. This controller guarantees almost global asymptotic stability of the pose-tracking error without requiring any information about the mass and inertia matrix of the chaser satellite. On top of that, this controller can identify the mass and inertia matrix

if certain sufficient conditions on the reference motion given in Chapter 4 are satisfied. Moreover, the relatively low order of the controller makes it suitable for satellites with limited computational resources. Note that by combining this inertia-free pose-tracking controller with the DQ-MEKF described in Section 4.4, one obtains a velocity-free inertia-free pose-tracking control scheme for space proximity operations.

With the ultimate goal of testing the controllers and estimators derived in this dissertation on the 5-DOF platform of the ASTROS facility, a high-fidelity simulation of the platform is developed in Chapter 6. The equations of motion of the platform are carefully derived for three cases: a 3-DOF case, a 5-DOF case, and a (2+1)-DOF case. In particular, a special effort is put on defining all the reference frames and stating all the assumptions. Hopefully, this groundwork will be useful to others in the upcoming years. The high-fidelity simulation has a modular design to permit the test of new modules, such as a new controller or a new control allocation method, while keeping the remaining modules unaltered. Based on experimental data, the limitations of all actuators and sensors are simulated. Thanks to Simulink's xPC Target environment, the exact same control software used in the high-fidelity simulation can also be uploaded to the platform and run hardware-in-the-loop. All the parameters of the simulation are defined in a single input file for easy access and modification.

To experimentally validate the high-fidelity simulation, the DQ-MEKF, and the inertia-free pose-tracking controller, four experiments were run in real-time on the 5-DOF platform. A direct comparison between experimental results and simulated results indicates that the high-fidelity simulation is able to predict with a reasonable degree of accuracy the behavior of the platform.

7.1 Future Work

Some possible directions for future work are highlighted next, in no specific order.

1. The next obvious step for this research is to demonstrate experimentally the

capability to track a time-varying reference pose with respect to a target object by using measurements from a camera.

2. It has been shown [16, 61, 80] that the separation principle holds for the attitude-tracking problem under some conditions, i.e., under some conditions a stable closed-loop can be obtained by independently designing and combining a stable observer and a stable controller. As far as the author knowns, a similar result has not been demonstrated for the pose-tracking problem. This seems like another good application for the dual quaternion technique proposed in this dissertation.

3. Most vision-based algorithms for pose estimation are based on detecting and matching point features. However, line features have the potential to work better in space proximity operations. First, because they only appear in man-made objects in space and, second, because they are visible under a wider range of lighting conditions [40]. Because lines can be compactly represented using dual vector quaternions and their relative pose can be compactly represented using unit dual quaternions, some vision-based algorithms have been developed in the past based on line features and dual quaternions [40, 6]. However, these algorithms were not specifically designed and tested with space applications in mind. Moreover, since these algorithms were published, much work has been done in computer vision. Furthermore, the DQ-MEKF was not available to efficiently process the measured line features. Therefore, it would be interesting to take advantage of these new results to develop a vision-based algorithm for pose estimation based on line features and dual quaternions specifically designed for space proximity operations. By combining the inertia-free pose-tracking controller, the DQ-MEKF, and this new vision-based algorithm, the pose-tracking problem would be completely solved using dual quaternions.

4. Although it has been said that the classical EKF is still the most useful and practical solution for nonlinear attitude estimation, newer approaches such as nonlinear observers, *Unscented Kalman Filters* (UKFs), and *Particle Filters* (PFs) have been shown to have some advantages over it [21]. Thus, it would be interesting to try to extend some of these newer attitude estimation results into pose estimation results using dual quaternions.

5. As mentioned in Remark 7, although the mass and inertia matrix of the chaser spacecraft do not need to be known to implement the inertia-free controller given by Eq. (158), the center of mass of the chaser spacecraft still needs to be known. This is because Eq. (71) is only valid if the origin of the body frame is located at the center of mass. Hence, it would be interesting to rewrite Eq. (71) with respect to an arbitrary system of axes, not necessarily centered at the center of mass. Then, it should be possible to derive a more general inertia-free controller that does not require the center of mass to be known. Moreover, such a controller would most probably be able to handle changes in the location of the center of mass, making it an ideal candidate for the capture phase of NASA's *Asteroid Redirect Robotic Mission* (ARRM) [84].

6. The pose-tracking controllers given by Eqs. (158) and (82) are derived using the dual quaternion norm defined in Eq. (36), which is based on the dual quaternion circle product. However, other dual quaternion norms exist, such as the dual quaternion norm based on the dual quaternion logarithm [94, 96, 97, 44, 95]. This dual quaternion norm can potentially be used to extend existing attitude-only results derived using the quaternion norm based on the quaternion logarithm. Moreover, it would be interesting to research other dual quaternion norms.

7. The gains k_p, described in Theorem 2, and k_d, described in Remark 3, of the

velocity-free pose-tracking controller are scalars. As a consequence, the angular motion and the linear motion share the same gains, which is not ideal. Hence, it would be interesting to create more general forms of Theorem 2 and Remark 3, where the gains k_p and k_d are 8-by-8 matrices. Moreover, the velocity-free controller is derived in continuous-time, but vision-based sensors have typically slow update rates. Hence, it would be interesting to re-derive this controller in discrete-time and compare its performance with the simulation results presented in Section 4.7.

8. Both the velocity-free and the inertia-free controllers require the angular and linear velocities and accelerations of the target spacecraft with respect to the inertial frame to be known. Whereas the DQ-MEKF can be used to estimate the velocities, for uncooperative satellite proximity operations, it would be interesting to develop a pose-tracking controller with some stability guarantees that does not require any information about the motion of the target satellite with respect to the inertial frame. As far as the author knows, such a controller does not exist, not even for the attitude-tracking problem.

9. In short-distance proximity operations, the exhaust-plumes produced by the thrusters of the chaser spacecraft can damage the target spacecraft. Hence, their magnitude and direction must be constrained. Moreover, fuel is a precious commodity in space. Thus, it is important to minimize its consumption. Neither of these problems is directly addressed in this dissertation, but both are important and interesting problems to investigate in the future.

10. Some possible upgrades to the hardware and software of the 5-DOF platform are suggested hereafter.

    10.1. Currently, the center of mass of the upper stage needs to be manually adjusted before each experiment to coincide with the center of rotation.

This is a time-consuming task that has the potential to be automated, as in Ref. [13].

10.2. As discussed in Section 6.2, the motors that control the gimbals of the VSCMGs cannot produce angular rates smaller than approximately 4 deg/s in absolute value. Hence, fine attitude control cannot be achieved. A deadzone compensation algorithm, like the one presented in Ref. [58], could potentially mitigate the effect of this deadzone.

10.3. The inertia-free controller is currently implemented in the Simulink model shown in Figure 44 as a C-code S-function. Alternatively, this controller can be implemented in Simulink as a *Matlab Function* block and a *Discrete-Time Integrator* block, like the DQ-MEKF. Although both implementations are equivalent, the latter would be easier to maintain and update. Once this is done, it would be interesting to add the term $\widehat{\boldsymbol{f}_d^{\mathrm{B}}}$ to the inertia-free controller currently implemented in the Simulink model. In theory, this term should help counteract the disturbance force due to the slope of the epoxy floor and help reduce the position-tracking error.

10.4. A nice feature to add to the virtual-reality environment driven by the Simulink model would be a visualization of the path of the platform.

APPENDIX A

DERIVATION OF THE QV-AEKF

Instead of representing the pose of a body with respect to the I-frame with a unit dual quaternion (expressed neither in the body frame nor in the I-frame), the attitude and position of a body can be represented separately with a unit quaternion and a translation vector (expressed either in the body frame or in the I-frame). This is the approach taken in Refs. [68, 50, 40]. Hereby, an additive EKF based on this representation of the pose is derived for comparison with the DQ-MEKF with no linear and angular velocity measurements.

The linear and angular velocity measurement model is still given by Eq. (103) by separating the real part from the dual part, i.e., $\omega^{\mathrm{B}}_{\mathrm{B/I},m} = \omega^{\mathrm{B}}_{\mathrm{B/I}} + b_\omega + \eta_\omega$ and $v^{\mathrm{B}}_{\mathrm{B/I},m} = v^{\mathrm{B}}_{\mathrm{B/I}} + b_v + \eta_v$, where $E\left\{\overline{\eta}_\omega\right\} = 0_{3\times1}$, $E\left\{\overline{\eta}_v\right\} = 0_{3\times1}$, $E\left\{\overline{\eta}_\omega(t)\overline{\eta}^{\mathsf{T}}_\omega(\tau)\right\} = \overline{Q}_\omega(t)\delta(t-\tau)$, $E\left\{\overline{\eta}_v(t)\overline{\eta}^{\mathsf{T}}_v(\tau)\right\} = \overline{Q}_v(t)\delta(t-\tau)$, $\dot{b}_\omega = \eta_{b_\omega}$, $\dot{b}_v = \eta_{b_v}$, $E\left\{\overline{\eta}_{b_\omega}\right\} = 0_{3\times1}$, $E\left\{\overline{\eta}_{b_v}\right\} = 0_{3\times1}$, $E\left\{\overline{\eta}_{b_\omega}(t)\overline{\eta}^{\mathsf{T}}_{b_\omega}(\tau)\right\} = \overline{Q}_{b_\omega}(t)\delta(t-\tau)$, and $E\left\{\overline{\eta}_{b_v}(t)\overline{\eta}^{\mathsf{T}}_{b_v}(\tau)\right\} = \overline{Q}_{b_v}(t)\delta(t-\tau)$.

The state and process noise of the QV-AEKF are initially selected as

$$x_{16}=[[\delta q_{\mathrm{B/I}}]^{\mathsf{T}}\ [r^{\mathrm{B}}_{\mathrm{B/I}}]^{\mathsf{T}}\ [b_\omega]^{\mathsf{T}}\ [b_v]^{\mathsf{T}}]^{\mathsf{T}} \in \mathbb{R}^{16} \text{ and } w_{16}=[[\eta_\omega]^{\mathsf{T}}\ [\eta_v]^{\mathsf{T}}\ [\eta_{b_\omega}]^{\mathsf{T}}\ [\eta_{b_v}]^{\mathsf{T}}]^{\mathsf{T}} \in \mathbb{R}^{16}.$$

The time derivative of $\delta q_{\mathrm{B/I}}$ is given by the real part of Eq. (120), i.e., $\frac{\mathrm{d}}{\mathrm{d}t}(\delta q_{\mathrm{B/I}}) \approx -\frac{1}{2}\hat{\omega}^{\hat{\mathrm{B}}}_{\mathrm{B/I}}\delta q_{\mathrm{B/I}} + \frac{1}{2}\delta q_{\mathrm{B/I}}\hat{\omega}^{\hat{\mathrm{B}}}_{\mathrm{B/I}} + \frac{1}{2}\delta q_{\mathrm{B/I}}\hat{b}_\omega - \frac{1}{2}\delta q_{\mathrm{B/I}}b_\omega - \frac{1}{2}\delta q_{\mathrm{B/I}}\eta_\omega$, whereas the time derivative of $r^{\mathrm{B}}_{\mathrm{B/I}}$ is given by

$$\dot{r}^{\mathrm{B}}_{\mathrm{B/I}} = v^{\mathrm{B}}_{\mathrm{B/I}} - \omega^{\mathrm{B}}_{\mathrm{B/I}} \times r^{\mathrm{B}}_{\mathrm{B/I}} = (\hat{v}^{\hat{\mathrm{B}}}_{\mathrm{B/I}} + \hat{b}_v - b_v - \eta_v) - (\hat{\omega}^{\hat{\mathrm{B}}}_{\mathrm{B/I}} + \hat{b}_\omega - b_\omega - \eta_\omega) \times r^{\mathrm{B}}_{\mathrm{B/I}}. \quad (245)$$

Hence, the state equations of the QV-AEKF are given by

$$f_{16}(x_{16}(t),t) = \begin{bmatrix} [-\frac{1}{2}\hat{\omega}^{\hat{\mathrm{B}}}_{\mathrm{B/I}}\delta q_{\mathrm{B/I}} + \frac{1}{2}\delta q_{\mathrm{B/I}}\hat{\omega}^{\hat{\mathrm{B}}}_{\mathrm{B/I}} + \frac{1}{2}\delta q_{\mathrm{B/I}}\hat{b}_\omega - \frac{1}{2}\delta q_{\mathrm{B/I}} b_\omega] \\ (\hat{v}^{\hat{\mathrm{B}}}_{\mathrm{B/I}} + \hat{b}_v - b_v) - (\hat{\omega}^{\hat{\mathrm{B}}}_{\mathrm{B/I}} + \hat{b}_\omega - b_\omega) \times r^{\mathrm{B}}_{\mathrm{B/I}} \\ 0_{4\times 1} \\ 0_{4\times 1} \end{bmatrix}, \tag{246}$$

$$g_{16\times 16}(x_{16}(t),t) = \begin{bmatrix} -\frac{1}{2}[\delta q_{\mathrm{B/I}}]^{\mathrm{L}} & 0_{4\times 4} & 0_{4\times 4} & 0_{4\times 4} \\ -[r^{\mathrm{B}}_{\mathrm{B/I}}]^{\times} & -I_{4\times 4} & 0_{4\times 4} & 0_{4\times 4} \\ 0_{4\times 4} & 0_{4\times 4} & I_{4\times 4} & 0_{4\times 4} \\ 0_{4\times 4} & 0_{4\times 4} & 0_{4\times 4} & I_{4\times 4} \end{bmatrix}. \tag{247}$$

At this point, reduced state and process noise vectors are selected, namely

$$x_{12} = [\overline{\delta q_{\mathrm{B/I}}}^{\mathsf{T}}\ (\overline{r}^{\mathrm{B}}_{\mathrm{B/I}})^{\mathsf{T}}\ \overline{b}^{\mathsf{T}}_{\omega}\ \overline{b}^{\mathsf{T}}_{v}]^{\mathsf{T}} \in \mathbb{R}^{12} \text{ and } w_{12} = [\overline{\eta}^{\mathsf{T}}_{\omega}\ \overline{\eta}^{\mathsf{T}}_{v}\ \overline{\eta}^{\mathsf{T}}_{b_\omega}\ \overline{\eta}^{\mathsf{T}}_{b_v}]^{\mathsf{T}} \in \mathbb{R}^{12}.$$

By replacing $\delta q_{\mathrm{B/I},0}$ through Eq. (19) in Eqs. (246) and (247) and using Eq. (93), $F_{12\times 12}(t)$ and $G_{12\times 12}(t)$ can be determined to be

$$F_{12\times 12}(t) = \begin{bmatrix} -[\overline{\hat{\omega}^{\hat{\mathrm{B}}}_{\mathrm{B/I}}}]^{\times} & 0_{3\times 3} & -\frac{1}{2}I_{3\times 3} & 0_{3\times 3} \\ 0_{3\times 3} & -[\overline{\hat{\omega}^{\hat{\mathrm{B}}}_{\mathrm{B/I}}}]^{\times} & -[\overline{\hat{r}^{\hat{\mathrm{B}}}_{\mathrm{B/I}}}]^{\times} & -I_{3\times 3} \\ 0_{3\times 3} & 0_{3\times 3} & 0_{3\times 3} & 0_{3\times 3} \\ 0_{3\times 3} & 0_{3\times 3} & 0_{3\times 3} & 0_{3\times 3} \end{bmatrix}, \tag{248}$$

$$G_{12\times 12}(t) = \begin{bmatrix} -\frac{1}{2}I_{3\times 3} & 0_{3\times 3} & 0_{3\times 3} & 0_{3\times 3} \\ -[\overline{\hat{r}^{\hat{\mathrm{B}}}_{\mathrm{B/I}}}]^{\times} & -I_{3\times 3} & 0_{3\times 3} & 0_{3\times 3} \\ 0_{3\times 3} & 0_{3\times 3} & I_{3\times 3} & 0_{3\times 3} \\ 0_{3\times 3} & 0_{3\times 3} & 0_{3\times 3} & I_{3\times 3} \end{bmatrix}. \tag{249}$$

A.1 Time Update

For the time update of the QV-AEKF, the estimates of $q_{\mathrm{B/I}}$, $r^{\mathrm{B}}_{\mathrm{B/I}}$, $\omega^{\mathrm{B}}_{\mathrm{B/I}}$, $v^{\mathrm{B}}_{\mathrm{B/I}}$, b_ω, and b_v are propagated using the real part of Eq. (115), i.e., $\frac{\mathrm{d}}{\mathrm{d}t}(\hat{q}_{\mathrm{B/I}}) \approx \frac{1}{2}\hat{q}_{\mathrm{B/I}}\hat{\omega}^{\hat{\mathrm{B}}}_{\mathrm{B/I}}$, $\frac{\mathrm{d}}{\mathrm{d}t}(\hat{r}^{\hat{\mathrm{B}}}_{\mathrm{B/I}}) =$

$\hat{v}^{\hat{\mathrm{B}}}_{\mathrm{B/I}} - \hat{\omega}^{\hat{\mathrm{B}}}_{\mathrm{B/I}} \times \hat{r}^{\hat{\mathrm{B}}}_{\mathrm{B/I}}$, $\hat{\omega}^{\hat{\mathrm{B}}}_{\mathrm{B/I}} \approx \omega^{\mathrm{B}}_{\mathrm{B/I},m} - \hat{b}_{\boldsymbol{\omega}}$, $\hat{v}^{\hat{\mathrm{B}}}_{\mathrm{B/I}} \approx v^{\mathrm{B}}_{\mathrm{B/I},m} - \hat{b}_v$, $\frac{\mathrm{d}}{\mathrm{d}t}(\hat{b}_\omega) = 0$, and $\frac{\mathrm{d}}{\mathrm{d}t}(\hat{b}_v) = 0$, respectively, given $\hat{q}_{\mathrm{B/I}}(t_0)$, $\hat{r}^{\hat{\mathrm{B}}}_{\mathrm{B/I}}(t_0)$, $\hat{b}_\omega(t_0)$, and $\hat{b}_v(t_0)$.

Numerical errors in the propagation of $q_{\mathrm{B/I}}$ can result in the violation of the algebraic constraint associated with unit quaternions. Hence, after each integration step, this algebraic constraint is enforced by using Eq. (125).

As for the covariance matrix of x_{12}, i.e., $P_{12\times12}(t) \triangleq E\left\{\Delta x_{12}(t)\Delta x_{12}(t)^{\mathsf{T}}\right\}]$ or

$$P_{12\times12}(t) \triangleq E\left\{\left(\begin{bmatrix}\overline{\delta q_{\mathrm{B/I}}}(t)\\ \overline{r}^{\mathrm{B}}_{\mathrm{B/I}}(t)\\ \overline{b}_\omega(t)\\ \overline{b}_v(t)\end{bmatrix} - \begin{bmatrix}0_{3\times3}\\ \hat{\overline{r}}^{\hat{\mathrm{B}}}_{\mathrm{B/I}}(t)\\ \hat{\overline{b}}_\omega(t)\\ \hat{\overline{b}}_v(t)\end{bmatrix}\right)\left(\begin{bmatrix}\overline{\delta q_{\mathrm{B/I}}}(t)\\ \overline{r}^{\mathrm{B}}_{\mathrm{B/I}}(t)\\ \overline{b}_\omega(t)\\ \overline{b}_v(t)\end{bmatrix} - \begin{bmatrix}0_{3\times3}\\ \hat{\overline{r}}^{\hat{\mathrm{B}}}_{\mathrm{B/I}}(t)\\ \hat{\overline{b}}_\omega(t)\\ \hat{\overline{b}}_v(t)\end{bmatrix}\right)^{\mathsf{T}}\right\}, \quad (250)$$

it is propagated according to Eq. (92) given $P_{12\times12}(t_0)$ and where

$$Q_{12\times12}(t) = \begin{bmatrix}\overline{Q}_\omega(t) & 0_{3\times3} & 0_{3\times3} & 0_{3\times3}\\ 0_{3\times3} & \overline{Q}_v(t) & 0_{3\times3} & 0_{3\times3}\\ 0_{3\times3} & 0_{3\times3} & \overline{Q}_{b_\omega}(t) & 0_{3\times3}\\ 0_{3\times3} & 0_{3\times3} & 0_{3\times3} & \overline{Q}_{b_v}(t)\end{bmatrix}. \quad (251)$$

Note that it is not very intuitive to define $P_{12\times12}(t_0)$. It is more intuitive to define the covariance matrix

$$\tilde{P}_{16\times16}(t_0) \triangleq E\left\{\left(\begin{bmatrix}[q_{\mathrm{B/I}}(t_0)]\\ [r^{\mathrm{B}}_{\mathrm{B/I}}(t_0)]\\ [b_\omega(t_0)]\\ [b_v(t_0)]\end{bmatrix} - \begin{bmatrix}[\hat{q}_{\mathrm{B/I}}(t_0)]\\ [\hat{r}^{\hat{\mathrm{B}}}_{\mathrm{B/I}}(t_0)]\\ [\hat{b}_\omega(t_0)]\\ [\hat{b}_v(t_0)]\end{bmatrix}\right)\left(\begin{bmatrix}[q_{\mathrm{B/I}}(t_0)]\\ [r^{\mathrm{B}}_{\mathrm{B/I}}(t_0)]\\ [b_\omega(t_0)]\\ [b_v(t_0)]\end{bmatrix} - \begin{bmatrix}[\hat{q}_{\mathrm{B/I}}(t_0)]\\ [\hat{r}^{\hat{\mathrm{B}}}_{\mathrm{B/I}}(t_0)]\\ [\hat{b}_\omega(t_0)]\\ [\hat{b}_v(t_0)]\end{bmatrix}\right)^{\mathsf{T}}\right\}.$$

Given $\tilde{P}_{16\times16}(t_0)$, $P_{12\times12}(t_0)$ can be calculated by first computing

$$P_{16\times16}(t_0) \triangleq E\left\{\left(\begin{bmatrix}[\delta q_{\mathrm{B/I}}(t_0)]\\ [r^{\mathrm{B}}_{\mathrm{B/I}}(t_0)]\\ [b_\omega(t_0)]\\ [b_v(t_0)]\end{bmatrix} - \begin{bmatrix}[1]\\ [\hat{r}^{\hat{\mathrm{B}}}_{\mathrm{B/I}}(t_0)]\\ [\hat{b}_\omega(t_0)]\\ [\hat{b}_v(t_0)]\end{bmatrix}\right)\left(\begin{bmatrix}[\delta q_{\mathrm{B/I}}(t_0)]\\ [r^{\mathrm{B}}_{\mathrm{B/I}}(t_0)]\\ [b_\omega(t_0)]\\ [b_v(t_0)]\end{bmatrix} - \begin{bmatrix}[1]\\ [\hat{r}^{\hat{\mathrm{B}}}_{\mathrm{B/I}}(t_0)]\\ [\hat{b}_\omega(t_0)]\\ [\hat{b}_v(t_0)]\end{bmatrix}\right)^{\mathsf{T}}\right\}$$

$$= S\tilde{P}_{16\times16}(t_0)S^{\mathsf{T}}, \tag{252}$$

where

$$S = \begin{bmatrix}[\hat{q}^*_{\mathrm{B/I}}]^{\mathrm{L}} & 0_{4\times12}\\ 0_{12\times4} & I_{12\times12}\end{bmatrix}. \tag{253}$$

Then, $P_{12\times12}(t_0)$ can be obtained from $P_{16\times16}(t_0)$ by removing the first, fifth, ninth, and thirteenth rows and columns of $P_{16\times16}(t_0)$.

A.2 Measurement Update

For direct comparison with the DQ-MEKF with output equation given by Eq. (137), it is assumed that the QV-AEKF is fed measurements of $q_{\mathrm{B/I}}$ and $r^{\mathrm{I}}_{\mathrm{B/I}}$ corrupted by additive white Gaussian noise. Hence, the output equation of the QV-AEKF is given by

$$\begin{bmatrix}[q_{\mathrm{B/I},m}(t_k)]\\ \overline{r}^{\mathrm{I}}_{\mathrm{B/I},m}(t_k)\end{bmatrix} = \begin{bmatrix}[\hat{q}_{\mathrm{B/I}}(t_k)\delta q_{\mathrm{B/I}}(t_k)]\\ \overline{\hat{q}_{\mathrm{B/I}}(t_k)\delta q_{\mathrm{B/I}}(t_k)r^{\mathrm{B}}_{\mathrm{B/I}}(t_k)\delta q^*_{\mathrm{B/I}}(t_k)\hat{q}^*_{\mathrm{B/I}}(t_k)}\end{bmatrix} + v_7(t_k). \tag{254}$$

Replacing $\delta q_{\mathrm{B/I},0}$ through Eq. (19) in Eq. (254) and calculating the measurement sensitivity matrix using Eq. (99) yields

$$H_{7\times12}(t_k) = \begin{bmatrix}[\hat{q}_{\mathrm{B/I}}]^{\mathrm{L}}_{4\times3} & 0_{4\times3} & 0_{4\times3} & 0_{4\times3}\\ -2\hat{R}^{\mathrm{I}\leftarrow\mathrm{B}}[\overline{\hat{r}^{\hat{\mathrm{B}}}_{\mathrm{B/I}}}]^{\times} & \hat{R}^{\mathrm{I}\leftarrow\mathrm{B}} & 0_{3\times3} & 0_{3\times3}\end{bmatrix}, \tag{255}$$

where $\hat{R}^{\mathrm{I}\leftarrow\mathrm{B}}$ is the expected value of $R^{\mathrm{I}\leftarrow\mathrm{B}}$, which can be formed from $\hat{q}_{\mathrm{B/I}}$.

In summary, for the measurement update of the QV-AEKF, the Kalman gain is calculated from Eq. (98), whereas the optimal Kalman state update is calculated from

Eq. (96) as

$$\Delta^{\star}\hat{x}_{12}(t_k) \triangleq \begin{bmatrix} \Delta^{\star}\overline{\delta\hat{q}_{\mathrm{B/I}}}(t_k) \\ \Delta^{\star}\overline{\hat{r}}^{\hat{\mathrm{B}}}_{\mathrm{B/I}} \\ \Delta^{\star}\overline{\hat{b}}_{\omega}(t_k) \\ \Delta^{\star}\overline{\hat{b}}_{v}(t_k) \end{bmatrix} = K_{12\times 7}(t_k)(z_7(t_k) - \hat{z}_7(t_k)). \tag{256}$$

The estimate of the state at time t_k after the measurement is then calculated from $\hat{q}^{+}_{\mathrm{B/I}}(t_k) = \hat{q}^{-}_{\mathrm{B/I}}(t_k)\Delta^{\star}\delta\hat{q}_{\mathrm{B/I}}(t_k)$, $\overline{\hat{b}}^{+}_{\omega}(t_k) = \overline{\hat{b}}^{-}_{\omega}(t_k) + \Delta^{\star}\overline{\hat{b}}_{\omega}(t_k)$, $\overline{\hat{b}}^{+}_{v}(t_k) = \overline{\hat{b}}^{-}_{v}(t_k) + \Delta^{\star}\overline{\hat{b}}_{v}(t_k)$, and

$$\overline{\hat{r}}^{\hat{\mathrm{B}},+}_{\mathrm{B/I}}(t_k) = \overline{\hat{r}}^{\hat{\mathrm{B}},-}_{\mathrm{B/I}}(t_k) + \Delta^{\star}\overline{\hat{r}}^{\hat{\mathrm{B}}}_{\mathrm{B/I}}, \tag{257}$$

where $\Delta^{\star}\delta\hat{q}_{\mathrm{B/I}}$ is defined as the unit quaternion

$$\left(\sqrt{1-\|\Delta^{\star}\overline{\delta\hat{q}_{\mathrm{B/I}}}\|^2}, \Delta^{\star}\overline{\delta\hat{q}_{\mathrm{B/I}}}\right), \text{ or } \left(\frac{1}{\sqrt{1+\|\Delta^{\star}\overline{\delta\hat{q}_{\mathrm{B/I}}}\|^2}}, \frac{\Delta^{\star}\overline{\delta\hat{q}_{\mathrm{B/I}}}}{\sqrt{1+\|\Delta^{\star}\overline{\delta\hat{q}_{\mathrm{B/I}}}\|^2}}\right) \tag{258}$$

if the norm of $\Delta^{\star}\overline{\delta\hat{q}_{\mathrm{B/I}}}$ is larger than one. Note that whereas the optimal Kalman state update is added in Eq. (257), it is multiplied in Eq. (133). Finally, the covariance matrix of the state immediately after the measurement at t_k is computed from Eq. (101).

Similarly to before, when position and attitude measurements are available, but linear and angular velocity measurements are not, estimates of $\omega^{\mathrm{B}}_{\mathrm{B/I}}$ and $v^{\mathrm{B}}_{\mathrm{B/I}}$ can be determined by setting $\omega^{\mathrm{B}}_{\mathrm{B/I},m}$, $v^{\mathrm{B}}_{\mathrm{B/I},m}$, $\overline{Q}_{\omega}$, and $\overline{Q}_{v}$ to zero, and by increasing $\overline{Q}_{b_\omega}$ and $\overline{Q}_{b_v}$ if necessary.

APPENDIX B

DERIVATION OF THE SQV-AEKF

Whereas the states of the DQ-MEKF and of the QV-AEKF include both the attitude and position of the body, the traditional approach to estimate the pose consists on developing separate estimators for the attitude and for the position [77]. To compare this traditional approach to the DQ-MEKF and to the QV-AEKF, the QV-AEKF is split here into two additive EKFs, one for the attitude and another one for the position. This alternative formulation is referred to as the *SQV-AEKF*.

B.1 Attitude Estimation with the SQV-AEKF

As in the QV-AEKF, the angular velocity measurement model is given by $\omega^{\mathrm{B}}_{\mathrm{B/I},m} = \omega^{\mathrm{B}}_{\mathrm{B/I}} + b_\omega + \eta_\omega$, where $E\{\overline{\eta}_\omega\} = 0_{3\times1}$, $E\{\overline{\eta}_\omega(t)\overline{\eta}^{\intercal}_\omega(\tau)\} = \overline{Q}_\omega(t)\delta(t-\tau)$, $\dot{b}_\omega = \eta_{b_\omega}$, $E\left\{\overline{\eta}_{b_\omega}\right\} = 0_{3\times1}$, and $E\left\{\overline{\eta}_{b_\omega}(t)\overline{\eta}^{\intercal}_{b_\omega}(\tau)\right\} = \overline{Q}_{b_\omega}(t)\delta(t-\tau)$.

The state and process noise of the attitude part of the SQV-AEKF are initially selected as

$$x_8{=}[[\delta q_{\mathrm{B/I}}]^{\intercal}\ [b_\omega]^{\intercal}]^{\intercal} \in \mathbb{R}^8 \text{ and } w_8{=}[[\eta_\omega]^{\intercal}\ [\eta_{b_\omega}]^{\intercal}]^{\intercal} \in \mathbb{R}^8.$$

As in the QV-AEKF, the time derivative of $\delta q_{\mathrm{B/I}}$ is given by $\frac{\mathrm{d}}{\mathrm{d}t}(\delta q_{\mathrm{B/I}}) \approx -\frac{1}{2}\hat{\omega}^{\hat{\mathrm{B}}}_{\mathrm{B/I}}\delta q_{\mathrm{B/I}} + \frac{1}{2}\delta q_{\mathrm{B/I}}\hat{\omega}^{\hat{\mathrm{B}}}_{\mathrm{B/I}} + \frac{1}{2}\delta q_{\mathrm{B/I}}\hat{b}_\omega - \frac{1}{2}\delta q_{\mathrm{B/I}}b_\omega - \frac{1}{2}\delta q_{\mathrm{B/I}}\eta_\omega$. Hence, the state equations of the attitude part of the SQV-AEKF are given by

$$f_8(x_8(t),t) = \begin{bmatrix} [-\frac{1}{2}\hat{\omega}^{\hat{\mathrm{B}}}_{\mathrm{B/I}}\delta q_{\mathrm{B/I}} + \frac{1}{2}\delta q_{\mathrm{B/I}}\hat{\omega}^{\hat{\mathrm{B}}}_{\mathrm{B/I}} + \frac{1}{2}\delta q_{\mathrm{B/I}}\hat{b}_\omega - \frac{1}{2}\delta q_{\mathrm{B/I}}b_\omega] \\ 0_{4\times1} \end{bmatrix}, \tag{259}$$

$$g_{8\times8}(x_8(t),t) = \begin{bmatrix} -\frac{1}{2}[\delta q_{\mathrm{B/I}}]^{\mathrm{L}} & 0_{4\times4} \\ 0_{4\times4} & I_{4\times4} \end{bmatrix}. \tag{260}$$

At this point, reduced state and process noise vectors are selected, namely

$$x_6 = [\overline{\delta q_{\mathrm{B/I}}}^{\mathsf{T}} \ \overline{b}_\omega^{\mathsf{T}}]^{\mathsf{T}} \in \mathbb{R}^6 \text{ and } w_6 = [\overline{\eta}_\omega^{\mathsf{T}} \ \overline{\eta}_{b_\omega}^{\mathsf{T}}]^{\mathsf{T}} \in \mathbb{R}^6.$$

By replacing $\delta q_{\mathrm{B/I},0}$ through Eq. (19) in Eqs. (259) and (260) and using Eq. (93), $F_{6\times6}(t)$ and $G_{6\times6}(t)$ can be determined to be

$$F_{6\times6}(t) = \begin{bmatrix} -[\overline{\hat{\omega}_{\mathrm{B/I}}^{\hat{\mathrm{B}}}}]^\times & -\frac{1}{2}I_{3\times3} \\ 0_{3\times3} & 0_{3\times3} \end{bmatrix}, \tag{261}$$

$$G_{6\times6}(t) = \begin{bmatrix} -\frac{1}{2}I_{3\times3} & 0_{3\times3} \\ 0_{3\times3} & I_{3\times3} \end{bmatrix}. \tag{262}$$

B.1.1 Time Update

For the time update of the attitude part of the SQV-AEKF, the estimates of $q_{\mathrm{B/I}}$, $\omega_{\mathrm{B/I}}^{\mathrm{B}}$, and b_ω are propagated using $\frac{\mathrm{d}}{\mathrm{d}t}(\hat{q}_{\mathrm{B/I}}) \approx \frac{1}{2}\hat{q}_{\mathrm{B/I}}\hat{\omega}_{\mathrm{B/I}}^{\hat{\mathrm{B}}}$, $\hat{\omega}_{\mathrm{B/I}}^{\hat{\mathrm{B}}} \approx \omega_{\mathrm{B/I},m}^{\mathrm{B}} - \hat{b}_{\boldsymbol{\omega}}$, and $\frac{\mathrm{d}}{\mathrm{d}t}(\hat{b}_\omega) = 0$, respectively, given $\hat{q}_{\mathrm{B/I}}(t_0)$ and $\hat{b}_\omega(t_0)$.

Numerical errors in the propagation of $q_{\mathrm{B/I}}$ can result in the violation of the algebraic constraint associated with unit quaternions. Hence, after each integration step, this algebraic constraint is enforced by using Eq. (125).

As for the covariance matrix of x_6, i.e., $P_{6\times6}(t) \triangleq E\left\{\Delta x_6(t)\Delta x_6(t)^{\mathsf{T}}\right\}$ or

$$P_{6\times6}(t) \triangleq E\left\{\left(\begin{bmatrix}\overline{\delta q_{\mathrm{B/I}}}(t) \\ \overline{b}_\omega(t)\end{bmatrix} - \begin{bmatrix}0_{3\times3} \\ \hat{\overline{b}}_\omega(t)\end{bmatrix}\right)\left(\begin{bmatrix}\overline{\delta q_{\mathrm{B/I}}}(t) \\ \overline{b}_\omega(t)\end{bmatrix} - \begin{bmatrix}0_{3\times3} \\ \hat{\overline{b}}_\omega(t)\end{bmatrix}\right)^{\mathsf{T}}\right\}, \tag{263}$$

it is propagated according to Eq. (92) given $P_{6\times6}(t_0)$ and where

$$Q_{6\times6}(t) = \begin{bmatrix} \overline{Q}_\omega(t) & 0_{3\times3} \\ 0_{3\times3} & \overline{Q}_{b_\omega}(t) \end{bmatrix}. \tag{264}$$

Note that it is not very intuitive to define $P_{6\times6}(t_0)$. It is more intuitive to define the covariance matrix

$$\tilde{P}_{8\times8}(t_0) \triangleq E\left\{\left(\begin{bmatrix}[q_{\mathrm{B/I}}(t_0)] \\ [b_\omega(t_0)]\end{bmatrix} - \begin{bmatrix}[\hat{q}_{\mathrm{B/I}}(t_0)] \\ [\hat{b}_\omega(t_0)]\end{bmatrix}\right)\left(\begin{bmatrix}[q_{\mathrm{B/I}}(t_0)] \\ [b_\omega(t_0)]\end{bmatrix} - \begin{bmatrix}[\hat{q}_{\mathrm{B/I}}(t_0)] \\ [\hat{b}_\omega(t_0)]\end{bmatrix}\right)^{\mathsf{T}}\right\}.$$

Given $\tilde{P}_{8\times 8}(t_0)$, $P_{6\times 6}(t_0)$ can be calculated by first computing

$$P_{8\times 8}(t_0) \triangleq E\left\{\left(\begin{bmatrix}[\delta q_{\mathrm{B/I}}(t_0)]\\ [b_\omega(t_0)]\end{bmatrix} - \begin{bmatrix}[1]\\ [\hat{b}_\omega(t_0)]\end{bmatrix}\right)\left(\begin{bmatrix}[\delta q_{\mathrm{B/I}}(t_0)]\\ [b_\omega(t_0)]\end{bmatrix} - \begin{bmatrix}[1]\\ [\hat{b}_\omega(t_0)]\end{bmatrix}\right)^{\mathsf{T}}\right\}$$
$$= S\tilde{P}_{8\times 8}(t_0)S^{\mathsf{T}}, \tag{265}$$

where

$$S = \begin{bmatrix}[\hat{q}^{*}_{\mathrm{B/I}}]^{\mathrm{L}} & 0_{4\times 4}\\ 0_{4\times 4} & I_{4\times 4}\end{bmatrix}. \tag{266}$$

Then, $P_{6\times 6}(t_0)$ can be obtained from $P_{8\times 8}(t_0)$ by removing the first and fifth rows and columns of $P_{8\times 8}(t_0)$.

B.1.2 Measurement Update

It is assumed that the attitude part of the SQV-AEKF is fed measurements of $q_{\mathrm{B/I}}$ corrupted by additive white Gaussian noise (whereas the position part of the SQV-AEKF is fed measurements of $r^{\mathrm{I}}_{\mathrm{B/I}}$ corrupted by additive white Gaussian noise). Hence, the output equation of the attitude part of the SQV-AEKF is given by

$$[q_{\mathrm{B/I},m}(t_k)] = [\hat{q}_{\mathrm{B/I}}(t_k)\delta q_{\mathrm{B/I}}(t_k)] + v_4(t_k). \tag{267}$$

Replacing $\delta q_{\mathrm{B/I},0}$ through Eq. (19) in Eq. (267) and calculating the measurement sensitivity matrix using Eq. (99) yields

$$H_{4\times 6}(t_k) = \left[[\hat{q}_{\mathrm{B/I}}]^{\mathrm{L}}_{4\times 3}\ 0_{4\times 3}\right]. \tag{268}$$

In summary, for the measurement update of the attitude part of the SQV-AEKF, the Kalman gain is calculated from Eq. (98), whereas the optimal Kalman state update is calculated from Eq. (96) as

$$\Delta^{\star}\hat{x}_6(t_k) \triangleq \begin{bmatrix}\Delta^{\star}\overline{\delta\hat{q}_{\mathrm{B/I}}}(t_k)\\ \Delta^{\star}\bar{\hat{b}}_\omega(t_k)\end{bmatrix} = K_{6\times 4}(t_k)(z_4(t_k) - \hat{z}_4(t_k)). \tag{269}$$

The estimate of the state at time t_k after the measurement is then calculated from $\hat{q}^{+}_{\mathrm{B/I}}(t_k) = \hat{q}^{-}_{\mathrm{B/I}}(t_k)\Delta^{\star}\delta\hat{q}_{\mathrm{B/I}}(t_k)$ and $\overline{\hat{b}}^{+}_{\omega}(t_k) = \overline{\hat{b}}^{-}_{\omega}(t_k) + \Delta^{\star}\overline{\hat{b}}_{\omega}(t_k)$, where $\Delta^{\star}\delta\hat{q}_{\mathrm{B/I}}$ is the unit quaternion defined in Eq. (258). Finally, the covariance matrix of the state immediately after the measurement at t_k is computed from Eq. (101).

Similarly to before, when attitude measurements are available, but angular velocity measurements are not, estimates of $\omega^{\mathrm{B}}_{\mathrm{B/I}}$ can be determined by setting $\omega^{\mathrm{B}}_{\mathrm{B/I},m}$ and $\overline{Q}_{\omega}$ to zero, and by increasing $\overline{Q}_{b_\omega}$ if necessary.

B.2 Position Estimation with the SQV-AEKF

As in the QV-AEKF, the linear velocity measurement model is given by $v^{\mathrm{B}}_{\mathrm{B/I},m} = v^{\mathrm{B}}_{\mathrm{B/I}} + b_v + \eta_v$, where $E\left\{\overline{\eta}_v\right\} = 0_{3\times1}$, $E\left\{\overline{\eta}_v(t)\overline{\eta}^{\mathsf{T}}_v(\tau)\right\} = \overline{Q}_v(t)\delta(t-\tau)$, $\dot{b}_v = \eta_{b_v}$, $E\left\{\overline{\eta}_{b_v}\right\} = 0_{3\times1}$, and $E\left\{\overline{\eta}_{b_v}(t)\overline{\eta}^{\mathsf{T}}_{b_v}(\tau)\right\} = \overline{Q}_{b_v}(t)\delta(t-\tau)$.

The state and process noise of the position part of the SQV-AEKF are initially selected as

$$x_8 = [[r^{\mathrm{B}}_{\mathrm{B/I}}]^{\mathsf{T}}\ [b_v]^{\mathsf{T}}]^{\mathsf{T}} \in \mathbb{R}^8 \text{ and } w_8 = [[\eta_v]^{\mathsf{T}}\ [\eta_{b_v}]^{\mathsf{T}}]^{\mathsf{T}} \in \mathbb{R}^8.$$

The time derivative of $r^{\mathrm{B}}_{\mathrm{B/I}}$ is given by Eq. (245). Hence, the state equations of the position part of the SQV-AEKF are given by

$$f_8(x_8(t),t) = \begin{bmatrix} (\hat{v}^{\hat{\mathrm{B}}}_{\mathrm{B/I}} + \hat{b}_v - b_v) - (\hat{\omega}^{\hat{\mathrm{B}}}_{\mathrm{B/I}} + \hat{b}_\omega - b_\omega) \times r^{\mathrm{B}}_{\mathrm{B/I}} \\ 0_{4\times1} \end{bmatrix}, \tag{270}$$

$$g_{8\times8}(x_8(t),t) = \begin{bmatrix} -I_{4\times4} & 0_{4\times4} \\ 0_{4\times4} & I_{4\times4} \end{bmatrix}. \tag{271}$$

At this point, reduced state and process noise vectors are selected, namely

$$x_6 = [(\overline{r}^{\mathrm{B}}_{\mathrm{B/I}})^{\mathsf{T}}\ \overline{b}^{\mathsf{T}}_v]^{\mathsf{T}} \in \mathbb{R}^6 \text{ and } w_6 = [\overline{\eta}^{\mathsf{T}}_v\ \overline{\eta}^{\mathsf{T}}_{b_v}]^{\mathsf{T}} \in \mathbb{R}^6.$$

Using Eq. (93), $F_{6\times6}(t)$ and $G_{6\times6}(t)$ can be determined to be

$$F_{6\times6}(t) = \begin{bmatrix} -[\overline{\hat{\omega}^{\hat{\mathrm{B}}}_{\mathrm{B/I}}}]^{\times} & -I_{3\times3} \\ 0_{3\times3} & 0_{3\times3} \end{bmatrix}, \tag{272}$$

$$G_{6\times6}(t) = \begin{bmatrix} -I_{3\times3} & 0_{3\times3} \\ 0_{3\times3} & I_{3\times3} \end{bmatrix}. \tag{273}$$

Note that $F_{6\times6}(t)$ is a function of $\overline{\hat{\omega}^{\hat{\mathrm{B}}}_{\mathrm{B/I}}}$, which is an output of the attitude part of the SQV-AEKF.

B.2.1 Time Update

For the time update of the position part of the SQV-AEKF, the estimates of $r^{\mathrm{B}}_{\mathrm{B/I}}$, $v^{\mathrm{B}}_{\mathrm{B/I}}$, and b_v are propagated using $\frac{\mathrm{d}}{\mathrm{d}t}(\hat{r}^{\hat{\mathrm{B}}}_{\mathrm{B/I}}) = \hat{v}^{\hat{\mathrm{B}}}_{\mathrm{B/I}} - \hat{\omega}^{\hat{\mathrm{B}}}_{\mathrm{B/I}} \times \hat{r}^{\hat{\mathrm{B}}}_{\mathrm{B/I}}$, $\hat{v}^{\hat{\mathrm{B}}}_{\mathrm{B/I}} \approx v^{\mathrm{B}}_{\mathrm{B/I},m} - \hat{b}_v$, and $\frac{\mathrm{d}}{\mathrm{d}t}(\hat{b}_v) = \mathtt{0}$, respectively, given $\hat{r}^{\hat{\mathrm{B}}}_{\mathrm{B/I}}(t_0)$ and $\hat{b}_v(t_0)$. Note that $\frac{\mathrm{d}}{\mathrm{d}t}(\hat{r}^{\hat{\mathrm{B}}}_{\mathrm{B/I}})$ is a function of $\hat{\omega}^{\hat{\mathrm{B}}}_{\mathrm{B/I}}$, which is an output of the attitude part of the SQV-AEKF.

As for the covariance matrix of x_6, i.e., $P_{6\times6}(t) \triangleq E\left\{\Delta x_6(t)\Delta x_6(t)^{\mathsf{T}}\right\}]$ or

$$P_{6\times6}(t) \triangleq E\left\{ \left(\begin{bmatrix} \overline{r}^{\mathrm{B}}_{\mathrm{B/I}}(t) \\ \overline{b}_v(t) \end{bmatrix} - \begin{bmatrix} \hat{\overline{r}}^{\hat{\mathrm{B}}}_{\mathrm{B/I}}(t) \\ \hat{\overline{b}}_v(t) \end{bmatrix} \right) \left(\begin{bmatrix} \overline{r}^{\mathrm{B}}_{\mathrm{B/I}}(t) \\ \overline{b}_v(t) \end{bmatrix} - \begin{bmatrix} \hat{\overline{r}}^{\hat{\mathrm{B}}}_{\mathrm{B/I}}(t) \\ \hat{\overline{b}}_v(t) \end{bmatrix} \right)^{\mathsf{T}} \right\}, \tag{274}$$

it is propagated according to Eq. (92) given $P_{12\times12}(t_0)$ and where

$$Q_{12\times12}(t) = \begin{bmatrix} \overline{Q}_v(t) & 0_{3\times3} \\ 0_{3\times3} & \overline{Q}_{b_v}(t) \end{bmatrix}. \tag{275}$$

B.2.2 Measurement Update

It is assumed that the position part of the SQV-AEKF is fed measurements of $r^{\mathrm{I}}_{\mathrm{B/I}}$ corrupted by additive white Gaussian noise (whereas the attitude part of the SQV-AEKF is fed measurements of $q_{\mathrm{B/I}}$ corrupted by additive white Gaussian noise). Hence, the output equation of the position part of the SQV-AEKF is given by

$$\overline{r}^{\mathrm{I}}_{\mathrm{B/I},m}(t_k) = \overline{\hat{q}_{\mathrm{B/I}}(t_k)\delta q_{\mathrm{B/I}}(t_k) r^{\mathrm{B}}_{\mathrm{B/I}}(t_k) \delta q^{*}_{\mathrm{B/I}}(t_k) \hat{q}^{*}_{\mathrm{B/I}}(t_k)} + v_3(t_k). \tag{276}$$

Calculating the measurement sensitivity matrix using Eq. (99) yields

$$H_{3\times 6}(t_k) = \left[\hat{R}^{\mathrm{I}\leftarrow\mathrm{B}}\ 0_{3\times 3}\right], \tag{277}$$

where $\hat{R}^{\mathrm{I}\leftarrow\mathrm{B}}$ is the expected value of $R^{\mathrm{I}\leftarrow\mathrm{B}}$, which can be formed from $\hat{q}_{\mathrm{B/I}}$, one of the outputs of the attitude part of the SQV-AEKF.

In summary, for the measurement update of the position part of the SQV-AEKF, the Kalman gain is calculated from Eq. (98), whereas the optimal Kalman state update is calculated from Eq. (96) as

$$\Delta^{\star}\hat{x}_6(t_k) \triangleq \begin{bmatrix} \Delta^{\star}\overline{\hat{r}}^{\hat{\mathrm{B}}}_{\mathrm{B/I}} \\ \Delta^{\star}\overline{\hat{b}}_v(t_k) \end{bmatrix} = K_{6\times 3}(t_k)(z_3(t_k) - \hat{z}_3(t_k)). \tag{278}$$

The estimate of the state at time t_k after the measurement is then calculated from $\overline{\hat{b}}^{+}_v(t_k) = \overline{\hat{b}}^{-}_v(t_k) + \Delta^{\star}\overline{\hat{b}}_v(t_k)$ and $\overline{\hat{r}}^{\hat{\mathrm{B}},+}_{\mathrm{B/I}}(t_k) = \overline{\hat{r}}^{\hat{\mathrm{B}},-}_{\mathrm{B/I}}(t_k) + \Delta^{\star}\overline{\hat{r}}^{\hat{\mathrm{B}}}_{\mathrm{B/I}}$. Finally, the covariance matrix of the state immediately after the measurement at t_k is computed from Eq. (101).

Similarly to before, when position measurements are available, but linear velocity measurements are not, estimates of $v^{\mathrm{B}}_{\mathrm{B/I}}$ can be determined by setting $v^{\mathrm{B}}_{\mathrm{B/I},m}$ and $\overline{Q}_v$ to zero, and by increasing $\overline{Q}_{b_v}$ if necessary.

REFERENCES

[1] Ahmed, J., Coppola, V. T., and Bernstein, D. S., "Adaptive asymptotic tracking of spacecraft attitude motion with inertia matrix identification," *Journal of Guidance, Control, and Dynamics*, vol. 21, pp. 684–691, September-October 1998.

[2] Air Force Research Laboratory, "XSS-11 micro satellite," tech. rep., Space Vehicles Directorate, December 2005.

[3] Akella, M. R., "Rigid body attitude tracking without angular velocity feedback," *Systems & Control Letters*, vol. 42, pp. 321–326, April 6 2001.

[4] Arthur E. Bryson, J., *Control of Spacecraft and Aircraft*. Princeton University Press, 1994.

[5] Aspragathos, N. and Dimitros, J., "A comparative study of three methods for robotic kinematics," *IEEE Transactions on Systems, Man, and Cybernetics, Part B: Cybernetics*, vol. 28, pp. 135–145, April 1998.

[6] Bayro-Corrochano, E. and Zhang, Y., "The motor extended Kalman filter: A geometric approach for rigid motion estimation," *Journal of Mathematical Imaging and Vision*, vol. 13, pp. 205–228, December 2000.

[7] Bhat, S. P. and Bernstein, D. S., "A topological obstruction to continuous global stabilization of rotational motion and the unwinding phenomenon," *Systems & Control Letters*, vol. 39, pp. 63 – 70, January 28 2000.

[8] Brodsky, V. and Shoham, M., "The dual inertia operator and its application to robot dynamics," *Journal of Mechanical Design*, vol. 116, p. 1089, December 1994.

[9] Brodsky, V. and Shoham, M., "Dual numbers representation of rigid body dynamics," *Mechanism and Machine Theory*, vol. 34, pp. 693–718, July 1999.

[10] Cabecinhas, D., Cunha, R., and Silvestre, C., "Output-feedback control for almost global stabilization of fully-actuated rigid bodies," in *Proceedings of the 47th IEEE Conference on Decision and Control*, (Cancun, Mexico), pp. 3583–3588, December 9-11 2008.

[11] Cairano, S. D., Park, H., and Kol, I., "Model predictive control approach for guidance of spacecraft rendezvous and proximity maneuvering," *International Journal of Robust and Nonlinear Control*, vol. 22, pp. 1398–1427, 2012.

[12] Chaturvedi, N. A., Sanyal, A. K., and McClamroch, N. H., "Rigid-body attitude control using rotation matrices for continuous singularity-free control laws," *IEEE Control Systems Magazine*, pp. 30–51, June 2011.

[13] Chesi, S., Gong, Q., Pellegrini, V., Cristi, R., and Romano, M., "Automatic mass balancing of a spacecraft three-axis simulator: Analysis and experimentation," *Journal of Guidance, Control, and Dynamics*, vol. 37, pp. 197–206, January-February 2014.

[14] Cho, D.-M., Jung, D., and Tsiotras, P., "A 5-DOF experimental platform for spacecraft rendezvous and docking," in *AIAA Infotech @ Aerospace Conference*, (Seattle, WA), April 6–9 2009. AIAA Paper 2009-1869.

[15] Cho, D.-M., Tsiotras, P., Zhang, G., and Holzinger, M. J., "Robust feature detection, acquisition and tracking for relative navigation in space with a known target," in *AIAA Guidance, Navigation, and Control Conference*, AIAA 2013-5197, (Boston, MA), August 19-22 2013.

[16] Chunodkar, A. A. and Akella, M. R., "Switching angular velocity observer for rigid-body attitude stabilization and tracking control," in *23rd AAS/AIAA Space Flight Mechanics Meeting*, no. AAS 13-216, (Kauai, Hawaii), February 10-14 2013.

[17] Clifford, W. K., "Preliminary sketch of bi-quaternions," *Proceedings of the London Mathematical Society*, vol. 4, pp. 381–395, 1873.

[18] Condurache, D. and Burlacu, A., "Dual Lie algebra representations of the rigid body motion," in *AIAA/AAS Astrodynamics Specialist Conference*, (San Diego, CA), August 4-7 2014.

[19] Condurache, D. and Burlacu, A., "On board exact solution to the full body relative orbital motion problem," in *AIAA/AAS Astrodynamics Specialist Conference*, (San Diego, CA), August 4-7 2014.

[20] Costic, B., Dawson, D., de Queiroz, M. S., and Kapila, V., "Quaternion-based adaptive attitude tracking controller without velocity measurements," *Journal of Guidance, Control, and Dynamics*, vol. 24, pp. 1214–2429, November-December 2001.

[21] Crassidis, J. L., Markley, F. L., and Cheng, Y., "Survey of nonlinear attitude estimation methods," *Journal of Guidance, Control, and Dynamics*, vol. 30, pp. 12–28, January-February 2007.

[22] Daniilidis, K., "Hand-eye calibration using dual quaternions," *The International Journal of Robotics Research*, vol. 18, pp. 286–298, March 1999.

[23] Delpech, M., Berges, J., S.Djalal, and J.Christy, "Vision based rendezvous experiment performed during the PRISMA extended mission," in *23rd*

International Symposium on Space Flight Dynamics, (Pasadena Convention Center), October 29 - November 2 2012.

[24] Dooley, J. and McCarthy, J., "Spatial rigid body dynamics using dual quaternion components," in *Proceedings of the 1991 IEEE International Conference on Robotics and Automation*, (Sacramento, California), pp. 90–95, April 1991.

[25] Durrant-Whyte, H., "Introduction to estimation and the Kalman filter," tech. rep., Australian Centre for Field Robotics, The University of Sydney, Australia, January 2 2001. Version 2.2.

[26] Fehse, W., *Automated Rendezvous and Docking of Spacecraft*. Cambridge Aerospace Series, Cambridge University Press, 2003.

[27] Filipe, N. and Tsiotras, P., "Adaptive model-independent tracking of rigid body position and attitude motion with mass and inertia matrix identification using dual quaternions," in *AIAA Guidance, Navigation, and Control Conference*, AIAA 2013-5173, (Boston, MA), August 19-22 2013.

[28] Filipe, N. and Tsiotras, P., "Rigid body motion tracking without linear and angular velocity feedback using dual quaternions," in *European Control Conference*, (Zürich, Switzerland), pp. 329–334, IEEE, Piscataway, NJ, July 17-19 2013.

[29] Filipe, N. and Tsiotras, P., "Simultaneous position and attitude control without linear and angular velocity feedback using dual quaternions," in *American Control Conference*, (Washington, DC), pp. 4815–4820, IEEE, Piscataway, NJ, June 17-19 2013.

[30] Filipe, N. and Tsiotras, P., "Adaptive position and attitude-tracking controller for satellite proximity operations using dual quaternions," *Journal of Guidance, Control, and Dynamics*, 2014. DOI: 10.2514/1.G000054.

[31] Filipe, N., Holzinger, M., and Tsiotras, P., "Pose-tracking controller for satellites with time-varying inertia," in *AIAA/AAS Astrodynamics Specialist Conference*, (San Diego, CA), August 4-7 2014.

[32] Filipe, N., Kontitsis, M., and Tsiotras, P., "An extended Kalman filter for spacecraft pose estimation using dual quaternions," in *American Control Conference*, (Chicago, Illinois), July 1-3 2015. (under review).

[33] Filipe, N., Kontitsis, M., and Tsiotras, P., "Extended Kalman filter for spacecraft pose estimation using dual quaternions," *Journal of Guidance, Navigation, and Dynamics*, 2015. (under review).

[34] Filipe, N. and Pritchett, A., "Applying problem-based learning to instruction of system dynamics and controls," in *American Control Conference*, (Portland, Oregon, USA), pp. 2530–2535, June 4-6 2014.

[35] Filipe, N. and Tsiotras, P., "Adaptive position and attitude tracking controller for satellite proximity operations using dual quaternions," in *AAS/AIAA Astrodynamics Specialist Conference*, AAS 13-858, (Hilton Head, South Carolina), pp. 2313–2332, August 11-15 2013.

[36] Filipe, N., Valverde, A., and Tsiotras, P., "Pose-tracking without linear and angular velocity feedback using dual quaternions," *IEEE Transactions on Aerospace and Electronic Systems*, 2015. (in preparation).

[37] Funda, J. and Paul, R., "A computational analysis of screw transformations in robotics," *IEEE Transactions on Robotics and Automation*, vol. 6, pp. 348–356, June 1990.

[38] Gan, D., Liao, Q., Wei, S., Dai, J., and Qiao, S., "Dual quaternion-based inverse kinematics of the general spatial 7R mechanics," *Proceedings of the Institution of Mechanical Engineers, Part C: Journal of Mechanical Engineering Science*, vol. 222, no. 8, pp. 1593–1598, 2008.

[39] Ge, Q. and Ravani, B., "Computer aided geometric design of motion interpolants," *Transactions of the ASME*, vol. 116, pp. 756–762, September 01 1994.

[40] Goddard, J. S., *Pose and Motion Estimation from Vision Using Dual Quaternion-based Extended Kalman Filtering*. PhD thesis, The University of Tennessee, Knoxville, 1997.

[41] Haddad, W. and Chellaboina, V., *Nonlinear Dynamical Systems and Control: A Lyapunov-Based Approach*. Princeton University Press, 2008.

[42] Hamilton, W., *Elements of Quaternions*. London: Longmans, Green, & Company, 1866.

[43] Han, D.-P., Wei, Q., and Li, Z.-X., "Kinematic control of free rigid bodies using dual quaternions," *International Journal of Automation and Computing*, vol. 5, pp. 319–324, July 2008.

[44] Han, D., Wei, Q., Li, Z., and Sun, W., "Control of oriented mechanical systems: A method based on dual quaternions," in *Proceeding of the 17th World Congress, The International Federation of Automatic Control*, (Seoul, Korea), pp. 3836–3841, International Federation of Automatic Control, Laxenburg, Austria, July 6–11 2008.

[45] Henshaw, C. G., Healy, L., and Roderick, S., "LIIVe: A small, lowcost autonomous inspection vehicle," in *AIAA SPACE 2009 Conference & Exposition*, AIAA 2009-6544, (Pasadena, California), 2009.

[46] Howard, R. T., Heaton, A. F., Pinson, R. M., and Carrington, C. K., "Orbital Express advanced video guidance sensor," in *2008 IEEE Aerospace Conference*, (Big Sky, MT), March 1-8 2008.

[47] Jung, D. and Tsiotras, P., "An experimental comparison of CMG steering control laws," in *AIAA/AAS Astrodynamics Specialist Conference and Exhibit*, AIAA Paper 04-5294, (Providence, RI), August 16-19 2004.

[48] Jung, D. and Tsiotras, P., "An experimental validation of spacecraft attitude and power tracking with variable speed control moment gyroscopes," in *AAS Spaceflight Mechanics Meeting*, AAS Paper 07-130, (Sedona, AZ), January 28 - February 1 2007.

[49] Kasai, T., Oda, M., and Suzuki, T., "Results of the ETS-7 mission - rendezvous docking and space robotics experiments," in *5th International Symposium on Artificial Intelligence, Robotics and Automation in Space*, pp. 299–306, June 1-3 1999.

[50] Kim, S.-G., Crassidis, J. L., Cheng, Y., Fosbury, A., and Junkins, J. L., "Kalman filtering for relative spacecraft attitude and position estimation," *Journal of Guidance, Control, and Dynamics*, vol. 30, pp. 133–143, January-February 2007.

[51] Kristiansen, R. and Nicklasson, P. J., "Spacecraft formation flying: A review and new results on state feedback control," *Acta Astronautica*, vol. 65, pp. 1537–1552, December 2009.

[52] Kristiansen, R., Nicklasson, P. J., and Gravdahl, J. T., "Spacecraft coordination control in 6DOF: Integrator backstepping vs passivity-based control," *Automatica*, vol. 44, pp. 2896–2901, November 2008.

[53] Krolikowski, A. and David, E., "Commercial on-orbit satellite servicing: National and international policy considerations raised by industry proposals," *New Space*, vol. 1, pp. 29–41, March 2013.

[54] Lee, T., Leok, M., and McClamroch, N. H., "Geometric tracking control of a quadrotor UAV on SE(3)," in *49th IEEE Conference on Decision and Control*, (Atlanta, GA, USA), pp. 5420–5425, December 15-17 2010.

[55] Lee, U. and Mesbahi, M., "Dual quaternions, rigid body mechanics, and powered-descent guidance," in *51st IEEE Conference on Decision and Control*, (Maui, Hawaii, USA), pp. 3386–3391, December 10-13 2012.

[56] Lee, U. and Mesbahi, M., "Dual quaternion based spacecraft rendezvous with rotationally and translationally constrained field of view constraints," in *AIAA/AAS Astrodynamics Specialist Conference*, (San Diego, CA), August 4-7 2014.

[57] Lefferts, E., Markley, F., and Shuster, M., "Kalman filtering for spacecraft attitude estimation," *Journal of Guidance, Control, and Dynamics*, vol. 5, pp. 417–429, September-October 1982.

[58] Lewis, F. L., Tim, W. K., Wang, L.-Z., and Li, Z. X., "Deadzone compensation in motion control systems using adaptive fuzzy logic control," *IEEE Transactions on Control Systems Technology*, vol. 7, pp. 731–742, November 1999.

[59] Lewis, F. L., *Optimal Estimation*, ch. 3.7 Discrete Measurements of Continuous-Time Systems, pp. 185–191. USA: John Wiley & Sons, Inc., 1986.

[60] Lizarralde, F. and Wen, J. T., "Attitude control without angular velocity measurement: A passivity approach," *IEEE Transactions on Automatic Control*, vol. 41, pp. 468–472, March 1996.

[61] Maithripala, D. H. S., Berg, J. M., and Dayawansa, W. P., "Almost-global tracking of simple mechanical systems on a general class of Lie groups," *IEEE Transactions on Automatic Control*, vol. 51, pp. 216–225, January 2006.

[62] Markley, F. L., "Attitude error representations for Kalman filtering," *Journal of Guidance, Control, and Dynamics*, vol. 26, pp. 311–317, March-April 2003.

[63] Mayhew, C. G., Sanfelice, R. G., and Teel, A. R., "Robust global asymptotic attitude stabilization of a rigid body by quaternion-based hybrid feedback," in *Joint 48th IEEE Conference on Decision and Control and 28th Chinese Control Conference*, (Shanghai, P.R. China), pp. 2522–2527, December 16-18 2009.

[64] McCauley, J., *Classical Mechanics: Transformations, Flows, Integrable and Chaotic Dynamics*. Cambridge University Press, 1997.

[65] Meirovitch, L., *Methods of Analytical Dynamics*. Advanced Engineering Series, McGraw-Hill Book Company, 1970.

[66] Misra, G. and Sanyal, A., "Analysis of orbit-attitude coupling of spacecraft near small solar system bodies," in *AIAA Guidance, Navigation, and Control Conference*, (Kissimmee, Florida), January 5-9 2015.

[67] Miwa, H. and Akella, M. R., "Global adaptive stabilization using output feedback for spacecraft attitude tracking," in *Spaceflight Mechanics 2002: Proceedings of the AAS/AIAA Space Flight Mechanics Meeting*, (San Antonio, Texas, USA), pp. 345–357, January 27-30 2002.

[68] Mourikis, A. I., Trawny, N., Roumeliotis, S. I., Johnson, A. E., Ansar, A., and Matthies, L., "Vision-aided inertial navigation for spacecraft entry, descent, and landing," *IEEE Transactions on Robotics*, vol. 25, pp. 264–280, April 2009.

[69] Murray, R. M., Li, Z., and Sastry, S. S., *A Mathematical Introduction to Robotic Manipulation*. CRC Press, 1994.

[70] NASA, "Overview of the DART mission mishap investigation results - for public release," tech. rep., May 15 2006.

[71] Obermark, J., Creamer, G., Kelm, B. E., Wagner, W., and Henshaw, C. G., "SUMO/FREND: vision system for autonomous satellite grapple," in *SPIE Proceedings*, vol. 6555, pp. 65550Y 1–11, 2007.

[72] Oda, M., "ETS-VII: Achievements, troubles and future," in *Proceedings of the 6th International Symposium on Artificial Intelligence and Robotics & Automation in Space (i-SAIRAS)*, (St.-Hubert, Quebec, Canada), Canadian Space Agency, June 18-22 2001.

[73] Pan, H. and Kapila, V., "Adaptive nonlinear control for spacecraft formation flying with coupled translational and attitude dynamics," in *Proceedings of the 40th IEEE Conference on Decision and Control*, (Orlando, Florida USA), pp. 2057–2062, December 2001.

[74] Perez, A. and McCarthy, J., "Dual quaternion synthesis of constrained robotic systems," *Journal of Mechanical Design*, vol. 126, pp. 425–435, September 2004.

[75] Pham, H.-L., Perdereau, V., Adorno, B. V., and Fraisse, P., "Position and orientation control of robot manipulators using dual quaternion feedback," in *IEEE/RSJ International Conference on Intelligent Robost and Systems*, (Taipei, Taiwan), pp. 658–663, October 18–22 2010.

[76] Rao, A., *Dynamics of Particles And Rigid Bodies: A Systematic Approach*. Cambridge University Press, 2006.

[77] Romano, M., Friedman, D. A., and Shay, T. J., "Laboratory experimentation of autonomous spacecraft approach and docking to a collaborative target," *Journal of Spacecraft and Rockets*, vol. 44, pp. 164–173, January-February 2007.

[78] Schaub, H. and Junkins, J., *Analytical Mechanics of Space Systems*. Education Series, American Institute of Aeronautics & Astronautics, 2003.

[79] Seo, D. and Akella, "High-performance spacecraft adaptive attitude-tracking control through attracting-manifold design," *Journal of Guidance, Control, and Dynamics*, vol. 31, pp. 884–891, July-August 2008.

[80] Seo, D. and Akella, M. R., "Separation property for the rigid-body attitude tracking control problem," *Journal of Guidance, Control, and Dynamics*, vol. 30, pp. 1569–1576, November-December 2007.

[81] Sinclair, A., Sherrill, R., and Lovell, T., "Review of the solutions to the Tschauner-Hempel equations for satellite relative motion," in *AAS/AIAA Space Flight Mechanics Meeting*, AAS 12-149, (Charleston, South Carolina), 29 January - 2 February 2012.

[82] Singla, P., Subbarao, K., and Junkins, J. L., "Adaptive output feedback control for spacecraft rendezvous and docking under measurement uncertainty," *Journal of Guidance, Control, and Dynamics*, vol. 29, pp. 892–902, July-August 2006.

[83] Slotine, J.-J. E. and Li, W., *Applied Nonlinear Control*, p. 366. Prentice Hall, 1991.

[84] Strange, N., Landau, D., McElrath, T., Lantoine, G., Lam, T., McGuire, M., Burke, L., Martini, M., and Dankanich, J., "Overview of mission design for NASA asteroid redirect robotic mission concept," in *33rd International Electric Propulsion Conference*, no. IEPC-2013-321, (Washington, D.C., USA), October 6-10 2013.

[85] Tanygin, S., "Generalization of adaptive attitude tracking," in *AIAA/AAS Astrodynamics Specialist Conference and Exhibit*, AIAA 2002-4833, (Monterey, California), August 5-8 2002.

[86] Thienel, J. K., Luquette, R. J., and Sanner, R. M., "Estimation of spacecraft inertia parameters," in *AIAA Guidance, Navigation and Control Conference and Exhibit*, AIAA 2008-6454, (Honolulu, Hawaii), August 18-21 2008.

[87] Tsiotras, P., "ASTROS: A 5DOF experimental facility for research in space proximity operations," in *AAS Guidance and Control Conference*, no. 2014-114, (Breckenridge, CO), January 31 - February 5 2014.

[88] Tweddle, B. E., Muggler, E., Saenz-Otero, A., and Miller, D. W., "The SPHERES VERTIGO goggles: Vision based mapping and location onboard the International Space Station," in *International Symposium on Artificial Intelligence, Robotics and Automation in Space*, (Turin, Italy), September 4-6 2012.

[89] Tweddle, B. E., "Computer vision based navigation for spacecraft proximity operations," Master's thesis, Massachusetts Institute of Technology, January 29 2010.

[90] U.S. Department of Defense, *Dictionary of Military Terms and Acronyms*. Praetorian Press, LLC, 2011.

[91] Vallado, D. and McClain, W., *Fundamentals of Astrodynamics and Applications*. Space Technology Library, Springer, third ed., 2007.

[92] Vallado, D. and McClain, W., *Fundamentals of Astrodynamics and Applications*, pp. 707–711 and 990. Space Technology Library, Springer, third ed., 2007.

[93] Wang, J. and Sun, Z., "6–DOF robust adaptive terminal sliding mode control for spacecraft formation flying," *Acta Astronautica*, vol. 73, pp. 676–87, April-May 2012.

[94] Wang, X., Han, D., Yu, C., and Zheng, Z., "The geometric structure of unit dual quaternion with application in kinematic control," *Journal of Mathematical Analysis and Applications*, vol. 389, pp. 1352–1364, 15 May 2012.

[95] Wang, X. and Yu, C., "Feedback linearization regulator with coupled attitude and translation dynamics based on unit dual quaternion," in *2010 IEEE International Symposium on Intelligent Control, Part of 2010 IEEE Multi-Conference on Systems and Control*, (Yohohama, Japan), pp. 2380–2384, September 8–10 2010.

[96] Wang, X. and Yu, C., "Unit dual quaternion-based feedback linearization tracking problem for attitude and position dynamics," *Systems & Control Letters*, vol. 62, pp. 225–233, March 2013.

[97] Wang, X., Yu, C., and Lin, Z., "A dual quaternion solution to attitude and position control for rigid-body coordination," *IEEE Transactions on Robotics*, vol. 28, pp. 1162–1170, October 2012.

[98] Weiss, A., Kolmanovsky, I., Baldwin, M., and Erwin, R., "Model predictive control of three dimensional spacecraft relative motion," in *American Control Conference 2012*, pp. 173 – 178, 27-29 June 2012.

[99] Weiss, A., Kolmanovsky, I., Baldwin, M., Erwin, R. S., and Bernstein, D. S., "Forward-integration Riccati-based feedback control for spacecraft rendezvous maneuvers on elliptic orbits," in *51st IEEE Conference on Decision and Control*, (Maui, Hawaii, USA), December 10-13 2012.

[100] Wen, J. T.-Y. and Kreutz-Delgado, K., "The attitude control problem," *IEEE Transactions on Automatic Control*, vol. 36, pp. 1148–1162, October 1991.

[101] Wie, B., *Space Vehicle Dynamics and Control*. AIAA Education Series, American Institute of Aeronautics and Astronautics, 1998.

[102] Wie, B., "Singularity escape/avoidance steering logic for control moment gyro systems," *Journal of Guidance, Control, and Dynamics*, vol. 28, pp. 948–956, September-October 2005.

[103] Wie, B. and Barba, P. M., "Quaternion feedback for spacecraft large angle maneuvers," *Journal of Guidance*, vol. 8, pp. 360–365, May-June 1985.

[104] Wong, H., Pan, H., and Kapila, V., "Output feedback control for spacecraft formation flying with coupled translation and attitude dynamics," in *Proceedings of the 2005 American Control Conference*, (Portland, OR, USA), pp. 2419–2426, June 8-10 2005. vol. 4.

[105] Wu, Y., Hu, X., Hu, D., Li, T., and Lian, J., "Strapdown inertial navigation system algorithms based on dual quaternions," *IEEE Transactions on Aerospace and Electronic Systems*, vol. 41, pp. 110–132, January 2005.

[106] Yang, A., *Basic Questions of Design Theory*, vol. 265, ch. Calculus of Screws, pp. 266–281. North-Holland, Amsterdam: W. R. Spillers, 1974.

[107] Yoon, H. and Tsiotras, P., "Spacecraft adaptive attitude and power tracking with variable speed control moment gyroscopes," *Journal of Guidance, Navigation, and Dynamics*, vol. 25, pp. 1081–1090, November-December 2002.

[108] Yoon, H. and Tsiotras, P., "Singularity analysis of variable-speed control moment gyros," *Journal of Guidance, Control, and Dynamics*, vol. 27, pp. 374–386, May-June 2004.

[109] Zanetti, R., Majji, M., Bishop, R. H., and Mortari, D., "Norm-constrained Kalman filtering," *Journal of Guidance, Control, and Dynamics*, vol. 32, pp. 1458–1465, September-October 2009.

[110] Zhang, G., Kontitsis, M., Filipe, N., Tsiotras, P., and Vela, P., "Cooperative relative navigation for space rendezvous and proximity operations using controlled active vision," *Journal of Field Robotics*, 2015. (under review).

[111] Zhang, G., Vela, P. A., Tsiotras, P., and Cho, D.-M., "Efficient closed-loop detection and pose estimation for vision-only relative localization in space with a cooperative target," in *AIAA Space 2014 Conference and Exposition*, no. AIAA 2014-4262, (San Diego, CA), August 4-7 2014.

[112] Zu, Y., Lee, U., and Dai, R., "Distributed motion estimation of space objects using dual quaternions," in *AIAA/AAS Astrodynamics Specialist Conference*, no. 2014-4296, (San Diego, CA), August 4-7 2014.

VITA

Nuno Filipe received a B.Sc. in Aerospace Engineering from the Instituto Superior Técnico, Portugal, in 2007 and a M.Sc. with honors in Aerospace Engineering from the Delft University of Technology, The Netherlands, in 2008. From April 2008 to July 2010 he worked for the Control Systems Division of the European Space Agency in The Netherlands. Since August 2010, he has been pursuing a Ph.D. in Aerospace Engineering at the Georgia Institute of Technology. His research interests are guidance, navigation, and control of space systems, nonlinear control and estimation, and modeling and simulation of dynamic systems.